Metallogenic controls of mantle plumes on platinum-group elements and precious metals

Jordan James Lindsay

Camborne School of Mines

College of Engineering, Mathematics and Physical Sciences

University of Exeter

March 2021

. . . . . .

For Mum, Dad and Amy

Abstract

Platinum-group elements (PGE) are important precious metals and critical raw materials, but are some of the rarest metals in the Earth's crust. The PGE are chalcophile elements and their distribution is largely controlled by the behaviour of sulphur (as sulphide) in magmatic environments. Mineralisation of PGE is most likely to occur in mafic and ultramafic intrusive systems and these share an inherent link with intraplate basaltic lavas produced by partial melting of the mantle, particularly associated with mantle plume thermal anomalies.

In this thesis, new whole-rock geochemical data from a range of basaltic lavas from geologically-recent intraplate (i.e., mantle plume-related) settings are presented with a particular emphasis on examining chalcophile elements such as Ni, Cu, Co, Au and particularly, the PGE. Much of these data represent the first complete suites of major and trace elements, including PGE and Au analyses for key regions, such as Paraná, Etendeka, and Tenerife. The relationship between the PGE compositions of intraplate magmas and the mantle plumes responsible for their generation is interrogated using the combined application of quantitative geochemical melt modelling and a novel machine learning workflow, created for this project and featuring the PCA, t-SNE and *k*-means clustering techniques.

Variations in melting processes due to different geodynamic conditions for each mantle plume studied dominates the controls on PGE abundances in magmas and thus lavas, as revealed by a quantitative account of partial melting of sulphide and silicate minerals in the mantle. In settings with deep, low degree partial melts (e.g., Canary Islands and Hawaii) chalcophile behaviour inhibits substantial source liberation from residual mantle sulphides. In settings with shallower, higher degree partial melts (e.g., Iceland and Kerguelen), chalcophiles are easily liberated from mantle sulphides. The most strongly PGE-enriched intraplate lavas are located at the edges of continents (e.g., East Paraná and East Greenland), where the incorporation of metasomatised sub-continental lithospheric mantle boosts the PGE budgets of parental magmas, leading to variation in the metal basket of lavas (e.g., changing Pd and Pt ratio). The geochemical and machine learning approach developed in the thesis describes this scenario as the optimal target for ore body formation within the context of a global intraplate PGE Mineral Systems model.

Acknowledgements

It is a daunting task to thank everyone who has had an impact on the last four years of my life and, crucially, the creation of this thesis, but I shall try my very best! I would firstly like to thank the University of Exeter for funding my PhD via the Vice-Chancellor Scholarship, which provided me with an exceptionally flexible approach to research and allowed me to drive the project independently.

A huge expression of gratitude must go to Camborne School of Mines and all within it. Whilst not related to my project, James, Sam H, Robin, Frances, Kate, Sam B-F, Paul, Laura, Benny, Malcolm, Sharon, Gavyn, Callum, Pat, Peter, Ben and Steve have made the past four years hugely enjoyable and I will miss this small but important research community at the seaside! The only person with two acknowledgements, Chris Y, has effectively stepped in as a fourth supervisor in this project and I cannot thank him enough for helping me find my niche within the machine learning and geochemistry worlds. Iain provided a piece of home whenever we met up, as two Glaswegians in southern UK – he is always supportive, switched-on and hilarious to work with. Jens stuck out to me as a lecturer during my MSc and it was an absolute privilege to have someone as knowledgeable and approachable as him as a supervisor. I will never forget our incredible trip to Brazil in my second year - a PhD highlight!

I probably would not have reached the end of this project intact without my fantastic friends, both at home and in Cornwall. Ross, Fiona, Nick and Jon have been my biggest supporters throughout this, at times, very tough journey and have truly made me strive to do my best even though I could only see them a few times a year. This also extends to Sarah, Ewan, Rory, Stuart, Claire, Julie, Sam, Dyer, Chelsea, and Aaron, for always being there for me. At times, living so far from home was difficult, but it was made immeasurably better by the wonderful friends I have made whilst in the south-west - Charlie, Charlotte, Chris Y, Rob, Laurens, Matt, Jess, Tess, Kez, Sam, Bex, Robyn, Doug, Sophie, Carlo, Fei, Abraham, Jane, Dickie, Chris E, Keiran, Violeta, Chris D, Teuntje, Alex, Jon, Katie, Nick, Matt, Richard and Scott. Thanks also to geo-friends across the world – Chris H, Alan, Marcell, Otavio, Edir, Katie, Laura and Will. And to Penny, Marie, Bob, Saemi, and Holger for contributing rock samples from their travels.

I also must thank my family, who have encouraged me to pursue my own path from the very start. Gran, Papa and Auntie for weekly motivating catch-ups. Amy, for always being straight-talking, practical and a best friend when I need it most. Dad, for always taking the utmost interest in what I am doing, and for guiding me through all of life's challenges. Mum, for being an all-round wee angel.

My final thanks go to Hannah, of course. I feel blessed to have had such an enthusiastic, helpful, funny and tough primary supervisor – there is no one better to have on your side if things go wrong *or* right! She constantly motivated me to become the best researcher I could, and into the bargain, I feel that I have made a lifelong friend who can drink me/anyone under the table if necessary.

List of Contents

List of Figures

List of Tables

List of Supplementary Material

Appendices

Digital Supplementary Files

Digital files have been supplied in suitable formats in a zipped folder as part of this submission.

Supplementary 1 (Sample database)

S1.1 Fieldwork sample acquisition database with sample nomenclature, hand specimen descriptions, locations and physical characteristics. Also includes lab-book for in-house analysis.

Supplementary 2 (Master geochemical database)

S2.1 Compiled (anhydrous) major, trace and PGE bulk geochemical data for all samples analysed throughout this study (introduced and interpreted separately in Chapters 3, 4, 6 and 7), classified by locality. Original analytical data files with standard and blank information also included.

Supplementary 3 (Chapter 3)

S3.1 Sample Database for Paraná.

S3.2 Literature Database for comparison plots for Paraná.

S3.3 Raw bulk geochemical data (XRF, ICP-MS, NiS Fire Assay) for Paraná.

S3.4 Full amalgamated data sheet used in analysis for Paraná.

S3.5 Modelling worksheets using mass balance equations for Paraná.

Supplementary 4 (Chapter 4)

S4.1 Sample hand-descriptions for Tenerife

S4.2 Raw bulk geochemical data (XRF, ICP-MS, NiS Fire Assay) for Tenerife, Kilauea and Iceland.

S4.3 Full amalgamated data sheet used in analysis (with literature data) for Tenerife, Kilauea and Iceland.

S4.4 Modelling worksheets using mass balance equations for Tenerife.

Supplementary 5 (Chapter 5)

S5.1 Master bulk geochemical data sheet for all NAIP literature (Hughes et al., 2015).

S5.2 Python code in Jupyter notebook files for PCA, t-SNE and *k*-means workflows.

S5.3 Principal Component Analysis eigenvalues & scaled co-ordinates.

S5.4 Master PCA, t-SNE and *k*-means data applied to NAIP geochemistry.

Supplementary 6 (Chapter 6)

S6.1 Raw bulk geochemical data (XRF, ICP-MS, NiS Fire Assay).

S6.2 Sample database for PELIP.

S6.3 Python code in Jupyter notebook files for PCA, t-SNE and *k*-means workflows for PELIP.

S6.4 Master PCA, t-SNE and *k*-means data applied to PELIP geochemistry (amalgamated from S6.1).

Supplementary 7 (Chapter 7)

S7.1 Raw bulk geochemical data (XRF, ICP-MS, NiS Fire Assay).

S7.2 Oceanic MLA database.

S7.3 Transitional MLA database.

S7.4 Continental and oceanic MLA database.

S7.5 Python code in Jupyter notebook files for PCA, t-SNE, UMAP and *k*-means workflows for each of the three data sets.

List of Abbreviations and Acronyms

Geochemistry/Geology

AFC	assimilation and fractional crystallisation
BMS	base metal sulphide (minerals)
C_0	starting compositions of a mantle source (in modelling)
CFB	continental flood basalt(s)
CLIP	continental large igneous province(s)
CMB	core-mantle boundary
D^x_y	partition coefficient of a given element (y) between two phases (x)
DMM	Depleted MORB Mantle component
EMI/EMII	Enriched Mantle I and II mantle components
F	Degree of partial melting
FC	fractional crystallisation
FOZO	Focus-Zone mantle component
HIMU	high-μ (i.e. high-Pb) mantle component
HSE	highly siderophile element(s)
IPGE	iridium-group PGE
LIP	Large Igneous Province(s)
LLSVP	Large Low Shear Velocity Province(s)
MORB	Mid-Ocean Ridge Basalt (magma type)
N-MORB	Normal MORB
MSE	moderately siderophile element(s)
Mss	monosulphide solution (*acronym not all-capitalised*)
OIB	Ocean Island Basalt (magma type)
OLIP	oceanic large igneous province(s)

PGE	platinum-group element(s)
PGM	platinum-group mineral(s)
PPGE	palladium-group PGE
REE	rare earth element(s) (LREE – light; HREE- heavy)
SSE	slightly siderophile element(s)
TAS	total alkali (Na_2O+K_2O) vs. silica (SiO_2) plot

Locations

BPIP	British Palaeogene Igneous Province
DPSD	Deep Sea Drilling Project
IODP	Integrated Ocean Drilling Program
NAIP	North Atlantic Igneous Province
PELIP	Paraná-Etendeka Large Igneous Province

Data science and machine learning

DBI	Davies-Bouldin Index
k	number of clusters in the *k*-means clustering algorithm
MLA	machine learning algorithm(s)
PCA	Principal Component Analysis
(PCs)	Principal Components (of variability)
t-SNE	t-Distributed Stochastic Neighbour Embedding

Lab techniques

ICP-MS	inductively-coupled plasma mass spectrometry/spectrometer
XRF	X-ray fluorescence

Author's Declaration

All content within this thesis has been planned, prepared, written, collated and presented by the candidate, Jordan James Lindsay. Lab work, data analysis, figure generation and interpretations were conducted exclusively by the candidate under supervision of the three project supervisors. All five research chapters have been constructed as both thesis chapters and journal articles, as described in Section 1.3, and as such, co-authors for each publication, accepted or otherwise, have contributed as detailed below.

Chapter 3 received draft edits from Hannah Hughes, Jens Andersen, Iain McDonald, Marcell Besser, Otavio Licht, Edir Arioli, Alan Hastie and Chris Hawkesworth following full preparation by the candidate. In addition, the modelling spreadsheet used for melt calculations was created with Alan Hastie. Samples were gathered by the candidate, Jens Andersen and Edir Arioli.

Chapter 4 received draft edits from Hannah Hughes, Jens Andersen, Iain McDonald and Alan Hastie following full preparation by the candidate. The modelling spreadsheet initially created for Chapter 3 alongside Alan Hastie was also used in this study. Samples were gathered by the candidate.

Chapter 5 (now published) received draft edits from Hannah Hughes, Chris Yeomans, Jens Andersen and Iain McDonald, plus three anonymous reviewers with the *Geoscience Frontiers* journal following full preparation by the candidate. The machine learning workflow was developed by the candidate and Chris Yeomans. Data taken from Hughes et al. (2015).

Chapter 6 (accepted for publishing) received draft edits from Hannah Hughes, Chris Yeomans, Jens Andersen, Iain McDonald and Chris Hawkesworth, plus two anonymous reviewers with *Earth Science, Systems and Society* following full preparation by the candidate. Samples were gathered primarily by the candidate, with supplementary samples supplied by Bob Trumbull (Potsdam University), Penny Weiser (University of Cambridge) and Sæmundur Ari Halldórsson (Nordvulk).

Chapter 7 received draft edits from Hannah Hughes, Chris Yeomans, Jens Andersen, Iain McDonald and Chris Hawkesworth following preparation by the candidate. All data is from prior chapters of this thesis or taken from literature.

Chapter 1

Thesis Introduction

1.1. Motivation – platinum-group elements as resources

Osmium (Os), iridium (Ir), ruthenium (Ru), rhodium (Rh), platinum (Pt) and palladium (Pd), known collectively as the platinum-group element(s) (PGE), are amongst the rarest and most valuable metals on the planet (Gunn et al., 2009). They are often considered together in economic, geological and chemical terms given their general association in nature, which sees them concentrated together in similar ore deposits and settings, often within the same mineral hosts (Barnes et al., 1985; Fleet et al., 1999; Holwell and McDonald, 2010; Lorand et al., 2013; Driscoll, 2016; Birke et al., 2017; Fernandez, 2017). In detail, their individual atomic properties differentiate their behaviour in Earth systems and their utilities in material science, but for decades, research has focused on studying the group as a whole. Perhaps the most defining feature of the PGE, when considering the non-radioactive elements of the periodic table, is their exceedingly sparse abundances on Earth's surface compared to primitive cosmic material (McDonough and Sun, 1995), with all six rarely found in concentrations of over a few parts per billion (ppb) each in crustal rocks. Unlike industrial metals like iron and aluminium, which are used in a host of applications and are amongst the most abundant elements in the Earth's crust, the PGE are both scarce and in demand in modern society.

The PGE, which are regarded as precious metals alongside Au and Ag, are often co-produced in mining operations due to their geological association, and are also sold as by-products in larger Ni, Cu, Co, Cr and Au production (Gunn et al., 2009). The main use of PGE is as catalysts within the petrochemical industry and particularly as auto-catalysts in catalytic convertors in car exhaust systems; the latter application will be slowly reduced in coming years, as we work towards achieving net-zero carbon emissions by 2030 (European Commission 2020a; BGS 2015). The utility of the PGE has also expanded beyond these two more traditional uses alongside technological advances in a variety of sectors.

Electronics, LED screens, magnet technology, high-tech alloys, data storage, medicine and modern dentistry all require PGE in increasing amounts (Gunn et al., 2009; BGS, 2015; Zientek et al., 2017; European Commission 2020a, 2020b). As world economies move away from a reliance on fossil fuels as energy sources, the PGE are more in demand now than ever before. In particular, hydrogen fuel cells in transport and energy storage, for which an ounce of Pt is required per cell (BGS, 2015), presents the biggest potential demands on the metals in the future (FCH, 2017; Zientek et al., 2017; FCHEA, 2018). Although PGE are suitable for recycling and retain much of their chemical utility following their reuse, the current stock of these metals simply cannot satisfy the rising demand (WPIC, 2020). The fine balance between supply and demand of each PGE has resulted in highly variable trading prices of the metals throughout the last decade (with an overall increase with time), and recently prices have recorded some of the highest historical values for Ir, Rh and Pd (Figure 1.1 and Table 1.1).

Rhodium in particular has seen an almost five-fold increase in price in the last two to three years alone, and is a key component in cutting-edge single-cell photocatalysis, which can create sustainable hydrogen reserves for use in renewable energy (Li and Nguyen, 2018; Peplow, 2020; Whittemore et al., 2020). As new research on fuel cell technology arises, the relative demand for each of the PGE fluctuates depending on which of the group is favoured in the newest, most efficient decarbonisation breakthroughs and which are affected by policy changes restricting the production of catalytic convertors. Much like Cu, the price of which can vary significantly depending of sensitive economic and industrial growth factors worldwide (i.e., if countries are building infrastructure or not), the PGE are intrinsically supply-and-demand driven (Mudd et al., 2018). Their current demand reflects both the remaining use in catalytic convertors and recent advancements in technology, and particularly their prevalence within the collective pursuit of carbon net-zero goals.

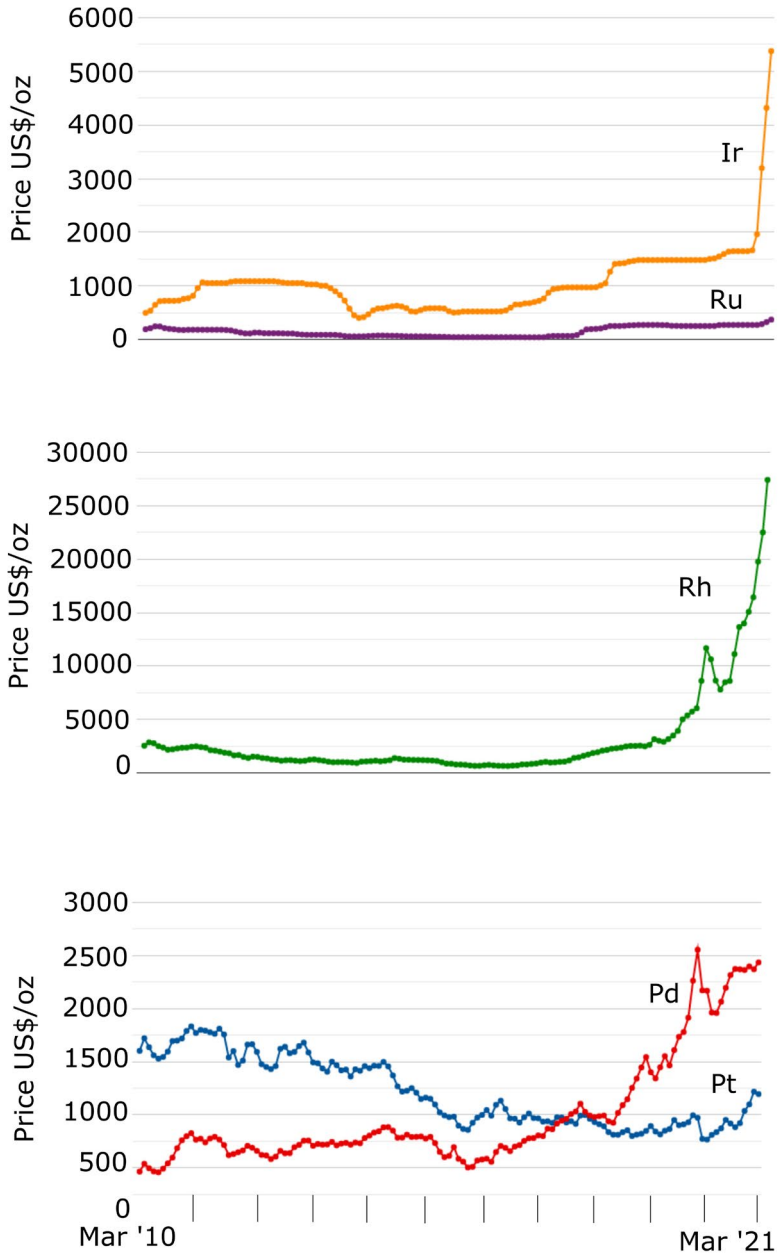

Figure 1.1 *– Plot of monthly prices (March 22nd 2021) in US$/oz. of Ir, Rh, Ru, Pt and Pd from March 2010 to March 2021. Prices from Johnson Matthey, 2021.*

Table 1.1 *– Current prices (March 22nd 2021) for five of the six PGE in US$ per troy oz. Osmium is frequently traded together with other PGE and is rarely priced on its own. Prices from Johnson Matthey, 2021.*

Metal	Ir	Ru	Rh	Pt	Pd
US$/oz	6,000	390	29,600	1,175	2,604

The PGE are concentrated into ore bodies via a series of geological mechanisms – chiefly via magmatic differentiation, but also precipitation from hydrothermal fluids and as placer deposits in river flow channels (Barnes and Picard, 1993; Gunn et al., 2009a; Naldrett, 2010; Barnes et al., 2016). Mineralised ore bodies bearing significant PGE resources (see Section 2.5) are inextricably linked to continental intraplate magmatism (e.g., Andersen et al., 2002; Momme et al., 2002; Zhang et al., 2008; Li et al., 2009; Day, 2013; Hughes et al., 2015), which in turn is associated with mantle plumes. Mantle plumes are thermal anomalies from deep in the Earth, and in some cases, they may transport hot material from the lower mantle to the asthenosphere, where they then induce partial melting and magma generation (see Section 2.2). Research into understanding metallogenesis of the PGE (i.e., the distribution and concentration of PGE via geological processes) has increasingly been a focus in the geoscience community (e.g., Maier et al., 2003a; Maier and Groves, 2011; Hughes, 2015 and references therein) in an effort to provide new insights into these critical metals in our pursuit of a 'net-zero' world (FCH, 2017).

The overwhelming majority of PGE mining operations are located in South Africa and Russia, with significant production also located in Canada, Zimbabwe and the USA (Cawthorn, 1999; Thormann et al., 2017; Mudd et al., 2018). Despite historically supplying over 80 % of global reserves, both South Africa and Russia have come under scrutiny due to common issues surrounding security of supply and socioeconomic pressure on various aspects of the production chain in each country (Mudd et al., 2018). This places PGE in the situation that their supply is not limited by geological depletion but social, economic and environmental factors instead. The risk involved with over-reliance on South African and Russian sources for the increasingly critical PGE has sparked an interest in exploring alternative resources. This has included re-visiting brownfield mining sites (i.e., previously mined for PGE or other metals), reprocessing mine tailings and exploring new environments hospitable to undiscovered PGE mineralisation worldwide (BGS, 2015; European Commission, 2020b). The pursuit of understanding and subsequently locating PGE mineralisation is supported by crucial academic research into the geochemical characteristics of PGE enrichment at surface (see Section 2.1), the identification of precious metal sources in the Earth system (see Section 2.3) and the origin of known PGE ore

bodies (see Section 2.5). This thesis contributes to the discussion surrounding the source-driven factors in global PGE distribution (i.e., how these metals can be brought to the crust from the Earth's interior), building on current literature (Chapter 2) to present five case studies in Chapters 3 through 7.

In addition to the more economic-driven motivations for studying PGE enrichment, the connection to magmatic systems brings any investigation involving these metals into contact with studies of the Earth's interior. The continental crust can be directly observed at surface to provide a wealth of *in situ* information on their petrological development; we may only use magmatic rocks to model and calculate the conditions of the mantle in combination with geophysical surveys. Geochemists use the compositions of lavas representing melts derived from the mantle to back-calculate to inferred mantle compositions and processes, and also use the more empirical approach of analysing mantle rocks and minerals (i.e., xenoliths and diamonds) to provide direct interpretations of the deep Earth. Such studies have received more than a century's worth of research, yet there remain innumerable questions regarding the nature of the mantle, which is the largest (by volume) sector of our planet. The research presented in this thesis ultimately contributes to the building of PGE geochemical databases to explore key processes in operation in the Earth's mantle, particularly in relation to mantle plumes.

1.2. Research aim, objectives and hypotheses

The overall aim of this thesis is to investigate the range and distribution of PGE abundances and geochemistry for basaltic lavas derived from a selection of recent (and/or active) mantle plumes around the world, in order to establish if different plumes have characteristic PGE signatures. Lavas represent the liquid composition of melts generated from the mantle and their bulk geochemistry can help indicate the conditions in each locality and how these affect metal contents. The mantle is a highly heterogeneous and dynamic region of the Earth that records billions of years of geochemical and geophysical processes as the planet slowly progressed to its present day state. The connection between PGE ore bodies, intraplate magmatism and mantle plumes drives the bulk of this thesis.

Many of the ideas presented in this introduction can be illustrated by Figure 1.2, which serves as a precursor to the detailed literature review contained within Chapter 2. The intricacies of intraplate magmatism described in this diagram are examined in each of the research chapters, and include:

- The incorporation of a variety of materials at plume origin (annotation 1), as covered in Chapters 4 and 7.
- The interaction between plumes and potential near-surface PGE reservoirs (annotation 2), as covered in Chapters 3, 5 and 6.
- The variability in intraplate magmas in different locations (annotation 3), as covered in Chapters 3, 4, 5, 6 and 7.
- The balance of upwards and downwards flow in the mantle (annotation 4), covered in Chapters 3, 4 and 7.

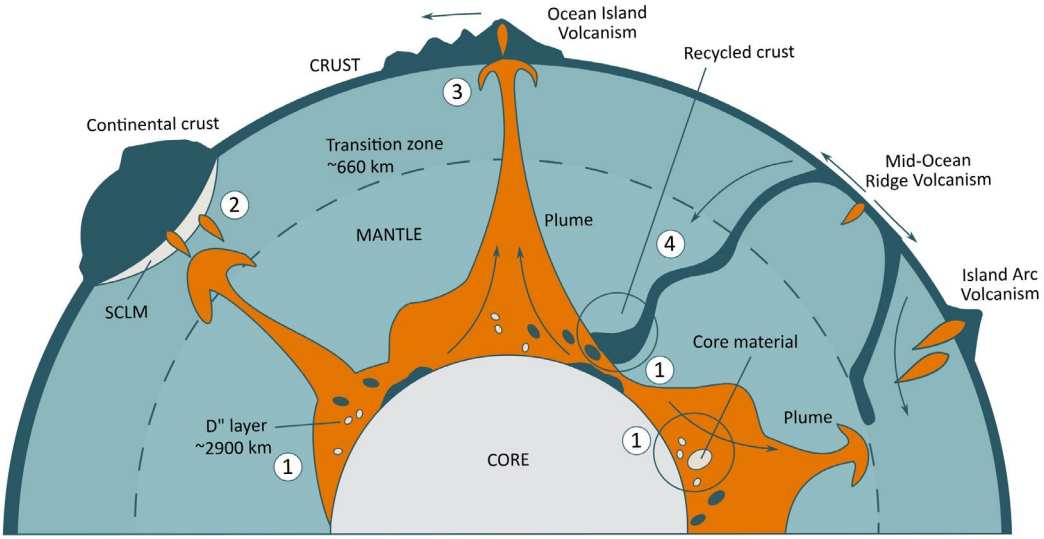

Figure 1.2 *– Schematic cross-section of the Earth, detailing some major concepts explored in this thesis. (1) – The heterogeneous core-mantle boundary (i.e., the D" layer) which influences the geochemistry of deep-origin magmas. (2) – The sub-continental lithospheric mantle (SCLM), a potential asthenospheric reservoir of precious metals for continental intraplate magmas due to prolonged metasomatic enrichment. (3) – Ocean island basalts, the surface expression of oceanic intraplate magmas. (4) – Recycled oceanic lithosphere, which can be incorporated into the D" layer. This thesis examines the relative effects these features play on magmatic PGE metallogenesis.*

The following testable hypotheses, referred to in the thesis as "H1", "H2" and "H3", are investigated in the research chapters of the thesis:

1. Magmas (and thus lavas) from oceanic plume settings have distinct PGE signatures related to their geophysical properties ***[H1]***.
2. PGE enrichment in intraplate magmas is caused by incorporation of continental lithospheric material (including metals) of transitional continent-ocean plume systems ***[H2]***.
3. Magmas from continental and purely-oceanic plumes have markedly different PGE enrichment signatures ***[H3]***.

In all cases, parental magma compositions investigated by lava samples taken from the plume sites being studied. The objectives of the research and the practical framework surrounding the hypotheses, are referred to as “O1”-“O5” and are as follows:

1. Acquire intraplate lava (basalt) samples from multiple plume localities around the world and analyse their bulk major, trace and PGE geochemistry using high precision laboratory techniques to compile an high quality geochemical database of young (< 150 Ma), fresh plume-derived lava samples (i.e. unaffected by alteration/metamorphism), alongside literature data ***[O1]***.
2. Compare and contrast PGE geochemistry from plume-derived lavas in relation to major and trace element trends, to test the effects different settings, geodynamic regimes and melting conditions have on precious metal budgets in intraplate magmas ***[O2]***.
3. Model metal concentrations of melts in continental and oceanic settings to determine the major controls on magma PGE content ***[O3]***.
4. Establish common features in intraplate magmatism across different localities that are conducive to significant PGE enrichment on a global scale, to determine the active/passive role plumes play in intraplate PGE metallogenesis ***[O4]***.
5. Develop an integrated machine learning workflow to optimise the identification and interpretation of multi-element trends within data sets, that is suitable for use in exploring large suites of bulk geochemical data both inside and outside this thesis ***[O5]***.

1.3. Thesis overview

This thesis comprises seven main chapters excluding this introduction. **Chapter 2** summarises key background knowledge from the wealth of literature on the topics of PGE geochemistry, mantle plumes, mantle geochemistry and ore deposits, and introduces some of the more technical aspects of the study (such as machine learning algorithms) expanded upon in the main research chapters. The content within this review provides a background relevant to all research chapters but is not locality-specific. The geology, geochemistry and geodynamics of the specific locations studied in the research contributions (Chapters 3 to 7) are explored in depth within the opening sections of the corresponding chapter, and build upon theories, concepts and data highlighted in Chapter 2.

The research chapters of the thesis (Table 1.2) are all at various stages of publication in peer-reviewed journals – one fully published (Chapter 5), one accepted (Chapter 6), two under review (Chapters 3 and 4) and one pre-submission (Chapter 7) at the time of thesis submission. As such, the content is presented in a similar format to that submitted to journals and each chapter is self-supporting as an independent study. However, the material herein is adapted for the purpose of a single flowing thesis narrative, with content arranged in a logical manner. The work grows in scope throughout the thesis and illustrates the variability of PGE metallogenesis on local (Chapters 3-4), regional (Chapters 5-6) and global (Chapter 7) scales. Chapters 3 and 4 are centred upon a more ‘traditional’ approach to modelling geochemical data in different plume settings, whilst the machine learning aspects of the thesis are integrated from Chapter 5 onwards.

Table 1.2 *– Summary of main research chapters included in this thesis, with an account of their main theme/locality and publication status (submitted or accepted for publishing), and indication if they contain data generated for new samples, traditional geochemical interrogations (including modelling), and/or machine learning. Discussed further in-text. * - in review.*

Chapter	Theme	New data	Geochem.	MLA	Publication
3	PGE geochemistry of Paraná lavas	✓	✓	✗	✓*
4	PGE geochemistry of Canary Islands lavas	✓	✓	✗	✓*
5	Machine learning in the NAIP – PGE signatures	✗	✗	✓	✓
6	Machine learning in the PELIP – PGE signatures	✓	✓	✓	✓
7	Global plume PGE signatures	✓	✗	✓	✗

Chapter 3 comprises a traditional geochemical study of flood basalts from the Paraná region in Brazil, with a focus on constraining the controls on PGE abundances in magmas generated by the underlying Tristan plume. The data produced for this chapter marks one of the first complete bulk major, trace, PGE and Au data sets for lavas in the Paraná region, and contributes substantive findings to our understanding of metal acquisition beneath continents. This has significant implications for potential ore genesis in South America. The content of this chapter is currently **under review** in manuscript form with *Geochimica et Cosmochimica Acta* (Lindsay et al., in review[a]).

Chapter 4 introduces a second plume locality, the Canary Islands, and conducts a similar study into the PGE metallogenesis of intraplate magmas, but offshore and in the absence of continental lithosphere. The data set presents an extension of a study by Day et al. (2010) that interpreted PGE enrichment patterns the western Canary Islands by adding Tenerife into the discourse. As with the Paraná study this is the first complete bulk major, trace, PGE and Au data set produced for the island at the time of writing, and presents an exciting opportunity to enhance previous ideas about metallogenesis in an oceanic plume setting, complementary to Chapter 3. The content of this chapter is currently **under review** in manuscript form with *Geoscience Frontiers* (Lindsay et al., in review[b]).

Chapter 5 is the first instance of machine learning being employed in the thesis to analyse geochemical data and contains the bulk of the methodology carried through to subsequent chapters. This chapter demonstrates the use of the Principal Component Analysis (PCA), t-Distributed Stochastic Neighbour Embedding (t-SNE) and *k*-means clustering algorithms on a sample data set from the North Atlantic Igneous Province (NAIP), linked to the Icelandic plume. The workflow created throughout this case study not only provides new insights into how the PGE behave within the context of a regional magmatic system, but an exploration framework suitable for any number of geochemistry-based research topics. The methodology allows for the recognition of complex data trends potentially imperceptible to human analysts and resolves high-dimensional information in an easily communicable format. This chapter has been **published** in *Geoscience Frontiers* (Lindsay et al., 2021).

Chapter 6 uses the framework established on the North Atlantic data set to return to the Paraná data set, but this time incorporates lavas from the entire Paraná-Etendeka Igneous Province (PELIP), which spans the width of the Southern Atlantic and mirrors the geodynamic history of the NAIP. The PELIP data set contains significantly more elements analysed per sample and highlights the importance and utility of dimensionality reduction in geochemical studies. The comparison between the North and South Atlantic plume systems features in the discussion. The content of this chapter is **accepted for publication** with *Earth Science, Systems and Society* (Lindsay et al., in accepted).

Chapter 7 acts as both a synthesis to the ideas running throughout the thesis and a stand-alone study into global plume metallogenic signatures, featuring all localities covered by new data in Chapters 3 through 6, plus literature data for Kerguelen, Ontong-Java and Hawaii plumes. By tying together many of the concepts discussed in detail for specific localities in the previous studies, and using the machine learning workflow successfully implemented in regional settings in previous chapters for a broader data set, plumes are considered with a Mineral Systems approach to prospectivity (see Section 2.5.4). This is being prepared for a short-format publication at the time of writing.

The thesis ends with some **Concluding Remarks** in **Chapter 8**, which reflect upon the overarching themes and outcomes from Chapters 3-7, and draw together their uniting features with attention to objectives and hypotheses laid out in Section 1.2. This final chapter also reflects upon the relevance of machine learning within the context of geochemical topics, and highlights opportunities to build upon the work laid out in the thesis.

The Appendices found at the end of the thesis serve as extra sources of information outside the main scope of each research chapter, and are referred to in-text when relevant. All Supplementary material is supplied alongside this thesis in digital format. For a full account of sample information relevant to this thesis, including hand specimen descriptions, see Supplementary S1.1. For the bulk geochemical database for all gathered samples, see Supplementary S2.1. These are both sub-divided between the appropriate chapters and discussed in detail therein, but there are also master databases in S1.1 and S2.1, for quick reference.

Chapter 2

Literature Review - Platinum-group elements — plumes, partial melting and inheritance in the Earth's mantle

2.1. Geochemical behaviour of the PGE

Goldschmidt (1937) defined major subdivisions in the periodic table as a function of which elements preferentially sit within different phases and portions of the Earth, and these terms are still used extensively in modern geochemistry. Lithophiles are most stable in oxygen-bearings compounds, most commonly silicate minerals (the major component of Earth). Chalcophiles are most stable in chalcogen compounds, most commonly sulphide. Atmophiles are most stable in gases and are depleted in the solid Earth, instead residing in the atmosphere. Finally, siderophiles have an affinity to iron metal phases (Goldschmidt, 1937).

A 'partition coefficient' is the experimental ratio of concentrations of a particular element in two different phases under a given set of dynamic physical conditions. These are normally measured via extensive laboratory-based projects comparing concentrations in a variety of substances throughout a chemical process such as melting or crystallisation (Goldschmidt, 1937; McIntire, 1963; Irving, 1978). As an example, the metal/silicate partition coefficient (e.g., $D^{(metal/silicate)}$) of an element at modern mantle pressure and temperature conditions may be >1, indicating that the element is more stable and thus found in higher abundance in metal than in the silicate (Beattie et al., 1993). $D^{(metal/silicate)}$ <1 indicates that the element will not ideally exist within a metal under these conditions and favour the silicate component. Slightly siderophile elements (SSE) include Zn, Ga, Mn, V and Cr, and generally have $D^{(metal/silicate)}$ between 0 and 10. Moderately siderophile elements (MSE) include Mo, As, Ge, W, P, Ni and Co, and have $D^{(metal/silicate)}$ between 10 and 1,000. Highly siderophile elements (HSE)

comprise the PGE (Ru, Rh, Pd, Os, Ir, Pt), Au and Re, and typically have $D^{(metal/silicate)}$ > 10,000 (partition coefficients from Siebert et al., 2011; Walker et al., 2015). This concept can also be applied to elemental abundances in liquids, gases and various minerals or rocks. Partition coefficients are sensitive to temperature, pressure, redox states and volatile composition/abundance among other factors. The element in question will preferentially migrate via diffusion to the stable phase (normally via diffusion) if given the space and time to equilibrate (Irving, 1978; Watson, 1985). The process of elements segregating into contrasting phases is 'fractionation' and determines the current distribution of elements throughout the entire planet.

The eight HSE are heavy, metallic, and refractory to transitional in terms of volatility, meaning they are resistant to heat and difficult to fuse compared to most other elements (Mann et al., 2009). Table 2.1 shows basic chemical properties for the HSE under early mantle conditions, whilst Figure 2.1 summarises the relative abundance of elements on Earth (with respect to chondritic meteorite concentrations) against their volatility. The affinity of HSE for metal phases in most conditions (e.g., $D^{(metal/silicate)}$ of between 10^4 and 10^7) make them very rare in the silicate portion of Earth (as seen on the y-axis of Figure 2.1), when compared to the refractory lithophile (silicate-loving) abundances. Platinum-group elements and Re are consistently measured in the crust at ppb or sub-ppb concentration levels, making them by far the most depleted metals in the crust (McDonough and Sun, 1995), whilst Au occurs at slightly higher abundances than PGE although still measured in ppb/ppm. The PGE physical and chemical affinity for liquid metal is a result of their unfilled high-energy *d*-orbitals and readily available unpaired electrons making metallic bonding a highly stable electronic arrangement (Lorand et al., 2008).

The HSE are regarded collectively as precious metals, and may be grouped into three sets based on their similar chemical properties: the palladium-group PGE (PPGE), Pt, Rh, Pd; the iridium-group PGE (IPGE), Os, Ir, Ru; and Au and Re, the non-PGE (Barnes et al., 1985). The main distinction between the three sets is their behaviour during silicate melting processes. In general, the IPGE act compatibly in mantle melting (i.e., $D^{(mineral/melt)}$ >1) and will remain in the solid source until high degrees of partial melting; PPGE are less compatible (i.e., $D^{(mineral/melt)}$ <1) and can be scavenged from a solid source into silicate melts

during melting (Barnes et al., 1985). Gold and Re are best considered separately from the PGE due to their unique physical properties, but Au especially can be affiliated with PPGE. All HSE also exhibit strong chalcophile behaviour in the absence of a metal phase, and therefore in most mantle conditions, the HSE will preferentially partition into sulphide over all other phases (Brenan et al., 2016 and references therein).

Table 2.1 *– Basic chemical properties of the eight HSE (after Gunn et al., 2009), including their metal/silicate partition coefficients based on experimental studies (Kimura et al., 1974; Brenan and McDonough, 2009; Mann et al., 2012). * Metal/silicate D values ($D^{M/S}$) given are for low pressure (3 GPa), moderate temperature (~2700 K), reducing conditions (equivalent to those on the early Earth). This is effectively maximum D values, which decreases as Earth formation proceeds (Mann et al., 2012).*

	Atomic #	Mass #	ρ (g/cm^3)	Melting T (K)	Vapor. T (K)	$D^{M/S}$*
Ru	44	101.1	12.45	2607	3900	10^6
Rh	45	102.9	12.41	2237	3727	10^5
Pd	46	106.4	12.02	1828	2927	10^4
Re	75	186.2	21.02	3459	5627	10^5
Os	76	190.2	22.61	3306	5027	10^7
Ir	77	192.2	22.65	2739	4527	10^7
Pt	78	195.1	21.45	2041	3827	10^5
Au	79	197	19.32	1337	2807	10^4

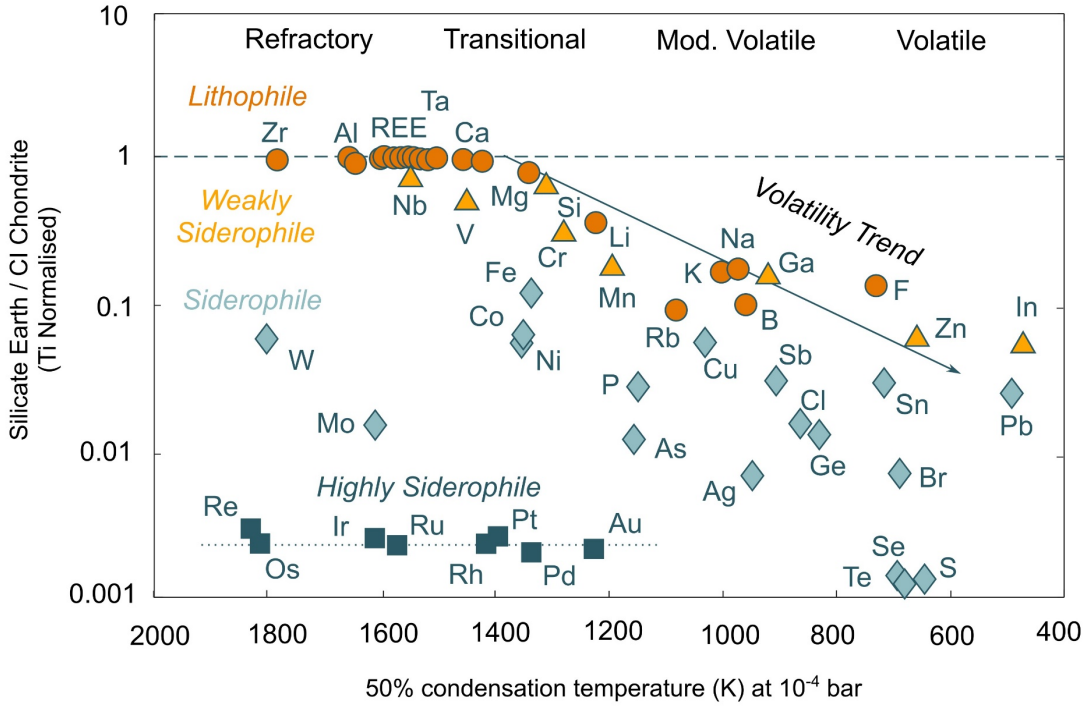

Figure 2.1 *- Plot of element condensation temperatures against chondrite-normalised abundance in silicate Earth, as estimated from mantle rocks. From this plot, subdivisions based on volatility and Goldschmidt classifications can be displayed (adapted from Mann et al., 2009).*

2.1.1. Formation of the Earth

This thesis primarily focuses on the PGE, their distribution throughout Earth, and the methods through which they are transported from reservoirs to the surface. The chemical behaviours of the PGE are intrinsically linked to our collective knowledge of the creation of Earth, and the history of mantle studies involves substantial overlap in PGE geochemistry and planetary accretion. The process of planetary amalgamation, beginning ~4.7 Ga, was dynamic - gravitational, collisional and radioactive energy amassed by the coalescence of planetesimals and cosmic dust from the solar system generated huge temperatures and pressures in the early celestial body (Kargel and Lewis, 1993). The raw elements of the universe converged chaotically into the proto-Earth in the very earliest stages of amalgamation (Wood et al., 2006).

The mass of Earth and the heat from accretionary impacts would have been sufficient to create gravitational melting, allowing diffusion-based internal chemical differentiation dictated by Goldschmidt behaviour. Goldschmidt's classification scheme rules that siderophiles and lithophiles were differentiated into metal and silicate phases respectively in the accreting Earth, with the denser metal falling to the centre of gravity (Figure 2.2). The segregating metal (mainly Ni and Fe) formed the core of the Earth along with 1-2 % oxygen and 2-13 % silicon (Kleine et al., 2004; Rubie, 2004; Siebert et al., 2012), separating siderophile elements from the silicate portion of Earth, which would later become the mantle (Kargel and Lewis, 1993; O'Brien et al., 2006; Ballhaus et al., 2013). Core formation was complete within 60 Myr of Earth's history, as evidenced by tungsten isotopes (see Section 2.4.3) (Walker, 2009). The mantle would have been relatively unmixed during core formation, leaving chemical heterogeneities (e.g., lower mantle vs. upper mantle) until convection and plate subduction began (Walker et al., 2015). Furthermore, the core itself differentiated into a solid inner core and liquid outer core due to pressure and temperature variability with depth to the centre (De Wijs et al., 1998), and the PGE were fractionated between the two phases – IPGE dominantly in the solid core, PPGE and Re dominantly in the outer core (Brandon and Walker, 2005).

The entirety of the mantle is thought to have been molten during earliest core formation due to the modelled P/T conditions for an accreting planet (typical minimum values of 3 GPa, 1850-2200°C; Siebert et al., 2011). As pressure increased with accretion and perovskite stabilised in the lowermost mantle, the remaining silicate Earth became a magma ocean (> 25 GPa, 2,000-3,000°C; Righter and Drake, 1997) extending from the surface down to depths of 1,200 km (Rubie, 2004; Righter, 2011) (Figure 2.2b). Although the settling of material into the core was originally believed to be a homogeneous process, later work has indicated that accretion was most likely a protracted multi-stage process with chemically variable impactors arriving on Earth throughout the first 60 Myr (Righter, 2003; Kaminski and Javoy, 2013) (Figure 2.2a). It is estimated that the earliest material accreting into the proto-Earth was mostly reduced, which increases siderophilic behaviour (Righter, 2003) – core segregation would have sequestered siderophiles in high concentrations in the earliest Earth with diminishing effectiveness with time (Siebert et al., 2011). The latter 20-30 % of

the accretionary volume was much more oxidising and volatile-rich (e.g., Drake and Righter, 2002; Siebert et al., 2011).

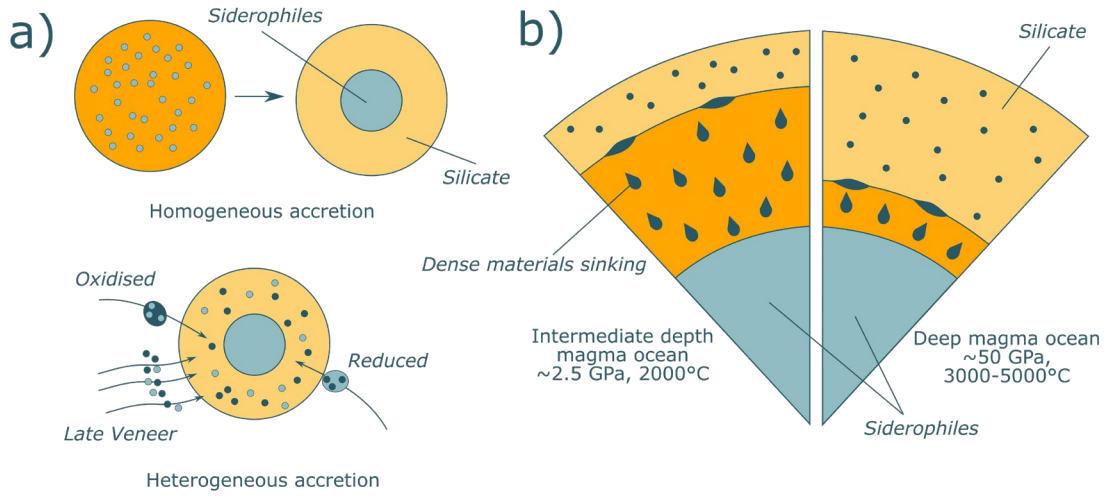

Figure 2.2 *– (a) Different accretionary models for early Earth and core formation, with the bottom model (heterogeneous accretion) proving to be the most satisfactory explanation for complex elemental behaviours through time. (b) Different models for magma ocean depth and conditions. Both adapted from Righter (2003).*

Variable equilibrium P/T and oxidation conditions in the magma ocean throughout accretion would have elicited different responses from each siderophile element, resulting in a variety of partition coefficients (Walter and Cottrell, 2013). The $D^{(metal/silicate)}$ values of SSE and MSE are especially sensitive to temperature changes, while pressure and oxygen fugacity have more influence on HSE $D^{(metal/silicate)}$ than temperature (Walter and Cottrell, 2013). Pressures > 3 GPa systematically reduce the metal-silicate partition coefficients of PGE in experiments (i.e., Figure 2.3), and allow SSE and MSE to be significantly retained in the mantle, in comparison to the HSE (Mann et al., 2012).

Meteorites provide our best estimate of the 'primitive' undifferentiated solar system material that created Earth, prior to segregation via terrestrial processes (Palme and O'Neill, 2003). Comparisons can be drawn between chondrite meteorite compositions and the overall composition of Earth, both in terms of the concentration of elements for a given planetary mass, and for relative element

abundances (McDonough and Sun, 1995). A major feature of modern geochemistry is to compare measured elemental abundances against the chondritic norm, and interpret any enrichments or depletions based on chemical behaviour. Carbonaceous CI chondrites were established as representing the 'normal' nebular composition (McDonough and Sun, 1995), and enstatite chondrites provide very similar isotopic compositions to Earth (Javoy et al., 2010). The concentration of elements in the Primitive Upper Mantle (PUM) (immediately after core formation) has been defined based on the reduction of siderophiles from chondritic abundances (McDonough et al., 1992; McDonough and Sun, 1995; Becker et al., 2006). Following core segregation, the formation of lithosphere, via magmatic processes differentiating mantle-derived melts, took place (Hastie et al., 2016). The total volume of material in the mantle and lithosphere is referred to as Bulk Silicate Earth (BSE).

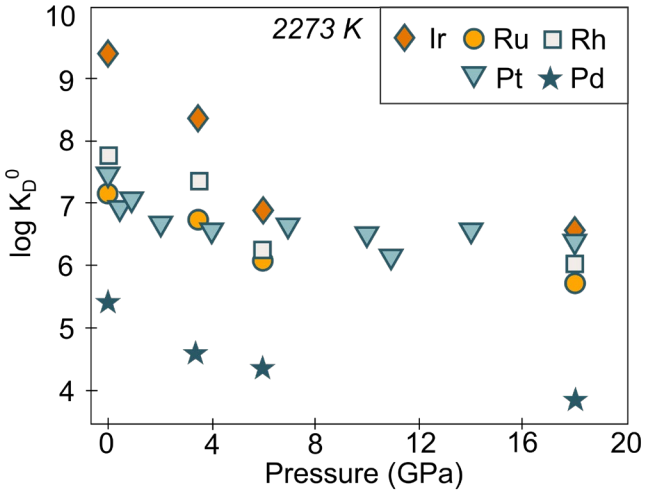

Figure 2.3 *- Bivariate plot of mantle pressure vs. metal-silicate partition coefficients (expressed as K_D^0) for PGE (excluding Os). All five elements show a systematic decrease in siderophile behaviour with increasing pressure, particularly within the first ~8 GPa of pressure increase. The IPGE are significantly more siderophile than the PPGE at all stages. By 20 GPa, there is a smaller deviation in individual PGE partition coefficients than there is at lower pressures (adapted from Mann et al., 2012).*

2.1.2. Distribution of PGE on Earth

On comparing PUM and BSE estimates with mantle xenoliths representative of modern mantle compositions and numerical models of core depletion, the physical conditions attributed to a primitive magma ocean can account for the proportions of SSE and MSE measured in present-day mantle (Siebert et al., 2012). However, HSE concentrations in the mantle do not match the predicted absolute concentrations from these same models (Holzheid et al., 2000). The PGE budget of the mantle is 100-400 times lower than chondritic values, as opposed to that predicted by the process of core segregation alone which would suggest that HSE should be 10,000 times lower than chondrite (Danielson et al., 2005). This is sometimes referred to as the 'siderophile problem'.

Variations of equilibrium conditions during accretion (as discussed in Section 2.1.2) have been suggested as an explanation for the modern distribution of siderophiles in Earth. Given that the silicate magma ocean on Earth slowly increased in pressure and oxidation state as the planet grew in mass (e.g., Rubie et al., 2011; Siebert et al., 2011; Wood et al., 2006), siderophiles would be held in the mantle in higher proportions than they were originally as time went on (Mann et al., 2012). A reduction of siderophility at increased pressure is observed for all siderophiles to varying degrees (Righter, 2011) (Figure 2.3). Under magma ocean pressures (over 20 GPa) suggested by most studies, the relative abundances of certain siderophiles (e.g., V/Nb, Ga/Mn, U/Ta, In/Pb and In/Zn) can be accounted for (e.g., Mann et al., 2009; Walker et al., 2015). Palladium and Au (the least siderophile HSE) can theoretically be retained in the mantle, at pressures of > 60 GPa (e.g., Holzheid et al., 2000; Mann et al., 2012). Anything less than this would not allow effective HSE retention in the mantle. However, such pressures would (a) be unrealistic for the depth of the proposed magma ocean, and (b) cause an inaccurate overstock of MSE in the mantle compared to the core (Münker et al., 2003). A single set of physical conditions and a single-stage accretion/segregation model cannot account for mantle abundances of all siderophiles simultaneously (Righter et al., 2008) and thus a further model must be considered.

The Late Veneer Hypothesis is the most robust and widely accepted explanation for the siderophile problem. By defining Earth accretion as a multi-stage, heterogeneous process (e.g., Figure 2.2a), elemental distribution is bolstered by the addition of new material following core formation, adjusting absolute and relative HSE concentrations in the mantle after core formation (Kimura et al., 1974). The late bombardment of Earth by meteorites is suggested to have occurred after both the Moon-forming impact and the cessation of core formation (e.g., in the last 0.5% of accretion) (Walker, 2009). This late bombardment is estimated to have brought 10^{22} kg of material to Earth in the last stages of accretion (Lorand et al., 2008), equating to 0.5 % of Earth's total mass (e.g., Kleine, 2011; Médard et al., 2015). Any siderophiles added to the Earth at this point would have remained in the mantle, re-stocking it after the strong depletion to the core in the first 60 Myr of Earth's history (O'Brien et al., 2006), and thereby estimated to satisfy the observation that HSE in the mantle are 100-400 times < chondrite (almost 100% depletion (Cottrell and Walker, 2006; Mann et al., 2012). This is reflected in chondritic relative ratios of most PGE and suprachondritic Pd/Ir (given that Pd was retained in the mantle to a higher degree than the other PGE) (Mann et al., 2012). Given that HSE were almost totally absent in the PUM, any addition via late veneer would be proportionately significant (Walker, 2009). Komatiites, rocks formed by high degrees of partial melting in the mantle, record progressively diminishing PGE concentrations from the Early Archaean onwards as the late siderophile contributions are slowly mixed into the deeper regions of the Earth (Maier et al., 2009).

Given the SSE, MSE and HSE concentration in the mantle, it is difficult to fit the distribution of all siderophiles to a single process and a combination of a late veneer and variable equilibrium conditions is most likely, even for the inter-element distribution of just the HSE. However, since the dawn of plate tectonics, the mantle became a highly heterogeneous region of the Earth, further differentiating the PGE concentrations from PUM via the flow of mantle material.

2.2. Mantle plume dynamics

2.2.1. Mantle convection and plume generation

Kinetic disturbances within the mantle due to chemical, mechanical instability or rheological disruptions cause material flow in the mantle to become more turbulent on a local scale; if the upwards pressure gradient is sufficient, hot material can begin to rise adiabatically towards the surface of the Earth through overlying cooler zones (Bercovici and Kelly, 1997). The concept of mantle stratification and convection has been highly controversial for almost a century, with many models, processes and rebuttals of such theories put forward through the years. For example, Becker and Boschi (2002) suggest that whole mantle convection is the default thermodynamic model for the Earth, but add the importance of subduction-enforced cooling in re-organising transition zone (660 km depth) flow channels between the upper and lower mantle. Popularised by Morgan (1971), the concept of *mantle plumes* has become the most robust theory for describing more regionalised mantle flow, but remains a controversial topic despite decades of studies furthering the understanding of such features.

Mantle plumes represent significant thermal, mechanical and seismic anomalies in the Earth's interior, and build upon the concept that buoyant material rises in situations of rheological (i.e., Rayleigh-Taylor) instability (Cagney et al., 2016). This normally occurs at significant thermal boundaries such as, but not restricted to, the core-mantle boundary (CMB). Immediately on top of the CBD resides the D" layer, a highly heterogeneous region comprising lower mantle material, recycled oceanic lithosphere, core metal dregs and small amounts of silicate melt (DePaolo and Manga, 2003; Jellinek and Manga, 2004; Lay et al., 2004). The compositional variability of the D" layer and the high heat transfer across the CMB makes initial instability events much more plausible than elsewhere in the mantle (e.g., the upper-lower mantle transition) (Davies, 1993). A variety of models have been proposed for plume initiation, summarised by Lay et al. (2004) and culminating in a hybrid model incorporating thermal and chemical boundary differences, recycled slab 'graveyards' and phase changes at the CMB (Figure 2.4a-f). A density deficit of 3-6% compared to the ambient mantle will initiate buoyancy in the D" layer (Kellogg and King, 1993). Following initial buoyant flow, low-pressure cells will form in the D" layer, drawing in and

mixing low-viscosity material from source into the proto-plume head, 'inflating' it and increasing temperature and flux (Figure 2.4a) (Bercovici and Kelly, 1997). Once ascent velocity exceeds the growth rate of the plume head, it will rise upwards in accordance with Stoke's Law (Griffiths and Campbell, 1990; Bercovici and Kelly, 1997). The strongest plumes, which give rise to large eruption events (e.g., the Deccan and Siberian Traps) will have high temperature and chemical density/thermal viscosity differences with the mantle (Figure 2.4b) (Deschamps et al., 2011) and high flux rates (Jellinek and Manga, 2004) allowing successful, stable transportation of deep material to the surface (Griffiths and Campbell, 1990). Cooler plumes with a weak flux will be contaminated on ascent, which can ultimately lead to plume stalling, widening and eventual cessation when buoyancy is overcome (Jellinek and Manga, 2004).

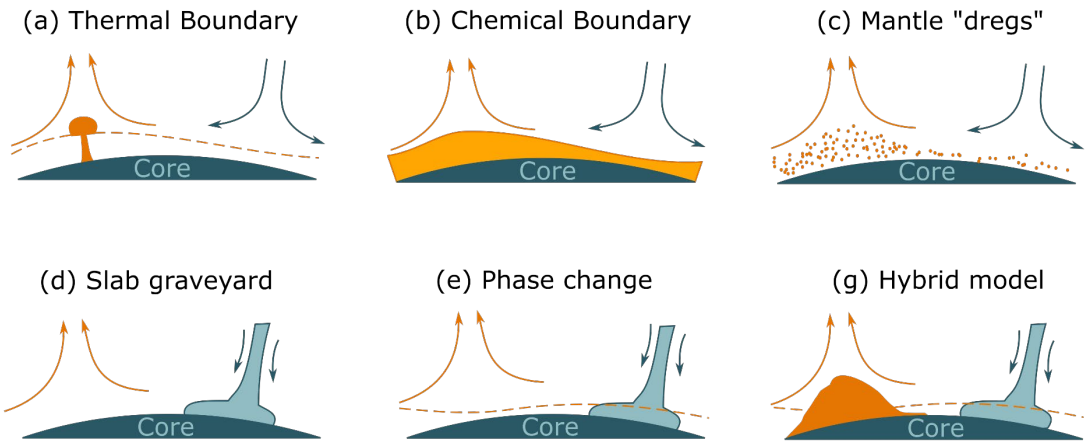

Figure 2.4 *– A variety of models for processes initiating plume anomalies from instability at the CMB: (a) difference across thermal boundaries; (b) differences across chemical boundaries; (c) accumulating dregs of heavier material from the mantle; (d) amalgamations of recycled oceanic lithosphere (slabs); (e) phase changes surrounding slab placement at the CMB; and (f) a hybrid model incorporating all previous features. Adapted from Lay et al. (2004).*

The geometry of ascending mantle plumes is a source of great debate in the geoscience community, with major theories summarised in Figure 2.5. This ranges from a continuous laminar 'tail' with an inflated 'head' (Morgan, 1971), through to upper mantle thermal anomalies (Foulger et al., 2000), substantial anchors at the core-mantle boundary (Torsvik et al., 2010) (see Section 2.2.2),

laterally expansive plume heads (French and Romanowicz, 2015) and hybrid complexes with “superplume” roots (Duncombe, 2019) (see Section 2.2.3). The debate over plume geometry spans the fields of geophysics and geochemistry, but regardless of the precise shape of such anomalies, plumes present an environment in which heat, chemical components and supercritical liquids are transferred between pre-existing reservoirs in the Earth, particularly those components absent from the asthenosphere and lithosphere (see Section 2.4).

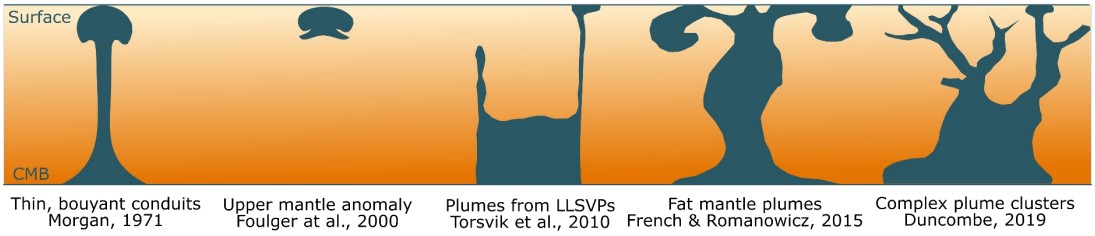

Figure 2.5 *– A variety of models for plume geometries through the literature. Adapted from Duncombe (2019). LLVSP – Large Low Shear Velocity Provinces.*

2.2.2. Core-mantle boundary heterogeneity

The D” layer, which comprises multiple Large Low-Shear Velocity Provinces (LLVSP) detected by seismic studies of the lower mantle, is widely regarded to contribute material into ascending mantle plumes as described in Section 2.2.1. As old, dense oceanic lithosphere is subducted beneath more buoyant younger oceanic or continental lithosphere, the down-going slab is pushed into the mantle, and a sixth of this slab material is thought to penetrate the upper-lower transition (~660 km depth), accumulating as pyroxenites at the CMB (Christensen and Hofmann, 1994; Boschi et al., 2007). This creates dense liquid melted slab graveyards (Figure 2.4d) that can be imaged by very slow-moving shear-wave seismology (Burke et al., 2008; Deschamps et al., 2011; Jones et al., 2016). This interface between materials of varying viscosity and density, particularly at the thermal boundary itself (Lay et al., 2004), can trigger the initial collapse necessary for proto-diapirism; disturbances in pressure due to sudden movements at the interface can have a runaway effect generating plumes (Bercovici and Kelly, 1997). As demonstrated in fluid dynamic experiments,

dense material within the LLSVP will ‘sweep’ horizontally along the D” layer, displaced by down-welling slabs towards the low pressure zones left by gravitational collapse at the LLSVP edges (e.g., Hassan et al., 2015; Lay et al., 2004). If buoyancy forces in the moving pile are high, a plume will generate (Garnero and McNamara, 2008).

Subduction zones and LLSVP have regular distribution with respect to each other, with areas of down-going cold material adjacent to areas of plume upwelling (and D” piles at their base) (Garnero and McNamara, 2008; Dziewonski et al., 2010) (Figure 2.6). An estimated 20% of the CMB is covered by LLSVP (e.g., Hassan et al., 2015; Richards et al., 1988). Major Large Igneous Provinces (LIP) with strong connections to plume-derived magmatism can correlate well with the edges of two major LLSVP; one under Africa, one under the centre of the Pacific Ocean, and a third smaller one is thought to be present under Siberia (Burke et al., 2008). In 3D spherical modelling simulations, between 65 and 75 % of all strong plume signals occur within 10 degrees of LLSVP margins (e.g., Davies and Davies, 2009; Li and Zhong, 2017; Torsvik et al., 2006). It is suggested by high-resolution seismological surveys that the shape of a LLSVP denotes its age – long-lived piles will have flat upper boundaries, while freshly accumulated piles will have diffuse, undulating upper boundaries (Garnero and McNamara, 2008).

Temperature and pressure conditions at the lowermost mantle permit metallic liquid from the outer core to percolate into, and become trapped in, the D” cumulate pile immediately above the CMB, which is compositionally dominated by perovskite and magnesiowustite (Shannon and Agee, 1998). The low dihedral angle of these lower mantle compositions allows upwards movement of core alloys (FeO-FeS-Fe) via capillary action across the CMB and into the silicate pile, which has been described as a ‘rainfall’ of liquid core (e.g., Brandon and Walker, 2005; Shannon and Agee, 1998). Seismic studies of the CMB detect significant anisotropy attributed to the admixture of metal and silicate material as described – the area of effect of this heterogeneity is twice as large as previously assumed (~ 300 km vertically), suggesting that core percolation into the D” layer is widespread (Vinnik et al., 1998). The CMB is effectively a eutectic boundary and components of both the core and mantle are free to interact chemically with each other (Lay et al., 2004). Disequilibrium and equilibrium reactions, isotopic

exchange, diffusive heat loss and light element exsolution are all thought to take place at the thermochemical boundary (Humayun et al., 2004 and references therein). Thermochemical erosion of the heterogeneous D" pile can then introduce core material into LLSVP and, consequently, plumes (Humayun, 2011). Further, volatile exsolution from cumulate piles can extract S and subsequently, more mobile chalcophiles, redistributing sulfide minerals and segregating them from their original setting (Godel and Barnes, 2008)

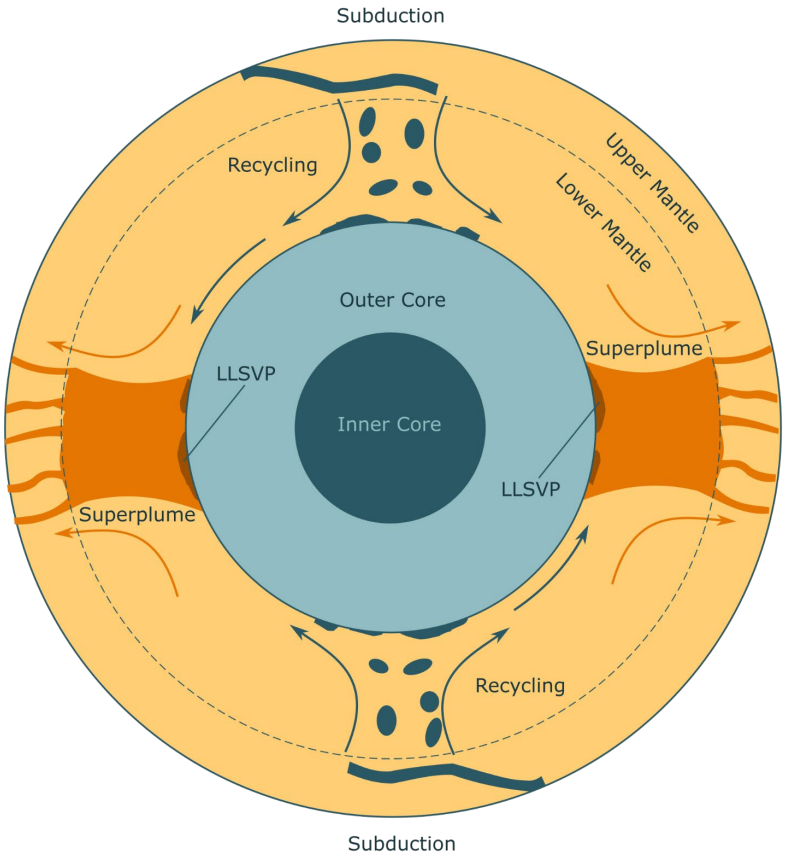

Figure 2.6 *– The geographic relationship between major subduction zones, slab graveyards, LLSVP and mantle plumes. The potential for superplume complexes is also highlighted at the upper-lower mantle transition. Adapted from Dziewonski et al. (2010). LLSVP – Large Low Shear Velocity Provinces.*

2.2.3. Intraplate magmatism

When plumes ascend to the upper mantle (i.e., the asthenosphere), they induce decompression-based partial melting of their surroundings, including components transported from depth, ambient upper mantle/asthenosphere and, potentially, the lithospheric mantle if melting is shallow enough (e.g., Turner et

al., 1996). This melting generates intraplate magmas that can rise through the lithosphere and erupt as lavas or intrude the crust to form intrusive bodies like dykes, sills and batholiths (e.g., Griffiths and Campbell, 1990). High-pressure (e.g., deeply sourced) xenoliths, xenocrysts and diamonds are often incorporated in hotspot lavas and intrusions (Ryabchikov and Kogarko, 2016) and act as tracers of deep mantle ascent.

Given the head-and-tail configuration of a plume (i.e., Figure 2.5), volcanism style changes throughout the lifecycle of a plume-derived melting environment (e.g., Hawkesworth and Scherstén, 2007). The head, which is able to entrain material from its surroundings, will be more contaminated and cooler, but volumetrically much larger, producing extensive flood basalt provinces on eruption via high degree partial melts in the asthenosphere (Campbell and Griffiths, 1990). This can generate continental large igneous provinces (CLIP) and oceanic large igneous provinces (OLIP). The tail, which is much thinner and hotter, often produces small-volume komatiites and picrites for the remainder of the volcanism (Griffiths and Campbell, 1990). Thermal boundaries are thought to exist between plumes and the surrounding mantle, which could consequently generate secondary thermal plumes and maintain volcanic flux (Figure 2.6) (Dziewonski et al., 2010). This “superplume” set-up seems to be the driving force underneath Polynesia, where a large LLSVP-derived plume anomaly has stalled at the transition zone, permitting smaller plumes to continue their ascent to the surface (Courtillot et al., 2003).

As melting and magma generation continues through the ‘tail’ stage and lithospheric plates move relative to this, usually in response to seafloor spreading, a ‘hotspot’ chain is formed where each volcanic edifice is superseded by a new one (ten Brink, 1991). According to Courtillot et al. (2003), a ‘true’ hotspot must fulfil the following criteria:-

1. Linear chain of volcanoes with age progression
2. Flood basalts at the origin of this track
3. Large buoyancy flux
4. Consistently high $^{3}He/^{4}He$ ratios (see Section 2.4.4)
5. Low shear wave velocity anomaly in the underlying mantle.

Most plumes in the world fulfil some of these conditions, with a sub-section of seven satisfying all five: Hawaii, Easter and Louisville in the Pacific hemisphere; Iceland, Afar, Reunion and Tristan in the Indo-Atlantic hemisphere. Hotspots in the same hemisphere (e.g., Pacific vs. African) migrate in unison with each other, but each hemispheric arrangement moves independent of the other (Courtillot et al., 2003). Mid-ocean ridges, such as that found in the Atlantic Ocean, have been seen to migrate over hotspot foci (in the South Atlantic case, the Tristan hotspot; see Chapters 3 and 6) without disrupting the intraplate volcanic flux (Fromm et al., 2017). This is seen as evidence for the deep origin of hotspot magmatism – if melting was generated in the upper 200 km of the mantle (similar to rift magmatism or the Foulger model in Figure 2.5), a migrating ridge would deflect and reposition the hotspot, thus necessitating the existence of a plume-type upwelling (DePaolo and Manga, 2003). The upwards flux of Hawaiian magmatism (50 cm/year) is ten times that of the velocity of plate migration, further strengthening the case that hotspot *positions* are independent of plate movements (DePaolo and Manga, 2003).

However, to say that plumes and plate tectonics are dynamically independent would be inaccurate. Convergent plate boundaries are always found above D” zones with high seismic velocity (e.g., no plate accumulation at the CMB), while hotspots are always above low velocity zones (Garnero and McNamara, 2008). Some studies cite incipient plumes as the cause of eventual continent break-up (e.g., Pirajno and Santosh, 2015), whilst others support the theory that rifting continents passively encourage mid-mantle upwelling into the pressure void created at the constructive boundary (McKenzie and White, 1989; Anderson and Natland, 2005). Others believe LLSVP act as sturdy mantle ‘anchors’, directly influencing superplume placement, convection cells and thus, plate tectonics (Dziewonski et al., 2010). The temperature anomalies supplied by plumes at rift zones (100-200 °C) can double or quadruple potential melt generation (Campbell and Griffiths, 1990) often producing continent margin flood basalt magmatism; such as the North and South Atlantic Igneous Provinces, and the Deccan and Karoo traps (e.g., McKenzie and White, 1989).

2.3. Mantle geochemistry

2.3.1. The mantle ‘zoo’

Following the initiation of mantle convection, plate tectonics and plume generation, the contents of the mantle were subject to redistribution from PUM paradigms. Regions of the mantle exhibited geochemical signatures based on their collective history. The recycling of oceanic lithosphere, which itself is the result of multiple fractionation (melting) events, drives a significant proportion of mantle heterogeneity (Christensen and Hofmann, 1994). The asthenosphere is frequently melted at rift zones, beneath continents and within plume columns, removing incompatible elements from the source, leaving *depleted* mantle behind (Peach et al., 1990; Bézos et al., 2005). The lower mantle retains the majority of its chemical constituents until incorporated into plumes, leaving *enriched*, primitive or simply undepleted mantle behind (Deschamps et al., 2011; Harrison et al., 2017).

The most basic geochemical classification of lavas produced from magmatism in different mantle sources are: Mid-Ocean Ridge Basalts (MORB) produced at constructive boundaries from shallow mantle; Arc lavas, produced at destructive boundaries from mantle wedges above subduction zones; and Ocean Island Basalts (OIB), produced from intraplate (i.e., plume-derived) deep mantle sources. Both MORB and Arc lavas (and thus their parental magmas) are derived from depleted sources within shallower mantle, relative to OIB. Accordingly, MORB and arc lavas tend to have lower concentrations of incompatible elements, such as Rb, Th, U and Ba (McDonough and Sun, 1995). Arcs may be rejuvenated by subduction-related fluid enrichment. In contrast, OIB magmas may sample areas of the mantle relatively untouched until plume interaction.

The degree of heterogeneity in the D” layer can provide ascending plumes with a wide variety of material, acquired via deep sampling/incorporation, hence the coining of the “mantle zoo” analogy (Stracke et al., 2005). The amount and lithology of recycled lithosphere incorporated in a plume is thought to be the major definitive factor in OIB variability (Christensen and Hofmann, 1994). Gathered oceanic lithosphere in LLSVP, as pyroxenite, will be relatively enriched compared to the rest of the lower mantle, given that they contain the elements expunged

from the asthenosphere during ridge melting, such as Ni and Zn (e.g. Howarth and Harris, 2017; Matzen et al., 2017). Pyroxenite mantle will also be comparatively Fe-rich due to their basaltic starting composition compared to the more Mg- and olivine-rich peridotite dominating the lower mantle (Burke et al., 2008). The most common OIB sources were established by Zindler and Hart (1986) (Figure 2.7) and are herein referred to as 'components', defined by Stracke et al. (2005) as "zones in the mantle that are isotopically different to other zones without considering size, distribution or properties". The literature typically defines mantle heterogeneity through isotopic variability – certain distinctive element pairs (and isotopes generated by the radiogenic decay of unstable elements) that have different compatibilities in mantle reservoirs are used to fingerprint 'components' and the processes at work in partial melting and magma sourcing. Section 2.4 describes these isotope systems in detail, and the mantle components are summarised below.

HIMU-type (high-μ; high radiogenic Pb concentrations) OIB are thought to be the product of re-melted recycled oceanic lithosphere that has lost alkalis and Pb while retaining (or being enriched in) U and Th through subduction (Chauvel et al., 1992). Uranium and Th are significantly depleted in the asthenosphere and incorporated into continental lithosphere; the lower mantle is less depleted, and replenished by recycled material (Hofmann, 1997). HIMU is regarded as the most radiogenic component with regards to the Pb isotope system in Figure 2.7 and is relatively rare in intraplate magmas compared to the other components (Stracke et al., 2005).

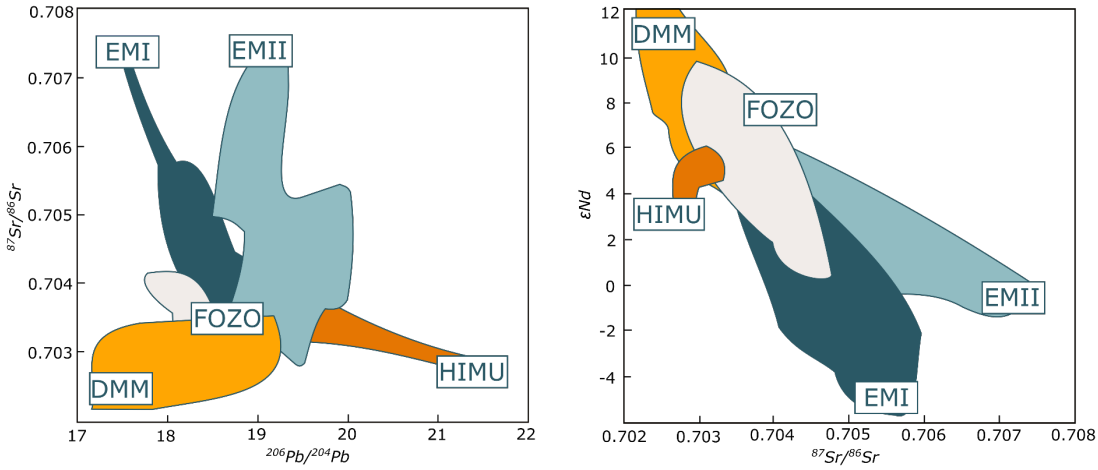

Figure 2.7 *– A summary of common mantle component signatures based on Sr, Nd and Pd isotope ratios* (Zindler and Hart, 1986; Stracke et al., 2005)

Enriched lower mantle EMI and EMII type OIB are similar to each other as they are thought to derive from recycled subcontinental lithosphere or pelagic sediments along with regular oceanic plates. They are radiogenic in their Sr and Nd isotopic compositions and unradiogenic in terms of Pb isotopes (Figure 2.7; e.g., Bennett et al., 1996; Zindler and Hart, 1986). Some authors believe this 'sedimentary' signature can be imparted when the plume arrives at the base of the lithosphere, as in Socorro Island in Mexico (Bohrson and Reid, 1995). EMII is slightly more radiogenic than EMI.

FOZO (previously PREMA) type OIB are thought to represent the general, un-enriched lower mantle composition. This is based on the premise that all other components radiate from their composition on a discriminant diagram, hence the name "focal zone" giving "fo-zo". FOZO is moderately more isotopically radiogenic than DMM ('depleted MORB mantle') in Sr, Nd and Pb systematics in Figure 2.7, and is suggested to represent a mixing component in all plume-derived magmas (Hart et al., 1992).

2.3.2. Plume components

As we begin to approach the central themes of the hypotheses introduced in Chapter 1, we consider plume geochemical signatures as a global phenomenon; each plume is a different age, occurs in a different setting under different types of lithosphere, and inherit different mantle components from the D" layer. Given their shared deep mantle origin and the wealth of literature written on the geochemical variability of the deep mantle (summarised in Zindler and Hart, 1986), we can deduce which geochemical components are common to all plumes, or if certain plumes bear a characteristic or even unique geochemical signature. Whilst individual mantle components may be recognised in OIB lavas, it is rare that a geographic location adheres to a single mantle component, instead changing over time, erupting two types at once or existing as a mix between multiple signatures (e.g., Griffiths and Campbell, 1990; Jones et al., 2016).

Axis plume flow has the least contaminated geochemical and isotopic signatures (Campbell and Griffiths, 1990) with source material from the D" layer dominating magma, and subsequently lava, compositions (Jones et al., 2016). Recycled oceanic lithosphere is preferentially incorporated into ascending plumes given that it is melted more easily than and has a density contrast with surrounding mantle peridotite (Cagney et al., 2016). Binary mixing of depleted mantle and recycled oceanic lithosphere alone cannot explain many deep plume magma compositions; for example, the isotopic signatures recognised in Hawaiian lavas are very likely to represent two deep sources (Bennett et al., 1996). Hawaii preserves a consistent spatial divide or zonation in source components, which can be traced along the axis of the plume trail (Figure 2.8). The northern side of the island lava chain belongs to the enriched 'Loa' group and the southern side belongs to the depleted 'Kea' group (e.g., Hanano et al., 2010; Weis et al., 2011; Harrison et al., 2017; DeFelice et al., 2019). This feature is also observed in other Pacific hotspot trails e.g., Samoa and Marquesan, perhaps related to their common source, the Pacific LLSVP (Huang et al., 2011; Chauvel et al., 2012; Jackson et al., 2014). More recently, the Gough hotspot track in the South Atlantic (belonging to the African LLSVP and the Tristan plume) has been recognised as a geochemically zoned hotspot chain – Rohde et al. (2013b) suggest that chemical zonation may be a feature of *all* lower mantle plume sources.

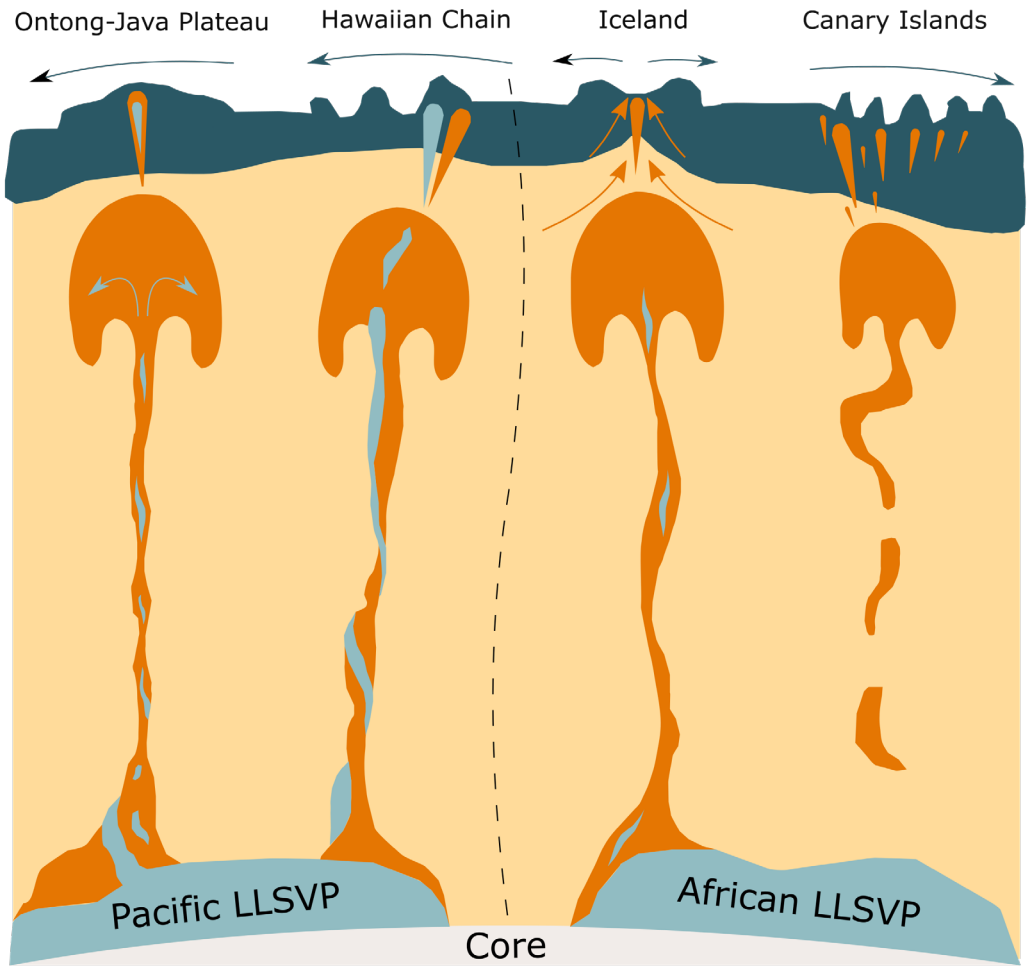

Figure 2.8 *– Schematic cross-section describing different forms of mantle plume heterogeneity. L-R: Ontong-Java with well-integrated components; Hawaii with spatially distinct surface components; Iceland with combined MORB and OIB influence; Canary Islands with complex temporal changes influencing magma compositions. Black dashed line separates the Pacific and African plumes.*

Heterogeneous ascending plumes can also be intercepted by, and mixed with, surrounding mantle material; density differences in components within a plume system can disrupt chemical zoning that would otherwise transfer to the surface expression (e.g., Hawaii) (e.g. Griffiths and Campbell, 1990; Harrison et al., 2017). In Iceland, and other mid ocean ridge-proximal plume settings, MORB and OIB components mingle and mix as plume-derived melts seep through perpendicular rift channels (Figure 2.8). This results in zones throughout the island with dominant depleted or enriched compositions depending on the prevailing source (e.g., Fitton et al., 1997; Momme et al., 2003; Peate et al., 2010; Jones et al., 2016; Béguelin et al., 2017). In Ontong-Java, Kerguelen, The Azores and Easter Island, plumes retain DMM with HIMU/EMI/EMII signatures at the

same time (Figure 2.8) (e.g., Fretzdorff et al., 1996; Neal et al., 2002; Ely and Neal, 2003; Chazey and Neal, 2004; Chazey and Neal, 2005; Béguelin et al., 2017; Sushchevskaya et al., 2017). In the Canary Islands, a host of geodynamic complexities are imposed by the proximity of the plume to the African continent. The resulting hotspot island geochemistry features components from a host of origins including HIMU, DMM and sub-African lithospheric mantle, which erupted sporadically through the lifecycle of the island chain (Figure 2.8) (Hernández-Pacheco and Ibarrola, 1973; Carracedo et al., 1998; Anguita and Hernán, 2000; Duggen et al., 2009; Taylor et al., 2020) (see Chapter 4).

Further heterogeneity and geochemical complexity may be imparted onto plume-derived magmas via crustal contamination. For example, the Galápagos Island lavas encompass a range of isotopic and compositional changes that indicate variable amounts of oceanic lithosphere being incorporated into ascending material (Fretzdorff et al., 1996; Loewen et al., 2013; Harpp and Geist, 2018). The interplay between peridotite (mantle) and pyroxenite (lithosphere) source compositions, revealed by distinctive isotopic signatures (Gurenko et al., 2009; Matzen et al., 2017), appear to show an increase in slab mixing in certain localities like the Canary and Galápagos island groups (Trela et al., 2015).

2.3.3. PGE in the mantle

Whilst the HSE, and especially the PGE, are chemically similar as described in Section 2.1, small differences in their partition coefficients for silicate, oxide and sulphide minerals cause them to fractionate from each other between different Earth reservoirs and through magmatic differentiation, including during partial melting of a mantle source region (Barnes et al., 1985). The physical state of PGE in the mantle is chiefly controlled by their relative compatibilities in typical mantle minerals (silicates, oxides and sulphides), and the thermal stability of host phases will determine the abundances of PGE in mantle partial melts.

In the mantle, the IPGE are commonly found in platinum-group minerals (PGM) (including alloys), Ni-Fe-rich mono-sulphide solution (Mss), and within the structure of high-temperature silicate minerals such as olivine or the spinel group (e.g., Capobianco and Drake, 1990; Peach et al., 1990; Barnes and Picard, 1993; Peach et al., 1994; Alard et al., 2000; Bockrath et al., 2004; Righter et al., 2004; Ballhaus et al., 2006; Pitcher et al., 2009). These mineral phases are all

refractory, and reasonably resistant to melting until high temperatures and pressures (Bockrath et al., 2004), which leaves mantle residues relatively enriched in IPGE compared to the partial melt extracted from the system. At high degrees of partial melting, 'clusters' of IPGE alloys can be incorporated into silicate melts as micro-xenoliths that can either stabilise in S-rich environments to coalesce with As, Te and Bi or act as nucleation sites for silicate and oxide minerals during crystallisation in S-poor environments (e.g., Tredoux et al., 1995, Lorand et al., 1999; Mansur and Barnes, 2020). Liberation of PGM clusters from the mantle can significantly increase metal concentrations in magmas due to their highly concentrated metal content (i.e., a high metal 'tenor'; Lesher, 2017).

The PPGE, (particularly Pt and Pd) are more often hosted in (typically interstitial) Cu-Ni-rich base metal sulphide (BMS) phases in the mantle, and are incompatible in both silicates and Mss (e.g., Mitchell and Keays, 1981; Barnes et al., 1985; Borisov et al., 1994; Barnes et al., 1997; Holzheid et al., 2000; Ballhaus et al., 2001; Mungall et al., 2005; Prichard et al., 2013; Driscoll, 2016). The distinction in host phases causes fractionation between IPGE and PPGE in partial melts of the mantle. During small degrees (e.g., < 10 %) of partial melting of a mantle source, we would expect a higher proportion of PPGE to enter a silicate magma than IPGE, given that the latter are often found within minerals that melt at very high degrees of partial melting (e.g., Keays, 1995; Ballhaus et al., 2001; Bockrath et al., 2004). With increasing degrees of melting, the PPGE/IPGE of a magma (often simply indicated by Pd/Ir) decreases as the more compatible elements are eventually released from their host minerals (e.g., Barnes et al., 1985). Furthermore, multiple melting events in succession can pre-condition the mantle for easier release of metals into later melts, negating the requirement for complete exhaustion in one event (Locmelis et al., 2016; Fiorentini et al., 2018).

The liberation of PGE from mantle phases during partial melting can be contrasted against other chalcophile elements (Figure 2.9). Given the extremely chalcophile nature of the PGE in comparison to Ni, and even Cu (an MSE), any minerals in a source subjected to partial melting will retain their PGE loads until the point where the mineral host approaches full consumption (e.g., Barnes et al., 1985; Rehkämper et al., 1999; Righter et al., 2004; Naldrett, 2010; Prichard et al., 2013; Mungall and Brenan, 2014). Recent studies highlight some alternative processes and conditions that describe the upwards entrainment of PGE besides

degree of partial melting – mantle CO_2 fluxing asthenospheric sulphides (Blanks et al., 2020), post-subduction magma redistributing metals into the crust (Holwell et al., 2019) and intra-lithospheric redistribution of metals via carbonated melts (Aulbach et al., 2021).

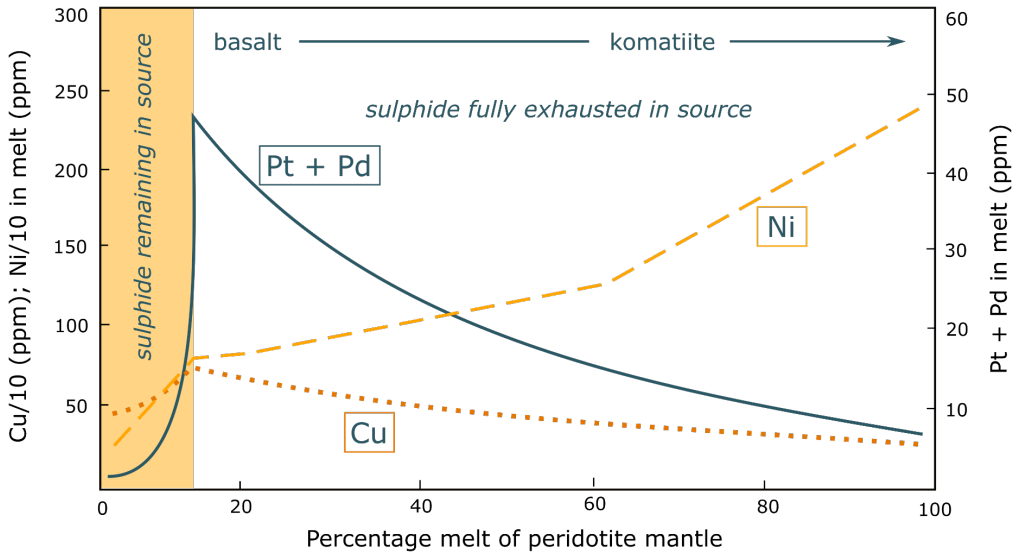

Figure 2.9 *– Concentrations of Pt, Pd, Ni and Cu in partial melts of a peridotite mantle source with increasing degrees of partial melting. Sulphide exhaustion in the source can release significant quantities of chalcophiles into melts previously locked within mantle phases, whilst Ni increases with increasing melting. Adapted from Naldrett (2010).*

The heterogeneity in mantle plume environments and the fractionation of PGE between different mantle phases leads us to consider the effects such variability has on PGE and HSE redistribution, summarised in a thought experiment in Figure 2.10. If plumes record different source signatures (potentially including core material and different mantle lithologies), it may be possible to establish a link between certain plume types (or specific plumes) and elevated precious metal abundances. Overall, we would expect the deepest-origin plumes (or those interacting with undepleted reservoirs) to contain higher concentrations of PGE than shallower-origin plumes (those with negligible contribution from enriched mantle components). Furthermore, plume environments featuring high degrees of partial melting, potentially as a result of an enhanced thermal anomaly, would be expected to liberate more PGE (both PPGE and IPGE) from the mantle into magmas. Finally, the lithology of the source being melted, and the assemblage of PGE-bearing minerals within (i.e.

lithospheric mantle vs. asthenosphere or peridotite vs. pyroxenite) will be expected to exert a control on the metal budget of magmas globally (e.g., Fiorentini et al., 2010; Fiorentini et al., 2011; Day et al., 2013; Barnes et al., 2015). These features are a key focus of the main body of this thesis, and will be explored in detail using several plume localities through Chapters 3 to 6, culminating in a global overview in Chapter 7.

The diversity of plume-derived magmas signal the significant fractionation of PGE between mantle phases, which reflect billions of years of mantle development and the impacts element compatibility has had on magmatic deposits on the surface. Despite being classified together as a chemically-similar unit, the intricacies of PGE geochemical behaviour fractionate the individual metals in magmatic systems (Figures 2.3, 2.9 and 2.10) and the relative concentrations of each PGE in intrusive and volcanic rocks provides a geochemical exploratory toolset to study the interior of the planet with (e.g., Lorand et al., 2008). By understanding fractionation patterns of PGE in magmatic rocks, we can imply the melting and geochemical history of the parental magmas.

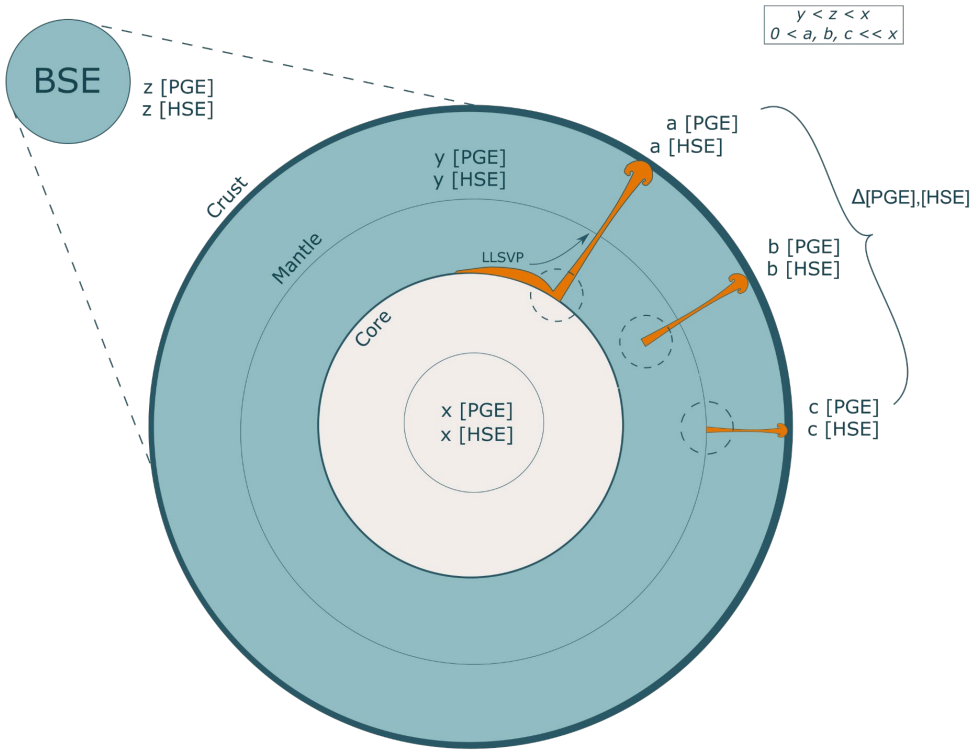

(Caption overleaf)

Figure 2.10 *– Theoretical considerations of plume PGE and HSE concentrations. The core contains the bulk of Earth's PGE (x), leaving the mantle (y) depleted. The modern mantle is significantly differentiated from earliest mantle (Bulk Silicate Earth - BSEE/Primitive Upper Mantle - PUM) concentrations (z). Plumes of different physical properties and of different origins are hypothesised to have different concentrations of PGE and HSE (a, b, c, etc.), as explored throughout this thesis, particularly Chapter 7.*

2.3.4. Lithospheric mantle

Although the conversation surrounding mantle heterogeneity generally involves deeper regions of the Earth, the lithospheric mantle is, although volumetrically much smaller and nearer surface, an important feature in the complete mantle story, especially when discussing PGE concentrations. As mantle convection, plate tectonics and plume cycles progress, the lithospheric mantle (i.e., the uppermost solid region of the mantle) inherits evolving geochemical changes as chemical components are melted, mobilised, removed or added (e.g., Downes, 2011; Wade et al., 2019). Geochemical processes beneath the continental and oceanic lithospheres vary as a function of physical conditions related to each. Continental lithosphere is generally older than oceanic lithosphere, as it is significantly more buoyant relative to the latter due to its average silica and alkali mineral dominated composition. This means that it is more difficult to subduct or destroy. Consequently, the subcontinental lithospheric mantle (usually referred to as the SCLM) below tends to be preserved over longer periods, assimilating geochemical characteristics with time as the continental lithosphere is subjected to collisions, rifting, melting and metasomatism (chemical interaction with fluids) (e.g., Lorand et al., 2004; Luguet and Reisberg, 2016). Although oceanic lithospheric mantle is subject to these same processes, the predominance of their density-driven subduction leads to their recycling into deeper mantle processes (e.g., Woodland et al., 2002; Willbold and Stracke, 2006) (Section 2.2).

Melting events and metasomatism in the SCLM in particular play key roles in PGE redistribution as an additional process to initial plume-derived transportation following core formation. Long-lived SCLM underneath stable continental cratons will become repositories for volatiles, melts and minerals stripped from subducted oceanic (and more dense continental) lithosphere, with new "enriched" SCLM mineral assemblages forming as a direct consequence

(e.g., Kepezhinskas et al., 2002; Rielli et al., 2018; Holwell et al., 2019). Metasomatism related to subduction or other tectonic events can dissolve, transport and deposit mobile elements throughout the SCLM using sub-lithospheric architecture (e.g., Larsen et al., 2003; Lorand et al., 2004; Powell and O'Reilly, 2007; Alard et al., 2011). Melting events, caused by mantle plumes or otherwise, can "pre-condition" the SCLM by preferentially melting and depleting more fusible mineral phases (e.g., Song et al., 2008; Fiorentini et al., 2020), changing the boundary conditions for further melting events potentially billions of years down the line (i.e., see Figure 2.9 for an account of sulphide exhaustion). Any of these process acting in the SCLM to reconfigure precious metal budgets can then be sampled by subsequent melts related to plume impingement beneath the lithosphere, and can promote the pre-emptive incorporation of precious metals into later melts at conditions contrary to those established in experimental settings (e.g., Handler and Bennett, 1999; Zhang et al., 2008; Wang et al., 2020a) (e.g. Section 2.1.2). The numerous processes that can contribute to the fertilisation of the SCLM can be preserved and recorded in xenoliths, chunks of the lithospheric mantle brought to the surface in magmas, in regions of sub-lithospheric melting (e.g., Delpech et al., 2012; Hughes et al., 2014; Maier et al., 2017; Aulbach et al., 2021). The role of the SCLM in global PGE prospectivity, especially when coupled with melting processes related to mantle plumes (i.e., Figure 1.2), is explored throughout this thesis, particularly Chapters 3, 6 and 7.

2.4. Isotope systems for plume studies

A variety of isotopic systems are central to the literature on mantle plumes, and are summarised herein.

2.4.1. Strontium, Neodymium and Lead systems

As discussed in Section 2.3.1, some common classifications of mantle components involve radiogenic Rb-Sr, Sm-Nd and various Pb systematics. These systems are incredibly diverse in terms of signatures generated in the mantle (Figure 2.8) and thus useful in determining the source of magmatic rocks, especially when their individual signatures are combined.

The Rb-Sr system primarily involves compatibility differences between parent (Rb) and daughter (Sr) isotopes and their fractionation within the Earth

(popularised by Steiger and Jäger, 1977). Unstable ^{87}Rb isotopes will stabilise as ^{87}Sr via beta decay (with a half-life of ~49 Gyr) (Long, 1964). Rubidium is more incompatible during partial melting of a silicate source rock, and will preferentially be concentrated in magmas, subsequently resulting in lavas and magmatic intrusions being enriched in radiogenic ^{87}Sr (which is normalised against ^{86}Sr; (Long, 1964; Minster et al., 1982). The upper mantle is normally Rb-depleted due to previous melting events throughout geological history, and the lower mantle is Rb-rich (Figure 2.11); this leads to low $^{87}Sr/^{86}Sr$ in MORB, high but variable $^{87}Sr/^{86}Sr$ in OIB (White and Hofmann, 1982; Zindler and Hart, 1986), and very high $^{87}Sr/^{86}Sr$ in continental crust formed from ancient melting events.

The Sm-Nd system (DePaolo and Wasserburg, 1976; Lugmair and Marti, 1978) is similar to Rb-Sr, but in reverse – the parent (^{147}Sm; half-life of ~100 Gyr) is compatible and the radiogenic daughter (^{143}Nd; produced via alpha decay and normalised by ^{144}Nd) is incompatible during partial melting (Arndt and Goldstein, 1987; DePaolo et al., 1991). This generates the negative relationship between $^{87}Sr/^{86}Sr$ and $^{143}Nd/^{144}Nd$ observed in Figure 2.11, which establishes a robust fingerprinting tool for MORB, OIB, mantle xenoliths, and oceanic and continental lithospheric material.

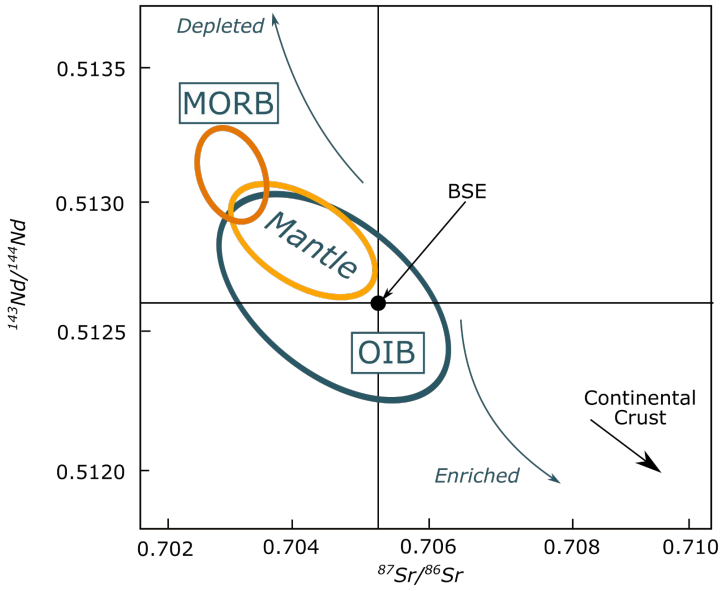

Figure 2.11 *– Summary of typical $^{87}Sr/^{86}Sr$ and $^{143}Nd/^{144}Nd$ values in the literature for MORB, OIB, BSE and mantle xenoliths, with an indication of depleted and enriched vector trends and continental crust values. Adapted from Rollinson (1993).*

In comparison to the Sr and Nd systems, there is a great deal of complexity in Pb isotopic systems, but the systematics of each branch have been studied for decades in a variety of contexts, most notably for dating early Earth processes and meteorites (Steiger and Jäger, 1977). Radiogenic daughter isotopes ^{206}Pb, ^{207}Pb and ^{208}Pb are created by extensive decay chains of unstable ^{238}U, ^{235}U and ^{232}Th isotopes, respectively (Tatsumoto et al., 1973). The ratios of radiogenic Pb isotopes to ^{204}Pb can describe a host of distinctive petrological and geochemical constituents in parent magmas, implying the presence of recycled lithosphere and sediments in OIB, usually alongside Sr-Nd systematics (Zindler and Hart, 1986; Holm, 1988; Rollinson, 1993; Peate and Stecher, 2003; Stracke et al., 2005). The Sr-Nd-Pb sequence has been vital for the description of mantle domains through decades of literature and have become the most robust, commonly used and widely understood isotope dating techniques available.

2.4.2. Osmium systems

The Re-Os isotope system has been extensively developed as a geochemical tool since the 1960s (Hirt et al., 1963) after decades of slow progress, when new thermal ionisation technology allowed for the accurate detection of these very low concentration elements for the first time (Creaser et al., 1991). Rhenium-187 decays to ^{187}Os via beta decay with a half-life of ~42 Gyr (Figure 2.12) (Hirt et al., 1963) and unlike other isotope systems used in geochemistry, parent and daughter have different compatibilities during mantle melting and can be segregated further than simply by D values. Rhenium is more incompatible than Os and is more likely to be carried to the surface in silicate melts (Shirey and Walker, 1998). The resultant crust formed from melts is thus enriched in Re relative to Os by a ratio of around 50:1 (Esser and Turekian, 1993). In the literature, ^{187}Os was normalised by stable ^{186}Os in early analytical work, but ^{188}Os has become the more popular and accepted stable denominator in recent years (Walker et al., 1991).

It is sometimes convenient to compare measured ^{187}Os/^{188}Os at a given time (t) to the near-chondritic modern mantle ratio of 0.12753 (Shirey and Walker, 1998) as 'γ-Os':

$$\gamma Os(t) = \left\{ \left[\frac{^{187}Os}{^{188}Os_{sample(t)}} / \frac{^{187}Os}{^{188}Os_{chon(t)}} \right] - 1 \right\} X\ 100$$

Modern upper mantle sources, from which multiple melting events have depleted Re (and other incompatible elements) over time, have very low $^{187}Os/^{188}Os$ (defining the baseline for γ-Os), while lower mantle sources that have only been melted to very low degrees have more Re and higher $^{187}Os/^{188}Os$ (positive γ-Os) (Hawkesworth and Scherstén, 2007). After lithosphere formation and subsequent recycling of plates back to the core-mantle boundary (CMB), the lower mantle is thought to inherit the positive γ-Os values of the lithosphere (Esser and Turekian, 1993). Plume magmas tend to have variable but positive γ-Os, which can be attributed to either the direct assimilation of recycled material or potentially outer core entrainment, where the original stock of HSE were stored before the late veneer (e.g., Brandon et al., 1999). Owing to their compatibilities with solid and liquid metal, Re is concentrated in the liquid outer core, while Os is concentrated in the solid inner core. The outer core consequently is estimated to have a higher $^{187}Os/^{188}Os$ than the inner core (Brandon et al., 1998). Crust, core material and ambient mantle thus all have distinctive Os isotopic signatures that can be used to pinpoint the source of plume components in their resultant intraplate lavas. Platinum-190 decays to ^{186}Os with a half-life of ~500 Gyr, and acts as a supplementary signature for more robust HSE characters of Earth components, based on the IPGE/PPGE partitioning behaviour of Os and Pt, respectively (e.g., Brandon et al., 1998; Brandon and Walker, 2005; Puchtel et al., 2009; Meisel and Horan, 2016). Together, the coupled ^{186}Os and ^{187}Os signatures of a magma can help reduce errors in interpretations, as Os is a particularly difficult element to accurately measure and the two isotope systems can complement each other (Brandon et al., 1998).

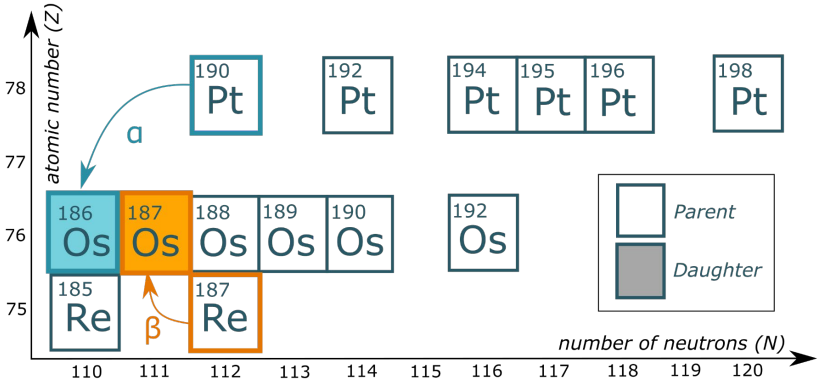

Figure 2.12 *– Nuclide chart for Re-Os and Pt-Os decay chains, contributing to 187Os/188Os and 186Os/188Os systematics, respectively.*

2.4.3. Hafnium-Tungsten system

Hafnium, a lithophile transition metal, was notably present as ^{182}Hf during the accretionary stage of Earth formation. Experimentally, it has been determined that due to a small half-life (8.9 ± 0.1 Myr; Kleine et al., 2009), ^{182}Hf would have become extinct within 50-60 Myr of solar system formation, stabilising as ^{182}W via beta decay (Walker et al., 2015) (Figure 2.13). This is a unique system, given that W is a MSE and Hf is a lithophile – any radiogenic ^{182}W produced from ^{182}Hf would have been exclusively found in the mantle, unlike the original non-radiogenic W that would have been sequestered to the core during planetary accretion (Kleine et al., 2009). Given that ^{182}Hf was only extant for the first 60 Ma of Earth's history (the same duration of core completion), the core should be almost devoid of radiogenic W (and therefore have a very low $^{182}W/^{184}W$ ratio) (Walker, 2009).

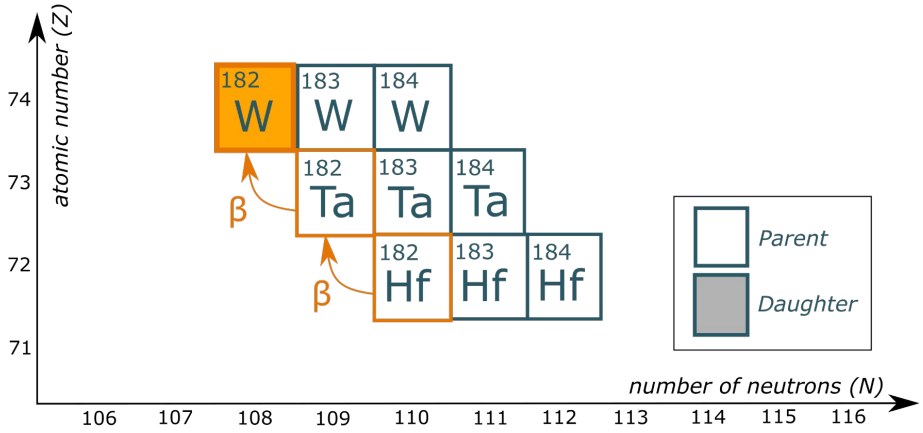

Figure 2.13 *– Nuclide chart for Hf-W decay chain, within 182Hf/184Hf systematics.*

The mantle will have produced a great deal of ^{182}W over time, given that it would have retained close to all ^{182}Hf in the accreting planet, and will have been depleted in the stable isotope ^{184}W, which is found in the core in higher abundance (Jones et al., 2019). '$\varepsilon^{182}W$' is shorthand for a measured $^{182}W/^{184}W$ against a chondritic standard (Kleine et al., 2009):

$$\varepsilon^{182}W = \left\{\left[\frac{^{182}W}{^{184}W_{sample}} / \frac{^{182}W}{^{184}W_{chon}}\right] - 1\right\} X\ 10^4$$

The late veneer would have brought extra siderophiles to the Earth post-core formation, and any ^{184}W added to the mantle will lower $^{182}W/^{184}W$ (Marchi et al., 2017). Thus, a downwards shift in $^{182}W/^{184}W$ of mantle rocks between 4 and 3 Ga (coupled with a similar $^{143}Nd/^{144}Nd$ decrease) signifies the arrival of post-core formation material (Willbold et al., 2011). It is postulated that entrainment of core material in deep magmatic plumes would produce lavas or intrusions with $\varepsilon^{182}W < 1$ (Jones et al., 2019) although this has been found to be difficult to fingerprint precisely (Willbold et al., 2011).

2.4.4. Helium system

Isotopes of He provide auxiliary information about mantle sources when combined with Sr, Nd, Os, W or Pb systems (de Leeuw et al., 2017; Mundl-Petermeier et al., 2019). Helium is a noble gas - chemically inert and atomically stable without the need for bonding. For this reason, much of Earth's He has been lost through time to the atmosphere and space, unable to be incorporated into crystal matrices as easily as H or O (Hopp and Trieloff, 2005; Moreira et al., 2012). It exists in ^{3}He and ^{4}He on Earth. Alpha particles emitted by U/Th-Pb radioactive decay systems create new ^{4}He atoms, with 2 protons and 2 neutrons. As radiogenic alpha particles are emitted constantly by the Earth, new ^{4}He is added to the planet's stockpile, while both ^{3}He and ^{4}He are being degassed from Earth as a whole (Ozima and Podosek, 1983; Anderson, 1998). The $^{3}He/^{4}He$ ratio ('R' ratio) of the Earth is slowly decreasing due to no new ^{3}He not being created (Anderson, 1998). However, it is postulated that the lower mantle is less successfully degassed than the upper mantle, and less prone to radiogenic ^{4}He addition given the incompatible nature of U and Th (Moreira et al., 1999). Theoretically, the lower mantle should have higher R in comparison to the atmospheric He ratio (Ra) for this reason. Courtillot et al. (2003) state that a high $^{3}He/^{4}He$ ratio is indicative of a classic deep-origin mantle plume signature, found in some of the most well-studied hotspot localities such as Hawaii, Iceland, the Canary Islands and Réunion (e.g., Mukhopadhyay et al., 2003; Hopp and Trieloff, 2005; Starkey et al., 2009; Day and Hilton, 2011; Day and Hilton, 2020). Where data are available, $^{182}W/^{184}W$ and $^{3}He/^{4}He$ are inversely correlated; previously Hf-poor magmas (lacking in radiogenic ^{182}W) are also ^{3}He-rich (Mundl et al., 2017) and this could be a robust indicator of source depth (Jones et al., 2019).

2.5. PGE ore deposits

A key consideration prior to the presentation of new research findings in this thesis is the relevance of the world's 'classic' PGE ore bodies, the processes that generated them, and their place within the broader context of precious metal distribution through Earth. Case studies of two major PGE-bearing ore deposits, the Skaergaard and Noril'sk Talnakh Intrusive Complexes (Table 2.2), are presented below and feature two notable similarities, as introduced in Chapter 1 – (i) they are associated with intraplate magmatism and LIP, and (ii) they reside within the ancient cratonic lithosphere. This thesis is focused on investigating how relevant each of these features are in global ore genesis [O1-O4] [H1-H3] (Chapter 1), especially in relation to the geochemistry of associated lavas. The deposits provide a unique perspective on the conditions optimal to PGE mineralisation at surface in each case, and the geochemical links they share with their respective LIP.

2.5.1. PGE mineralisation processes and the link to flood basalts

The 55 Ma Skaergaard Intrusion is located on the eastern coast of Greenland amongst the magmatic rocks of the North Atlantic Igneous Province (NAIP; McKenzie and White, 1989; Saunders et al., 1997; Jerram et al., 2009). The intrusion features a unique, continuous layered mafic intrusive body (~280 km^3; Nielsen, 2004), within which resides horizons enriched in Au and PGE, in particular, Pd (Bird et al., 1991; Andersen et al., 1998; Nielsen et al., 2014; Andersen et al., 2017). Protracted *in situ* fractional crystallisation of a single parental magma (i.e., a closed magmatic system) in a large oval-shaped chamber produced distinctive mineral assemblage horizons through Bowen's reaction series (i.e., olivine, pyroxene and plagioclase with minor magnetite and chromite; Wager and Brown, 1968; Bowen, 1979; McBirney and Noyes, 1979). Elements that are incompatible in these silicate phases, including S and chalcophiles, became progressively enriched in the residual silicate liquid until the point of S-saturation (Andersen et al., 1998; Momme et al., 2002b; Tegner et al., 2009; Holwell et al., 2012; Andersen et al., 2017). Following this point, Pd-Au alloys crystallised within BMS alongside the normal fractionating phases, concentrated into the sub-horizontal Platinova reefs (Andersen et al., 1998; Nielsen et al., 2014).

Due to its remote location, Skaergaard is not mined for PGE but represents a significant economic-grade stock of precious metals, with an estimated bulk 2 ppm of both Au and Pd within the reefs and ~90 million tonnes of ore-grade material (Andersen et al., 1998; Andersen et al., 2002). Similar layered PGE-bearing intrusions can also be found on the other side of the Icelandic plume, on the Isles of Rum, Skye and Mull in Scotland (Butcher et al., 1999; Pirrie et al., 2000; O'Driscoll et al., 2009; O'Driscoll et al., 2010) and the NAIP of Northern Ireland has been the focus of exploration for PGE mineralisation for decades.

Table 2.2 *– Summary of key characteristics of two major PGE ore bodies related to flood basalt provinces – the Skaergaard Intrusion* (Andersen et al., 1998; Andersen et al., 2002; Tegner et al., 2009) *and Noril'sk Talnakh* (Naldrett, 1997; Arndt et al., 2003)*. NAIP – North Atlantic Igneous Province, BMS – base metal sulphides, FC – fractional crystallisation, AFC – assimilation and fractional crystallisation. *Noril'sk Talnakh comprises multiple branches with average dimensions given here.*

	Skaergaard	**Noril'sk Talnakh**
Location	East Greenland	Siberia
LIP	NAIP	Siberian Traps
Age (Ma)	55	250
Size (approx.)	11x8x4 km	15x2x0.2 km*
Mineralisation	Pd-Au	Ni-Cu-PGE
Host	BMS	BMS
Mechanism	FC, closed system	AFC, sulphur addition

Lavas surrounding Skaergaard exhibit PGE-enriched signatures (Momme et al., 2002a; Momme et al., 2002b) and share isotopic characteristics with the intrusion and other smaller Greenlandic dykes and sills nearby. The shared parent magmas from the proto-Icelandic plume melting event beneath Laurentia (>60 Ma) evidently contained elevated precious metal abundances at source, which were then drawn out and focused via chromitite formation within intrusive bodies (Kent and Fitton, 2000; Andersen et al., 2002; Power et al., 2003). Studies

appear to link the incorporation of heterogeneously-enriched SCLM in asthenospheric partial melts beneath Greenland, Ireland and Scotland to elevated PGE concentrations in continental NAIP lavas (Hughes et al., 2014; Hughes et al., 2015), a concept explored in Chapters 5-7.

Noril'sk Talnakh, a 250 Ma complex network of magmatic conduits, including dykes and sills within the Siberian Traps continental flood basalt (CFB) province (Lightfoot and Keays, 2005; Sobolev et al., 2009; Izokh et al., 2016), contains PGE-sulphide enriched horizons within individual intrusion branches including the eponymous Noril'sk and Talnakh intrusions (Naldrett et al., 1992; Arndt et al., 2003; Li et al., 2009). Sulphide saturation occurred within the intrusive plume-derived Siberian magmas due to significant crustal contamination on late-stage ascent by assimilated sulphur-rich gypsum-anhydrite country rock, forming an immiscible sulphide liquid(s) exsolved from the silicate magma(s) within certain intrusion branches (Lightfoot et al., 1993; Wooden et al., 1993; Ripley et al., 2003; Li et al., 2009; Keays and Lightfoot, 2010). The geometry of numerous channels within the complex acted as physical traps for the immiscible sulphide liquid, leading to accumulate and crystallise as flat, pod- or lens-like massive ores (hosting the PGE) at the base of individual gabbroic intrusions (Naldrett et al., 1992; Naldrett, 1997; Kerr and Leitch, 2005; Li et al., 2009; Maier and Groves, 2011). The majority of Noril'sk PGE are held within Cu-rich minerals and pentlandite, with as much as 0.13 wt.% Pt and 4.62 wt.% Pd in single pentlandite crystals (Brovchenko et al., 2020).

The surrounding Siberian lavas share geochemical characteristics with the Noril'sk Talnakh intrusions, but unlike Skaergaard, the connection between intrusive and extrusive chemistry is more direct given that Noril'sk is thought to be a feeder system to the flood basalts (Arndt et al., 2003). The intrusions, which lie ~ 1 km below the Siberian Traps, detail the strong partitioning of chalcophile elements into the in-situ BMS deposits within the crust (Naldrett, 2010). Lavas above the intrusions are consequently depleted in Ni, Cu and PGE by 50-90 % compared to the metalliferous intrusive bodies, illustrating the significant fractionation of such elements in the event of S-saturation and sulphide immiscibility (Lightfoot and Keays, 2005; Lightfoot, 2007; Izokh et al., 2016). The abundance of sulphur and the stages of S-saturation can be traced through the stratigraphic lava sequence and correlated directly with ore-bearing horizons in

the intrusion using palaeomagnetic data (Latyshev et al., 2020) – the appearance of S-saturated lavas on the surface coincide with the most highly mineralised intrusions at depth.

The examples of Skaergaard and Noril'sk Talnakh highlight the importance of considering the metallogenesis of LIP as a whole, beyond the localised ore bodies. Although the two ore deposits represent the optimisation of different crustal-level mineralisation processes in intraplate settings, the magmatic system responsible for their genesis, represented by the composition of related flood basalts, likely exerts a control on regional magma fertility prior to PGE mineralisation.

2.5.2. Intraplate PGE Mineral Systems

In this section, intraplate magmatic events are considered as potential Mineral Systems, based on the framework introduced by studies such as (McCuaig et al., 2010). The placement of Skaergaard and Noril'sk Talnakh within relatively young (< 250 Ma) CLIP suggests some commonality to the PGE fertility of these regions and intraplate magmatism, and Maier and Groves (2011) suggest an apparent connection between mantle plumes and PGE mineralisation on a global scale. Whilst the exact crustal mechanisms and mineralisation styles vary between Skaergaard and Noril'sk Talnakh, they both likely featured (i) precious metal fertility of the parent magmas and the mantle source; (ii) sufficient pathways to transport metal-bearing agents (i.e., magma) to the lithosphere; and (iii) efficient geochemical and physical processes leading to fractionation and 'deposition' (mineralisation) of PGE into focused ore bodies (Wyborn et al., 1994; McCuaig et al., 2010).

Figure 2.14 provides an example of a Mineral Systems approach to Ni-sulphide mineralisation in komatiites from McCuaig et al. (2010), highlighting the components necessary at different scales to generate a Ni-bearing orebody. This ranges from source and pathway characteristics on a district (i.e., regional) scale, pathways and chemical processes at a camp (i.e., local) scale, and physical processes at a prospect (i.e., ore deposit) scale. This is provided as an example of a Mineral Systems model only, as an equivalent diagram does not yet exist for PGE mineralisation. Throughout the course of this thesis, the various research

contributions will be used to consider the same diagrammatic format for PGE systems, and a complete model encompassing various intraplate mineralisation processes will be suggested as a final chapter output. Unlike Ni in magmas, when dealing with HSE (and specifically PGE), sulphide exhaustion (and mobilisation of PGM) of a mantle source (Figure 2.2) is an important control on magma fertility and thus every subsequent stage in a potential Mineral System. This enforces a strict district-scale control on the success of a potential PGE Mineral System at the earliest stages, and highlights the degree of partial melting as a vital component in precious metal liberation from the mantle. The opposite is true for crystallisation – PGE and Au will be sequestered into sulphides as soon as they become a fractionating phases (i.e., upon sulphide saturation), and the timing of this is key for crustal levels in the Mineral System (Barnes et al., 1985; Naldrett, 2010; Mungall and Brenan, 2014).

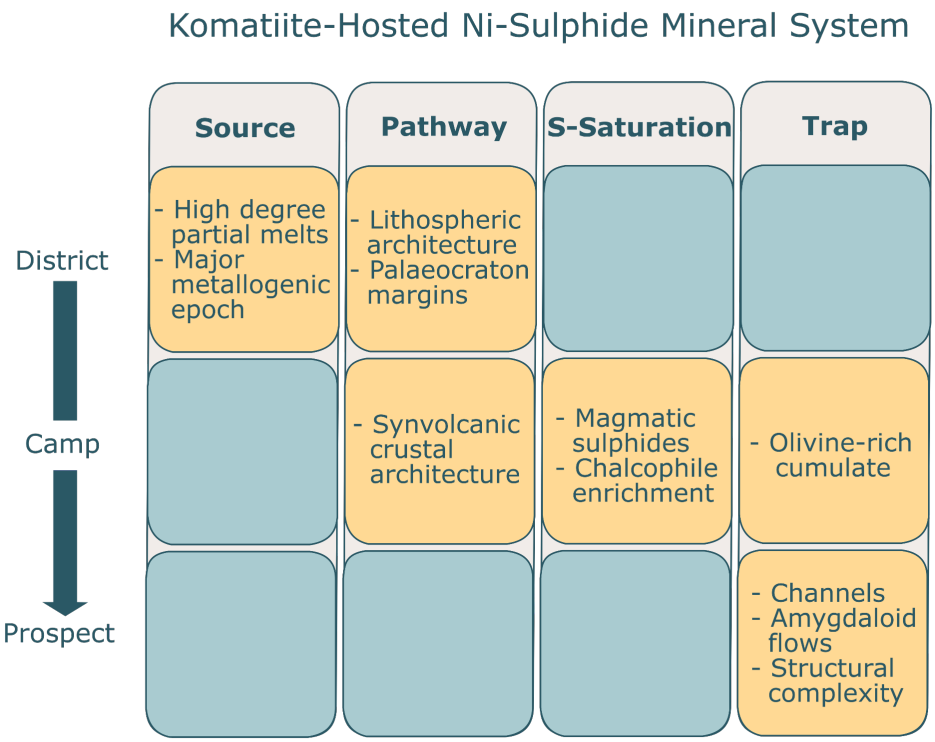

Figure 2.14 *– Generalised example of the source, pathway and depositional characteristics of a komatiite-hosted Ni-sulphide Mineral System, with critical steps at various scales of targeting (from district to camp to prospect scale). Orange boxes denote critical steps in the system, whilst blue boxes signify that a certain system component is less relevant at the given scale. A successful Ni orebody will see the features of all orange boxes present within a magmatic environment. Adapted from McCuaig et al. (2010).*

The link between coeval lavas and ore bodies has been demonstrated for metalliferous intrusions, and forms a cornerstone of this thesis – by investigating the detailed bulk geochemistry of easily-accessible, well-preserved flood basalts within LIP, we can infer characteristics of parent magmas in the region. Given that the bulk geochemistry of both Greenlandic and Siberian lavas synergise with signatures from the Skaergaard and Noril'sk intrusions, respectively, our study aims to investigate lavas from similar provinces to identify key metallogenic features in regions of significant enrichment. Through the course of this thesis, the contributing factors to intraplate PGE metallogenesis will be considered in detail for specific localities, in wider plume settings and finally on a global scale, to arrive at a Mineral Systems interpretation for such environments in Chapter 7. This can plausibly act as an early-stage exploratory tool for likely sites of PGE mineralisation.

2.6. Machine learning in geochemistry

Presentation of trends, patterns and general interpretations of large data sets can involve challenges in terms of computational capacity and general efficiency for analysts. This is particularly true when dealing with geochemical data sets that can often contain concentrations for over 50 measured elements for hundreds or thousands of samples (Davis, 2002). This thesis presents novel ways to approach such data by turning to modern applications of data science to streamline and enhance geochemical analyses.

2.6.1. Machine learning categories

Machine learning is an umbrella term for a vast sub-section of data science that primarily deals with pattern recognition in large data sets (Ripley, 1996; Hastie et al., 2009; Marsland, 2009). Machine learning algorithm(s) (MLA) have been developed for decades to assist in data interpretation and are now more accessible than ever before due to data-sharing capabilities afforded by open-access learning, and the leap in computational power, especially on desktop machines. This opens up new methods of analysis to more traditional branches of science. There are ample opportunities to incorporate cutting-edge MLA into geological, geochemical, geophysical and geospatial investigations to increase to impact of the contributions made to our collective knowledge as we venture

into a future dominated by computer-based learning. This thesis suggests a simple, novel approach to geochemistry using MLA that can be applied to a variety of similar studies, and aims to demonstrate the utility of data science within geosciences.

There are three major categories of MLA – supervised, unsupervised and reinforcement (Figure 2.15). Supervised MLA must be trained to recognise patterns in a portion of the project data (the training set) before making predictions or interpretations about the remainder of the data; a popular example of this is regression analysis. Unsupervised MLA do not require *a priori* information to run and are primarily used to classify or 'cluster' similar data points in a population without the need to train beforehand (Ripley, 1996; Hastie et al., 2009; Marsland, 2009). The algorithms can thus objectively create clusters in data using any number of metrics, but do so on the entire data set at once. Whilst human analysts can conceivably construct clusters based on bivariate relationships in data, as is often done in geochemistry using two-dimensional discriminant plots, the true utility of unsupervised clustering MLA lies in their ability to classify data across many more than two variables simultaneously (Iwamori et al., 2017). A human brain cannot easily comprehend relationships beyond three dimensions, but trends will exist between elements in as many dimensions present within a data set (i.e., the number of elements measured). It is this field of machine learning that most appeals to the work contained within this thesis and geochemistry as a whole – unsupervised MLA can detect relationships in sample geochemistry across all measured elements at once, revealing a plethora of previously undetectable information in an efficient manner (Ripley, 1996; Clare and Cohen, 2001; Wagstaff et al., 2001). This not only provides information beyond our understanding of two-dimensional geochemical relationships, but also resolves previously available trends in a much quicker timeframe.

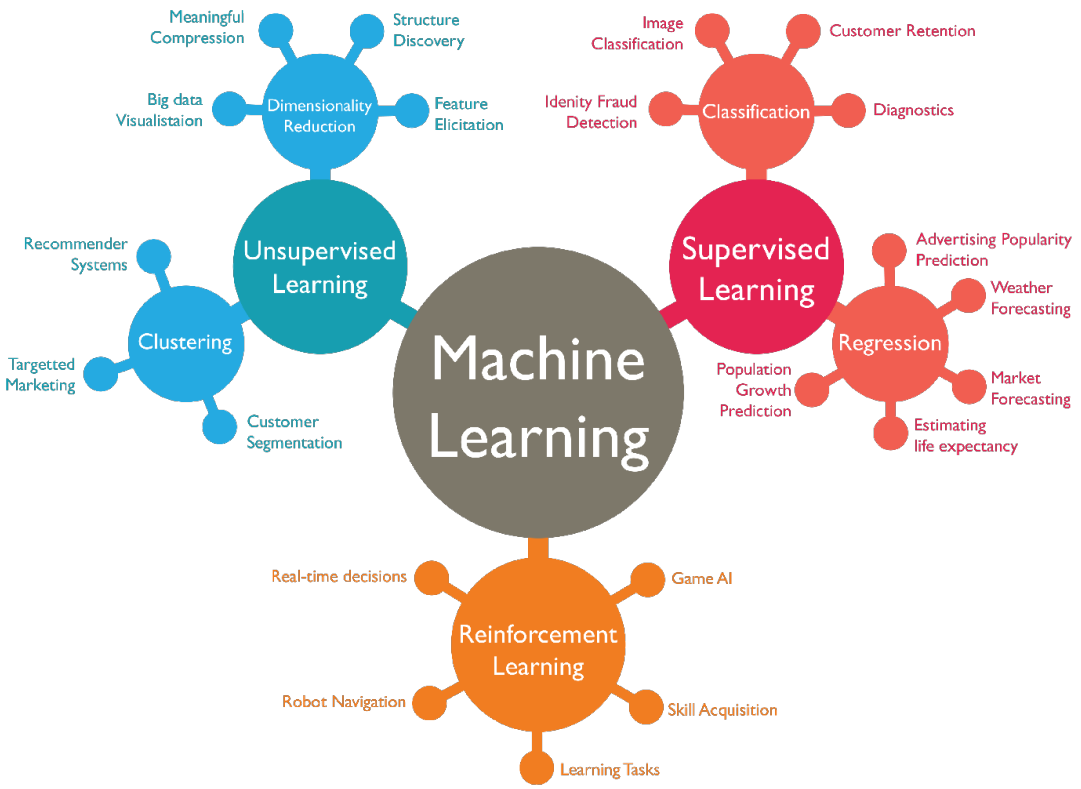

Figure 2.15 *– The three major branches of machine learning algorithms (MLA) – supervised, unsupervised and reinforcement. Examples are given for applications of these MLA in modern society, generally outside geoscience. This thesis focuses on unsupervised MLA for clustering and dimensionality reduction (Wahid, 2017).*

Some data scientists consider a further example of unsupervised MLA in *dimensionality reduction* (Figure 2.15), although the exact placement within the machine learning bracket can vary depending on the individual (Wahid, 2017; Bushkovskyi, 2020). Dimensionality reduction offers a means of presenting information regarding the high-dimensional trends inherent in a large data set, by visualising results in an easily digestible manner (as per the simple example in Figure 2.16) (Nguyen and Holmes, 2019). Techniques like Principal Component Analysis (PCA) and t-Distributed Stochastic Neighbour Embedding (t-SNE) can analyse said trends whilst presenting the information in a two-dimensional space, portraying high-dimensional interpretations in more classic plots (Jolliffe, 2002; van der Maaten and Hinton, 2008; Abdi and Williams, 2010; van der Maaten, 2014). As such, dimensionality reduction plays a crucial role in bridging the gap between machine learning and geoscience within this thesis, illustrating complex information in logical and visually-impactful diagrams.

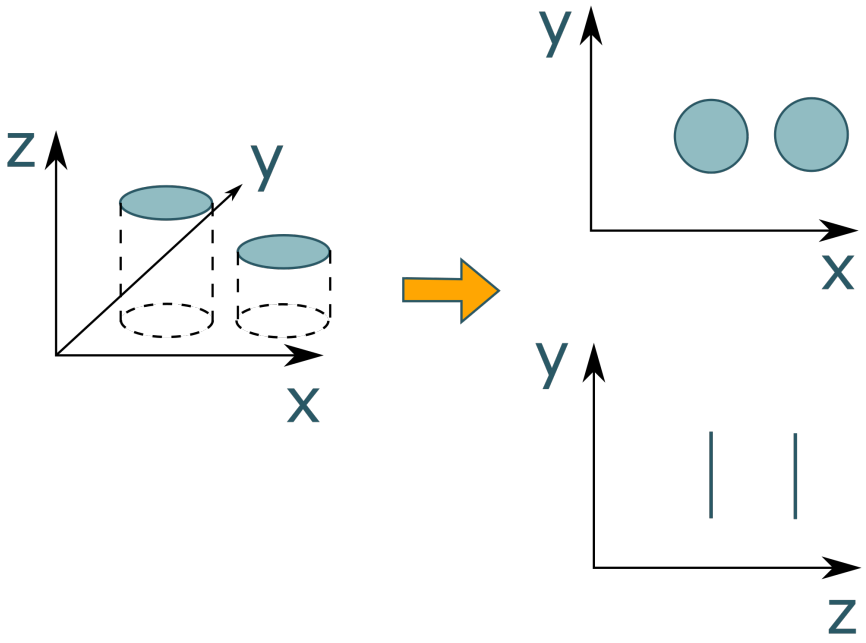

Figure 2.16 *– A simple demonstration of dimensionality reduction. In this example the three dimensional shape of the blue disc in translated into two lower-dimension plots. Dimensionality reduction can resolve much higher dimension trends than this with small computational intensity. Adapted from Bushkovskyi (2020).*

Reinforcement MLA use a complex interplay of learning and exploitation via data interaction and feedback loops to make highly efficient frameworks for data analysis (Marsland, 2009). Perhaps the most mechanically advanced of the three branches, reinforcement MLA share many similarities with artificial intelligence (AI) in that they adapt to information in a dynamic manner to predict outcomes from a variety of parameter inputs (Dayan and Niv, 2008). Ultimately, reinforcement MLA help to recognise optimal process pathways that maximise positive outcomes and minimise negative outcomes in a system via a holistic approach. These algorithms can be model-based or model-free and are particularly useful for neuroscience, biochemistry and medical applications, in addition to economics, mathematics, robotics, psychology and videogame AI (Andrew, 1999; Wahid, 2017).

2.6.2. Applications of machine learning in geoscience

Machine learning is already well-integrated in bioscience research (reviewed in Ching et al., 2018; Webb, 2018; Zitnik et al., 2019). The geosciences feature a steadily increasing incorporation of MLA into research frameworks, with more contributions towards uniting the fields of data science and Earth Science studies appearing every month. Some pertinent examples are described below:

- Mapping geochemical domains using supervised MLA as an efficient means of digital geological surveying, advancing classic interpolation techniques like kriging (Cracknell, 2014; Kirkwood et al., 2016).
- Mapping rock hydration processes using unsupervised MLA in an attempt to isolate base metal anomalies from a large set of element concentrations, for use in mineral exploration (Horrocks et al., 2019).
- Exploring known regions of active or historic mining and using supervised MLA to predict areas of undiscovered mineralisation from a wide range of geospatial variable inputs (Cracknell and de Caritat, 2017; Yeomans et al., 2020).
- Estimating values of missing variables in core logging or groundwater geochemical surveys (amongst other applications) using regressive relationships as analysed by the Random Forest supervised MLA (Schnitzler et al., 2019) and multi-variate analysis (Farnham et al., 2002).
- Classifying seismic events and eruptive responses of the Cotopaxi Volcano (Ecuador) using unsupervised *k*-means clustering on a variety of geophysical input variables (Duque et al., 2020)
- Modelling the predicted petrological implications of a variety of global geodynamic and magmatic systems using dimensionality reduction techniques (Rummel et al., 2020).
- Identifying anomalous metal enrichment throughout stream-sediment samples using various dimensionality reduction techniques as a vectoring system towards polymetallic mineralisation (Zuo, 2011; Ghannadpour et al., 2013; Liu et al., 2016; Wang et al., 2017; Zuo, 2017; Steiner et al., 2019; Wang et al., 2020b).
- Building a petrological database for lunar and Martian basalts using unsupervised dimensionality reduction techniques, allowing for the establishment of detailed multi-element domains on the surface of the

moon in response to variable magmatic processes (Taylor et al., 2010; Cone et al., 2020).

- Creating a robust multi-variable barometer for diamond-hosted garnet formation in deep mantle pressure conditions (Thomson et al., 2021).

The relevance and importance of machine learning in the geosciences cannot be overstated, and has led to the inclusion of the final research objective for this thesis found in Section 1.2.

Considering the scope of this study, and the large database of geochemical information generated as part of the objectives, the inclusion of machine learning into the analytical process allowed for efficient data processing and presented a different perspective on geochemical problems central to the investigation. Chapter 5 details the testing of the bespoke workflow (which is focused exclusively on unsupervised MLA), and assesses the pros and cons of such an approach. Ultimately, this chapter serves as the blueprint for all subsequent MLA-based content in the thesis (Chapters 6 and 7), and should be referred to as both a methodological framework and a research-based study with significant impacts for the overarching geochemical and geodynamic themes of the project.

Chapter 3

Platinum-group element geochemistry of the Paraná flood basalts - modelling metallogenesis in rifting continental plume environments

Chapter Summary

The 135 Ma Paraná-Etendeka Large Igneous Province (PELIP) is one of the largest areas of continental flood basalt (CFB) volcanism in the world and is widely agreed to be a product of intracontinental melts related to thermal anomalies from Tristan mantle plume. The province rifted during the break-up of Gondwana, as the plume transitioned into an oceanic geodynamic environment. This chapter defines three distinct metallogenic groupings using a newly analysed geochemical suit for the mafic lavas (the Serra Geral Group) that fit with modern multi-element magma classifications in Licht (2018). *Type 4* lavas contain a distinctive PGE-poor signature, *Type 1 (Central-Northern)* lavas are enriched in Pd, Au and Cu, and *Type 1 (Southern)* lavas are enriched in Ru and Rh. New quantitative trace element melt modelling indicates that the differing compositions result from changes in the melting regime between the garnet and spinel stability fields, in response to the thinning and 'unlidding' of the rifting lithosphere above. This imposes progressively shallower melting depths and higher degrees of partial melting for the CFBs. *Type 1 (Central-Northern)* magmas incorporated components of sub-continental lithospheric mantle (SCLM)-derived partial melts. The SCLM was heterogeneously enriched prior to plume melting, and this provided enrichment in volatile metals (Pd, Cu, and Au) to these magmas. In contrast, the Ru-Rh enrichment in *Type 1 (Southern)* lavas is attributed to increased spinel-group mineral *and* sulphide incorporation in even higher degree partial melts close to the continental rift zone. Modelling in this chapter confirms the importance of SCLM melts in precious metal abundances within CFB provinces, and reinforce the role of heterogeneous metasomatic enrichment underneath cratons in boosting intracontinental melt prospectivity.

3.1. Introduction

Many of the world's important magmatic sulphide deposits are found within continental flood basalt (CFB) provinces (e.g., Lightfoot et al., 1993; Naldrett, 1997). Whilst the mineralisation processes at work in each CFB are primarily controlled by mid- to upper-crustal differentiation mechanisms (e.g., Thompson and Gibson, 1991; Ellam, 1992; Maier and Groves, 2011), the initial geochemical fingerprint of CFB magmas can have important implications for metallogenic fertility and understanding how metals are mobilised from the mantle (e.g., Hawkesworth et al., 1988; Wooden et al., 1993; Wilson et al., 1996; Bierlein et al., 2009). Localities with prominent PGE orthomagmatic sulphide deposits share a similar geodynamic setting, with plume-derived (i.e., intraplate) magmas interacting with thick continental cratons. Plumes represent buoyant material from mantle discontinuities that rise to the base of the lithosphere (e.g., Morgan, 1971; Morgan, 1972; Shannon and Agee, 1998; Jellinek and Manga, 2004; Burke et al., 2008; Deschamps et al., 2011; Li and Zhong, 2017), inducing partial melting and magma generation in the asthenosphere and lowermost lithosphere (Jerram and Widdowson, 2005 and references therein). Decompression models for CFB melting predict ~ 5 % of the lithosphere (particularly the sub-continental lithospheric mantle or SCLM) is involved in melt generation, and this is isolated to the initiation stages of rifting (e.g., McKenzie and White, 1989; White and McKenzie, 1995; Turner et al., 1996; Howarth and Harris, 2017). A spatial association between PGE-rich ore deposits and Archaean lithosphere has previously been noted, indicating that the 'inheritance' of precious metals may play an important role in dictating aspects of the geochemistry of plume-derived magmas and mineralisation (e.g., Downes, 2001; Hawkesworth and Scherstén, 2007; Zhang et al., 2008; Maier and Groves, 2011; Maier et al., 2012; Griffin et al., 2013; Barnes et al., 2015), although the relationship is still being explored.

Here, we examine the nature of the interaction between plumes and the SCLM and its potential role as a control on PGE (and other metal) abundances within CFB parental magmas. Work on the North Atlantic Igneous Province (NAIP) demonstrates that in plume environments that transition from continental to oceanic settings, changes in the thickness of lithosphere above the melt region and the degrees of partial melting directly affect the PGE geochemistry of ascending plume-derived magmas (e.g., Andersen et al., 2002; Hughes et al.,

2015). Continental lavas from Greenland and the British Isles exhibit distinctly higher Pt/Pd ratios than oceanic lavas from Iceland, attributed to a shifting “metal basket” (i.e., the concentration and variety of precious and/or base metals) and variable SCLM incorporation in partial melts (Hughes et al., 2015). In this chapter, we investigate lavas associated with the Tristan plume and the Paraná-Etendeka Large Igneous Province (PELIP) in the South Atlantic in order to test how (if) the PGE, Au and base metal geochemistry of the CFB province changes through time and space. The PELIP shares a similar transitional continent-to-ocean geodynamic setting to the NAIP. If the inherent controls of trace element and isotopic variation in regional magmas reflect distinct geodynamic controls, this should be evident in highly siderophile and chalcophile elements. New geochemical data for onshore South American PELIP flood basalts are compared and used in quantitative geochemical melt modelling, to assess how PGE geochemistry changes through the evolution of the CFB province, with a focus on the link between variable SCLM properties and resulting partial melt compositions.

3.1.1. Formation of the Paraná-Etendeka Large Igneous Province

Currently positioned in the centre of the southern Atlantic Ocean, the Tristan plume has migrated through a cratonic, to continental margin, to mid-oceanic setting throughout the Cretaceous and Cenozoic (Fodor and Vetter, 1984). It is active today under the islands of Tristan da Cunha and Gough, but has a > 130 million year history of volcanism that spans two continents and the entire width of the South Atlantic (Stewart et al., 1996). The plume head stage is thought to be responsible for the eruption of the PELIP, one of the largest CFB provinces in the world (Courtillot et al., 2003), in addition to the Rio Grande Rise and Walvis Ridge topographic features on the ocean floor (e.g., Camboa and Rabinowitz, 1984; O’Connor and Duncan, 1990; Ussami et al., 2013) (Figure 3.1a). The Tristan plume is one of the world’s “primary hotspots” according to Courtillot et al. (2003), satisfying the criteria of creating linear chains of age-progressive volcanics, exhibiting large flood basalt buoyancy flux, high $^{3}He/^{4}He$ isotope ratios and significant low shear wave velocity anomalies in the mantle below.

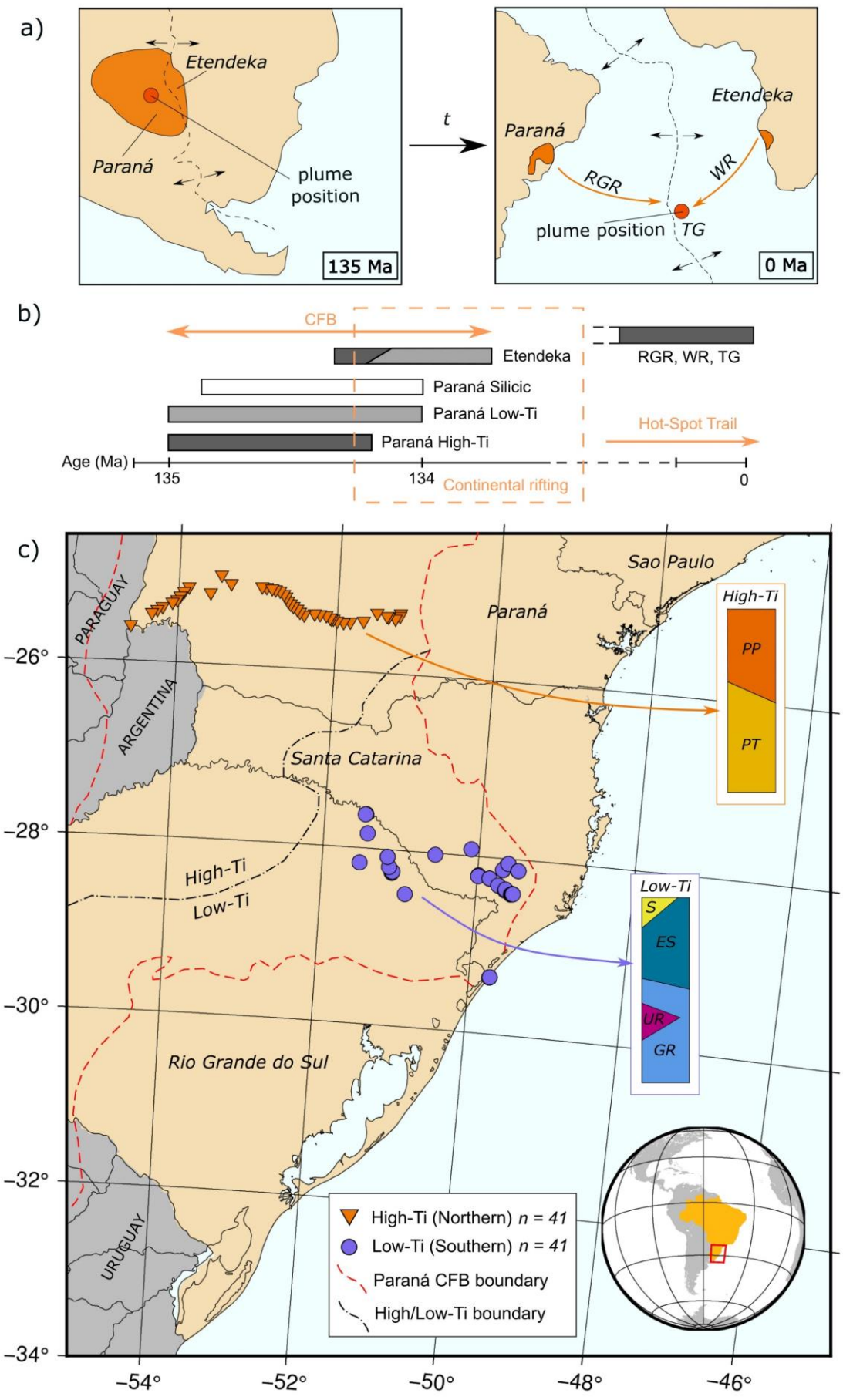

(Caption overleaf)

Figure 3.1 – (*a) Schematic map showing the eruption of the Paraná-Etendeka flood basalts over the conjoined South American and African continents (135 Ma) and their current formation with the Rio Grande Rise (RGR), Walvis Ridge (WR) and Tristan-Gough islands (TG) in between. (b) Representative summary timeline of eruptive products of the PELIP with incipient rifting. (c) Sample map for this study (Paraná region) with High-Ti and Low-Ti provinces and CFB boundaries. Markers denote sample localities – see Supplementary S3.1 for further sample details. Representative stratigraphy is given for the north and south with magma-types classified as: north - Pitanga (PT) and Paranapanema (PP); south - Gramado (GR), Esmeralda (ES), Urubici (UR) and Silicic (S), based on Turner et al. (1999).*

The ~ 1.7 km^3 PELIP is spread asymmetrically between (primarily) Paraná, Brazil and Etendeka, Namibia (which were conjoined in the Cretaceous; Figure 3.1a), with fifteen times higher volume of lavas found in South America than Africa (Fodor et al., 1989). Intraplate magmas are typically chemically variable and are derived from relatively undepleted mantle (e.g., Zindler and Hart, 1986; Stracke et al., 2005; Hawkesworth and Scherstén, 2007). The Tristan plume arrived at the Gondwanan lithosphere under the modern day central Paraná region in Brazil ca. 135 Ma, inducing partial melting in the asthenosphere (Stewart et al., 1996). The duration of eruption of the onshore PELIP has been debated, ranging from < 1 million years (suggesting a high eruption rate of around 1.5 km^3/year; Renne et al., 1996) to 10 million years (suggesting a much lower eruption rate of under 0.1 km^3/year; Stewart et al., 1996). Recent studies suggest a conservative 0.8 km^3/year for the majority of the flood eruption (Beccaluva et al., 2020), comparable to other CFB provinces, such as those that produced the Deccan and Karoo traps (Natali et al., 2017 and references therein). This eruption rate is slightly higher than the NAIP (a mean of 0.6 km^3/year; Eldholm and Grue, 1994).

From 134 to 128 Ma (Stewart et al., 1996), rifting initiated in the thermally thinned Gondwanan continental lithosphere (e.g., McKenzie and White, 1989; Turner et al., 1996; de Wit et al., 2008). North-westerly plate movement migrated plume activity to the Etendeka-Angola margin, synchronous with the eruption of the south-eastern lavas in Paraná (Beccaluva et al., 2020) (Figure 3.1b). Following significant extension and basin formation as the South American and African continents drifted apart (Martins-Ferreira et al., 2020 and references therein), the asthenosphere above the Tristan plume continued to undergo partial

melting and eruption of lava on the seafloor throughout the Cretaceous. Sustained volcanism formed ridges on either side of the mid-oceanic rift, the Rio Grande Rise (west) and the Walvis Ridge (east) that connect the PELIP to the modern active hotspot islands of Tristan da Cunha and Gough (e.g., O'Connor and Duncan, 1990; O'Connor and Jokat, 2015; Homrighausen et al., 2019). Figure 3.1b summarises the different stages of PELIP magmatism with respect to congruent rifting.

3.1.2. Geochemical classification of the Paraná flood basalts

The South American portion of the PELIP erupted over the Botucatu Sandstones and Proterozoic basement of the Paraná Basin. The basin is oriented NE-SW with its morphology controlled by three major underlying structures – the Ponta Grossa and Rio Grande arcs, and the Torres Trough (e.g., Cordani and Vandoros, 1967; Peate et al., 1992; Besser et al., 2018). On average, the basin-filling lavas in the region are > 1 km thick overall, and up to 1.7 km towards the north (Gordon, 1947; Leinz, 1949; Leinz et al., 1966; Peate et al., 1990). The Paraná lavas, referred to more formally as the Serra Geral Group in Brazil (e.g., Licht, 2018; Rossetti et al., 2018), are primarily basaltic to basaltic-andesitic and compositionally grouped into High-Ti (HT) in north-central Paraná and Low-Ti (LT) in the south-east. Volcanism in the south-east laterally evolved into bimodal mafic-felsic volcanism, producing significant amounts of silicic lavas (e.g., Peate et al., 1992; Polo et al., 2018).

Given that the Serra Geral lavas are thought to have erupted simultaneously throughout the province via different melting sources rather than by differentiation processes from a single source (Peate, 1997), the underlying stratigraphy of the Paraná Basin is complex (Turner et al., 1999; Rossetti et al., 2018). The literature supports the theory that the synchronous HT and LT lavas were erupted from separate sub-surface magma plumbing systems spawned from plume-derived melting, and followed separate magmatic differentiation routes (Natali et al., 2016; Licht, 2018), with rare evidence for minor interaction between HT and LT magmas in plumbing systems (De Min et al., 2017). It is generally agreed that the HT and LT split represents spatial compositional zoning in the mantle plume and subsequent localised melting processes. LT magmas reflect higher degrees of crustal contamination in contrast to limited (or absent) crustal contamination for the HT magmas (e.g., Piccirillo et al., 1988; Peate et al.,

1992; Peate and Hawkesworth, 1996; Turner et al., 1996; Rocha-Júnior et al., 2013; Natali et al., 2017; Marques et al., 2018). Whilst the mafic Serra Geral lavas are similar in both hand specimen and thin section, the magma-types exhibit slight differences in modal mineralogy and larger differences in bulk geochemical compositions. Consequently, pioneering studies on the geochemistry of the Serra Geral Group further classified the HT, LT and silicic magma-types based on major and trace element, and isotopic variations (e.g., Bellieni et al., 1984; Fodor, 1987; Peate et al., 1992; Peate, 1997). With time, increasingly more sophisticated distinctions across multi-element parameters have been sought (e.g., the sixteen Si-Ti-Zr-P divisions introduced by Licht, 2018). A generalised northern and southern stratigraphy for Serra Geral is given in Figure 3.1c.

3.1.3.1. Low-Ti Group

The LT lavas comprise around 50 % of the total eruptive volume of the Serra Geral Group and are found in the south of the CFB province. Over a third of the total lava volume belongs to the Gramado magma-type, and 5-10 % to the Esmeralda magma-type (Peate et al., 1992). As per Peate (1997), both magma-types see distinctive enrichment of heavy rare earth elements (HREE) and large-ion lithophile (LIL) elements relative to high field strength (HFS) elements and light rare earth elements (LREE), and a negative Ti anomaly when normalised against mantle compositions. Esmeralda has highly variable εNd, while maintaining consistent initial Sr isotope values (with $(^{87}Sr/^{86}Sr)_i$ = 0.7046-0.7086; Peate et al., 1992). Gramado lavas have the lowest TiO_2 concentrations and εNd in the Serra Geral sequence, and higher and much more varied $(^{87}Sr/^{86}Sr)_i$ ratios (0.7075-0.7167) relative to Esmeralda, which sets it apart from all other mafic lavas in the Serra Geral Group (Peate and Hawkesworth, 1996). The Gramado magma-type is considered to be formed from the most crust-contaminated Tristan plume-derived magmas. In the southern Paraná Basin, Gramado is normally found on the flanks of the Serra Geral escarpment and at the coast near Torres, whilst Esmeralda is found on the flatter plateau tops (Peate, 1997). This reflects their general relative positioning within the lava pile but not strictly their stratigraphy as per Figure 3.1c. Recent studies have further subdivided Gramado into the Torres and Vale do Sol Formations in the modern framework (Rossetti et al., 2018 and references therein). The Gramado and Esmeralda magma-types

comprise the Type 1 (Southern) classification from Licht (2018) (< 2.85 wt.% TiO_2).

Rarely found exposed at the surface, the LT Ribeira lavas have low TiO_2 concentrations, but slightly higher Ti/Y than Gramado and Esmeralda (Ti/Y ratio has occasionally been used in place of TiO_2 as a more specialised LT/HT group discriminator - Peate et al., 1992; Peate and Hawkesworth, 1996). In contrast, the LT Ribeira ($^{87}Sr/^{86}Sr)_i$ signature is more in line with HT magma-types (0.7055-0.7060 compared to 0.7046-0.7167 for LT; Peate et al., 1992), but lacks the accompanying HFS and LREE enrichment expected of the HT group. Despite having more in common geochemically with the LT group, the transitional Ribeira lavas are found interbedded with HT lavas in the northern zone (Peate et al., 1992), essentially an intermediate lava overlapping the geochemical properties of both HT and LT magma-types.

3.1.3.2. High-Ti Group

Like the LT lavas, the HT lavas are classified into three major magma-types – Paranapanema, Pitanga and Urubici. Pitanga and Urubici lavas have the highest TiO_2 concentrations (> 3 wt.%) (Peate et al., 1992). Pitanga and Paranapanema are found exposed almost exclusively in central-northern Paraná, while Urubici outcrops between the LT and HT provinces as shown in Figure 3.1c (Peate et al., 1999), often intercalated with LT flows. Paranapanema lavas belong to the HT group despite having a lower TiO_2 concentration than the other two HT members (between Esmeralda and Pitanga at 1.7-3.2 wt.%; Peate, 1997) and being found throughout the region. Urubici is significantly enriched in LREE and HFS in comparison to the other HT lava magma-types (Peate et al., 1999). It is suggested that lower oxygen fugacity in the Urubici magma source could have been a factor in its trace element enrichment (Bellieni et al., 1984). Pitanga is generally slightly more enriched than Paranapanema in most trace elements, excluding the transition metals Ni, Co, Cr and Sc (Rocha-Júnior et al., 2013).

Despite major and trace element differences, the three magma-types have similar isotopic signatures, leading to them being grouped together as the “northern basalts” in many early Sr-Nd-Pb isotope studies (e.g., Richardson et al., 1982; Peate et al., 1992; Peate and Hawkesworth, 1996). Licht (2018) classifies Urubici and Pitanga as Type 4 (> 2.85 wt.% TiO_2) and Paranapanema

as Type 1 (Central-Northern) (< 2.85 wt.% TiO_2), a significant distinction from classic studies. Paranapanema and Pitanga each contribute to 20 % of the total Serra Geral volume, and Urubici contributes ~ 5 %. Urubici lavas are the most sparsely observed at surface, although it is seen in the highlands of São Joaquim and as sills interbedded with Vale do Sol in the south-east of the CFB province (Besser et al., 2018). Paranapanema overlies Pitanga throughout most of the flood sequence; however, it underlies Gramado in the very south of the basin (Bellieni et al., 1984).

3.1.3.3. Silicic Group

Mafic lavas in central and southern Paraná are often associated with the silicic lavas of the Chapecó and Palmas magma-types, mainly within the bimodality of south-eastern LT group (Figure 3.1c) (e.g., Bellieni et al., 1984; Peate et al., 1990; Peate et al., 1992; Garland et al., 1995; Peate, 1997). Chapecó lavas are higher in TiO_2 than Palmas, and their relative geographic location mimics that of the mafic HT/LT split, placing Chapecó further northwest than its counterpart. The rhyolites, dacites and related alkali complexes of Paraná have been dated to co-exist with the pre-rift stages of flood basalt volcanism, which further reinforces the complexity of the multi-source melting beneath the province – the silicic lavas are likely derived from mid- to upper-crustal differentiation processes from the source of flood basalt volcanism (e.g., Milner et al., 1995b).

The Serra Geral silicic rocks have been interpreted to be genetically related to their mafic equivalents via fractional crystallisation – Chapecó represents partial melt extraction in HT basalts in the lower crust whilst Palmas represents the differentiation of LT basalts in the upper crust (Garland et al., 1995). Licht (2018) provided distinctions for eight high-Si magma-types with varying Zr, TiO_2 and P_2O_5 concentrations – Palmas fits within Type 9 and Chapecó within Type 14, and they contribute to around 20 % of samples classified in the region. However, as silicic rocks are very rarely associated with PGE mineralisation, the focus of this chapter lies on the mafic magma-types whilst using these more evolved compositions as reference material for geochemical trends. The specific and intricate high-Si magma-types described by Licht (2018) are insignificant for our purposes.

3.2. Materials and Methods

3.2.1. Sample acquisition

This chapter presents a new suite of major, trace and PGE data for 85 basalt and 7 rhyolite samples from the Serra Geral Group. Samples were collected during two field expeditions, one in the north (focusing on HT lavas of Paraná State) and one in the south (focusing on LT and Silicic groups of the Santa Catarina and Rio Grande do Sul States). Figure 3.1c shows the general sample localities within the context of the Paraná Basin, with reference to underlying lava group. A complete sample database with field descriptions is provided in Supplementary S3.1.

3.2.2. Laboratory techniques

Weathered material and amygdales were removed from all samples prior to preparation, as these would interfere with primary geochemical concentrations. Rock samples were crushed to 1-2 mm chips using a jaw crusher before being milled in a chrome-steel TEMA mill to produce fine powders, which were used in all subsequent bulk geochemical analyses.

Major element oxides were measured using X-ray fluorescence (XRF) (after Kystol and Larsen, 1999; Tegner et al., 2009) at Camborne School of Mines, University of Exeter. Dried and ignited samples were fused in a furnace in platinum crucibles with lithium borate flux. Ammonium iodide solution was added to the molten sample to act as a wetting agent when poured into moulds. Cooled samples were analysed at 50-111 mA and 27-60 kV using a Bruker S4 Pioneer XRF spectrometer. Concentrations were corrected to anhydrous values. The AGV-1, BHVO-2, BIR and DNC-1 standards were used in analyses. Trace elements were measured using inductively coupled plasma mass spectrometry (ICP-MS) (after McDonald and Viljoen, 2006), also at Camborne School of Mines. Powdered samples were dissolved using 4-Acid digestion technique, and elemental concentrations were detected by an Agilent 7700 Series mass spectrometer. The BCR-2 and Bir-1a standards were used in analyses.

The PGE (Os, Ir, Ru, Rh, Pt, Pd) plus Au were measured using Ni-S fire assay followed by tellurium co-precipitation and ICP-MS analysis at Cardiff University (using methods developed by Huber et al., 2001; McDonald and

Viljoen, 2006). Fifteen grams of sample was mixed with 12 g of borax flux, 6 g $NaCO_3$, 0.9 g solid sulfur, 1.08 g Ni and 1 g silica, before being melted in a furnace at 1000°C for 1.5 hours. The sulfide bead separated from the cooled melt was removed, dissolved in hydrochloric acid, co-precipitated with Te, filtered and diluted before element detection using a mass spectrometer. It should be noted Os was not measured for the northern sample set due to method availability at the time of analyses. The TBD1 and WPR1 standards were used in analyses. Detection limits (i.e., lowest recorded blank values) were 0.0052 ppb for Os, 0.0026 ppb for Ir, 0.0603 ppb for Ru, 0.0152 ppb for Rh, 0.1458 ppb for Pt, 0.0662 ppb for Pd and 0.0070 ppb for Au. Full raw major, trace and PGE-Au data, plus standard measurements for each method are available in Supplementary S3.3. An amalgamated data sheet with duplicate measurements is available in Supplementary S3.4.

3.2.3. Petrology of samples

In general, basalts from each magma-type are aphyric/fine- to medium-grained with small phenocrysts of pyroxene or plagioclase (up to 1 mm), and are exceptionally fresh for lavas of their age (alteration information in Appendix A1). In thin section, olivine is notably sparse or absent in most mafic rocks, with orthopyroxene (normative 10-30 wt.%), clinopyroxene (normative 5-40 wt.%), plagioclase (normative 20-50 wt.%), and spinel-group minerals (normative 1-5 wt.%) dominating in the majority of samples. Silicic rocks (likely rhyolites to dacites) are fine grain-sized, with plagioclase (20-30 wt.%), clinopyroxene (~ 10 wt.%) and magnetite (1-5 wt.%) phenocrysts, in a plagioclase-quartz-K-feldspar groundmass. Volcanic glass and quartz-feldspar aggregates (spherulites) are common throughout. Chapecó samples have larger and more frequent plagioclase phenocrysts than Palmas. There are no visible sulphides in any of our Serra Geral hand specimens, but rare traces (< 1 wt.%, < 0.1 mm crystals) can be found in thin sections.

We have used a combination of two classification schemes alongside sampling locations in order to utilise the wealth of literature already available describing the characteristics of lavas belonging to each magma-type. In this way, we can contextualise subtleties in the dataset according to PGE and Au and therefore metallogenic processes in the new precious metal data set. Accordingly, lava samples have been classified into their classic magma-types

(except Ribeira, which wasn't sampled) based on bulk concentrations of MgO and TiO_2, plus Ti/Y and Ti/Zr ratios (established by Peate et al., 1992) and MgO vs. Zr, with literature data used for comparison (Figure 3.2a-c; Supplementary S3.2). Classifications from Licht (2018) are also given for each sample (denoted by symbology), based on Si, Ti, Zr and P concentrations. The inherent issue with classifying samples based on limited bivariate relationships is evident – samples SG11-12, SG56 and SG78-79 do not conform to the Peate et al. (1992) classification for example, and thus their designation was assessed subjectively based on adjacent literature data clouds for the purpose of this study; Licht (2018) classifications are wider, but more robust.

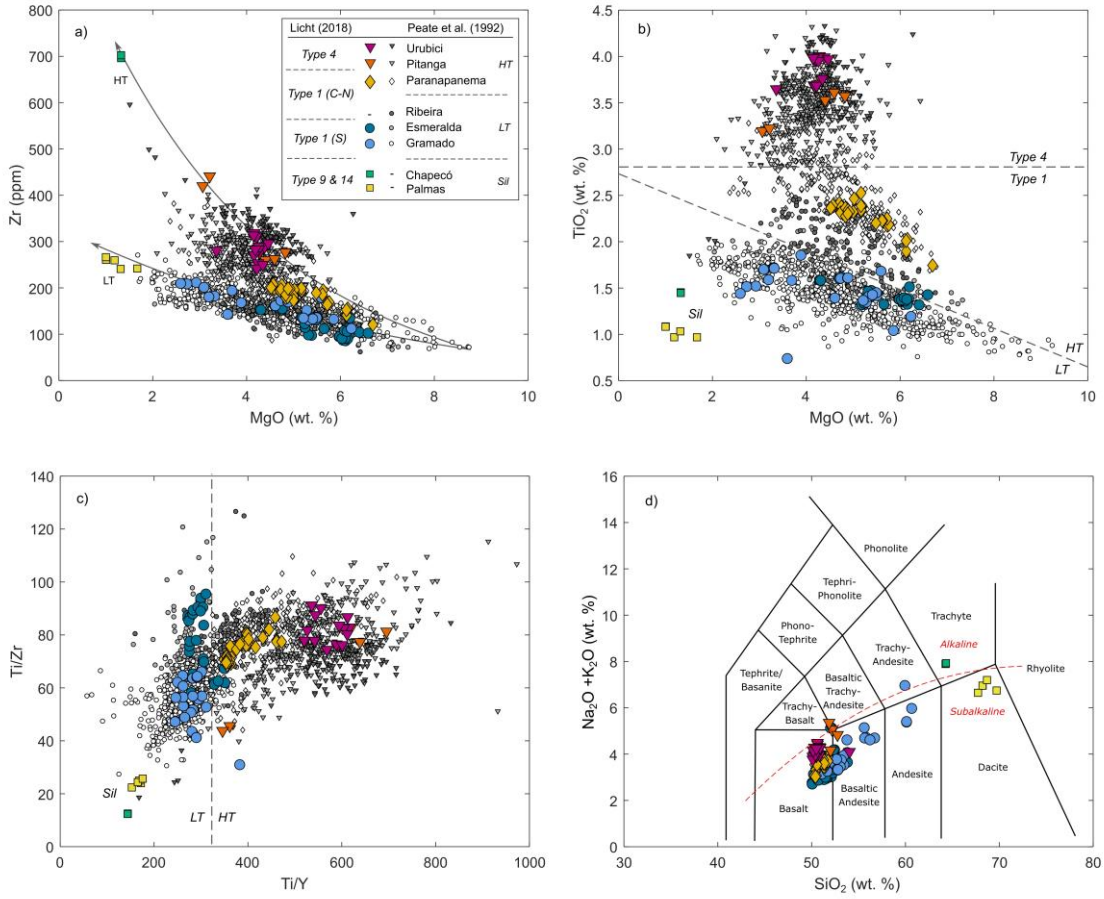

Figure 3.2 – *Classification diagrams based on Peate et al. (1992): (a) MgO vs. Zr; (b) MgO vs. TiO_2; (c) Ti/Y vs. Ti/Zr. (d) Total Alkali vs. Silica (TAS) petrological/geochemical discriminant diagram for the Serra Geral sample set. Colours refer to Peate classifications and symbols for Licht classifications as per the legend in 3.2a. Dashed lines for approximate HT/LT division are from Peate (1997). Dashed lines for approximate Type 1 and 4 division (2.85 wt. % TiO_2) from Licht (2018). Arrows refer to approximate development trajectory. In the key, dashes indicate that no data was*

Figure 3.2 (cont'd) - *available for that particular magma-type either in this study (large coloured markers) or the literature (small greyscale markers). Literature database with references is provided in Supplementary S3.2.*

The sample set is also classified using a total alkali vs. silica (TAS) plot in Figure 3.2d. The mafic samples are predominantly basalts to basaltic andesites, with some Gramado samples classifying as andesites. Palmas samples plots within the dacitic field, while the two Chapecó samples plot with trachytes. All Paraná lavas analysed fall within the sub-alkaline to transitional alkali-tholeiitic fields.

3.3. Results

3.3.1. Major and trace element geochemistry

3.3.1.1. Major element oxides

Table 1 displays mean concentrations for all sampled Serra Geral lava classifications. A selection of anhydrous major element bivariate plots for the Serra Geral samples are shown in Figures 3.3a-h against MgO concentrations. Serra Geral basalts tend to have MgO concentrations consistently between 2 and 7 wt.%; silicic lavas plot between 1 and 2 wt.% MgO. Concentrations of TiO_2 highlight the established literature magma-types – > 3 wt.% for Urubici/Pitanga or Type 4, 1.5-2.5 wt.% for Paranapanema or Type 1 (Central-Northern), and < 1.5 wt.% for Gramado/Esmeralda or Type 1 (Southern), plus the silicic lavas (Figure 3.3a). All basic lavas exhibit Fe_2O_3 between 10 and 16 wt.% (Figure 3.3b), with HT samples generally higher than LT. In Figure 3.3c, LT lavas exhibit higher Al_2O_3 concentrations than HT lavas (the opposite to Fe_2O_3), with a slightly positive relationship with MgO; MnO concentrations follow this same slight positive relationship but between 0.15 and 0.35 wt.% (Figure 3.3d). There is a distinctly positive correlation between MgO and CaO (Figure 3.3e), and negative correlations between MgO and Na_2O (Figure 3.3f), and MgO and K_2O (Figure 3.3g) do not show clear HT-LT distribution patterns. Finally, P_2O_5 exhibits a bifurcated negative trend with MgO, with a shallow slope for LT and silicic lavas, and a steeper slope for HT lavas (Figure 3.3h).

Table 1 – *Mean concentrations for major element oxides, trace elements and PGE for all Serra Geral magma-types (full data in Supplementary S3.4). S – Southern, C-N – Central-Northern, GRA- Gramado, ESM – Esmeralda, PAR – Paranapanema, PIT – Pitanga, URU – Urubici, PAL – Palmas, CHA – Chapecó. * - Total Fe oxides.*

	Low-Ti		**High-Ti**			**Silicic**	
	Type 1 (S)		**Type 1 (C-N)**	**Type 4**		**Type 9 & 14**	
	GRA	**ESM**	**PAR**	**PIT**	**URU**	**PAL**	**CHA**
wt.%							
SiO_2	54.62	51.73	50.90	51.64	50.72	68.51	64.29
Al_2O_3	13.82	13.85	12.84	12.84	12.51	12.86	13.43
Fe_2O_3*	12.78	13.68	15.21	14.05	15.17	6.50	7.48
MgO	4.46	5.67	5.22	4.18	4.19	1.24	1.32
CaO	8.10	10.14	9.15	7.83	8.19	2.93	3.22
Na_2O	2.69	2.46	2.50	2.66	2.64	3.07	3.66
K_2O	1.55	0.90	1.15	1.95	1.45	3.84	4.25
TiO_2	1.48	1.42	2.27	3.49	3.86	1.03	1.45
MnO	0.20	0.21	0.22	0.18	0.20	0.11	0.15
P_2O_5	0.23	0.18	0.27	0.67	0.58	0.30	0.45
SO_3	0.06	0.07	0.01	0.05	0.02	0.07	0.01
LOI	0.98	0.56	0.55	0.70	0.69	1.01	0.68
Total	100.02	100.33	99.78	99.64	99.62	100.5	99.84
ppm							
Sc	34	37	42	28	33	15	15
V	348	365	466	327	435	81	34
Cr	52	81	74	42	12	53	6
Co	41	44	52	39	46	11	13
Ni	39	63	57	38	33	46	2
Cu	159	245	257	239	204	190	9
As	5.5	14.1	0.5	6.3	0.5	30.0	0.4
Se	3.2	2.8	3.1	5.5	4.3	4.5	7.0
Rb	52	27	29	44	37	137	85
Sr	261	188	287	570	507	109	342
Y	32	29	35	42	40	37	60
Zr	165	113	183	327	284	254	699

Nb	11	7	13	26	17	21	60
Te	0.04	0.06	0.01	0.02	0.02	-	-
Ba	376	217	332	617	568	578	1085
La	25	14	23	47	42	38	72
Ce	52	30	49	103	89	74	142
Pr	6.5	4.0	6.4	13.1	11.6	9.4	19.8
Nd	26	17	27	55	49	35	81
Sm	5.9	4.4	6.3	11.9	10.4	7.8	16.8
Eu	1.65	1.41	2.00	3.67	3.27	1.62	4.58
Gd	6.3	5.2	7.1	11.5	10.4	7.6	15.8
Tb	0.94	0.81	1.09	1.56	1.45	1.14	2.22
Dy	6.14	5.45	6.85	8.99	8.37	7.04	12.66
Ho	1.24	1.12	1.37	1.67	1.56	1.40	2.35
Er	3.53	3.20	3.98	4.46	4.28	3.97	6.49
Tm	0.50	0.46	0.54	0.58	0.55	0.58	0.86
Yb	3.27	2.96	3.62	3.62	3.55	3.72	5.50
Lu	0.49	0.44	0.53	0.51	0.50	0.56	0.77
Hf	4.55	3.20	4.69	8.21	7.05	7.09	16.83
Ta	1.30	0.91	1.21	2.04	1.29	1.87	4.52
W	7.79	3.80	20.68	8.59	8.84	0.76	45.78
Pb	14.7	17.7	3.7	14.4	5.9	33.1	8.9
Bi	0.09	0.13	0.02	0.07	0.03	0.44	0.02
Th	5.69	2.70	2.39	4.34	3.82	10.83	8.01
U	1.38	0.65	0.52	0.96	0.85	3.76	1.89
ppb							
Os	0.27	0.30	-	0.37	-	-	-
Ir	0.26	0.29	0.09	0.22	0.04	-	0.03
Ru	2.24	2.88	0.27	1.27	0.22	-	0.13
Rh	1.14	1.08	0.53	0.86	0.16	-	0.10
Pt	9.06	6.72	10.47	4.50	2.93	-	2.90
Pd	4.76	4.90	16.17	2.30	2.29	-	2.87
Au	2.53	2.32	6.46	1.88	2.71	-	3.12

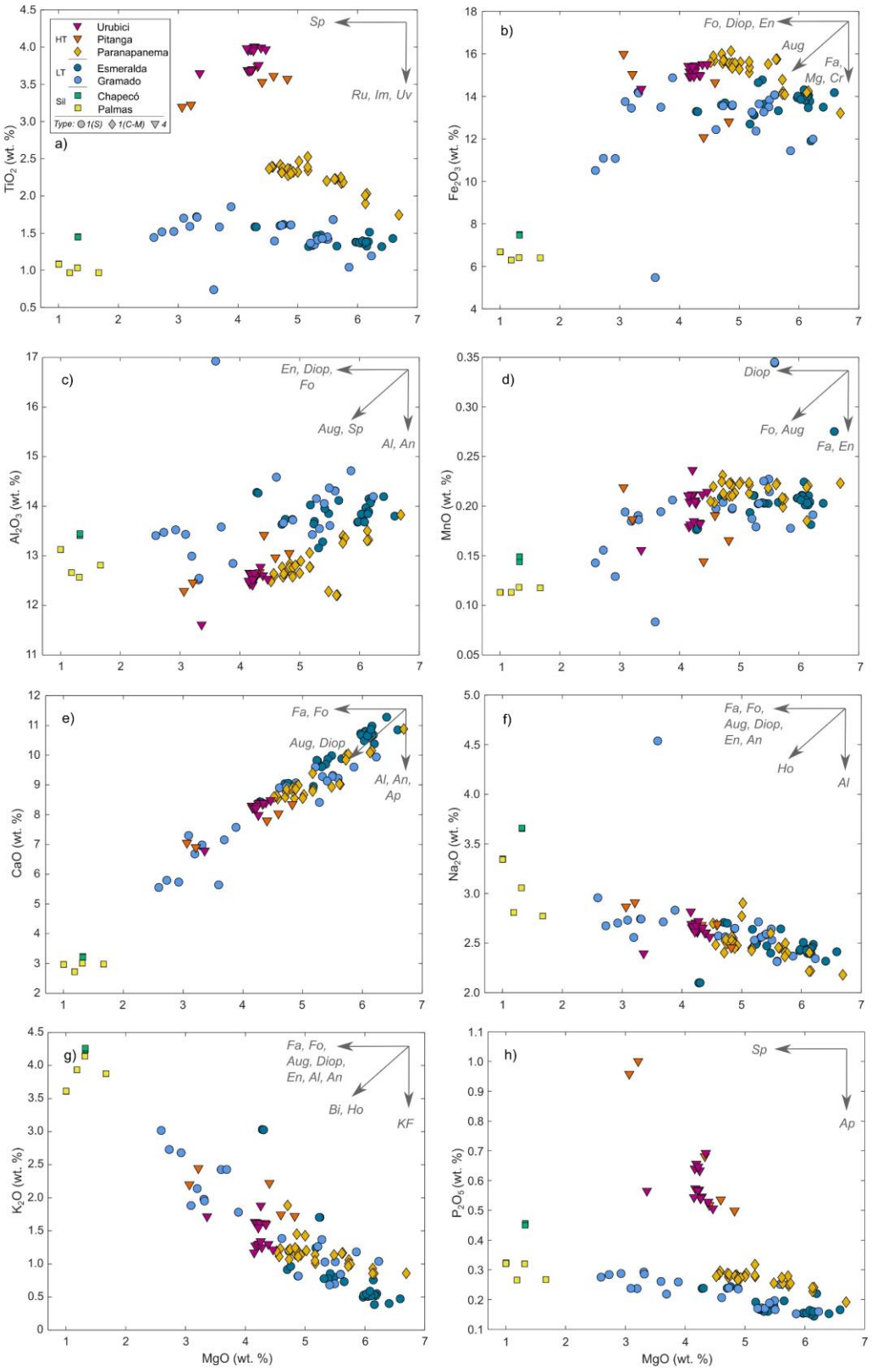

Figure 3.3 – *Harker bivariate plots for Serra Geral lavas: MgO vs. (a) TiO_2, (b) Fe_2O_3, (c) Al_2O_3, (d) MnO, (e) CaO, (f) Na_2O, (g) K_2O, (h) P_2O_5. With fractionation vectors for evolving liquid compositions for Fo – forsterite, Fa – fayalite, Aug – augite, En – enstatite, Diop - diopside, an – anorthite, Al – albite, Sp – spinel, Uv – ulvospinel, Mg – magnetite, Cr – chromite, Ru – rutile, Im – ilmenite, Bi – biotite, Ho – hornblende, KF – K-feldspar.*

3.3.1.2. Base metals

Trends in base metal enrichment are limited for the Serra Geral data set, with distinctively low overall Ni (< 140 ppm; Figure 3.4a) and Cr (< 160 ppm; Figure 3.4d) contents compared to other CFB provinces (e.g., the NAIP where onshore lavas generally exhibit Ni concentrations of 100-1,000 ppm and Cr concentrations of 100-2,000 ppm; Hughes et al., 2015). The Paranapanema samples display positive correlations between MgO and Ni, Co and Cr concentrations (Figures 3.4a, 3.4c, 3.4d) that are similar in shape to but higher in magnitude than Gramado and Esmeralda samples; Urubici and Pitanga samples lack strong trends in all instances. Enrichment of Ni, Cr and Co (Figure 3.4c) follow very similar trends to Fe_2O_3 relative to MgO (Figure 3.3b), with HT lavas generally containing slightly higher concentrations. Overall, Cu concentrations are better clustered into locality classifications, with Paranapanema lavas exhibiting the highest mean Cu content at 254 ppm and Esmeralda exhibiting the highest single-sample concentrations (Figure 3.4b and Table 1). Unlike the Ni and Cr, concentrations of Cu and Co (Figures 3.4b-c) are comparable to NAIP onshore lavas from Hughes et al. (2015), at around 10-500 ppm for Cu and 10-70 ppm for Co.

3.3.1.3. Rare earth elements and lithophiles

Chondrite-normalised (McDonough and Sun, 1995) REE plots for lavas belonging to each Serra Geral magma-type are shown in Figures 3.5a-f. All plots have fractionated REE patterns, with LREE > HREE in all samples. Silicic and LT lavas have prominent Eu troughs, with the Silicic group generally showing more enriched concentrations of all elements, particularly Chapecó (Figure 3.5a). The LT REE arrays (Figures 3.5b-c) have more variable LREE concentrations than HT lavas, particularly in the more incompatible REE such as La, Ce, Pr, Nd and Sm. Esmeralda is the most depleted magma-type in all element concentrations (Figure 3.5c). Steeper gradients are observed in the HT lavas (Figures 3.5d-f), with distinctive light REE enrichment especially in Pitanga (Figure 3.5e) and Urubici (Figure 3.5f); these two magma-types also exhibit parallel arrays, and all HT lavas have a narrower spread of concentrations. Paranapanema lavas (Figure 3.5d) feature similar enrichment patterns to the LT group, not their designated HT group.

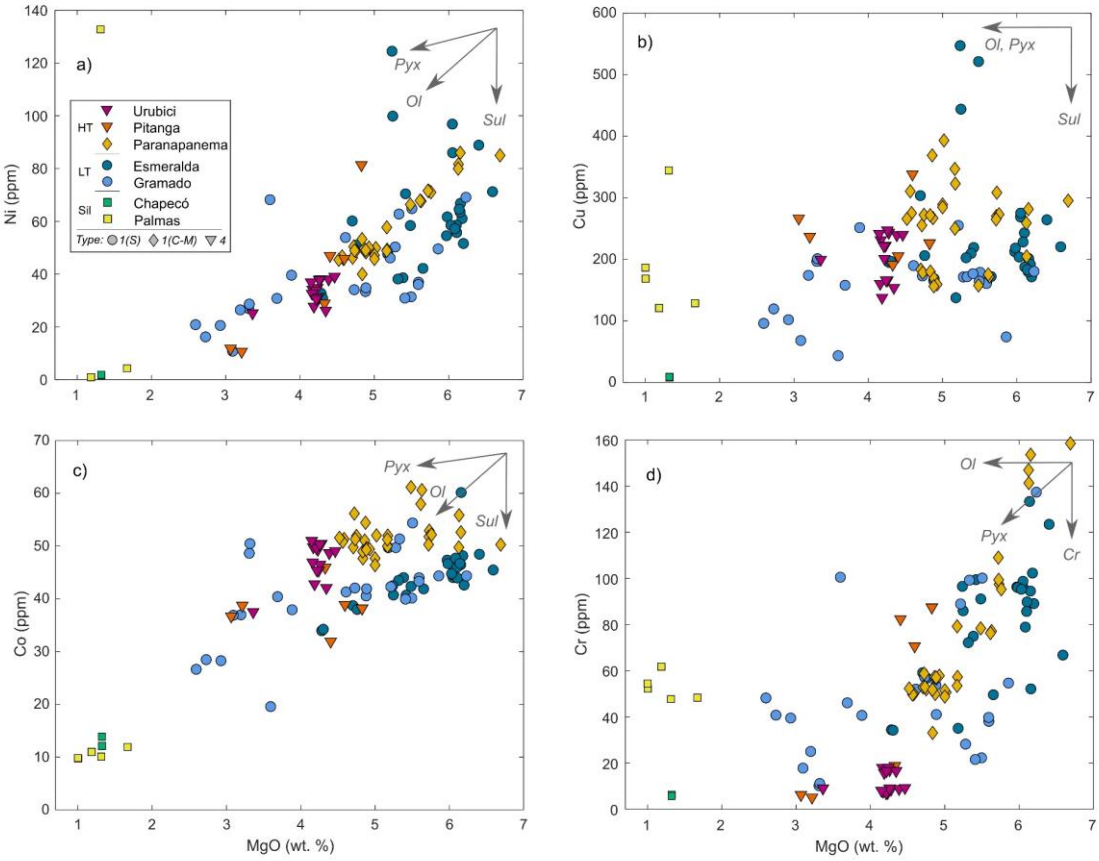

Figure 3.4 – *Bivariate plots for base metal concentrations in Serra Geral lavas: MgO vs. (a) Ni, (b) Cu, (c) Co, (d) Cr. With fractionation vectors for evolving liquid compositions for Ol – olivine, Pyx – pyroxene, Sul – sulphide, and Cr – chromite.*

In Figure 3.6a, some Gramado lavas trend towards high SiO_2 concentrations and progressively lower Nb/La ratios associated with assimilation and fractional crystallisation in CFB magmas (Xiao et al., 2004). In Figures 3.6b and 3.6c, chondrite-normalised (McDonough and Sun, 1995) $(Th/Ta)_n$, $(Sm/Yb)_n$ and $(La/Sm)_n$ ratios demonstrate the different source affinities of the magma-types. From this, HT lavas are associated with OIB, while LT lavas trend towards classic Low-Ti signatures found in Gondwana CFBs (Wooden et al., 1993). Paranapanema, Gramado and Esmeralda magma-types, or Type 1 from Licht (2018), share a strong association in Figures 3.6b and 3.6d at (Sm/Yb)n ~ 2. Meanwhile, Urubici and Pitanga lavas (i.e., Type 4 in Licht, 2018) trend together towards higher (Sm/Yb)n > 3 (plots taken from Xiao et al., 2004).

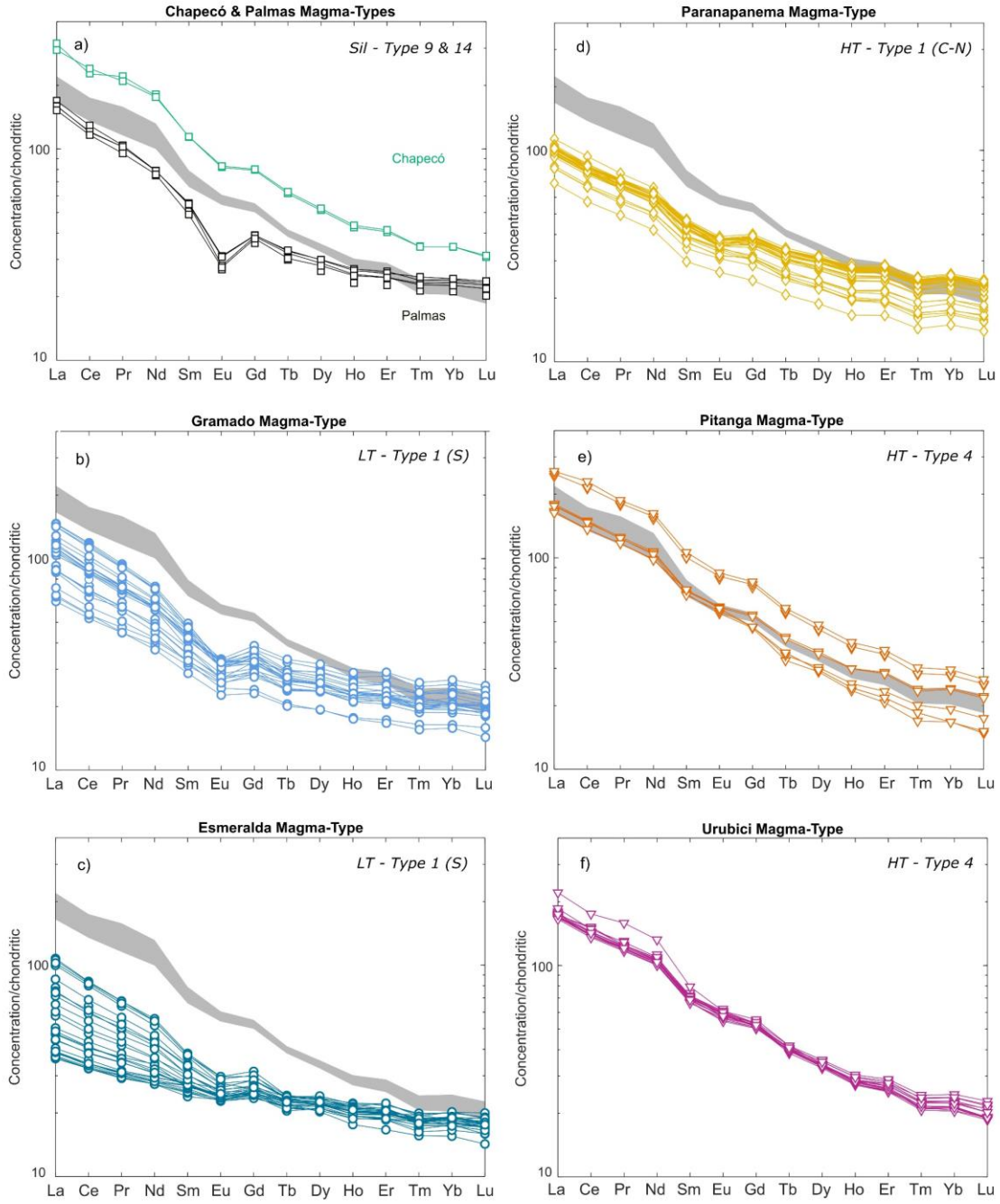

Figure 3.5 – *Chondrite-normalised (McDonough and Sun, 1995) rare earth element plots for Serra Geral lavas: (a) silicic Palmas and Chapecó; (b) Gramado; (c) Esmeralda; (d) Paranapanema; (e) Pitanga; (f) Urubici. Grey shaded area – Urubici magma-type for reference.*

In primitive mantle normalised plots (McDonough et al., 1992) (Figures 3.7a-f), Chapecó and Palmas display similar patterns with Chapecó slightly more enriched overall – pronounced Nb, Sr and Ti negative anomalies, and high Rb, Th, U, K, Hf and Zr. Chapecó features a positive Ba anomaly, while Palmas

features a negative one. Gramado (Figure 3.7b) and Esmeralda (Figure 3.7c) exhibit a wide range of multi-element normalised signatures, primarily lower than all other magma-types, with Ba, Nb, Sr, P and Ti negative anomalies and depletions in the most incompatible elements including Hf, Zr, Sm and Tb in particular. The three HT magma-types (Figures 3.7d-f) exhibit similar patterns to one another and are enriched in the more compatible elements like Nd, Hf and Zr, featuring positive Ba anomalies, and small negative Sr, P and Ti anomalies. Overall, the HT and Silicic groups tend to exhibit concentrations above 10 x Primitive Mantle values, while LT groups frequently lie below this line, particularly for Sr and Ti.

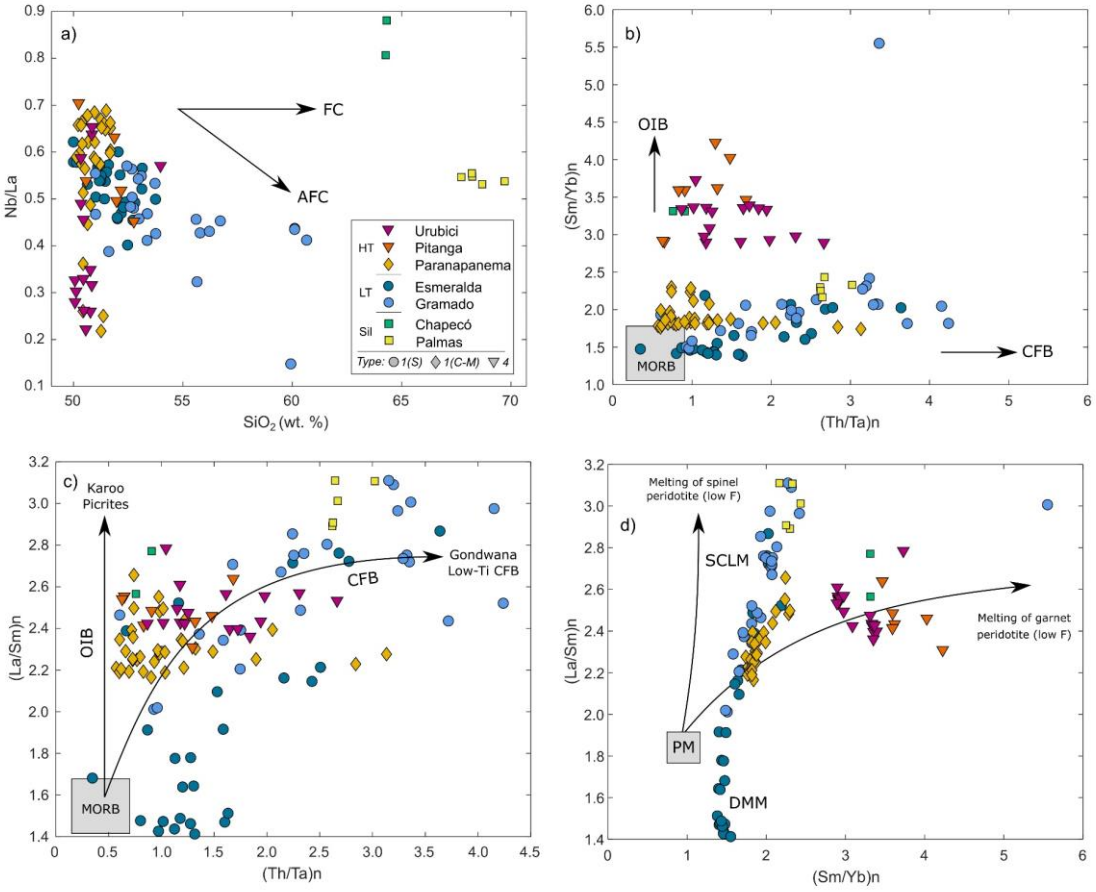

Figure 3.6 – *Selection of lithophile and REE ratio discriminant plots for Serra Geral lavas. (a) SiO_2 vs. Nb/La, (b) $(Th/Ta)_n$ vs. $(Sm/Yb)_n$; (c) $(Th/Ta)_n$ vs.$(La/Sm)_n$; (d) $(Sm/Yb)_n$ vs. $(La/Sm)_n$. (Annotations for 3.6b and 3.6c based on Wooden et al., 1993; for 3.6a and 3.6d based on Xiao et al., 2004).*

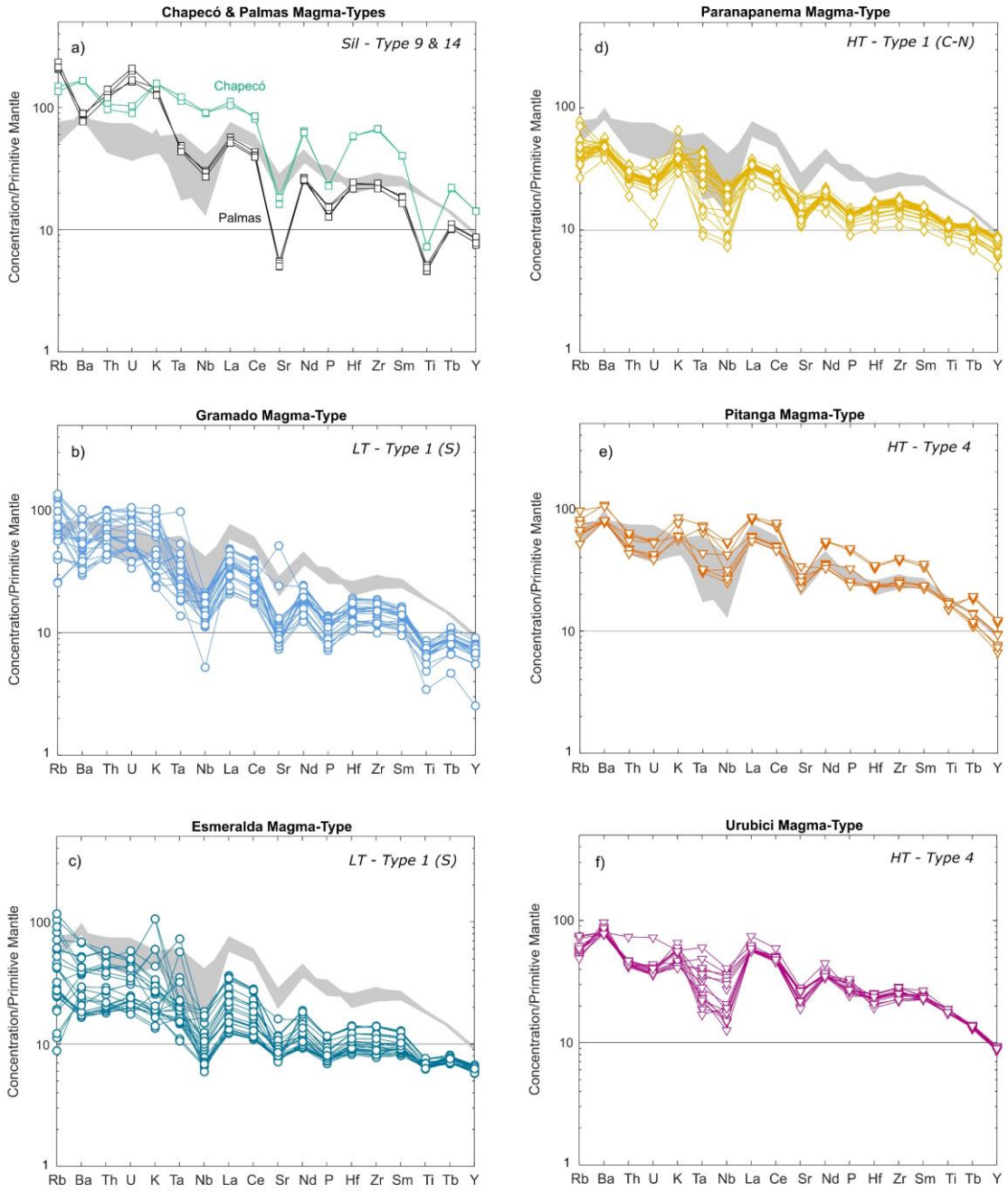

Figure 3.7 – *Trace element concentrations normalised by Primitive Mantle values (McDonough et al., 1992), arranged according to increasing compatibility, for the Serra Geral lavas: (a) silicic Palmas and Chapecó; (b) Gramado; (c) Esmeralda; (d) Paranapanema; (e) Pitanga; (f) Urubici. Grey shaded area – Urubici magma-type for reference.*

3.3.2. PGE and Au

Figures 3.8a-f display chondrite-normalised PGE and Au plots (McDonough and Sun, 1995) for lavas from all Serra Geral magma-types except Palmas, which was not analysed. Lavas from all locations have a relative

enrichment of Pd-group PGE (PPGE; Rh, Pt, Pd) and Au compared to Ir-group PGE (IPGE; Os, Ir, Ru). However, the degree of enrichment varies significantly across the sample set. This is most obvious between Serra Geral HT and LT groups, with HT exhibiting a steep slope from IPGE to PPGE (Figure 3.s 8d-f) and the LT showing normalised IPGE concentrations an order of magnitude higher than HT samples, producing a flatter gradient into PPGE (Figure 3.8b-c). Most importantly, Serra Geral LT samples, or Type 1 (Southern) samples, frequently display an unusual, distinctive 'hump' between Ru, Rh and Pt concentrations instead of the gradual slope seen in the HT plot. Paranapanema lavas, or Type 1 Central-Northern, have the highest Pd concentrations (mean of 16.17 ppb in Table 1) as shown by up to 0.1 x chondritic values (compared to 0.001-0.01 x chondrite for other lavas) in Figure 3.8d.

Figures 3.9a-f display bivariate plots for the PGE vs. MgO. The highest concentrations of Ir, Ru and Rh (Figures 3.9b-d) are found in LT rocks (around 1.2, 13.5 and 5.75 ppb, respectively), while Pt is most enriched in LT and Paranapanema (up to 30-40 ppb; Figure 3.9e). Paranapanema lavas are distinctly Pd-rich in most instances (ranging 5-35 ppb compared to 1-15 ppb in all other lavas; Figure 3.9f). Although Os concentrations are unavailable for HT lavas, LT lavas contain concentrations of a similar level to Ir in the same rocks (up to 1.2 ppb; Figure 3.9a). Paranapanema samples have the lowest Cu/Pd of the PELIP lavas (Figure 3.10a). Figure 3.10b demonstrates the IPGE/PPGE enrichment split between LT and HT, such that LT lavas tent to have the lowest Pd/Ir ratios, in a similar range to most NAIP lavas from Hughes et al. (2015). Urubici and Pitanga magma-types evidently contain less PPGE compared to the LT samples in Figure 3.10b. Figure 3.10c demonstrates that Gramado, Esmeralda and Paranapanema (constituents of Type 1; Licht, 2018) have significantly higher total PGE contents (~ 5-52 ppb) relative to the Type 4 and silicic lavas (< 10 ppb). Figure 3.10d displays Au concentrations for the magma-types according to Ti/Y – Paranapanema lavas contain the most Au, reaching ~ 20 ppb, followed by all other lavas, which bear a maximum of 8 ppb. Figures 3.10e-f contextualise PGE ratios alongside trace element ratios from Figure 3.6.

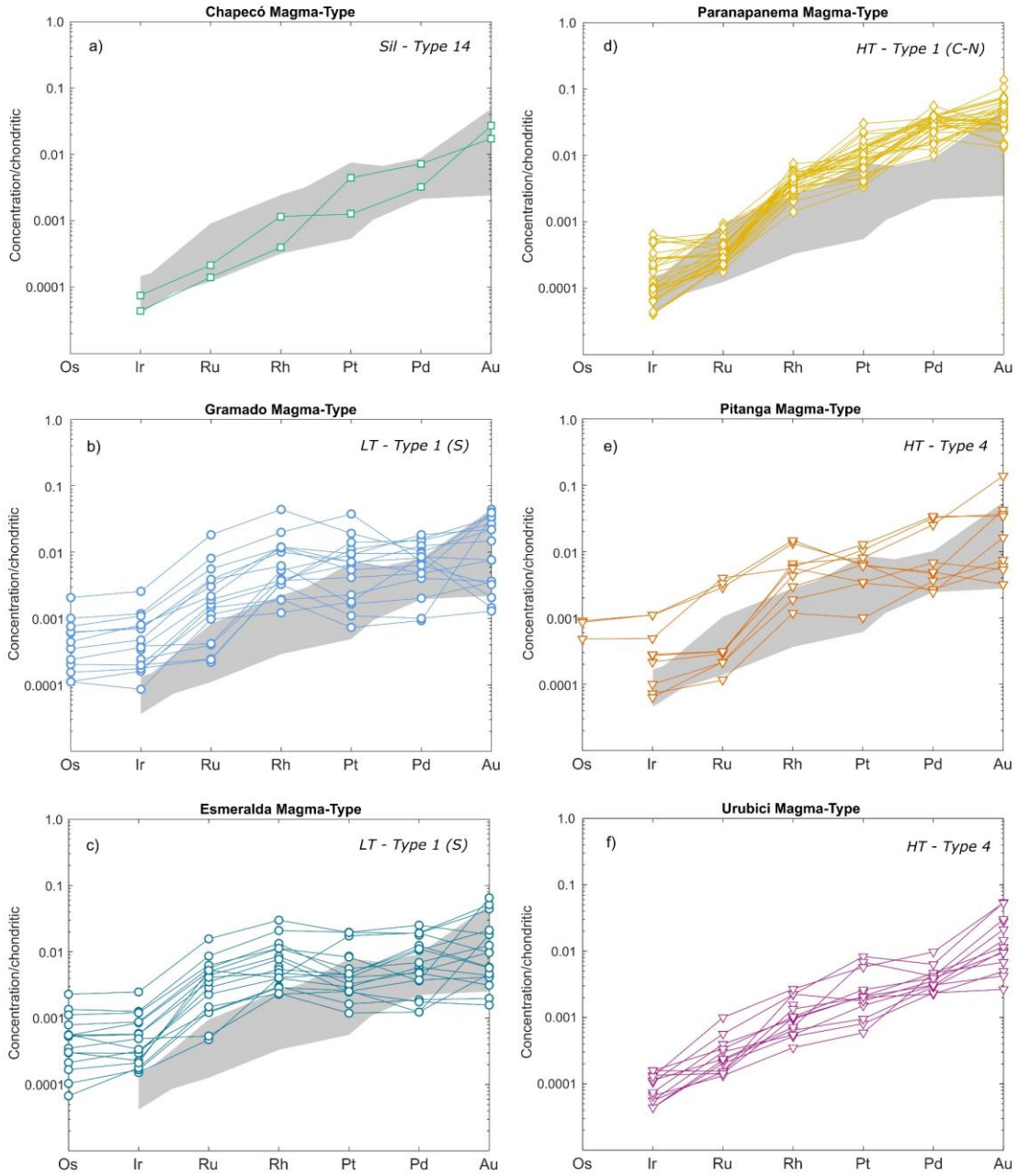

Figure 3.8 – *Chondrite-normalised (McDonough and Sun, 1995) PGE plots for Serra Geral lavas and locations. (a) Chapecó; (b) Gramado; (c) Esmeralda; (d) Paranapanema; (e) Pitanga; (f) Urubici. Grey shaded area – Urubici magma-type for reference.*

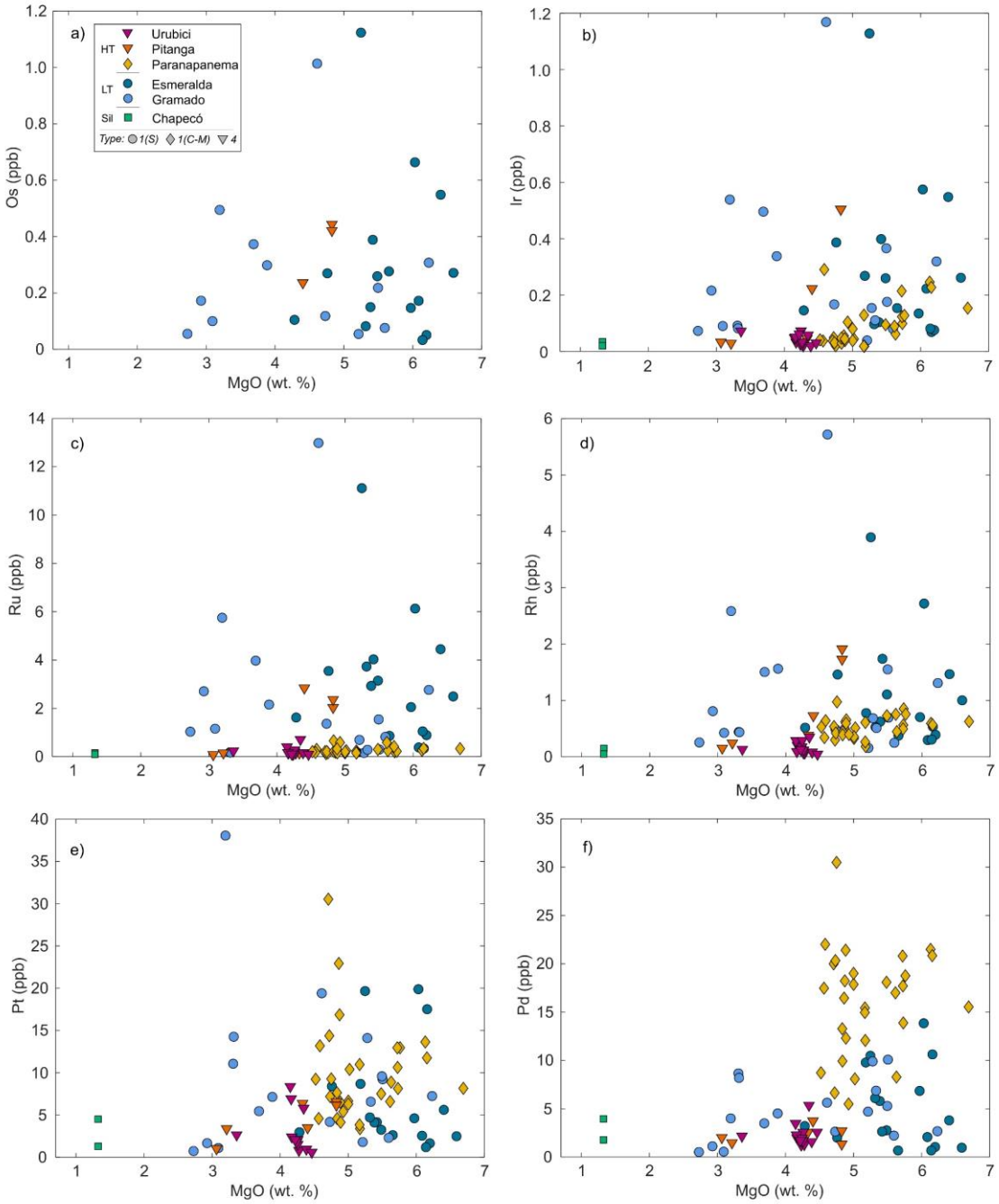

Figure 3.9 – *PGE Bivariate plots of Serra Geral lavas for MgO vs (a) Os, (b) Ir, (c) Ru, (d) Rh, (e) Pt and (f) Pd.*

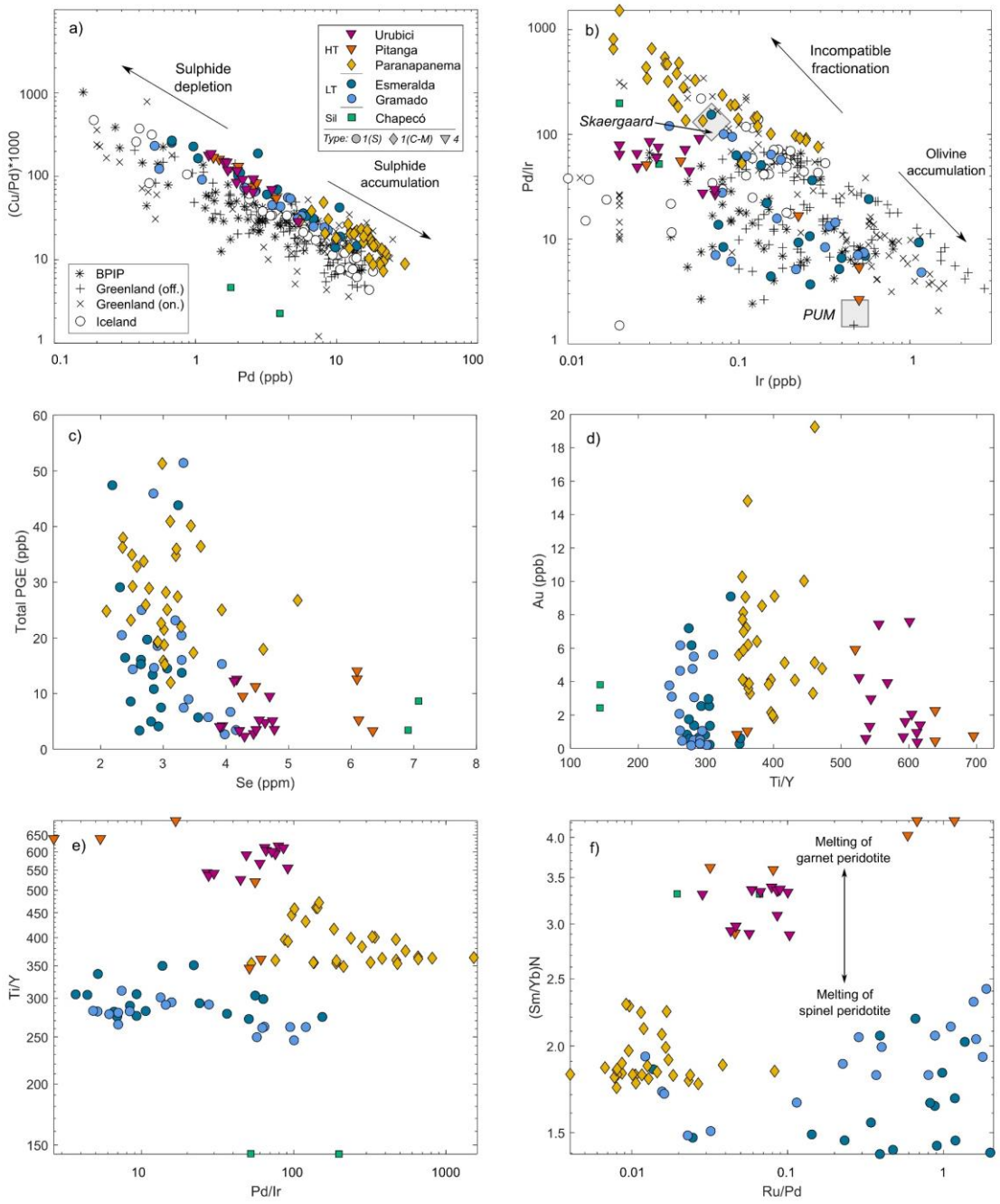

Figure 3.10 – *Bivariate plots for PGE concentrations as ratios for Serra Geral lavas. (a) Pd vs. (Cu/Pd)*1000; (b) Ir vs. Pd/Ir with vectors for incompatible fractionation and olivine accumulation, and markers for Primitive Upper Mantle and Skaergaard compositions from Hughes et al. (2015); (c) Se vs. Total PGE; (d) Ti/Y vs. Au; (e) Pd/Ir vs. Ti/Y; (f) Ru/Pd vs. $(Sm/Yb)_n$. Literature data used in 3.10a and 3.10b from: Lightfoot et al. (1997); Philipp et al. (2001); Momme et al. (2002); Momme et al. (2003); Hughes et al. (2015).*

3.4. Discussion

3.4.1. Magmatic trends

Our results show important geochemical trends across both the Peate et al. (1992) and Licht (2018) classification schemes that help contextualise precious metal trends, summarised and interpreted herein. Low MgO content (2-7 wt.%; Figures 3.3a-h) and Ni concentrations (< 125 ppm; Figure 3.4a) across all Serra Geral lavas implies that they are not primary mantle melts and have undergone significant differentiation, likely via fractional crystallisation (Xiao et al., 2004). Mineral fractionation vectors in Figures 3.3a-h strongly suggest that olivine, clinopyroxene and plagioclase (plus minor amounts of spinel-group minerals) were progressively removed from the parent magmas leading to decreases in Fe_2O_3, CaO, MnO and Al_2O_3, and increases in incompatible Na_2O and K_2O with decreasing MgO content (Fodor, 1987; Peate et al., 1990). As observed in thin section, the dominant mineral phase in all mafic samples is orthopyroxene, with clinopyroxene, plagioclase and spinel-group minerals, and a notable absence of olivine (typically 0-5% of assemblages), likely due to the earlier removal. Most major elements exhibit a single fractionation trend for each magma-type with a possible slight change in slope and groupings below ~ 4 wt.% MgO, indicating that the fractionating mineral(s) were reasonably consistent for mafic lavas. For TiO_2 and P_2O_5 (Figures 3.3a and 3.3h), the fractionation trends indicate at least two liquid lines of descent, with Type 4 lavas (Urubici and Pitanga) exhibiting much more pronounced negative slopes with MgO compared with Type 1 lavas (Paranapanema, Esmeralda and Gramado), which are weakly negative. These branching fractionation trends indicate differing accessory/minor mineral constituents between magma-types and localities. We suggest that Type 4 lavas fractionated TiO_2 and P_2O_5-poor accessories such as chromite (which may also explain the more prominent Cr depletion with decreasing MgO in this group in Figure 3.4d), while Type 1 lavas fractionated magnetite, titanomagnetite and/or apatite.

Olivine fractionation would efficiently remove compatible Ni ($D_{Ni}^{ol-melt}$ = 7.21) and Co ($D_{Co}^{ol-melt}$ = 2.28) (Spandler and O'Neill, 2010). Serra Geral mafic lavas are particularly olivine-deficient in thin section and reasonably evolved with respect to SiO_2 and MgO concentrations (Figures 3.2d and 3.3a-h), which means

that a significant amount of compatible base metals may have been removed from the parent magmas prior to eruption in all magma-types. In a similar manner, Cr is depleted in lavas throughout the region, which we attribute to the removal of both olivine and chromite. Copper appears to be the only base metal/chalcophile retained in the lavas in any significant amount (Figure 3.4b), and thus is incompatible in the fractionating silicate and oxide mineral phases. If sulphide fractionation drove chalcophile depletion, Cu would be uniformly removed from melts given its strong affinity for sulphide liquids in silicate melts ($D_{Cu}^{sulphide-melt}$ = 1,470; Mungall and Brenan, 2014). Since this is not the case, we propose that large degrees of olivine and chromite fractionation experienced by such MgO-depleted magmas would effectively remove Ni, Co and Cr while leaving Cu in melts.

Trace element concentrations and ratios provide evidence for markedly different geochemical processing between magma-types within the Serra Geral Group. From Figure 3.5, Type 4 lavas feature an order-of-magnitude enrichment in LREE compared to Type 1 lavas (particularly Southern), suggesting differing degrees of partial melting or assimilation of continental crust. Combined with the trends of HT lavas towards OIB signatures in Figure 3.6b and high-Ti melts akin to Karoo CFBs in Figure 3.6c, we suggest Type 4 represents more strongly plume-related magmas in agreement with Rämö et al. (2016), who attribute HT lava $^{87}Sr/^{86}Sr$ and εNd signatures to an enriched mantle (EMI) component. Given that the HT/Type 4 lavas align with the plume focus ca. 135 Ma (Beccaluva et al., 2020), their signatures in our data signify the strongest asthenospheric signal.

More pronounced negative Eu anomalies in the LT group than HT lavas (Figure 3.5) suggest that a more significant amount of plagioclase has fractionated from the parent magma, signalling a higher degree of crystal fractionation (FC) in this group compared to HT. The LT lavas, particularly Gramado, exhibit decreasing Nb/La with increasing SiO_2 (Figure 3.6a), indicating the role of assimilation and fractional crystallisation (AFC) in the parent magmas. The depletion in trace element signatures and strongly negative Ta-Nb anomalies (Figures 3.7b-c) suggest that contamination by continental crust material during magma ascent may have been important in their geochemical development, as widely documented by isotopic studies of the LT group (e.g., Peate et al., 1992; Rocha-Júnior et al., 2013; Natali et al., 2017; Marques et al., 2018). The Ta-Nb

anomalies in HT lavas (Figures 3.7d-f) are significantly less pronounced, indicating a lower degree of crustal contamination in these magmas. Chapecó and Palmas typically trend with HT and LT, respectively, in Figures 3.5a, 3.6a-d and 3.7a, suggesting they share a common source and perhaps evolved towards silicic compositions from their associated mafic magma-types.

The steeply negative medium to HREE trends for Type 4 multi-element patterns in Figures 3.5e and 3.5f, along with Type 4 samples trending towards high $(Sm/Yb)_N$ values in Figure 3.6d suggest an association with the melting of a garnet peridotite source. This would imply high pressure melting conditions commonly associated with plume melts beneath thick continental cratons, where the majority of the melting occurs in the garnet-bearing asthenosphere (e.g., Arndt et al., 1998; Jourdan et al., 2007). In comparison, Type 1 lavas are strongly associated with trace element trends produced by the melting of spinel peridotite (Figure 3.6d) (e.g., White and McKenzie, 1995), which corresponds with their shallow medium to HREE slopes in Figures 3.5b and 3.5c. The Paranapanema lavas, thought to represent a transitional member between HT and LT and classified separately in Type 1 (Central-Northern), exhibits a combination of trace element signatures associated with the two groups in Figures 3.5-3.7. Paranapanema lavas trend with Type 1 (Southern) towards spinel peridotite melts (Figure 3.6d), exhibits medium to heavy REE slopes between those Type 1 (Southern) and Type 4, but is grouped with Type 4 OIB sources in other discriminant diagrams (e.g., Figure 3.6c) and as such must be regarded separately in terms of source interpretation, as in Licht (2018).

The spinel to garnet transition occurs where pressures and temperatures exceed 3 GPa and 1,570°C (Milholland and Presnall, 1998; Walter et al., 2002). This translates to depths of 50-70 km in asthenospheric regions and 120-180 km in colder sub-cratonic settings (Kent and Fitton, 2000; Ziberna et al., 2013). In Cr-rich mantle sources or depleted rocks such as harzburgite, the transition can occur at significantly higher pressures (up to 10 GPa) and typically increases the depths at which both spinel and garnet are stable simultaneously (Klemme, 2004; Ziberna et al., 2013). The different spinel/garnet melting trends exhibited by the Serra Geral lavas reflect either (a) different degrees of melting of a garnet-bearing mantle source (with garnet exhaustion in the most extreme cases) or (b) separate melting sources and depths (between 50 and 100 km; Gibson et al., 2006) as a

function of the rapidly evolving geodynamic setting. Both scenarios would require a change in melting depth between magma-types, to facilitate differential degrees of partial melting (Beccaluva et al., 2020), and polybaric melting processes are favoured by Rämö et al. (2016) in their assessment of Pitanga and Paranapanema geochemical differences. We model the trace element geochemistry of Serra Geral lavas, including chalcophile elements, in Section 3.4.2.3.

3.4.2. PGE enrichment

Trends in PGE enrichment fall consistently into the three major mafic subdivisions established by Licht (2018) in Figures 3.8 and 3.9 – Pitanga and Urubici in Type 4, Paranapanema in Type 1 (Central-Northern), and Gramado and Esmeralda in Type 1 (Southern). As such, it is most appropriate to primarily use these newer classifications in lieu of the classic groups when discussing metallogenesis going forward.

Type 1 (Southern) lavas are more enriched in IPGE than all other lavas (Figure 3.8a-f). This is especially true for Ru concentrations, which are an order of magnitude higher than typical intracontinental lavas (Barnes et al., 2015). Furthermore, Rh, the transitional PGE that shares properties with both IPGE and PPGE (Holwell and McDonald, 2010 and references therein), is also enriched in Type 1 (Southern) lavas, forming a ‘humped’ shape on their plots in Figures 3.8b-c. Contrasting this trend to the significant Pd and Au enrichment (and steep slope in the multi-element diagram) in the Type 1 (Central-Northern) lavas (Figure 3.8d) and general depletion in PGE in Type 4 lavas (Figure 3.8f), it is clear that PGE signatures are heterogeneous in the region. The discrepancy with depleted Ni and Co, and relatively enriched Cu in Figures 3.4a and 3.4b supports preferential fractionation of Ni and Co via olivine, in the absence of significant Cu depletion via sulphide removal. As noted in Section 4.1, we suggest that sulphide fractionation did not control base metal and PGE concentrations in the PELIP magmas. Thus, we must identify different geochemical processes outside sulphide depletion to explain the separate Ir-Ru-Rh and Pd-Au-Cu enrichment associations in Type 1 lava varieties that make sense when integrated with their major and trace element interpretations.

3.4.2.1. Palladium in Type 1 (Central-Northern) lavas

The Pd-Au-Cu enrichment in Type 1 (Central-Northern) samples is clearly illustrated by their steep multi-element slope in Figure 3.8d and high Pd/Ir ratios in Figure 3.10b, which place the lavas as 1-2 orders of magnitude more Pd-rich than all other lavas in this study. These lavas often contain up to 30 ppm more Pd than any other classification (Figure 3.9f), particularly Type 4, and contain slightly higher mean Cu and Au concentrations than others (Figure 3.4b and 3.10f). Given that Pd, Cu and Au are all mobile incompatible chalcophiles commonly associated with each other in fluid-rich environments (e.g., Holwell et al., 2019; Choi et al., 2020 and references therein), we propose that Pd, Cu and Au-bearing material is being preferentially incorporated into Type 1 (Central-Northern) melts. This supports Type 1 (Central-Northern) as a separate compositional group by Licht (2018) despite earlier classification alongside Urubici and Pitanga by Peate et al. (1992); the fundamental geochemical controls on Si, Ti, Zr and P in Serra Geral magmas established from this study evidently have an impact on PGE concentrations. Enrichment in Pd-Cu-Au is unique to Type 1 (Central-Northern) lavas in this Paraná sample set, and thus a different partial melting model is required to generate the compositional variances from other samples. If, as suggested by Rocha-Júnior et al. (2013), the significant stratigraphic and spatial distance between individual magma-types observed as lavas at surface represents physically distinct sources in the mantle, we would expect each of the parental magmas to feature their own set of geodynamic controls on geochemistry.

The three metals enriched in Type 1 (Central-Northern) lavas - Pd, Au and Cu - are notable for being more incompatible in silicate melting environments than the other five PGE and base metals (e.g., Mitchell and Keays, 1981; Borisov et al., 1994; Holzheid et al., 2000; Righter et al., 2008; Tassara et al., 2017). Furthermore, Pd does not form micronuggets like the other PGE, tending to exist in base metal sulphides alongside Cu and Au (Holzheid et al., 2000). Metasomatic activity can easily redistribute such metals via fluids and melts at the asthenosphere and base of the lithosphere in sub-cratonic settings over long periods of time (e.g., Zhang et al., 2008; Maier and Groves, 2011). Given that the Paraná Basin exists on Proterozoic Gondwanan basement, the SCLM beneath modern day Brazil will have been subjected to numerous fertilisation events

(Rocha-Júnior et al., 2013) via subduction around the cratonic margin (Tassara et al., 2017). Subducting oceanic lithosphere can release mobile elements in dehydrating fluids or small-degree melts as the plate descends, and these become concentrated in a mantle wedge and SCLM (e.g., Woodland et al., 2002; Griffin et al., 2013; Tassara et al., 2017; Rielli et al., 2018; Wade et al., 2019), similar to the origins of Cu-porphyry environments. Metasomatic sulphide minerals, and by extension chalcophile elements, can then be scavenged by melts generated in an intracontinental setting (Powell and O'Reilly, 2007). Generally, Pd will follow Cu during partial melting of the mantle and can be found in similar sulphide phases at upper mantle P/T conditions (e.g., Barnes et al., 1997; Mungall et al., 2005; Lorand et al., 2013 and references therein), which further links their metallogenic processing. If Cu- and Pd-bearing sulphides are melted and incorporated into magmas interacting with the SCLM, the two metals can share a coupled enrichment in resulting volcanic and intrusive products (e.g., Bockrath et al., 2004; Alard et al., 2011; Delpech et al., 2012; Lorand et al., 2013; Lorand and Luguet, 2016; McDonald et al., 2017; Tassara et al. 2017).

An alternative theory is that whilst the SCLM still received enrichment via metasomatic processes, subduction did not supply the metals. In Figure 3.11a-b, relative PGE concentrations are compared to some classic sub-lithospheric rocks from the literature, including pyroxenite xenoliths from Cameroon (Abeng et al., 2012). Here, Type 1 (Central-Northern) samples plot far from classic intraplate xenoliths and instead are much more alike the pyroxenites. Thus, the enrichment of PPGE in the parent magma could have resulted from pyroxenite (i.e., recycled oceanic lithospheric components) in the melt column and/or SCLM. Further, a study by Fiorentini et al. (2020) suggests that plume events related to Bushveld magmatism ~2.06 Ga could have pre-fertilised the lithospheric mantle under the Gondwanan continent, later to be sampled by subsequent Phanerozoic melts, as occurred in Western Australia. Given the long history of the Gondwanan SCLM likely including many metasomatic and partial melting events, and the tendency of mantle plumes to sample both pyroxenite and peridotite from the deep mantle, this is plausible, yet would require Os-isotope data to accurately confirm. Regardless of mechanism (subduction or mantle component-driven), the Type 1 (Central-Northern) parent magmas require enrichment in PPGE, Cu and Au prior to ascent via a metasomatic event to produce such PGE signatures.

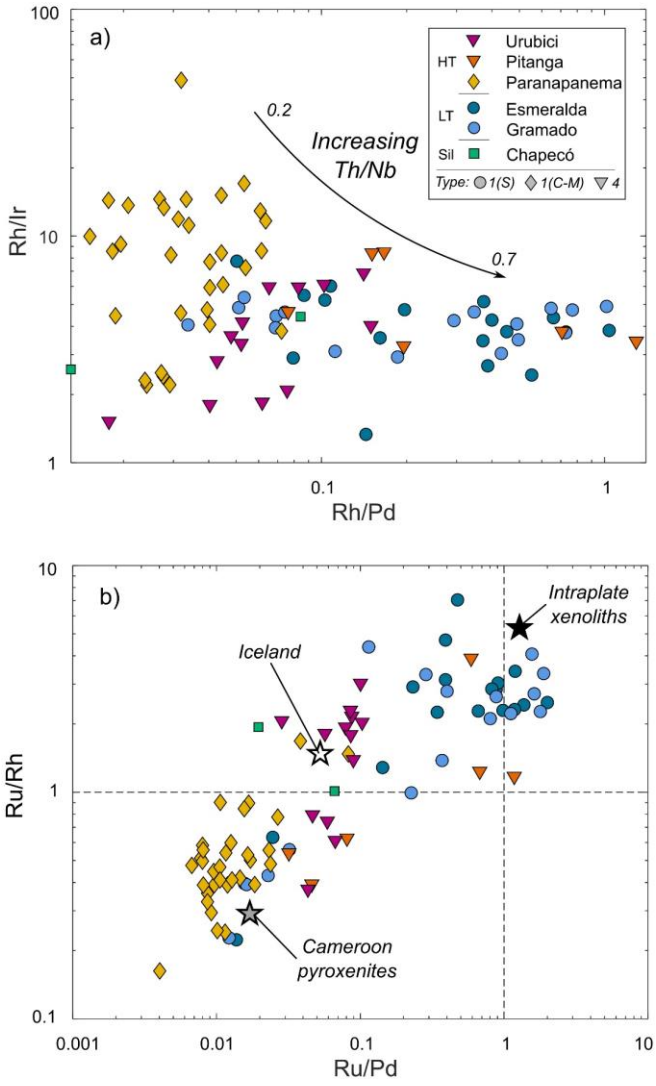

Figure 3.11 – *Bivariate plots of (a) Rh/Pd vs. Rh/Ir and (b) Ru/Pd vs. Ru/Rh, demonstrating the differences between the Serra Geral lava PGE ratios, with comparison data for intraplate xenoliths (Maier et al., 2012), Iceland (Momme et al., 2003) and Cameroon pyroxenites (Abeng et al., 2012)*

In a study comparing intracontinental melts from depleted asthenospheric and metasomatised SCLM sources in the North China Craton, Wang et al. (2020a) determined that the latter were 3-4 times more enriched in precious and base metals, likely via efficient extraction of SCLM sulphides during melting. Furthermore, spinel lherzolite xenoliths in intracontinental lavas from Ethiopia (Lorand et al., 2003), showing evidence of metasomatic deformation and melt percolation, see a characteristic enrichment in S-Cu-Pd-Au. Given the unique geochemical characteristics of Type 1 (Central-Northern) lavas for the PELIP, our

metallogenic model must provide a mechanism for differentiating the magma-type from the others, particularly the Type 1 (Southern) group given that they melt at a similar depth according to garnet-spinel information in Figure 3.6d. We propose that given the documented metasomatic association of Pd, Au and Cu (e.g., Tassara et al., 2017; Holwell et al., 2019; Choi et al., 2020), and the consistently higher concentrations in shallower-derived continental melts from the PELIP (e.g., potentially involving more SCLM than asthenosphere), the Type 1 (Central-Northern) lavas obtained elevated concentrations of Pd, Au and Cu by the passive melting of pre-enriched metasomatised SCLM by the Tristan plume. Indeed, studies of Brazilian mantle xenoliths indicate a protracted metasomatic history beneath the craton (e.g., Rivalenti et al., 2000; Carlson et al., 2007), supporting this hypothesis.

3.4.2.2. Ruthenium and rhodium in Type 1 (Southern) lavas

The plateau between Ru, Rh and Pt in Type 1 (Southern) samples (Figure 3.8b-c) likely reflects the source minerals included in parental melts. This likely indicates that Ru-Rh-bearing minerals are being incorporated into Type 1 (Southern) magmas from a mantle source in a separate system from other magmas. The melting depth and source for Type 1 magmas are different to Type 4 (Rämö et al., 2016; Licht, 2018) (Figure 3.6d), implying distinct melting processes in the northern and southern basalts (Beccaluva et al., 2020) that could explain the groups' differing metallogenic characters. Overall, the PGE behave in a similar manner chemically – in the presence of a sulphide melt portion, all six will be overwhelmingly concentrated within it rather than the silicate melt. However, the individual partition coefficients of the PGE between silicate minerals and melt vary significantly when not in the presence of sulphides (e.g., Peach et al., 1990; Peach et al., 1994; Righter et al., 2004; Park et al., 2017 and references therein), and the melting of a sulphide-deficient mantle will facilitate the heterogeneous incorporation of PGE into melts. It follows that the enrichment and depletion of PGE in Serra Geral lavas must be controlled by silicate or oxide differentiation processes in the magma. If the melts were depleted in sulphide, the majority of their PGE basket would also be removed and they would have higher Cu/Pd than what is displayed in Figure 3.10a. To add Ru and Rh to Type 1 (Southern) in the quantities observed in Figures 3.8b-c and 3.9c-d would require

melting of a source rich in these PGE alone, or at least in higher proportions than the other PGE.

As per Figure 3.6d, Type 1 (Southern) and (Central-Northern) lavas follow a liquid line of descent commonly associated with the melting of spinel peridotites at shallower depths and lower pressures than Type 4 magmas. Experimental studies found Ru and Rh to be compatible in spinel-group minerals (Capobianco and Drake, 1990; Barnes and Picard, 1993; Pitcher et al., 2009), with spinel-silicate melt partition coefficients of 400-900 (Righter et al., 2004). This synchronises well with our trace element ratios (Figure 3.6) – by melting a source with normative spinel-group mineral content, the generated magma would contain relatively high concentrations of the two PGE. In the mantle, Os, Ir, Ru and Rh are also highly compatible with sulphides, platinum-group minerals (PGM) and alloys, different mineral phases from the base metal sulphides, tellurides and arsenides that Pt and Pd are commonly found in (e.g., Mitchell and Keays, 1981; Alard et al., 2000; Helmy and Bragagni, 2017; Helmy and Fonseca, 2017). As such, the variety of sulphide compositions in the mantle source can be a crucial factor in fractionating the PGE from each other and isolating an IPGE and Rh rich mineral phase (i.e., Ni-sulphides, alloys or even spinel) for preferential melt incorporation (e.g., Keays et al., 1982; Barnes and Picard, 1993; Rehkämper et al., 1997; Maier et al., 2003a). A combination of spinel-group minerals and IPGE-sulphides at source may provide the necessary PGE signatures to Type 1 (Southern) melts. However, Type 1 (Central-Northern) sample trace element signatures also indicate spinel peridotite as a melting source in Figure 3.6d, cluster with Type 1 (Southern) in Figure 3.6b, and sit distinct from the other magma-types in the Licht (2018) study. Type 1 (Central-Northern) lavas do not have the characteristic Ru-Rh enrichment in Figure 3.8b-c and 3.9c-d. This suggests that although all Type 1 lavas likely formed by the partial melting of spinel peridotite mantle, the melting processes for the Southern and Central-Northern varieties must have been different to incorporate a different suite of PGE, or the mantle sources being melted exhibited different metasomatic characters.

3.4.2.3. Modelling melt compositions

Based on the interpretations of all Type 1 lava PGE signatures, we forward-modelled melt compositions appropriate for pressures of 2.0-3.0 GPa in a sub-lithospheric setting, using mass balance calculations from Shaw (1970) and experimental melting mode values from Johnson (1998) (Figure 3.12a-b). Mineral-melt partition coefficient sources are given in Figure 3.12 and Table 3.2. Starting with bulk concentrations of Co, Ni, Cu, PGE and Au from (i) metasomatised arc, (ii) normal arc, (iii) cratonic, and (iv) off-craton peridotite xenoliths collated by Barnes et al. (2015), and the mineral mode (X) and melt mode (p) values displayed in Table 3.2, we successfully generated chondrite-normalised multi-element PGE plots representative of the Serra Geral Type 1 magmas (summarised in Figure 3.12; see Supplementary S3.5 for modelling worksheets). Metasomatised and normal arc xenoliths represent re-enriched and depleted asthenospheric sources in our Type 1 (Central-Northern) models, respectively. On-craton xenoliths are generally from kimberlites within the thickest area of a craton block whilst off-craton are from kimberlites in thinner mobile belts surrounding cratons (e.g., Wildman et al., 2017); these represent a progressively thinning intracontinental setting in our Type 1 (Southern) models.

An important caveat for our models is that strongly chalcophile elements (such as the PGE) will preferentially stay in sulphide minerals until the phase is melted entirely, and as such, sulphide melting strongly controls the concentration of PGE in the resulting magmas. In order to attain PGE concentrations contained in any of our samples (between 0.0001 and 0.1 x chondritic values; Figure 3.8a-f), the sulphide phase, if present in the source (~ 1 wt.% in our model), must be exhausted. Similarly, for IPGE and Rh compatible in spinel, this mineral phase must be entirely melted to release the metals into magmas. Given the spinel-melt partition coefficients for IPGE are often 3-4 orders of magnitude smaller than those for sulphides (Table 3.2), the effect on resulting concentrations pre-exhaustion is much less pronounced. Further, it must be noted that chalcophile sulphide-melt partition coefficients can be highly variable from experiment to experiment, so we have maintained those found by Mungall and Brenan (2014) for consistency whilst acknowledging the challenges of modelling sulphide melts.

To generate Type 1 (Central-Northern) magmas, our models (Figure 3.12a) show that elevated bulk Cu, Pt, Pd and Au concentrations in the source

strongly influence the resulting melt enrichment. Metasomatised continental arc xenoliths (as in Wilson et al., 1996) typically feature such enrichment of Cu, Pt, Pd and Au. Beneath ancient cratons, the SCLM can be pre-conditioned by repeated enrichment events throughout history (e.g., Mitchell and Keays, 1981; Powell and O'Reilly, 2007; Zhang et al., 2008; Hughes et al., 2014; Hughes et al., 2015; Holwell et al., 2019). The model predicts that at melting degrees of around 20 %, metasomatic sulphides in an arc-like mantle will be exhausted at the conditions from Table 3.2, releasing chalcophile elements into the melt ('metasomatised arc' in Figure 3.12a). This is similar to the range of 20-23 % partial melting suggested by Gibson et al. (2005) for syn-rift melting in the PELIP. Identical melting conditions with a less Pt, Pd, Au and Cu-enriched source would produce chondrite-normalised plots with shallower gradients ('normal arc' in Figure 3.12a, also from Wilson et al., 1996), indicating that bulk source composition is the key factor in melt enrichment. Further, a mantle source without sulphide in the mineral mode cannot sufficiently produce melts with elevated Pt, Pd or Au concentrations, as the elements in question do not partition strongly into the remaining silicate or oxide mineral phases. It should be noted that PGM and alloys are also known to host small amounts of the SCLM's PGE budget (e.g., Hughes et al., 2015; González-Jiménez et al., 2020), but our model does not account for these phases. If Brazilian SCLM *does* host Pd-bearing PGM this would only work to boost our model further and reinforce the idea of metasomatically-enriched Pd-Au-Cu SCLM components.

Table 3.2 **(overleaf) -** *Parameters used in melting models.* [a] *Spinel peridotite melt modes from Johnson (1998) and Kinzler (1997), with addition of sulphide.* [b] *D-values for olivine from Brenan et al. (2003) and Spandler and O'Neill (2010).* [c] *D-values for orthopyroxene from Beattie et al., (1991) and Liu et al. (2014).* [d] *D-values for clinopyroxene from Hill et al. (2000) and Righter et al. (2004).* [e] *D-values for spinel from Liu et al. (2014), Park et al. (2017) and Righter et al. (2004).* [f] *D-values for sulphide from Mungall and Brenan (2014).* [g] *Arc xenolith concentrations from Wilson et al. (1996).* [h] *Craton xenolith concentrations from Maier et al. (2012).* [i] *Off-craton xenolith concentrations from Schmidt et al. (2003). Italicised values were unavailable in the literature for silicates, but assigned neutral values based on olivine values, given their lesser significance to melt composition compared to spinel and sulphide.*

Setting	Mode (X)[a]	Melt Mode(p)[a]
Arc		
Olivine	0.52	-0.06
Opx	0.27	0.28
Cpx	0.17	0.62
Spinel	0.03	0.11
Sulphide	0.01	0.05
Craton		
Olivine	0.52	-0.06
Opx	0.27	0.28
Cpx	0.17	0.62
Spinel	0.03	0.12
Sulphide	0.01	0.04

Element	D olivine/liq[b]	D opx/liq[c]	D cpx/liq[d]	D spinel/liq[e]	D sulphide/liq[f]
Co	2.28	3	1.3	5	230
Ni	7.21	5	2.6	10	500
Cu	0.14	0.09	0.23	0.77	1470
Os	1.2	*0.05*	0.01	30	740000
Ir	0.77	*0.4*	*0.5*	132	458000
Ru	0.23	*3*	4.27	871	415000
Rh	1.94	*0.2*	0.25	400	205000
Pt	0.009	*1*	1.5	0.1	317000
Pd	0.12	*0.1*	*0.1*	0.14	190000
Au	0.12	*0.01*	*0.01*	0.076	10000

Source/C0	Meta. Arc[g]	Normal Arc[g]	Craton[h]	Off-Craton[i]
Co (ppm)	80	100	100	108
Ni (ppm)	810	1980	2159	2240
Cu (ppm)	168	30	16.7	6.1
Os (ppb)	0.49	0.76	2	1.43
Ir (ppb)	0.31	1.26	2.33	2.3
Ru (ppb)	2	0.82	3.36993	3.43
Rh (ppb)	0.9	0.41	0.84030	1.21
Pt (ppb)	14.96	1.97	3.89172	6.91
Pd (ppb)	6.42	0.86	1.85781	3.28
Au (ppb)	14.3	1.69	1.06642	0.79

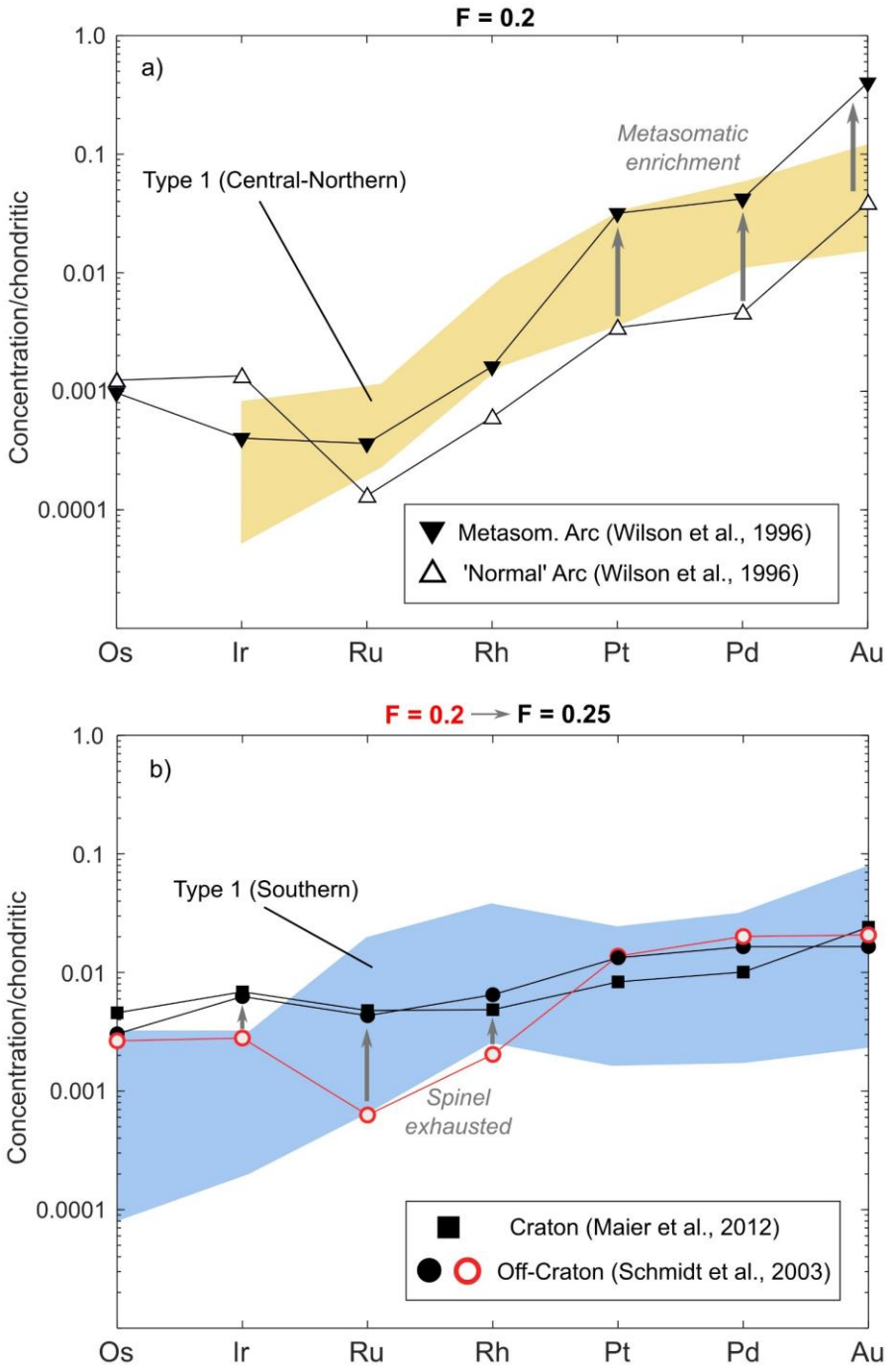

Figure 3.12 – *Melt modelling for Serra Geral magma PGE and Au concentrations based on the parameters from Table 3.2. (a) Arc xenolith starting compositions, representing Type 1 (Central-Northern) magma generation. Metasomatised mantle sources can produce the characteristic Pt-Pd-Au enrichment in the corresponding Paranapanema samples at ~ 20 % partial melting. (b) Cratonic and off-cratonic xenolith starting compositions, representing Type 1 (Southern) magma generation. Magma produced at 20 % partial melting (i.e., sulphides exhausted) releases PGE to roughly the chondrite-normalised concentrations in Gramado and Esmeralda samples, but the Ru-Rh 'hump' is not achieved until spinel is also exhausted (25 % partial melting with this set-up).*

Cratonic (Maier et al., 2012) and off-cratonic (Schmidt et al., 2003) peridotite xenoliths have a more even distribution in PGE concentrations, but in most cases are enriched in Ir, Ru and Rh, and depleted in Pt, Pd and Au with respect to arc sources (Table 3.2). Our models predict that once sulphides are exhausted, the resulting on/off craton melts produce nearly flat chondrite-normalised PGE-enrichment patterns (Figure 3.12b), but not the Ru-Rh 'hump' from Figure 3.8b-c. However, given that evidence shows that Type 1 lavas were derived from melts nearer the locus of lithospheric rifting (Beccaluva et al., 2020), we assume a higher-degree (i.e 25 %) melt fraction in the off-craton setting (i.e., thinner lithosphere, shallower/higher degree partial melts) as a best fit the PGE patterns in our Gramado and Esmeralda samples. This allows more spinel to be melted which increases Ir, Ru and Rh concentrations to match Type 1 (Southern) patterns (Figure 3.8b-c). In the absence of sulphide, our model can produce similar PGE enrichment curves, implying that these lavas, unlike Type 1 (Central-Northern), do not rely on metasomatic sulphides in the melting system. Elevated source bulk concentrations in the relevant metals are the key driver in resulting melt composition in all models, provided the host phase can be sufficiently melted. Sulphide exhaustion can plausibly occur at lower degrees of partial melting (down to 12%; Rehkämper et al., 1999), via quicker consumption rates. This would reduce the overall melting degree required in our system, which is approaching rift magmatism and whilst possible, may be restricted by lithospheric thickness (Gallagher and Hawkesworth, 1994).

Our modelling demonstrates that Type 1 (Central-Northern) magma compositions are best explained by a mantle source region with metasomatic sulphides which become exhausted during partial melting, while Type 1 (Southern) magmas can be generated by higher degrees of partial melting to exhaust *both* sulphides and spinel-group minerals (if sulphides were present at all). Locally heterogeneous SCLM beneath Brazil (Fodor et al., 2002; Carlson et al., 2007), as exists in other CFB provinces worldwide (Karoo in Jourdan et al., 2007; Emeishan in Song et al., 2008; the North Atlantic in Hughes et al., 2015; and South Australia in Wade et al., 2019), can generate diverse PGE signatures in melting signatures.

3.4.3. Melt components and the role of the SCLM in CFB magmatism

A unifying metallogenic model for Serra Geral must incorporate aspects of geodynamic, mineralogical and melting models to explain major and trace element signatures in the region. The variable enrichment and depletion of PGE and Au in Paraná CFB magma-types immediately characterises Type 4 (the highest-Ti magma-type of the HT group) as relatively deficient in all seven precious metals. In contrast, the Type 1 mafic magma-types contain the modelled enrichments in two different sets of PGE/chalcophiles – Pd, Au and Cu in Type 1 (Central-Northern), and Ru and Rh in Type 1 (Southern). As per Figure 3.12a-b, the concentrations can be explained by variable element compatibility and mineral assemblages expected in the melting region, which in turn implies changing conditions beneath the Tristan plume. Between the generation of Type 4 and Type 1, the mantle source has changed to distinctly spinel lherzolite (Figure 3.6d) (in agreement with Rämö et al., 2016). This indicates a progressive shift to shallower melting depths, which may have allowed higher degrees of partial melting (i.e., 20-25 %, as modelled in Figure 3.12a-b), permitting access to different zones and/or greater amounts of the SCLM as a melting source. Whilst alkaline-carbonatitic magmatism in LIPs can provide direct evidence of SCLM-derived melts (and hint as to potential PGE-bearing mineral transportation mechanisms via fluxing of mantle carbon; Blanks et al., 2020), rocks of this variety are rare in Paraná. However, contemporaneous Cretaceous lavas in eastern Paraguay, still within the PELIP (Figure 3.1c) bear strong alkaline-carbonatitic signatures (Comin-Chiaramonti et al., 2007), validating the potential presence of SCLM-derived materials in melts in the region generated in this wider event.

We propose a multi-component metallogenic model (Figure 3.13) to describe the incorporation of variable PGE assemblages throughout the geochemical magma-types in the Paraná CFB, in line with the region's geodynamic development in the Cretaceous (135-128 Ma; Figure 3.1a-b) and modelling from Figure 3.12.

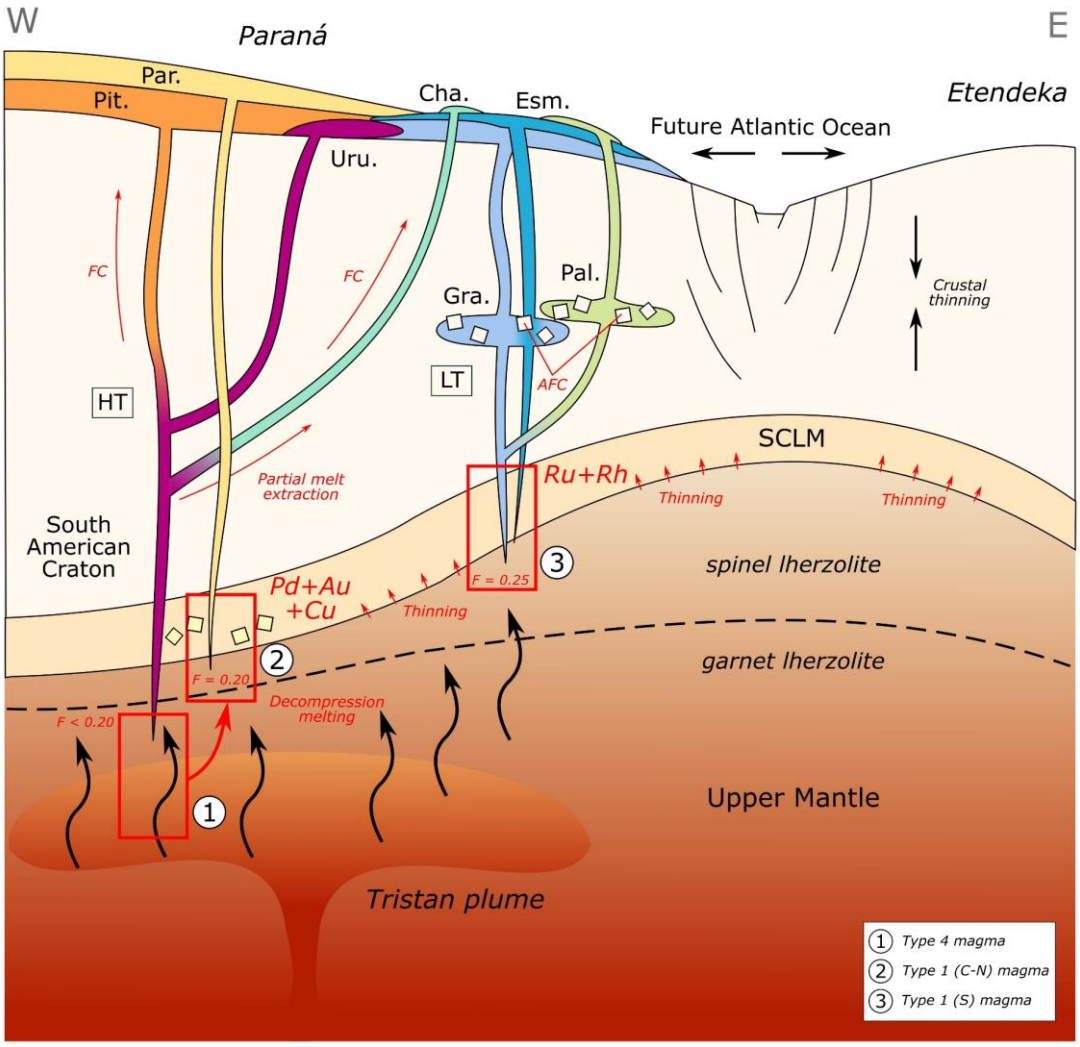

Figure 3.13 – *Metallogenic model for the Serra Geral flood basalts and their parent magmas based on geochemical interpretations, literature information and modelling (Figure 3.12). Thinner lithosphere above the Tristan plume, either situated nearer to the future Atlantic rift (i.e., south-east Paraná and Etendeka) or from progressive craton extension (i.e., north-west Paraná) promotes higher degrees of partial melting at shallower depths. Type 4 magmas diversify mainly by partial melt extraction and fractional crystallisation (FC) from a plume-proximal source with minimal crustal contamination. Type 1 (Central-Northern) magmas, generated when the HT source begins melting in shallow SCLM regions (F = 0.2), incorporate Pd, Au and Cu from metasomatic sulphides. Type 1 (Southern) lavas diversify by assimilation and fraction crystallisation (AFC), and mafic varieties contain elevated Ru and Rh content via higher degree melts (F = 0.25) of SCLM spinel and sulphides. Based on work by Beccaluva et al. (2020); Rämö et al. (2016); Turner et al. (1999).*

Firstly, we must establish the evolving geodynamic setting in Cretaceous Brazil as the mechanism behind the differing PGE enrichment. Prior to extension, a thick continental lithospheric 'lid' suppressed the degree of melting beneath the Gondwanan continent and confined CFB melt generation to deeper in the upper mantle (i.e., at the plume head), firmly within the upper mantle garnet lherzolite stability field (as in Arndt et al., 1993; White and McKenzie, 1995; Turner et al., 1996; Kerr, 1997). Following lithospheric thinning as a consequence of thermal weakening by the underlying mantle plume and the onset of continental rifting from the south-east ca. 134 Ma, the underlying mantle decompressed and enabled partial melting at shallower depths i.e., within the spinel lherzolite stability field (e.g., Ellam, 1992; Stein and Stein, 1992). This thinning would be most prevalent in south-eastern Paraná, near the future Atlantic coast, forming geographically-bound differences in lithospheric thickness and melting depth (Turner et al., 1996), decreasing from the north-west (HT lavas) to the south-east (LT lavas) (Gallagher and Hawkesworth, 1994; Beccaluva et al., 2020). This echoes the geodynamic setting of the Palaeogene proto-Icelandic rift-plume system in the North Atlantic – magmas from under the intact Greenlandic lithosphere and magmas at/near the developing Atlantic rift zone record different depths of melting and markedly different melt geochemistry as a result (e.g., Saunders et al., 1997; Kent and Fitton, 2000; Hughes et al., 2015; Lindsay et al., 2020). The transition from thick North Atlantic Craton to rifted lithosphere resulted in high- then low-Ti continental magma generation (Momme et al., 2006), reflected in their apparent depth and degree of melting, and garnet/spinel source signatures.

In the case of Paraná, we propose that partial melts generated at the garnet-spinel transition as a function of lithosphere extension can directly control the variable metal baskets in the Serra Geral magma-types as modelled (in line with Kerr, 1995; Klemme and O'Neill, 2000; Gibson et al., 2006). Although Serra Geral lavas generally follow the classic stratigraphy of Gramado to Esmeralda and Palmas (with minor Urubici intercalated) in the south and Pitanga to Paranapanema and Chapecó in the north (Figure 3.1c), it must be reiterated that the lavas are synchronous across the Paraná Basin. Evidence for synchronicity includes mixing between Esmeralda and Pitanga (De Min et al., 2017), Urubici occurrence between successive Gramado layers (Turner et al., 1996) and

Paranapanema underlying the ‘older’ Gramado in places (Turner et al., 1999). The ongoing development and diversification of the magmas does not necessarily equate to their complex temporal and spatial surface distribution sequence.

The smaller degree of crustal contamination and more enriched mantle melt signatures place Type 4 lavas as close to a plume component as possible in the region, such that Urubici and Pitanga lavas are enriched in LREE and incompatible elements (Figure 3.5e-f and 3.7e-f). Through time, as the lithosphere thinned, the melting region shifted to shallower depths in response to the lid effect, producing Type 1 (Central-Northern) magmas from a HT source (albeit with a drop in bulk TiO_2 concentration), evidenced by the transition from garnet to garnet-spinel to spinel lherzolite (Figure 3.6d) (Rämö et al., 2016). These melts successfully incorporated metasomatised (i.e., Pt, Pd, Au and Cu bearing) SCLM sulphides given the presumed increased degree of melting possible at reduced depths, modelled in Figure 3.12a. Silicic Chapecó magmas that were formed by small degree partial melt extraction from the HT magmas would not inherit the Pd, Au or Cu concentrations contained within Type 1 (Central-Northern) because their subsequent upper crustal development would have fractionated such elements into early crystals and removed them from the felsic system. It is unclear whether the differences in melting depth were a) progressive from a single evolving and shallowing melting site or b) spatially distinct despite the general ‘northern’ HT source. Given the synchronous nature of Serra Geral lavas, we opt for the latter view.

Further to the east, Type 1 (Southern) magmas were sourced from beneath thinner lithosphere still, near the Atlantic rift and further from the plume focus – this produced higher degree partial melts within the spinel lherzolite mantle (Figure 3.6d) with much more dilute TiO_2 concentrations (Figure 3.3a). This coincides with greater amounts of extension in Low-Ti dykes in the region compared to High-Ti dykes (Gallagher and Hawkesworth, 1994), indicating significant progress in continental rifting between these stages. These higher-degree melts were able to exhaust sulphide and spinel, to produce the IPGE and Rh dominant signatures in Figures 3.8b-c and 3.12b. Beccaluva et al. (2020) suggest that where HT magmas were less viscous and were able to rise to the surface with minor assimilation of crustal material, LT magmas stalled in

subsurface chambers prior to eruption. All LT Type 1 (Southern) lavas consequently exhibit geochemical evidence for contamination, such as high $^{87}Sr/^{86}Sr$, low εNd and crustal U-Th-Pb isotopic signatures (Peate, 1997). The transition from Gramado to Esmeralda within Type 1 (Southern) did not visibly affect PGE concentrations (Figures 3.9a-f). Palmas lavas formed from protracted upper crustal development of LT lavas, in this case with more extensive AFC than the mafic melts (Garland et al., 1995; Milner et al., 1995b), which may explain the loss of PGE from parental Type 1 magmas.

Overall, the shifting melting depth imposed on the Tristan plume in response to the breakup of Gondwana drives regional variations in metallogenesis. It is highly likely that the SCLM beneath Brazil is heterogeneous in terms of precious metal content hosted in metasomatic sulphide phases in the mantle. Whilst Type 4 magmas did not receive ‘spiked’ PGE signatures from increased degrees of melting, the shallower-sourced Type 1 melts exhausted sulphides and, for the Southern magmas, spinel-group minerals to attain elevated precious metal contents. Future multiple sulphur isotope and radiogenic isotope studies of the Paraná rocks alongside these PGE analyses may help pinpoint the exact source of enrichment and support the SCLM theory built in this chapter. The scale of the PELIP, localised nature of metasomatism, and synchronicity of geochemically diverse regional lavas reinforces the idea that a variety of concurrent magmatic systems worked in unison to produce the complex stratigraphy of Serra Geral.

3.5. Conclusions

The bulk major and trace element, PGE and Au data and quantitative modelling presented in this chapter support a progressively thinning lithosphere in response to thermal uplift from the upwelling Tristan plume and congruent crustal extension. This in turn directly affects the depth and source of Paraná intracontinental partial melts and their resulting metal baskets.

1. Serra Geral Type 4 lavas (i.e., Urubici and Pitanga) do not contain any significant enrichment in precious metals, primarily due to their origin as deeper asthenospheric melts with plume-derived trace element enrichments but no obvious precious metal contribution from the SCLM.
2. Serra Geral Type 1 (Central-Northern) lavas (i.e., Paranapanema) contain elevated Pd concentrations, coupled with higher mean Au and Cu than the other magma-types, which we attribute to a shallower melting environment, but still primarily within the asthenosphere, promoting the incorporation of metasomatically-enriched Proterozoic SCLM.
3. Serra Geral Type 1 (Southern) lavas (i.e., Gramado and Esmeralda) display unique Ru-Rh enrichment that can be linked to shallow SCLM melting at the developing rift zone, and spinel and/or sulphide incorporation from the melting source.
4. The heterogeneous PGE enrichment of cratonic SCLM by metasomatism in intracontinental settings, as exhibited beneath the North Atlantic Igneous Province, the North China Craton and Ethiopia, promotes variable metallogenic characters throughout CFB provinces. This highlights the crucial role of plume-SCLM interaction as a potential precursor to the generation of PGE ore deposits in the upper crust from intracontinental magmas.

Chapter 4

Precious metals in Tenerife: Investigating metallogeny in plume-derived lavas from the western Canary Islands and beyond

Chapter Summary

The Canary Islands chain, consisting of seven age-progressive main islands, is the volcanic expression of an oceanic intraplate thermal anomaly imposed by a mantle plume close to the passive margin of NW Africa. Magmatism in the area is heterogeneous in temporal and volcanological terms, and this is reflected in the variable lava geochemistry across some islands and between the islands. This chapter presents a new suite of whole-rock major element oxide, trace element, PGE and Au data for basalts on Tenerife, the largest of the Canary Islands. Through analysis of the geochemistry of Tenerife basalts, particularly in comparison to the adjacent, younger islands of El Hierro and La Palma, the chapter demonstrates how melting heterogeneities in the mantle source could influence the precious metal budget of the Canary Islands plume and its volcanic products. Tenerife basalts are alkaline, generated by 1-5 % partial melting in the plume source and are depleted in total PGE (mean 1.63 ppm) with respect to El Hierro and La Palma (mean 3.27 and 6.13 ppm, respectively); Pt and Pd in particular are often an order of magnitude lower in Tenerife. Modelling of Tenerife melt compositions indicates that the more compatible Os, Ir, Ru and Rh are retained in the mantle source in higher amounts than Pt, Pd and Au due to the varying melting susceptibility of their respective mineral hosts, particularly silicates and oxides, as well as sulphides. A further fractionation of Pt and Pd in Tenerife lavas can be explained by a multi-stage melting model, in which the less compatible PGE signatures are inherited from recycled plume components, previous partial sulphide melting events or early removal of sulphur from the mantle source. Consequently, even small changes in melting degree and source composition have significant impacts the metal budget of plume-derived lavas.

4.1. Introduction

Mantle plumes and related intraplate magmas are commonly associated with Ni-Cu-PGE mineralisation (e.g., Lightfoot et al., 1993; Hawkesworth and Scherstén, 2007; Zhang et al., 2008; Sobolev et al., 2009; Naldrett, 2010; Maier and Groves, 2011; Hassan et al., 2015). However, the role that plumes play in controlling precious metal abundances in intraplate magmas (and thus metallogenesis) is debated. Some studies highlight the inherent diapiric nature mantle plumes to imply that siderophile precious metals may be sourced from the outer core at the core-mantle boundary (Hauri and Hart, 1997; Brandon and Walker, 2005; Humayun, 2011; Cagney et al., 2016). Other workers suggest that plumes play a passive role in precious metal sourcing, only providing heat to melt other metal reservoirs, such as the sub-continental lithospheric mantle (SCLM) (e.g., Kepezhinskas et al., 2002; Begg et al., 2010; Griffin et al., 2013; Hughes et al., 2014; Hughes et al., 2015; Tassara et al., 2017; Holwell et al., 2019; Wade et al., 2019). The relationship between plumes and their associated mineral deposits are poorly constrained in comparison to other magmatic mineral systems such as Cu-porphyries.

Shallow crustal processes, including assimilation, fraction crystallisation and contamination, may concentrate precious metals to form ore deposits (e.g., Thériault et al., 1997; Andersen et al., 1998; Arndt et al., 2003; Li et al., 2009; Keays and Lightfoot, 2010; Nielsen et al., 2014). Therefore, whilst crustal mineralising processes are crucial to the formation of ore, in the case of orthomagmatic deposits, the initial fertility of a magma feeding that crustal system is important in dictating the metal basket of mineralisation. Intraplate magmatism often leads to the eruption of flood basalts during initial voluminous plume head melting of the asthenosphere (e.g., McKenzie and White, 1989; Campbell and Griffiths, 1990; Griffiths and Campbell, 1990), and lavas in such regions typically share genetic geochemical signatures with underlying intrusive bodies that may bear elevated PGE concentrations (Kent and Fitton, 2000; Ripley et al., 2003). Thus, we can use detailed geochemical data from plume-derived lavas to study the parent magmas in a volcanic system and investigate source properties conducive to mineralisation elsewhere in an igneous province. By studying plume-derived lavas from a purely oceanic setting, we remove the late-stage influence of continental crustal processes, to isolate signatures associated with

mantle source properties only. However, even these ocean island basalts (OIB) have significant geochemical and isotopic heterogeneity, and can indicate a wide variety of source regions, mutable melt components, and variable degrees of partial melting, oxygen fugacity or sulphide saturation, all of which impact on the eventual composition of plume-derived magmas (e.g., Zindler and Hart, 1986; Hofmann, 2003; Stracke et al., 2005; Deschamps et al., 2011; Xia and Li, 2019).

In this chapter, we interrogate a new suite of bulk geochemical data, including major element oxide, trace element, PGE and Au concentrations in plume-derived mafic lavas from the island of Tenerife from the Canary Island chain. Herein, we investigate how PGE behave in an oceanic plume environment, with the support of data from other islands generated by the same plume and two other similar oceanic plumes – Hawaii and Iceland. The objective of the chapter is to characterise the metallogenic behaviour of a single isolated and well-preserved recent (active) oceanic plume environment with view to examine how plume properties and melting processes through time affect intraplate magma metal baskets, and if this differs throughout the Canary Island chain.

4.1.1. Geodynamics of the Canary Islands plume

The Canary Islands are a series of subaerial oceanic volcanic landmasses off the Atlantic north-west coast of Africa, that are generally thought represent the surface expression of the Canary mantle plume (Carracedo et al., 2002; Hoernle and Carracedo, 2009) (Figure 4.1a). They comprise the main islands of Fuerteventura, Lanzarote, Gran Canaria, Tenerife, La Gomera, La Palma and El Hierro, which young progressively to the west (Abdel-Monem et al., 1972) (Figure 4.2). Smaller satellite islands can be found north of the main island chain, including the Selvagen Islands and associated seamount complexes. Like the Hawaiian-Emperor chain in the Pacific Ocean (Morgan, 1971; Jackson et al., 1972; Hieronymus and Bercovici, 2001; Harrison et al., 2017), the Canary Islands are a hotspot trail generated by tectonic plate motion relative to a thermal anomaly in the mantle. Volcanic activity in the Canary Islands spans from the inception of seafloor magmatism (ca. 70-60 Ma according to Steiner et al., 1998; ca. 35-30 Ma according to Cantagrel et al., 1993), to initial subaerial volcanism in Fuerteventura (ca. 24-21 Ma; Carracedo et al., 1998) and until the present day.

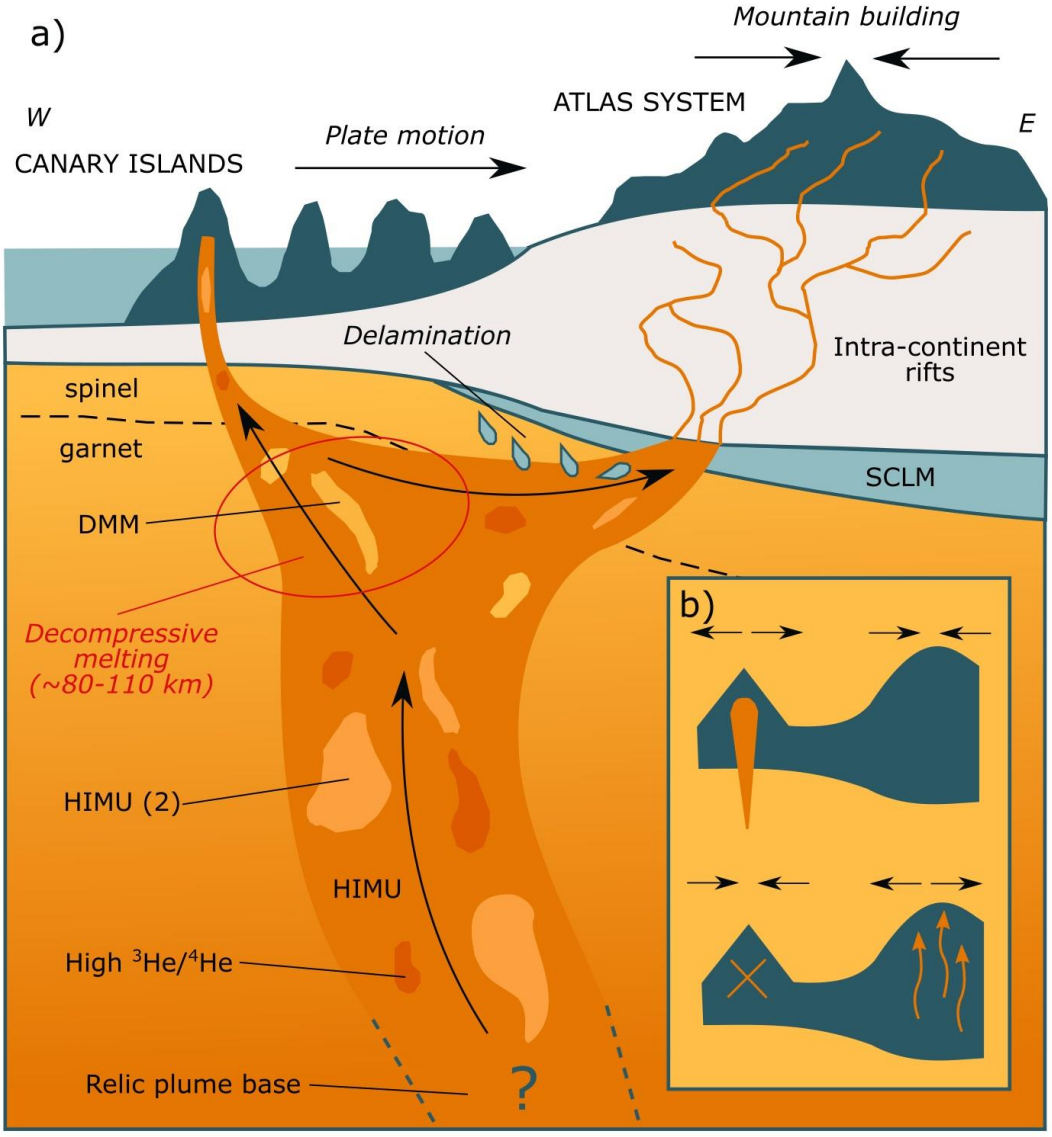

Figure 4.1 – *(a) Schematic cross-section of the Canary Islands plume, summarising heterogeneity in magma geochemistry and the relationship with the Atlas Mountain system on the northwest African coast. (b) Interrelationship between Canary Island and Atlas volcanism in response to tectonic forces. Adapted from Carracedo et al. (1998); Anguita and Hernán (2000); Duggen et al. (2009); Day et al., 2010; Taylor et al. (2020).*

The hotspot trail morphology broadly reflects the ENE movement of the African plate above the Canaries plume, with periodic fluctuations in the rate of volcanism (Hoernle and Schmincke, 1993; Wysession et al., 1995). The African Plate is regarded as a “slow” moving plate, moving only 9-12 mm per year at its passive margin (O’Connor and Duncan, 1990; Hoernle and Carracedo, 2009), which generally creates more complex eruption sequences in comparison to

faster-moving Pacific hotspot trails (Carracedo et al., 1998). The Canary Islands provide representation for all three stages in a volcanic lifecycle along the length of the chain: Lanzarote, Fuerteventura and Gran Canaria are erosional; Tenerife is at the peak of edifice construction verging on erosional; and La Gomera, La Palma and El Hierro are still under their construction stage (Carracedo, 1994). All of the islands excluding La Gomera have erupted in the last five centuries (Cantagrel et al., 1984; Hoernle and Carracedo, 2009). The age progressive island chain is bifurcated from La Gomera onwards (Figure 4.2). This resembles the Tristan-Gough plume-related hotspot trail further south from the Canaries, part of the 135 Ma-present Paraná-Etendeka Large Igneous Province (PELIP), which formed a split morphology following a sudden tectonic adjustment above the plume focus ca. 70 Ma (e.g., Le Roex et al., 1990; Gibson et al., 2005; Rohde et al., 2013a; Rohde et al., 2013b; O'Connor and Jokat, 2015; O'Connor et al., 2018; Homrighausen et al., 2019). The complexity and perceived temporal irregularity of genesis of the Canary Islands is further exemplified by La Gomera having a radiometric age that is older than Tenerife despite being in a "younger" geographic position in the chain (Guillou et al., 2004); disruption in plate motion and/or melting at this stage is highly likely.

The Canary Islands share a possible genetic link with the contemporaneous inland Atlas fault system (e.g., Duggen et al., 2009), an area of intense active deformation and mountain building in the NW African continental margin including the Atlas and Rif mountains. Originally, the Canary chain was thought to be an oceanic ridge branching off from the Atlas fault system, but this was disproved by bathymetric orientation studies (Carracedo et al., 1998; Anguita and Hernán, 2000). The plume model is broadly supported for the islands, with deep mantle isotopic source components recognised in lavas throughout the Canaries, particularly on the islands of El Hierro, La Palma and Gran Canaria (Marcantonio et al., 1995; Gurenko et al., 2009; Day et al., 2010; Day and Hilton, 2011). Compression from Atlas tectonics altering the pathway for the plume melting column above the slow African plate migration could explain the temporal disruptions to chain progression (Carracedo, 1994; Carracedo et al., 1998). The push-pull relationship between the Canaries and Atlas systems may determine the productivity of Canarian oceanic volcanism depending on the availability of low-pressure zones in response to lithospheric flexion (Figure 4.1b) (Anguita and

Hernán, 2000). Duggen et al. (2009) extend this Atlas-Canaries relationship to the SCLM – lavas produced during infrequent Atlas volcanism share clear $^{207}Pb/^{204}Pb$ and $^{206}Pb/^{204}Pb$ similarities to lavas from the Canary Islands plus delaminated SCLM material, and are distinct from onshore intraplate lavas in Egypt and Sudan. The study describes a subcontinental lithospheric “corridor” under the passive margin that promotes the sporadic lateral inflow of Canary Island mantle material (Figure 4.1a), aided by the plume thermal anomaly and thinning lithosphere at the edge of Africa (Duggen et al., 2009).

The Canary Islands present an interesting location for investigating plume magmatism compared to Hawaii and Iceland, as they exhibit differences in key intraplate magmatic characteristics established by the latter two settings (summarised in Belay et al., 2019). The proximity of the chain to the African passive margin imposes different mantle conditions than other OIB localities far from the continent with geodynamic implications for such a relationship (Carracedo et al., 1998). Unlike the highly productive Hawaiian and Icelandic plumes (Courtillot et al., 2003), in which volcanism progressed relatively smoothly with consistent time-progressive lava generation, well-constrained by radiometric dating, the Canaries have been characterised as temporally patchy, spatially irregular, prone to eruption hiatuses, and difficult to date (Hoernle and Schmincke, 1993; Taylor et al., 2020). Furthermore, the Canary Island chain presented major challenges to bathymetric swells normally associated with thermal anomalies from the lower mantle. Through time, the “blob” theory came to prominence (Hoernle and Schmincke, 1993; Anguita and Hernán, 2000; Aulinas et al., 2010), in which heterogeneous mantle component inclusion in the rising plume column produced highly variable melting and eruption rates resulting in fluctuating geochemical and isotopic signatures in lavas. This developed into the recent “pulsing” plume theory (Taylor et al., 2020), which refined and unified concepts from the prior model whilst satisfying the majority of anomalies that contrasted with the original simple plume theory, including the transpression-transtension relationship with inland Atlas tectonic activity (Duggen et al., 2009; Wittig et al., 2010a).

Geochemical variability in lavas from the Canary chain reflects the complicated geodynamics in the region enforced by its unique plume properties. Multiple mutable mantle components (recognised by their distinctive isotopic

properties) are incorporated into lavas on the islands. These include HIMU (i.e., recycled oceanic lithosphere with highly radiogenic Pb isotope signatures), depleted MORB-like mantle (DMM), in addition to high $^{3}He/^{4}He$ domains from the lowermost mantle, each of which vary in prominence throughout the islands (Day et al., 2010; Day and Hilton, 2011) (Figure 4.1a). In general, the Canary Islands are notably more alkaline than typical tholeiite-dominated hotspot islands like in Hawaii or Iceland, which is generally an early indication that there are smaller degrees of partial melting involved in magma generation for the region (Hoernle and Schmincke, 1993). The chain hosts two separate alkalinising trends – slowly alkalinising (Lanzarote, Fuerteventura, La Gomera and El Hierro) and rapidly alkalinising (Gran Canaria, Tenerife and La Palma) (Cantagrel et al., 1984). The different geochemical trends reflect variable influence of competing African and Atlantic mantle sources, further implying heterogeneity in the material melting in the system (Hernández-Pacheco and Ibarrola, 1973), and the prevalence of depleted mantle sources in magmas from the region (Day et al., 2010; Day and Hilton, 2011). The geochemical heterogeneity in surface lavas resemble the Loa and Kea compositional split in the Hawaiian chain (e.g., Huang et al., 2011; Hofmann and Farnetani, 2013; Harrison et al., 2017; DeFelice et al., 2019; Harrison et al., 2020). Unlike in Hawaii, where two bulk geochemical trends exist parallel to each other often within single islands, the stresses of adjacent lithospheric blocks in the Canaries chain are thought to have delayed and eventually split the progression into two distinct lines (Hieronymus and Bercovici, 1999) (Figure 4.2).

4.1.2. Geology of Tenerife

Tenerife is the largest and highest of the seven Canary Islands, with an areal extent of 2,058 km^2 and maximum elevation of 3,718 m from the seafloor (Hoernle and Carracedo, 2009). It initially formed from three individual edifices of basaltic magmatism in the Miocene-Pliocene, preserved today in the north-western, north-eastern and southern tips of the island to form a triangular landmass with the more recent, evolved volcanics in the centre. The mafic corners (i.e., massifs) are collectively referred to as the Tenerife Old Basalt Series (Ancochea et al., 1990; Araña et al., 1994; Thirlwall et al., 2000; Longpré et al., 2009; Geyer and Martí, 2010). The distribution of major geological units of Tenerife and their relative ages are summarised in Figure 4.2.

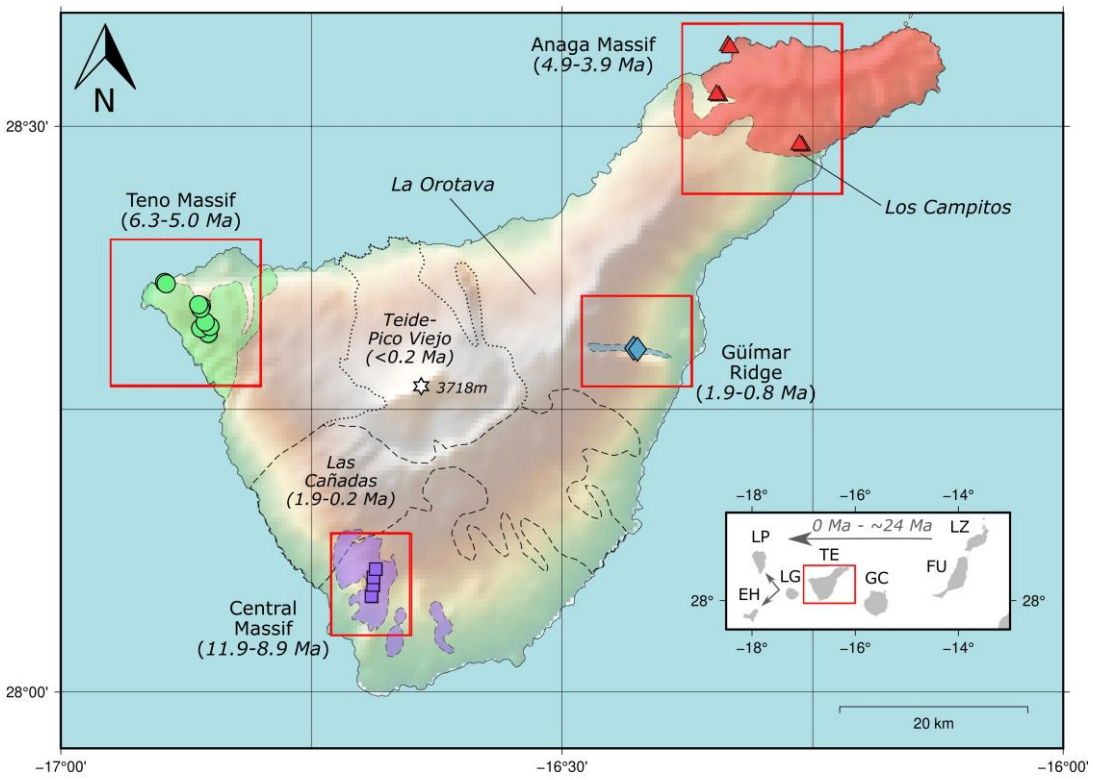

Figure 4.2 – *Locality map of Tenerife within the Canary Islands (inset). The relative spatial extent of each of the three Old Basalt massifs (shaded) plus the Güímar ridge and modern volcanics (dotted and dashed areas) are highlighted within. Area between highlighted massifs are primarily ridge volcanic series. Samples collected for this study are shown with the four symbol classes. The inset map provides a generalised younging direction for the Canaries from east to west over ~24 Ma. Ages taken from Guillou et al. (2004). LZ – Lanzarote, FU – Fuerteventura, GC – Gran Canaria, TE – Tenerife, LG – La Gomera, LP – La Palma, EH – El Hierro.*

The southern Roque del Conde Old Basalt massif is entirely made of basaltic lava flows (11.9-8.9 Ma; Guillou et al., 2004), is the least preserved of the series, and had an estimated original flow thickness of > 1,000 m (Abdel-Monem et al., 1972; Ancochea et al., 1990). It is the only exposed section of the former Central edifice and hosts the oldest basalts on the island. The north-western Teno Old Basalt massif comprises a Lower Unit of basalt pyroclastics and lavas (6.3-6.1 Ma) and a much thinner Upper Unit of basaltic and trachytic lavas (5.6-5.0 Ma) (Guillou et al., 2004; Leonhardt and Soffel, 2006). The Teno basalts erupted in a single melting event of varying degrees of partial melting (Longpré et al., 2009), relatively rapidly in comparison to the other two edifices.

The north-eastern basalts of the Anaga Old Basalt massif were previously dated to be the oldest of the three massifs, with K-Ar ages of 16.1 Ma (Abdel-Monem et al., 1972). However, issues with discerning alteration of potassic phases in the lavas were rectified by more modern K-Ar and $^{40}Ar/^{39}Ar$ dating which eventually refined the date range of the series to a much more recent 4.9-3.9 Ma (Guillou et al., 2004). Unlike the Central and Teno massifs, the Anaga series is polygenetic and its eruptive sequence is more complex that the others. Its Lower Unit consists of primarily volcaniclastic flows, with a 1,000 m thick Middle Unit of basaltic lavas and pyroclastics unconformably overlying the earlier rocks. The Upper Unit completes the Anaga series with a thinner layer of basaltic to phonolitic lavas (Ancochea et al., 1990). The three edifices were built throughout the Miocene and Pliocene via cycles of independent magmatism with significant and frequent time-gaps likely associated with mantle plume pulses and/or transpression from inland tectonics (Carracedo et al., 1998; Duggen et al., 2009).

A large composite edifice, the Las Cañadas member, produced multiple amalgamating eruptions peaking between 1.9 and 0.2 Ma (Ancochea et al., 1990), uniting the previous Old Basalts as one island. The three-stage development of Las Cañadas saw trachybasaltic, trachytic and finally phonolitic lavas erupted in succession (Cantagrel et al., 1999; Bryan et al., 2002), building the centre of the island to its current height centred round the active Teide volcano. The triangular island shape may reflect eruption of Las Canadas via a centred triple-junction fault system (Carracedo, 1994). A dorsal ridge of Las Cañadas lava reached north-eastwards towards the Anaga Old Basalts, today framed by the La Orotava and Güímar valleys on either side. Modern volcanism is dominated by Teide-Pico Viejo eruptions (< 0.2 Ma; Ancochea et al., 1990), the final petrological member of the Tenerife igneous pile; the youngest flows on the island, Lavas Negras, erupted just 1,171 years ago (Carracedo et al., 2007).

This chapter attempts to reconcile geological and geochemical information from the Tenerife massifs to characterise the metallogenic controls exerted by the Canaries plume, with particular attention to how geochemical signatures vary throughout the earliest lavas on Tenerife and between the individual Canary Islands. Considering the marked isotopic heterogeneity described in the literature throughout the island chain through a relatively short time span, this may also be reflected in precious metal abundances across the constituent lavas.

4.2. Materials and methods

4.2.1. Tenerife samples

Basaltic lava samples were collected primarily from the Anaga, Teno and Roque del Conde Old Basalt provinces, to represent the initial plume melts on Tenerife prior to the more recent evolved lava compositions from the Las Cañadas, Teide and Pico Viejo edifices. The sample set comprises 24 basalts from separate lava flows (5 from the Roque del Conde area, 10 from the Teno area, 2 from Barranco del Badajoz in the Güímar valley, and 7 from the Anaga area). The younger Güímar samples were primarily collected for reference against the three older massifs. Supplementary S4.1 summarises the hand-specimen petrology of the sample set and sample localities are displayed in Figure 4.2. Fresh, unaltered and amygdale-free samples were prioritised. Samples are primarily divided into phenocryst-rich and phenocryst-poor varieties. The former variety is referred to as ankaramite in the literature and is characterised by 40-60 % euhedral clinopyroxene and olivine phenocrysts in a mafic groundmass comprising predominantly clinopyroxene and plagioclase (as also described by Thirlwall et al., 2000). The less phyric samples (i.e., < 20 % phenocrysts) have a similar groundmass to the ankaramites, dominated by clinopyroxene and plagioclase. The rare phenocrysts in these samples are smaller, more skeletal olivine.

4.2.2. Laboratory techniques

New whole-rock geochemical data were generated for the 24 Tenerife samples, including measurements for major element oxide, trace element, PGE and Au concentrations. Amygdales and weathered material were removed from samples to ensure primary elemental concentrations were detected, before samples were crushed using a hardened steel crusher and ground to analytical-grade powders using a chrome-steel TEMA mill at Camborne School of Mines, University of Exeter.

Laboratory methods broadly follow those from Chapter 3 (i.e., Lindsay et al., in review[a]). Major element oxides were measured using X-Ray Fluorescence (XRF) at Camborne School of Mines. Following Kystol and Larsen (1999) and Tegner et al. (2009), dried and ignited samples were mixed with lithium borate flux in platinum crucibles and fused in a furnace. Molten samples were cooled in

platinum moulds with the aid of an ammonium iodide wetting agent to form fused beads. Beads were analysed alongside standards (AGV-1, BHVO-2, BIR and DNC-1) using a Bruker S4 Pioneer XRF Spectrometer, running at 50-111 mA and 27-60 kV. Measured concentrations were corrected to anhydrous values prior to interpretation. Trace element concentrations were measured using Inductively-Coupled Plasma Mass Spectrometry (ICP-MS), also at Camborne School of Mines. The technique involved the dissolution of powdered samples using the 4-Acid method, as per McDonald and Viljoen (2006). Element detection was performed on dissolved samples and standards (BCR-2 and Bir-1a) using an Agilent 7700 Series mass spectrometer.

Six PGE and Au concentrations were measured using the NiS Fire Assay technique with tellurium co-precipitation following Huber et al. (2001) and McDonald and Viljoen (2006), conducted at Cardiff University. By mixing and melting 15 g of sample, 12 g borax flux, 6 g sodium carbonate, 0.9 g solid sulphur, 1.08 g nickel and 1 g silica in a furnace at 1000°C, a sulphide bead was separated from each quenched sample silicate matrix. The beads were then dissolved in hydrochloric acid, re-precipitated (alongside tellurium), filtered and diluted, and the precious metal content of the final solutions were measured using a mass spectrometer. Blanks and standards (TBD1 and WPR1) were run alongside samples through the full process, plus duplicates. Standard measurements are in agreement with the published values (see Supplementary S4.2). Detection limits (i.e., lowest recorded blank values) were 0.0052 ppb for Os, 0.0026 ppb for Ir, 0.0603 ppb for Ru, 0.0152 ppb for Rh, 0.1458 ppb for Pt, 0.0662 ppb for Pd and 0.0070 ppb for Au.

Supplementary S4.2 provides all raw measured bulk element concentrations in each sample, separated by method, in addition to blank, standard and duplicate measurement information where appropriate. Supplementary S4.3 also provides an amalgamated data sheet with all measured elements for all sample localities.

4.2.3. Literature data

To contextualise our new data within the Canary Islands and on a global scale, we have incorporated bulk geochemical data from other studies for the islands of El Hierro, La Palma, Gran Canaria, Iceland and Kilauea (Hawaii). All islands are of oceanic plume-derived origin and feature minimal interaction with continental lithosphere. El Hierro and La Palma data are from Day et al. (2010) and comprise major element oxide, trace element and PGE (excluding Rh) concentrations. The Gran Canaria data set from Asavin et al. (1997) is significantly smaller, and comprises selected major element oxide and PGE concentrations. The full suite of major element oxide, trace element, PGE and Au concentrations from Iceland and Kilauea were run exclusively for this thesis and analysed alongside the Tenerife samples, with the same methodology. These two localities are primarily used for trace element and PGE interpretations, to allow for the easier identification of major element oxide fractionation processes in the Canary Islands only. Supplementary S4.3 provides the complete set of new and published data for each locality to be used in this chapter, with a variety of normalisations to published chondritic and primitive mantle concentrations (McDonough and Sun, 1995) in Appendix B1.

4.3. Results

4.3.1. Major and trace element geochemistry of the Tenerife lavas

4.3.1.1. Major element oxides

Mean concentrations for each of the four Tenerife sample localities are given in Table 4.1. Figure 4.3 arranges the Canary Island samples in a Total Alkali-Silica (TAS) diagram, and classifies the majority of rocks as basalts to basanites, within the alkali developmental trend. Teno samples tend to be the least alkali-rich of the Tenerife samples, while Roque del Conde and the majority of Anaga samples plot closer to trachy-basalts than the remaining rocks. Samples from Güímar and two from Anaga are significantly more alkaline, plotting within the phono-tephrite and tephra-phonolite regions of the diagram. From the literature set, La Palma samples are highly variable, but are largely classified as basanites, as are El Hierro samples but with slightly lower alkali concentrations. Gran Canaria samples are more silicic, with some plotting within trachy-basalt

region. Selected La Palma and Gran Canaria outliers are extremely alkali and silica enriched, classified as trachytes to phonolites.

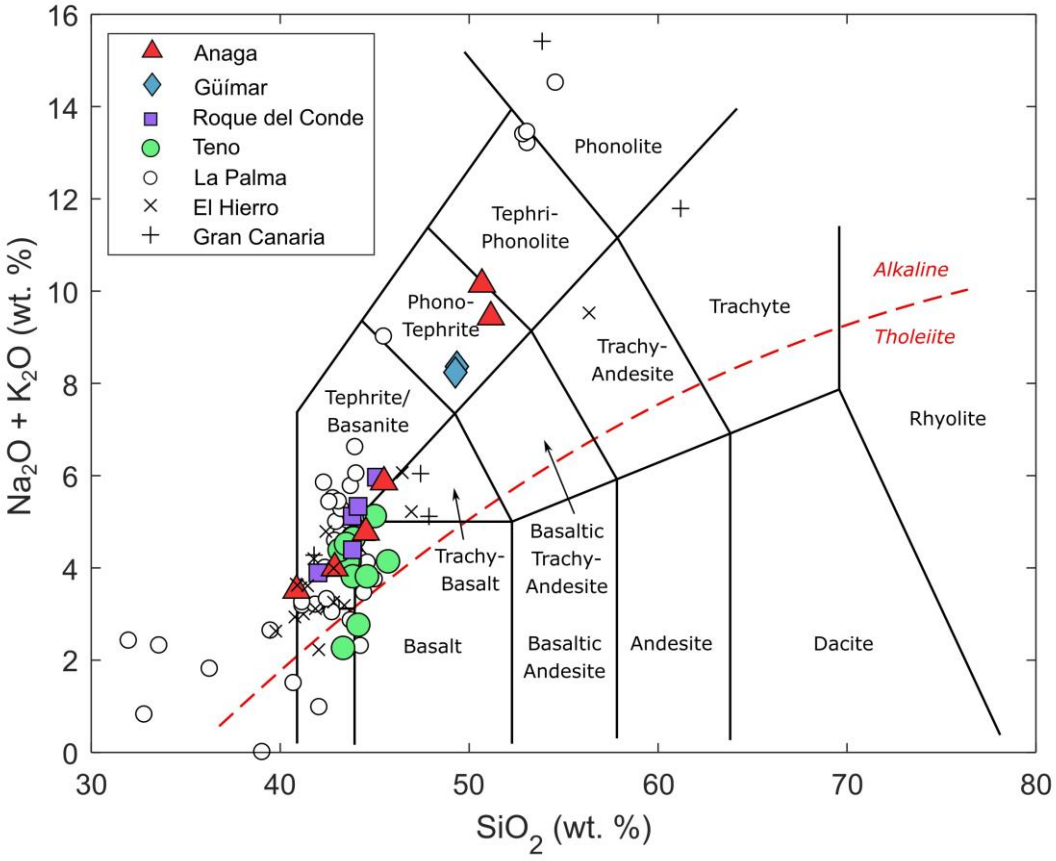

Figure 4.3 – *Total Alkali vs. Silica (TAS) diagram for Tenerife samples plus literature data for El Hierro and La Palma (Day et al., 2010), and Gran Canaria (Asavin et al., 1997). Canary Island samples lie distinctly along the alkaline development trend.*

Table 4.1 (overleaf) - *Mean bulk major element oxide (in wt.%) and trace element (in ppm) concentrations of Anaga (n = 7), Güímar (n = 2), Roque del Conde (n = 5) and Teno (n = 10) basalt samples from Tenerife. For full bulk geochemical measurements, see Supplementary S4.2 and S4.3.*

	Anaga	Güímar	Roque del Conde	Teno
SiO_2 (wt.%)	45.6	50.0	44.1	44.4
TiO_2	3.60	2.47	3.65	3.44
Al_2O_3	15.3	17.9	14.2	14.1
Fe_2O_3	12.4	9.1	13.1	13.8
CaO	9.7	7.8	11.0	11.2
MgO	6.12	2.77	7.41	7.83
SO_3	0.14	0.09	0.08	0.07
Na_2O	4.12	6.16	3.51	2.87
K_2O	1.48	2.07	1.39	1.13
P_2O_5	0.61	0.84	0.91	0.64
MnO	0.20	0.21	0.18	0.18
Sc (ppm)	23.8	10.2	27.4	30.2
V	269	139	295	312
Cr	173	48	290	319
Co	42	16	50	58
Ni	65	3	109	143
Cu	53	9	91	97
As	5.2	4.9	6.1	6.3
Se	7.4	7.8	8.0	6.4
Rb	73	47	368	130
Sr	1208	1251	1146	975
Y	35	37	33	30
Zr	406	577	302	286
Nb	108	167	104	80
Ba	784	900	644	433
La	83	115	82	64
Ce	162	210	160	118
Pr	19	22	19	15
Nd	74	82	75	59
Sm	13	14	14	11
Eu	4.14	4.17	4.22	3.50
Gd	11.1	11.3	11.6	9.89
Tb	1.48	1.51	1.50	1.31
Dy	8.12	8.36	8.00	7.06
Ho	1.39	1.45	1.33	1.19
Er	3.53	3.80	3.33	2.96
Tm	0.45	0.50	0.42	0.37
Yb	2.77	3.20	2.50	2.22
Lu	0.39	0.46	0.34	0.30
Hf	8.84	11.65	7.02	6.69
Ta	5.94	9.51	14.40	4.82
W	1.97	2.87	4.07	2.89
Pb	11.4	10.2	41.3	9.47
Bi	0.07	0.03	1.23	0.62
Th	8.07	15.7	10.2	6.96
U	1.92	4.51	3.18	1.96

Figure 4.4 displays a selection of anhydrous major element oxide concentrations against MgO for all Canary Islands samples, along with approximate mineral fractionation vectors. Overall, Tenerife samples have relatively low MgO concentrations, primarily between 5 and 10 wt.%, whilst La Palma and El Hierro span between 5 and 18 wt.%. The small population of Gran Canaria samples plot mainly < 5 wt.% MgO, with a single sample closer to 15 wt.%. Tenerife, La Palma and Gran Canaria share reasonably similar TiO_2 concentrations (~ 4 wt.%), with El Hierro generally more enriched at ~ 6 wt.% (Figure 4.4a). A similar trend is observed in Fe_2O_3 (Figure 4.4b), CaO (Figure 4.4e) and P_2O_5 (Figure 4.4h) with MgO, in terms of relative element enrichment/depletion of each locality. There is a negative correlation between Al_2O_3 and MgO, with Tenerife significantly more enriched in Al_2O_3 (12-20 wt.%) than the other islands (< 12 wt.%) (Figure 4.4c). In Figures 4.4f-g, Na_2O and K_2O have a less pronounced negative correlation with MgO, with Tenerife slightly more enriched in Na_2O and K_2O (3-7 wt.% and 1-4 wt.%, respectively) compared to the majority of the other island samples. No obvious trends are recognised in Figure 4.4d, with similar MnO concentrations across most samples (0.16-0.24 wt.%) with two Anaga, two La Palma and one El Hierro sample > 0.24 wt.%. There is a significant change in fractionation trend at ~ 7 wt.% MgO across TiO_2, Fe_2O_3, CaO, Na_2O, K_2O and P_2O_5 plots; Al_2O_3 has a consistent negative slope with MgO, and there is no correlation with MnO.

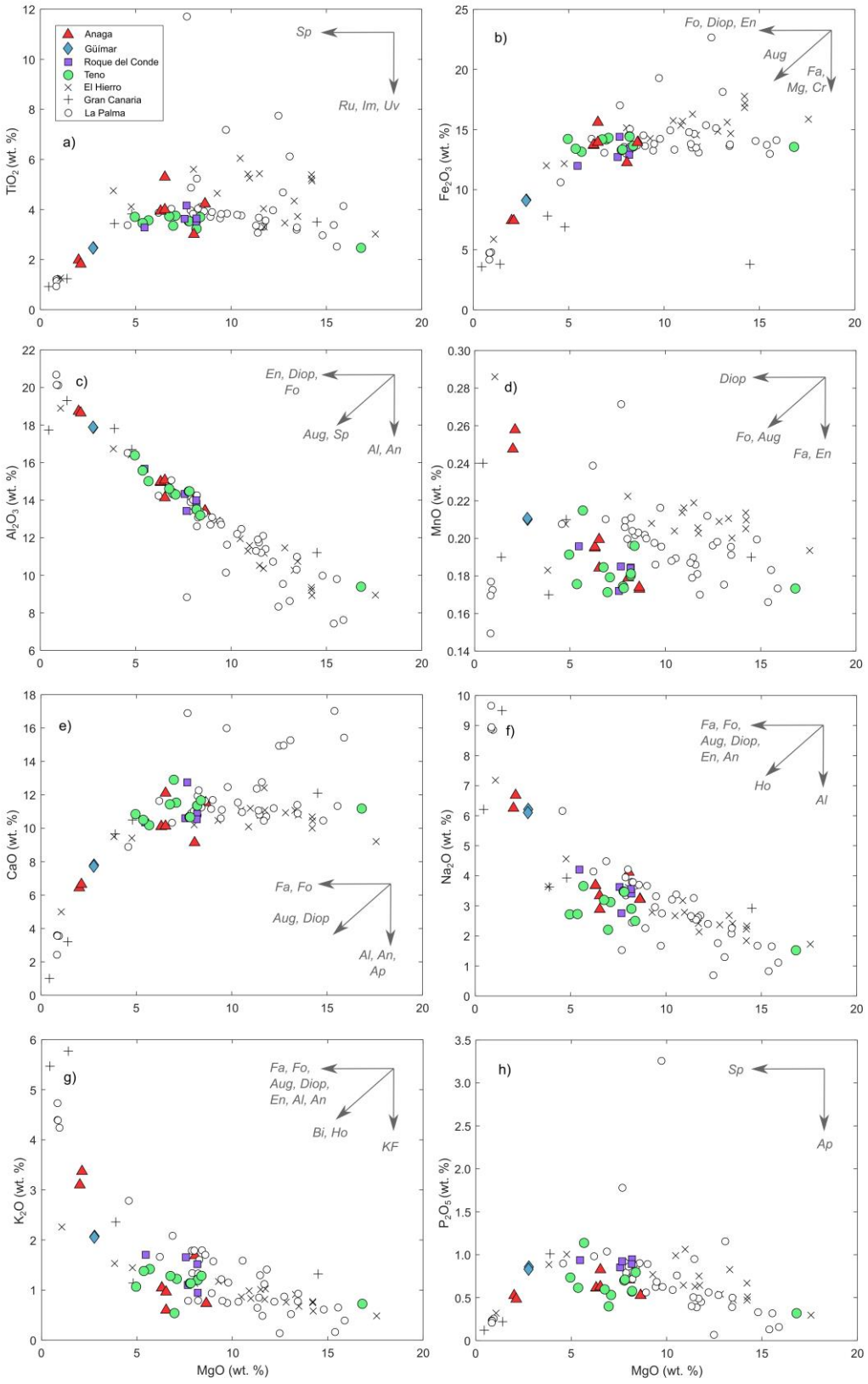

Figure 4.4 – *Harker bivariate plots for Tenerife lavas plus El Hierro and La Palma (Day et al., 2010), and Gran Canaria (Asavin et al., 1997). Plots show MgO vs. (a) TiO_2, (b) Fe_2O_3, (c) Al_2O_3, (d) MnO, (e) CaO, (f) Na_2O, (g) K_2O, (h) P_2O_5. With fractionation vectors for evolving liquid compositions for Fo – forsterite, Fa – fayalite, Aug – augite,*

Figure 4.4 (cont'd) - *En- enstatite, Diop - diopside, an – anorthite, Al – albite, Sp – spinels, Uv – ulvospinel, Mg – magnetite, Chr – chromite, Im – ilmenite, Bi – biotite, Ho – hornblende, KF – K-feldspar, Ap – apatite, Ru - rutile.*

4.3.1.2. Base metals

Figure 4.5 displays a selection of MgO vs. trace element bivariate plots, showing base metal trends through the Canaries excluding Gran Canaria as these elements were not measured in samples from this island (Asavin et al., 1997). As with major element oxides in Figure 4.4, there is a contrast in most minor element concentrations between low-MgO Tenerife samples and high-MgO La Palma and El Hierro samples along a single fractionation trend. In Figure 4.5a and 5b, Sc and V have positive correlations with MgO, for Tenerife samples (< 10 wt.% MgO) and La Palma and El Hierro (> 10 wt.% MgO). Vanadium concentrations plateau at ~ 400 ppm with occasional La Palma outliers (Figure 4.5b).

In Figure 4.5c-e, Cr, Co and Ni trend positively with increasing MgO. Tenerife samples have < 400 ppm Cr, < 60 ppm Co and < 200 ppm Ni, except one high-MgO Teno sample with 1000 ppm Cr, 95 ppm Co and 500 ppm Ni; the outlier also has high MgO, and thus reflects the same overall fractionation trend as the other samples. La Palma samples generally have slightly higher Sc, V, Cr, Co and Ni than El Hierro and both are more enriched than Tenerife. Unlike the other five base metals, Cu distribution is distinct in each island (Figure 4.5f). For Tenerife samples, Cu and MgO are positively correlated, with Cu concentrations up to ~ 120 ppm and one Teno sample with ~ 150 ppm. La Palma and El Hierro Cu concentrations are more variable although the range in Cu concentrations is generally similar to that of the Tenerife samples (up to ~ 160 ppm). Fractionation trends again have a kink at ~ 7 wt.% MgO for Sc and V, but a more consistent gradient for Cr, Co and Ni with a slight change in slope at the kink.

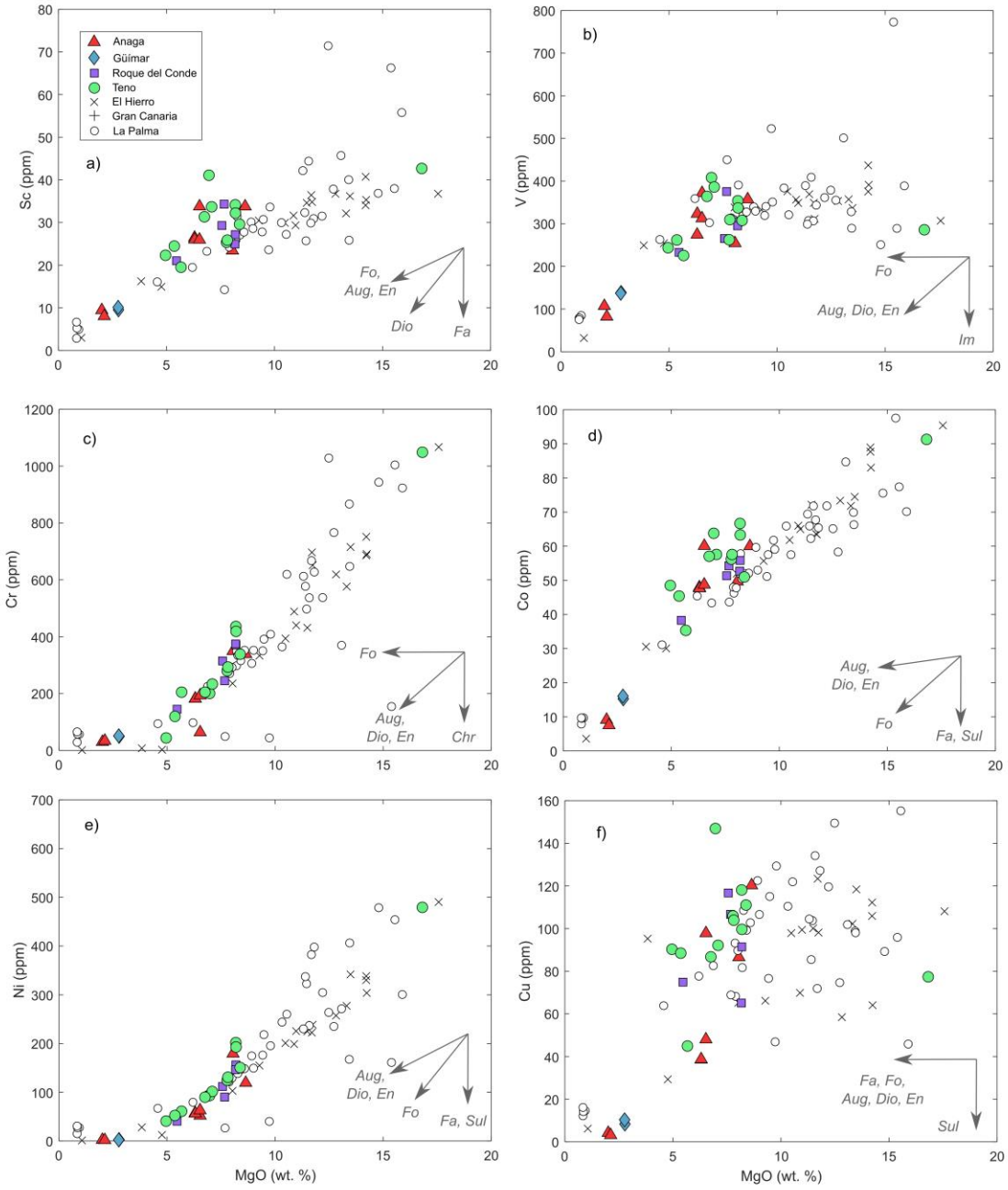

Figure 4.5 – *Bivariate plots for base metal concentrations in Tenerife lavas plus El Hierro and La Palma (Day et al., 2010), and Gran Canaria (Asavin et al., 1997). Plots show MgO vs. (a) Sc, (b) V, (c) Cr, (d) Co, (e) Ni, (f) Cu. With fractionation vectors for evolving liquid compositions for Fo – forsterite, Fa – fayalite, Aug – augite, En- enstatite, Diop - diopside, Im – ilmenite, Sul – sulphide, and Chr – chromite.*

4.3.1.3. Rare earth elements and lithophiles

Trace element concentrations for the four Tenerife localities plus El Hierro and La Palma (Day et al., 2010) are compared and contrasted alongside Kilauea (Figures 4.6-4.8) and Iceland (Figure 4.8) values (from Appendix B1 and Supplementary S4.3) and a representative mean normal mid ocean ridge basalt (N-MORB) composition (Gale et al., 2013) (Figures 4.6-4.8).

Figure 4.6 displays chondrite-normalised (McDonough and Sun, 1995) rare earth element (REE) multi-element diagrams. All four Tenerife sample localities have enriched REE patterns compared to Kilauea and MORB, particularly the light REE (LREE). Tenerife localities lack strong positive or negative anomalies throughout their REE array (even Eu that is often anomalous in igneous rocks), except a slightly steeper Nd-Sm slope (i.e., Nd enrichment). Anaga (Figure 4.6a) has two distinct trends, with one more enriched than the other in all REE concentrations. Güímar and Roque del Conde samples (Figure 4.6b-c) are more enriched than Teno (Figure 4.6d), although the latter location has a larger spread in concentrations with respect to chondritic from ~ 500 x chondritic La to concentrations closer to that of Kilauea samples. For the literature data, the general REE slope shape is similar to Tenerife in both islands, with El Hierro (Figure 4.6e) bearing a close resemblance to Teno, and La Palma (Figure 4.6f) showcasing a wide array of concentrations compared to its neighbours. El Hierro and La Palma have similar normalised patterns to Kilauea and their heavy REE (HREE) concentrations lie below the N-MORB concentration line from Tb onwards. In Tenerife, only Ho or Er onwards plot below N-MORB values.

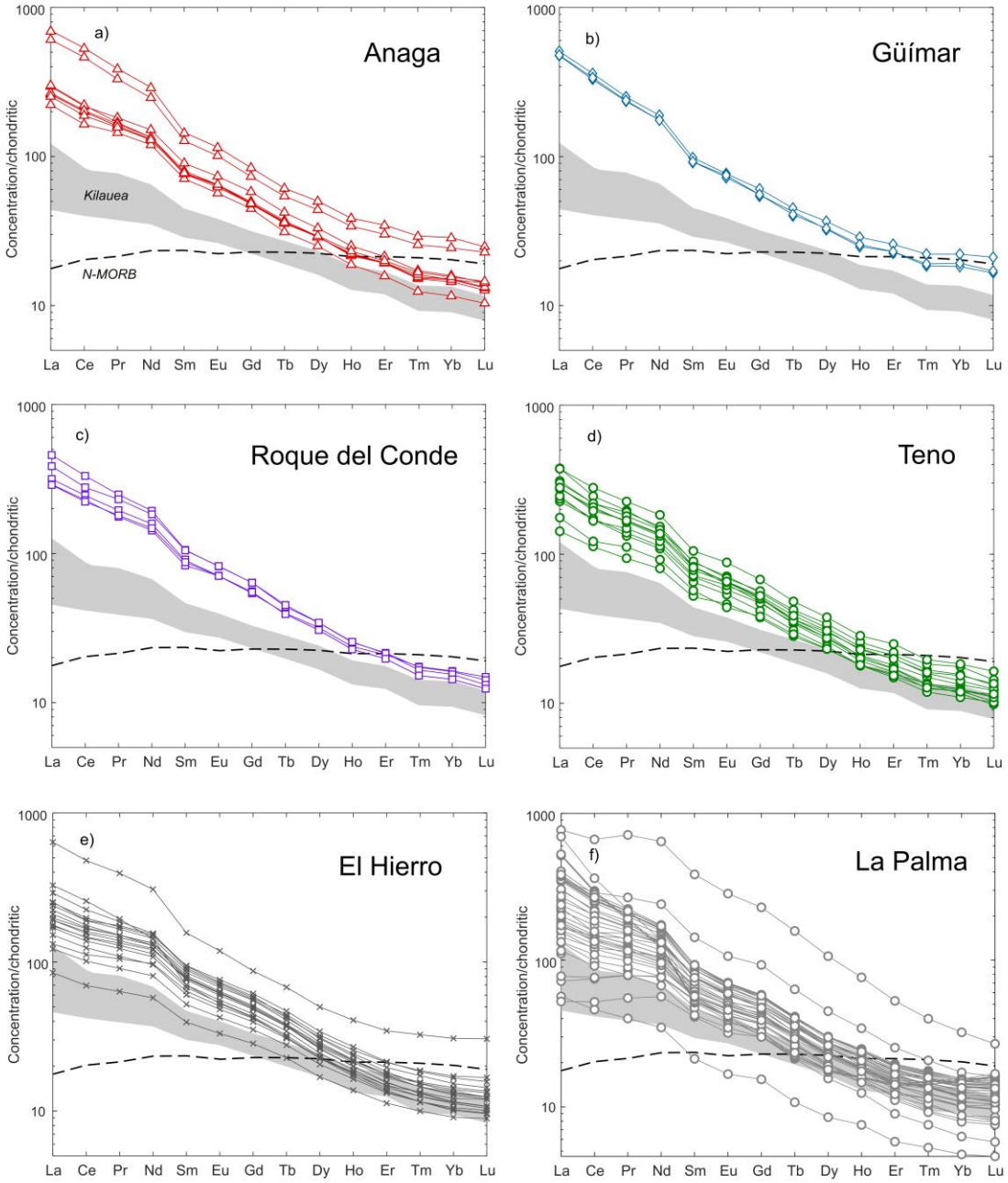

Figure 4.6 – *Chondrite-normalised (McDonough and Sun, 1995) rare earth element plots for Canary Island lavas. Tenerife: (a) Anaga; (b) Güímar; (c) Roque del Conde; (d) Teno. Other islands (Day et al., 2010): (e) El Hierro; (f) La Palma. Also includes Kilauea trend range for reference (see Appendix B1) plus normal MORB (N-MORB) mean value line (Gale et al., 2013).*

Figure 4.7 displays incompatible trace element concentrations normalised by Primitive Mantle values (McDonough et al., 1992). Samples from all four Tenerife localities are more enriched overall than Kilauea and N-MORB. Anaga samples (Figure 4.7a) have two different trends: the first is more enriched in

almost all incompatible elements with significant Rb, K, P and Ti negative anomalies; and the second is less enriched and shows less prominent or absent anomalies for the four aforementioned elements. Güímar samples (Figure 4.7b) have signatures similar in shape with the more enriched Anaga samples, with Rb, K and Ti negative anomalies (where measured). Roque del Conde samples (Figure 4.7c) are enriched in the most incompatible elements (i.e., Rb, Th, U) with negative K and Hf anomalies. Teno signatures (Figure 4.7d) are similar to Roque del Conde, but with less prominent anomalies and an overall depletion in all incompatible elements. El Hierro (Figure 4.7e) is significantly less enriched in all elements than Tenerife samples (largely similar to Kilaeau), with strong positive Ta and Nb anomalies. La Palma (Figure 4.7f) has a wide range of normalised signatures, but the majority are slightly higher than Kilauea with prominent negative Rb, K, Sr, P, Zr, Ti and Y anomalies.

The majority of Tenerife samples have low $(Th/Ta)_N$ and high $(La/Sm)_N$ values akin to classic ocean island basalts with minimal affinity for continental flood basalt signatures (using annotations from Wooden et al., 1993) (Figure 4.8a). This is also illustrated in Figure 4.8b using $(Sm/Yb)_N$ (also from Wooden et al., 1993). In Figure 4.8c, Nb/U and Ce/Pb ratios describe the trace element compositions connected to specific mantle isotopic components (from Day et al., 2010). Here, Tenerife, Hawaii and Iceland show significantly lower values for both ratios than N-MORB, La Palma and El Hierro, although some Anaga samples trend with the more enriched groups with Ce/Pb of > 30. Roque del Conde and Teno samples have particularly low ratios in this space. In Figure 4.8d, using $(Sm/Yb)_N$ and $(La/Sm)_N$ to assess likely mantle melting sources (Xiao et al., 2004), almost every sample from the Canary Islands has an affinity for generalised trends associated with melting of garnet peridotite at low degrees of partial melting (F), particularly Roque del Conde and Teno. Kilauea also plots towards the garnet peridotite vector but much closer to the origin (i.e., N-MORB) and Iceland plots almost entirely within the N-MORB region. Three La Palma samples trend with vectors for melting of spinel peridotite at higher F values.

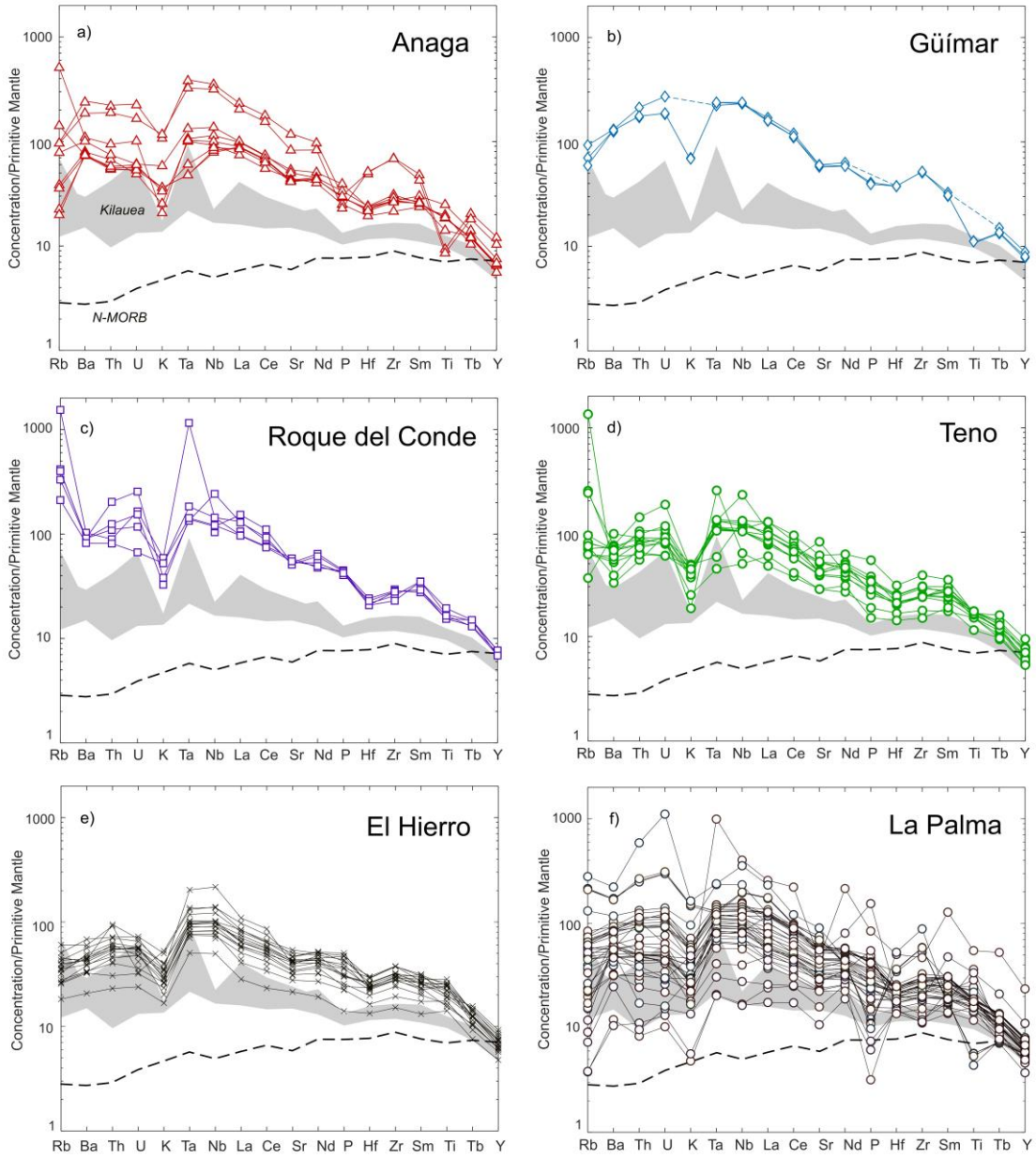

Figure 4.7 – *Incompatible trace element plots for the Canary Islands with concentrations normalised by Primitive Upper Mantle (PUM) (McDonough et al., 1992). Tenerife: (a) Anaga; (b) Güímar; (c) Roque del Conde; (d) Teno. Other islands (Day et al., 2010): (e) El Hierro; (f) La Palma. Also includes Kilauea trend range for reference (see Appendix B1) plus normal MORB (N-MORB) mean value line (Gale et al., 2013).*

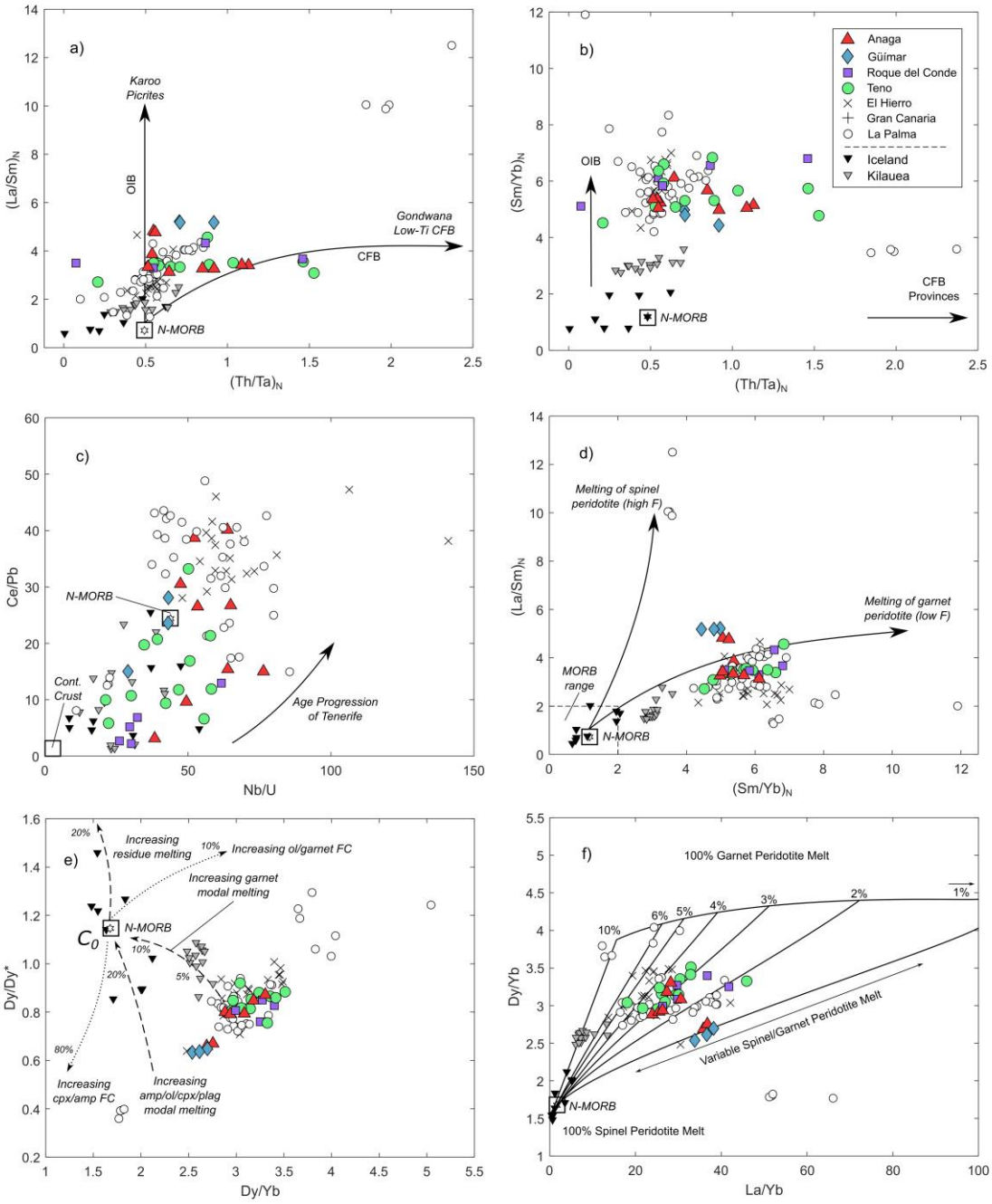

Figure 4.8 – *Selection of lithophile and rare earth element ratio plots for Tenerife, Kilauea and Iceland lavas, plus El Hierro and La Palma (Day et al., 2010), Gran Canaria (Asavin et al., 1997), and N-MORB (Gale et al., 2013). (a) $(Th/Ta)_N$ vs. $(La/Sm)_N$ (plot and vectors from Wooden et al., 1993); b) $(Th/Ta)_N$ vs. $(Sm/Yb)_N$ (plot and vectors from Wooden et al., 1993); c) Nb/U vs. Ce/Pb (plot from Day et al., 2010); d) $(Sm/Yb)_N$ vs. $(La/Sm)_N$ (plot and vectors from Xiao et al., 2004); e) Dy/Yb vs. Dy/Dy* (plot and vectors from Davidson et al., 2013); La/Yb vs. Dy/Yb (plot and calculated melting degrees from Day et al., 2010).* *F - degree of partial melting, FC – fractional crystallisation, CFB – continental flood basalt, OIB – ocean island basalt.*

In Figure 4.8e, a variety of mineral controls on geochemistry are mapped from Davidson et al. (2013) using Dy/Yb and Dy/Dy*. In this plot, Canary Island samples also trend with vectors representing the generalised signature for melting of small degrees (< 5 %) of a garnet-bearing mantle source. Icelandic samples plot close to N-MORB compositions, with Kilauea between the Canaries and Iceland. In Figure 4.8f, we use the La/Yb versus Dy/Yb plot from Day et al. (2010), which originally featured in the original El Hierro and La Palma study, and is now updated with new Tenerife samples plus Kilauea and Iceland. Here, Tenerife samples have variable spinel/garnet melting signatures but generally plot with lower degrees of partial melting than all other localities, excluding a sub-set of La Palma. Iceland trends strongly with high degrees of partial melting of a spinel peridotite mantle, Kilauea with ~ 10% melting of a more garnet-rich mantle and El Hierro and La Palma largely exhibit a similar mantle mineralogy to Tenerife but with slightly higher degrees of partial melting.

4.3.2. PGE and Au

Table 4.2 displays PGE and Au concentrations for all newly analysed samples, plus mean values for El Hierro, La Palma, Kilauea, and Iceland for comparison. Tenerife samples contain up to 0.2 ppb Os, up to 0.1 ppb Ir, up to 0.6 ppb Ru, up to 0.2 ppb Rh, up to 1.5 ppb Pt, up to 2 ppb Pd and up to 2 ppb Au. Figures 4.9a-f show PGE and Au concentrations plotted against MgO. Overall, Tenerife samples are distinctly PGE-depleted compared to El Hierro, La Palma and Gran Canaria in all Figure 4.9 plots. A single enriched Roque del Conde sample is 2-4 times higher concentrations of Ir, Ru, Rh, Pt and Au than other Tenerife samples. Gran Canaria samples, whilst low in number, are often enriched in measured PGE (Os, Ir, Pt, Pd). Samples from Kilauea and Iceland have PGE and Au concentrations comparable to most Tenerife samples.

Figure 4.10 displays multi-element PGE and Au plots, with concentrations normalised by chondritic values (McDonough and Sun, 1995). Overall, Tenerife samples are more enriched in Os, Ir and Ru (the Iridium-group PGE, IPGE) and more depleted in Rh, Pt and Pd (the Palladium-group PGE, PPGE) than the mean N-MORB concentration from Peucker-Ehrenbrink et al. (2003). Anaga (Figure 4.10a) samples have PGE concentrations akin to the least enriched Hawaiian lavas, with a very similar normalised fractionation pattern (relatively shallow from IPGE to PPGE). Güímar samples (Figure 4.10b) and the majority of Roque del

Conde samples (Figure 4.10c) follow very similar trends to Anaga, but a single sample from Roque del Conde has PGE concentrations an order of magnitude higher than the others. Teno (Figure 4.10d) is also similar to Anaga, but with slightly higher PPGE and Au concentrations. Both El Hierro and La Palma (Figures 4.10e and 4.10f) are generally more enriched in PGE than Tenerife, and La Palma in particular plots with or above the highest Kilauea signatures.

Table 4.2 – *Whole-rock PGE and Au concentrations for Tenerife lavas (in ppb) with MgO. (in wt.%). '-' - not measured. * - mean value of parts A and B (processed separately). El Hierro and La Palma mean values taken from Day et al. (2010) and Iceland and Kilauea means of measured values as part of this thesis. See Supplementary S4.3 for full major and trace element data for all localities.*

Sample	**Locality**	**Os** *ppb*	**Ir** *ppb*	**Ru** *ppb*	**Rh** *ppb*	**Pt** *ppb*	**Pd** *ppb*	**Au** *ppb*	**MgO** *wt.%*
TE01	Roque del Conde	0.15	0.17	1.58	0.50	5.84	0.63	7.60	7.57
TE02	Roque del Conde	0.06	0.03	0.25	0.05	0.24	0.09	0.22	5.46
TE03	Roque del Conde	0.17	0.07	0.25	0.03	0.14	0.28	0.49	8.19
TE04	Roque del Conde	0.02	0.02	0.06	0.03	0.15	0.23	0.23	7.67
TE05	Roque del Conde	0.04	0.04	0.18	0.03	0.59	0.50	0.76	8.17
TE06	Teno	0.10	0.07	0.16	0.05	0.64	0.75	0.25	6.97
TE07	Teno	0.03	0.05	0.16	0.05	0.49	0.50	0.30	8.18
TE08	Teno	0.06	0.03	0.34	0.06	1.25	0.75	1.73	8.38
TE09	Teno	0.03	0.03	0.10	0.05	0.11	0.16	0.10	4.95
TE10	Teno	0.11	0.09	0.16	0.13	0.88	0.91	1.59	7.09
TE11	Teno	0.05	0.03	0.13	0.03	0.21	0.11	0.28	5.67
TE12	Teno	0.08	0.03	0.13	0.06	1.21	0.95	1.50	5.36
TE13*	Teno	0.01	0.03	0.26	0.04	0.32	0.41	0.37	7.82
TE14	Teno	0.02	0.02	0.07	0.04	0.27	0.23	1.14	6.76
TE15	Teno	0.02	0.03	0.12	0.07	0.17	0.26	0.44	16.81
TE16	Güímar	0.03	0.03	0.21	0.12	0.32	1.57	0.21	2.78
TE17	Güímar	0.03	0.03	0.16	0.05	0.32	0.31	0.17	2.76
TE18	Anaga	0.02	0.02	0.28	0.10	0.23	0.30	0.15	2.01
TE19	Anaga	0.02	0.02	0.09	0.04	0.13	0.15	0.09	8.64
TE20	Anaga	0.07	0.07	0.55	0.10	0.32	0.53	0.16	2.12
TE21	Anaga	0.08	0.03	0.25	0.13	0.52	0.41	0.06	6.53
TE22	Anaga	0.02	0.05	0.30	0.06	0.51	0.41	0.14	8.05
TE23*	Anaga	0.03	0.05	0.23	0.09	0.26	0.65	0.34	6.31
TE24	Anaga	0.08	0.03	0.36	0.19	0.22	0.14	0.77	6.53
Mean	El Hierro	0.12	0.10	0.48	-	1.95	0.57	-	10.78
	La Palma	0.09	0.23	0.39	-	3.09	2.33	-	9.49
	Iceland	0.09	0.09	0.47	0.10	0.90	0.69	0.16	19.22
	Kilauea	0.15	0.13	0.74	0.19	0.83	0.78	0.53	8.79

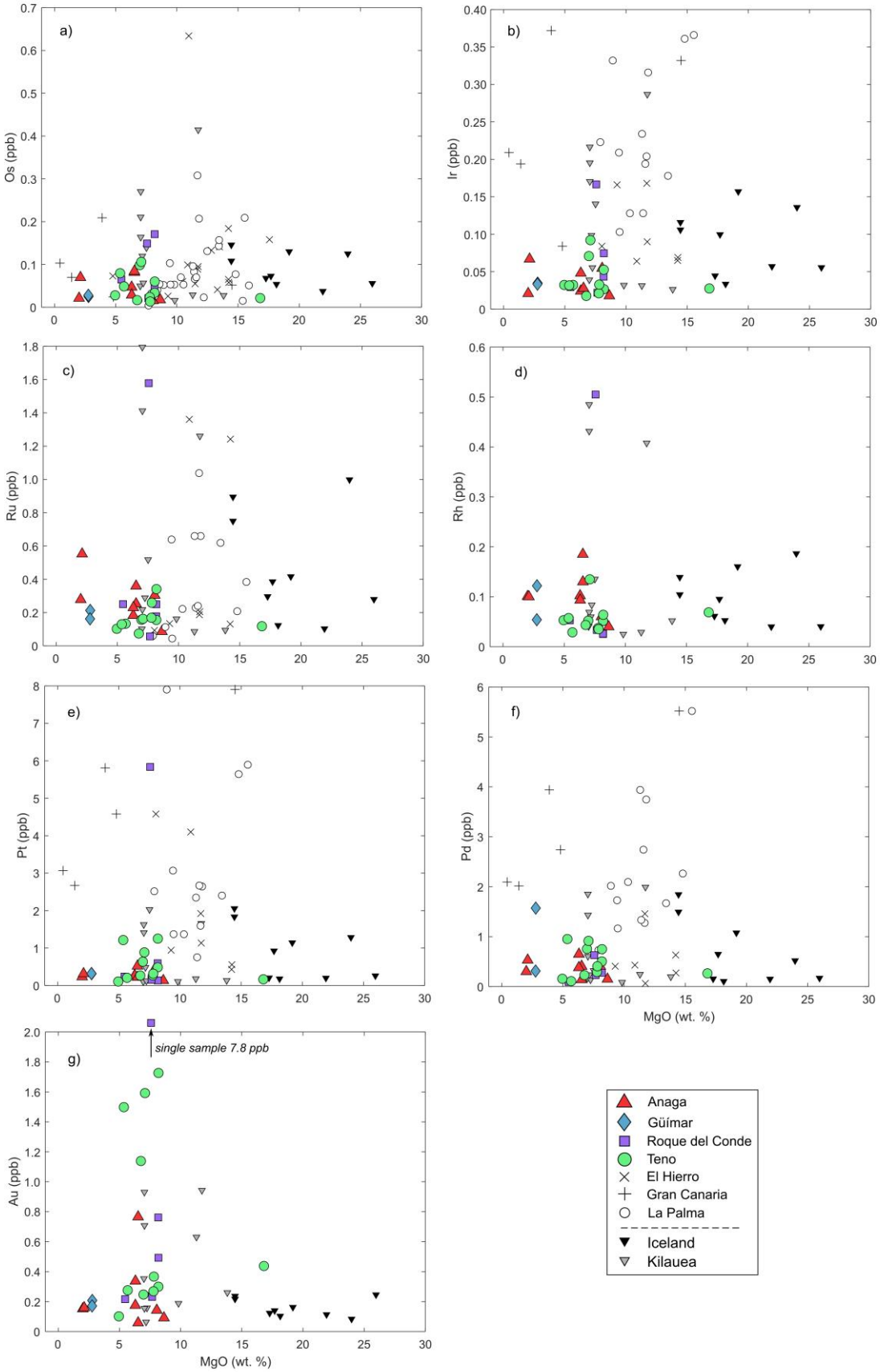

Figure 4.9 – *PGE Bivariate plots for Tenerife, Kilauea and Iceland lavas, plus El Hierro and La Palma (Day et al., 2010), and Gran Canaria (Asavin et al., 1997). Plots of MgO vs (a) Os, (b) Ir, (c) Ru, (d) Rh, (e) Pt, (f) Pd and (g) Au.*

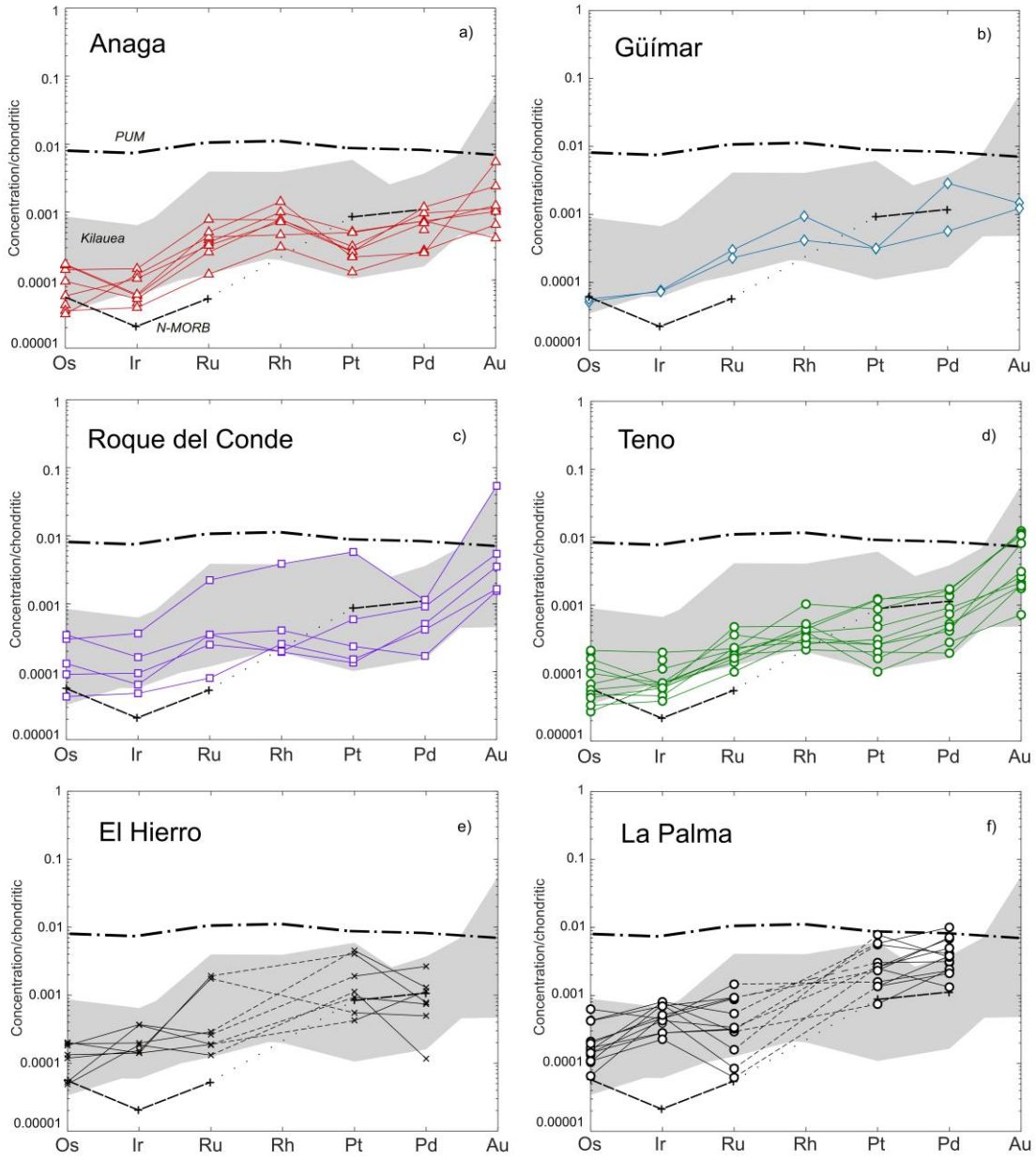

Figure 4.10 – *Chondrite-normalised (McDonough and Sun, 1995) PGE and Au plots for the Canary Islands. Tenerife: (a) Anaga; (b) Güímar; (c) Roque del Conde; (d) Teno. Other islands (Day et al., 2010): (e) El Hierro; (f) La Palma. Also includes Kilauea trend range for reference (see Appendix B1) plus mean value lines for N-MORB (Peucker Ehrenbrink et al., 2003) and Primitive Upper Mantle (PUM) (Becker et al., 2006).*

Figure 4.11 shows some PGE, chalcophile and trace element ratios in bivariate plots. Tenerife, Kilauea and Iceland lavas have Cu/Pd ratios of between 100 and 1,000, whilst El Hierro and La Palma are generally between 30 and 100. In Figure 4.11b, all plume-derived lavas are spread between generalised trend lines for olivine accumulation and incompatible element fractionation, however

Tenerife samples have notably lower Ir concentrations associated with the latter process. Gran Canaria and Kileauea have Pt/Pd ~ 1, whilst Tenerife, La Palma and Iceland are highly variable (Figure 4.11c). Tenerife samples have higher Pd/Ir and Dy/Yb (Figure 4.11d), and higher La/Yb (Figure 4.11e) than other localities. The highest total PGE concentrations (Figure 4.11f) are correlated with Ce/Pb >20 (i.e., with El Hierro and La Palma).

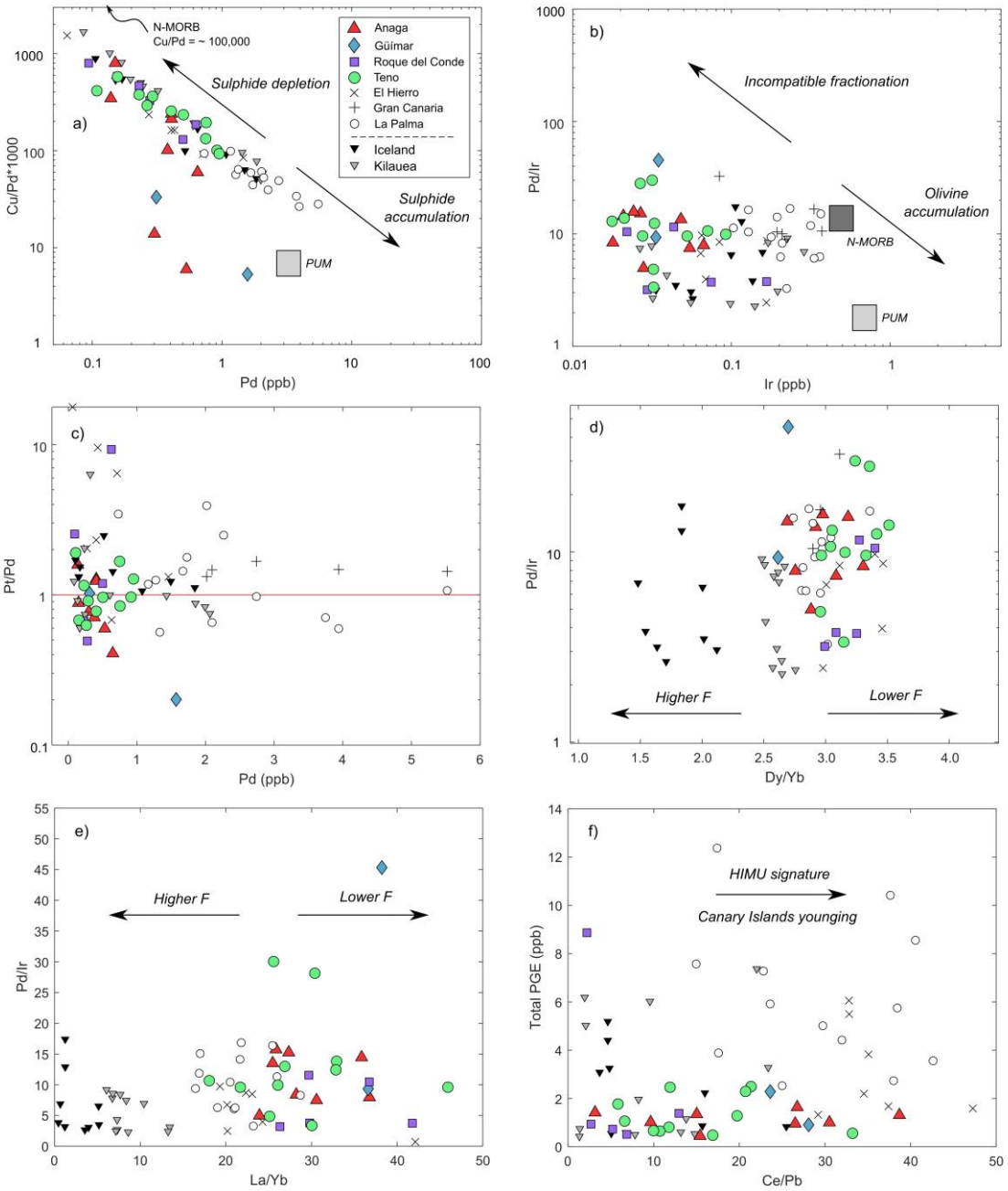

Figure 4.11 – *Bivariate plots for PGE or PGE-REE concentrations as ratios for Tenerife, Kilauea and Iceland lavas, plus El Hierro and La Palma (Day et al., 2010), and Gran Canaria (Asavin et al., 1997). Includes mean values for N-MORB (Peucker Ehrenbrink et al., 2003) and Primitive Upper Mantle (PUM) (Becker et al., 2006) where appropriate.*

Figure 4.11 (cont'd) - *(a) Pd vs. (Cu/Pd)*1000 with vectors for sulphide enrichment and depletion from Barnes and Picard (1993); (b) Ir vs. Pd/Ir with vectors for incompatible fractionation and olivine accumulation from Hughes et al. (2015); (c) Pd vs. Pt/Pd; (d) Dy/Yb vs. Pd/Ir (vectors from Day et al., 2010); (e) La/Yb vs. Pd/Ir (vectors from Day et al., 2010); (f) Ce/Pb vs. Total PGE (vectors from Day et al., 2010). F = degree of partial melting.*

4.4. Discussion

4.4.1. Magmatic trends in the Tenerife lavas

The low degrees of alteration in the sample set (Appendix B2) indicate that all geochemical signatures are primary, as interpreted herein. The TAS diagram for Figure 4.3 clearly illustrates the alkaline nature of the Canary Islands, with all Tenerife, El Hierro, La Palma and Gran Canaria samples plotting above the alkali-tholeiitic discriminant line. In general, alkali lavas are generated by smaller degrees of partial melting than tholeiites and/or ultramafic rocks, given that alkali minerals are more fusible than mafic minerals like olivine or pyroxene (Bowen, 1979; McKenzie and O'Nions, 1991; Sharkov et al., 2017). Mineral fractionation vectors from Figures 4.4 and 4.5 show variable trends indicating different minerals fractionating from Canary Island magmas with decreasing MgO (i.e., with increased fractional crystallisation). The change in direction at ~ 7 wt.% in the majority of the plots implies a difference in fractionation phase(s). The flatter trend from 20 to 7 wt.% MgO recognised mainly by El Hierro and La Palma is aligned with olivine vectors (particularly forsterite) and the pronounced decrease in TiO_2, Fe_2O_3 and CaO in < 7 wt.% MgO samples consistently align with clinopyroxene (augite/diopside) vectors through the plots, and this is likely alongside minor plagioclase. This combination would also explain the relatively shallower fractionation trends in Al_2O_3, Na_2O and K_2O in more evolved lavas (Figures 4.4c, 4.4f and 4.4g), and the corroborating shallow-to-steep Sc, V and Co (compatible in pyroxene) fractionation trends with decreasing MgO. Furthermore, Ni and Cr (compatible in olivine) show a shallowing trend at < 7 wt.% MgO, indicating the relative reduction in the role of olivine in fractionating the bulk geochemistry by this stage of magmatic differentiation. These findings are in agreement with published trends for Tenerife (Thirlwall et al., 2000) and the western Canary Islands (Day et al., 2010). The significant depletion of olivine-

compatible Co and Ni (Spandler and O'Neill, 2010) in Tenerife lavas compared to other samples in the Canary Islands (Figure 4.5d and 5e) suggests that, along with their distinctively low MgO concentrations, the composition of Tenerife lavas are the result of removal of high proportions of olivine during earlier stages of fractional crystallisation.

The shape of REE enrichment curves from all four Tenerife sample localities (Figure 4.6a-d) are similar to each other - relatively smooth slopes with no major positive/negative anomalies except slightly steeper Nd-Sm ratios. This Nd-Sm slope could suggest an enriched Sm/Nd (i.e., deeper) mantle source with a large proportion of ^{147}Sm decaying to ^{143}Nd, increasing overall Nd concentrations beyond those acquired from source (Depaolo and Wasserburg, 1976; McCulloch and Wasserburg, 1978; Jackson et al., 2012). The split REE signature of Anaga samples (Figure 4.6a) reflects the multi-event eruptive sequence of this massif in comparison to the more consistent signatures in other parts of the island (Abdel-Monem et al., 1972; Ancochea et al., 1990; Carracedo et al., 1998; Guillou et al., 2004). Between lava sequences, the geochemistry of the parent magma altered slightly, producing more enriched (TE18-20 from Los Campitos) and more depleted (TE21-24) members. Higher LREE-HREE slopes (mean $(La/Sm)_N$ of ~ 3.8; Figures 4.6a-f, 4.8a and 4.8d) in the Canaries implies a more incompatible element-enriched and garnet-bearing mantle source for parent magmas (Day et al., 2010).

In plots concerning generalised intraplate magma compositions ranging from continental to oceanic (Figures 4.8a and 4.8b), Canary Islands express strong affinity for the latter setting, trending towards vectors produced by Wooden et al. (1993) indicating OIB compositions (i.e., high $(La/Sm)_N$ and $(Sm/Yb)_N$ with low $(Th/Ta)_N$). By this metric, we confirm the (previously assumed) absence of continental lithosphere in magma generation and recognise the fingerprint of a deep mantle source in melting. Comparatively, the Canary Islands have higher $(La/Sm)_N$ and $(Sm/Yb)_N$ than Kilauea and Iceland samples (Figures 4.8a-b). The unique placement of Iceland astride an active mid-ocean rift introduces the chemically-complex combination of plume-derived and shallow mantle-derived melt components (similar to N-MORB in Figure 4.8) that can obscure the deeper influence of lavas in the absence of isotopic fingerprints (McKenzie and White,

1989; Fitton et al., 1997; Foulger et al., 2005; Momme et al., 2006; Koornneef et al., 2012; Shorttle et al., 2013).

Day et al. (2010) used Nb/U versus Ce/Pb for El Hierro and La Palma samples to describe trace element ratios related to mantle isotopic components involved in melt generation. In our recreation with the new data (Figure 4.8c), we see a clear differentiation between the two islands from the original study plus some Tenerife samples (Anaga and Güímar) and the remaining Tenerife, Kilauea and Iceland samples, primarily based upon Ce/Pb (divided at ~25). In this plot, we see also see a roughly age-progressive trend in Tenerife lavas from low to high Nb/U and Ce/Pb. Pulses in plume productivity and geochemistry are frequent throughout the length of the Canary Islands chain (Hoernle and Schmincke, 1993; Taylor et al., 2020), and individual islands express different isotopic characters pertaining to heterogeneous mantle component inclusion. La Palma and El Hierro lavas have strong HIMU components as per their elevated Ce/Pb (Hofmann, 2003; Day et al., 2010) and the separation of Anaga and Güímar from other, older lavas on Tenerife with low Ce/Pb in Figure 4.8c may establish the introduction of this mantle 'flavour' to the Canary system during Tenerife eruption.

All samples in the study (with the exception of three La Palma outliers) trend towards vectors established by Xiao et al. (2004) for magma generation via melting of garnet peridotite under low degrees of partial melting (F) (Figure 4.8d), which in turn implies a deep melting environment (see Chapter 3). As with Figures 4.8a-b, the Canaries have the highest ratio signatures in each plot, this time implying that they are formed from even deeper, smaller degree melts than Kilauea and Iceland (which again trends with N-MORB compositions). The spinel-garnet stability transition zone occurs at pressures of ~ 3 GPa and temperatures of ~ 1,570°C in the mantle (Milholland and Presnall, 1998; Kent and Fitton, 2000; Klemme and O'Neill, 2000; Walter et al., 2002; Ziberna et al., 2013), although specific mineralogical controls such as an abundance of Cr in mantle phases can increase this to depths equating to pressures of 10 GPa (Klemme, 2004; Ziberna et al., 2013). Workers identified that beneath oceanic asthenosphere, the garnet-spinel transition is shallower than underneath continents due to excess pressure from the continental landmass (White and McKenzie, 1995; Arndt et al., 1998; Jourdan et al., 2007). This shallower spinel-garnet transition is particularly

evident under thinner, younger oceanic lithosphere – most MORB lavas have trace element signatures relating to spinel peridotite melts (Ellam, 1992; Stein and Stein, 1992; Peucker-Ehrenbrink et al., 2003). The Canary Islands placement within some of the oldest parts of the Atlantic seafloor (150-180 Ma; Hoernle, 1998), which has thickened via underplating with time and distance from the active mid-oceanic ridge, may have imposed deeper melting than a plume closer to the ridge. The thermal anomaly from the mantle plume allows melting to occur deeper in the mantle than in a ridge melting environment (suggested to be 80-110 km beneath the Canaries; Thirlwall et al., 2000; Carracedo et al., 2002; Gurenko et al., 2006; Day et al., 2010), leading to garnet-dominated trace element controls (Hoernle and Schmincke, 1993).

The majority of OIB lava samples trend with the vector calculated by Davidson et al. (2013) that describes incremental melting of modal garnet in the mantle (i.e., decreasing Dy/Yb, increasing Dy/Dy*) (Figure 4.8e). The Canary Islands occupy space denoting < 5 % partial melting of a garnet peridotite, Kilauea represents ≥ 5 % partial melting of a similar source, and Iceland does not appear to adhere to this developmental trend, possibly due to the influence of spinel- or plagioclase-normative shallow (MORB) mantle compositions (Johnson, 1998). Canary Island lavas are 1-5 % partial melts of a more garnet-rich peridotite, compared to 6-10 % partial melts of a less garnet-rich peridotite in Kilauea and 10 % partial melts MORB-like spinel-rich peridotite (Figure 4.8f). Roque del Conde samples generally plot towards the lowest degrees of partial melting of a similar mantle source to the other Tenerife lavas (Figure 4.8d and 8f). This indicates a slight increase in melting degree with time in parent magmas from Roque del Conde to the younger Teno and Anaga, and on to the subsequent mafic magmas of El Hierro and La Palma. Degrees of partial melting evidently control the trace element signatures of plume-derived lavas, even down to single-digit variations between Tenerife and La Palma. The type and amount of mantle phases involved in partial melting impose limitations on the abundances of compatible and incompatible elements in intraplate magmas, and this most likely has an impact on precious metal concentrations too.

4.4.2. Tenerife PGE geochemistry

The shapes of PGE multi-element enrichment in Tenerife lavas (Figure 4.10a-d) are broadly comparable, with shallow positive slopes from IPGE to PPGE, slightly enriched Rh concentrations, and more fractionated (Steeper normalised signatures) than N-MORB (Peucker-Ehrenbrink et al., 2003). Tenerife samples have PGE concentrations within the lower end of Kilauea range (Figure 4.10a-d), something acknowledged by Day et al. (2010) for El Hierro and La Palma (Figure 4.10e-f). The alkaline lavas found in El Hierro and La Palma differ slightly in their PGE concentrations (Figure 4.10e-f) - the contrasting low Pd/Ir El Hierro rocks and the high Pd/Ir La Palma rocks are attributed to variable pyroxenite mantle source components in small degree (< 6 %) partial melts in the Canary Islands plume (Day et al., 2010). We expect similar overall melting conditions were present for Tenerife melt generation based on trace element interpretations (Figures 4.8c-f). However, the subtle differences in Pd/Ir (and by extension the degree of fractionation between the PGE) on lavas from Tenerife and the other Canary Islands may reflect small differences in degrees of partial melting in each locality.

Fractionation between PGE in magmas generally reflects differences in the minerals that commonly host each metal in the mantle, and the control this exerts on PGE liberation from source during partial melting. For example, the IPGE and Rh are known to have a degree of compatibility with olivine and spinel, two early-forming (i.e., high-temperature) silicate minerals in a mafic magmatic system, whilst Pt and Pd are strongly incompatible in silicates (Barnes et al., 1985; Brenan et al., 2003; Righter et al., 2004; Spandler and O'Neill, 2010; Park et al., 2017). Some PGE are found as discrete, refractory platinum-group minerals (PGM) and alloys within silicates in the mantle, typically the IPGE and Pt (Lorand et al., 1999; Rehkämper et al., 1999; Ballhaus et al., 2006). Arsenides and tellurides are also known to contain PGE (Mansur and Barnes, 2020). Interstitial base metal sulphides (BMS) can also host PGE in varying concentrations, depending on their relative compatibility with each base metal phase (i.e., Ni- or Cu-rich) (Alard et al., 2000; Prichard et al., 2013; Helmy and Bragagni, 2017). Overall, IPGE and Rh are more likely to be hosted by Ni-Fe-rich base metal sulphides (BMS), whilst Pt and Pd tend to be hosted by Cu-rich BMS (Bockrath et al., 2004; Ballhaus et al., 2006; Lorand et al., 2008). The different

responses to melting and the ease of fusion in this variety of potential mineral hosts (e.g., PGM in olivine vs. Cu-sulphide) can drive strong fractionation in the PGE budget incorporated into melts (Barnes et al., 1985; Rehkämper et al., 1999).

The shape of Tenerife chondrite-normalised PGE signatures (Figure 4.10a-d) is comparable to the mean N-MORB composition (Peucker-Ehrenbrink et al., 2003), although the island lavas are more IPGE-rich and slightly more PPGE-poor. Oceanic lithosphere is sourced from the shallow, depleted mantle, so precious metal enrichments recorded for mantle-derived lavas such as those in the Canaries must reflect a different source composition or region from N-MORB, likely deeper in the mantle (Peucker Ehrenbrink et al., 2003). In this study, the Anaga, Güímar, Roque del Conde and Teno samples have slightl differences in individual PGE and Au concentrations, but overall, lavas from El Hierro and especially La Palma are the most PGE-rich of the western Canaries, with mean concentrations around 2 and 4 times those observed in Tenerife, respectively (Table 4.2; Figure 4.9a-f). The higher degree partial melts within the Canaries chain (El Hierro and La Palma, according to Figures 4.8d-f and Day et al., 2010) are the most IPGE-enriched in Figures 4.9a-f. This may simply reflect the highly chalcophile partitioning behaviour of PGE, and IPGE in particular, meaning that they will be retained in residual mantle sulphides until exhaustion in the source (generally thought to be around 20 % for mantle rocks with ~250 ppm S; Rehkämper et al., 1999; Luguet et al., 2003). The PGE and other chalcophiles will enter melts in very small amounts (inversely proportional to their relative sulphide-silicate melt partition coefficients) until the point all sulphides are consumed, after which concentrations will spike (Hamlyn et al., 1985; Hamlyn and Keays, 1986; Peach et al., 1990; Tredoux et al., 1995; Naldrett, 2011) (see Section 2.5.4 and Figure 2.14 of this thesis). This makes wholesale sulphide acquisition from mantle sources in small degree asthenospheric melts such as those in OIB settings very hard, given that, as shown in Figures 4.8e-f, Canary Islands have trace element ratios indicative of a maximum of 6 % partial melting of a garnet peridotite, and even less beneath Tenerife. It follows that the Canary Islands' general depletion in PGE could be a result of their geodynamic setting – deep melting with highly alkaline (small degree) melts failing to melt significant amounts of sulphides at source (i.e., Figures 4.11d-f). Regardless of whether

plume material entrains precious metals from depth or not, these metals cannot be incorporated into melts without sufficiently high degrees of partial melting.

Sulphide saturation at any stage in magma development can overwhelmingly partition Ni, Cu and PGE into immiscible sulphide liquids given their high sulphide-silicate partition coefficients, which can exceed 400,000 for the IPGE (Barnes and Picard, 1993; Mungall and Brenan, 2014). This would subsequently partition chalcophile elements away from silicate melts. Most western Canaries lavas are described as S-undersaturated compared to N-MORB in the literature (Marcantonio et al., 1995; Bézos et al., 2005; Day et al., 2010). In particular, Day et al. (2010) note that El Hierro and La Palma lavas are S-undersaturated based on Re/Os ratios and variable PGE concentrations, suggesting partial sulphide retention in the mantle source. No such assessment has been made for Tenerife beyond Figure 4.11a, which suggests a small degree of sulphide depletion may have occurred in Tenerife lavas due to relatively high Cu/Pd ratios. Depletion of Ni and Co appear to be intrinsically linked to olivine removal via fractional crystallisation or minimal olivine melting due to the small degrees of partial melting in Tenerife magmas (Figures 4.5d-e and 11b). Consequently, we suggest that sulphide fractionation may have occurred in some Tenerife magmas in small amounts, prior to El Hierro and La Palma eruption. This would have left the relative PGE enrichments shapes from Figure 4.8 unchanged (given wholesale chalcophile removal), and simply slightly reduce their magnitudes, rather than causing further IPGE/PPGE fractionation.

4.4.3. Modelling chalcophile elements and magmatic differentiation

We forward-model partial melt compositions in a plume melting environment using mass balance calculations derived from Shaw (1970), in order to further investigate the PGE geochemistry of the Tenerife and overall Canaries datasets, reconciling this with major and lithophile trace element compositions. Given the trace element indicators (high Sm/Yb_N, Dy/Yb; Figures 4.8d-f) for melting of garnet peridotite in magma generation at all Canary localities, we use experimental garnet peridotite mode values appropriate for pressures of > 2.5 GPa under relatively old oceanic lithosphere, from Johnson (1998) and melting mode values from Walter (1998) to simulate deeper melting conditions. Mineral-melt partition coefficient values are taken from a variety of studies, cited in Table 4.3 alongside all other model parameters. Bulk concentrations of Co, Ni, Cu, PGE

and Au are taken from studies of DMM (Salters and Stracke, 2004) and PUM (Becker et al., 2006) to represent the end-members of mantle enrichment beneath the Canary Islands, in the absence of base and precious metal data for Canaries xenoliths. We also use mantle peridotite xenolith data for Kerguelen plume-derived lavas (Lorand et al., 2004) for a comparison to mantle in a similar intraplate/oceanic plume locality. Further models adjust these parameters to produce favourable magma compositions. The results of different parameter set-ups are shown in Figures 4.12a-d, next to ranges for Tenerife (using Anaga as the most representative), La Palma and Kilauea for reference. Full modelling data sheets are available in Supplementary S4.4.

In Figures 4.12a-c, all PGE signatures require the exhaustion of any sulphide phases present in the mantle source before concentrations in magmas can reach between 1 x 10^{-5} and 0.1 times chondritic values, observed in Anaga, La Palma or Kilauea. Any chalcophiles will preferentially remain in sulphide phases until the point of exhaustion (i.e., F = 0.2 for our set-up assuming 250 ppm S in the mantle source; Table 4.3), and once these phases are consumed, PGE and Au are released into the melt. Our models demonstrate this effect, with concentrations for all PGE and Au in magmas held at very low levels (1 x 10^{-7} to 1 x 10^{-6} times chondritic values) until the point of sulphide depletion for a starting sulphide mode (X) of 1 % and melt mode (*p*) of 5 %. Crucially, the chalcophile-based estimated 20 % partial melting of the mantle (~ 250 ppm S) conflicts with the lithophile geochemistry of our sample set (e.g., Figure 4.8) and literature on the Canary Islands (e.g., Day et al., 2010) that places melting at closer to 5 %. Sulphide depletion can occur at lower degrees of partial melting provided the source has < 250 ppm S (Luguet et al., 2003). Additionally, BMS in the mantle can have highly heterogeneous PGE contents depending on their formation and metasomatic history (e.g., Lorand and Luguet, 2016), even if the phase is often associated with one or more of the PGE. This allows flexibility in source bulk PGE compositions used in the model, which we explore through Figure 4.12. It should be noted that this model does not include modal PGM, which may provide significant PGE enrichment in magmas, but will follow a similar consumption process to sulphides, albeit at higher degrees of partial melting.

Table 4.3 – *Parameters used in melting models. a - Garnet peridotite melt modes from Johnson (1998) and Walter (1998), with addition of 0.01 sulphide borrowed from Opx mode. b - D-values for olivine from Brenan et al. (2003) and Spandler and O'Neill (2010). c - D-values for orthopyroxene from Beattie et al. (1991) and Liu et al. (2014). d – D-values for clinopyroxene from Hill et al. (2000) and Righter et al. (2004). e - D-values for base metals in garnet from Liu et al. (2014), Park et al. (2017). f - D-values for sulphide from Mungall and Brenan (2014). g - Kerguelen xenolith concentrations from Lorand et al. (2004). h - Depleted MORB Mantle (DMM) concentrations from Salters and Stracke (2004). i - Primitive Upper Mantle (PUM) concentrations from Becker et al. (2006). Italicised values were unavailable in the literature for silicates, but assigned neutral values based on olivine values, given their lesser significance to melt composition compared to garnet and sulphide. * - Garnet D-values were adjusted to simulate IPGE+Rh retention in silicate phases during melting. *2 – DMM Pt, Pd and Au concentrations were adjusted to very low levels to simulate source depletion.*

Mineral	Mode (X)[a]	Melt Mode (*p*)[a]	Consumption (F)
Olivine	0.6	0.03	20.0
Opx	0.20/0.19	-0.16	-1.188
Cpx	0.1	0.88	0.114
Garnet	0.1	0.09	1.111
Sulphide	0/0.01	0/0.05	0.2

Element	D olivine/liq[b]	D opx/liq[c]	D cpx/liq[d]	D garnet/liq[e]	D sulphide/liq[f]
Co	2.28	3	1.3	5	230
Ni	7.21	5	2.6	10	500
Cu	0.14	0.09	0.23	0.77	1470
Os	1.2	*0.05*	0.01	*	740000
Ir	0.77	*0.4*	*0.5*	*	458000
Ru	0.23	*3*	4.27	*	415000
Rh	1.94	*0.2*	0.25	*	205000
Pt	0.009	*1*	1.5	*	317000
Pd	0.12	*0.1*	*0.1*	*	190000
Au	0.12	*0.01*	*0.01*	*	10000

Source (C_0)	Kerguelen[g]	DMM[h]	PUM[i]
Co (ppm)	-	106	-
Ni (ppm)	-	1960	-
Cu (ppm)	-	30	-
Os (ppb)	2.42	2.99	3.90
Ir (ppb)	1.81	2.90	3.50
Ru (ppb)	3.93	5.70	7.00
Rh (ppb)	0.57	1.00	1.12
Pt (ppb)	2.31	6.20*[2]	7.60
Pd (ppb)	2.48	5.20*[2]	7.1
Au (ppb)	-	1.00*[2]	1.9

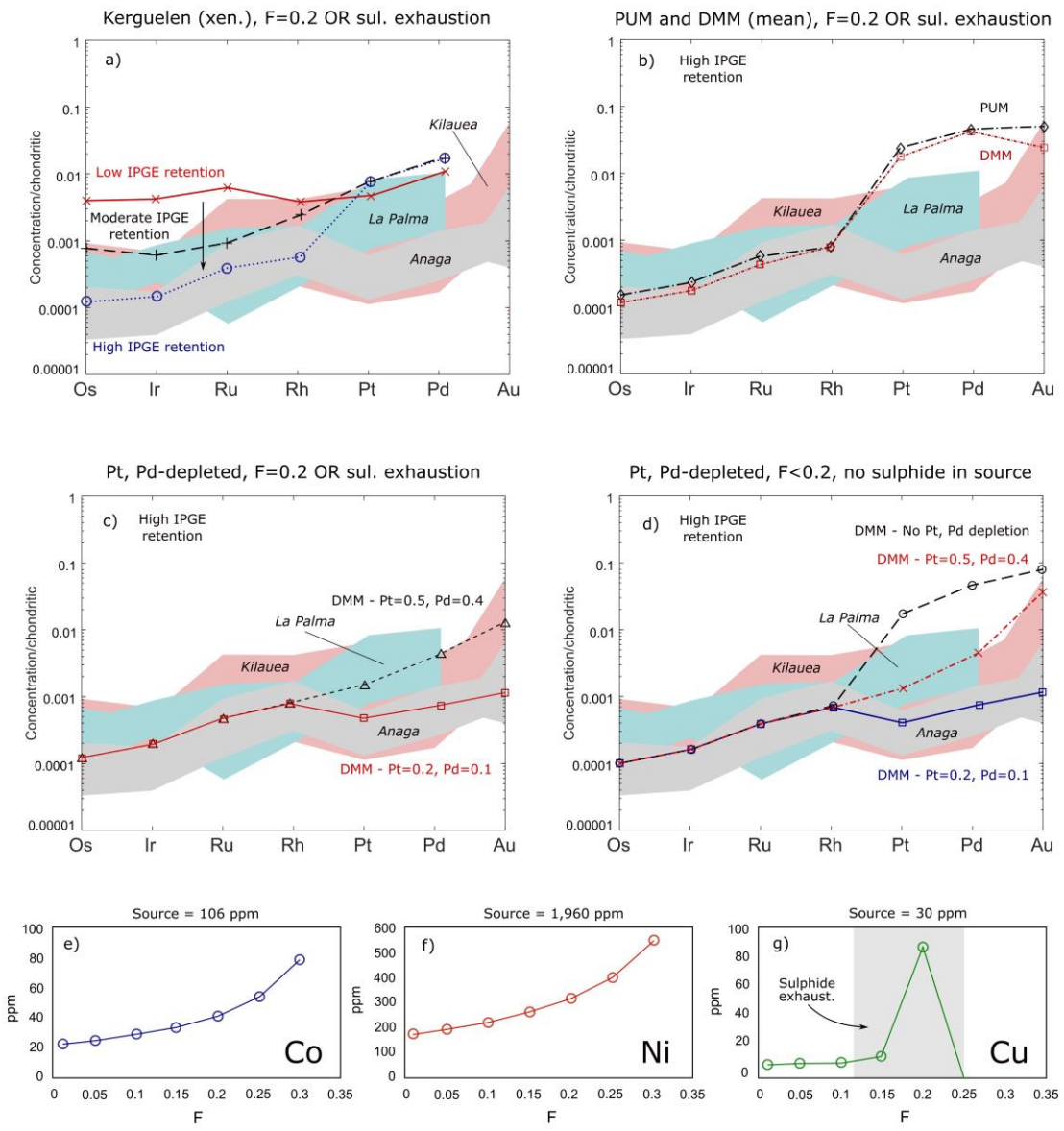

Figure 4.12 – *Melt modelling for Tenerife magma PGE and Au concentrations based on the parameters from Table 4.3. Anaga, La Palma and Kilauea ranges from Figure 4.10 are shown next to modelled trends for reference. (a) Modelling using starting concentrations in Kerguelen mantle xenoliths (Lorand et al., 2004), and alteration of IPGE and Rh partition coefficients for low, moderate and high levels of retention in silicate phases. (b) Modelling using Depleted MORB Mantle (DMM) (Salters and Stracke, 2004) and Primitive Upper Mantle (PUM) (Becker et al., 2006) starting concentrations, with high IPGE and Rh retention in silicates as per 12a. (c) Modelling using hypothetical adjusted DMM starting concentrations from 12b, with moderate and strong Pt and Pd pre-depletion. Plots (a) to (c) assume sulphide exhaustion in a garnet peridotite source (i.e., ~ 20 % partial melting). (d) Modelling using DMM starting compositions (original, moderate and strong Pt-Pd depletion) without sulphide in source, allowing for much lower degrees of partial melting.*

Using the starting composition of Kerguelen harzburgite xenoliths (Lorand et al., 2004), our model generates magma with a very flat PGE enrichment trend in Figure 4.12a, at around 0.004 x chondritic values for the PGE (note that Au data for the Kerguelen xenoliths is unavailable). The resulting chondrite-normalised signature of the melt is 100 times more enriched in IPGE and around 10 times more enriched in PPGE than our observed Tenerife range. A simple uniform PGE depletion at source would still result in imbalanced PPGE/IPGE (i.e., Pd/Ir) with respect to our Tenerife concentrations. This necessitates a mechanism for supressing IPGE significantly in the resulting magma via either a more depleted source composition or retention in a residual mantle phase during melting. We reflect this in our bulk model in the partition coefficients we use for IPGE and Rh into olivine, garnet or orthopyroxene (any of the three will produce the same effect) to simulate their partial retention in the mantle even past sulphide exhaustion. By increasing IPGE and Rh retention by a moderate and high degree (Figure 4.12a) we approach IPGE and Rh concentrations akin to those observed in the Canary Islands lava sample suite. In the given conditions, compatibility of PGE with garnet/olivine/orthopyroxene is a reliable melt suppression mechanism, as the minerals are only consumed in very small degrees (i.e., low *p* values; Table 4.3). Clinopyroxene is the dominant melting phase in garnet peridotites (Walter, 1998) and is consumed at 11.4 % partial melting in our models; since PGE are not strongly compatible with clinopyroxene, its role in PGE distribution is minimal. Conversely, given that Pt and Pd are not readily compatible with silicates (and are purely controlled by BMS and PGM), we require a different mechanism to adjust their concentrations in the model.

In Figure 4.12b, we observe the effects that different source compositions have on magma PGE concentrations in the calculation. Overall, PUM represents mantle compositions soon after differentiation of the Earth, prior to significant melting-induced fractionation of PGE (Becker et al., 2006; Lorand et al., 2008; Lorand et al., 2009; Walker, 2009; Laurenz et al., 2016). DMM represents a pre-depleted portion of the mantle subjected to multiple melting events and removal of less compatible elements (Peucker-Ehrenbrink et al., 2003; Salters and Stracke, 2004; Stracke et al., 2005). Since Pt and Pd are more easily liberated from the mantle via partial melting than the other PGE, and DMM has generally experienced higher degrees of partial melting prior to inclusion in plume-derived

melts, we assume $Pd/Ir^{PUM} > Pd/Ir^{DMM}$. The two compositions, in the context of our modelling, represent end-members of standard mantle components in terms of PGE concentrations from enriched (PUM) to depleted (DMM). However, the adjustments observed in source composition from Figure 4.12a to 4.12b are insufficient to generate Tenerife multi-element signatures, and Pt and Pd concentrations are still higher than observed with both of these mantle end-members. In Figure 4.12c, we start with a DMM source composition but reduce the Pt and Pd to significantly lower levels (0.5 ppb Pt, 0.4 ppb Pd; and 0.2 ppb Pt, 0.1 ppb) not observed in any of the xenolith or experimental arrays (i.e., Pd/Ir < 1). As shown in this plot, by combining silicate suppression of IPGE melt incorporation with a strongly Pt- and Pd-depleted starting composition, we can successfully model the observed trends in Tenerife and La Palma.

To address the sulphide exhaustion issue, we run the model in the absence of a sulphide mantle phase for experimental purposes only in Figure 4.12d – a complete lack of sulphide in the mantle is petrologically unrealistic and presents the issue that Pt and Pd are incompatible with all input source phases. The model essentially demonstrates that the enrichment patterns produced via IPGE suppression in silicates and Pt-Pd depletion in the mantle source can be recreated at any melting degree. Changes from F = 0.01 to F = 0.3 are minimal, provided Pt and Pd can be hosted in a phase not accounted for in the model, such as the (as yet) unquantifiable PGM. Evidently the true process lies somewhere between sulphide depletion at a given degree of partial melting and sulphide absence, as both end-members present inconsistencies. This allows flexibility in starting sulphide compositions in melting models to trigger sulphide exhaustion (and chalcophile release) at lower degrees of partial melting.

DMM compositions for Co, Ni and Cu (Salters and Stracke, 2004) work very well with the models from Figures 4.12a-d (106, 1960, 30ppm at source; 42, 315, 86ppm in melts post-sulphide exhaustion) (Figures 4.12e-g). Sulphide exhaustion in the source causes a sharp increase in Cu concentrations in generated melts (Figure 4.12g). Modelled final melt compositions broadly reflect the ranges in Figures 4.5d-f. In the absence of sulphide from the system (Figure 4.12d), Co and Ni are unaffected due to affinity for and subsequent control by mafic silicates (Table 4.3), and Cu ends up at similar levels in both sulphide normative and depleted situations, after ~ 20% partial melting. In the absence of

sulphide in the mantle mode, Cu concentration is highest in smaller-degree melts, because it has low compatibility in silicates – this potentially reinforces the sharp relationship between Cu and MgO in Tenerife samples with respect with other islands (Figure 4.5f). The ratios of Cu/Pd (Figure 4.11a) in our samples provide evidence for a small degree of crustal S-saturation and sulphide depletion. Whilst fractionating sulphides are likely to have drawn down the PGE concentration of many of the Tenerife lavas *as a whole* (i.e., the partition coefficient of the PGE into sulphides is large for all PGE), this will retain the shape of the chondrite-normalised pattern established by our models (Figure 4.12a-d) and merely shift absolute PGE concentrations down slightly with respect to less sulphide-depleted lavas.

4.4.4. Implications for OIB precious metal budgets

Having satisfied IPGE and Rh concentration requirements in via encapsulation in silicate phases (Figure 4.12a), we must address (i) the apparent source depletion in Pt and Pd, and (ii) sulphide exhaustion in relation to degree of partial melting. It is rare in surface magmatic rocks that bulk rock Pd/Ir is lower than 1, given the general enrichment of PPGE with respect to IPGE in most rocks (e.g., McDonough and Sun, 1995; Bennett et al., 2000; Lorand and Alard, 2001; Barnes et al., 2015; Driscoll, 2016). However, when we consider the heterogeneity of a mantle sources potentially included in plume melts, and in particular the Canaries plume (i.e., Figure 4.1a), incorporation of recycled oceanic lithospheric material may impart Pt and Pd depletion relative to the remaining PGE in a melting source. La Palma and El Hierro lavas have HIMU (high-Pb) isotopic signatures that indicate the presence of recycled crust and lithosphere in the plume column (Day and Hilton, 2011). Other studies on the Canary Islands comment on the long-term persistence of HIMU signatures through different islands (Day et al., 2010; Taylor et al., 2020). The subduction of oceanic plates at convergent margins often leads to significant dehydration of slab material, which in turn can scavenge metals from the subducted crust to the overriding asthenospheric mantle wedge and SCLM - this is particularly the case for Cu, Pt, Pd and Au, the least compatible of the highly siderophiles elements (e.g., Woodland et al., 2002; Powell and O'Reilly, 2007; Alard et al., 2011; Delpech et al., 2012; Griffin et al., 2013; Lorand et al., 2013; Lorand and Luguet, 2016; McDonald et al., 2017; Tassara et al., 2017; Rielli et al., 2018; Holwell et

al., 2019; Wade et al., 2019). If the Canary Islands preserve the isotopic properties of HIMU components (e.g., Day et al., 2010 and Day and Hilton, 2011), the Pt and Pd depletion signatures of subducted lithosphere can also be retained. This would lead to a melting system enriched in IPGE and Rh relative to Pt and Pd (resulting in low Pd/Ir) when present as a melt component.

If pre-depletion did not occur in melt components *before* their involvement in OIB magma generation beneath the Canaries, a multi-stage melting process (as seen in the early lavas of the Icelandic plume in Keays and Lightfoot, 2007, and Pacific hotspot trails in Ren et al., 2005; Jones et al., 2017) may have played a crucial role in generating Canary Island PGE signatures. As featured in our models, the retention of IPGE and Rh as PGM and alloys in silicate minerals in addition to interstitial phases when compared with Pt and Pd-bearing interstitial BMS will aid in their fractionation. However, if an initial melting event began the process of sulphide consumption prior to the generation of western Canary Islands magmas, perhaps earlier in the island chain, the interstitial sulphides would be the first to be partially depleted in the subsequent plume mantle source, be it DMM, HIMU or another composition. Given that partial melting is often a multi-stage process, and the literature describes significant gaps in Canary Island volcanic productivity that may have facilitated fluctuating melting rates (e.g., Hoernle and Schmincke, 1993; Marcantonio et al., 1995; Anguita and Hernán, 2000; Day et al., 2010; Taylor et al., 2020), this pre-depletion via earlier partial melting could set the scene for low source Pt and Pd concentrations necessitated by Figure 4.12c, leaving a dominant IPGE presence in silicate-encapsulated PGM. Furthermore, by removing a portion of mantle sulphides in the source, the modal assemblage (i.e., 'X' in Table 4.3) may alter in such a way that subsequent melting events could exhaust the remaining sulphides at a greater rate, bringing F values in successful models (Figure 4.12c) closer to those observed in the island chain from other major and trace element (lithophile) geochemical evidence (~ 5 %; Figures 4.8e-f).

Until this point, our models have dealt with sulphide minerals as a single phase observed in xenoliths, to describe the bulk mobility of chalcophiles in melting systems. However, even beyond the differences in speciation between intra-silicate and interstitial sulphides affecting IPGE+Rh/PPGE fractionation, the two groups of PGE have different affinities for different base metal sulphides.

Furthermore, although xenoliths can represent mantle assemblages, the elevated P/T conditions in true mantle conditions can alter the solidus of sulphide minerals, which has implications for PGE partitioning (Becker et al., 2006). In the mantle, IPGE and Rh are frequently hosted in Fe-rich mono-sulphide solutions (Mss), and PGM within silicate minerals, whilst Pt and Pd are hosted in comparatively Cu-rich sulphide phases (e.g., Barnes et al., 1985; Bockrath et al., 2004; Mungall et al., 2005; Naldrett, 2011). These distinct host phases will melt at different rates, with the Pt and Pd-bearing Cu-rich phases more easily melted, leaving an Mss-rich residue and IPGE/Rh-bearing silicates, oxides or PGM in the melting source (Ballhaus et al., 2001). Magmas produced from a subsequent melting event of the same source, or increased degrees of partial melting (perhaps exhausting sulphide phases in the source) will be relatively IPGE- and Rh-rich (mobilising these once residual phases) relative to Pt and Pd (Keays, 1995). We envisage a multi-stage melting event and pre-depletion by earlier partial sulphide consumption (in addition to distinct silicate and sulphide melting) could contribute to the subsequent Pt and Pd depletions in Tenerife lavas compared to El Hierro and La Palma lavas.

Heterogeneous melting events and subsequent fractionation in included chalcophile concentrations has been recognised in Hawaiian and Icelandic plume-derived magmas. Bennett et al. (2000) suggest that PGE-deficient Koolau lavas in the Hawaiian chain relate to signatures for increased residual sulphide in the plume and relatively PGE-rich Kilauea and Loihi lavas in the same chain relate to signatures for small amounts of residual sulphide in the plume. Alkaline Maui lavas (i.e., low degree partial melts of the Hawaiian plume source) are also PGE-poor compared to Kilauea (Crocket, 2002b). In Iceland, increased chalcophile content at lower degrees of partial melting (i.e., < 20 %) are associated with liberation of sulphide phases in S-depleted plume material, potentially due to prior partial exhaustion from multiple melting events (Webber et al., 2013). It follows that a complex array of melting-induced PGE fractionation processes are common in plume settings beyond the Canary Islands, which suggests that this may be a feature inherent in long-lived oceanic intraplate volcanism in general.

The gradual shift in PGE concentrations throughout the Canary Island chain (Tenerife to El Hierro and La Palma) fits well with the pulsing plume model

established by Taylor et al. (2020) and highlights the importance of slight changes in melting regime and/or source components have on precious metal acquisition in intraplate magmas. Ultimately, future $^{187}Os/^{188}Os$ data would clarify the concepts suggested as explanations for Tenerife PGE trends, and complete the geochemical assessment of the western products of the Canary Island plume. This chapter provides significant headway in linking the metallogenic character of the Canary Islands region to the complexities introduced to a magmatic system by high degrees of heterogeneity in plume characteristics with time.

4.5. Conclusions

The heterogeneous properties of the Canary Islands plume imprint distinctive and variable geochemical signatures in mantle melts, as recorded by lavas spread throughout the seven main islands. This heterogeneity has been shown through the chapter to impact upon the precious metal basket of basaltic lavas, which we successfully modelled for Tenerife and the western Canary Islands:

1) Tenerife represents ≤ 5 % partial melts of a garnet peridotite source beneath the western Canary Islands, with strongly alkaline, incompatible element and light REE-enriched, olivine-deficient lavas found in the Old Basalt massifs at each of the island's three corners.
2) Precious metal signatures in Canary Islands lavas vary through Tenerife, El Hierro and La Palma, and feature increasing PGE-enrichment overall with time, which may reflect increasing degrees of partial melting forming the magmas that fed later lavas.
3) Modelling of PGE concentrations in Canary plume melts indicate the importance of IPGE and Rh retention within less fusible mantle phases such as olivine, and significant Pt and Pd depletion in the mantle source (due to relic signatures in plume material) in generating observed PGE signatures.
4) A combination of inherent Pt and Pd depletion in HIMU (recycled oceanic lithosphere) plume components, pre-conditioning of melting sources via preferential fractionation of Pt- and Pd-bearing sulphides, incremental sulphide exhaustion via multi-phase melting, and suppression of IPGE in silicate phases control the PGE geochemistry of magmas in the western Canaries, as represented by basaltic lavas.

Chapter 5

A machine learning approach for regional geochemical data - Platinum-group element geochemistry vs geodynamic settings of the North Atlantic Igneous Province

Chapter Summary

Whilst traditional approaches to geochemistry provide valuable insights into magmatic processes such as melting and element fractionation, by considering entire regional data sets on an objective basis using machine learning algorithms (MLA), we can highlight new facets within the broader data structure and significantly enhance previous geochemical interpretations. The PGE budget of lavas in the North Atlantic Igneous Province (NAIP) has been shown to vary systematically according to age, geographic location and geodynamic environment. Given the large multi-element geochemical data set available for the region, MLA are employed in this chapter to explore the magmatic controls on these shifting concentrations. The NAIP data set is manipulated herein using Principal Component Analysis (PCA) and t-Distributed Stochastic Neighbour Embedding (t-SNE) techniques to increase separability in the data alongside clustering using the *k*-means MLA. The workflow provides a methodology for conducting an objective high-dimensional investigation on a geochemical data set and particularly enhances the identification of metallogenic anomalies across the region. Crucially, the variability of Pt and Pd are not reflected in MLA-based clustering trends, suggesting that they vary independently through controls not readily demonstrated by the NAIP major or trace element data structure (i.e., other proxies for magmatic differentiation, perhaps SCLM enrichment). The workflow contained within this chapter is used in Chapter 6 and 7.

5.1 Introduction

Machine learning is a powerful data science tool used to investigate large data sets and is increasingly integrated into novel scientific applications. Bulk geochemical data sets are excellent targets to analyse using machine learning algorithms (MLA) considering they often comprise large sample sets with a multitude of elements measured for each sample. Furthermore, global and regional geochemical data sets are becoming less expensive to create, and more accessible through analytical development and data sharing capabilities. Previous studies have successfully implemented MLA-based methodologies to investigate geochemical domains on Mars (Taylor et al., 2010), hazardous groundwater geochemistry (Farnham et al., 2002), and Pb behaviour in the Kerman Copper Belt, Iran (Ghannadpour et al., 2013). Recently, efforts have been made to enhance the link between traditional geochemical investigations and data science, such as the revisiting of traditional basalt geochemical sub-groups (Iwamori et al., 2017) and mapping mineral distributions in lunar basalts (Cone et al., 2020) using multivariate statistical analyses.

Herein, this chapter tests a combined classical and MLA approach applied to a large magmatic geochemical data set, with the aim to establish a framework that can be replicated for a variety of studies in the field of geochemistry. The comparison of descriptor-based labelling (e.g., geographic location or lithological classification) and algorithmic clusters is of particular interest in geochemistry, since geochemical studies often partition data based on a small number of variables selected by the user and do not incorporate the larger-scale similarities across all variables. In this respect, simplifying data sets may resolve major trends, but bypass more subtle relationships that exist across multiple elements and that could enhance the interpretation. Machine learning provides a means for more sophisticated analysis alongside classical geochemical techniques.

By exploring an example data set, the bulk geochemistry of North Atlantic Igneous Province (NAIP) lavas, we contribute to the discussion surrounding mantle plume and sub-continental lithospheric mantle (SCLM) controls on PGE and precious metal abundances in basaltic magmas. The application of data science techniques such as MLA allows for the critical examination of elemental concentrations from a different, objective perspective by analysing geochemistry

in multi-dimensional space – something not attainable through traditional geochemical data analyses. The workflow presented in this chapter, including dimensionality reduction and clustering methods, can be used for a variety of similar studies alongside prior or concurrent classical discriminant diagrams, for example, forming a framework for comparisons of plume geochemical signatures at a global scale (Chapter 7).

5.1.1. Geological background

5.1.1.1. Mantle plumes and continent break-up

Mantle plumes are hot upwellings from the lowermost portions of the silicate Earth. Initiated by chemical or physical instability at depth (Kellogg and King, 1993; Bercovici and Kelly, 1997; Jellinek and Manga, 2004), they form rising diapirs of buoyant high-temperature mantle material that can induce decompression-driven partial melting of the upper mantle, asthenosphere and lithosphere (Griffiths and Campbell, 1990). Continental landmasses uplifted and thinned by impinging plumes will eventually extend and rift apart, ultimately leading to the formation of oceanic lithosphere (Pirajno and Santosh, 2015). The material melted by plumes under continental lithosphere changes through their lifetime as the geodynamic environment shifts towards an oceanic setting, and the geochemistry of subsequent lavas produced from plume magmas will reflect these changes (Howarth and Harris, 2017). Decompression models for flood basalt melting predict < 5% of the lithosphere is involved in melt generation, and this is isolated to the initiation stages (i.e., when the continental lithosphere is available to melt prior to rifting; McKenzie and White, 1989; White and McKenzie, 1995). If the lithosphere is thick, larger amounts of crust and the SCLM are involved in melt generation; underneath lithosphere thinned by extension, melts will incorporate higher proportions of asthenospheric (i.e., plume-derived) material (Turner et al., 1996). In addition to the reduction of continental contamination of plume magmas with time, initial melts coinciding with the buoyant, laterally expansive and voluminous plume head are typically interpreted to have stemmed from higher degrees of partial melting and produced extensive eruption of flood basalts (Campbell and Griffiths, 1990). With time, the degree of partial melting may decrease, as the narrower plume tail becomes the primary melting source (e.g., Griffiths and Campbell, 1990; Trela et al., 2015).

5.1.1.2. The North Atlantic Igneous Province

The Icelandic hotspot, the surface expression of the underlying (proto-) Icelandic mantle plume, first erupted lava ca. 65 Ma (Berggren et al., 1995), heralding the opening of the North Atlantic Ocean in the Palaeogene (Hole and Natland, 2019). Greenland and the British Isles began to rift apart while mantle plume-derived magmas fed volcanism persisting into the newly opened ocean basin (Fitton et al., 1997; Saunders et al., 1997; Kent and Fitton, 2000). Collectively, the igneous rocks produced from this event belong to the NAIP (Horni et al., 2017; Figure 5.1a). Today, intraplate and rift volcanism are active simultaneously on Iceland (McKenzie and White, 1989; White and McKenzie, 1995; Momme et al., 2003), and the plume has transitioned through continental to oceanic geodynamic settings throughout the last ~ 62 Myr (Figure 5.1b).

The Icelandic hotspot extruded (and continues to extrude) unusually high volumes of lava with respect to similar plumes around the world (Courtillot et al., 2003), especially in its earlier stages (e.g., Greenland and the British Palaeogene Igneous Province or BPIP) (Larsen and Pedersen, 2000). Lavas in the region are primarily basaltic but range from picrites to more evolved andesites and rhyolites (Kent and Fitton, 2000). The region is recognised as having high potential for hosting Ni-Cu-PGE deposits, partly attributed to its plume setting (Andersen et al., 2002) and has been a focus for PGE research in the last two decades. In some PGE-mineralised localities elsewhere in the world, such as the Bushveld (South Africa) and Stillwater (North America) complexes the suggestion that the SCLM plays a key role in contaminating plume magmas with the metals that form ore deposits through mineralisation remains controversial, yet persistent (e.g., Maier and Groves, 2011 and references therein). Intrusive complexes in the NAIP, such as Skaergaard in East Greenland and the Rum Layered Complex in western Scotland, host mineralised PGE reefs and a key debate concerns the source of these metals within the NAIP magmatic system (e.g., Andersen et al., 1998, 2002; Butcher et al., 1999; Pirrie et al., 2000; Hughes et al., 2015, 2017).

In one study, Hughes et al. (2015) demonstrated a systematic shift in the relative PGE abundances of NAIP basaltic lavas from oldest to youngest (e.g., continental to oceanic). Lavas in West Greenland and the BPIP (the earliest products of plume magmatism) typically have Pt/Pd ratios of 1.9; later lavas in East Greenland and its offshore regions have Pt/Pd ~ 0.79; and contemporary

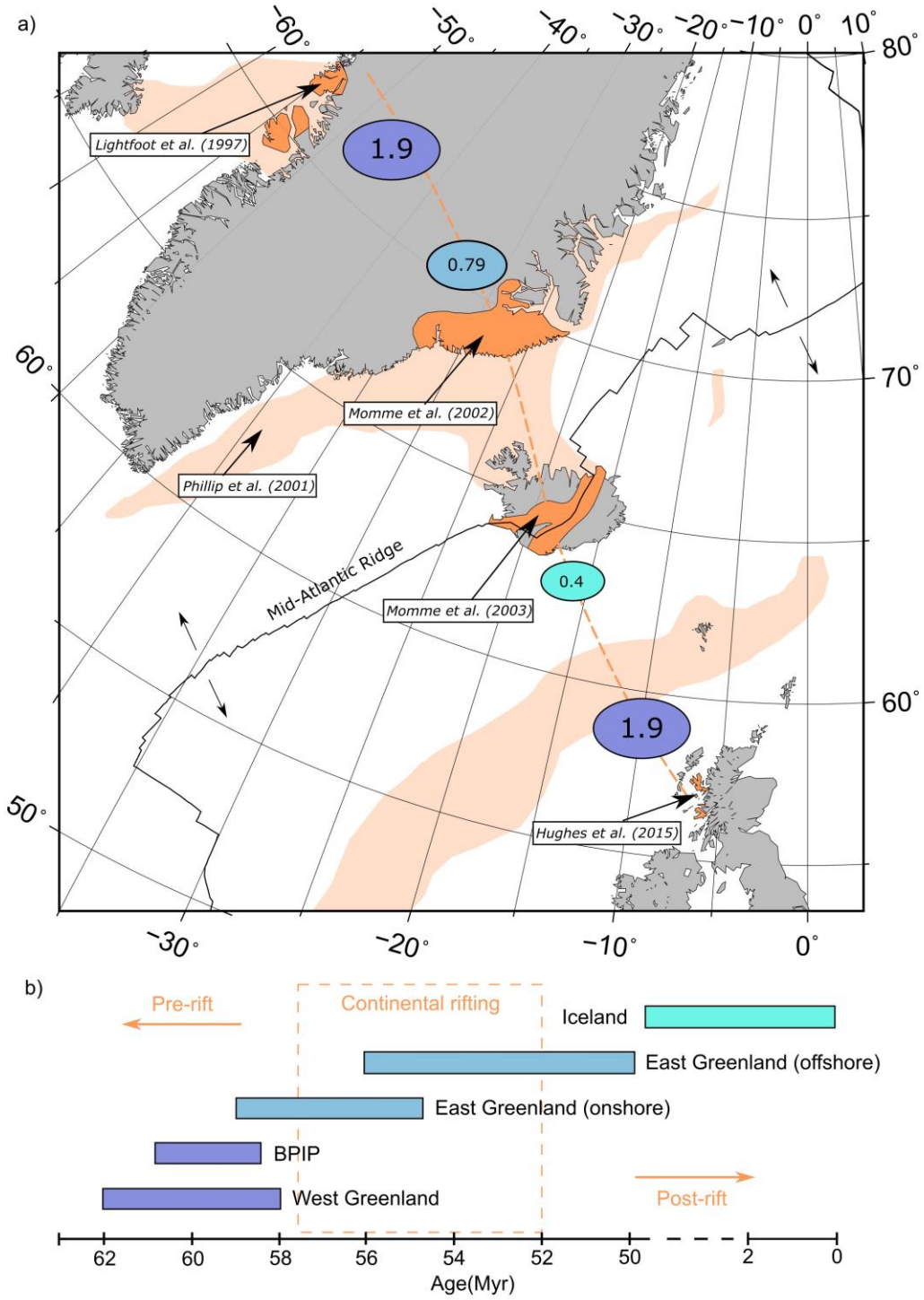

Figure 5.1 *– (a) Schematic map of the North Atlantic Igneous Province. Onshore and offshore lavas are shown in orange. Pt/Pd for each locality are shown in the purple to light blue bubbles, lightening towards lower values. The orange dotted line describes the trail of the proto-Icelandic plume from ca. 65 Ma onwards (based on Lawver and Muller, 1994). Study localities from which data are drawn are shown in white boxes. (b) Timeline of eruption in localities in the NAIP throughout the last ca. 62Ma, divided into pre-, syn-, and post-rift periods. Adapted from Hughes et al. (2015).*

Icelandic lavas have Pt/Pd ~ 0.4 (Figure 5.1a). The metal signature of NAIP plume-derived melts (i.e., the metal basket) appears to have changed alongside the chemo-dynamic setting. After critiquing a variety of possible explanations for this Pt/Pd shift, Hughes et al. (2015) suggested the contaminating influence of SCLM-derived melts and metals on the plume-derived basaltic magmas was the most likely control. More specifically, mantle peridotite xenoliths entrained within Scottish lamprophyre dykes, representative of the mineralogy of the SCLM underneath the current margins of the North Atlantic craton, contain two populations of base metal sulphides, one of which is notably Pt-rich due to their inclusion of PtS, the platinum-group mineral cooperite (Hughes et al., 2017). If plume magmas from the earlier stages of the NAIP (e.g., West Greenland and Scotland) incorporated portions of the SCLM during asthenospheric melting, assimilation of such platinum-group minerals (PGM) would be reflected in higher Pt/Pd in bulk geochemistry of the lavas produced. This effect would reduce in line with the progressively decreasing role of SCLM contamination of plume-derived magmas in oceanic settings (e.g., more recent East Greenland offshore and Iceland lavas), reducing Pt/Pd ratios and therefore signalling an inherent linkage between enriched mantle keels and metal prospectivity (e.g., Hawkesworth and Scherstén, 2007; Hughes et al., 2014).

The validity of the apparent shift in Pt/Pd ratio is tested in this chapter by assessing the precious metal compositions of NAIP lavas in context with their major and trace element geochemistry across multi-dimensional (multi-element) space. By using MLA to objectively classify the high-dimensional trends in the data, we seek to comment on the major processes captured in a regional-scale magmatic differentiation system and whether controls on metallogenesis are truly localised according to geodynamic setting.

5.2. Materials and Methods

The purpose of using machine learning to analyse the NAIP data set is to explore different facets and enhance our understanding of a previously-studied geochemical system. Geochemistry has, until recently, rarely been coupled with data science (Zuo, 2017) and there are significant opportunities to develop an integrated geochemical workflow for high-dimensional data analysis using MLA,

as proposed in Figure 5.2. Traditional geochemical investigations are essential for understanding the geological processes behind magma compositions, but a data science approach is hereby used to maximise the information obtained from such data sets and complement findings from earlier investigations. Dimensionality reduction techniques like Principal Component Analysis (PCA) and t-Distributed Stochastic Neighbour Embedding (t-SNE) describe the large-scale variability of a large data set in an intuitive way. A variety of MLA process large amounts of data and identify high-dimensional trends unresolvable to a human analyst. The changing Pt/Pd ratio across NAIP lavas is documented by Hughes et al. (2015), and reflected in their changing geography. By using a data science approach supported by dimensionality reduction, we investigate how elemental concentrations behave with respect to each other and geographic information. The large-scale structure of the data will inform the investigation of controls on shifting PGE ratios (and other elemental concentrations) while directly comparing the new findings to those from earlier studies.

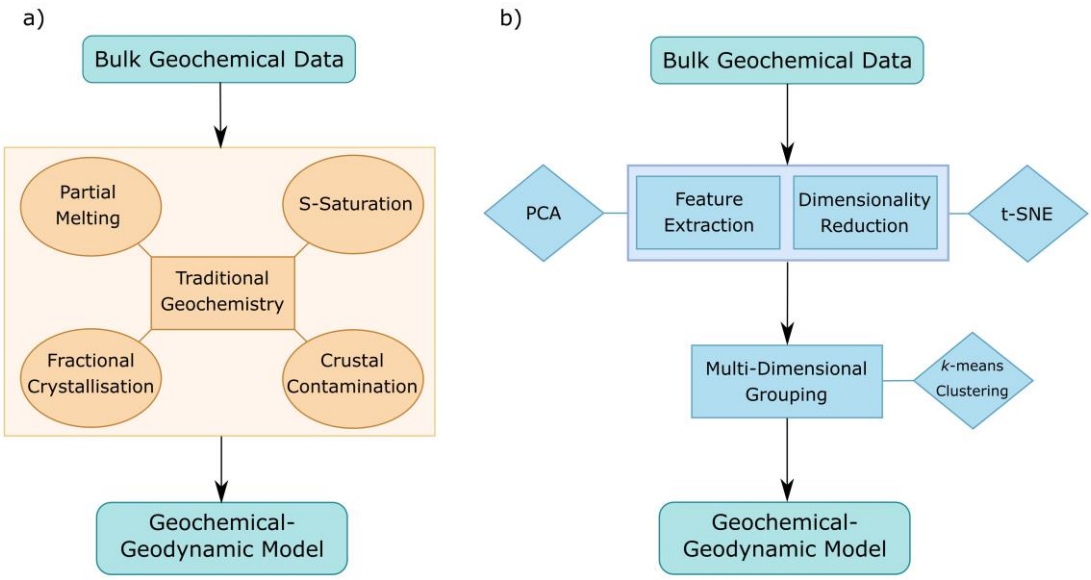

Figure 5.2 *– Geochemical workflow introduced in this study featuring concurrent (a) traditional and (b) data science based methods towards a geochemical-geodynamic model. Dimensionality reduction is used to create more concise, descriptive multi-element clusters using MLA.*

5.2.1. Data

The NAIP data set from Hughes et al. (2015) contains new bulk concentrations of 49 major and trace elements from Scottish basalts in addition to existing literature data for basaltic lavas from West and East Greenland, offshore Greenland, and Iceland (Table 5.1; Figure 5.1). Hughes et al. (2015) used their own data alongside a compilation of other PGE-bearing data sets from across the NAIP for their study (Table 5.1) – the amalgamated data set is presented in Supplementary S5.1. The data were classified by locality (i.e., five categories) and the study compared major, trace and PGE concentrations in lavas between these locations. This chapter uses new methods to produce different categories based on multi-element geochemical variability, to determine how well sample localities (and by extension, geodynamic stages in the NAIP) are reflected in numerical clustering techniques.

Table 5.1 *– Summary of data used in this study listed according to geographic regions, localities, reference and number of basaltic lava samples (n).*

NAIP Region	Locality	Study	n
Scotland	Mull, Rum & Skye	Hughes et al. (2015)	51
West Greenland	Disko Island & Nuussuaq	Lightfoot et al. (1997)	48
East Greenland (onshore)	Sortebre flood basalts	Momme et al. (2002)	33
East Greenland (offshore)	ODP 917-918; ODP 988-990	Philipp et al. (2001)	97
Iceland	West, East and South Rift Zones	Momme et al. (2003)	30
		Total	***259***

The dimensionality reduction and machine learning techniques used in this study necessitate a complete data set with no missing information. The number of elements analysed and available in each of the five sample sets varied greatly, leaving eleven variables present in every North Atlantic locality with mainly non-zero concentrations – major element oxides Fe_2O_3, MgO and TiO_2, and trace elements Cr, Ni, Cu, Ir, Ru, Rh, Pt, and Pd. This is by no means an exhaustive variable set, missing lithophiles, alkalis and rare earth elements, but by itself can provide a great deal of information towards large-scale plume melting processes. The eleven modelled elements are important proxies for magmatic differentiation

processes in mafic magmatic systems and are key for mineralisation of Ni-Cu-PGE ores, explaining their consistent inclusion in all five sample sets. Of these selected variables, where occasional blank/non-numerical observations existed, a process of rounded-zero imputation was applied following the approach by Martín- Fernández et al. (2012), using the mean least-squares regression values against all other variables. This gives previously missing observation cells meaningful concentrations below the elemental detection limits, without implying detectable concentrations or disrupting the variance of the data as a whole. The final data set used is supplied in Supplementary S5.1 and all Python code in Supplementary S5.2. The following sections describe the workflow used to analyse the data.

To avoid biasing the clustering through variables with mixed-unit concentrations (major oxides in percent, minors in ppm and PGE in ppb) z-scores were generated for the data set as a standardisation procedure. The following equation was used to produce z-scores for all data observations (as per Kreyszig, 1979) when z is the z-score, x is the raw concentration, μ is the population mean, and σ is the standard deviation of the population:

$$z = \frac{x - \mu}{\sigma}$$

Standardising the data ensures that variability in a given variable can be directly compared to another, regardless of raw data units, leading to more effective clustering.

5.2.2. Principal Component Analysis

Popularised by Hotelling (1933) after Pearson (1901), PCA is a multivariate analysis tool commonly used to transform a data set in such a way that the variances of each dependent variable can be viewed in unison in a low dimensional space (Davis, 2002; Jolliffe, 2002 and references therein). It functions as an effective linear dimensionality reduction technique. The method creates individual Principal Components (PCs), which describe the contributions to data variance, where the first order PC is aligned to capture the maximum variance in the data spread, the second order PC will then be aligned orthogonal to the first and so on. The main purpose of using PCA for the NAIP geochemical data set is to determine how elemental concentrations in the basaltic lavas are

correlated to these PCs and by extension, which concentrations are controlled by similar factors. PCA also allows us to display multi- element information in biplots (Hyvärinen et al., 2001) using the PCA *sci-kit learn v0.21.3*, *NumPy v1.16.5* (Harris et al., 2020) and *Pandas v0.25.1* (McKinney, 2010) packages on Python 3.7.4 (Pedregosa et al., 2011), and effectively discuss the structure of the data set using minimal dimensions (Chang, 1983). The package automatically standardises raw concentrations using z-scores. For a large geochemical data set, PCA can describe the contribution from each element to the overall variance of the data set, allowing for a simple comparison of correlations between elemental concentrations, analogous to the relationships for the eleven NAIP elements shown in a correlation matrix (Figure 5.3). Elements with high correlation coefficients will likely be represented in the same PCs, and thus, reflect similar underlying controls.

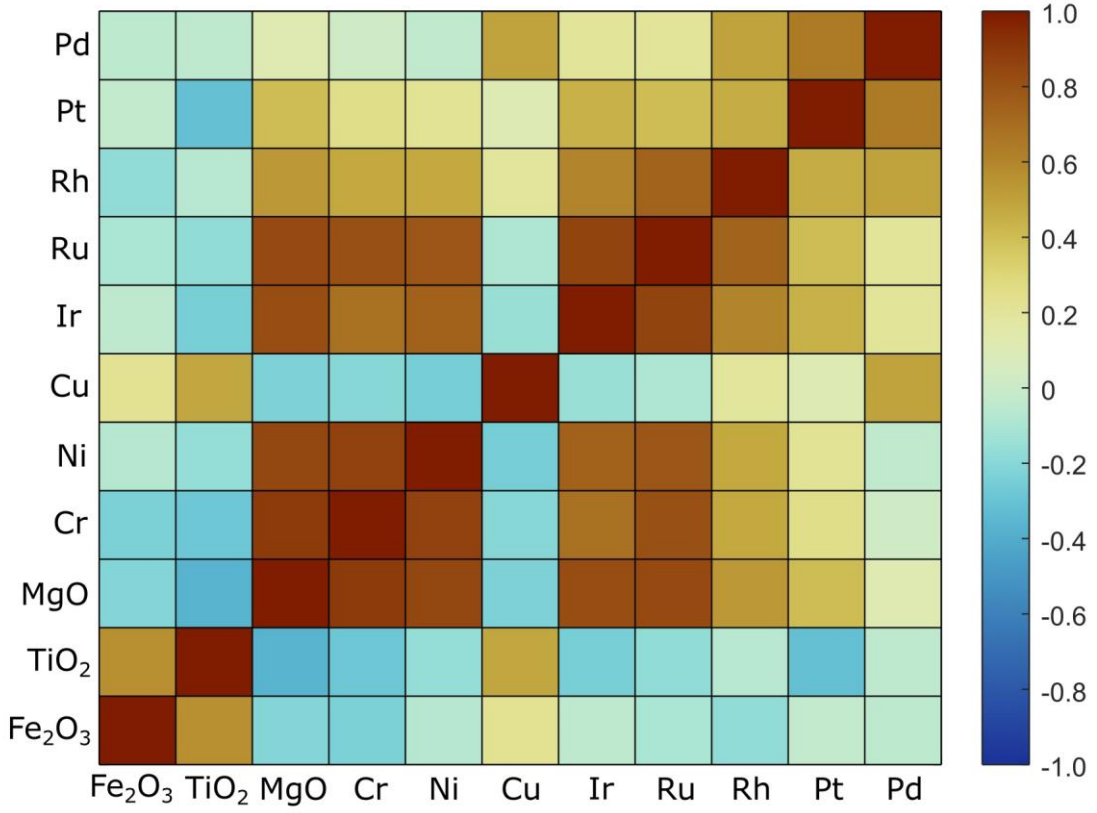

Figure 5.3 *– Correlation Matrix for all eleven elements included in the bulk geochemical data set for the North Atlantic Igneous Province. Both individual and group correlations are indicated on a scale from −1 to 1, highlighting multi-element trends in a simple manner prior to data science analyses.*

5.2.3. t-SNE

Similar to PCA, t-SNE is a dimensionality reduction technique used to display multi-dimensional data in an easily interpretable manner. The algorithm was developed by van der Maaten and Hinton (2008) and translates high-dimensional data (with each dimension representing one variable from the data set) into a low-dimensional bivariate space using two new computed features referred to as embeddings. Using the Kullback-Leibler Divergence (Kullback and Leibler, 1959), the algorithm maximises the similarity between the positions of all data points in high-dimensional space and their position in the embedding plot. The advantage of this approach is that it retains the original data structure while significantly reducing dimensionality, compared to PCA. Data points with similar multi-element concentrations will plot closely in the resulting two-dimensional embedding (van der Maaten and Hinton, 2008; van der Maaten, 2014). This technique acts as a data structure map and the transformed data points can be overlain with their MLA-based or descriptor-based classifications. Contributing element concentrations can also be mapped on to the embedding space, to determine how their abundances are distributed through the overall data structure.

Studies have successfully used t-SNE as a geochemical discriminant tool for alteration indicators (Horrocks et al., 2019) and geological domain mapping (Balamurali and Melkumyan, 2016), and the method is applied in a similar fashion to the NAIP data to identify metallogenic signatures. Here, we use the t-SNE algorithm from the *sci-kit learn* package in Python 3.7.4 (Pedregosa et al., 2011) to resolve and display the z-scored elemental contributions to overall NAIP data structure, with close reference to PCA results derived herein. Key input parameters were set up is as follows: perplexity of 80, 5,000 maximum iterations and learning rate of 200, based on recommendations for 259 samples by Krijthe (2015). Geographic categories from Hughes et al. (2015) and MLA-based clusters developed in this study are overlain on the generated t-SNE embedding, to allow for a simple comparison of the different clustering methods.

5.2.4. *k*-means clustering

Machine learning techniques fall into three major categories: supervised learning, in which you train an algorithm on a portion of a data set to analyse or

make predictions about the remaining portion; unsupervised learning, in which the algorithm finds its own structure in the data without the need for class labels; and reinforcement learning, where algorithms perform sequences of decisions based on both exploration and exploitation of knowledge (e.g., Hastie et al., 2009; Marsland, 2009; Witten et al., 2016). One of many unsupervised MLA used to cluster multivariate data is the *k*-means clustering technique (MacQueen, 1967), which has been selected as an analytical technique for the NAIP data set on account of its versatility, ease of use, and ability to cluster data based on user-selected parameters. The distance-based algorithm partitions a data set based on similarities amongst a large number of variables simultaneously so that occurrences within the same grouping are more similar to each other than occurrences in another grouping (e.g., Michie et al., 1994; Hastie et al., 2009; Marsland, 2009). The analyst must select the desired number of clusters (*k*) and the algorithm then randomly assigns *k* centroids to the data set. All observations are attributed to the nearest centroid to form clusters. The algorithm repositions the centroids and iterates until the sum of square Euclidian distances from each data point to their mean centre are minimised across the entire data set, to find the optimum centroid positions and corresponding clustering formation (Howarth, 1983). Crucially, this technique can be used with a high-dimensional data set, something unattainable via manual interpretations, and consequently will produce more objective and statistically-robust clusters than a manual clustering exercise. For the chosen set of variables, screening of outliers was unnecessary.

The unsupervised *k*-means algorithm does not require *a priori* sample labels to produce clusters and as such, the optimum *k* can be difficult to discern; a heuristic approach is recommended when selecting *k*-values, which promotes running the model multiple times with different input parameters to achieve a satisfactory result. The Davies-Bouldin Index (DBI) (Davies and Bouldin, 1979) can be used to retrospectively assess the statistical performance of different input parameter setups in a model, but model selection should also consider more subjective qualifiers in the context of the data set. Ideally, classifications should have small intra-cluster distances and high inter-cluster distances. In this study, the *k*-means algorithm from the *sci-kit learn* package in Python 3.7.4 (Pedregosa et al., 2011) was implemented including the z-scores of (i) all 11 available variables, (ii) PGE and trace elements Cr, Ni and Cu, (iii) PGE only, and (iv) a

selection of generated PCs, to observe the differences these inputs had on cluster size, shape, placement and DBI.

5.3. Results

5.3.1. Dimensionality reduction

5.3.1.1. Principal components

PCA was performed for the eleven elements in the NAIP data set. PCs 1 through 6 account for 92.17 % of the variability in the NAIP data set combined (43.99 %, 20.06 %, 13.53 %, 6.78 %, 5.11 % and 2.70 %, respectively). A scree plot is provided in Figure 5.4a that summarises the relative importance of each PC. As a rough guide, eigenvalues beyond ~ 90 % cumulative contribution are normally considered to be background noise and not substantially adding to data set variability, denoted by the flattening of the scree slope. PC7 and onwards are superfluous and not discussed herein. Full PCA statistics, including eigenvalues, eigenvectors and scaled co-ordinates are displayed in Supplementary S5.3. Figures 5.4b–d displays PC score biplots (combined variable and sample information) for (b) PC1-PC2, (c) PC3-PC4, and (d) PC5-PC6. Eigenvectors for each element are plotted as lines from the origin, and individual samples are plotted and attributed to their geographic categories (Hughes et al., 2015). Biplots allow for simultaneous interpretation of both element and sample variance. Vector lengths and directions represent the degree to which each PC describes the variability of the corresponding element.

As shown in Figure 5.4b, there are three major element vector groups in the PC1-PC2 space: MgO, Ni, Cr, Ir and Ru, positively attributed to PC1; Fe_2O_3, TiO_2 and Cu, positively attributed to PC2; and Pd, Pt and Rh, positively attributed to both PC1 and PC2. In Figure 5.3, these groups tend to have positive correlation coefficients with other members of their group. In Figure 5.4c, Pt, Pd and Rh retain their association from Figure 5.4b and are the only variables to plot positively against PC3; all other elements plot to the left-hand side of the PC3-PC4 space, with the MgO-Ni-Cr- Ru-Ir group displaying shorter vector lengths than the Fe_2O_3-TiO_2-Cu group. The majority of the variables have negligible to negative association with PC4, with only Pt, Ir and Fe_2O_3 vectors plotting positively. In Figure 5.4d, Pt and Pd appear correlated with the previously

identified MgO-Ni-Cr group in the negative direction of both PC5 and PC6. In this space, TiO_2 exhibits an opposite vector direction to Fe_2O_3 and Cu. Finally, Ir, Ru and Rh exhibit positive trends with PC5, with increasing vector length in that order; Ir and Ru are positively correlated with PC6. In terms of sample variance, onshore West and East Greenlandic lavas are coupled with MgO and its correlated vectors discussed above, while East Greenlandic (offshore), Icelandic and BPIP lavas plot in the opposite direction to most multi-elemental vector groups in higher order PCs (Figures 5.4b-c). It appears that in some instances (Figures 5.4c-d), extreme West Greenlandic outliers with high single-element contributions (notably Pt, TiO_2 and Rh) have an influence on eigenvector length.

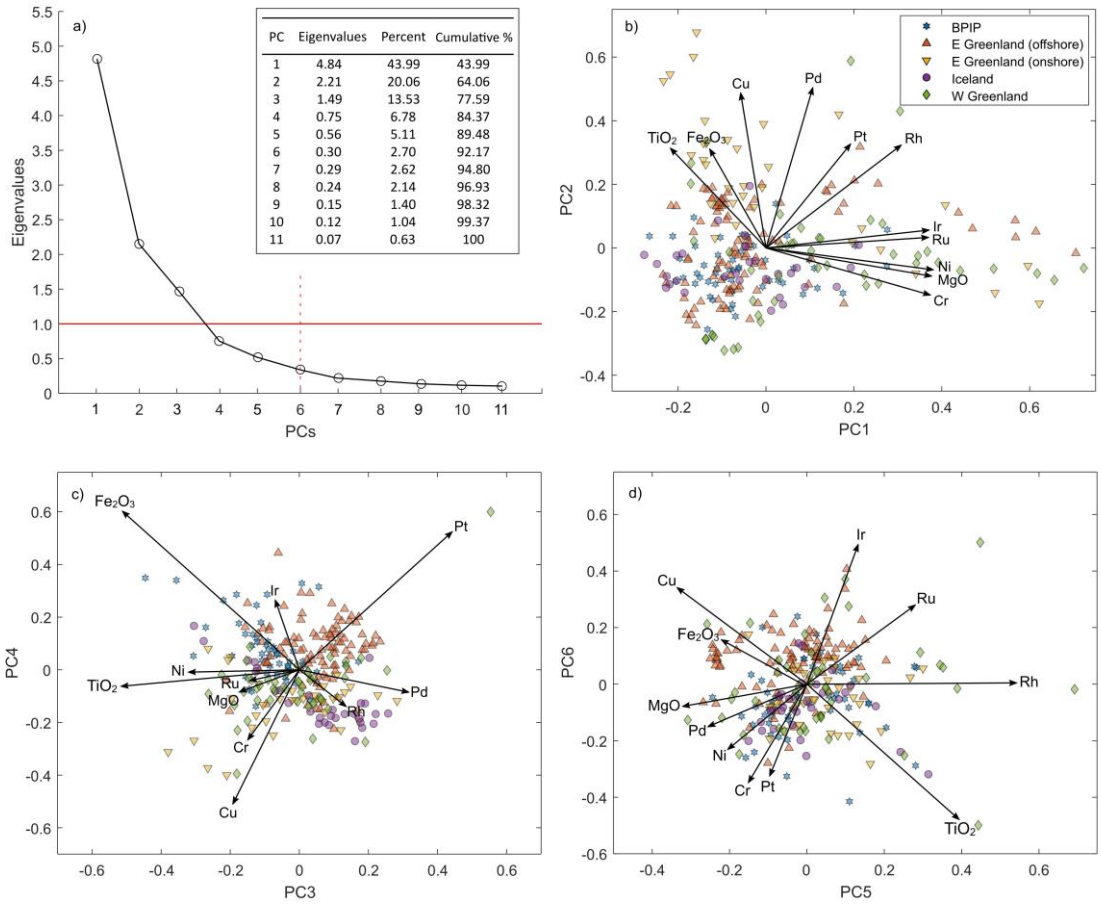

Figure 5.4 *– PCA for the NAIP data set. (a) Scree plot of eigenvalues for the eleven created PCs and corresponding cumulative percentages; (b) biplot for PC1 vs. PC2; (c) biplot for PC3 vs. PC4; and (d) biplot for PC5 vs. PC6, with variables (elements) plotted as vectors and samples plotted as points classified by their respective geographic grouping in all biplots.*

5.3.1.2. Embedding

A t-SNE analysis of the NAIP data set created using the z-scores of all eleven elements as input variables is displayed in Figure 5.5. The transformed data distribution is coloured by the individual elemental concentrations for each data point, giving an account of how each element contributes to the variability of the entire data set. The newly computed features, Embedding 1 and 2, arrange the data points in a roughly spherical shape with prominent protrusions on the top-left, top-right and bottom-middle of the distribution. Elements that exhibit clear bimodality through the embedding significantly contribute to the data set structure and corresponding low-dimensional shape (Horrocks et al., 2019). For example, high concentrations of MgO are found in the bottom of the embedding, and data points outside this zone have reduced MgO content comparatively. From this logic, the inverse relationship between MgO-Ni-Cr-Ir-Ru and TiO_2-Fe_2O_3-Cu-Pd trends from PCA (Figures 5.4b–d) is clear along the length of Embedding 2 in the form of opposed bimodal distributions. A smaller separation is also visible between Cu (top-left), TiO_2 (top-right) and Fe_2O_3 (top-spread) in the uppermost zone of the embedding. A third group of Pd, Pt and Rh expresses bimodality along Embedding 1, particularly Pd, with all three plotting highest values on the left of the embedding. This is in direct opposition to the major bimodality distribution shown in the other elements.

Extreme outlier values of Pt and Rh concentrations do not interfere with this trend. The ratio of Pt/Pd does not appear to have any distinctive trends in the embedding. As per their correlation in Figure 5.3, Pd and Cu are seen to have reasonable overlap in the embedding space. In addition to overall trends, t-SNE can isolate data set anomalies within the context of the data structure and attribute their segregated nature to single or multi-element concentrations. Sub-clusters can be seen to host distinctive concentrations pertaining to either the MgO or TiO_2-led trends from Figure 5.4, and high single element concentrations define individual outlier samples e.g., the segregated high-Ni (top-centre), high-Rh (bottom-right) and Pt (bottom-left) occurrences in the embedding space.

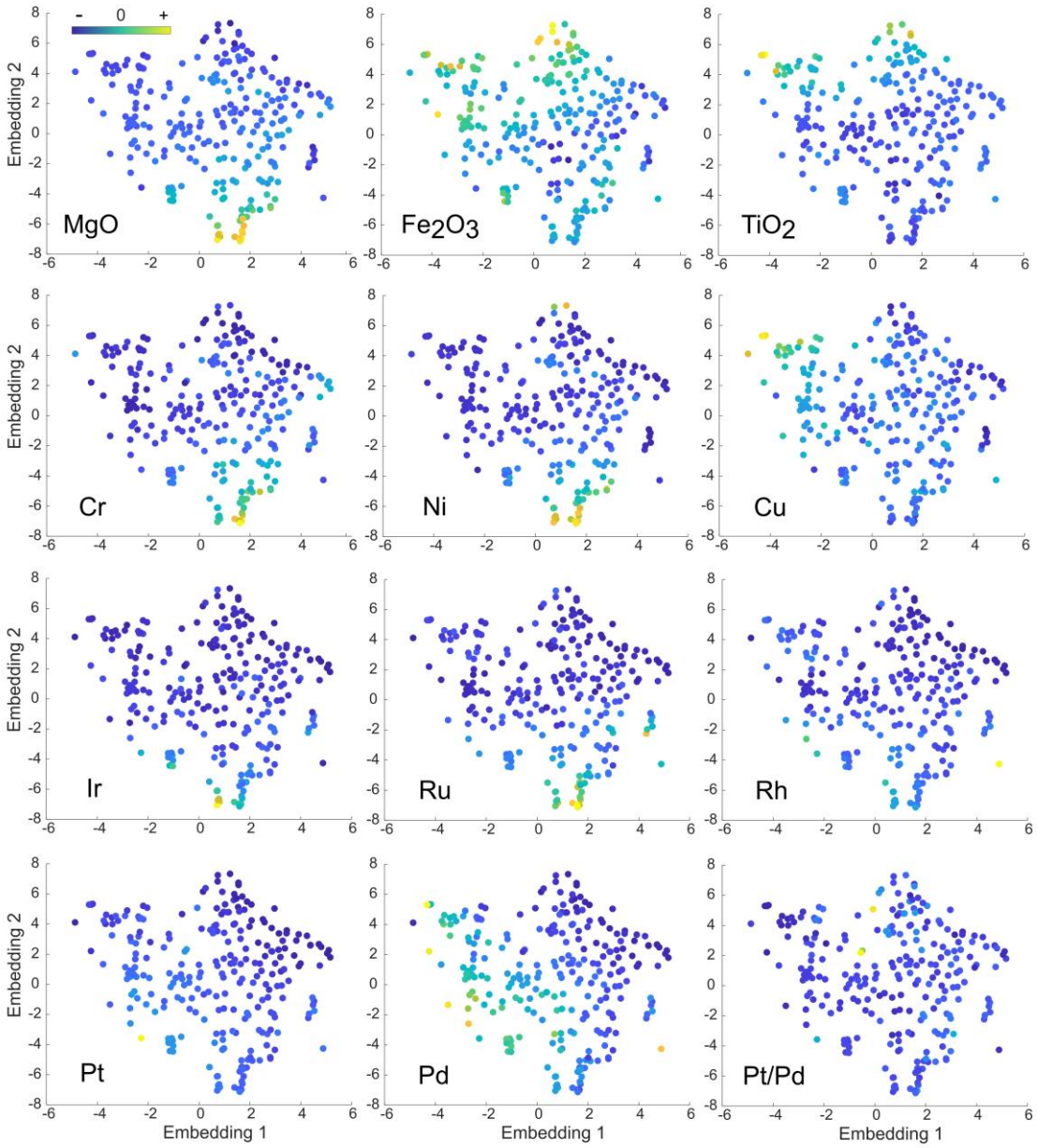

Figure 5.5 *– t-SNE plots based on eleven variables, with data points coloured by the relative values of a given constituent element for all eleven analysed variables and Pt/Pd. Dark blue represents the lowest values for a given variable and yellow represents the highest values. Note that Rh and Pt have significant outliers and otherwise less distinctive trends.*

5.3.2. MLA model selection

The NAIP data set was clustered using the *k*-means algorithm for *k*-values of 2, 3, 4 and 5, with the different variable arrays detailed in the methodology, including variable z-scores and PC1–6 (selected as per Figure 5.4a). Davies-Bouldin Indices (DBI), which account for cluster performance in all configurations,

are shown in Figure 5.6. A high DBI signifies that the density function of each defined cluster is larger, meaning more diffuse or looser clustering. In this instance, a low DBI is desirable, reflecting tighter, more well-defined clusters (Davies and Bouldin, 1979).

Models using *k*-values of 2, whilst consistently having some of the lowest DBI of the model set (< 1.40), appear too simplistic to describe the evolving geochemistry of the NAIP lavas, especially considering the number of groups defined by Hughes et al. (2015) were either 3 (Pt/Pd subdivisions) or 5 (geographic categories). After discounting $k = 2$ models due to their simplicity, and all models using z-scores of raw concentrations as variables due to their higher DBI, the parameter setup of $k = 3$ with PC1–6 as input variables is selected as the best model (highlighted by the black square in Figure 5.6). It is clear that in data sets with large variable numbers, using new features produced via dimensionality reduction is vital to help focus high-dimensional trends, recognise multivariate structures and create robust clustering models (Nguyen and Holmes, 2019). Figure 5.7 shows a comparison of clustering models using PC1–6 as variables and *k* ranging from 2 to 5. This is useful to demonstrate how high-dimensional clusters from different parameter set-ups relate in a bivariate space, in the case of Figure 5.7, PC1 against PC2. Surplus models are displayed in Appendix C1-7 and all clustering results compiled in Supplementary S5.4.

5.3.3. Clustering

The clusters created by the chosen *k*-means algorithm are referred to as Group 1 (red circles), Group 2 (blue squares) and Group 3 (yellow diamonds). It is convenient to display newly assigned multivariate cluster information in bivariate plots to determine the relative contributions each element's variability made to the overall cluster formation. Elements that are important to overall data structure will have easily identifiable and distinct clusters along the corresponding axes of a bivariate plot. Figure 5.8 displays MLA-clustered bivariate plots of elemental concentrations from the NAIP data set. Major element oxides MgO and TiO_2 cluster with a progressive negative trend (Figure 5.8a). By contrast, Fe_2O_3 does not exhibit a linear trend, with Groups 1 and 2 perhaps exhibiting slightly higher concentrations in a wider range than Group 3 (Figure 5.8b).

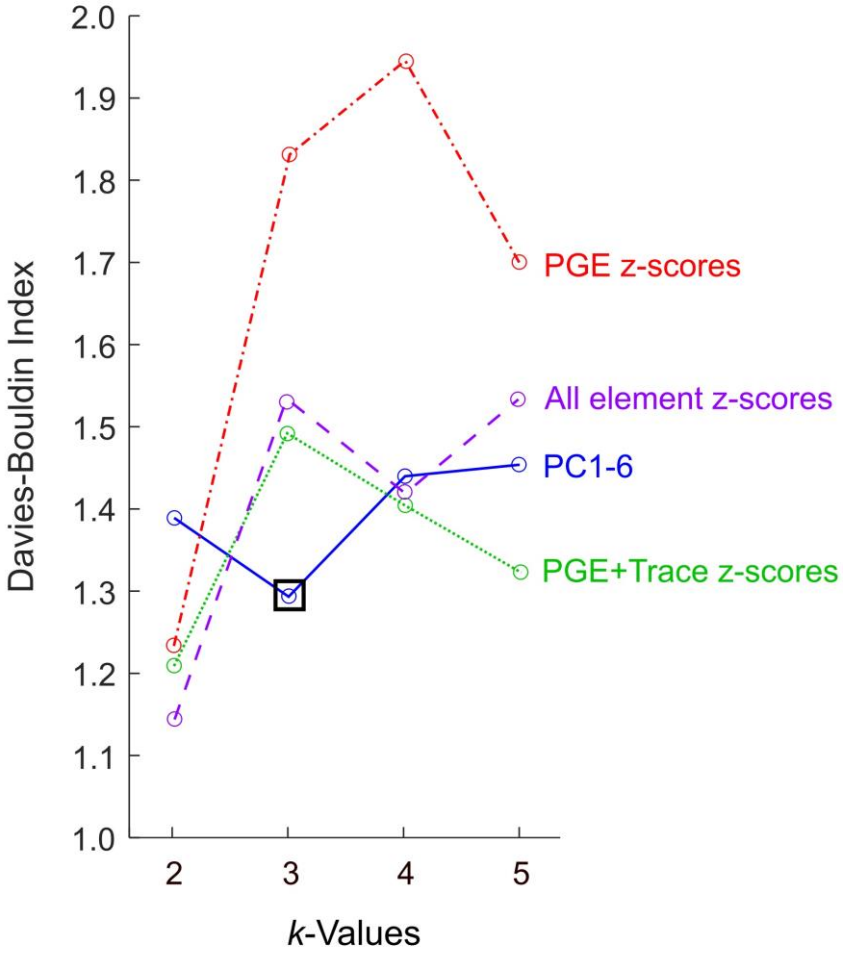

Figure 5.6 *– Davies-Bouldin Indices (DBI) for all parameter setups run for k-means clustering models, with the chosen model (k = 3, using PC1–6 as input variables) highlighted by the black square. By using PC1–6 as variables, the clusters formed are more efficient than using raw data in almost all cases.*

Trace elements Cr and Ni, and Ir, Ru and Rh from the PGE all cluster neatly in Figure 5.4b–f, with the highest concentrations of each belonging to Group 3 (corresponding to higher MgO and lower TiO_2); this again reflects their high correlation coefficients with each other in Figure 5.3. Copper does not cluster as distinctly as the other trace elements, but a slight negative relationship with Ni is visible, with the highest Cu concentrations in Group 1 and comparable low concentrations in Groups 2 and 3 (Figure 5.8c). The correlation matrix for the NAIP data set (Figure 5.3) accordingly describes Cu as lacking in strong affinity with any other elements other than TiO_2 and Pd. It appears that Group 2, the

smallest by sample number, exists as an intermediate cluster with no significant enrichments, whereas Groups 1 and 3 have enrichments in elements from opposing PCA and t-SNE trends (Figures 5.4b–d and 5.5) and act as geochemical end-members in the system. Overall, Group 1 is defined by higher concentrations of TiO_2, Fe_2O_3 and Cu, Group 2 is defined by background to very low concentrations for most elements and Group 3 is defined by higher concentrations of MgO, Ni, Cr, Ir Ru and Rh.

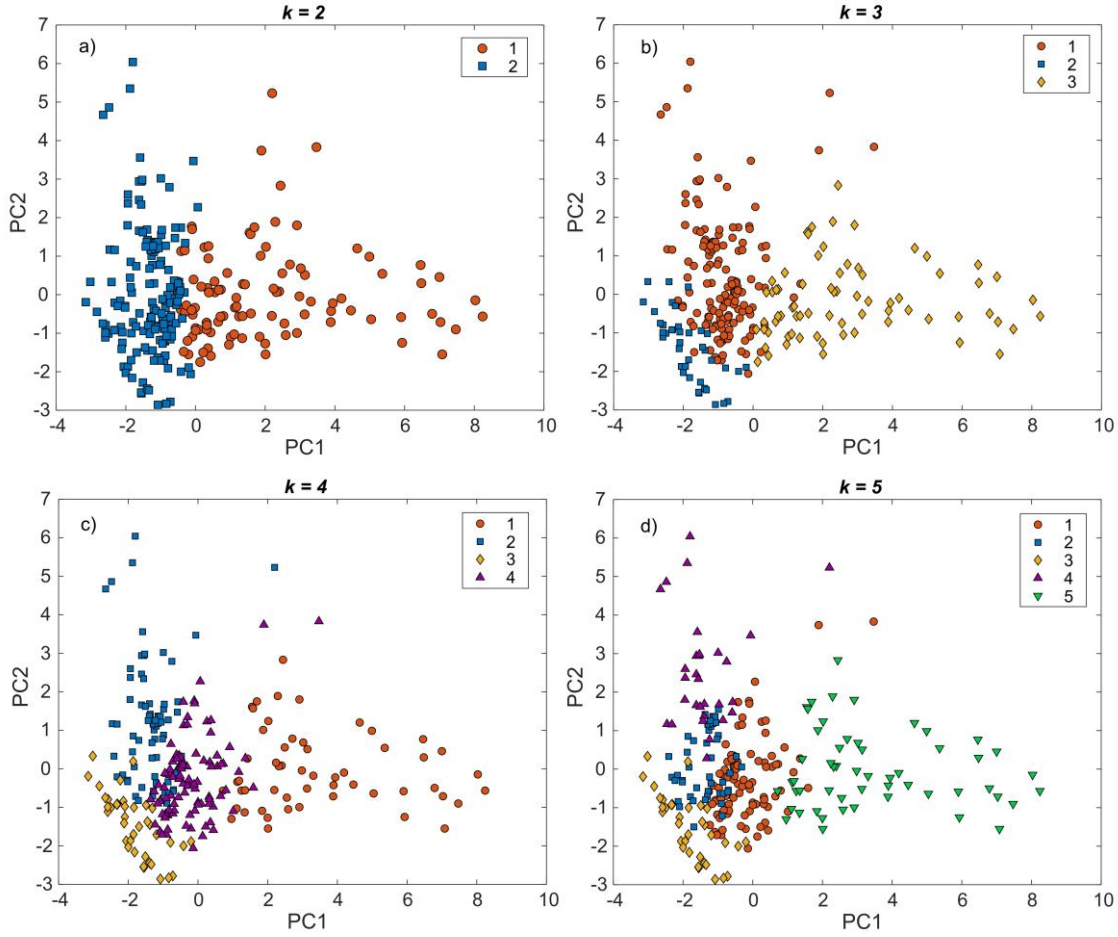

Figure 5.7 *– Selection of bivariate PC1 v PC2 plots displaying selected input parameter configurations for k-means clustering models. (a) k = 2, PC1–6 as variables; (b) k = 3, PC1–6 as variables; (c) k = 4, PC1–6 as variables; (d) k = 5, PC1–6 as variables. Cluster numbering is randomised by the algorithm and the group order is not relevant to interpretation.*

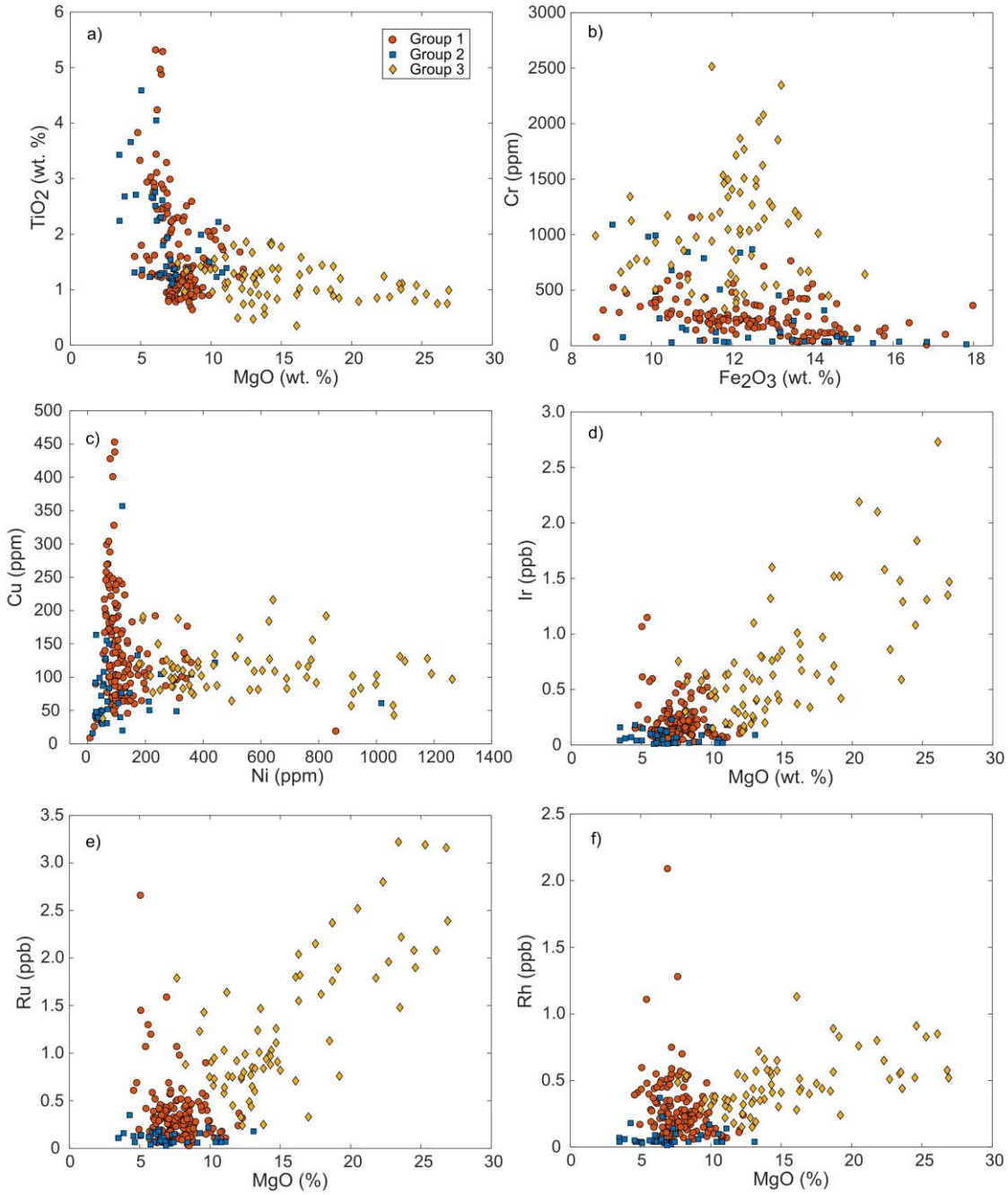

Figure 5.8 *– Bivariate geochemical plots of all NAIP data points, clustered by k-means clustering (k = 3, PC1–6 as variables in the clustering process). (a) MgO vs. TiO_2, (b) Fe_2O_3 vs. Cr, (c) Ni vs. Cu, (d) MgO vs. Ir, (e) MgO vs. Ru, (f) MgO vs. Rh.*

There are no distinct clustering trends in two particular variables – Pt and Pd. Figure 5.9a shows an MLA-clustered bivariate plot of Pt and Pd, and highlights the lack of definition in both variables. Group 2 appears to host the lowest concentrations for both elements, although all three groups share similar distribution of higher concentrations and clusters are indistinct. Figure 5.9b

illustrates a similar absence of trend in terms of Pt/Pd ratio as a function of Pd. Overall, the *k*-means model successfully clustered data in nine elements based on the chosen input parameters of *k* = 3 and PC1–6 as variables. The remaining two elements, Pt and Pd, present an interesting anomaly in the clustering process, and this would appear to be in agreement with the lack of strong correlation coefficients (Figure 5.3), unique PCA characters (Figure 5.4) and t-SNE concentration trends opposed to all other elements (Figure 5.5) for these two elements, with a weak to moderate relationship with Rh in some cases.

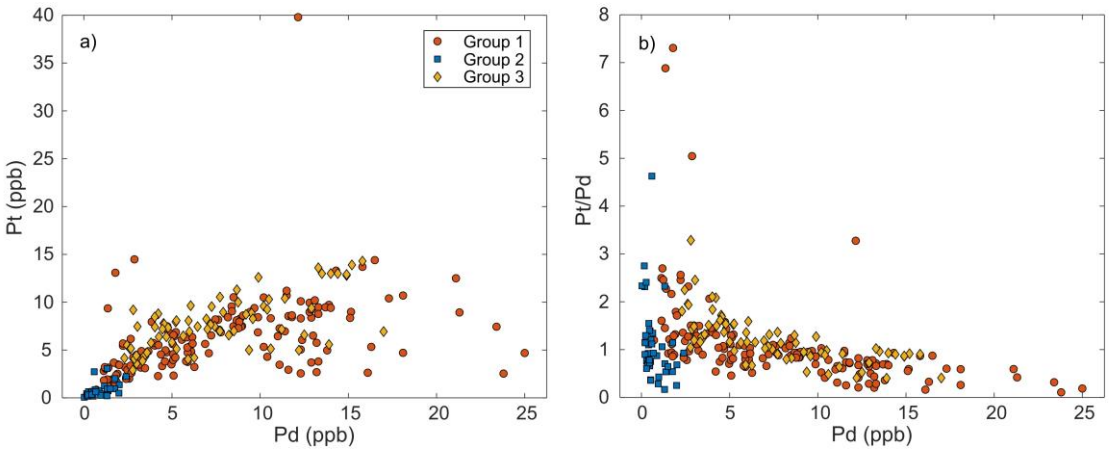

Figure 5.9 *– Bivariate geochemical plots of all NAIP data points, clustered by k-means Clustering (k = 3,PC1–6 as variables in the clustering process). (a) Pd vs. Pt, (b) Pd vs. Pt/Pd.*

5.3.4. Comparison to prior NAIP categories

A key check on the effectiveness of using the MLA-integrated workflow as a geochemical tool is comparing algorithm-based clustering to information already established by classical studies using discriminant plots, to identify similarities and differences in element behaviour. Figure 5.10 displays a histogram of the five geographic groups and their new equivalent cluster distribution based on the chosen *k*-means model. The Iceland group comprises similar proportions of Group 1, 2 and 3 samples (roughly a third of each). BPIP lavas are 51 % within Group 1, 24 % within Group 2 and 25 % within Group 3, making a roughly 2:1:1 split. East Greenland offshore and onshore lavas belong largely to the Group 1 end-member (71 % and 75 %, respectively); they differ in that the former contains small proportions of Group 2 and 3 and the latter is

completely devoid of Group 2 in the chosen clustering set-up. Finally, West Greenland contains the largest proportion of Group 3 samples (48 %) and the smallest proportion of Group 1 samples (29 %) in the region.

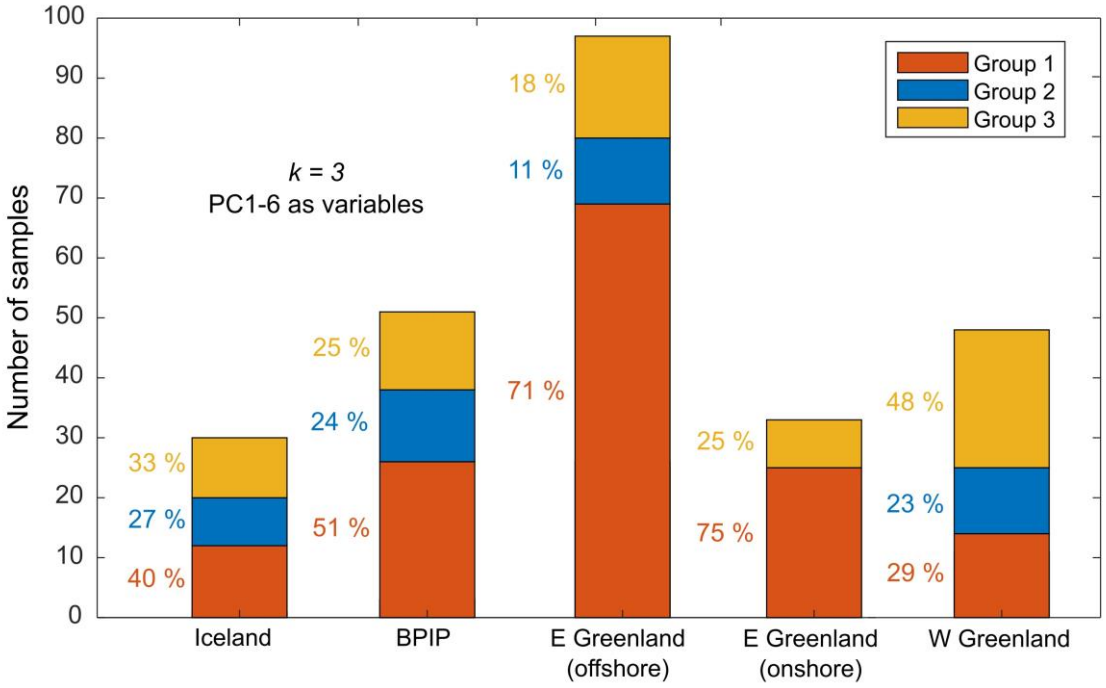

Figure 5.10 *– Histogram of MLA-based cluster distribution within each geographic category.*

A further effective visual comparison of the MLA workflow results can be achieved by overlaying data distributions in bivariate plots and t-SNE embeddings with new clusters and geographic categories. A selection of key bivariate PGE relationships is shown in Figure 5.11. Trends and anomalies in the newly clustered classifications both complement and differ from the NAIP geographic categories in a variety of manners.

As shown in Figure 5.11a, the average Pt/Pd ratios neatly described by geographic groupings (Figures 5.1a and 5.11b) by Hughes et al. (2015) do not form as clear a trend with the *k*-means clustering method, which echoes the lack of distinct clusters for those individual variables in Figure 5.9. A very slight decrease in average Pt/Pd is observed from Group 3 to 2 to 1, but this is on a much smaller degree than the trends in geographic categories. It should be noted that although the regression lines for Pt/Pd in East Greenland (onshore) lavas were not as distinct as other localities in the original study (Momme et al., 2002;

Hughes et al., 2015), the basic age-progressive reduction in average Pt/Pd does persist throughout, using the data available.

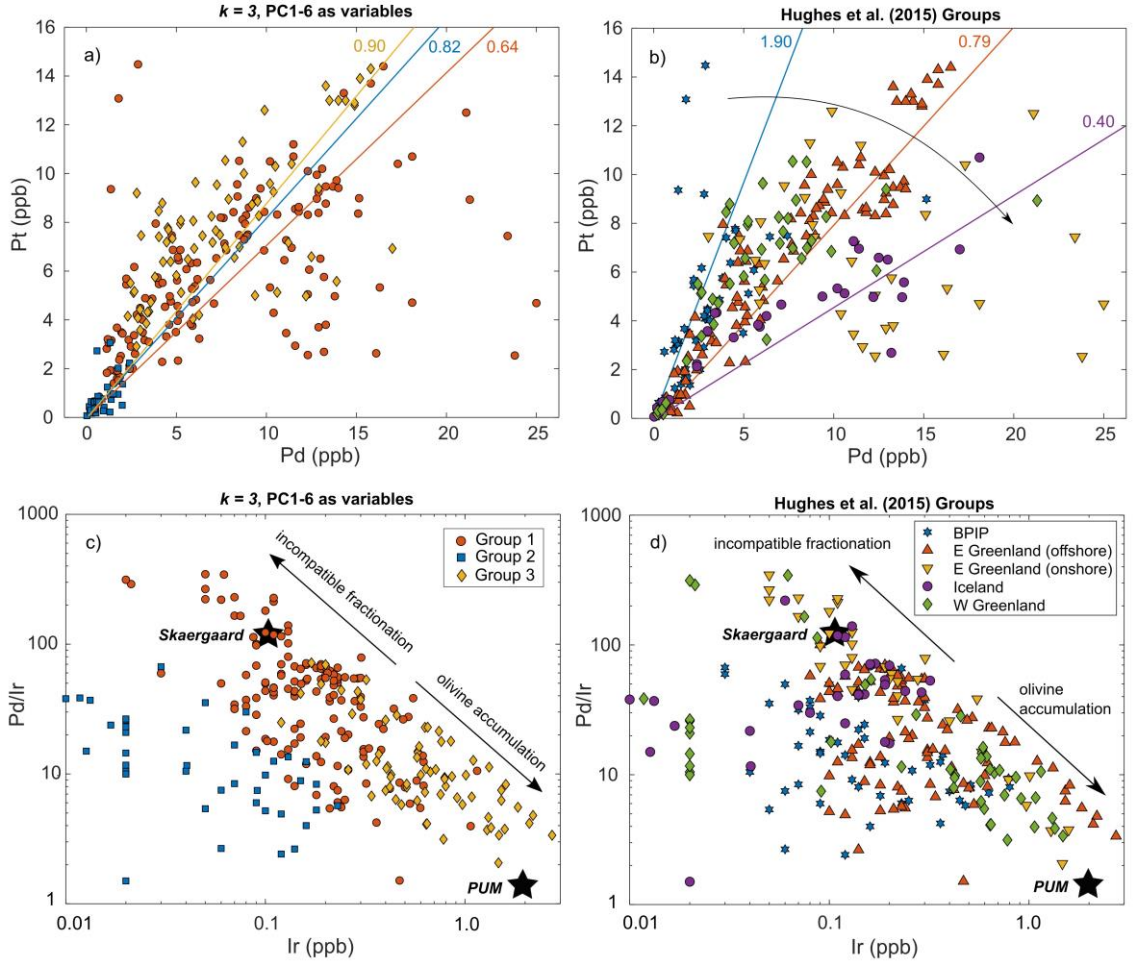

Figure 5.11 *– Comparison of MLA-based (clustering) groupings and geographic location categories from Hughes et al. (2015). (a) MLA-based Pd v Pt with average Pt/Pd for each group; (b) geographic-based Pd v Pt with average Pt/Pd lines for major trends (with values for W Greenland/BPIP in blue, E Greenland (onshore and offshore) in orange and Iceland in purple); (c) MLA-based Ir v Pd/Ir; (d) geographic-based Ir v Pd/Ir. Sub-plots (c) and (d) show trends for olivine accumulation and incompatible fractionation in the system, based on Hughes et al. (2015). Skaergaard (Vincent and Smales, 1956) and Primitive Upper Mantle (PUM) (McDonough and Sun, 1995) estimates are given for reference.*

In Figures 5.11c-d, plots of Ir vs. Pd/Ir ratio convey trends typical of olivine accumulation and incompatible element fractionation as controls on PGE distribution within magmas. Group 1 plots neatly along the incompatible

fractionation trend and Group 3 plots with olivine accumulation. Group 2 does not appear to have a strong affinity with either trend, plotting in low-Ir regions far from the major fractionation population (Figure 5.11c). In Figure 5.11d, West Greenlandic lava Pd/Ir ratios are attributed mainly to olivine accumulation (and thus, correlated with Group 3 as per Figure 5.10). East Greenlandic (onshore) and, to a lesser extent, Icelandic samples correspond well with Group 1 being driven by the fractionation of elements incompatible in modal silicate minerals (e.g., Cu and Pd as per; Naldrett, 2004; Keays and Lightfoot, 2007). The geochemistry of the East Greenlandic (offshore) lavas, BPIP lavas and a portion of the Icelandic lavas do not correspond well with either control, with a comparable distribution to Group 2 (Figure 5.11c) off the main trend axis – these locations also have the highest proportion of points designated to Group 2 in Figure 5.10.

Figure 5.12 displays the embedding from Figure 5.5 created using t-SNE, with all data points classified by (a) *k*-means clustering using the selected model and (b) geographic groupings, summarising how the different clusters interact with the broad structure of the data set. As detailed in van der Maaten and Hinton (2008), t-SNE retains important multivariate data information in a bivariate plot. Groups 1, 2 and 3 plot in distinct regions within the newly created embedding in Figure 5.12a, with Group 1 distributed mainly in the centre and left, Group 2 in the upper right and Group 3 in the bottom of the distribution. One notable outlier of Group 2 is located in the far right of the embedding. The split between Group 3 and the other two clusters is similar to their relationships in Figure 5.8, where Group 3 often plots distinctly from all other points. Group 1 has the largest spread in variability, physically taking up the most space in the embedding. In contrast, Groups 2 and 3 have much more concentrated distributions in the embedding, which likely relate to their more consistent individual element concentrations throughout Figure 5.8. Group 3 generally acts as the ‘anomalous’ cluster of highest MgO, Ni, Cr, Ir and Ru, and lowest Fe_2O_3, TiO_2 and Cu concentrations (Figures 5.8a–f), and these enrichments and depletions evidently create a distinctive character for each group's chemistry in Figure 5.12a in strong agreement with individual element trends in Figure 5.5. Although less distinct, Group 1 shares a sector of the embedding with higher concentrations of Fe_2O_3, TiO_2 and Cu (Figure 5.5).

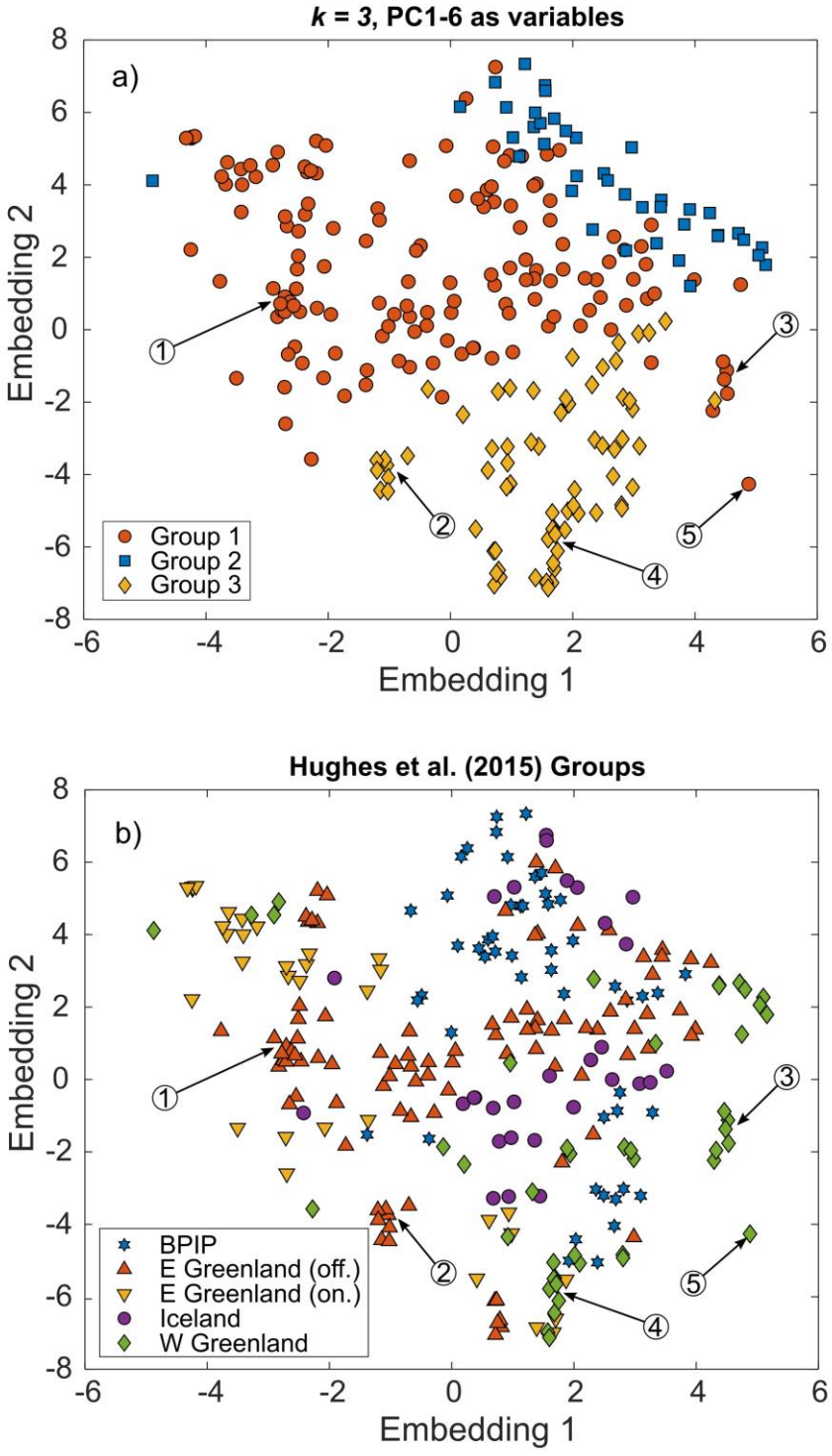

Figure 5.12 *– t-SNE plots from Figure 5.5 with data points assigned to (a) k-means clustering groups using k = 3 and PC1–6 as input variables; (b) geographic localities. 1 – Tight sub-cluster dominated by Group 1 and East Greenland (off.) (n = 10). 2 – Sub-cluster of Group 3 and East Greenland (off.) (n = 8). 3 – Sub-cluster of Group 1 and West Greenland (n = 6). 4 – Sub-cluster of Group 3 and West Greenland (n = 13). 5 – Single point defined by Group 1, East Green- land (off.) and high Rh concentration in Figure 5.5 (n = 1).*

In general, the t-SNE embedding is not clustered as clearly when classified by geographic location in Figure 5.12b, but structures are still observable. The majority of West Greenlandic lavas (bottom-right) have multi-elemental compositions physically opposed to onshore and offshore East Greenlandic lavas (centre and top-left) in the embedding. Icelandic lavas are concentrated in the boundary between West Greenland and East Greenland (offshore) in the centre of the embedding, and the bulk of BPIP samples appear in the top of the embedding. A large proportion of West Greenland lavas and around half of Icelandic lavas plot in the section of the embedding strongly associated with high MgO, Ni, Cr, Ir, Ru and Rh in Figure 5.5 and Group 3 in Figure 5.12a (which agrees with large proportions of their lavas belonging to Group 3 in Figure 5.10). East Greenland (offshore and onshore) is associated with high Fe_2O_3, TiO_2 and Cu (Figure 5.5) and Group 1 (Figure 5.12), as per Figure 5.10 (< 70% Group 1 lavas). BPIP appears evenly spread between prior identified regions in the embedding. Individual sub-clusters forming distinct populations outside and within the main data structure and can be observed in Figure 5.12a and 5.12b. These were defined subjectively as breaks from the otherwise continuous cumulative variability map and are always dominated by a particular high concentration in Figure 5.5, a particular Group in Figure 5.12a or a particular locality in Figure 5.12b. Selected prominent sub-clusters are indicated by numbered annotations.

A series of summary box-and-whisker plots with elemental concentrations for each MLA-based cluster is shown in Figure 5.13 to summarise their typical geochemical signatures. Even in these simple plots, the lack of significant inter-cluster Pt and Pd variations are clear when compared to the other elements, which normally see reasonable shifts in quartile ranges between Groups 1, 2 and 3.

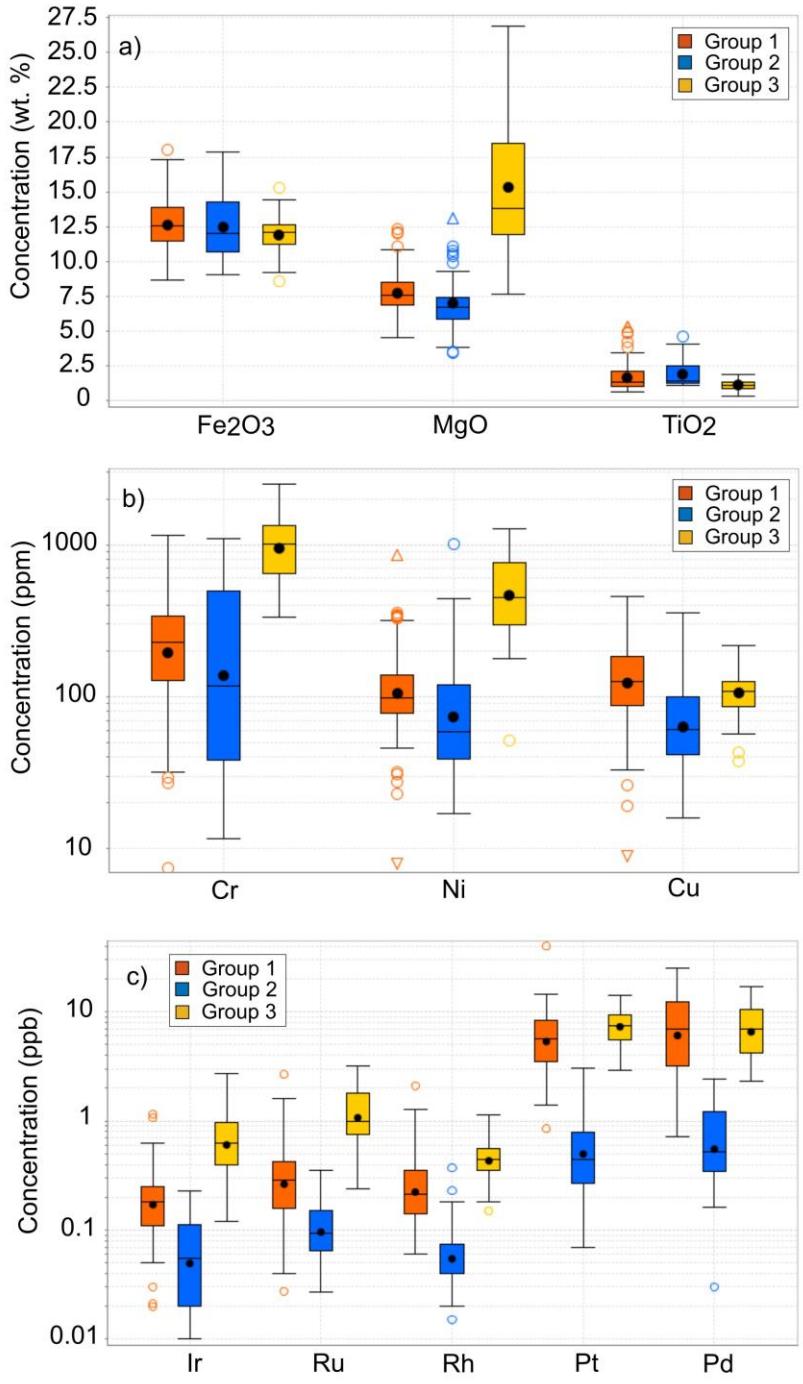

Figure 5.13 *– Box-and-whisker plots for all elemental concentrations in each MLA-based cluster (k = 3, PC1–6 as variables). Displays interquartile ranges (within box), minimum and maximum values excluding outliers (whiskers) and outliers (circles for lower outliers, triangles for extreme outliers) for: (a) major oxides; (b) trace elements; and (c) PGE.*

5.4. Discussion

5.4.1 Performance of MLA-based geochemical workflow

Utilising data science techniques to explore the NAIP data set has allowed us to analyse and display data in a variety of ways not attainable by a classic interrogation of geochemistry. Not only does establishing a MLA-integrated workflow save processing time and provide a framework easily applied to other data sets, it reveals unique information about how elemental concentrations vary alongside each other. The correlation matrix (Figure 5.3) delineates which elements varied with respect to each other, expanded upon by PCA in Figure 5.4. At least two multi-elemental geochemical end-member associations exist within the broad data structure – a high MgO group, and a high-TiO_2 group. t-SNE displayed complete chemical variability information about NAIP lavas across eleven elements, while simultaneously identifying anomalous multi-element sub-clusters distinct from the main population and attributed to a particular grouping. The technique further reduced dimensionality and independently replicates the MgO- and TiO_2-led end-members identified by PCA in the context of data structure. In both PCA and t-SNE dimensionality reduction results, Rh, Pt and Pd are highlighted as not strongly conforming to either of the major end-member groups. Sub-clusters identified by t-SNE can be investigated in isolation and are often attributed to individual sample localities; it is likely that these distinct masses represent a unique chemistry still conforming to the overall algorithm-based clusters but with individual elemental concentrations outside the norm. This finding agrees with Figure 5.5, in which sub-clusters can often be explained by particularly high concentrations of a single variable.

Using machine learning to cluster the data set beyond arbitrary single element concentrations further explores these multi-elemental end-members and classifies data points broadly in line with findings from dimensionality reduction. The intricacies of a high-dimensional data set can be resolved and presented in a logical manner, with the three techniques complementing and enhancing the findings from other steps. Multi-element patterns can be observed through all three techniques (Figures 5.4, 5.5 and 5.8), PC features were directly used in the best-fit clustering model (Figures 5.6–5.9), and t-SNE was used to visualise overall differences in MLA-based classifications and geographic categories from

other steps in the workflow (Figure 5.12). Whilst the NAIP variable set of eleven elements is certainly large enough to merit exploration using an MLA approach and the applicability of dimensionality reduction prior to clustering is reflected in Figure 5.6, this would become increasingly relevant as a data set integrates more variables. By condensing large-scale elemental behaviour into fewer features whilst retaining variability information, the workflow makes geochemical interrogation significantly more manageable.

Despite the success of the workflow results, some caveats must be acknowledged when utilising clustering algorithms and dimensionality reduction for geochemistry. The selection of input parameters for most machine learning techniques is an analyst-dependent pursuit – *k*-means clustering cannot optimise parameters and model selection requires a set of considerations unique to the job the algorithm will be applied to. Furthermore, while clustering data points based on a large set of elements can be viewed as objective by encompassing all variable concentrations, elements that do not conform to the overall variance of the data set can impede perceived algorithm success. Similarly, if certain input parameter set-ups are chosen (e.g., with inefficient *k*-value and t-SNE input parameters, non-standardised data or incomplete variable sets) any of the models used in this study may be unsuccessful or unrepresentative. However, as long as considerations are made regarding the set-up of the methodology, a MLA approach does not become a 'black box' process, and offers new prospects in understanding a data set. While data science provides important and unique information about a data set, a reasonable knowledge of the subject being investigated is essential to aid in the interpretation of results – a careful balance must be maintained between sensible user input to drive MLA success and background geochemical understanding of the project without bias. The following discussion takes findings from the NAIP workflow – namely the three multi-element clusters and the seemingly isolated behaviour of certain PGE – and contextualises them by relating data anomalies and trends to geochemical processes.

5.4.2. MLA mapped on to geochemical indicators for magmatic differentiation in the NAIP

Further to establishing a new approach for the analysis of regional geochemical data sets, a major feature of this study concerns the behaviour of

groups of elements in relation to the data structure. In PCA, t-SNE and *k*-means clustering methods, distinct variability trends are exhibited by most of the elements included in MLA-based analyses. Magnesium (as MgO), Cr, Ni, Ir and Ru are strongly controlled by PC1 (Figure 5.4b) and Fe_2O_3, TiO_2 and Cu are strongly controlled by PC2 (Figure 5.4c); the two sets of elements also replicate similar trends in t-SNE embeddings in Figure 5.5 through a different mathematical process. Platinum, Pd and Rh exhibit a mixed influence of PC1–2, and PC3 (and to an extent PC4) further isolates them from every other element. The lower-influence PC5 and PC6 separate the previous elemental groups (Figure 5.4d), although their cumulative importance to data variability is much lower (Figure 5.4a). These multi-element patterns are broadly reflected in clustering in Figures 5.7–5.9.

The concentration of an element in a magma reflects the combined effect of several differentiation processes and the geochemical behaviour of that element. For example, Ni and Cr are compatible in olivine, and clinopyroxene and spinel-group minerals, respectively, and therefore these elements correlate well with MgO, TiO_2 and Fe (in this data set expressed as Fe_2O_3) in mafic lavas (Figure 5.8). In comparison, chalcophile elements, such as Cu and especially the Pd-group PGE (PPGE; Rh, Pt, Pd), are controlled almost exclusively by sulphides, whether as sulphide liquid or base metal sulphides (BMS) and PGM (e.g., Naldrett, 2004; Keays and Lightfoot, 2007; Lorand and Luguet, 2016 and references therein). Iridium-group PGE (IPGE; Os, Ir and Ru) although chalcophile, are also compatible in spinel (especially chromite) and olivine (Barnes and Picard, 1993; Pitcher et al., 2009). With higher degrees of partial melting, BMS will eventually be exhausted in the mantle source, and spinel and olivine will begin to melt, therefore increasing the abundance of IPGE broadly in correlation with increasing MgO, Ni, and Cr in the silicate magma produced. During ascent through the lithosphere, this magma will undergo magmatic differentiation via fractional crystallisation of olivine, pyroxene, spinel-group minerals and other silicate and oxide mineral phases, thereby further modifying the concentration of MgO, Ni, Cr and the IPGE in combination with other major and trace element proxies for fractionation and contamination.

If PCs can loosely be viewed as proxies for processes controlling element variability (e.g., Steiner et al., 2019), in this case as a result of magmatic

differentiation, we can begin to interpret the elemental correlations consistently displayed through dimensionality reduction as constituents to overall magma geochemical variability. PC1 (43.99 % of data set variability) is likely to represent the fractionation of olivine from the parental magma, given the close correlation with olivine-compatible MgO, Ni, Cr and the IPGE in Figure 5.4b. PC2 (20.06 % of data set variability), which primarily influences TiO_2, Fe_2O_3, Cu and Pd concentrations (Figure 5.4b), could represent a more complicated combination of silicate, oxide and sulphide fractionation controls within parental magmas. For example, as mafic magmas crystallise silicate minerals, the chalcophile elements (e.g., Cu and Pd) will become increasingly concentrated in the residual melt until an immiscible sulphide liquid is exsolved (following sulphide saturation). At this point, chalcophiles will partition into the sulphide liquid, depleting these elements in the remaining silicate melt (Naldrett, 2011 and references therein; Ripley and Li, 2013). Meanwhile, the concentration of Ti in the magma will be affected by the fractional crystallisation of silicate minerals (incorporating minor amounts of Ti; e.g., in clinopyroxene) and oxide minerals (such as the spinel-group) depleting the residual liquid composition vs potential addition of Ti to the magma via crustal contamination.

In the context of the NAIP, the three MLA-based geochemical end-members established from Figures 5.7–5.9 may be framed in terms of the evolving plume environment across this region. Geographic categories from Hughes et al. (2015) can be seen to ascribe to different dominant MLA-based end-members in Figures 5.10–5.12 (elemental concentrations are summarised in Table 5.2). In Figure 5.10, West Greenland has the highest proportion of Group 3 lavas of all localities (48 %); East Greenland (onshore and offshore) has dominant Group 1 affiliations (> 70 %); BPIP also has a prominent Group 1 affiliation (51 %); and Iceland has a more equal split of each cluster.

Group 3 is the end-member most easily characterised within the NAIP setting given its distinctive strong association with the dominant PC1 and corresponding enrichment in olivine-compatible elements MgO, Ni, Cr and the IPGE (Figures 5.4b, 5.5 and 5.12a). With MgO concentrations mainly between 15 wt.% and 25 wt.% (Figure 5.8a), we suggest that Group 3 could represent higher degree partial melts of a mantle source, sequestering compatible elements like Ni and IPGE into the magma, followed by subsequent fractionation and

accumulation of olivine (Figure 5.11c). A sensible petrological NAIP association with this end-member would be the picrites temporally related to early NAIP lavas in West Greenlandic plateaus (e.g., the uncontaminated members of the Vaîgat Formation; Lightfoot et al., 1997), that are interpreted to have formed from magmas produced by up to 25 % partial melting (Larsen and Pedersen, 2000; Andersen et al., 2002) – Figures 5.10 and 5.12. Vaîgat tholeiites record low $^{87}Sr/^{86}Sr$, high εNd and high γOs values consistent with asthenospheric plume melts with minimal SCLM interaction (Larsen et al., 2003).

Table 5.2 *– Summary of elemental concentrations in each MLA-based group (presented as a range from lower to upper quartile as per Figure 5.13, excluding outliers).*

Interquartile Ranges	Group 1	Group 2	Group 3
MgO (wt. %)	6.9-8.5	5.9-7.4	11.9-18.5
TiO_2 (wt. %)	1.0-2.1	1.3-2.5	0.9-1.4
Fe_2O_3 (wt. %)	11.4-13.9	10.7-14.3	11.2-12.7
Cr (ppm)	128-337	38-495	646-1,340
Ni (ppm)	78-138	39-120	296-763
Cu (ppm)	87-185	42-100	86-126
Ir (ppb)	0.11-0.25	0.02-0.11	0.40-0.97
Ru (ppb)	0.16-0.42	0.07-0.15	0.75-1.79
Rh (ppb)	0.14-0.35	0.04-0.07	0.35-0.56
Pt (ppb)	3.49-8.40	0.27-0.78	5.51-9.39
Pd (ppb)	3.20-12.19	0.35-1.20	4.22-17.0

Group 1 is primarily characterised by concentrations of MgO < 8.5 wt.% and TiO2 ~ 2.0–2.5 wt.%, in addition to up to five times enrichment in Cu compared to other groups (Figures 5.8c, 5.13 and Table 5.2), as expressed by PC2 (Figure 5.4b). Figure 5.11c appears to suggest that the fractionation of elements incompatible in certain silicate minerals controls this group. The concentration of Cu will increase in fractionated magmas in the absence of a sulphide phase (Holwell et al., 2012 and references therein), and combined with earlier fractional crystallisation of olivine (or a similar mineral in which Ti was incompatible), TiO_2 would be elevated in the Group 1 component. In plume environments, higher TiO_2 concentrations are also thought to indicate magma erupting through thicker lithosphere and SCLM, which correlates with longer residence time, more differentiated/evolved compositions and increased

incorporation of high field strength and lithophile elements from crustal sources (e.g., Arndt et al., 1993; Gibson et al., 1995). We envisage the high-Ti basalts of East Greenland (such as those in Kangertittivaq) could represent the product of this end-member as a more contaminated or differentiated melt (Tegner et al., 1998), tying with Group 1 prominence in both East Greenland categories from Hughes et al. (2015). Lavas from East Greenland have been noted to have high $^{87}Sr/^{86}Sr$ and low εNd, often cited as an indication of lithospheric contamination (Kent and Fitton, 2000). However, it must be considered that due to consistency of data with PGE geochemistry available to this study, we deal with eleven elements commonly used to document Ni-Cu-PGE mineralisation and mafic-ultramafic magmatic systems; the data set does not include alkali, lithophile or rare earth element concentrations. While TiO_2 is often a good initial indicator of mafic magma contamination, interrogating a wider palette of lithophile elements could enhance clustering and interpretations. Further testing on a larger element suite is necessary to confirm the link between Group 1, TiO_2 and crustal contamination in combination with silicate-incompatible element fractionation.

Group 2, the smallest group by sample number, does not exhibit the enrichments captured by Groups 1 and 3, and almost always has the lowest range of concentrations for all variables (Figure 5.13 and Table 2). As the intermediate end-member, it can be viewed in one of two ways – that it represents a geochemically depleted source (although this is difficult to test without a wider elemental suite) or, more likely, that it is a mixed source with no single dominant geochemical control. If Groups 1 and 3 represent the end-members for higher amounts of incompatible fractionation and higher degrees of olivine accumulation and/or partial melting in the NAIP asthenosphere, respectively, Group 2 could simply represent the absence of strong multi-element geochemical contributions from these factors. It could also represent a different higher-Fe_2O_3 (i.e., previously melted) mantle source component (as per Korenaga and Kelemen, 2000). This end-member may relate to the North Atlantic End-Member (NAEM) proposed by Ellam and Stuart (2000), a ubiquitous ‘background’ component in NAIP melts defined by its distinctive Pb-isotopic signature through all NAIP lavas. It is possible that this end-member is derived mainly from depleted upper mantle material, which couples well with our multi-element assessment of the group.

An interesting feature presented by the MLA workflow is that categories of a similar age in the NAIP (and by extension belonging to a similar geodynamic setting) do not necessarily share the same high-dimensional data interpretation. The BPIP category shares more in common in terms of multi-element variability with later lavas in East Greenland or Iceland than it does with West Greenland despite being the same age (Figure 5.1b). We would expect that BPIP lavas would share (i) a similar degree of partial melting and (ii) similar potential for crustal contamination to Greenlandic lavas, given the comparable geodynamics at this point in NAIP development (pre-rift continental flood basalts; Figure 5.1b). Isotope data for both localities confirm their inherent link to the plume source (Saunders et al., 1997), so the discrepancy in cluster distribution must be associated with differences in the high-dimensional data structure as per their distinct positioning within t-SNE plots in Figures 5.12a-b. We suggest that, given BPIP is not defined by the absence of Groups 1 or 3 but simply reduced proportions of them, there are asymmetrical localised variations in magma sources on either side of the sampled hotspot, similar to other localities like the Tristan plume in the southern Atlantic (e.g., Peate, 1997; Hoernle et al., 2015; Rämö et al., 2016). In summary, the MLA end-members demonstrate that there are a combination of magmatic differentiation processes taking place in the NAIP system, and that the net effect of those processes has been to produce an array of lava compositions that fall largely into three categories in multi-dimensional (multi-element) space.

5.4.3. Platinum and palladium: impacts on metal basket

The most prominent and significant finding from our study, the unique behaviour of specific PGE within the NAIP high-dimensional data structure, demonstrates the utility of the MLA workflow for exploring magmatic provinces from a ‘mineral systems’ perspective (e.g., McCuaig et al., 2010). Using a holistic approach to metallogenic systems, we can examine regional fertility on different scales and begin to understand the metal basket available to intraplate magmas.

It should be noted that Rh appears to fulfil a chemically intermediate role between IPGE and PPGE, appearing between the two populations in Figure 5.4b and 5.4c; Rh also shows more distinct clustering in Figure 5.8f. The mineralogical and chemical division of the IPGE and Rh from Pt and Pd is potentially reflected in their separate contribution to NAIP data set variability - Figures 5.4b–d

consistently separates the two groups in terms of dominant PC influence. Controls on Pt and Pd concentrations (particularly Pt) in NAIP lavas cannot be described as succinctly as the other nine elements, i.e., via Groups 1 to 3 and their collective geochemical significance, and it is likely that instead of a major dominant control linked to magmatic differentiation (e.g., PC1 or PC2) Pt and Pd are controlled by smaller-scale processes that affect them exclusively. The workflow is able to effectively work with major data trends while simultaneously identifying more subtle features extrinsic to these dominant multi-element interpretations, which we can interrogate further in the framework of low-level or localised geochemical controls within our system.

Whilst PC1–2 have a combined contribution to Pt and Pd variability between the Group 1 and 3 end-members, PC3–4 (which account for ~ 20% of data set variability; Figure 5.4a) have a unique influence on these two elements, far from the neat vector trends in the featured bivariate plots. Hence, the controls on Pt and Pd concentrations appear to be more complex and cryptic than other modelled elements in PCA (Figure 5.4b–d). This is further evidenced by the digression from significant patterns in the subsequent stages of the workflow - firstly in the embedding created via t-SNE, which shows Pt and Pd variability contradicting the major bimodal trends established by the other elements (Figure 5.5); and secondly in *k*-means clustering in all attempted model set-ups, which fails to capture distinct populations in these two variables (Figure 5.9a). Consistently high Pt/Pd signatures are found in BPIP and West Greenland lavas (Hughes et al., 2015), yet these two localities exhibit different multi-element variability trends in the rest of the MLA results, clearly indicating that the geographic Pt/Pd trend is more nuanced than other grouped elements captured within the data structure (as in Figure 5.5).

Platinum is visibly separated in Figure 5.4c from all other elements (even Pd and Rh) implying that whatever control PC3–4 represents, Pt is the element chiefly affected. In comparison, Pd, while lacking affinity for multi-element classification models, does correlate moderately with Cu (Figure 5.3) likely on account of similarities in the mineralogical controls on their fractionation (Barnes et al., 1985). Together with the t-SNE embedding (Figure 5.5) and clusters outside the dominant multi-element categories (Figures 5.8 and 5.9), the independent variation of Pt appears to be a small but significant control.

As illustrated, multi-element geochemistry can vary locally as a function of the components available to the melting environment (Figure 5.10). For example, the Hebridean Basin in western Scotland could provide large amounts of sedimentary material via contamination during magma ascent, different from those available to magmas ascending through the Greenlandic lithosphere. These mid- to shallow-crustal contaminants provide effective localised signatures, changing the resulting geochemistry of melts and potentially their metal basket (Andersen et al., 2002), which is of particular importance to our work in the form of PGE prospectivity. In the absence of a full set of major, trace and precious element data for all localities, we can use metallogenic studies of the region to inform our assessment of Pt and Pd behaviour, specifically addressing the independent roles of the elements in high-dimensional space as resolved by MLA and the apparent localised controls on their enrichment. The 'nugget effect' of discontinuous geological occurrence (e.g., Dominy et al., 2003) is common for metals with complex geochemical and physical partitioning behaviour, such as Au, base metals and the PGE, emphasising the importance of recognising spatial and temporal variations in magma enrichment detached from major element oxides like MgO, Fe_2O_3 and TiO_2. Gold has been seen to vary locally in lavas from Iceland and its adjoining Reykjanes Ridge, in relation to sulphide saturation conditions and differing mantle sources of the plume-derived melts, rather than as a direct function of the degree of partial melting (Webber et al., 2013). Webber et al. (2013) therefore illustrate the impact of source heterogeneity in regional metal basket variation and metallogenesis in a manner analogous to magma isotopic signatures transgressing petrological classifications. Additionally, Au, Co, Cu and the PGE amongst other elements have been speculated to be locally enriched via metasomatism into the lithospheric mantle (e.g., Mitchell and Keays, 1981; Tassara et al., 2017). Metal enrichment of the SCLM through subduction-related volatile and fluid transportation is widely documented, and Pt, Pd and Au are particularly thought to be mobilised in these metasomatic environments (e.g., Hughes et al., 2017; Tassara et al., 2017; Holwell et al., 2019; Choi et al., 2020). We envisage that metasomatism (or similar hydro-magmatic processes) could have resulted in the 'pre-conditioning' of the SCLM above the proto-Icelandic plume, leading to its heterogeneous enrichment in Pt and a shift in local metal basket. Such controls evidently do not map onto our three MLA-based multi-

element end-members, reinforcing the potential localised nature of high concentrations within the broader system.

The complexities of localised PGE behaviour and partitioning during partial melting of the mantle has been studied experimentally and empirically (e.g., Keays, 1982; Hamlyn and Keays, 1986; Peach et al., 1990; Rehkämper et al., 1997; Lorand et al., 1999; Ballhaus et al., 2001; Lorand and Alard, 2001; Luguet et al., 2003; Bockrath et al., 2004; Righter et al., 2004; Pitcher et al., 2009; Locmelis et al., 2013; Lorand et al., 2013; Mungall and Brenan, 2014; Lorand and Luguet, 2016; Luguet and Reisberg, 2016). IPGE are considered compatible during partial melting, with an affiliation for some silicate and oxide minerals, and thus behave in a similar fashion to Ni and Cr (e.g., Fleet et al., 1996, 1999; Brenan and Andrews, 2001; Maier et al., 2003a; Pitcher et al., 2009; Pagé et al., 2012). On the other hand, PPGE (especially Pd) are largely hosted by BMS (e.g., Mitchell and Keays, 1981; Alard et al., 2000; Lorand and Luguet, 2016; Luguet and Reisberg, 2016 and references therein) and are incompatible in silicates and oxides (e.g., Hill et al., 2000; Righter et al., 2004). Melting-induced fractionation of PGE may also stem from the co-existence of two mantle sulphide phases in the mantle source: a crystalline monosulphide enriched in Fe, Ni and IPGE vs an immiscible sulphide enriched in Cu, Ni and PPGE (e.g., Ballhaus et al., 2001; Lorand et al., 2013; Lorand and Luguet, 2016; Luguet and Reisberg, 2016). Significant fractionation between PPGE and IPGE can be caused by low degree partial melting as the immiscible sulphide becomes mobilised into silicate magma, leaving a monosulphide residue. With increasing partial melting, sulphide phases, including the monosulphide, may be exhausted and silicates and oxides (such as olivine and chromite) will also begin to release their IPGE budget (e.g., Keays, 1982; Rehkämper et al., 1997; Maier et al., 2003a; Mungall and Brenan, 2014). Accordingly, komatiites have much lower Pd/Ir ratios than basalts (e.g., Rehkämper et al., 1999).

Fractionation between individual elements of the PPGE may theoretically be possible during partial melting on account of their extremely high sulphide-silicate partitioning coefficients ($D_{Pt}^{sulphide-silicate}$ = 317,000 vs. $D_{Pd}^{sulphide-silicate}$ = 190,000; Mungall and Brenan, 2014). However, such strong chalcophile behaviour of both elements (extremely high partition coefficients, D) mean that this fractionation effect is likely to be marginal at best, and dwarfed in comparison

to the efficiency of sulphide melting and extraction from the mantle. Even a small residue of sulphide in the source can significantly inhibit the concentration of PGE in the silicate melt generated. It has been suggested that repeated partial melting events of the same source region record increasing Pt/Pd ratios via early depletion in Pd (e.g., Keays, 1982; Keays et al., 1982; Hamlyn et al., 1985). Further, of the PPGE, Pt in particular can also occur in PGM and these may behave differently from BMS during partial melting (depending on whether these are as PGM-sulphides or alloys). Regardless of the precise mechanisms for Pt and Pd decoupling, crucial empirical evidence from mantle peridotite xenoliths indicates that there may be regional and local variations in the composition of mantle BMS and PGM and thus domains particularly enriched in Pt (Wittig et al., 2010b; Hughes et al., 2017). For example, Hughes et al. (2017) found that mantle xenoliths from the keel of the Scottish portion of the North Atlantic Craton (which underlies portions of the BPIP) contain BMS enriched in PGE and characteristically bear micron-scale Pt-sulphides (cooperite). In context with the shift in NAIP lava Pt/Pd ratios through time, Hughes et al. (2015) suggested that the high Pt/Pd of earlier NAIP lavas resulted from entrainment of these Pt-sulphides, thereby 'spiking' the composition of the asthenosphere-derived mantle plume magmas during their ascent to the base of the lithosphere.

Ultimately, the MLA approach to geochemical data analysis developed in this chapter provides robust evidence that Pt (and to some extent Pd) is truly decoupled from the rest of the major and trace element geochemistry of the NAIP province. The Pt/Pd shift in the NAIP lavas with time is more complex than a systematic geographic variation; Pt is evidently being added to partial melts from a reservoir outwith the main process of magma generation via asthenospheric partial melting, and we suggest the potential role of a locally metasomatised SCLM in this process. The use of MLA demonstrates a new approach to investigating mantle source fertility and the manner in which the methodology can isolate specific nonconforming trends in high-dimensional space. This can then be related back to chalcophile modelling conducted in Chapter 3 that offers more precise process-based explanations of PGE behaviour to complement data structure conclusions (i.e., variable partition coefficients with sulphide and silicate minerals as a control on PGE distribution in melts). As suggested in the early sections of this chapter, a MLA approach to geochemistry should not be an

isolated pursuit. Whilst MLA models elucidate objective multi-dimensional trends that expand upon basic/bivariate geochemical relationships, traditional modelling conversely allows for plausible interpretations, with the two methodologies complementing, not replacing, each other towards a unified approach to global PGE patterns. Chapters 6 and 7 build upon the scale and scope of these ideas.

5.5. Conclusions

The benefits of using machine learning to explore high dimensional data sets have been clearly outlined by a detailed study of NAIP lava geochemistry. By using a novel combined data science and classical approach to bulk geochemical data sets, we have identified some key contributions to the investigation into PGE metallogenic controls in plume environments:

1. PCA, t-SNE and *k*-means clustering identified major multi- element trends in NAIP lava geochemistry and established three distinct geochemical end-members in the data set, which represent the net result of magmatic differentiation processes in the geodynamic system.
2. The workflow captured consistent variability information in nine of the eleven included variables, importantly isolating Pt and Pd as exceptional to end-member trends in all methods and input formations, implying a localised geochemical control for these two metals in the NAIP.
3. We suggest a locally metasomatised and Pt-sulphide-rich SCLM reservoir being incorporated into plume melts as a reasonable explanation for the unique Pt/Pd variability, based on previous findings regarding asthenospheric heterogeneity in the NAIP.
4. The role of feature extraction via dimensionality reduction is important for manageable high-dimensional geochemical investigations as illustrated by consistently improved clustering performance using Principal Components as input variables for MLA.
5. Further advances in understanding this wide topic may be possible by integrating more elements in larger data sets from other plume regions (where PGE are of significant interest), particularly lithophile elements.

Chapter 6

From Continent to Ocean - Investigating the multi-element and precious metal geochemistry of the Paraná-Etendeka Large Igneous Province using machine learning

Chapter Summary

Large Igneous Provinces (LIP), and by extension the mantle plumes that generate them, are frequently associated with platinum-group element (PGE) ore deposits, yet the process of metal acquisition in plume-derived magmas remains debated. In this chapter, we present a new bulk geochemical data set from the Paraná-Etendeka LIP (PELIP) in the South Atlantic, which includes major and trace element concentrations (including PGE and Au) for onshore and offshore lavas from different developmental stages in the province. The underlying Tristan plume initially generated continental PELIP lavas prior to the rifting of South America and Africa 135-128 Ma, when it passively transitioned to an oceanic setting. The novel geochemical and machine learning approach introduced in Chapter 5 is used to investigate PGE signatures in PELIP lavas, to test the hypothesis that plume-derived magmas can scavenge precious metals from the sub-continental lithospheric mantle (SCLM) and explore how this might change the metal basket. The PELIP presents an opportunity to observe magma geochemistry as the continent and the SCLM are progressively removed from a melting environment. Of the four onshore lava types on the Paraná side of the PELIP, the Type 1 (Southern) and Type 1 (Central-Northern) localities exhibit separate PGE-enriched assemblages (Ir-Ru-Rh and Pd-Au-Cu, respectively). Onshore lavas on the Etendeka side are without significant PGE enrichment. Offshore lavas on both sides exhibit similarities through the multi-element space to their onshore equivalents, but again lack PGE enrichment. It follows that there is significant asymmetry to the metallogenic character of the PELIP, with enrichment focused specifically on lavas from the continent edge in Paraná.

6.1. Introduction

Near-surface intrusive Ni-Cu-PGE deposits are famously located in the Noril'sk Talnakh intrusion in Siberia (e.g., Lightfoot, 2007), the Skaergaard Complex in Greenland (e.g., Andersen et al., 1998) and the Bushveld Complex in South Africa (e.g., Maier and Groves, 2011), as reviewed by Naldrett (1997) and Barnes et al. (2016). These locations share a similar geodynamic setting, with intraplate magmas interacting with thick, stable (i.e., older) continental lithosphere, and this setting may directly influence the precious metal budget of magmas in this context (e.g., Zhang et al., 2008; Maier and Groves, 2011).

Mantle plumes, buoyant diapirs of material from the mantle, can rise to the base of the lithosphere, introducing a thermal anomaly and inducing partial melting at the base of the lithosphere and asthenosphere, generating intraplate magmas (e.g., Morgan, 1971; Morgan, 1972; Griffiths and Campbell, 1990; Kellogg and King, 1993; Shannon and Agee, 1998; Jellinek and Manga, 2004). Intraplate magmas are thought to be sourced from a range of asthenospheric mantle reservoirs, many of which are relatively undepleted in incompatible elements (Zindler and Hart, 1986; Hawkesworth et al., 1988; Stracke et al., 2005; Hawkesworth and Scherstén, 2007). Furthermore, studies highlight the sub-continental lithospheric mantle (SCLM) below cratons as a potential source of metals, indicating that plume-derived magmas that ascend through Archaean lithosphere are enriched in precious metals compared to those that do not feature significant lithospheric interaction (e.g., Hawkesworth and Scherstén, 2007; Zhang et al., 2008; Bierlein et al., 2009; Begg et al., 2010; Griffin et al., 2013; Barnes et al., 2015). This is particularly evident in regions in which the SCLM has been significantly pre-enriched by successive metasomatic events throughout their tectonic development (e.g., Wilson et al., 1996; Handler and Bennett, 1999; Powell and O'Reilly, 2007; Tassara et al., 2017; Rielli et al., 2018; Holwell et al., 2019; Wang et al., 2020a).

This chapter looks at the nature of precious metal (PGE and Au) variations in plume-derived magmas, generated by the Southern Atlantic Tristan plume, alongside a large suite of major and trace element concentrations. For the past ~ 135 Myr, the environment above the Tristan plume has transitioned from a continental to oceanic setting, effectively removing the availability of the SCLM

reservoir during melting and/or contamination. Herein, we investigate the effects this substantial geodynamic shift had on the relative concentrations of precious metals (i.e., the metal basket) in magmas generated in the region, with a focus on correlations with major and trace element variability and the geochemical processes implied therein. Flood basalts can often share chalcophile, siderophile and incompatible trace element signatures with underlying Ni-Cu-PGE mineralised magmatic intrusions, as exhibited in the PGE-rich East Greenlandic lavas near Skaergaard (e.g., Momme et al., 2002; 2006) and S-saturated Siberian Traps near Noril'sk (e.g., Ripley et al., 2003; Lightfoot and Keays, 2005). This connection has not been explicitly investigated in the flood basalts associated with the Tristan plume in this context, and our study aims to provide insight into the PGE mineralisation potential of magmas in the region.

We use an integrated machine learning approach based on work from Lindsay et al. (2021) (i.e., Chapter 5) to analyse our new whole-rock geochemical data suite from onshore and offshore Tristan plume lavas, which comprise the Paraná-Etendeka Large Igneous Province (PELIP). Bulk geochemical data sets are excellent candidates for exploration using machine learning algorithms (MLA), often comprising upwards of 50 measured elemental concentrations and hundreds of samples. Using an MLA approach allows for the exploration of multi-element trends and relationships challenging for a human observer to extract, whilst contributing to the study of the Earth's mantle geochemistry. By comparing and contrasting our new data to the North Atlantic Igneous Province (NAIP) from Chapter 5, which shares a similar plume-rift geodynamic setting to the Tristan plume, we work towards a multi-element variability model for plume metallogenesis in the Atlantic Ocean.

6.1.1. The Paraná-Etendeka Large Igneous Province

The Tristan mantle plume is responsible for the eruption of the lavas of PELIP, one of the largest continental flood basalt (CFB) provinces in the world (e.g., Stewart et al., 1996; Courtillot et al., 2003; Gibson et al., 2005). Lavas are preserved asymmetrically between (primarily) Brazil in South America, and (to a lesser extent) Namibia in Africa, with fifteen times greater volume of lavas found in South America (around 1.2×10^6 km^2; Fodor et al., 1989). The lavas range in composition from basalts through to rhyolites and, even amongst the mafic rocks, there is geochemical evidence for multiple mantle sources (e.g., Le Roex et al.,

2002; Gibson et al., 2005; Beccaluva et al., 2020). After the Tristan plume arrived at the Gondwanan lithosphere under the modern day central Paraná region in Brazil ca. 135 Ma (e.g., Douglass et al., 1999; Gibson et al., 2005; Fromm et al., 2015), it induced partial melting of the asthenosphere and erupted lava at a rate of 0.8 km^3/year (Renne et al., 1996). These early Tristan lavas were primarily basaltic and were compositionally zoned into High-Ti compositions in central and north-west Paraná, and Low-Ti compositions in the south-east, the latter of which eventually progressed into bimodal mafic-felsic volcanism (Peate et al., 1992; Polo et al., 2018).

From 134 to 128 Ma (Stewart et al., 1996), rifting initiated in the thermally thinned and weakened lithosphere (McKenzie and White, 1989; Turner et al., 1996) as north-westerly plate movement migrated the magmatic activity to the Etendeka-Angola margin, synchronous with the eruption of the south-eastern Low-Ti lavas in Paraná (Beccaluva et al., 2020). Etendeka lavas are also sub-divided into High-Ti and Low-Ti groups and are bimodal throughout (Milner et al., 1995a; Marsh et al., 2001). After Gondwana rifted (e.g., de Wit et al., 2008; Jokat and Reents, 2017; Martins-Ferreira et al., 2020), the plume produced volcanics in the newly-opened ocean, creating the seafloor Rio Grande Rise and Walvis Ridge topographic features (e.g., O'Connor and Duncan, 1990; Ussami et al., 2013) (as shown in Figure 6.1a). These erupted at a less productive volcanic flux, given the transition from plume head to tail (Camboa and Rabinowitz, 1984; Gibson et al., 2005; Fromm et al., 2015). The Rio Grande Rise on the Southern American plate and the Walvis Ridge on the African plate connect the PELIP to the active hotspot focus, currently in the centre of the southern Atlantic Ocean (O'Connor and Duncan, 1990; O'Connor and Jokat, 2015; Homrighausen et al., 2019). Figure 6.1b summarises the PELIP timeline.

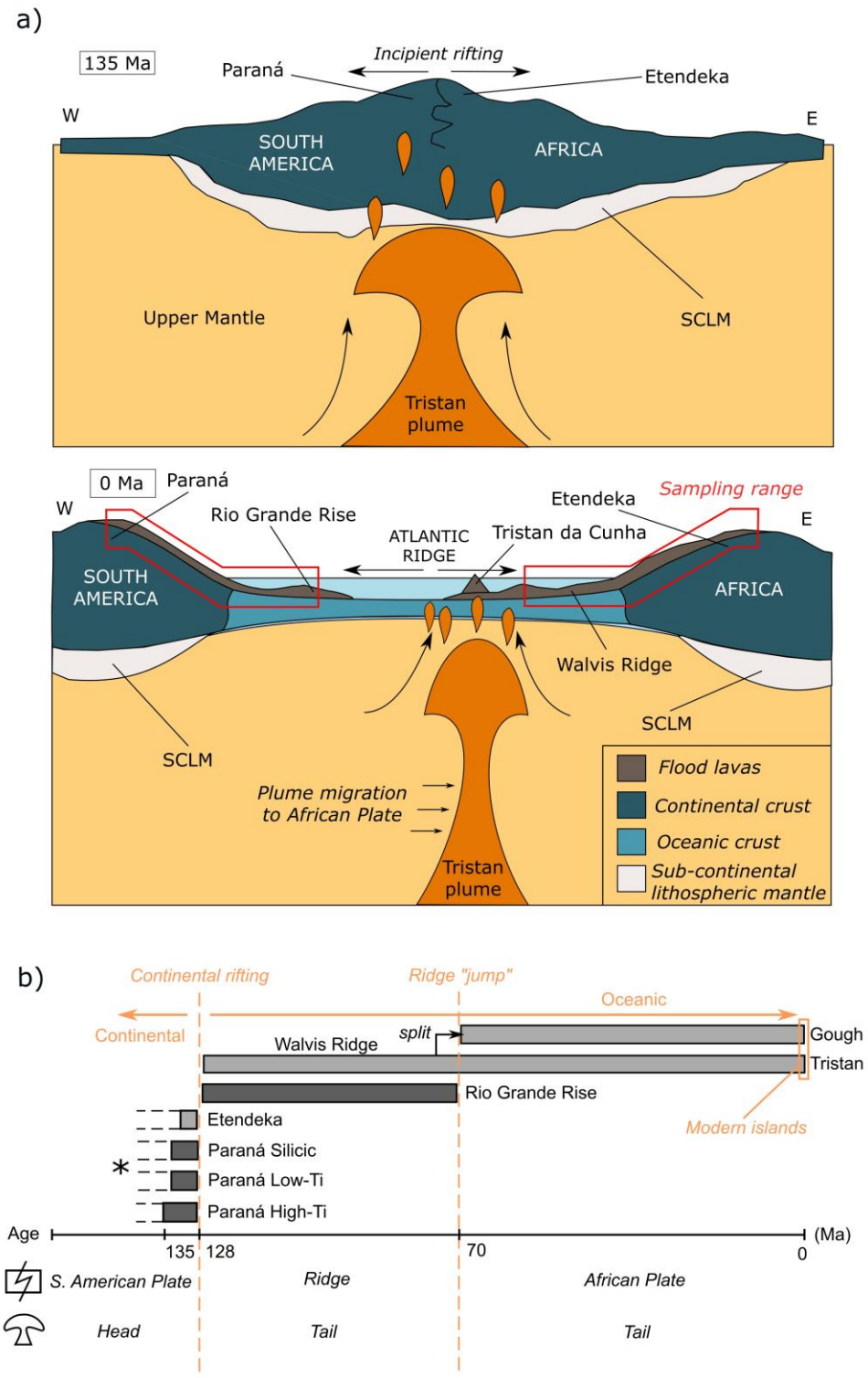

Figure 6.1 - *(a) Schematic two-part cross-section of the formation of the southern Atlantic Ocean, detailing the arrival of the Tristan plume beneath Gondwanan lithosphere 135-128 Ma, melting of the asthenosphere and SCLM, incipient continental rifting beginning after 128 Ma, and the eventual formation of oceanic hotspot trails connected to the plume until 0 Ma. Sample range for this study is indicated by the red boxes – refer to Table 6.1.*

Figure 6.1 (cont'd) - *(b) Schematic timeline for the PELIP, showing the eruption scales for each major locality from 135 Ma to present and major tectonic events such as rifting at 128 Ma and the ridge-jump at 70 Ma. Also included are the plate position of the plume focus and the head-to-tail plume transition. (* = although dated primarily between 135 and 128 Ma, the large majority of onshore lavas erupted between 135 and 134 Ma on the Paraná side)*

6.1.2. Petrology and geochemistry of the PELIP

6.1.2.1. Paraná

The predominantly basaltic and basaltic-andesitic lavas of the Paraná CFB sequence erupted on to the Botucatu Sandstone Formation and Proterozoic basement of the late Gondwanan continent, peaking between 135 and 134 Ma but continuing to 128 Ma (e.g., Gordon, 1947; Leinz, 1949; Leinz et al., 1966; Peate et al., 1990; Marques et al., 1999; Thiede and Vasconcelos, 2010; Rocha-Júnior et al., 2012; Hartmann et al., 2019). Previous studies on the geochemistry of the Paraná lavas, referred to more formally as the Serra Geral Formation in Brazil, classified them based on major and trace element concentrations, and isotopic variations (e.g., Fodor, 1987; Peate et al., 1992). The primarily tholeiitic High-Ti, Low-Ti and Silicic groups present throughout the creation of the CFB, were initially proposed by Fodor (1987) but later given more distinct magma-type subdivisions. For example, the Urubici sub-group represents the highest-Ti lavas in the Serra Geral Formation, and is often separated from Pitanga and Paranapanema within the High-Ti bracket (Peate et al., 1992). Relatively scarce in the region compared to the other main lava types, Ribeira is primarily distinguished isotopically, forming an intermediate lava with properties of both High-Ti and Low-Ti sub-groups (Peate et al., 1992; Peate and Hawkesworth, 1996). Gramado and Esmeralda are often associated with the Chapecó and Palmas members within the bimodality of south-eastern Low-Ti lavas in Paraná (Bellieni et al., 1984; Peate et al., 1990; Peate et al., 1992; Peate, 1997). Licht (2018) further classified all mafic and silicic lavas in the region into sixteen types based on Si, Ti, Zr and P concentrations. In this new scheme, Gramado and Esmeralda comprise Type 1 (Southern), Ribeira and Paranapanema comprise Type 1 (Central-Northern), Pitanga and Urubici are Type 4, and Palmas and Chapecó belong to Types 9 and 14, respectively (Licht, 2018). These types were

explored in depth in Chapter 3. The remaining 12 types are significantly less common volumetrically (Licht, 2018) and do not feature in this chapter.

The literature supports the theory that lavas belonging to the various magma-types erupted in a synchronous manner from separate subsurface melt systems (Peate, 1997; Rämö et al., 2016; Beccaluva et al., 2020; Lindsay et al., in review[a]; Chapter 3), with each system being subject to distinct differentiation processes and geochemical development (Turner et al., 1999; Rossetti et al., 2018).

6.1.2.2. Etendeka

The African equivalents of the Serra Geral lavas are dated consistently ~ 130 ±2 Ma (by $^{40}Ar/^{39}Ar$ mineral dating as per Renne et al., 1996; Stewart et al., 1996), coinciding with the late-stage bimodal Paraná lavas and earliest Atlantic opening (Milner et al., 1995c). The Etendeka Group is distributed roughly parallel to the coastline, split into two mafic regions separated into northern and southern sections by Möwe Bay (Ewart et al., 1998a). The lavas collectively contribute a much smaller volume to the total preserved throughout the PELIP, covering ~ 80,000 km^2 (Erlank et al., 1984) or 6 % of the preserved CFB area (Miller, 2008). The Etendeka Group Lavas, comprising basalts, basaltic-andesites and andesites with quartz latites (Erlank et al., 1984; Marsh et al., 2001), overlie the mixed sedimentary/volcanic rocks of the Neoproterozoic Damara Sequence and the Mesozoic Karoo sediments (Miller, 2008 and references therein). Similar to Paraná, the northern region is dominated by High-Ti signatures and the southern region by Low-Ti lavas. Silicic lavas are typically located in the south, such as in the Goboboseb Mountains (Ewart et al., 1998b) and the province hosts many intrusive dolerite complexes (Milner et al., 1995c).

The Etendeka Group features two main geochemical sub-groups in the Tafelberg and Khumib, which represent the bulk of the Type 1 and Type 4 Serra Geral magma classifications, respectively (Erlank et al., 1984; Marsh et al., 2001; Ewart, 2004; Miller, 2008). Minor Esmeralda and Kuidas groups complete the Low-Ti components of the Etendeka Group Lavas (Ewart, 2004), showing slight trace element and isotopic differences to Tafelberg. Most noteworthy is the observation that the lavas and intrusive complexes in Etendeka generally have markedly higher MgO (15-25 wt.%; Teklay et al., 2020) than their equivalents in

Serra Geral (typically < 8 wt.%; Peate, 1997), denoted to represent a differing degrees of partial melting and/or different mineral fractionation systematics in each (Teklay et al., 2020). The Etendeka part of the onshore PELIP is considered a better geochemical representation of the deep Tristan plume mantle source component through the Cretaceous (Hoernle et al., 2015; Jennings et al., 2019).

6.1.2.3. Rio Grande Rise and the Walvis Ridge

The formation of the age-progressive seafloor volcanic ridges in the developing South Atlantic Ocean ca. 128 Ma onwards resulted from a combination of mid-ocean ridge and intraplate magmatism following the breakup of Gondwana (O'Connor and Jokat, 2015; Homrighausen et al., 2019). The submarine ridges present the unusual situation in which OIB and MORB of the same age exist adjacent to each other, as normally, plume lavas intersect much older oceanic lithosphere in hotspots (e.g., Morgan, 1971; O'Connor and Duncan, 1990; Fromm et al., 2017). The Rio Grande Rise on the South American Plate has average bathymetries of 3,000 m in the west to 1,000 m in the central region (Camboa and Rabinowitz, 1984). Drill core samples from the plateau comprise mainly tholeiitic and alkali basalts (O'Connor and Duncan, 1990; Gibson et al., 2005). Working eastwards from the continent, the trail becomes significantly less prominent after 34°S 29°W (Figure 6.2). At this stage, the plume focus abruptly transitioned from the centre of the mid-ocean ridge to on top of the Africa Plate ca. 70 Ma (Figure 6.1b) (e.g., Camboa and Rabinowitz, 1984; Gibson et al., 2005; Fromm et al., 2015; O'Connor and Jokat, 2015; Graça et al., 2019).

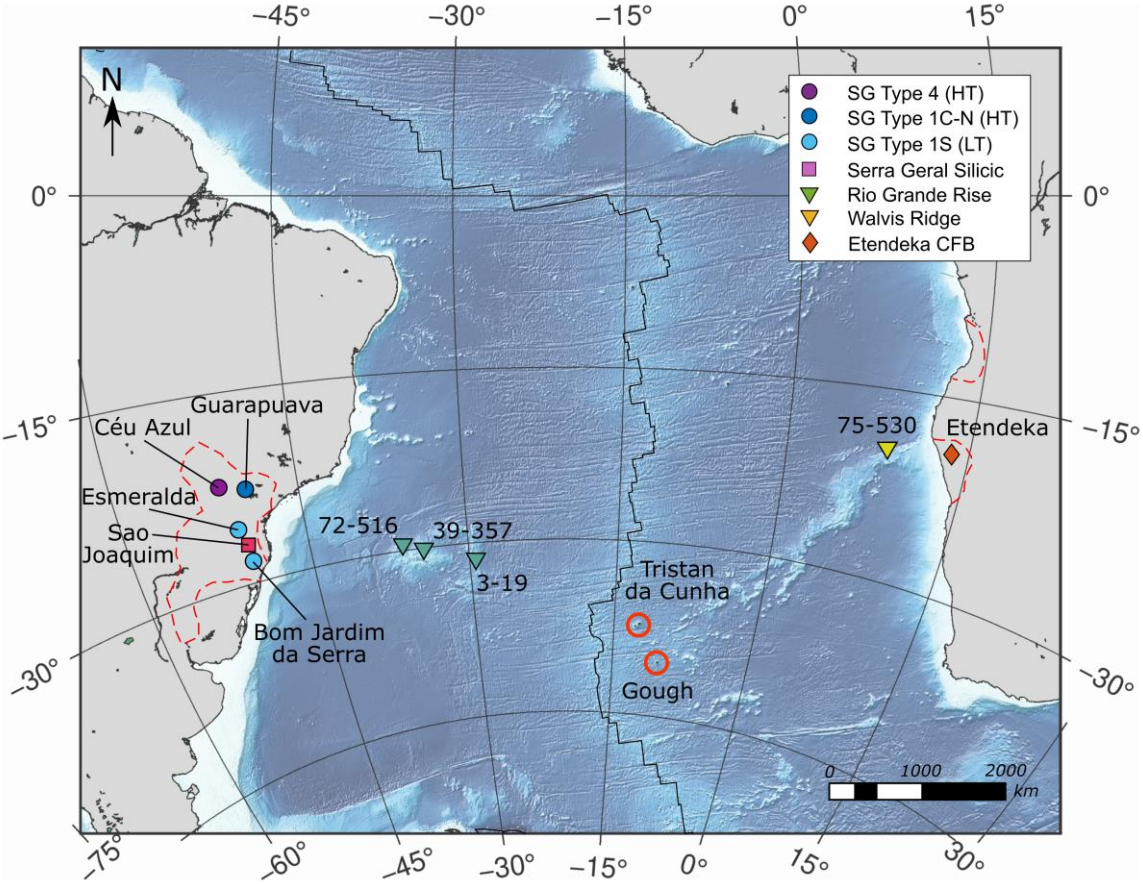

Figure 6.2 - *Schematic map of eastern South America, western Africa and the South Atlantic Ocean with ocean floor bathymetry, detailing the site localities for rock samples analysed in this study. Symbology is used throughout all plots related to these localities. For offshore samples, the IODP drill site and core numbers are displayed, and the current focus of the Tristan plume (beneath Tristan da Cunha and Gough) is shown in red. Also outlined onshore are the rough boundaries of the continental lavas.*

The Walvis Ridge, on the African Plate, is of a similar age to the Rio Grande Rise (Milner et al., 1995c) and forms a narrow trail westwards from the High-Ti Khumib lava exposures in Namibia (Homrighausen et al., 2019). Bathymetric data places it at between 2,500 and 1,600 m below sea level, with the ridge increasing in height from east to west (Der Verfasser et al., 2011). At around 29°S 2°E, the trail bifurcates into two younger ridges, the Tristan and Gough tracks (O'Connor and Duncan, 1990; Rohde et al., 2013a; Rohde et al., 2013b), eponymous with the islands associated with the current plume focus (Figure 6.2). The significant jump in tectonic plate movement at ~ 70 Ma resulted in the splitting of the Walvis hotspot trail and the cessation of Rio Grande Rise

volcanism, after which the Tristan plume focus lay to the east of the ridge for the first time, and volcanism occurred exclusively on the African plate (Rohde et al., 2013a; Graça et al., 2019). Prior to the jumps, it is suggested that the two > 70 Ma ridges would have been analogous with Iceland, as a conitguous volcanic ocean island formed by sustained ridge opening and addition of plume-derived lavas (Graça et al., 2019). The seafloor Walvis-Tristan-Gough hotspot track thus represents all stages of the transition from continental to modern day oceanic plume.

6.2. Materials and Methods

6.2.1. Samples

Table 6.1 displays sample information for our new PELIP suite (n = 134). Whole rock samples were collected for fossil onshore lavas in Paraná (n = 102). Etendeka samples (n = 10) were acquired from a collaboration with Potsdam University, and represent the Low-Ti end-members of the Namibian continental flood basalts (the Tafelberg Formation). Drill core samples (n = 22) were collected from the International Offshore Drilling Programme (IODP) repository in Bremen, Germany for offshore sites along the Rio Grande Rise (DSDP Leg 3-19, 39-357 and 72-516) and Walvis Ridge (DSDP Leg 75-530). Given the higher degree of geochemical variability and their potential to reflect sensitive changes in geodynamics, these Paraná lavas formed the bulk of the sample set in this study and have already undergone detailed investigation and melt modelling in Lindsay et al. (in review[a]); Chapter 3. For the present chapter, we have classified Paraná samples based on their Si-Ti-Zr-P concentrations as per Licht (2018), resulting in Serra Geral Type 1 (Southern), Type 1 (Central-Northern), Type 4 and Silicic groups.

To account for sample size differences (e.g., ~ 1kg for Paraná lavas to ~ 50g for IODP core sections) and to assess quality control of geochemical analyses, randomly selected larger samples were cut into pieces equivalent in weight to core samples and processed individually as separate runs i.e., sample A and B belonging to a single original rock. The geochemistry of each was compared as a check on the processing methodology and as a comparison

between samples of significantly different sizes from different localities. Further QAQC details are available in the Supplementary S6.1. Figure 6.2 shows the general sample localities within the context of the Southern Atlantic. A full sample database with rock descriptions and physical properties is presented in Supplementary S6.2.

Table 6.1 - *Samples used in this study with the locality, formation (or drill core for offshore samples), rock type and quantity (excluding duplicates). Samples listed west to east as per Figure 6.2. SG – Serra Geral, C-N – Central-Northern, S- Southern.*

Locality	Formation or Drill Core	Rock type	n
SG Type 4	Urubici, Pitanga (High-Ti)	Basalt	24
SG Type 1 (C-N)	Paranapanema (High-Ti)	Basalt	30
SG Type 1 (S)	Gramado, Esmeralda (Low-Ti)	Basalt	42
SG Silicic	Chapecó (High-Ti), Palmas (Low-Ti)	Dacite	6
Rio Grande Rise	DSDP Legs 3-19, 39-367, 72-516	Basalt	14
Walvis Ridge	DSDP Leg 75-530	Basalt	8
Etendeka	Tafelberg (Low-Ti)	Basalt	10
		Total	***134***

6.2.2. Laboratory techniques

Laboratory techniques follow those set out in Chapters 3 and 4 are described briefly herein. Rock samples were crushed to 1-2 mm chips using a jaw crusher following removal of weathered material and amygdales. They were then milled in a chrome-steel TEMA mill for use in bulk geochemical analysis techniques. Major elements were measured using X-ray fractionation (XRF) (using methods from Kystol and Larsen, 1999; Tegner et al., 2009). Dried and ignited samples were fused in a furnace in platinum crucibles with lithium borate flux, and cooled samples were moulded into beads using ammonium iodide as a wetting agent. Fused beads were analysed using a Bruker S4 Pioneer XRF spectrometer at Camborne School of Mines, alongside AGV-1, BHVO-2, BIR and DNC-1 standards. Trace elements were measured using inductively coupled plasma mass spectrometry (ICP-MS) at Camborne School of Mines (following the methodology of McDonald and Viljoen, 2006). This method used the 4-Acid

sample dissolution technique before element detection using the Agilent 7700 Series mass spectrometer, alongside BCR-2 and Bir-1A standards.

Finally, Os, Ir, Ru, Rh, Pt, Pd, and Au were measured at Cardiff University using the Ni-S fire assay and tellurium co-precipitation technique for PGE analysis outlined by Huber et al. (2001), and McDonald and Viljoen (2006). For this method, 15 g of sample was mixed with 12 g of borax flux, 6 g $NaCO_3$, 0.9 g solid sulphur, 1.08 g Ni and 1 g silica, and the mixture was melted in a furnace at 1000°C for 1.5 hours. The sulphide bead segregated from the quenched silicate matrix was dissolved in hydrochloric acid, re-precipitated with Te, filtered and diluted. The final solutions were then analysed for precious metal concentrations using ICP-MS, alongside the TBD1 and WPR1 standards. Full (anhydrous) major, trace and PGE+Au data are provided in Supplementary S6.1, with standard measurements, blank measurements and detections limits where applicable.

6.2.3. Machine learning workflow

We have implemented the machine learning workflow introduced by Lindsay et al. (2021) (Chapter 5 of this thesis) to examine the multi-element geochemistry of the PELIP and the Southern Atlantic plume-rift system. The workflow combines Principal Component Analysis (PCA) and t-Distributed Stochastic Neighbour Embedding (t-SNE) feature extraction methods with *k*-means clustering, as reviewed in Chapter 5. All methods used algorithms from the *sci-kit learn v0.21.3* package for Python 3.7.4 (Pedregosa et al., 2011) in addition to *NumPy v1.16.5* (Harris et al., 2020) and *Pandas v0.25.1* (McKinney, 2010) packages. All code used is available in Supplementary S6.3.

Both PCA and t-SNE are effective dimensionality-reduction techniques that allow for the management of data sets with high dimensionality (i.e., a large number of variables/features). These techniques provide a means for digesting and presenting substantial amounts of variability information contained within a large geochemical suite. By reducing the dimensionality of our data down to more manageable low-dimensional components we can effectively discuss complex multi-elemental trends. Principal components (PCs) generated during PCA, features that describe the directions of largest variability trends throughout the entire data structure (Pearson, 1901; Hotelling, 1933; Chang, 1983), can highlight inter-element associations, identify key drivers behind fluctuations in variable

associations and recognise multi-element enrichment signatures (Hyvärinen et al., 2001; Davis, 2002; Jolliffe, 2002). This information is generally displayed in 'biplots' which illustrate both sample and element variability through the entire data set. The PCs can then be used as optimised variables in the clustering steps of the workflow.

In comparison, the slightly more advanced, non-linear t-SNE method summarises the variability of all elements in a high-dimensional data set by visualising this information in a single newly-generated low-dimensional space referred to as an embedding (van der Maaten and Hinton, 2008; van der Maaten, 2014). This technique uses the Kullback-Leibler Divergence (Kullback and Leibler, 1959) to preserve similarity between data points within high-dimensional space and transform this information into the embedding. This creates a summary "map" of cumulative sample variability across all included elements. The positions of data points within an embedding space are strongly indicative of how geochemically similar or different they are to other data points, although it should be noted that the high-dimensional similarity of proximal points is preserved better than dissimilarity between distal points (Baramurali et al., 2019). Individual element variability, sample classifications and multi-element clusters recognised through PCA can be contextualised within the overall data structure in embeddings to quickly and efficiently describe a wealth of information for a complete data set. We work with three user-determined "hyperparameters" in our models – perplexity (the balance between portraying local and global trends in the data), learning rate (the increments taken to find the optimal embedding layout) and maximum iterations (the number of times the algorithm will try to optimise) (van der Maaten and Hinton, 2008).

We also use *k*-means clustering, an unsupervised MLA that clusters data into a pre-determined number of classification groups (*k*), based on an iterative density function that seeks out optimum similarity between samples across high dimensional space (MacQueen, 1967; Howarth, 1983; Michie et al., 1994; Hastie et al., 2009; Marsland, 2009). This allows for objective classification using a multitude of variables simultaneously, identification of multi-dimensional trends in the sample space and tests the similarity of previous classification clusters through the data structure. We can retrospectively assess clustering performance using the Davies-Bouldin Index (DBI) calculation (Davies and Bouldin, 1979),

which highlights the statistically-optimum cluster number as a function of intra-cluster density. A low DBI is desirable and denotes a high degree of similarity between points in each cluster, and *k*-means models with the lowest DBI are prioritised in the study. For an in-depth account of the MLA methodology, algorithm details and review of the techniques within, refer to Lindsay et al. (2021) and/or Chapter 5.

The techniques herein require data sets without zeroes, missing (blank) or non-numerical (e.g., below detection limit) entries. For this reason, despite being measured in some localities in the sample set, Te, W and Os were omitted from the working data set given the high volume of missing values. Further, BaO and Cr_2O_3 were removed from the XRF-derived data set as the concentrations of Ba and Cr were measured separately using the higher-precision ICP-MS technique, rendering the equivalent oxide values unnecessary. Rounded-zero imputation, as recommended by Horrocks et al. (2019) and Lindsay et al. (2021), was not utilised in this instance to fill gaps in the data sheet. Finally, two Rio Grande Rise samples were removed from the data set due to anomalously high (~ 19 wt.%) loss-on-ignition (LOI) values, likely indicating a high degree of alteration of these basaltic samples. The final data set used in all analyses consisted of 116 samples, with concentrations for 51 major element oxides and trace elements measured for each. The final processed data is available in Supplementary S6.4, alongside new PCA, t-SNE and *k*-means information discussed herein.

Since this data set is compositional in nature, standardisation of all measurements is required before any statistical analyses (e.g., Chayes, 1960; Palowsky-Glahn and Egozcue, 2006; Buccianti and Grunsky, 2014). Standardisation of data via the z-score calculation (Kreyszig, 1979) was performed on the data set prior to use in algorithms. The calculation presents all measured concentrations as a function of standard deviations from the mean value for each element. This validates the use of compositional data in this workflow and allows for more accurate comparison of mixed-unit concentrations across the different methods used by eliminating bias from, for example, high numerical values for elements measured in ppm (e.g., Ni, Cu) compared to small values measured in ppb (e.g., PGE). This process of standardisation, either using z-scores or other similar calculations, is recommended for data treatment prior to most unsupervised learning MLA (e.g., Taylor et al., 2010; Wang et al., 2020b).

6.3. Results

6.3.1. Major and trace element geochemistry

The table provided in Appendix D1 gives minimum, maximum and mean measured values for all elements included in the MLA workflow. The full processed geochemical data set, with z-scores, is available in Supplementary S6.4.

A selection of important anhydrous major element plots are shown in Figure 6.3, including an alkali-Fe_2O_3-MgO (AFM) ternary diagram (Figure 6.3a) and Harker plots with mineral fractionation vectors (Figures 6.3b-d); further Harker and classic normalised multi-element plots and are provided in Appendix D2-4 for reference. Appendix D12 provides alteration plots for our samples, indicating low degrees of alteration throughout the set and establishing all geochemistry herein as primary signatures (Mathieu, 2018). In Figure 6.3a, Etendeka and Walvis Ridge samples represent the least evolved samples (i.e., high MgO, low SiO_2), followed by Rio Grande Rise and Serra Geral mafic samples which plot tightly in the tholeiitic peak on the AFM triangle. Silicic lavas and a single mafic lava plot in the most fractionated sector. Serra Geral lavas, classified according to Licht (2018), have MgO concentrations consistently < 7 wt.% while samples from Etendeka range from 5 to 15 wt.%. Rio Grande Rise lavas are subdivided into a majority ~ 5 wt.% (similar to Serra Geral) and Walvis Ridge samples are clustered at 7-8 wt.% MgO. All Serra Geral samples form a positive linear array in the MgO-CaO plot in Figure 6.3b, while the other localities have more subtle trends, with mean CaO of ~ 10 wt.% (Figure 6.3b). Concentrations of TiO_2 groups Serra Geral lavas effectively as seen in Figure 6.3c – one group at > 3 wt.% (Type 4), one at 2-2.5 wt.% (Type 1 Central-Northern) and one at < 2 wt.% (Type 1 Southern and Silicic). Etendeka, Rio Grande Rise and Walvis Ridge generally have TiO_2 concentrations of < 2.5 wt.%. In Figure 6.3d, samples show a similar MgO-Al_2O_3 spread to MgO-CaO, with Serra Geral lavas forming a roughly positive array with Walvis Ridge samples, and lavas from the other localities show a more diffuse and slightly negative trend. An inflection in dominant trend direction is observed in all three bivariate plots at 6-7 wt.% MgO.

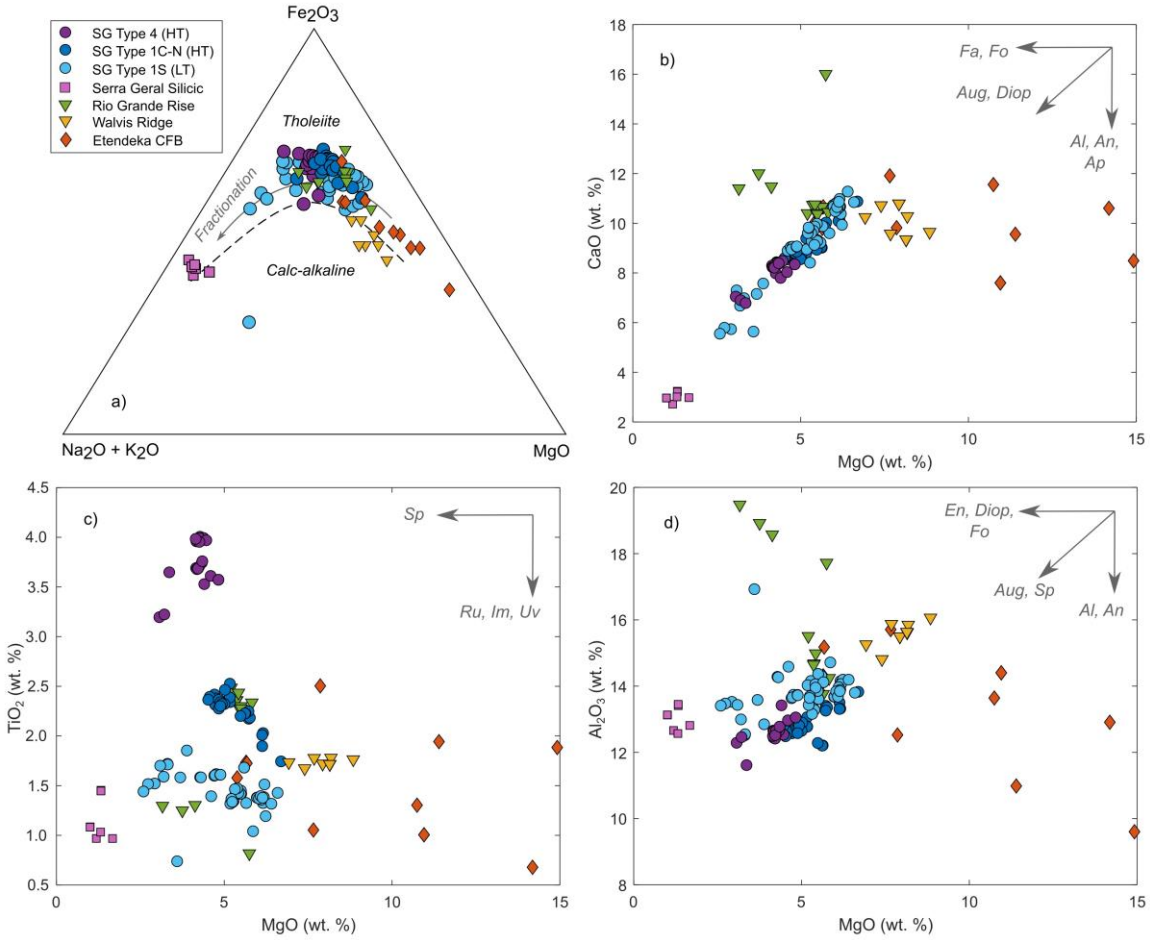

Figure 6.3 - *Ternary and bivariate geochemical plots for major elements in the PELIP data set, classified by locality. (a) AFM (alkali-Fe_2O_3-MgO) ternary plot; (b) MgO vs. CaO; (c) MgO vs. TiO_2; (d) MgO vs. Al_2O_3. With fractionation vectors for evolving liquid compositions for Fo – forsterite, Fa – fayalite, Aug – augite, En – enstatite, Diop - diopside, an – anorthite, Al – albite, Sp - spinel, Uv – ulvospinel, Mg – magnetite, Ru – rutile, Im – ilmenite.*

6.3.2. High-dimensional geochemistry using all variables

6.3.2.1. Principal Component Analysis

Dimensionality-reduction via PCA was performed using the concentrations of the full suite of 51 elements measured for all samples in the PELIP data set; the method standardises concentrations using z-scores within the script (see Supplementary 6.3). In this variable set-up, PC1 to PC8 account for 89.06 % of all data set variability (Figure 6.4a); information in higher order PCs (i.e., PC9 and upwards above the ~ 90 % mark in Figure 6.4a) have minimal overall contribution

to variability, hence the focus on the more significant PC1-8. A summary of PCA cumulative variability and eigenvalues are provided in Figure 6.4a, showing PC1-2 alone accounting for 56 % of data set variability.

Across the biplots in Figures 6.4b-e, data point and eigenvector interactions indicate how strongly a sample or element varies throughout the data set as a whole, respectively. Although all elements were resolved individually during the PCA process, we present eigenvectors with similar lengths and directions as groups for visual clarity in Figures 4b-e. Overall, PC7-8 relationships (Figure 6.4e) do not depict strong or consistent trends compared to the other PC biplots (Figures 6.4b-d) described below, working west to east across the PELIP.

- *Serra Geral Type 4* variability is governed by: TiO_2, P_2O_5, K_2O, Rb, Zr, Hf, and light rare-earth elements (LREE) in PC1-2; MgO, Fe_2O_3, Co, V, Sc, Mn, Ni, and LREE in PC3-4; and TiO_2, LREE, Eu, Sr, Nd, Sm, and As in PC5-6.
- *Serra Geral Type 1 (Central-Northern)* variability is governed by: Fe_2O_3, Sc, V, Cu, Pd, and Au in PC1-2; Cr, Pd, and Au in PC3-4; and La, Ce, Ni, Co, U, Th, Pt, Pd, and Au in PC5-6.
- *Serra Geral Type 1 (Southern)* variability is governed by: SiO_2, Na_2O, CaO, Co, As, Ir, Ru, and Bi in PC1-2; K_2O, Al_2O_3, SiO_2, Rb, Ba, U, Th, As, Ir, Ru, Rh, Pb, and Bi in PC3-4; and a wide variety of elements in PC5-6.
- *Serra Geral Silicic* variability is governed by: the same elements as Serra Geral Type 4 in PC1-2; the same elements as Serra Geral Type 1 (Southern) in PC3-4; and CaO, SO_3, Y, Zr, Nb, Ta, and heavy rare-earth elements (HREE) in PC5-6.
- *Rio Grande Rise* variability is governed by: Al_2O_3, Fe_2O_3, Co, As, Mn, Sc, V, Cu, Ir, Ru, Rh, Pt, Pd, and Au in PC1-2; TiO_2, CaO, SO_3, Se, Sr, Eu, Cu, and Pt in PC3-4; and Al_2O_3, P_2O_5, Na_2O, CaO, SO_3, Se, Y, Zr, Hf, and HREE in PC5-6.
- *Walvis Ridge* variability is governed by: CaO, Co, As, Ir, Ru, and Bi in PC1-2; the same elements as Serra Geral Type 1 (Southern) in PC3-4; and the same elements as Rio Grande Rise in PC5-6.
- *Etendeka* variability is governed by: MgO, Ni, Cr, and SO_3 in PC1-2; MgO, Fe_2O_3, Co, V, Sc, Mn, Ni, Cr, Ta, Pd and Au in PC3-4; and a wide variety of elements in PC5-6.

6.3.2.2. t-SNE

Dimensionality-reduction using t-SNE was performed using z-scores of the 51 variables. A parameter set-up of 5,000 maximum iterations, learning rate of 200 and perplexity of 50 was selected through a heuristic approach and provided the most well-defined, evenly spaced cluster structure - Figure 6.5 displays the chosen data set embedding classified by sample locality. Embeddings produced from different perplexity set-ups are shown in Appendix D5 for reference.

The t-SNE algorithm effectively discriminates the PELIP geographical groups in Figure 6.5, with all sample types excluding Rio Grande Rise occupying a unique sector of the embedding; Rio Grande Rise forms three nearby sub-clusters. Serra Geral Type 4 and Silicic samples plot distinctly from the other lavas, which form a continuum of multi-element compositions with smaller physical separation between each type. Etendeka and Walvis Ridge plot at the bottom of the Embedding 2. Both Serra Geral Type 1 localities occupy the centre of the embedding, with Type 1 (Southern) displaying a larger spread across the space compared to other groups. The three sub-clusters for Rio Grande Rise samples bracket Etendeka, Walvis and Serra Geral Type 1 samples, which appears to be a borehole control on geochemistry (i.e., Figure 6.2).

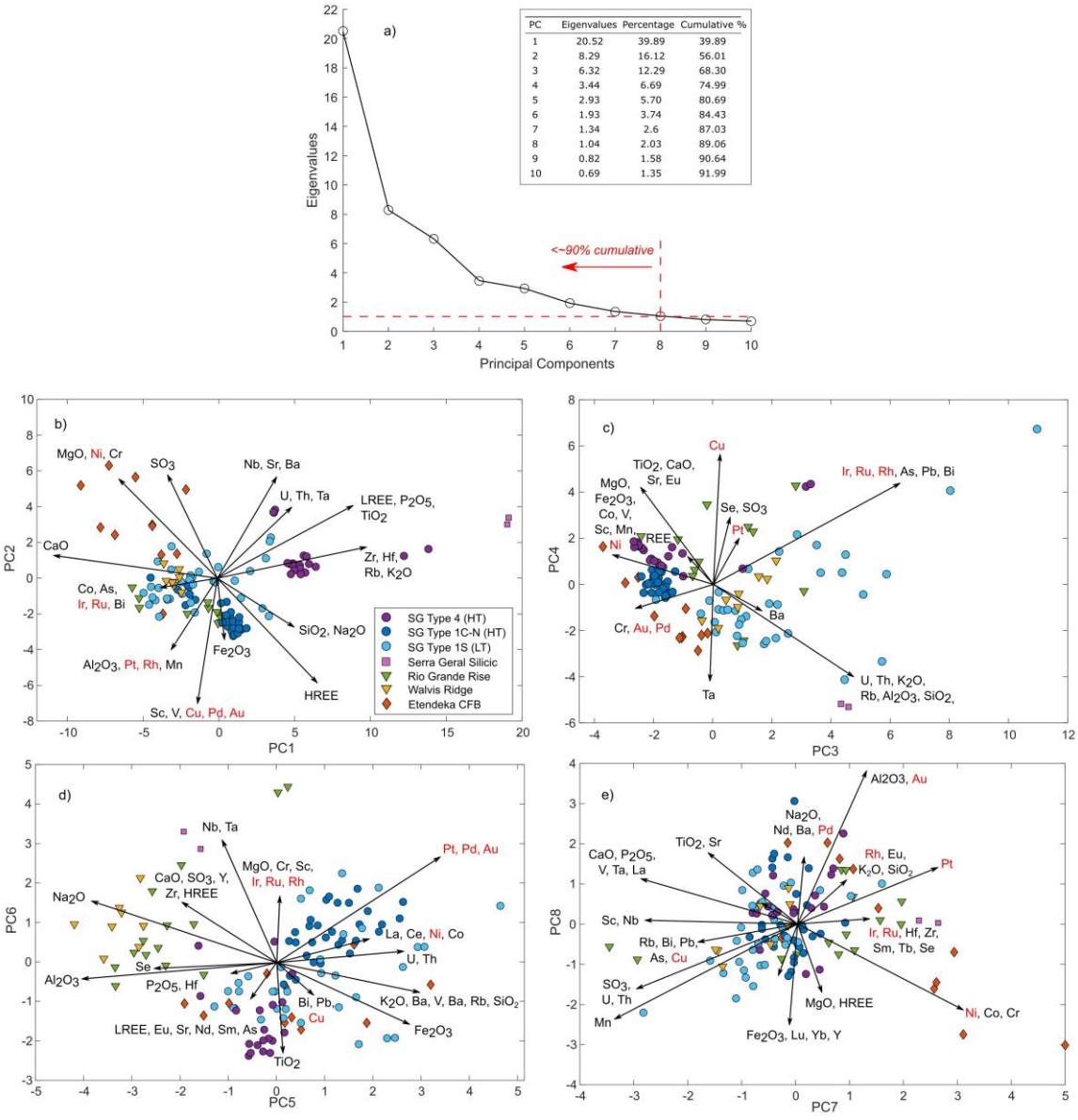

Figure 6.4 - *PCA statistics and summary biplots (combined eigenvector and data point information) for 51 elements in the PELIP data set. (a) Eigenvalues, percentage variance and cumulative percentage variance for PC1-10, with a scree plot denoting PC8 as the highest relevant component (i.e., flat slope, cumulative percentage ~ 90 % and eigenvalues > 1.0). (b) Biplot for PC1 vs. PC2; (c) Biplot for PC3 vs. PC4; (d) Biplot for PC5 vs. PC6; (e) Biplot for PC7 vs. PC8. Data points classified by locality and eigenvectors are summarised/grouped together with similar elemental trends for ease of presentation. Red elements are of critical interest to Ni-Cu-PGE-Au studies.*

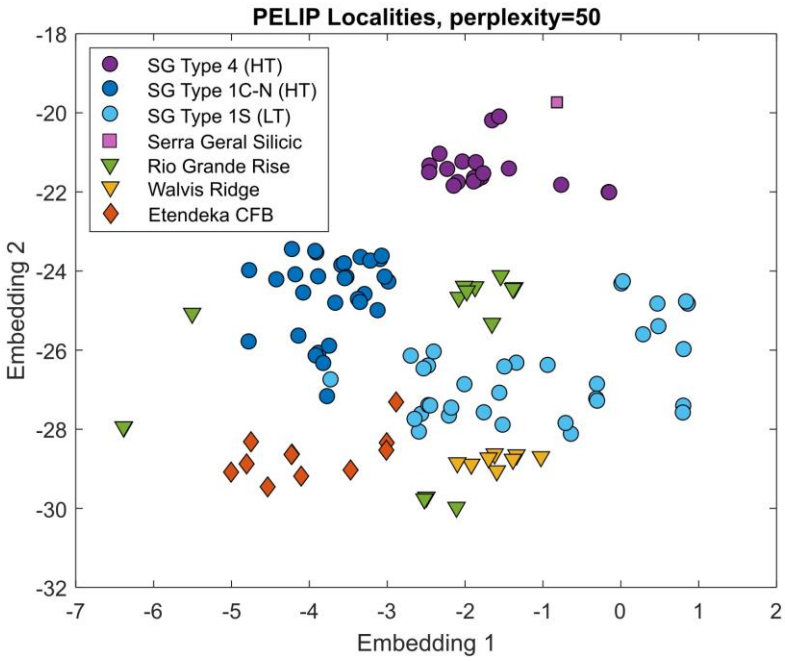

Figure 6.5 - *Embedding generated using t-SNE algorithm using all 51 element z-scores. Optimum embedding selected with perplexity of 50 for best separability and cluster definition. Data points classified by locality.*

Figure 6.6 displays PELIP sample data arranged in the embedding space from Figure 6.5, with points coloured by z-scores for 45 of the measured major and trace elements (excluding PGE and Au), to give an account of how individual elements vary through the new embedding (as per Horrocks et al., 2019; Lindsay et al., 2021). Elements with strong bimodal distribution (i.e., with clear, distinct zones of high and low z-scores) contribute significantly to overall data structure, whilst those with more even or scattered z-score distributions do not. For the major elements, MgO, CaO, TiO_2, K_2O, P_2O_5 and BaO concentrations exhibit strong bimodality across the data set, whilst SiO_2, Al_2O_3, Fe_2O_3, SO_3, Na_2O and MnO are more uniform or do not appear to have distinct variability trends apart from occasional outliers. For trace elements, Sc, V, Cr, Co, Ni, Cu, Se, Rb, Y, Zr, Hf, Th and U exhibit bimodality of varying strength. Conversely, As, Sr, Nb, Ta, W, Pb and Bi do not exhibit bimodal distributions. For the REE, the high z-scores progressively shift location from the top to the centre of Embedding 2 (y-axis) with increasing atomic number. This mimics a shift from Serra Geral Type 4 to Type 1 (Central-Northern) in Figure 6.5.

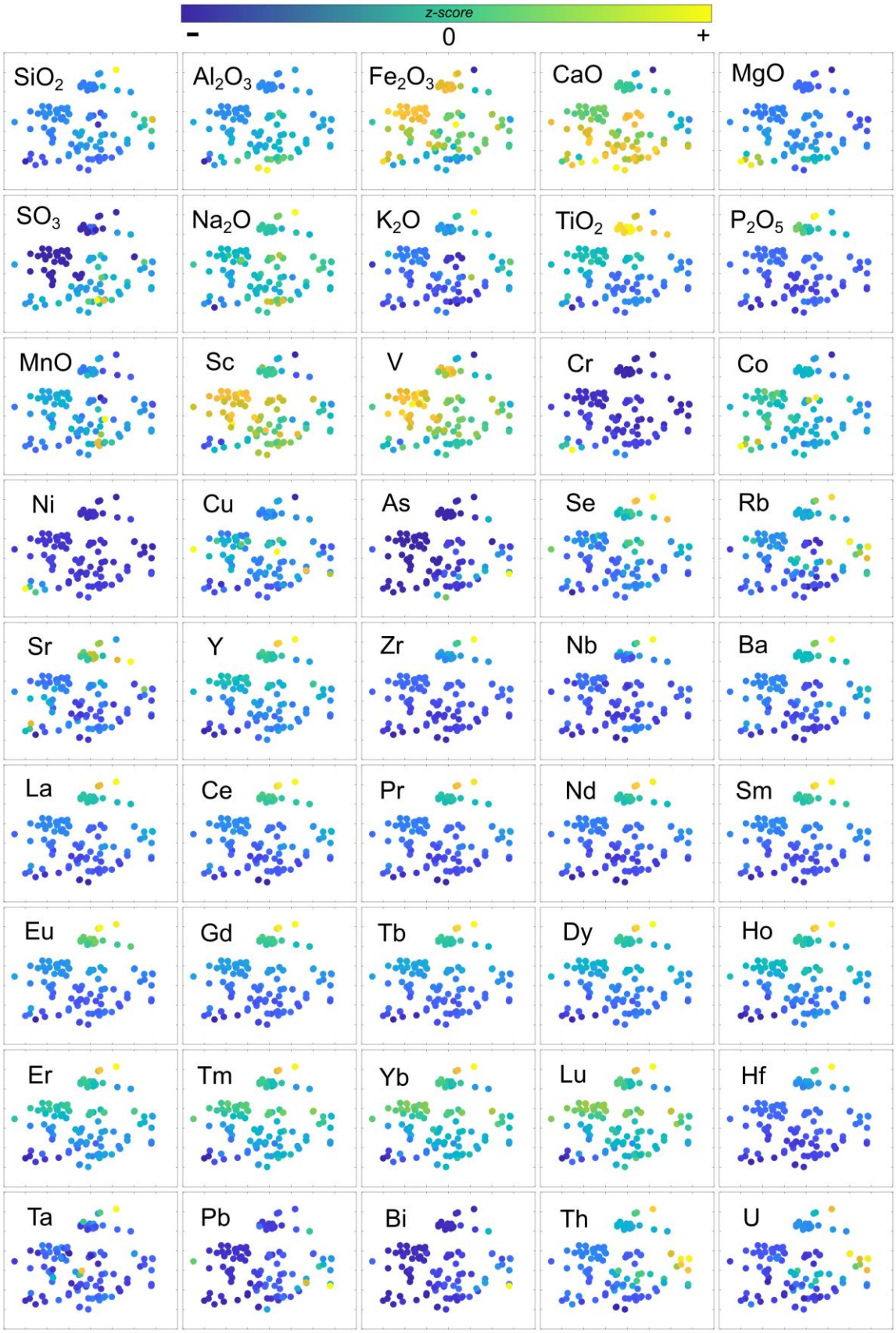

(Caption overleaf)

Figure 6.6 *- Embedding from Figure 6.5 with data points coloured by z-scores for 45 major and trace elements (excluding PGE and Au).*

Figure 6.7 displays PELIP sample data arranged in the embedding space from Figure 6.5, with points coloured by z-scores for the PGE (excluding Os) and Au. Compared to major and trace element embedding plots, these metals are much more "nuggety", with high concentrations much rarer than low concentrations. A small sub-cluster of Serra Geral Type 1 (Southern) samples in the far right (Figure 6.5) host very high Ir, Ru and Rh concentrations (Figure 6.7). The highest concentrations of Pt, Pd and Au are strongly concentrated with Serra Geral Type 1 (Central-Northern) on the left-hand side, particularly Pd and Au (again, comparing Figures 6.5 and 6.7). Overall, Serra Geral Type 4 and Silicic, Etendeka, Walvis Ridge and Rio Grande Rise zones from Figure 6.5 do not host high PGE concentrations, with the two Serra Geral Type 1 lavas appearing to dominate in this aspect, reflecting their statistics from Appendix Table D1 and PGE plots in Appendix D3 and D4.

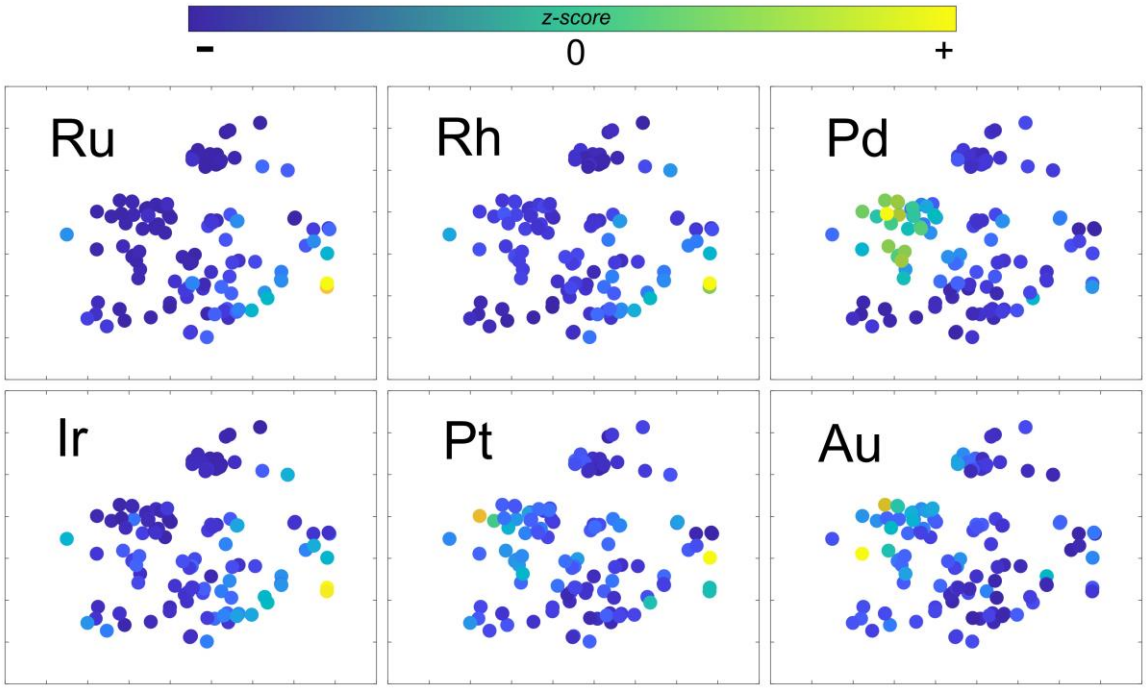

Figure 6.7 *- Embedding from Figure 6.5 with data points coloured by z-scores for PGE (excluding Os) and Au, arranged by atomic number.*

6.3.2.3. k-means clustering

Clustering using the *k*-means algorithm was performed on the (i) PCs and (ii) z-scores of the 51 variables. Models were run for *k*-values of 2 to 7. By comparing DBI for all model parameter set-ups, we find that the most robust model was clustering samples using PC1-8 (up to ~ 90% of variability; Figure 6.4a) for all variables (as suggested by Lindsay et al., 2021), with *k*=7. However on considering cluster formations, *k*=7 only produces a further localised 2-point outlier cluster with otherwise identical clusters to *k*=6, hence we use the *k*=6 model going forward as it best describes global trends in the data set. All models from all parameter set-ups and their corresponding DBI are displayed in Appendix D6-8.

Figure 6.8a displays the t-SNE layout from Figure 6.5, again classified by locality, with the same embedding classified by the *k*-means clusters from the optimal set-up displayed adjacent in Figure 6.8b. A histogram describing the subscription of new cluster classifications (Groups 1-6) in terms of their prevalence in each sample locality is given in Figure 6.8c. These six clusters define the main multi-element end-members in the lavas analysed, independent of geographic classifiers. Overall, Group 1 is exclusively found in Serra Geral Type 1 (Southern), Group 2 is exclusively found in Serra Geral Silicic, Group 4 is exclusively found in Serra Geral Type 4 and Group 6 is exclusively found in Etendeka. Group 3 appears primarily in Serra Geral Type 1 (Central-Northern) (making up the vast majority of the locality's new classification), but some Group 3 are also found in Type 1 (Southern) and Rio Grande Rise samples. Group 5 is found in all localities except Serra Geral Type 4 and Silicic (i.e., the lower half of Embedding 2 from Figures 6.5 and 6.8b).

A box-and-whisker plot detailing PGE concentrations (excluding Os due to its absence from some Serra Geral samples) per MLA-based cluster is provided in Figure 6.9. Group 1 hosts the highest mean, median and maximum values in the data set for Ir, Ru and Rh, and has a comparable spread of Pt concentrations to Group 3. Mean, median and maximum Pd concentrations are significantly higher in Group 3 than all other groups. Group 5 often hosts intermediate concentrations of each PGE between Groups 1 and 3. Groups 2, 4 and 6 are generally the least PGE-enriched clusters.

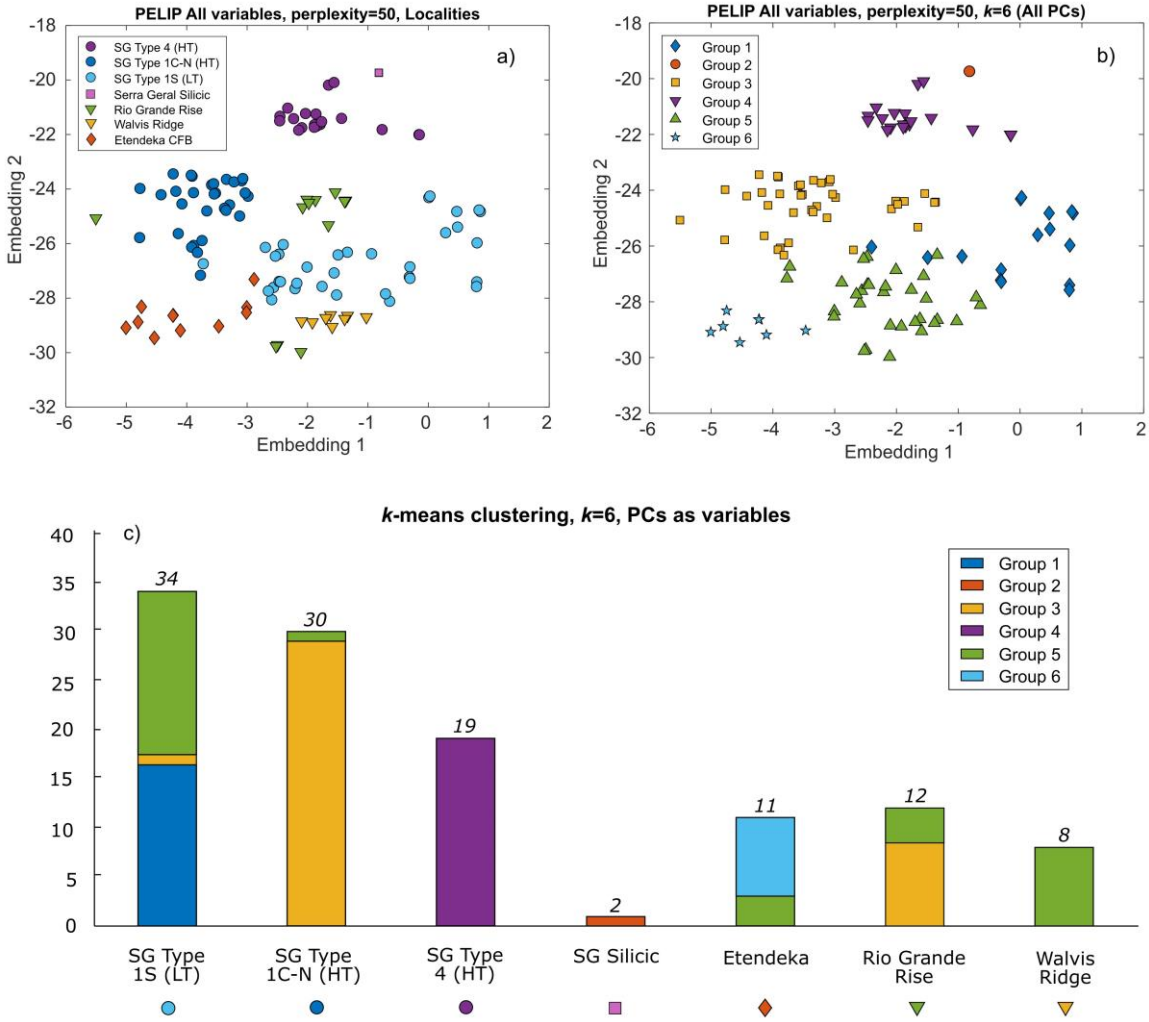

Figure 6.8 *- k-means clustering model selection with comparison to locality classifications – (a) Original t-SNE embedding from Figure 6.5 classified by locality (for reference); (b) t-SNE embedding classified by selected k-means clustering model (using PC1-8 from Figure 6.4 as variables, k=6); (c) Histogram comparing new cluster information from Groups 1-6 to localities.*

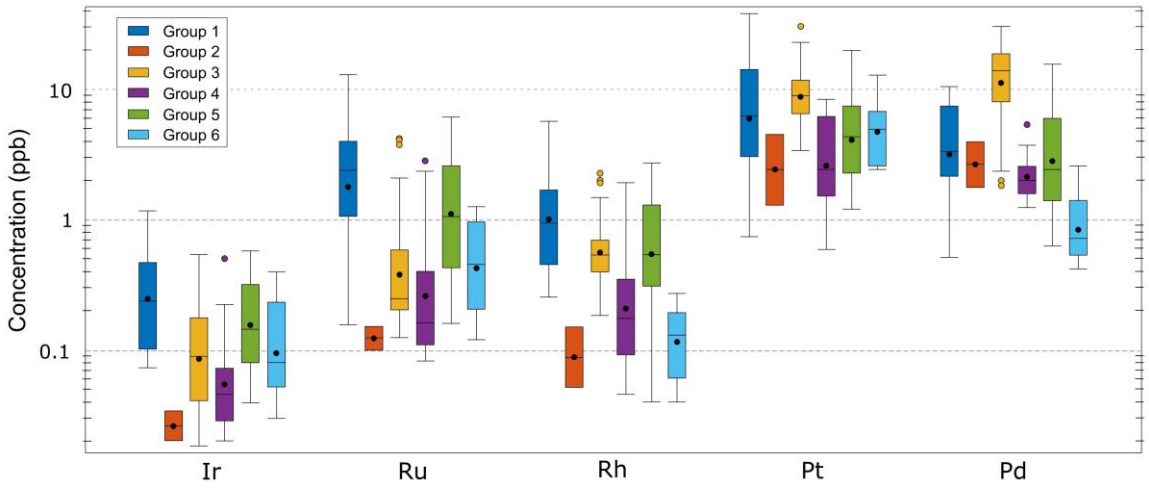

Figure 6.9 *- Box-and-whisker plot for PGE (excluding Os) concentrations in the selected k-means clustering model (PC1-8 as variables, k=6). Black circle – mean; horizontal line – median; box – interquartile range (Q1-Q3); whiskers – "maximum and minimum" i.e., Q1 or Q3 + 1.5 x interquartile range; coloured circles – outliers (above 1.5 x interquartile range).*

6.3.3. High-dimensional geochemistry using reduced variables

An important application of this study is comparing results to the test study from Lindsay et al. (2021) (Chapter 5) using the NAIP data set, both in terms of MLA workflow performance, and geochemical and geodynamic implications from their respective results. By running aspects of the MLA workflow using a reduced array of input variables, matching the eleven variables established in the NAIP data set, we can make a substantial assessment of the relative multi-element geochemistry of the two similar plume-rift environments. As explained in Chapter 5, these eleven elements were measured for samples in each NAIP locality and are synonymous with mafic-ultramafic magmas (e.g., Barnes et al., 2015). It would be inappropriate to judge interpretations of a 51-variable MLA investigation and an 11-variable MLA investigation, and by running the PELIP data through with these 11 variables only, we are better place to compare and contrast the two settings.

Accordingly, we re-run PCA and t-SNE for the PELIP data set using *only* MgO, Fe_2O_3, TiO_2, Ni, Cu, Cr, Ir, Ru, Rh, Pt, and Pd (as the 11 elements included in the NAIP study of Lindsay et al. (2021) comprising Chapter 5). This has

enabled us to directly compare the data sets and interpretation for lavas derived from the two mantle plumes associated with the opening of the Atlantic Ocean, both in the North (Icelandic plume) and South (Tristan plume) – see Section 6.4.3. In this reduced variable set-up, PC1-6 account for 93.10 % of cumulative variability (Figure 6.10a) and PC7-11 are disregarded. Across the biplots in Figures 6.10b-d:

- *Serra Geral Type 4* variability is governed by TiO_2 in PC1-2; TiO_2, Ir, Ru and Rh in PC3-4; and TiO_2, Ir and Rh in PC5-6.
- *Serra Geral Type 1 (Central-Northern)* variability is governed by Fe_2O_3, Cu and Pd in PC1-2; Pt and Pd in PC3-4; and MgO, Cr, Cu and Pd in PC5-6.
- *Serra Geral Type 1 (Southern)* variability is governed by Ir, Ru, Rh, and Pt in PC1-2; Ir, Rh and Ru in PC3-4; and Fe_2O_3, Ni, Ru, and Pt in PC5-6.
- *Serra Geral Silicic* variability is governed by no particular elements in PC1-2 or PC3-4; and TiO_2 in PC5-6.
- *Rio Grande Rise* variability is governed by Ir, Ru, Rh, Pt and Cu in PC1-2; TiO_2, Ir and Rh in PC3-4; and MgO, TiO_2, Cu, Cr and Pd in PC5-6.
- *Walvis Ridge* variability is governed by MgO, Cr, Ni and Ir in PC1-2; Ru in PC3-4; and MgO, Cr and Pd in PC5-6.
- *Etendeka* variability is governed by MgO, Cr, and Ni in PC1-2; Fe_2O_3, TiO_2, MgO, Cr, Ni, and Cu in PC3-4; and Fe_2O_3 and Ni in PC5-6.

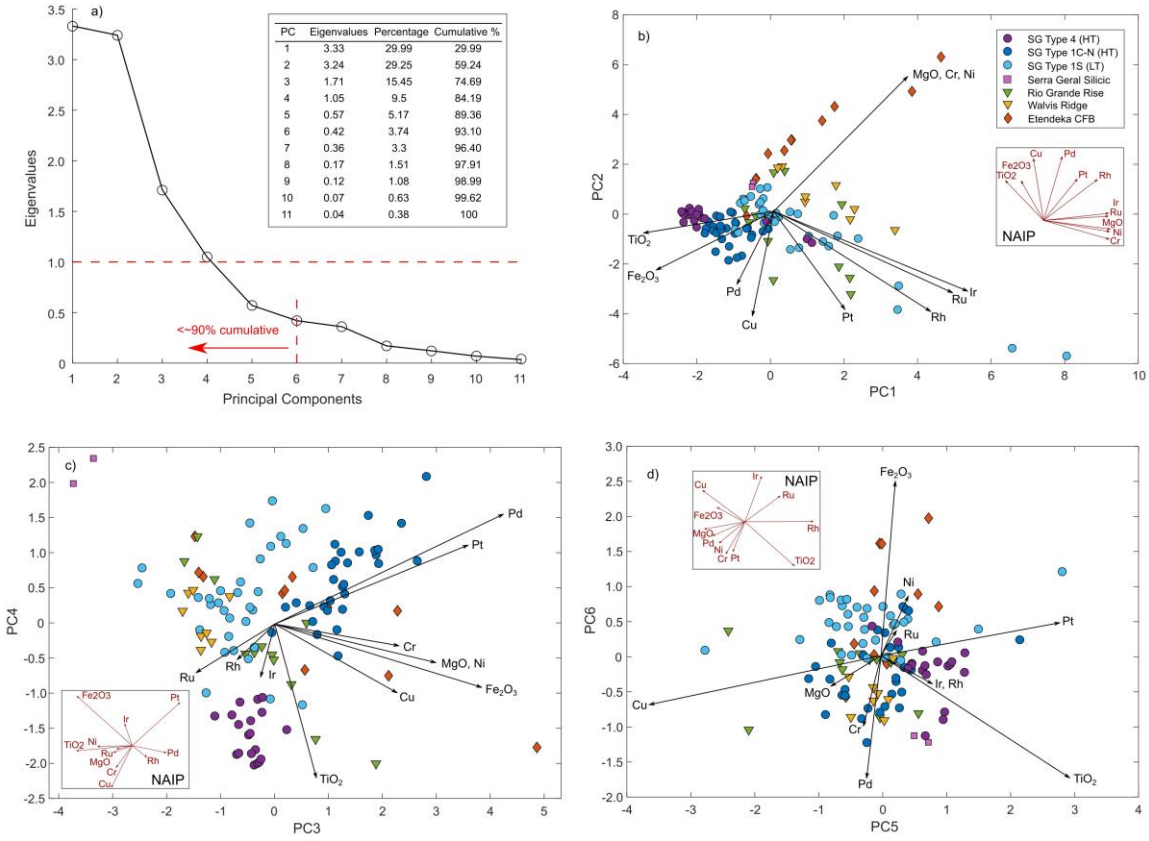

Figure 6.10 *- PCA statistics and summary biplots (combined eigenvector and data point information) for 11 elements in the reduced PELIP data set. (a) Eigenvalues, percentage variance and cumulative percentage variance for PC1-11, with a scree plot denoting PC6 as the highest relevant component (i.e., flat slope and cumulative percentage ~ 90%). (b) Biplot for PC1 vs. PC2; (c) Biplot for PC3 vs. PC4; (d) Biplot for PC5 vs. PC6. Data points classified by locality and eigenvectors are summarised/grouped together with similar elemental trends for ease of presentation where appropriate. NAIP eigenvectors for equivalent plots in red sub-plots, from Lindsay et al. (2021).*

Figure 6.11 displays the reduced variable embedding, (a) classified by locality (for reference) and (b) coloured by z-scored elemental concentrations for the eleven included variables. A parameter set-up of 5,000 maximum iterations, learning rate of 200 and perplexity of 50 was selected as the best embedding; extra models are presented in Appendix D9. Through the new embedding space, some elements share trends – high concentrations of MgO, Ni and Cr are found in the top left, Fe_2O_3 and TiO_2 in the bottom centre, Ir, Ru and Rh in the top right, and Pt and Pd on the right-hand side. Only Cu is distributed less clearly, although a general association with Pd is visible. Sample locality zones are reasonably

clear, with Etendeka, Serra Geral Type 4 and Silicic samples sitting separate from the rest of the localities in the central population (Serra Geral Type 1 and the ridge lavas). However, unlike the embedding using all 51 elements (i.e., Figure 6.5), individual samples often plot far from the main cluster centres, particularly for Etendeka, Walvis Ridge and Rio Grande Rise.

6.4. Discussion

6.4.1. MLA-based geochemical interpretation

6.4.1.1. Magmatic differentiation according to major elements

Figure 6.3 suggests that Etendeka and Walvis Ridge lavas are the most primitive in the sample suite with the highest MgO contents (Appendix Table D1). This is particularly notable in the AFM diagram in Figure 6.3a, in which Etendeka/Walvis samples plot earlier in the tholeiitic fractionation trend (Kuno, 1968), whilst the Serra Geral and Rio Grande Rise lavas are more evolved. Serra Geral Silicic samples are the most alkali-rich and compositionally evolved, and some Type 1 (Southern) are basaltic-andesites. The Serra Geral lavas form positive linear trends between MgO-CaO and MgO-Al_2O_3 in Figure 6.4b-c, indicating fractionation of minerals containing these elements from the parent magma, like olivine, pyroxene, plagioclase and/or spinel-group minerals (in agreement with Peate, 1997). Mineral fractionation vectors (e.g., Richter and Moore, 1966; Cox et al., 1979; Rollinson, 1993 and references therein) in Figures 6.3b-d and Appendix D2-3 indicate stronger removal of olivine in Rio Grande Rise, Walvis Ridge and Etendeka parent magmas compared to Serra Geral magmas, which trend more with pyroxene and plagioclase removal (i.e., more advanced fractionation). The corroborates with Serra Geral positioning further along the AFM fractionation vector in Figure 6.3a.

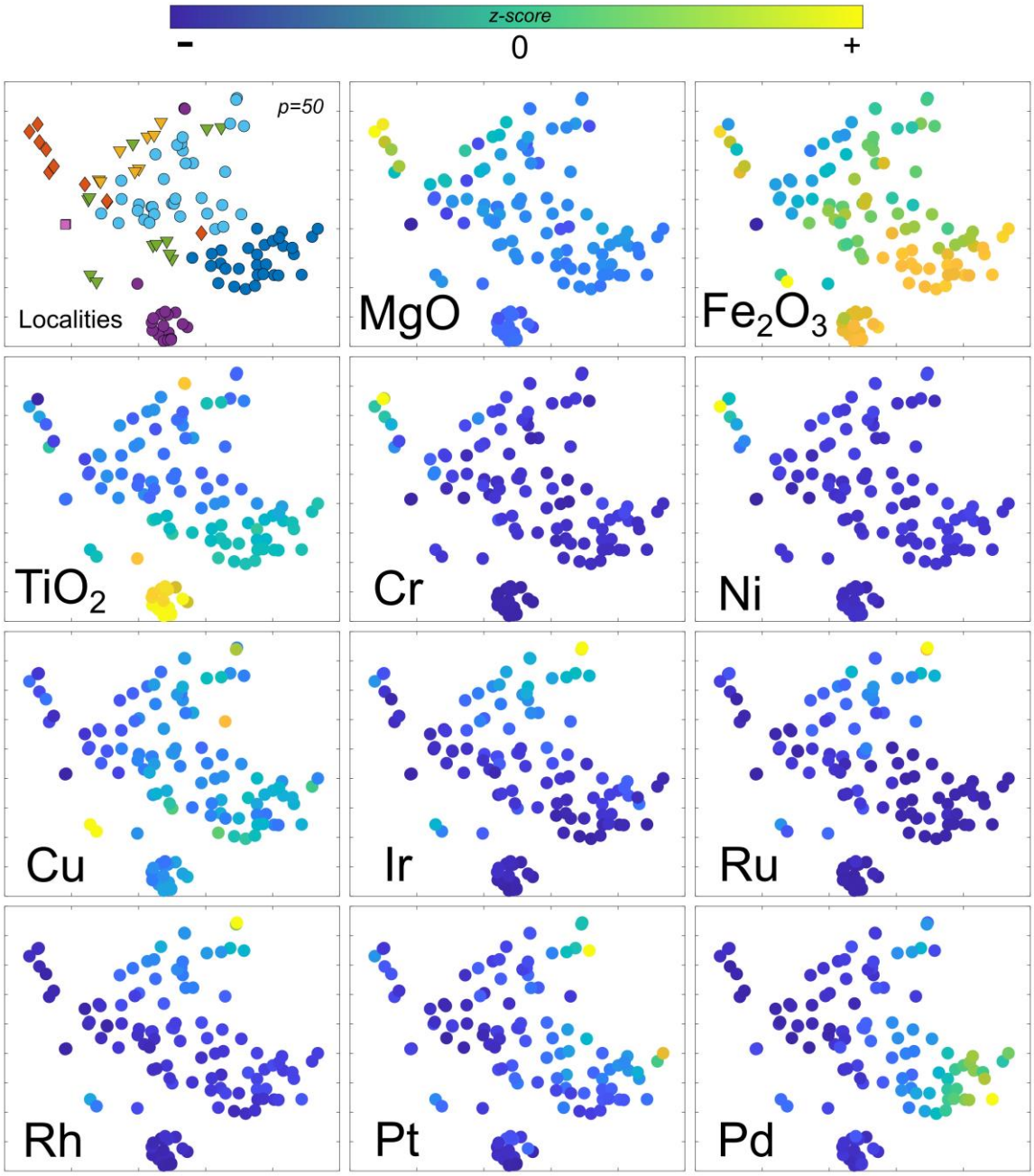

Figure 6.11 *- Embedding generated for the reduced PELIP data set (11 variables), coloured by z-scores for all elements used in the model. The embedding is also classified by sample locality in the top left for reference; key is the same used in all other plots for localities (e.g., Figures 6.3, 6.4, 6.5, 6.8 and 6.10).*

6.4.1.2. Reconciling PELIP localities & MLA-defined groupings

Table 6.2 summarises the major and trace element associations captured by the six MLA-based clusters by comparing their positions in Figure 6.8b with Figures 6.6 and 6.7. These classifications reinforce and allow us to succinctly describe multi-element signatures (i.e., geochemical end-members) that pervade through PCA (Figure 6.4) and t-SNE (Figures 6.5-6.7) interpretations for PELIP samples. We interpret the enrichment (or lack thereof) exhibited by each locality, working west to east, herein.

Serra Geral Type 4 samples are defined exclusively by the Group 4 end-member in Figure 6.8c and Table 6.2. They are the highest-Ti mafic lavas, show an expectedly strong affinity for TiO_2 eigenvectors in Figures 6.4a-d, and high-TiO_2 regions in the embedding space in Figures 6.5 and 6.6. This end-member also features enrichment in incompatible elements like Zr, Hf, Rb and LREE. High-Ti Paraná basalts are typically interpreted to be from a more trace element enriched mantle source in the literature, often connected to OIB Tristan plume signatures more than lower-Ti South American CFBs (e.g., Peate, 1997; Rämö et al., 2016; Weit et al., 2017; Beccaluva et al., 2020; Zhou et al., 2020).

Table 6.2 *- Summary of the cluster-defining multi-element associations in each of the six groups generated for the data set by the k-means MLA, including precious metal contents of interest (highlighted in Figure 6.4) and localities displaying these end-members, cross-referenced with Figures 6.4-6.9.*

***k*-means cluster**	**Major/Trace Associations**	**Metals of interest**	**Localities**
Group 1	U, Th, As, Pb, Bi	Ir, Ru, Rh, Pt	SG 1(S)
Group 2	SiO_2, Na_2O, K_2O, Se, Y, Zr, Nb, Ba	-	SG Silicic
Group 3	Fe_2O_3, Sc, V	Pt, Pd, Au, Cu	SG (C-N), 1(S) and RGR
Group 4	TiO_2, P_2O_5, K_2O, Zr, Hf, Rb, LREE	-	SG 4
Group 5	-	Moderate PGE	SG 1(S), (C-N), RGR, WR, ET
Group 6	MgO-Ni-Cr	-	ET

Serra Geral Silicic samples are defined by the Group 2 end-member (Figure 6.8c, Table 6.2), enriched in SiO_2, alkalis and, like Type 4, incompatible elements such as Zr and Rb (reflected in Figures 6.4-6.6). Silicic magmas likely evolved and differentiated in the crust over time to generate their more silica- and alkali-rich compositions (e.g., Bellieni et al., 1984; Garland et al., 1995; Milner et al., 1995) and may have acquired incompatible elements from the crust via extensive contamination (as per Simões et al., 2019). Precious (PGE and Au) and base metals (Ni, Cu and Co) are notably depleted in both Type 4 and Silicic samples (Figure 6.6 and 6.7, Table 6.2).

Both Southern and Central-Northern Serra Geral Type 1 samples occupy adjacent spaces within the centre of the embedding from Figure 6.5, which supports their more recent classification as one major magma-type (e.g., Gomes et al., 2018; Licht, 2018), despite historically being separated into Low-Ti and High-Ti, respectively, in prior studies (Fodor, 1987; Peate et al., 1992; Peate, 1997). However, their detailed multi-element geochemistry illustrates differences within their data structure, including a moderate difference in TiO_2 (Figure 6.3c; Appendix Table D1). MLA-based clustering assigned the Group 1 and Group 5 end-members in roughly equal proportions to Type 1 (Southern) (Figure 6.8c, Table 6.2), the former designation being exclusive to the locality. Group 1 occupies an embedding space defined by very high concentrations of U, Th, As, Pb, and Bi (Figures 6.6 and 6.7), elements all commonly concentrated in continental crust. Of the Serra Geral mafic lavas, Type 1 (Southern) is the most crust-contaminated magma-type and acquires much of its isotopic and lithophile geochemical characteristics from mid-upper crustal differentiation processes (e.g., Peate et al., 1992; Peate and Hawkesworth, 1996; Rocha-Júnior et al., 2013; Licht, 2018; Marques et al., 2018). Group 1 also represents lavas with the highest Ir, Ru and Rh concentrations.

Serra Geral Type 1 (Central-Northern) lavas express a consistent character through the MLA workflow, associated with Fe_2O_3, Sc, V, Cu, Pd and Au eigenvectors (Figure 6.4), and high concentrations of these elements in the far left of the t-SNE plots (on comparing Figures 6.6 and 6.8b). The Group 3 end-member, found primarily in Type 1 (Central-Northern) lavas, captures the majority of the multi-element signature from this association (Figures 6.8a-c, Table 6.2). Evidently, the main difference between the two Type 1 varieties is the metal

basket associated with their dominant end-members, given that their petrological definitions (Figure 6.3a-d) are reasonably consistent.

Rio Grande Rise and Walvis Ridge samples are generally less tightly defined in PCA and t-SNE spaces, but overall plot similarly to Serra Geral Type 1, appearing between clusters of Type 1 (Southern) and Type 1 (Central-Northern) in Figure 6.4b and below them as linear arrays in the embedding space (Figure 6.5). The two ridge lava types were classified primarily into Group 5 (Figure 6.8c), which is found in most localities in some amount and could thus be described as a background end-member, occupying the central embedding zone of high CaO and moderate Fe_2O_3, Na_2O, Al_2O_3, MnO, Sc, and V (i.e., z-score ≈ 0; Figures 6.4b-d, 6.6 and 6.7, Table 6.2). This end-member is poorer in REE than other localities (especially Serra Geral Type 4 and Silicic), denoting a less enriched mantle source (i.e., shallower, higher degree partial melts) and/or minimal crustal involvement (e.g., Le Roex et al., 1990; Gibson et al., 2005; Willbold and Stracke, 2006; Homrighausen et al., 2019). It should be noted that although Rio Grande Rise fits within similar multi-element clusters to Walvis Ridge, there is a degree of geochemical variability between the three IODP drillholes from which the lavas were sampled (Figure 6.2), with t-SNE and *k*-means clustering clearly segregating them in Figures 6.5 and 6.8a-c. Rio Grande Rise also features a significant amount of points classified as Group 3, which otherwise defines Serra Geral Type 1 (Central-Northern). However, these points plot as a separate sub-cluster of Group 3 in the centre of the embedding (Figures 6.8a-b) indicating differences between localities within the classification (Figure 6.8c).

Finally, Etendeka samples show a strong trend towards MgO, Ni and Cr eigenvectors (Figure 6.4b) and embedding sectors (Figures 6.5 and 6.6), a multi-element association also identified in NAIP lavas (Hughes et al., 2015; Lindsay et al., 2021; Chapter 5). Etendeka is the only locality to be classified in Group 6 (Figure 6.8c, Table 6.2), a multi-element end-member that likely represents high degree partial melts with predominant asthenospheric signatures (e.g., Gibson et al., 2005; Zhou et al., 2020). The literature suggests that many basalts from the Etendeka CFB were particularly enriched in MgO due to higher temperature melting (e.g., Jennings et al., 2017; Natali et al., 2017; Jennings et al., 2019; Beccaluva et al., 2020), producing different magma compositions to the entire

Paraná CFB sequence, which is less primitive in terms of MgO concentrations in comparison (Figure 6.3). The exclusivity of Group 6 to Etendeka and Groups 1-4 to Paraná and Rio Grande Rise suggests a strong asymmetry to melting-induced geochemical controls on either side of the Tristan plume-rift system, explored further in the following sections.

6.4.1.3. Onshore vs. offshore trends in the PELIP

The clustering of localities into distinct *k*-means groups indicates that, despite all PELIP lavas being attributed to melting imposed by the temperature anomaly from the Tristan plume, mutable source components exist in the corresponding parent magmas. This may reflect the rapidly shifting geodynamic conditions in the (now) PELIP during the Creataceous and the knock-on effect this has on melting processes. For the onshore portions, the High-Ti/Low-Ti split is thought by some authors to represent thermal zonation in the plume (i.e., deeper lavas produced in line with the plume head focus, and shallower lavas that are more peripheral, respectively) (e.g., Gibson et al., 1999; Zhou et al., 2020). This led to localised heterogeneous melting processes producing distinct multi-element signatures as a net effect (as per Rämö et al., 2016). In general, Low-Ti content represents crust-contaminated and High-Ti content represents less contaminated intracontinental magmas (e.g., Peate et al., 1992; Rocha-Júnior et al., 2013; Natali et al., 2017; Licht, 2018; Marques et al., 2018). However, there are many other processes affecting the final signatures including melt regime differences, mantle source composition and fractional crystallisation. All Type 1 (Southern) and Silicic onshore PELIP lavas exhibit geochemical evidence for crustal contamination, such as elevated heavy REE, Rb, U and Th, and low Nb and Ta (Pearce, 2008) (Figure 6.6). These signatures are not present in volcanic ridge or active hotspot lavas, suggesting that the processes or mantle components creating these melts were only present during the plume head CFB phase (c. 135 to 128 Ma) (e.g., Ussami et al., 2013; Graça et al., 2019). As the plume focus moved offshore into the new ocean basin, this CFB geochemical signature was no longer generated, reinforcing the link between Low-Ti lavas and the continental lithosphere and SCLM (Thompson and Gibson, 1991; Gibson et al., 2005).

There is a well-established asymmetric distribution in isotope and trace element geochemistry across the PELIP (e.g., Piccirillo et al., 1988; Peate and

Hawkesworth, 1996; Turner et al., 1996), and this together with greater preserved volumes of lava in Paraná and different sub-lithospheric thicknesses under both CFB regions (Gallagher and Hawkesworth, 1994) demands care in reconciling MLA-based interpretations with geodynamic processes. Despite a common regional rifting event in the opening of the South Atlantic, centred roughly on the Tristan plume, the multi-element geochemistry of PELIP lavas on the South American and African plates are different in terms of end-members identified using MLA (summarised in Figure 6.8) and PGE concentrations (Figure 6.9). In both Paraná and Etendeka, the High-Ti lava types are the products of partial melting of a mantle source enriched in incompatible elements and LREE, suggesting that they likely represents a deeper asthenospheric source undergoing low-degrees of partial melting under a thick lithosphere lid (Rämö et al., 2016; Jennings et al., 2019; Zhou et al., 2020). Similar signatures are observed in Walvis Ridge and contemporary Tristan da Cunha lavas (Gibson et al., 2005). Most of these have distinctive high $^{87}Sr/^{86}Sr$ and low $^{143}Nd/^{144}Nd$ signatures, interpreted as the Gough mantle component indicative of on-axis plume melts (Le Roex et al., 1990; Weaver, 1991; Willbold and Stracke, 2006; Homrighausen et al., 2019; Zhou et al., 2020), similar to Enriched Mantle I (EMI) OIB signatures (e.g., Zindler and Hart, 1986). In Paraná, the Gough isotopic component is not present in Serra Geral lavas (particularly Type 1) despite major and trace element similarities to OIB, implying that although representing plume-derived melts, these magmas may be from a more passive plume melting influence compared to Etendeka (Turner et al., 1996), and at the very least involve different mantle components to begin with. Paraná and Etendeka CFBs could consequently represent geochemical end-members of SCLM and asthenospheric material in intracontinental magmas, respectively (e.g., Stroncik et al., 2017; Beccaluva et al., 2020).

6.4.2. Precious metals

6.4.2.1. PGE variations throughout the PELIP

Throughout the PELIP, the concentrations and multi-element signatures of PGE and Au are distinctive in each locality (Table 6.2; Figure 6.9). In PCA biplots (Figures 6.4b-e) and embeddings (Figure 6.7), eigenvectors and/or high-concentrations for individual metals of the PGE and Au generally pair with each other, described herein. The MLA-based multi-element end-members defined by

precious metal concentrations in Table 6.2 are: Group 1 (high Ir, Ru, Rh and Pt), found in Serra Geral Type 1 (Southern); Group 3 (high Pt, Pd, Au, Cu), found in Serra Geral Type 1 (Central-Northern); and, to a lesser extent, Group 5 (moderate concentrations of Ir, Ru, Rh, Pt, Pd) found throughout the PELIP. This is further illustrated by the box-and-whisker plots in Figure 6.9, and classic PGE plots from Appendix D3-4. Groups 2, 4 and 6 have the lowest mean and minimum concentrations of Ir, Ru, Rh and Pd and comparable Pt concentrations to Group 5. They therefore represent geochemical end-members defined by PGE depletion, further to their major/trace element patterns in Table 6.2.

The balance between Ir-group PGE (IPGE – Os, Ir, Ru) and Pd-group PGE (PPGE – Rh, Pt, Pd) in a mafic rock generally reveals melting and mineralogical information about the parental magma. We have established that Serra Geral Type 1 (Southern) lavas are enriched in IPGE and Rh (i.e., a Group 1 signature). These metals are much more compatible during melting and require higher degrees of partial melting in order to be extracted from host phases (typically PGE alloys and platinum-group minerals; PGM) into a silicate magma (e.g., Barnes and Picard, 1993; Rehkämper et al., 1997; Alard et al., 2000; Helmy and Bragagni, 2017). PPGE (especially Pd) are more incompatible, so can be assimilated into melts from mantle phases at lower degrees of partial melting and at lower temperatures than IPGE (e.g., Holzheid et al., 2000; Maier et al., 2003a; Bockrath et al., 2004; Righter et al., 2008). The Group 1 link to As and Bi variability (Table 6.2) emphasises the segregation of Ir, Ru and Rh from the other PGE, given that phase relations have been established between Te-As-Bi-Sb-Sn (the TABS series) and Os-Ir-Ru-Rh in pyrrhotite in orthomagmatic sulphide systems (Mansur and Barnes, 2020). Modelling from Lindsay et al. (in review[a]) and Chapter 3 revealed the increase in partial melting in the mantle below the thinnest section of pre-Atlantic Brazilian lithosphere facilitated melting of not only IPGE-bearing sulphides and PGM/TABS phases in the SCLM, but spinel-group minerals in which IPGE have high partition coefficients (e.g., Capobianco and Drake, 1990; Barnes and Picard, 1993; Peach et al., 1994; Pitcher et al., 2009; Park et al., 2017). This may have boosted IPGE concentrations in Type 1 (Southern) magmas.

The Group 3 association of Pd, Au and Cu found in Serra Geral Type 1 (Central-Northern) lavas, could be indicative of a metasomatically-enriched

mantle source. Studies suggest that the SCLM and upper asthenosphere are enriched by fluids and partial melts released from down-going oceanic plates at subduction zones, effectively re-fertilising a region of the sub-continent (e.g., Mitchell and Keays, 1981; Borisov et al., 1994; Righter et al., 2008). The metals typically associated with this process include Pd, Au and Cu, some of the least compatible precious and base metals, which would preferentially be exsolved from a dehydrating slab (e.g., Woodland et al., 2002; Lorand et al., 2013; Tassara et al., 2017; Rielli et al., 2018; Wade et al., 2019). This process leads to the formation of base metal sulphides and accessory minerals (enriched in Pd, Au and Cu) within metasomatised SCLM. Magmas generated below this SCLM can melt these metasomatic mineral phases, incorporating their metal budget; this mechanism has been highlighted in many cratonic settings including Brazil (e.g., Zhang et al., 2008; Maier and Groves, 2011; Rocha-Júnior et al., 2013; Holwell et al., 2019; Choi et al., 2020). Data from PELIP lavas indicates degrees of partial melting around 22.5 % during plume head magmatism under a thinning lithosphere (Gibson et al., 2005), suitable for exhausting sulphides in melting sources. The presence of a metasomatic component in the melting SCLM has been identified as a key driver in near-surface precious metal content of intraplate magmas (e.g., Powell and O'Reilly, 2007; Tassara et al., 2017). A shallower melting imposed by the thinning Brazilian landmass may have allowed for higher degrees of partial melting of the SCLM and thus elevated Pd, Au and Cu in Serra Geral Type 1 (Central-Northern), in accordance with Lindsay et al. (in review[a]); Chapter 3. The link to Sc and V variability (Table 6.2) may further suggest significant metasomatic activity in rocks bearing a Group 3 signature, given the sensitivity of these elements to fluid interaction and redox conditions in the mantle (e.g., Chassé et al., 2018; Woodland et al., 2018 and references therein).

The more comparable Pt concentration levels through all localities (Figure 6.7; Appendix D3) and *k*-means clusters (Figure 6.9) is likely a representation of an absence of significant Pt anomalies. This may indicate that there are no Pt-enriched domains within the melt environment and therefore no increased abundance in Pt-bearing PGM. Whereas Os, Ir, Ru Rh and Pd (plus Au) each tend to form more element-specific mineralisation phases (Lorand et al., 2008 and references therein), Pt can be found in a wider range of hosts (i.e., Mss, Cu-sulphides and Pt-alloys) largely on account of its complex partitioning behaviour

under upper mantle conditions (Lorand and Alard, 2001). Therefore, low levels of Pt could be introduced to the magma from a wide variety of locations, contrasting with the spiked Ir-Ru-Rh and Pd-Au-Cu signatures from SCLM-derived Type 1 melts.

The fact that other localities in the PELIP do not have significant PGE enrichments further reinforces the ideas of Gibson et al. (2005), Rämö et al. (2016), Beccaluva et al. (2020), Lindsay et al. (in review) and Chapter 3 of this thesis that suggest variable melting processes under Paraná and the rest of the PELIP in response to lithospheric thinning drive variable incorporation of SCLM metals. The PGE signatures are unlikely to be inherited from the plume, otherwise they would be ubiquitous in melts in the region, especially in Rio Grande Rise and Walvis Ridge, which are distal to the SCLM. Modelling from Chapter 3 directly attributed PGE enrichment in Serra Geral Type 1 lavas to enhanced degrees of partial melting exhausting SCLM sulphides and spinel. It should be noted that Rio Grande Rise samples were mainly clustered into Group 3 (Figure 6.8a-c), the end-member otherwise typifying Serra Geral Type 1 (Central-Northern) lavas and their distinctive enrichment in Pd, Au and Cu. The Rio Grande Rise samples occupy a small population of Group 3 points in the very centre of the embedding space (Figure 6.5), where Pt, Pd, Au and Cu concentrations are moderate to low (Figure 6.7). As such, whilst the majority of Rio Grande Rise lava major and trace element concentrations are similar enough to Type 1 (Central-Northern) to merit their classification in a single end-member cluster, the high Pd-Au-Cu association is unique to the continental lavas alone. This is an important feature in the argument for SCLM involvement in metallogenesis, as whilst we have magmas generated to feature similar multi-element signatures, the connection to the Brazilian and African cratons must drive the individual precious metal deviations expressed. This may also potentially reflect different metal inheritance or “pre-conditioning” on either side of the (current) Atlantic, as described by Lindsay et al. (in review) and Chapter 3 for the Brazilian craton and by Hughes et al. (2015) across the North Atlantic craton and NAIP.

6.4.2.1. Implications for geodynamics and metallogenesis

With a focus on PGE, Cu and Au, it is evident that specific stages in PELIP development are prone to higher metal concentrations than others. The Serra Geral Type 1 (Southern) and Type 1 (Central-Northern) samples in particular are

the major hosts for elevated PGE contents through the region; Ir-Ru-Rh-Pt for the Southern magma-type and Pt-Pd-Cu-Au for the Central-Northern magma-type. In terms of processes controlling these differences, by combining information from all aspects of the MLA workflow and data from associated literature, we can suggest a working model for metallogenesis in the PELIP, centred around the temporal changes to regional multi-element geochemistry and PGE concentrations in this new data set. This builds upon Lindsay et al. (in review) and Chapter 3 of this thesis by considering localities outside Paraná (i.e., the broader PELIP).

There have been three geochemical/geodynamic developmental stages in the PELIP: (i) continental lavas in Paraná and Etendeka, featuring the zoned plume head and High/Low-Ti bimodality; (ii) Rio Grande Rise and Walvis Ridge plume tail hotspot trails, featuring the absence of crustal contaminated components; (iii) separated Tristan and Gough trails representing two 'flavours' of concurrent mantle plume magma and the cesstion of South American plate volcanism (Figure 6.1a-b). The relative timing of eruptive sequences in Paraná is complicated given the high flux rates (Bellieni et al., 1984; Thiede and Vasconcelos, 2010; Licht, 2018; Rossetti et al., 2018), but overall, Type 4 progresses stratigraphically in most sequences to Type 1 (Central-Northern) in the north-west, whilst Type 1 (Southern) and Silicic lavas erupted in the south-east of the basin. Their geochemical characteristics (Figures 6.3a-d, 6.4b-e and 6.5) and the cluster designation of each magma-type (Figure 6.8c) are distinct enough to be considered as four individual but synchronous geochemical processes between 135 and 134 Ma. Etendeka lavas erupted at a similar time to Type 1 (Southern) at around 134 Ma, and Rio Grande Rise and Walvis Ridge lavas erupted once the rifting had progressed to an oceanic setting from 128 Ma until the Tristan-Gough bifurcation at ~ 70 Ma (Figure 6.1a-b). The overall transition from thick to thin continental lithosphere and finally to oceanic lithosphere is the control on all magma geochemical variability from a single plume source, and we suggest that the PGE distribution varies as a function of this.

The High-Ti lavas of Paraná were generated by small degrees of melting as the plume head decompressed beneath the thickest part of the Brazilian lithosphere. Despite being enriched in REE elements as per Enriched Mantle I

(EMI) OIB geochemistry, this melting regime (deeper asthenosphere, low degree partial melting) did not allow PGE acquisition on Type 4 magma ascent due to inefficient sulphide exhaustion in the mantle source (Rämö et al., 2016; Lindsay et al., in review; Chapter 3). Geographically closer to the rift-zone, and on the axial sections of the plume head, Type 1 magmas were generated at shallower asthenospheric/SCLM depths, and higher degrees of partial melting (Beccaluva et al., 2020), which allowed for the melting and integration of SCLM PGE-bearing suphides into magmas. Isotopic signatures from such melts can often be matched to cratonic xenolith compositions representative of the local SCLM (e.g., Gibson et al., 2005 and references therein). Type 1 (Central-Northern), from slightly thicker lithosphere, exceeded melting conditions for PPGE sulphides (including Au and Cu). Type 1 (Southern), adjacent to the incipient ocean opening and thus under thinner lithosphere, incorporated even shallower and higher degree partial melts and IPGE-bearing sulphides and/or spinel-group minerals to boost their concentrations in line with the Group 1 end-member (Lindsay et al., in review). On the African plate, Etendeka parent magmas were extrated under similar plume and asthenospheric conditions, but evidence suggests that (like Serra Geral Type 4 magmas) the involvement of deeper, hotter and more plume-derived melts in their genesis (e.g., Marsh et al., 2001; Rämö et al., 2016; Jennings et al., 2019) did not facilitate incorporation of PGE from the shallower SCLM. An alternative explanation could be simply that SCLM components involved in Type 4 and Etendeka melts were not significantly pre-enriched, leading the resulting net multi-element geochemistry to be dominated by the asthenospheric components. From their similar chalcophile concentrations, the sulphide saturation histories of each region appear broadly equivalent (i.e., Appendix D3), so it is unlikely that this process differentiated the precious metal signatures.

Rio Grande Rise and Walvis Ridge lavas feature the background/non-enriched signatures also common in the Type 1 lavas (i.e., Groups 2 and 5; Figure 6.8), with the lack of PGE-rich end-members reflecting the absence of SCLM input in offshore melting (e.g., Gibson et al., 1999; Hoernle et al., 2015; Zhou et al., 2020). Whilst early oceanic PELIP lavas show isotopic evidence for a small component of SCLM present in melts (e.g., high $(La/Nb)_n$, low εNd and $^{206}Pb/^{204}Pb$), this has been attributed to contamination by delaminated cratonic slivers from continental break-up in the sub-oceanic melt column (Douglass et

al., 1999; Le Roux et al., 2002; Gibson et al., 2005). More recent enriched oceanic ridge lavas with isotopic compositons unlike Brazilian or African SCLM components (high $^{206}Pb/^{204}Pb$ and $^{87}Sr/^{86}Sr$; Gibson et al., 2005) have instead been linked to a deep mantle source and are thus more akin to classic EMI signatures (e.g., Wilson, 1992). The incorporation of SCLM remnants in westernmost Rio Grande Rise magmas are potentially reflected in their multi-element resemblance to onshore Type 1 lavas in terms of *k*-means cluster distribution (i.e., the ubiquitous Group 5; Figure 6.8c), but this is restricted purely to major and trace element similarities, not precious metals.

In summary, the manner in which different melts are generated directly affects resultant magma multi-element geochemistry and, in particular, PGE concentrations, as demonstrated across the PELIP. The “sweet spot” for PGE enrichment in magmas across the region appears to be linked to late-stage Serra Geral Type 1 lavas. This is demonstrated to be a product of the imminent separation of South America and Africa, where lithospheric un-lidding promoted higher degrees of partial melting and therefore incorporation of a greater proportion of SCLM-derived metals (whether through direct partial melting of the SCLM itself and/or through contamination; Chapter 3). The geochemical signature increasingly found in PELIP hotspot trail lavas through time denote a more prevalent involvement of the Tristan-Gough plume component, accompanied by the waning of SCLM-derived components as the South Atlantic opened. This is similar to the observation that the metal basket of the NAIP changed spatially and temporally as the North Atlantic rifted (Hughes et al., 2015; Lindsay et al., 2021).

6.4.3. Comparison with the Icelandic plume

The extra step of recreating the input parameter set-up from the NAIP study in Chapter 5 for the PELIP set has enabled us to directly compare the interpretations for lavas derived from the two mantle plumes associated with the opening of the Atlantic Ocean.

Broadly, the multi-element associations for major and trace elements in PCA biplots for both regions are similar – the two persistent associations are MgO-Ni-Cr and Fe_2O_3-TiO_2-Cu (Figure 6.10b and its inset NAIP eigenvector arrays, and Figures 6.11a-b). However, PGE distribution differs between the

regions, particularly for Ir-Ru-Rh eigenvectors in the highest-order PCs (i.e., the majority of data set variability). In the NAIP, these metals are always associated with MgO-Ni-Cr in dimensionality reduction results, with particularly high multi-element concentrations found in Greenlandic onshore lavas (Lindsay et al., 2021). In the PELIP, Ir, Ru and Rh variabilities are rarely associated with the MgO-Ni-Cr group eigenvector(s), even at lower-order PCs (Figures 6.10b-d). For the PELIP, the highest PGE concentrations are not associated with the two major multi-element end-members, which is logical given that the Serra Geral Type 1 hosts are neither the highest-Ti localities (like Type 4) or the highest-MgO localities (like Etendeka and the ridges). Thus, PGE variability in the PELIP decouples from the trends established in the NAIP, immediately differentiating the metallogenic characters of the two regions. We know from MLA results using all PELIP variables that PGE enrichment coincides with distinct sets of lithophile indicators, differentiating the processes that generate high Ir-Ru-Rh lavas.

In the Lindsay et al. (2021) study (i.e., Chapter 5), heterogeneous Pt/Pd variability throughout the NAIP reinforced prior work suggesting that the lithospheric keels around continent edges (i.e., modern day Scotland and Greenland) were variably enriched in metals added through metasomatic processes (Hughes et al., 2014 and references therein). This gives rise to notable PGE-bearing magmatic deposits on both sides of the plume-rift system in the Isle of Rum (Scotland) and the Skaergaard Complex (Greenland) (e.g., Andersen et al., 1998; Pirrie et al., 2000; Power et al., 2000; Nielsen et al., 2014; O'Driscoll et al., 2014; Andersen et al., 2017). In the PELIP, at least for Pd concentrations, enrichment associated with the Group 3 end-member (Figure 6.9) appears much more consistent and focused in a single locality, Serra Geral Type 1 (Central-Northern).

Models of melting beneath the Brazilian craton contained within Chapter 3 and Rämö et al. (2016) revealed that by transitioning to shallower melting depths from the deeper-sourced (i.e., garnet lherzolite zone) Type 4 magmas and into the spinel lherzolite zone, an increased degree of partial melting can effectively sequester Pd-bearing metasomatic sulphides from the SCLM. Overall, Pd distribution is described more concisely by the MLA approach in the PELIP compared to the NAIP, even with reduced variable information. No major PGE-bearing ore bodies have been discovered in the Paraná Basin at the time of

writing, but judging by the signatures in contemporaneous lavas, from a Mineral Systems perspective, intrusive bodies akin to Type 1 (Southern) or (Central-Northern) composition may prove fruitful for mineral exploration. A recent study by de Farias and Filho (2021) recognised relatively localised Ni-Cu-PGE mineralised intrusions related to an enriched Meso-Proterozoic SCLM source from the Amazon craton (north-west of the Paraná CFB), an encouraging development that supports a significantly metal-enriched and long-lived SCLM beneath the craton.

This chapter further reiterates a finding from the NAIP study – Pt is overall a sporadically distributed metal in comparison to the other PGE. Its disordered placement in embedding plots (Figures 6.7 and 6.11), more even enrichment in all PELIP multi-element signatures (Figure 6.9) and overall decoupling from major eigenvector associations (Figures 6.4b-e and 6.10b-d) illustrates this behaviour. By recognising such distribution in the PELIP, via both full and reduced data set MLA results, it supports the true “nuggety” geochemistry of Pt (Section 6.4.2.1) and genuine heterogeneity of SCLM metal enrichment is persistent through different plume-rift systems.

Overall, the PELIP has a much more distinctive locality-based classification system, and MLA-based clusters generally support separate localities having unique geochemical signatures. In contrast, in the NAIP all three *k*-means clusters generated for the data set can be found in all five localities, indicating that each sample location exhibits a degree of similarity with the others and no single area has its own exclusive signature. This of course does not extend to Pt and Pd, which behave independent from all other variables in the NAIP as per Chapter 5. Comparing this to the PELIP, four of the six optimum *k*-means clusters generated for the full data set (51 variables) are exclusive to a single locality, a fifth is almost wholly found in Serra Geral Type 1 (Central-Northern) and the sixth as a background end-member (Figures 6.8b-c; Table 6.2). Even when using *k*=3 and the PCs of eleven variables (see Appendix D10 and D11 for selected reduced-variable clustering results), the model best-suited to the NAIP data set, PELIP localities cluster far more neatly into three groups than the NAIP (roughly correlated to Low-Ti, High-Ti and anomalously high PGE), despite a smaller sample set. This illustrates that overall the PELIP is asymmetrical with stronger and more distinct multi-element signatures in each sample locality (i.e.,

end-member distribution in Figure 6.8c), whilst the NAIP is more symmetrical with more geochemical similarity in each locality.

Despite numerous differences, we can draw important similarities between the two plume-rift localities as PGE metallogenic systems. East Greenland (i.e., lava samples from the region near the Skaergaard Complex), where many of the highest multi-element PGE concentrations were found in the Chapter 5 and the original investigations (Lightfoot et al., 1997; Philipp et al., 2001; Momme et al., 2002; Momme et al., 2003; Hughes et al., 2015), is the geographic equivalent of the Serra Geral Type 1 lavas in the PELIP. Both localities are west of the rift, constitute some of the youngest continental lavas, and feature notable PGE enrichments, with the specific precious and base metal basket per locality varying between the north and south. In this sense, there appears to be a continent-edge (i.e., newly rifted craton margin) control on PGE enrichment (e.g., Gibson et al., 1999; Hughes et al., 2015; Hughes et al., 2017). However, as demonstrated in this chapter, the PELIP does not mirror this enrichment in the east and Etendeka lavas are consistently different from all onshore Paraná lavas through all MLA results (best summarised in Figure 6.8c), particularly in PGE concentrations. In contrast, Scotland and Ireland in the NAIP (the northern geographic equivalents of Etendeka onshore lavas) have similar multi-element geochemistry to Greenlandic lavas (Lindsay et al., 2021; Chapter 5) and also host PGE-bearing intrusions in the Isles of Rum, Mull and Skye (e.g., Andersen et al., 2002).

Evidently, the subtle differences in plume-rift architecture significantly influence regional geochemistry despite contemporary lavas being erupted very close together before drifting to their current geographic position. The notable missing EMI isotopic component through much of the Serra Geral lavas plays a key role in PELIP heterogeneity, by emphasising the more passive plume melting regime in comparison to the rest of the region. This may be a result of (i) changes in mantle sources as a response to differential lithospheric un-lidding; (ii) markedly different cratonic composition or structure in the melting environment; or (iii) heterogeneous melting sources. The marked decrease in precious metal content as the plume progressed further from the continent in both the PELIP and NAIP serves as substantial evidence that metal baskets are inherently linked to SCLM input in transitional continent-ocean plume settings.

6.5. Conclusions

A widespread account of PGE concentrations across the PELIP using a combined geochemical-MLA workflow has illustrated the importance of continent-edge geodynamic conditions in controlling the metal basket of plume-derived intraplate melts. Dimensionality reduction and multi-element analyses describe distinct signatures for each of the PELIP sample localities.

1. PGE are elevated in the Serra Geral Type 1 (Southern) and Type 1 (Central-Northern) lavas in Paraná, with each having their own set of associated metals – Ir-Ru-Rh-Pt for the former, Pt-Pd-Au-Cu for the latter. These enrichments are driven by enhanced degrees of partial melting attributed to shallowing melt foci in response to lithospheric thinning between 134 and 128 Ma.
2. PGE enrichment is asymmetrical across the PELIP, as the Etendeka equivalents of the Type 1 lavas are notably depleted in all PGE, which is attributed to the dominance of deeper, hotter but lower degree plume-derived partial melts instead of the passive melting of SCLM material under Paraná.
3. The western and eastern oceanic ridges in the PELIP show multi-element similarities to their onshore equivalents when considering major and trace elements, but lack high concentrations of precious metals, which reinforces the hypothesis that PGE are being supplied to Serra Geral Type 1 magmas by the melting of SCLM under a progressively thinning Brazilian lithosphere.
4. On comparing the Tristan plume system to the similar Icelandic plume system (from which the test of the MLA workflow was conducted), despite recognising some multi-element associations common in both regions, PGE enrichment is different in each. The Icelandic system does not feature asymmetry in PGE enrichment either side of the Atlantic Ridge. Therefore we conclude that, whilst SCLM enrichment is complex and variable in a plume-rift mineral system, there are common processes for how these metals are acquired.

Chapter 7

Mantle plumes and PGE Mineral Systems – using machine learning to explore patterns in global metallogenesis

Chapter Summary

The final research chapter of this thesis presents a global perspective on the PGE geochemistry of plume-derived lavas, and incorporates the localities discussed throughout Chapters 3-6 in addition to new data from ocean islands and oceanic plateaus. The chapter synthesises many of the theories discussed throughout the previous chapters within a single geochemical and machine learning investigation. Three major subdivisions of the data set are covered; oceanic plume settings, transitional plume settings (i.e., from continental rifting through to the formation of ocean lithosphere; Chapters 5 and 6) and finally all continental and oceanic localities simultaneously. The MLA workflow from Chapter 5 is used to reduce dimensionality in the largest sample set of the thesis, and cluster global plume-derived geochemistry to identify major metallogenic trends inherent to mantle plume environments. In oceanic plume settings, the degree of partial melting in the mantle source largely controls the precious metal budget of associated intraplate lavas. In transitional plume settings, the lavas erupted beneath the thinnest continental lithosphere in rifting systems yield the highest PGE concentrations – an effect of variable degrees of partial melting and sub-continental lithospheric mantle magma enrichment. Crucially, in the final data set, encompassing all settings featured in the oceanic and transitional data sets, the effect of continent-edge metal acquisition outweighs oceanic enrichments. These findings are applied to a framework for intraplate PGE Mineral Systems in order to illustrate patterns in metallogeny from mantle-derived magmatic environments such as Large Igneous Provinces (LIP).

7.1. Introduction

The PGE are amongst the rarest and most valuable metals on Earth (McDonough and Sun, 1995). In the past, these six metals (Os, Ir, Ru, Rh, Pt and Pd) were primarily used in catalytic converters, but future demand has grown and diversified significantly with the advent of PGE-dependent hydrogen fuel development, electronics, electrics, batteries, data storage and magnet technology (e.g., Lightfoot, 2007; Peplow, 2020; Whittemore et al., 2020). The supply of PGE is of increasing importance to future economies and understanding their metallogenesis on a global scale is of great interest within the fields of geochemistry, mining and energy science.

The scarcity of PGE at the surface is chiefly a result of strong sequestration of heavy metals, including Fe, Ni and the PGE, into the Earth's core during its formation in the first ~60 Myr of the planet's history, as revealed by Hf-W and Os isotope chronology (e.g., Kleine et al., 2002; Righter, 2003; Kleine et al., 2004; Kleine et al., 2009; Walker, 2009; Humayun, 2011). Due to their highly siderophile nature, and unlike the other, more abundant metals initially drawn into the core, the majority of the planet's PGE budget remained in the core (Holzheid et al., 2000; Mann et al., 2012; Siebert et al., 2012). This left a highly PGE-depleted Primitive Upper Mantle (PUM) with respect to chondritic values (McDonough and Sun, 1995). Whilst the stock of PGE in the Silicate Earth was slightly replenished by later heavy bombardment by meteorites, modern day mantle values are still 0.1-0.00001 times chondritic values (e.g., Kimura et al., 1974; Maier et al., 2009; Walker, 2009; Kleine, 2011; Rubie et al., 2011; Willbold et al., 2011).

Despite their rarity, PGE have been sourced from the Earth interior and deposited into ore deposits in the crust, typically as Ni-Cu-PGE orthomagmatic intrusive complexes (e.g., Naldrett, 2004; Maier, 2005; Lightfoot, 2007; Ernst, 2010; Maier and Groves, 2011). The largest PGE producers in the world, South Africa and Russia, mine 80 % of the world's PGE reserves from the Bushveld Complex and Noril'sk Talnakh, respectively (Thormann et al., 2017; Mudd et al., 2018). Both of these localities sit within LIP, which occur in intraplate settings and are thought to have formed following significant melting of the asthenosphere beneath the continental lithosphere to produce voluminous Continental Flood

Basalts (CFB) and associated intrusions (Coffin and Eldholm, 1994; Sobolev et al., 2009; Sharkov et al., 2017). Whilst shallower crustal processes are essential in forming mineable ore bodies, the metal content of an intraplate magma inevitably plays an important role in the delivery of metals from the mantle to the surface as a complete Mineral System (Wyborn et al., 1994; McCuaig et al., 2010; Naldrett, 2010; Barnes et al., 2016).

There are two common geodynamic features persist across these deposits; (i) their emplacement within continental landmasses far from contemporaneous tectonic boundaries, and (ii) the involvement of intraplate magmatism in their generation alongside CFB provinces (Naldrett, 1997; Maier, 2005; Pirajno and Santosh, 2015). From a Mineral Systems perspective (e.g., McCuaig et al., 2010), the inherent link between CFB provinces, intraplate magmas, and Ni-Cu-PGE deposits is clear. This geodynamic setting may provide a means to boost magma precious metal fertility at source, as well as pathways and agents by which to upgrade magmas into ore deposits in the upper crust. Intraplate magmas are frequently associated with mantle plumes, buoyant sectors of the silicate Earth that are generated from mineralogical or mechanical instability at the chemically and physically heterogeneous core-mantle boundary (CMB) (e.g., Morgan, 1971; Morgan, 1972; Klosko et al., 2001; DePaolo and Manga, 2003; Hawkesworth and Scherstén, 2007; Day, 2013; Ryabchikov and Kogarko, 2016). Some plumes may interact with and incorporate material from the Ni and PGE-rich outer core contained within the CMB layer, although this feature is oft-debated (Brandon et al., 1998; Chazey and Neal, 2004; Brandon and Walker, 2005; Cagney et al., 2016; Rizo et al., 2019). As a result, intraplate magmas can exhibit a wide range of compositions influenced by the chemistry of mantle sources (Zindler and Hart, 1986; Hart et al., 1992; Stracke et al., 2005; Cagney et al., 2016) *and* the lithosphere (McKenzie and White, 1989; White and McKenzie, 1995; Prytulak and Elliott, 2007; Zhang et al., 2008), in addition to the more controversial contribution of deep mantle and outer core material.

7.1.1. Plume geodynamics and precious metal acquisition

The physical origin of plumes have regularly been detected using seismic tomography, which illustrates a connection to the edges of Large Low Shear Velocity Provinces (LLSVPs) in the CMB interface (Richards et al., 1988; Christensen and Hofmann, 1994; Torsvik et al., 2006; Burke et al., 2008; Davies

and Davies, 2009; Deschamps et al., 2011). LLSVPs are thought to represent the amalgamated remnants of subducted oceanic lithosphere, core melts, and ambient lower mantle (Shannon and Agee, 1998; Vinnik et al., 1998; Becker and Boschi, 2002; Jellinek and Manga, 2004; Lay et al., 2004). Plumes act as significant thermal anomalies (often up to 100-200°C higher than the surrounding upper mantle; McKenzie and White, 1989) as they travel towards the surface, and can induce partial melting in the asthenosphere and lowermost lithosphere to generate intraplate magmas independent of tectonic boundaries (Campbell and Griffiths, 1990; Griffiths and Campbell, 1990; Courtillot et al., 2003).

If mantle plumes rise to the base of the continental lithosphere, they impart different melting conditions than under thinner oceanic lithosphere, which can directly influence what is melting, how much, and at what depths. This is most evident in the systematically variable geochemistry of lavas generated from transitional plumes that initiate magmatism underneath continental lithosphere prior to large-scale rifting events, and eventually generate melts beneath oceanic lithosphere, such as the Tristan and Icelandic plumes (McKenzie and White, 1989; Peate, 1997; Gibson et al., 2005; Storey et al., 2007; Hughes et al., 2015). Thicker (i.e., continental) lithosphere imposes smaller degree asthenospheric melts under higher pressures (McKenzie and Bickle, 1988; Ellam, 1992; Stein and Stein, 1992; Arndt et al., 1993; Turner et al., 1996) but also present opportunities for contamination of plume-derived magmas with continental material, enriched in rare earth elements (REE) and other lithophile elements, imparting distinctive isotopic signatures (Gibson et al., 1999; Zhang et al., 2008). Furthermore, ancient cratons that have survived millions or billions of years of destructive tectonism host an SCLM that, on account of previous metasomatic activity throughout geologic history, are often enriched in rare metals including PGE, Au and Cu (Woodland et al., 2002; de Wit and Thiart, 2005; Powell and O'Reilly, 2007; Maier and Groves, 2011; Griffin et al., 2013; Lorand et al., 2013; Rocha-Júnior et al., 2013). Often, these metals are originally contained within subducting lithosphere, which dehydrates, releases fluids and along with it scavenges the more volatile and/or incompatible elements to then deposit in the SCLM (Wilson et al., 1996; Alard et al., 2011; Rielli et al., 2018; Wade et al., 2019). Recent studies link high metal concentrations in magmatic bodies and lavas to incorporation of pre-enriched mantle (Kepezhinskas et al., 2002; Hughes

et al., 2015; Tassara et al., 2017; Holwell et al., 2019; Wade et al., 2019; Z. Wang et al., 2020a), and this hypothesis forms a cornerstone of our study.

Further, it cannot be ruled out that the core may act as a metal reservoir to plumes of deep origin. Oceanic intraplate magmas occasionally exhibit rare Os and W isotope anomalies that are notoriously difficult to pinpoint but consistent with incorporation of core material at the CMB (Brandon and Walker, 2005; Hawkesworth and Scherstén, 2007; Lorand et al., 2008; Rizo et al., 2019). It is estimated that the addition of as little as 0.5 % of outer core material into a plume-derived melt could boost Os concentrations (the most compatible of the PGE) by 4 times, given that the core is 100-300 times more enriched in PGE (Andersen et al., 2002; Brandon and Walker, 2005). Controversially, it is plausible that plumes that do not interact with continents can gain anomalous metal baskets elsewhere (Day et al., 2013; Cagney et al., 2016). Subsequent crustal processes ultimately form ore deposits from intraplate magmas, regardless of from where source enrichment is derived. These processes range from external sulphur input to drive S-saturation, to assimilation and fractional crystallisation (AFC) or magmatic-hydrothermal reactions with country rocks and crystallised intrusions themselves.

Plume-derived lavas share a geochemical and isotopic ‘genetic fingerprint’ with associated intrusive bodies (Mitchell et al., 1999; Ledevin et al., 2012), and are more easily sampled given their surface exposure throughout LIP, hence their utility in investigating plume systems. Furthermore, lavas are the fine-grained products of quenched liquids, differentiating them from cumulate intrusive rocks in which the cumulate is not directly representative of parent magma compositions. Thus, information gleaned from the study of lava samples can be more readily used to imply the geochemical properties of parent magmas that fed potentially ore-hosting plume-derived CFB.

Intraplate magmas inherit their highly variable geochemical and isotopic signatures from a plethora of melt components attributed to various mantle regions (e.g., Zindler and Hart, 1986). Whether of continental or oceanic affinity, the multi-element geochemistry of plume-derived lavas record the net effect of multiple geochemical processes at work within intraplate melt generation (Hastie et al., 2016; Harrison et al., 2017) that can then be upgraded to ore-grade concentrations in the crust. By interrogating a large suite of fresh, unaltered (i.e., geologically young or active) plume-derived lavas from around the world, this

chapter investigates the following hypotheses (introduced in Chapter 1) that follow on from regional studies in Chapters 3 through 6:

1) Magmas from oceanic plume settings have distinct PGE signatures related to their geophysical properties [H1].
2) PGE enrichment in magmas is linked to the continental portion of transitional continent-ocean plume systems [H2].
3) Magmas from continental vs. purely oceanic plumes have markedly different PGE enrichment signatures [H3].

Herein, we use an integrated geochemical and machine learning workflow to draw out as much information from our data sets as possible, contributing to the use of multivariate techniques as exploratory tools in geosciences.

7.1.2. Machine learning as a global geochemical tool

Machine learning is an umbrella term for data science techniques that allow for pattern recognition, prediction and classification in large data sets, which makes such methods of data analysis particularly relevant in the field of geochemistry. Often, geochemical studies produce data sets with over 50 elemental concentrations for hundreds of samples, and these can be combined with data from similar studies to generate high-dimensional data sets, thanks to advances in database sharing capabilities within the scientific community. Using machine learning algorithms (MLA) to investigate these large data sets is increasingly applicable and accessible. By using MLA for geochemical data interrogation, we are able to summarise complex trends that are difficult for a human analyst to resolve, allowing us to discuss and interpret multi-element signatures in a robust, resourceful and efficient manner.

This chapter interrogates a large bulk geochemical data set (n ~ 500) from a variety of locations, geodynamic settings and ages, combining new analyses of plume-related lavas (from this study) and multiple sets of published data for similar rocks from the literature. We use a novel machine learning workflow developed in Chapter 5 and Lindsay et al. (2021) for analysing large geochemical data sets, which includes Principal Component Analysis (PCA), t-Distributed Stochastic Neighbour Embedding (t-SNE), and *k*-means clustering. Here, we supplement the workflow with Uniform Manifold Approximation and Projection (UMAP), which works similarly to t-SNE and allows us to reinforce dimensionality

reduction outcomes. The workflow has been successfully tested on two smaller geochemical data sets (both in terms of included variables and/or sample numbers) contributing significantly to our understanding of plume-derived metallogenesis (Chapters 5 and 6). In contrast, in this chapter we use MLA to interrogate lavas from multiple intraplate settings simultaneously in a single model to draw out significant multi-element trends within or between localities.

7.2. Materials and Methods

7.2.1. Data

7.2.1.1. Samples

Our data catalogue for intraplate lava bulk geochemistry comprises data from previous studies (including some by the authors) and a small set of new data for the Hawaiian and Icelandic plumes. Table 1 summarises the localities included in this chapter, with an account of sample numbers, original studies (when applicable), the associated plume, and the particular hypotheses they contribute towards within the context of this study [H1, H2 and H3]. These localities are shown geographically in Figure 7.1. The sample set includes onshore and offshore flood basalts, ocean island basalts and offshore IODP/DSDP drill cores (collected from the IODP Repository in Bremen, Germany) of hotspot trails from prominent plumes. All samples are tholeiitic basalts to transitional basanites (excluding five andesites included in the Tristan set), to allow for like-for-like comparison across the sub-studies.

7.2.1.2. Localities

We have sub-divided the data into three groups (i.e., Table 1) to address the factors associated with each plume setting, as per the hypotheses being tested. The oceanic plume data set [H1] focuses on islands from oceanic hotspot trails (the Canary Islands and Hawaiian plumes) and oceanic large igneous provinces or OLIP (the Kerguelen plateau and two islands within the Ontong-Java province). We also use data from oceanic sections of transitional plume settings, namely the Tristan and Icelandic plumes. The Canaries and Hawaiian chains are age-progressive ocean islands comprised primarily of ultramafic to mafic OIB lavas, the geochemistry of which vary spatially and temporally. Kerguelen and

Ontong-Java (represented here by the islands of Malaita and Makira) comprise huge expanses of oceanic flood volcanism produced by plume head thermal anomalies and large degrees of partial melting of the oceanic lithospheric mantle and asthenosphere. All cases represent plume-derived lavas that lack continental interaction, allowing us to examine the PGE signatures acquired solely from the asthenospheric mantle and, potentially, the outer core.

Table 7.1 - *Summary of localities (from new samples and thesis chapters) included in the global plume study, broken down into oceanic and transitional data sets in reference to the three testable hypotheses in this chapter (H1, H2, H3). Con. – continental, oc. – oceanic, BPIP includes Skye and Mull. * - constituents of chapters taken from literature data, see relevant Chapter for sources.*

Locality	Province	Plume	H*	*n*	Data
Oceanic					
El Hierro	Canaries	Canaries	1, 3	7	Chapter 4*
La Palma	Canaries	Canaries	1, 3	13	Chapter 4*
Tenerife	Canaries	Canaries	1, 3	26	Chapter 4
Haleakala	Hawaii	Hawaiian	1, 3	6	Crocket (2002b)
Kilauea	Hawaii	Hawaiian	1, 3	12	This chapter
West Maui	Hawaii	Hawaiian	1, 3	2	Crocket (2002b)
Kerguelen	Kerguelen	Kerguelen	1, 3	22	Chazey & Neal (2005)
Iceland (1)	NAIP (oc.)	Icelandic	1, 3	9	This chapter
Makira	Ontong-Java	Louisville	1, 3	4	Ely & Neal (2003)
Malaita	Ontong-Java	Louisville	1, 3	8	Ely & Neal (2003)
Transitional					
Paraná	PELIP (con.)	Tristan	2, 3	85	Chapter 3
Etendeka	PELIP (con.)	Tristan	2, 3	11	Chapter 6
RGR	PELIP (oc.)	Tristan	1, 2, 3	14	Chapter 6
Walvis Ridge	PELIP (oc.)	Tristan	1, 2, 3	8	Chapter 6
W. Greenland	NAIP (con.)	Icelandic	2, 3	48	Chapter 5*
E. Greenland	NAIP (con.)	Icelandic	2, 3	33	Chapter 5*
BPIP	NAIP (con.)	Icelandic	2, 3	51	Chapter 5*
E.Greenland	NAIP (oc.)	Icelandic	1, 2, 3	97	Chapter 5*
Iceland (2)	NAIP (oc.)	Icelandic	1, 2, 3	30	Chapter 5*

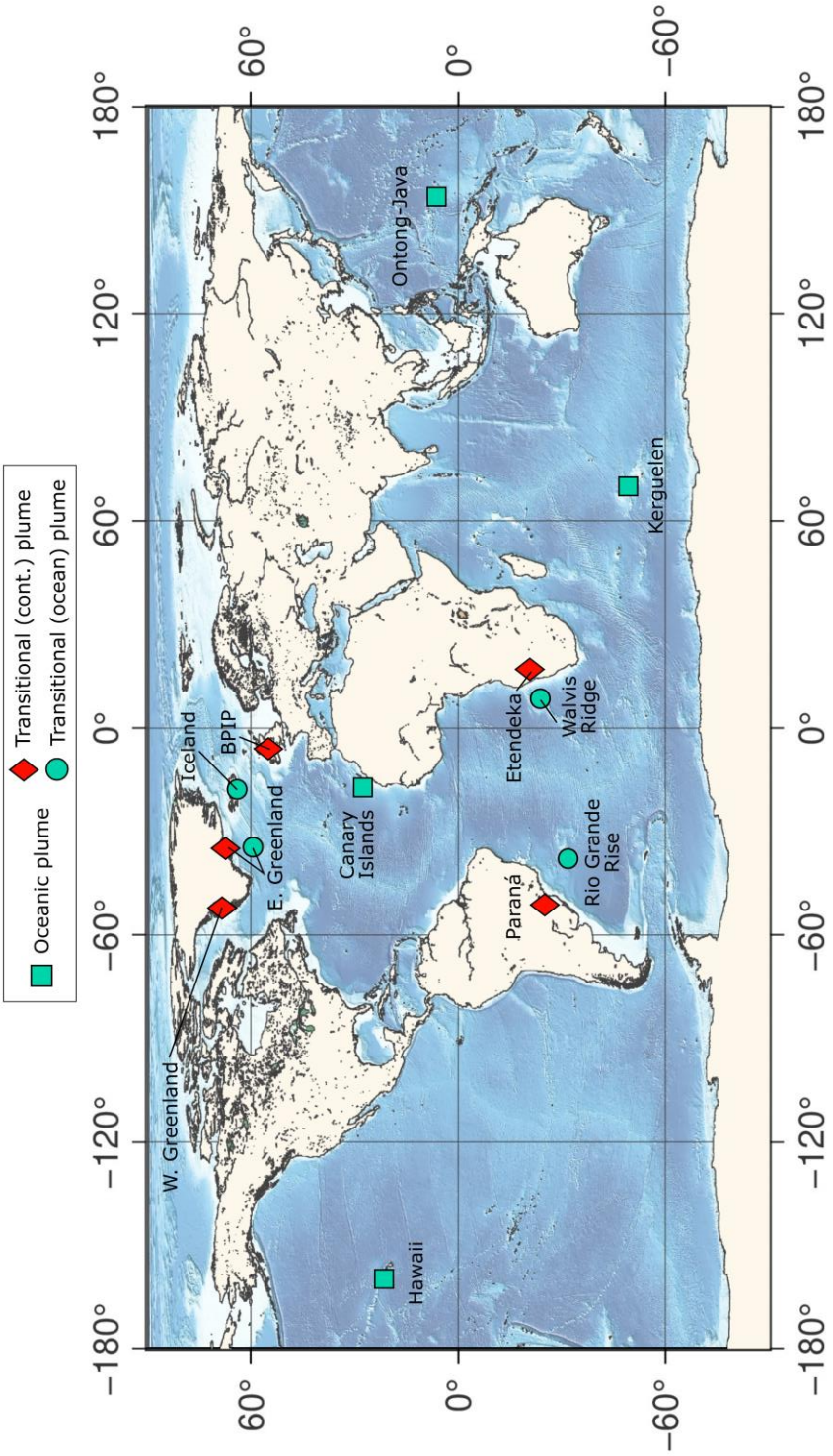

Figure 7.1 - *World map with study localities from which samples or data are used for this study. The map classifies localities into one of three plume types – continental, oceanic or transitional (i.e., continent-to-ocean). The data used for these localities are described in Table 1.*

The transitional plumes [H2] include the Tristan and Icelandic plumes, residing in the South and North Atlantic Ocean, respectively. In both of these regions, mantle plumes impinged underneath continental lithosphere, generating substantial volumes of intracontinental flood basalt volcanism. This was followed by continental rifting, the opening of the Atlantic from the south upwards, and the continuation of plume magmatism throughout, resulting in hotspot trails towards their current oceanic positions under Tristan da Cunha and Iceland. The volcanic products of the Tristan plume are the Paraná-Etendeka Large Igneous Province (PELIP), including the Paraná (Serra Geral Group) and Etendeka continental lavas, and the Rio Grande Rise and Walvis Ridge oceanic lavas. The volcanic products of the Icelandic plume are the North Atlantic Igneous Province (NAIP), and includes Greenlandic and British continental lavas and offshore Greenlandic and Icelandic oceanic lavas. Both settings provide an opportunity to observe changes in PGE concentrations in lavas as the geodynamic environment progressively transitions from continent to ocean, and each region presents quirks to their magmatic system that differ from the other.

Finally, we combined data from the transitional and oceanic sets to amalgamate information from continental and oceanic geochemical end-members and stages in between [H3]. By combining all plumes from the previous studies from a variety of settings, we can approach a global model for multi-element geochemistry and metallogeny in intraplate magmas. We have deliberately not included data from continental LIPs (such as the Siberian or Emeishan Traps) chiefly because these are significantly older than the PELIP and NAIP onshore portions, and thus subject to a host of geochemical alteration, metamorphism and preservation biases. Whilst we acknowledge there may be an age-related control on PGE prospectivity due to different mantle and/or lithospheric configurations, the scope of this chapter is on modern magma fertility in recent or active plume settings, under current mantle conditions.

7.2.2. Laboratory techniques

The laboratory techniques covered in this chapter follow those described in Chapters 3, 4 and 6, and are briefly summarised below. For samples processed and analysed as part of this study and prior studies leading to this work, whole rock lava specimens were crushed and ground to analytical-grade powders using a chrome-steel TEMA Mill. Impurities, amygdales and weathering were removed

prior to crushing and grinding to ensure the detection of primary elemental concentrations. Major element oxides were measured at Camborne School of Mines, University of Exeter using XRF. Sample powders were dried in an oven before being mixed with lithium borate flux; the resulting powder was melted in platinum crucibles. Molten samples were moulded into fused beads, with the aid of an ammonium iodide wetting agent, and the cooled beads were analysed using a Bruker S4 Pioneer XRF spectrometer. Samples and standards (AGV-1, BHVO-2, BIR, DNC-1) were analysed at 50-111 mA and 27-60 kV. Method and instrumentation follows Kystol and Larsen (1999); Tegner et al. (2009). Trace elements were measured using ICP-MS at Camborne School of Mines. This technique involved the dissolution of sample powders using 4-acid digestion and subsequent elemental detection via plasma ionisation using an Agilent 7700 Series mass spectrometer in He (collision) mode. Samples were analysed alongside the BCR-2 and Bir-1a standards. Method and instrumentation follows McDonald and Viljoen (2006).

For the six PGE and Au, we used the Ni-S fire assay and tellurium co-precipitation technique to separate precious metals from silicate material, followed by element detection using ICP-MS. For each sample, 15 g of powder was mixed with 12 g borax flux, 6 g sodium carbonate, 0.9 g sulphur solids, 1.08 g nickel and 1 g silica, and melted in a 1000°C furnace for 1.5 hours. This produced sulphide bead separates from the melted rock, which were dissolved in hydrochloric acid, co-precipitated using Te, filtered and diluted prior to element detection (alongside blanks plus the TBD1 and WPR1 standards). Method and instrumentation follows Huber et al. (2001); McDonald and Viljoen (2006). It should be noted that whilst all sample sets processed by the authors detected Os, Rh and Au, these are often omitted from literature PGE data sets using different detection methodologies.

Supplementary S7.1 contains all measured elemental concentrations, separated by technique with standard and blank measurements where applicable. The final amalgamated data sets used for H1, H2 and H3 herein are available in Supplementary S7.2, S7.3 and S7.4, respectively.

7.2.3. Machine learning workflow

For this study we replicate the workflow set out in Chapter 5 and in Lindsay et al. (2021) for each of the three plume bulk geochemical data sets. The MLA used throughout the workflow are from the *sci-kit learn v0.21.3* (Pedregosa et al., 2011), *NumPy v1.16.5* (Harris et al., 2020) and *Pandas v0.25.1* (McKinney, 2010) packages for Python 3.7.4, and all code is provided in Supplementary S7.5 as Jupyter Notebooks. We standardised elemental concentrations using the z-score (i.e., standard score) calculation (Kreyszig, 1979) prior to use in all processes, to avoid biasing the compositional data via mixed-unit measurements (e.g., Palowsky-Glahn and Egozcue, 2006; Buccianti and Grunsky, 2014).

The first technique applied to the data set is PCA. PCA is a linear dimensionality reduction technique that assesses variability in sample sets (developed by Pearson, 1901; Hotelling, 1933). The method generates new features, Principal Components (PCs), which describe variability in the elemental concentrations of all samples, especially in relation to each other, whilst reducing the number of dimensions within which we describe trends. Of the new features, PC1 represents the direction of highest variability across the high-dimensional data structure, PC2 is orthogonal to this (i.e., the likely next level of maximum variance), and so on until PC*n* when *n* is the number of variables (Chang, 1983; Hyvärinen et al., 2001; Davis, 2002). This information is arranged in *biplots*, which display sample variability with respect to the PCs in addition to vectors representing how strongly the variability of each variable (i.e., element concentrations) contributes to each PC, called *eigenvectors* (Jolliffe, 2002 and references therein). Using PCs allows for the effective communication of high-dimensional data information and subsequent multi-element anomaly detection.

As a non-linear dimensionality reduction technique, t-SNE allows for the conversion of high-dimensional data information into a single two-dimensional plot, effectively summarising all variability across all variables in all samples at once (developed by van der Maaten and Hinton, 2008). This produces an *embedding* that acts as a map of data set variability (see Section 7.3.1.2), arranging sample data points in a new space so that proximal samples have a high degree of similarity across the data set compared to distal samples (van der Maaten, 2014; Horrocks et al., 2019), using the Kullback-Leibler Divergence (Kullback and Leibler, 1959). UMAP works in a similar manner, but is generally

regarded as preserving information about distal samples more accurately than t-SNE (which is more suited to defining similarity in localised clusters) (McInnes et al., 2018; Becht et al., 2019). For this study, we opted to use t-SNE embeddings for the majority of data presentation, as their function as a variability map allows classification schemes to be overlain in the low-dimensional space. UMAP is used alongside certain t-SNE plots to further illustrate the high-dimensional separability of samples for reference only (within Appendix E).

Finally, *k*-means clustering (an unsupervised MLA developed by MacQueen, 1967; expanded upon by Howarth, 1983), is used to objectively classify samples based upon similarity across multiple variables. This is beneficial compared to classic geochemical studies, which generally classify data based on a selection of bivariate relationships. MLA-based clustering identifies high-dimensional trends, producing robust categories that capture a significantly larger amount of variability information (Howarth, 1983; Michie et al., 1994; Hastie et al., 2009; Marsland, 2009); this is especially true when using newly-generated PCs as input variables (as tested by Lindsay et al., 2021). The effectiveness of a *k*-means set-up can be assessed by the Davies-Bouldin Index (DBI; Davies and Bouldin, 1979), which describes the overall intra-cluster density for all groups and assigns low DBI to the optimal model. Compared to prior studies on plume geochemistry using the MLA workflow (Lindsay et al., 2021; Lindsay et al., in review) *k*-means clustering is used in a reduced capacity, as the study does not explicitly require sample categorisation. Instead, we use *k*-means to assign end-members to the partitioning of data sets based on high-dimensional associations from PCA, which can be then compared with t-SNE outcomes.

The MLA techniques used herein require full data sets with no missing, negative, zero or non-numeric values. This presents complications in selecting published data sets for analyses, given that the larger the stock of included elements is, the more likely a sample will be removed by the algorithm for an absent value. Hence, we have reduced the elements included as variables in each technique to 11 for the transitional plume data set (MgO, Fe_2O_3, TiO_2, Cr, Ni, Cu, Ir, Ru, Rh, Pt and Pd) and 10 for the remaining two data sets (all elements in the previous list excluding Rh). This ensured hundreds of samples were included with full variable suites for each study, providing robust and well-rounded data sets for MLA-based exploration. The 11 elements listed comprised the

original variable set for the NAIP study (Chapter 5; Lindsay et al., 2021) and are elements all associated with various aspects of mafic-ultramafic Ni-Cu-PGE magmatic/mineralisation systems, hence their inclusion in all original studies (Table 7.1). Previous chapters using the workflow have shown that this variable set can provide substantial insights into PGE-focused multi-element melting interpretation (Chapters 5 and 6).

In the rare occasion that single PGE values were below-detection in a sample, we utilised the “rounded-zero” technique (see Martín-Fernández and Thió-Hernestrosa, 2006; Martín-Fernández et al., 2012) to assign a value (below the detection limit for the given element) to such cells, without artificially influencing data set variability. This was only used for select samples in the second two studies, and such cells are italicised in data sheets. All MLA results can be found in Supplementary S7.2-7.4.

7.3. Results

The following results are presented according to the hypotheses being investigated. Firstly we describe results for oceanic plumes only [H1], followed by our two Atlantic localities representing transitional continent-to-oceanic plumes [H2], and finally all localities combined [H3]. Bivariate geochemical plots are provided for reference in Appendix E1-3.

7.3.1. Oceanic plumes

7.3.1.1. PCA

Figure 7.2a-d displays PCA information for the first sub-study on purely oceanic plumes [H1], including a scree plot with eigenvalues and cumulative variability (Figure 7.2a) and biplots for PC1-2, PC3-4 and PC5-6 (Figures 7.2b-d, respectively). From Figure 7.2a, PC1-6 account for 94.2 % of all data set variability across the ten included elements; PC7 onwards are considered noise and disregarded. Plume localities exhibit distinct eigenvector associations through each of the biplots. In Figure 7.2b, within the PC1-2 space (58.7 % of all variability), Icelandic samples trend with MgO, Ni and Cr, and some offshore East Greenlandic samples trend similarly, but with an association with Ru and Ir eigenvectors. Canary Islands and Hawaiian samples are associated with TiO_2,

whilst Kerguelen, PELIP, Ontong-Java and the remaining East Greenlandic samples trend with Fe_2O_3, Cu, Pt and Pd eigenvectors. In the PC3-4 space (Figure 7.2c), contributing 24.7 % to all data set variability, Canary Islands (especially El Hierro) and Kerguelen samples trend with TiO_2, alongside Fe_2O_3 and Ni. There is a strong PELIP association with Ru and Cu, and a moderate trend amongst some East Greenlandic and Ontong-Java samples towards Pt, Pd and Ir eigenvectors. In the PC5-6 space (Figure 7.2d), accounting for a further 10.8 % of data set variability, some sparse trends can be recognised – Rio Grande Rise with Cu, East Greenland and Kerguelen with Ir, Walvis Ridge with TiO_2 and Ru, Icelandic with MgO, Fe_2O_3 and Cr, Ontong-Java with Pd.

7.3.1.2. Embedding

Figure 7.3 displays the oceanic plume data set arranged in an embedding space generated by t-SNE, the representation of all variability of all elements throughout the sample set, with samples classified by locality. The model was run with a perplexity of 40, 5000 maximum iterations and learning rate of 200 (models with different set-ups are displayed in Appendix E4 for reference). This gives an account of sample variability across all 10 included variables. Most sample localities are arranged into distinct sectors of the embedding by the algorithm. Canary Island samples occupy the bottom-right of the space, with Hawaiian samples adjacent. Icelandic samples are located in the bottom-left, East Greenlandic and Walvis Ridge samples in the centre, and Kerguelen samples in the top. Rio Grande Rise and Ontong-Java clusters are less distinct, spread across the embedding but primarily in the top half. As with the oceanic plumes, trends in the transitional plume sub-study are exaggerated by UMAP (Appendix E5).

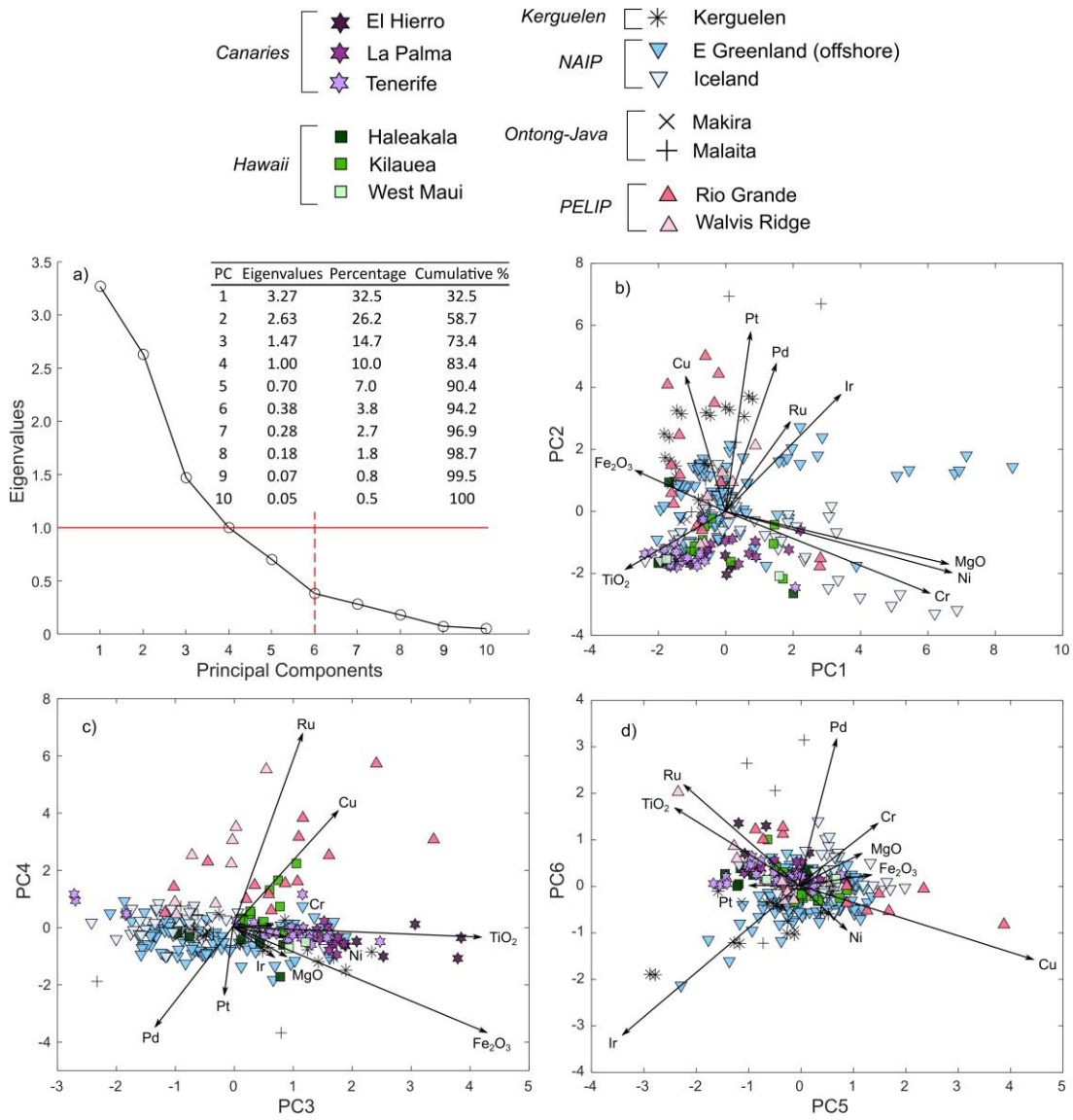

Figure 7.2 - *PCA results for the oceanic plume sub-study: (a) eigenvalue information including cumulative variability; (b) PC1 v PC2; (c) PC3 v PC4; (d) PC5 v PC6. Sample data points are classified by locality.*

Figure 7.4 displays the embedding from Figure 7.3 with sample points coloured by z-score concentrations of each of the 10 elements used as a variable. In this instance, the geochemical data exhibits a degree of bimodal variability across the embedding space in terms of concentration distribution. Groups of elements share similar trends: (i) MgO, Cr and Ni; (ii) Fe_2O_3 and TiO_2; (iii) Cu, Pt and Pd; (iv) Ir and Ru.

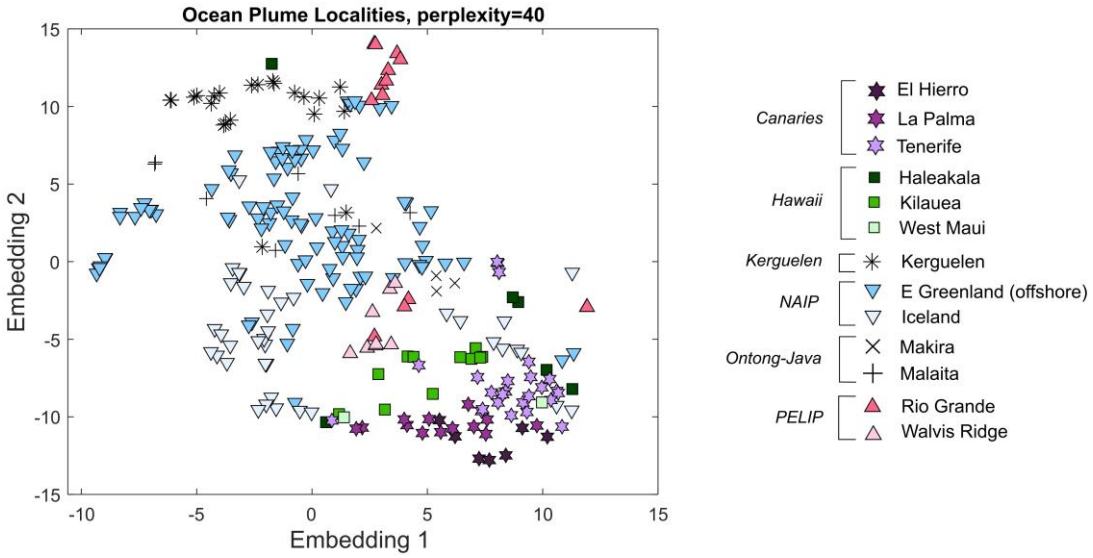

Figure 7.3 - *t-SNE plot for the oceanic plume sub-study, with data points classified by locality.*

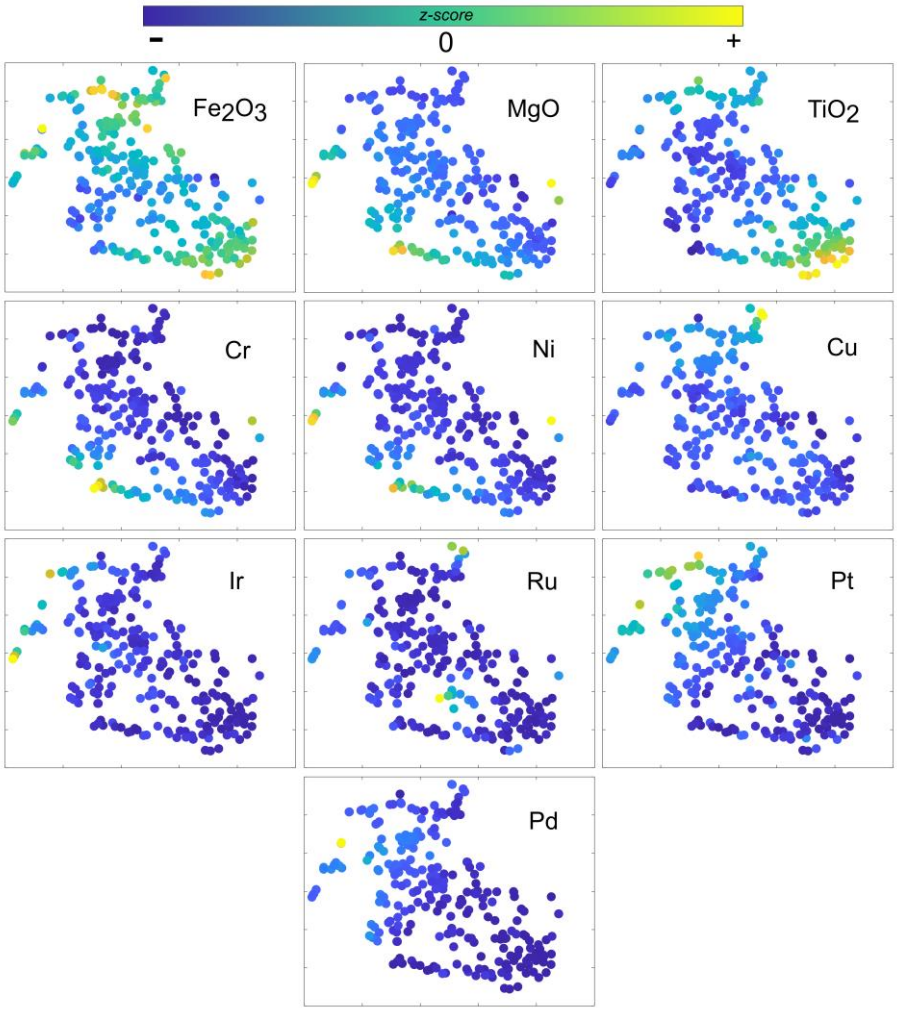

Figure 7.4 - *t-SNE plot for oceanic plumes from Figure 7.3 with data points coloured by element z-scores.*

7.3.1.3. k-means clustering

In Figure 7.5, the most robust (i.e., lowest DBI) *k*-means clustering model for the oceanic plumes (*k* = 7, with PC1-6 as variables) is displayed with data arranged in the embedding space from Figures 7.3 and 7.4. All models for *k*-values of 2-7 are provided in Appendix E6 alongside the DBI assessment in Appendix E7.

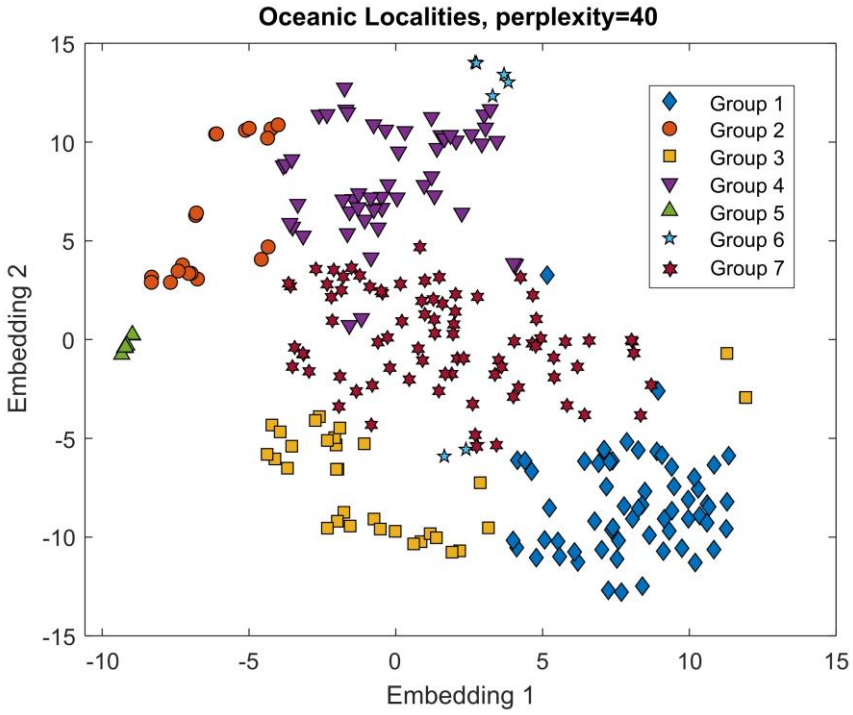

Figure 7.5 - *Clusters (k=7) for the oceanic data set, defined based on PCs 1-6, and mapped here onto t-SNE embedding from Figure 7.3. Number of clusters based on DBI (see Appendix E6-E7).*

On comparing Figure 7.5 with locality classifications from Figure 7.3 and elemental concentrations from Figure 7.4, we can describe the main features of each cluster.

- Group 1 comprises primarily the Canary Island and Hawaiian samples with high TiO_2 and Fe_2O_3 concentrations.
- Group 2 comprises a mix of East Greenlandic, Kerguelen and Malaita (Ontong-Java) samples in the top-left of the embedding, which feature high Fe_2O_3, Pt and Pd concentrations.

- Group 3 comprises the Icelandic and East Greenlandic samples in the bottom-left with high MgO, Ni and Cr concentrations, plus two outliers (Iceland and Rio Grande Rise) on the right.
- Group 4 comprises the Kerguelen and East Greenlandic samples in the top of the embedding with high Fe_2O_3 and Pt concentrations.
- Group 5 comprises a very small cluster of East Greenlandic samples on the left with particularly high MgO, Ni and Ir concentrations.
- Group 6 comprises Walvis Ridge and Rio Grande Rise (PELIP) samples with high Fe_2O_3, Cu and Ru concentrations.
- Group 7 comprises the central East Greenlandic, PELIP and Ontong-Java samples with no strongly defined elemental associations (i.e., a background signature).

7.3.2. Transitional plumes

7.3.2.1. PCA

Figure 7.6a-d displays PCA information for the second sub-study on transitional plumes [H2], including a scree plot with eigenvalues and cumulative variability (Figure 7.6a) and biplots for PC1-2, PC3-4 and PC5-6 (Figures 7.6b, 7.6c and 7.6d, respectively). From Figure 7.6a, PC1-6 account for 92.3 % of all data set variability across the eleven included elements; PC7 onwards are considered noise and are disregarded. There is a visible split in dominant variability controls in the PC1-2 space (59.9 % cumulative variability) in Figure 7.6b – NAIP samples (particularly Greenlandic onshore and offshore) trend with MgO, Cr, Ni and Ir eigenvectors, whilst PELIP samples trend with TiO_2, Fe_2O_3 and Cu eigenvectors, with multiple Serra Geral Type 1 outliers strongly attributed to Ru, Rh, Pt and Pd. In the PC3-4 space (a further 23.8 % cumulative variability) in Figure 7.6c, these trends mostly persist with some changes – Serra Geral Type 1 (Southern) trend strongly with Ru and Rh, Serra Geral Type 1 (Northern) with Pd, Greenland onshore with Pt, and the majority of the other localities across both regions trending with the remaining eigenvectors. The final biplot for PC5-6 (Figure 7.6d) accounts for 8.6 % cumulative variability and displays less clear sample-eigenvector relationships.

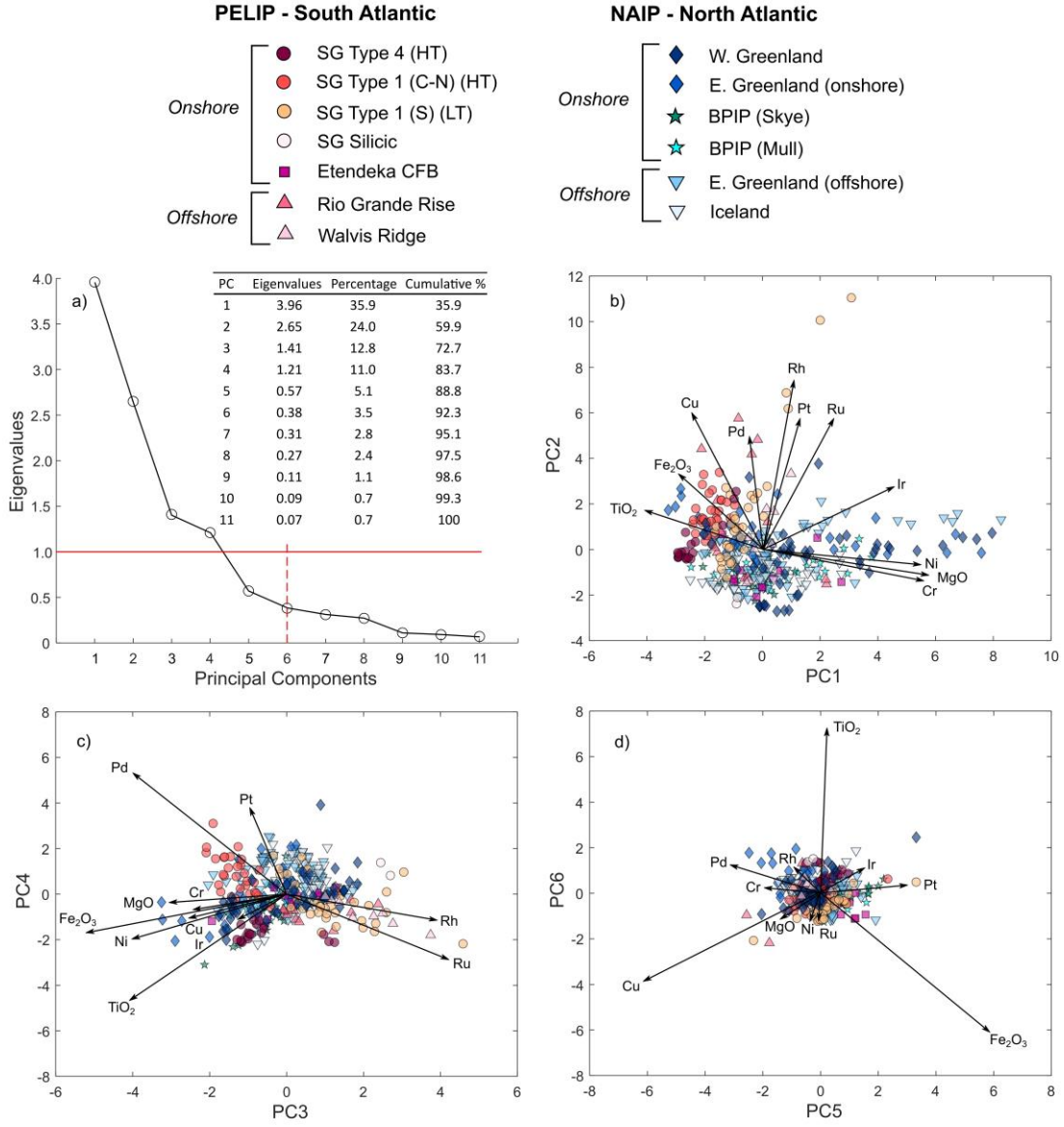

Figure 7.6 - *PCA results for the transitional plume sub-study: (a) eigenvalue information including cumulative variability; (b) PC1 v PC2; (c) PC3 v PC4; (d) PC5 v PC6. Sample data points are classified by locality. HT – High-Ti, LT – Low-Ti, SG – Serra Geral, C-N – Central-Northern, S – Southern, CFB – Continental Flood Basalts, BPIP – British Palaeogene Igneous Province.*

7.3.2.2. Embedding

Figure 7.7 displays the transitional plume data set arranged in an embedding space generated by t-SNE, with samples classified by locality; this model was run with a perplexity of 20, 5000 maximum iterations and learning rate of 200 (models with different set-ups are displayed in Appendix E8 for reference). This gives an account for sample similarity across all 11 variables. The sample points are arranged in a triangular shape, and there is a generalised left-right split between NAIP and PELIP, respectively. Onshore lavas from each region arranged in the top left and right corners of the embedding (Greenlandic and Serra Geral Type 4, respectively). At the bottom, samples from predominantly Serra Geral Type 1 (Central-Northern) and East Greenland plot closely. Between the top left and bottom corner, offshore NAIP lava samples plot in a near-linear array. Between the top right and bottom corner, Serra Geral Type 1 (Southern) and PELIP offshore samples plot in a near-linear array. Etendeka lavas (i.e., PELIP onshore) plot with NAIP onshore samples. BPIP samples are split, with Mull next to Greenlandic lavas and Skye next to Serra Geral Type 4. These trends are repeated with increased separability by UMAP in Appendix E9.

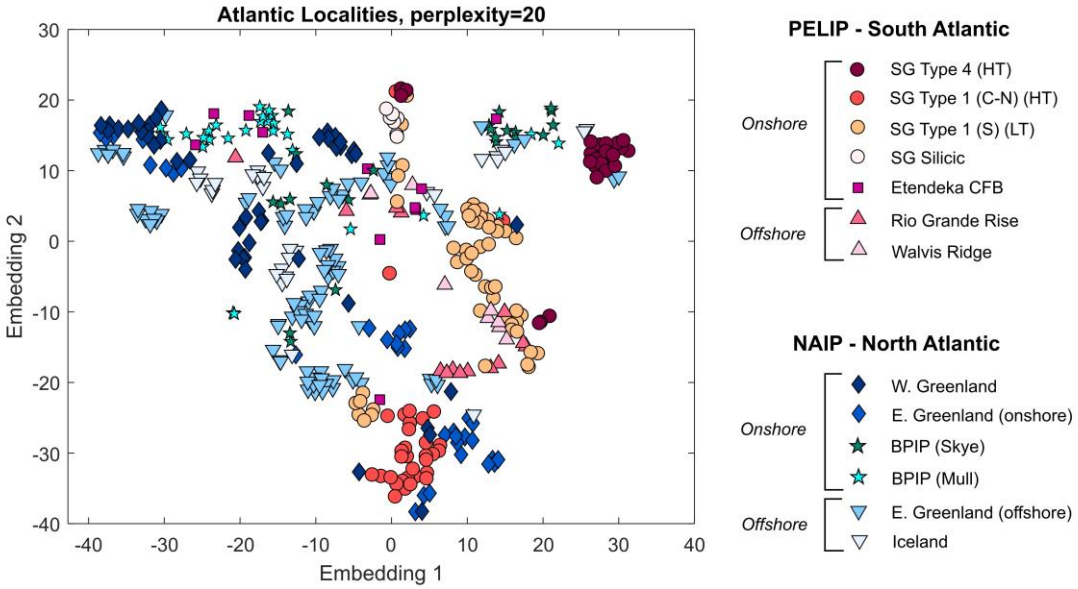

Figure 7.7 - *t-SNE plot for the transitional plume sub-study, with data points classified by locality. HT – High-Ti, LT – Low-Ti, SG – Serra Geral, C-N – Central-Northern, S – Southern, CFB – Continental Flood Basalts, BPIP – British Palaeogene Igneous Province.*

Figure 7.8 displays the embedding from Figure 7.7 with sample points coloured by z-score concentrations of each element used as a variable. Through the embedding space, MgO, TiO_2, Cr, Ni, Cu, Ir, Ru, Rh and Pd exhibit strongly bimodal concentrations, whilst Fe_2O_3 and Pt do not. Groups of elements exhibit associations (i.e., similar concentration distribution): (i) MgO, Cr, Ni and Ir; (ii) TiO_2, Cu and Pd; (iii) Ru and Rh.

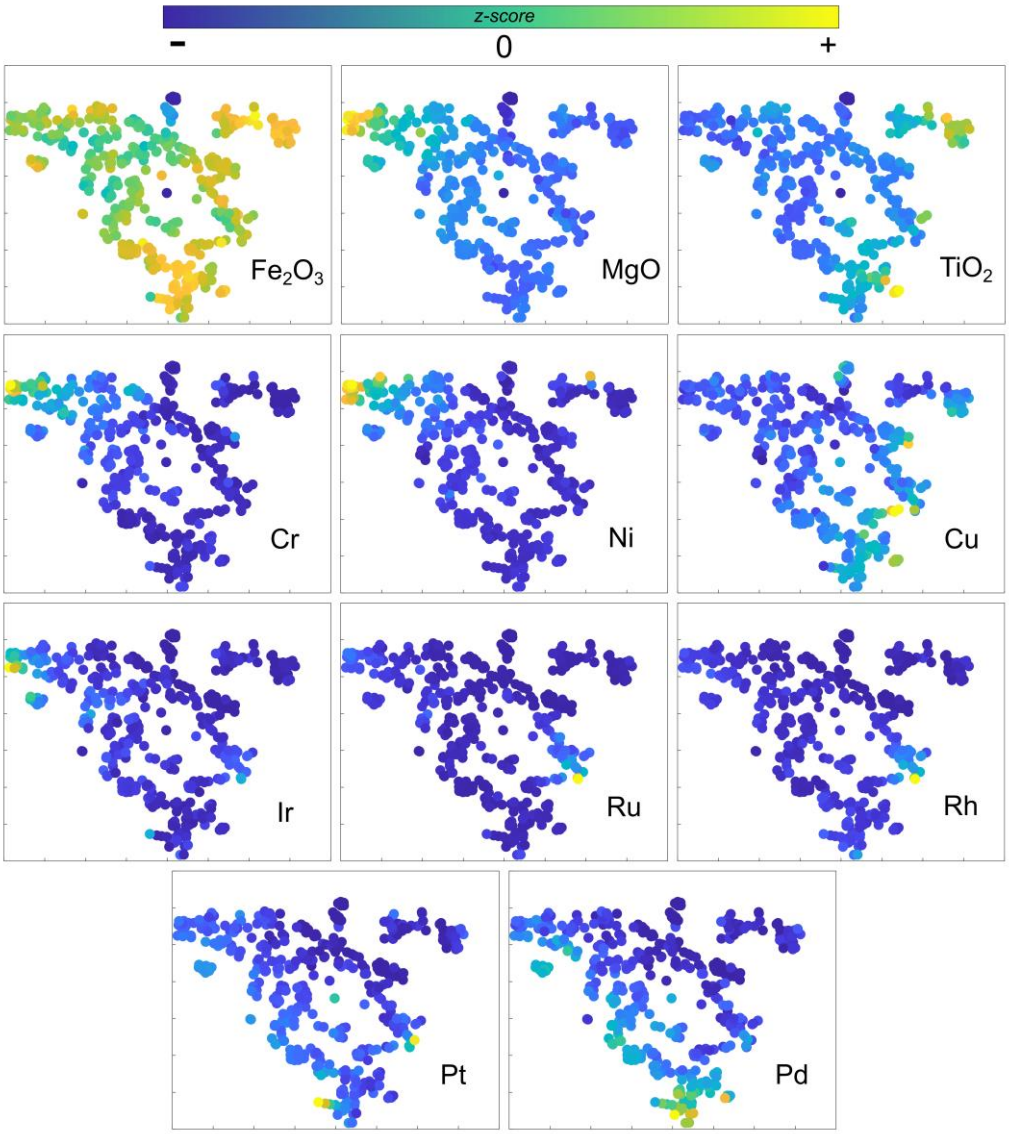

Figure 7.8 - *t-SNE plot for transitional plumes from Figure 7.7 with data points coloured by element z-scores*

7.3.2.3. k-means clustering

In Figure 7.9, the most robust (i.e., lowest DBI) *k*-means clustering model for the transitional plumes (*k* = 6, with PC1-6 as variables) is displayed with data arranged in the embedding space from Figures 7.7 and 7.8. All models for *k*-values of 2-7 are given in Appendix E10, alongside the DBI assessment in Appendix E11. On comparing with locality classifications from Figure 7.7 and elemental concentrations from Figure 7.8, we can describe the main features of each cluster.

- Group 1 comprises predominantly offshore NAIP samples with high Fe_2O_3 and moderate MgO, Cr and Ni concentrations.
- Group 2 comprises the high Fe_2O_3 and Pd samples from Serra Geral Type 1 (Central-Northern) and East Greenland (onshore), in addition to East Greenland (offshore).
- Group 3 comprises the highest MgO, Cr, Ni and Ir samples in the top-left of the embedding, comprising West and East Greenlandic, Mull and Etendeka localities.
- Group 4 comprises Serra Geral Type 1 (Southern), Rio Grande Rise and Walvis Ridge samples with high Ru and Rh, and moderate TiO_2 concentrations.
- Group 5 comprises a very small cluster of extremely high Ru and Rh Serra Geral Type 1 (Southern) samples.
- Group 6 comprises the high Fe_2O_3 and TiO_2 Serra Geral Type 4 samples, plus Skye and offshore NAIP localities.

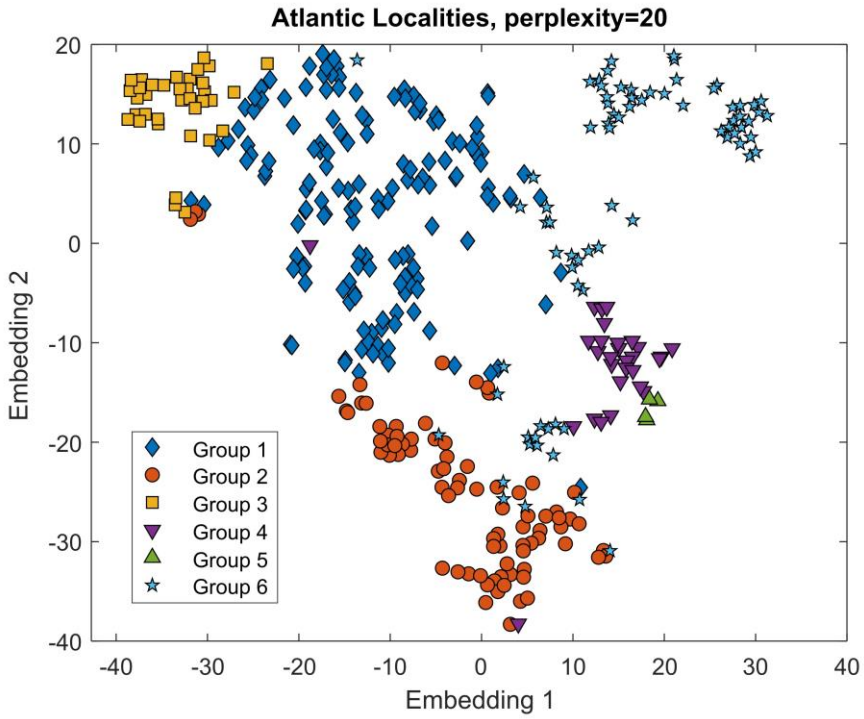

Figure 7.9 - *Clusters (k=6) for the transitional data set, defined based on PCs 1-6, and mapped here onto t-SNE embedding from Figure 7.7. Number of clusters based on DBI (see Appendix E10-E11).*

7.3.3. Continental and oceanic plumes

7.3.3.1. PCA

Figure 7.10a-d displays PCA information for the third sub-study on continental and oceanic plumes [H3], including a scree plot with eigenvalues and cumulative variability (Figure 7.10a) and biplots for PC1-2, PC3-4 and PC5-6 (Figures 7.10b-d, respectively). From Figure 7.10a, PC1-6 account for 92 % of all data set variability across the ten included elements; PC7 onwards are considered noise and disregarded. Plume localities exhibit distinct eigenvector associations through each of the biplots.

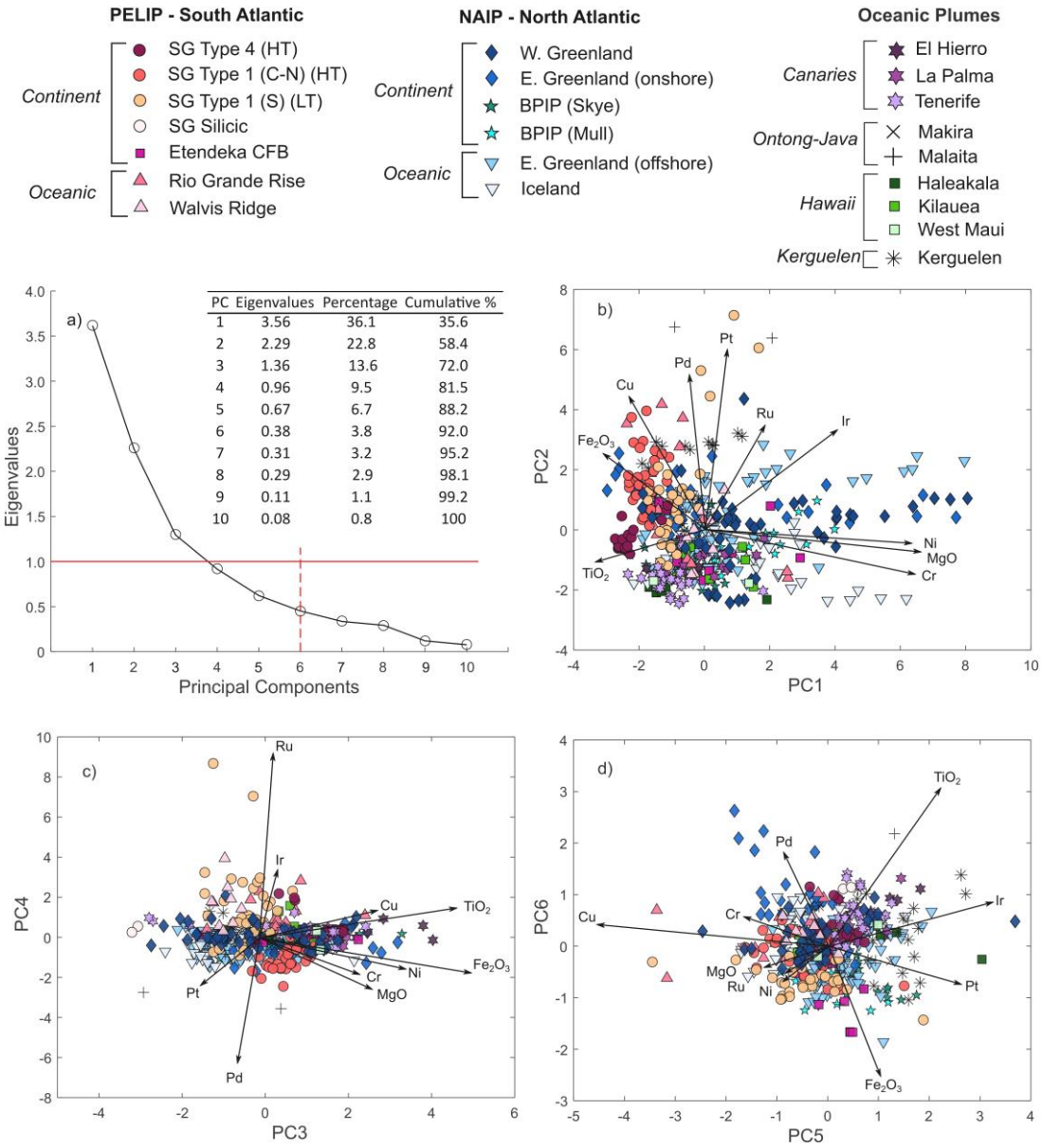

Figure 7.10 - *PCA results for the continental vs. oceanic plume sub-study: (a) eigenvalue information including cumulative variability; (b) PC1 v PC2; (c) PC3 v PC4; (d) PC5 v PC6. Sample data points are classified by locality. HT – High-Ti, LT – Low-Ti, SG – Serra Geral, C-N – Central-Northern, S – Southern, CFB – Continental Flood Basalts, BPIP – British Palaeogene Igneous Province.*

In Figure 7.10b, within the PC1-2 space (58.4 % of cumulative data set variability), NAIP lavas (onshore and offshore) trend with MgO, Cr, Ni, Ir and Ru eigenvectors alongside a small number of Etendeka samples. Kerguelen, Ontong-Java and PELIP (onshore and offshore) samples trend with Fe_2O_3, Cu, Pt and Pd. PELIP onshore (particularly Serra Geral Type 4) and the Canary

Islands have an association with TiO_2. Hawaiian samples show mostly weak associations with MgO, Ni and Cr but otherwise plot near the Canary Islands. In Figure 7.10c, within the PC3-4 space (23.1 % towards data set variability), PGE are strongly defined by PC4. Some prominent associations are: PELIP (onshore and offshore) and Kerguelen with Ru and Ir; Canary Islands, Hawaii and NAIP onshore with MgO, TiO_2, Fe_2O_3, Cr, Ni, Cu; NAIP offshore, Serra Geral Type 1(Central-Northern) and Ontong-Java with Pt and Pd. In Figure 7.10d, within the PC5-6 space (10.5 % of data set variability), trends are more subtle than in Figure 7.10b-c. Canary Islands samples once again trend towards the TiO_2, PELIP (onshore and offshore) between Fe_2O_3, MgO, Ni and Ru, NAIP (onshore) towards Cr and Pd, and a small mix of NAIP, Kerguelen, Hawaii and Etendeka samples towards Ir and Pt. Anomalously high Cu associations are exhibited by selected PELIP samples.

7.3.3.2. Embedding

Figure 7.11 displays the combined continental and oceanic plume data set arranged in an embedding space generated by t-SNE, with samples classified by locality (Figure 7.11a) and setting (Figure 7.11b); the chosen model was run with a perplexity of 40, 5,000 maximum iterations and learning rate of 200 (models with different set-ups are displayed in Appendix E12-13 for reference). This gives an account of sample variability across all 10 included variables simultaneously. Compared to the previous two sub-studies, the t-SNE results for this larger data set are slightly more complex, but prominent trends are exhibited in degrees of similarity between localities. For the continental samples, the bulk of localities are grouped into either the bottom left or top right of the embedding (Figure 7.11b) – West Greenland, BPIP and Etendeka in the former, and Serra Geral and East Greenland (onshore) in the latter (Figure 7.11a). A distinct sub-population, dominated by Serra Geral Type 4, can be seen on the right of the embedding. For oceanic samples, there is a single major population space, this at bottom right of the embedding (Figure 7.11b), with the remaining oceanic data found distributed in the centre of the plot. NAIP offshore lavas dominate the central group, whilst the purely oceanic Canary Islands and Hawaii lavas cluster tightly in the bottom right. Ontong-Java and Kerguelen plot close to the Serra Geral continental lavas at the top of the embedding (Figure 7.11a). UMAP plots

(Appendix E14) also capture the dominant trends and increase their separability, but ultimately still retain the general setting and locality clusters from t-SNE.

Figure 7.12 displays the embedding from Figure 7.11 with sample points coloured by z-score concentrations of each of the 10 elements used as a variable. All variables except Ru, which is concentrated in a single central sub-cluster dominated by Serra Geral Type 1 (Southern) samples in Figure 7.11a, exhibit bimodality, and once again some can be partnered with other elements with similar variability. In this instance, the main associations are: (i) MgO, Cr, Ni and Ir; (ii) Cu, Pt and Pd. Unlike previous sub-studies, TiO_2 and Fe_2O_3 exhibit strong but unique variability trends, most clear in TiO_2.

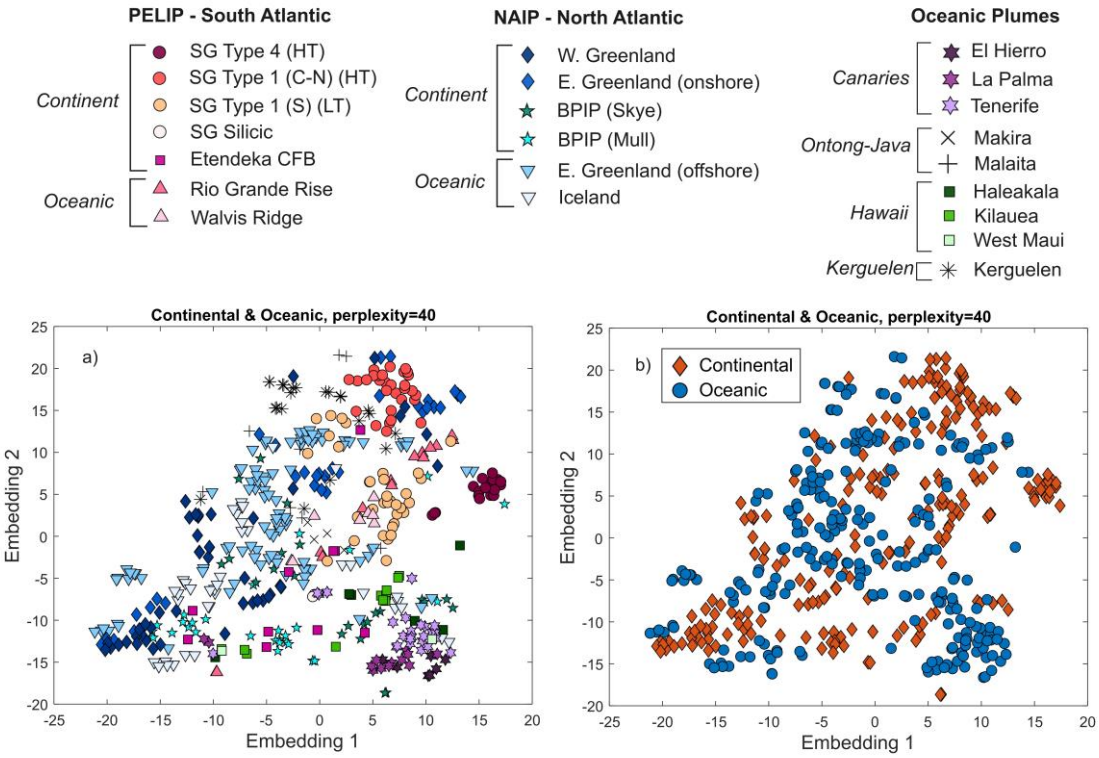

Figure 7.11 - *t-SNE plots for the continent vs. ocean plume sub-study, with data points classified by a) locality; b) setting. HT – High-Ti, LT – Low-Ti, SG – Serra Geral, C-N – Central-Northern, S – Southern, CFB – Continental Flood Basalts, BPIP – British Palaeogene Igneous Province.*

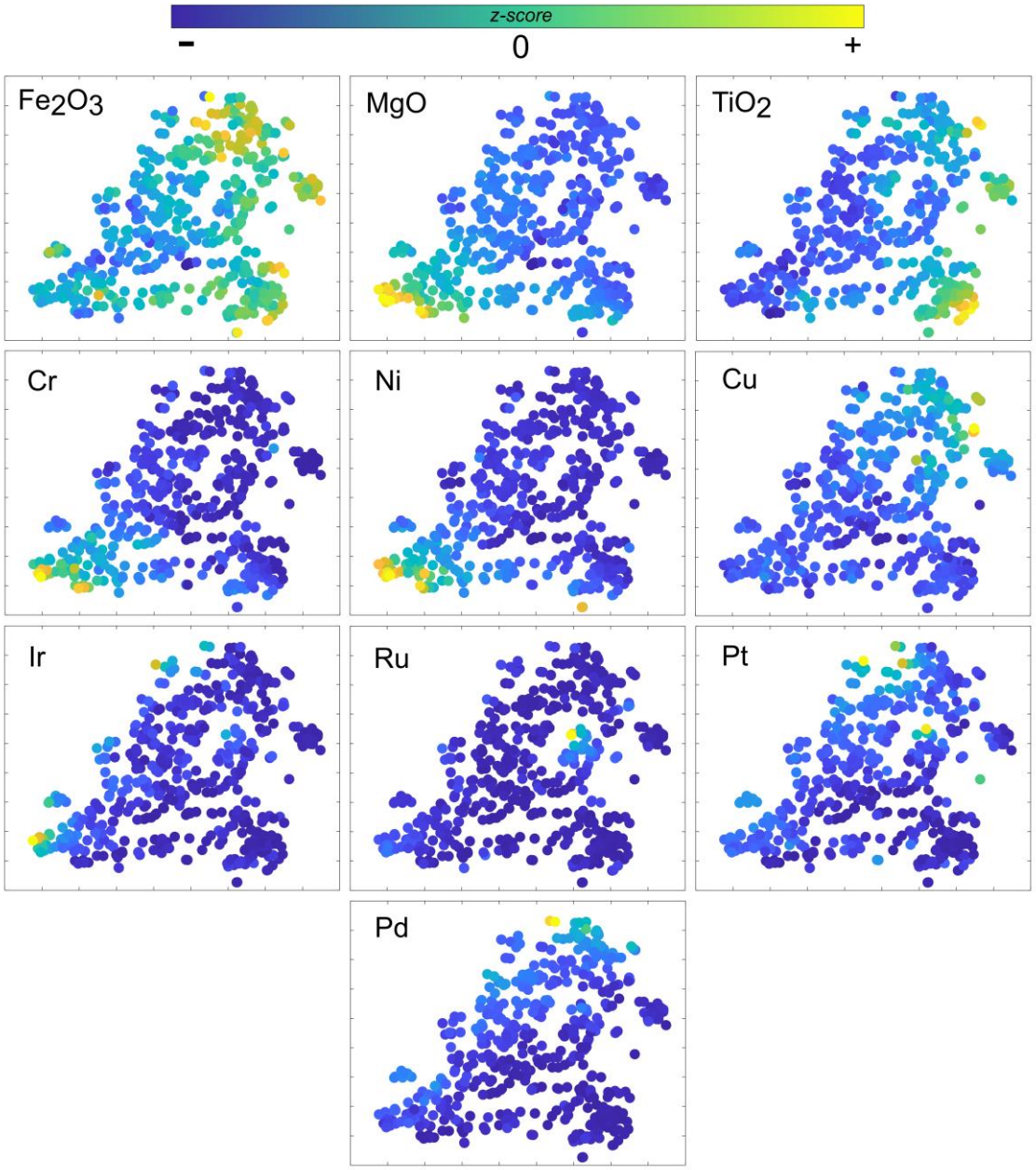

Figure 7.12 - *t-SNE plot for continental and oceanic plumes from Figure 7.11 with data points coloured by element z-scores*

7.3.3.3. k-means clustering

In Figure 7.13, the most robust (i.e., lowest DBI) *k*-means clustering model for continental and oceanic plumes (*k* = 7, with PC1-6 as variables) is displayed with data arranged in the embedding space from Figures 7.11 and 7.12. All models for *k*-values of 2-7 are given in Appendix E15-16 alongside the DBI assessment. On comparing with locality classifications from Figure 7.11 and elemental concentrations from Figure 7.12, we can describe the main features of each cluster.

- Group 1 comprises moderately high MgO, Cr, Ni and Ir samples from the NAIP (onshore and offshore) and Etendeka (continental).
- Group 2 comprises the bottom right of the embedding, dominated by Canary Island and Hawaiian oceanic samples, and BPIP (Skye) and PELIP continental samples, all with high TiO_2 and Fe_2O_3 concentrations.
- Group 3 comprises a very small sub-cluster identified in Figure 7.11a hosting Serra Geral Type 1 (Southern, continental) samples with very high relative Ru concentrations.
- Group 4 comprises samples with the highest MgO, Cr, Ni and Ir concentrations in the embedding, an extreme end-member extension of Group 1 (onshore and offshore).
- Group 5 comprises a large cluster in the top of the embedding featuring a diverse group of many localities (Serra Geral Type 1 varieties (continental), East Greenland onshore and offshore, Kerguelen and Malaita (oceanic)) with high Fe_2O_3 moderate TiO_2, Pt and Pd concentrations.
- Group 6 comprises a disparate group of samples that appear to border areas of strong enrichment (i.e., Groups 1 and 5; continental and oceanic), but are depleted in comparison to their neighbours. Concentrations of Ir, Pt, and Pd are moderately high, however. Kerguelen and Ontong-Java (oceanic) samples are situated here.
- Group 7 comprises a large group in the centre of the embedding comprising mainly NAIP (onshore and offshore) and Makira samples (oceanic) with occasional Etendeka (continental), Hawaii and PELIP (offshore) samples (all oceanic), all with moderate concentrations representing background multi-element signatures.

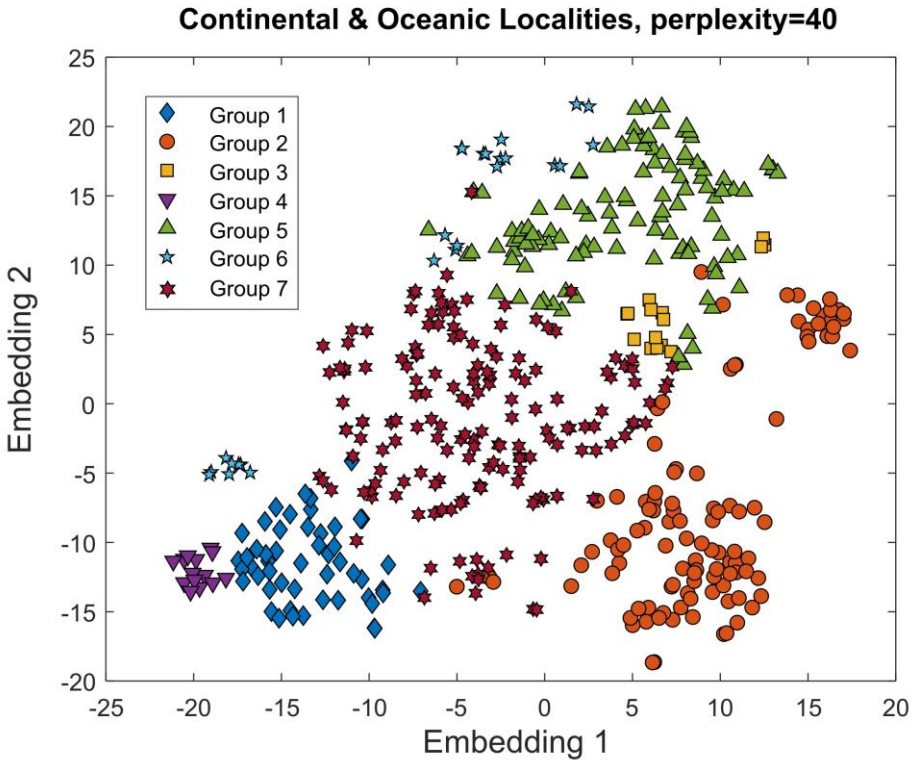

Figure 7.13 - *Clusters (k = 7) for the continental vs. oceanic data set, defined based on PCs 1-6, and mapped here onto t-SNE embedding from Figure 7.11. Number of clusters based on DBI (see Appendix E15-16).*

7.4. Discussion

The similarity expressed between localities through the high-dimensional space (be it their cluster designation or affinity for similar PCA eigenvectors) translate to their net geochemical variabilities being well-matched, indicating that the controls on their magmatic composition and metal basket could be comparable within the sample set. This is explicitly expressed via sample proximity in t-SNE plots. We can target precious metal variations as a function of these magmatic controls, to work towards a model for metal acquisition in intraplate magmas.

7.4.1. Multi-element trends

7.4.1.1. Oceanic plumes

Oceanic plumes are found far from the continental lithosphere, and thus their multi-element signatures represent a combination of fractional crystallisation and primarily processes operating in the mantle during partial melting, with no input (i.e., contamination) by more evolved continental crustal material. The degree of variation portrayed in the MLA workflow from Figures 7.2-7.5 is substantial, indicating that even when considering oceanic plumes with similar geochemical reservoirs or degrees of magmatic differentiation, there is no fixed or 'typical' signature for the included variables. The major trends from all MLA outcomes for the oceanic set (summarised in Figure 7.14) are interpreted herein.

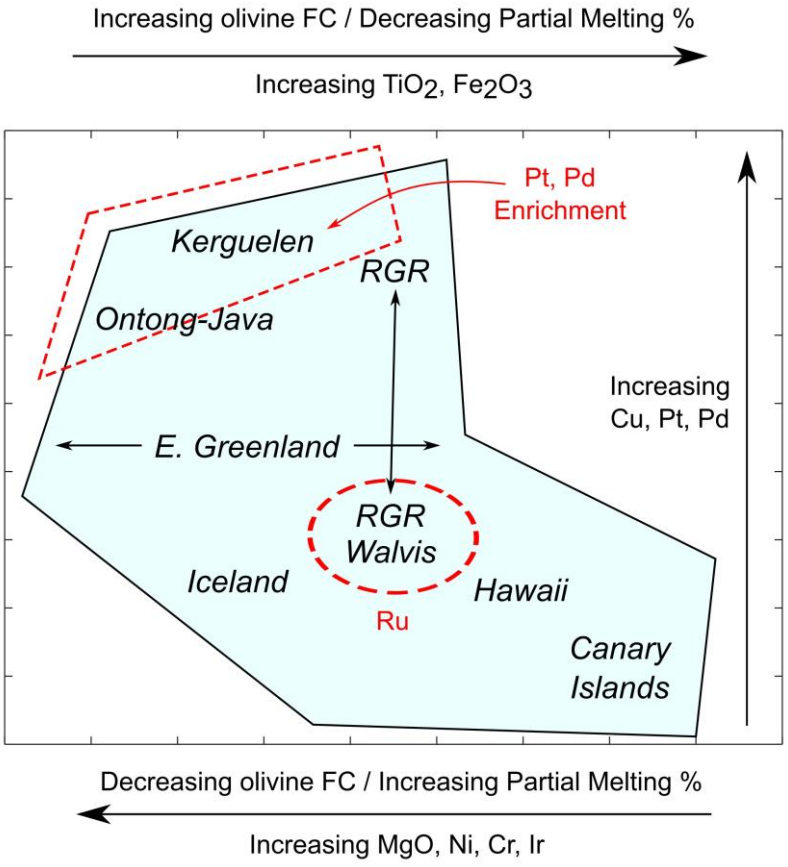

Figure 7.14 – *A summary of information gained from MLA results for the oceanic data set, arranged in a simplified embedding shape (Figure 7.3). The dominant trends of multi-element associations are indicated by arrows alongside the geochemical controls implied by each. Individual (i.e., localised) PGE enrichments are highlighted in red outlines. FC – fractional crystallisation, RGR – Rio Grande Rise. Blue shading represents the distribution of oceanic plume lava samples in Figure 7.3.*

The variability of NAIP samples (in this sub-study Iceland and East Greenland (offshore) only) is strongly controlled by MgO, Cr and Ni in the highest-order PCs, with a smaller influence from Ir (Figure 7.2b). Whether being melted from common mantle peridotite phases (Larsen and Pedersen, 2000; Matzen et al., 2017) or being removed via subsequent fractional crystallisation, MgO, Cr and Ni are seen to vary in unison. Whilst low-MgO lavas could have developed their signatures due to either minimal mantle melting or extensive olivine fractionation of those two processes, high-MgO lavas must have formed from high degrees of partial melting in order to incorporate significant mantle olivine into melts in the first place. As such, positive MgO-Ni-Cr multi-element anomalies can identify plumes that feature relatively high degrees of partial melting in a data set. The modern-day Icelandic plume is one of the highest buoyancy, deep-origin plumes of the world (Courtillot et al., 2003), and also intersects with mid-oceanic ridge magmas. This combination of features likely plays a direct role in the observed signatures by imparting high degrees of partial melting on the asthenosphere. In t-SNE plots, Iceland and East Greenland are separated into the lower and upper sections of the map, respectively (Figures 7.3 and 7.14), and clustered differently (Iceland in Group 1 or 3, East Greenland in Group 4, 5 or 7; Figures 7.3 and 7.5). Differences could arise in geography-based input to geochemistry – East Greenland offshore lavas were erupted shortly after the early opening of the Atlantic and, like the Rio Grande Rise, a component of remnant SCLM input may factor into the final lava composition. Comparatively, Iceland is far from the continents and is unlikely to be contaminated by SCLM; the proximity to the Atlantic Ridge also introduces significant MORB components to modern Icelandic melts (e.g., Tegner et al., 1998; Momme et al. 2003), further differentiating the two offshore NAIP localities on the y-axis of Figure 7.14.

Oceanic PELIP samples also exhibit similar trends to their inclusion in the first sub-study, associated with Fe_2O_3, Cu, Ru, Pt and Pd eigenvectors in Figure 7.2b, a trend shared with Kerguelen and Ontong-Java lavas in this data set. The Rio Grande Rise and Walvis Ridge samples from the PELIP represent the mid-stage of volcanism attributed to the Tristan plume, and the first major oceanic lavas in the system. In the absence of strong MgO (plus Cr, Ni and Ir) variability, as observed in the NAIP, PELIP lava variability is dominated by Fe_2O_3, Cu, Pd and Pt. In general, Rio Grande Rise samples bear stronger affinity for Fe_2O_3, Cu,

Pd and Pt eigenvectors (e.g., Figure 7.2b-d) than Walvis Ridge samples, with higher concentrations of each of these four elements indicated in the eigenvector association as per Appendix E1. In Chapter 6 (Lindsay et al., accepted), similarities between Rio Grande Rise and the youngest (Low-Ti) Paraná onshore lavas, and Walvis Ridge and the Etendeka lavas, were identified and described as geochemical constants in the Tristan plume melt system on either side of the opening Atlantic. Studies indicate that remnants of delaminated SCLM persist in the oceanic melt column following continental break-up, which can induce isotopic and geochemical similarities in the resulting magmas despite the removal of the bulk of the continental crust from the differentiating system of the magma(s) (Douglass et al., 1999; Le Roux et al., 2002; Gibson et al., 2005). Crucially, we see remnants of PGE enrichment in the Rio Grande Rise lavas (Figure 7.14) (albeit not as enriched as their onshore counterparts), which are significant when seen alongside purely oceanic data and distinct enough to merit the classification of Rio Grande Rise samples as a single, unique cluster (i.e., Group 6 when comparing Figures 7.3 and 7.5).

The oceanic Kerguelen and Ontong-Java plume lavas have certain similarities in the multi-element analyses – the aforementioned general Fe_2O_3, Cu, Pt and Pd eigenvector association in the PC1-2 space (Figure 7.2b), and occupying the upper section of the embedding generated for oceanic plumes (Figure 7.3 and 7.14). Kerguelen plume lavas consistently have < 10 wt.% MgO (low compared to other plumes in the data set – Appendix E1), likely due to 20-25 % olivine fractionation, and their otherwise high degree of partial melting (20-30 %) is masked by fractional crystallisation signatures (Neal et al., 2002; Chazey and Neal, 2005). The multi-element geochemistry of Ontong-Java samples is generally more diverse than Kerguelen lavas, spread across the centre of the embedding (Figure 7.3) and being assigned into multiple clusters (Figure 7.5), indicating their similarity to various other localities. Like Kerguelen and PELIP, both islands feature significantly olivine-fractionated basalts (Ely and Neal, 2003), supported by their preclusion of olivine-compatible element (MgO-Cr-Ni) enriched trends in Figures 7.2 and 7.4. The Malaita samples are generally more enriched in Fe_2O_3, Pt and Pd than the Makira samples (with geochemical distinctions likely related to their >27 Myr age difference; Ely and Neal, 2003). Geochemical and isotopic studies indicate that Malaita, the older of the islands, features multiple

OIB mantle components, whilst Makira features significant input from upper mantle MORB components in addition to OIB (Tejada et al., 1996; Tejada et al., 2002), which will contribute to their slightly different multi-element characters demonstrated in this data set.

Canary Island lava variability is dominated by TiO_2 in all three PC spaces (biplots in Figures 7.2b-d) and t-SNE embeddings (Figures 7.3, 7.4 and 7.14), indicating that these are the highest-Ti of the oceanic plumes included in this study (see Appendix E1). All three sampled islands from the west of the island chain (the youngest edifices) plot closely through the various workflow steps and are classified primarily in the Group 1 end-member (on comparing Figures 7.3 and 7.5). The Canary Islands plume is unique within our data set in that it features the most contentious plume connection, however a complex model involving a 'relic' plume thermal anomaly, 'pulsing' heterogeneities in flux and geochemistry, and interaction with onshore tectonic forces in the Atlas orogen satisfy most arguments (Carracedo et al., 1998; Day et al., 2010; Day and Hilton, 2011; Fullea et al., 2015; Taylor et al., 2020). Low $^{3}He/^{4}He$ signatures throughout the chain (Courtillot et al., 2003; Day and Hilton, 2011) imply that a portion of melt components are derived from the shallow asthenosphere, despite HIMU (i.e., enriched) mantle component signatures (Day et al., 2010). Chapter 4 (Lindsay et al., in review[b]) illustrates the difficulties of PGE enrichment in deep, low degree partial melts such as those in the Canaries. Accordingly, the general depletion of all Canary Island lavas in precious metals with respect to other localities in this MLA-based chapter (no strong PGE eigenvector relationships in Figure 7.2 and low concentrations in Figures 7.3 and 7.4; also see Appendix E1 for absolute concentrations) ties into the logic that a system requires a substantial degree of melting to liberate PGE from mineral hosts.

Hawaii presents an interesting anomaly, featuring no pertinent eigenvector associations in Figures 7.2b-d and occupying an embedding space defined only by moderate Fe_2O_3 and TiO_2, and low MgO concentrations in Figures 7.3, 7.5 and 7.14. Hawaiian lavas have $^{187}Os/^{186}Os$ between 0.12856 and 0.13851 (Brandon et al., 1999) in addition to high Re/Os and Pt/Os, a signature widely attributed to inclusion of LLSVP material and firmly establishing Hawaiian plume roots at the CMB (Sleep, 1990; Bennett et al., 1996; Harrison et al., 2017; Béguelin et al., 2019). However, unlike Kerguelen, we do not observe enrichment

in any of the base and precious metals in Hawaiian lavas (Crocket, 2002a; Crocket, 2002b; and new data from this study). The LLSVP signatures of Hawaiian lavas fall into two end-members: Loa, which is the isotopically enriched member associated with geochemistry indicating an inheritance from recycled lithosphere; and Kea, the more isotopically depleted member from the lower mantle (Jackson et al., 1972). Haleakala, Maui and Kilauea (used in our study) primarily lie within the depleted Kea trend (Hanano et al., 2010), perhaps suggesting an origin of their shared low PGE signatures separate from the enriched Loa islands.

7.4.1.2. Transitional plumes

Building upon prior studies that used MLA to assess PGE concentrations in the NAIP (Chapter 5; Lindsay et al., 2021) and the PELIP (Chapter 6; Lindsay et al., accepted), our new combined model strengthens our understanding of plumes that slowly migrate from intracontinental settings, through active rifting environments and continue their lifecycle as purely oceanic plumes. The major trends from all MLA outcomes for the transitional set (summarised in Figure 7.15) are interpreted herein.

From both PCA (Figure 7.6a-d) and t-SNE (Figures 7.7, 7.8 and 7.15), a clear split between north (NAIP) and south (PELIP) geochemistry is evident, something suggested on a qualitative basis in Chapter 6 (Lindsay et al., accepted) and described conclusively here. Analysing both regions simultaneously illustrates that variability in NAIP lavas is strongly controlled by MgO, Cr, Ni and Ir (clustering them mainly in Groups 1 and 3 in Figure 7.9), whilst variability in the PELIP is associated with TiO_2, Fe_2O_3 and Cu (clustering them mainly as Groups 4-6 in Figure 7.9). Although we observe the same geodynamic development in both intracontinental lavas prior to rifting and oceanic trail lavas, each plume has its own geochemical character.

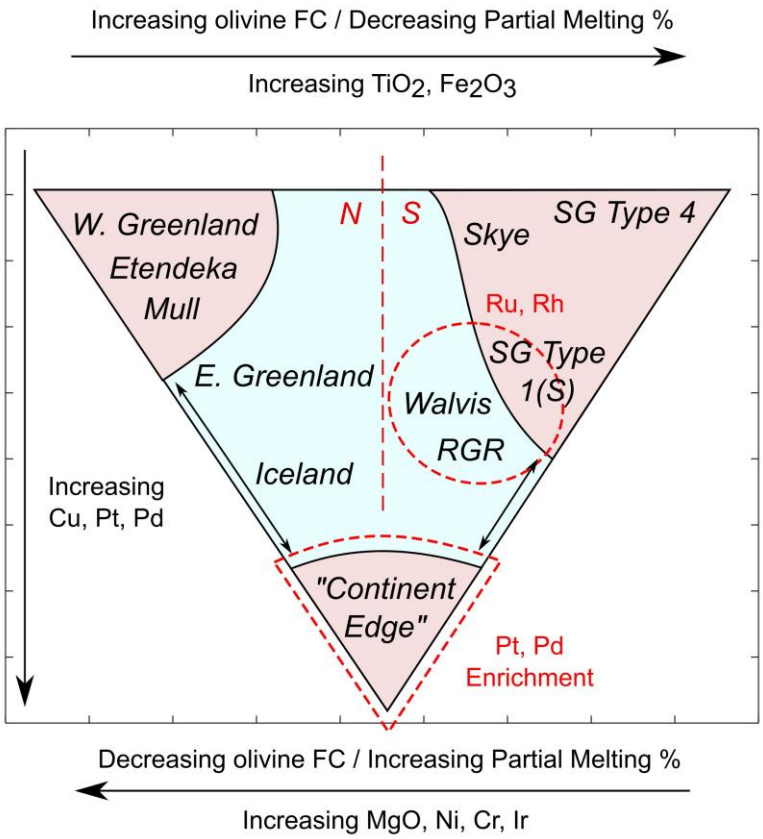

Figure 7.15 – *A summary of information gained from MLA results for the transitional data set, arranged in a simplified embedding shape (Figure 7.7). The dominant trends of multi-element associations are indicated by arrows alongside the geochemical controls implied by each. Individual (i.e., localised) PGE enrichments in the sample set and the approximate north-south split are highlighted in red dashed outlines. N – North Atlantic, S – South Atlantic, FC – fractional crystallisation, RGR – Rio Grande Rise, SG – Serra Geral, S – Southern. Continent-edge includes East Greenland and Serra Geral Type 1 (Central-Northern). Red and blue shading represents the distribution of continental and oceanic plume lava samples in Figure 7.7, respectively.*

Overall, NAIP lavas have significantly higher MgO than PELIP lavas (excluding Etendeka, discussed separately), and as established by Lindsay et al. (2021), Cr and Ni (which partition readily into Mg-bearing minerals such as olivine and the spinel group) accordingly share variability patterns. As per Section 4.1.1, positive MgO-Ni-Cr anomalies reflect localities with higher degrees of partial melting attributed to the Icelandic plume. In the PELIP, the dominant TiO_2-Fe_2O_3-Cu trend is more complex to decipher, but can be related back to previous results from Chapter 3, which attribute the majority of Paraná onshore lava major and

trace element geochemistry to a high degree of olivine fractionation prior to lava eruption. This will have removed MgO, Cr and Ni in large amounts from the resulting lava composition, allowing for elements such as TiO_2 and Fe_2O_3 to dominate the higher-level data structure for the region. In the absence of MgO enrichment, fluctuations in the other major element oxides drive the multi-element signatures in Paraná. Indeed, the Serra Geral Group lavas are classically defined by their TiO_2 concentrations (e.g., Fodor, 1987; Peate et al., 1992; Peate, 1997) and variations throughout the province are widely agreed to reflect the underlying plume geometry (e.g., Bellieni et al., 1984; Piccirillo et al., 1988; Gibson et al., 1995; Peate and Hawkesworth, 1996; Beccaluva et al., 2020).

For the majority of data set variability, Ru, Rh, Pt and Pd appear to be shared between NAIP and PELIP (with eigenvectors positioned between the groups in Figure 7.6b, representing more than half of cumulative variability). In lower-order PC3-6 (Figures 7.6c-d), PGE trends are more distinct, indicating that their variability is more localised. In general, Ru-Rh enrichment is found in Serra Geral Type 1 (Southern) lavas, which is attributed to the incorporation of spinel into Paraná melts, as well as SCLM sulphides (Chapter 3; Lindsay et al., in review[a]). The high degrees of partial melting (between 22 and 25 % of a metasomatised lithospheric mantle at ~1,500°C; Gibson et al., 2005) afforded by maximised lithospheric thinning in the final stages of CFB magmatism in Brazil allowed for the substantial melting and exhaustion of SCLM mineral phases, introducing the more compatible PGE to magmas (Chapter 3). The rapidly changing pressure conditions beneath a thinning lithosphere likely introduced features of high degrees of partial melting not often experienced by purely oceanic plume settings such as Hawaii or the Canary Islands (Section 7.4.1.1), particularly those with deep melting signatures.

An exception to the distinct north-south geochemical split lies in the Group 2 signature (the lowermost region of Figure 7.9), shared by many lavas from Serra Geral Type 1 (Central-Northern) and East Greenland (onshore) (Figures 7.7 and 7.15). The defining characteristic of these lavas appears to be a strong enrichment in Cu, Pt, and especially Pd (Figure 7.8) in addition to similar, moderate major element concentrations. Forward melt modelling from Chapter 3 (Lindsay et al., in review[a]) indicated that the incorporation of metasomatised SCLM, within which Pd, Cu and Au amongst other metals would be pre-enriched,

drove the distinctive Type 1 (Central-Northern) flavour in the Paraná CFB. In East Greenland, plume-derived magmas were upgraded at crustal levels to create the highly enriched Pt-Pd Skaergaard intrusion. The placement of both the Serra Geral Type 1 (Central-Southern) and East Greenlandic lavas at the same stage (final continental lavas) and on the same side of their respective plumes makes for compelling evidence that the process of Pt-Pd acquisition is common to both settings and is not a region-specific anomaly. Having very similar multi-element signatures (i.e., plotting closely in Figure 7.7) also implies that the major and trace element controls (i.e., melting, fractionation, contamination) may be aligned in these melts, which may indicate a “sweet spot” for Pt-Pd enrichment mantle conditions in a plume-rift setting.

An interesting feature of our multi-element analyses affecting a smaller set of localities lies in their relative positioning within t-SNE maps – Etendeka within a predominantly NAIP cluster (despite belonging to the PELIP), and Skye within a predominantly PELIP cluster (despite belonging to the NAIP) (Figures 7.7). This indicates that, given t-SNE is best suited for retaining similarities in high-dimensional space (as per Becht et al., 2019) these localities share more in common with lavas from the opposite region (Etendeka with the Icelandic plume, Skye with the Tristan plume), which is juxtaposed against the otherwise clear north-south differentiation in Figure 7.15. Within the PELIP, Etendeka lavas are thought to be derived from particularly deep asthenospheric melts from beneath the African continental lithosphere with elevated MgO levels (> 15 wt.%) (e.g., Gibson et al., 2005; Natali et al., 2017; Jennings et al., 2019; Beccaluva et al., 2020; Zhou et al., 2020), which contrasts with all of the Paraná lavas (maximum of 7 wt.% MgO). Whether olivine fractionation was markedly different on each side of the PELIP, or melting conditions varied beneath different portions of the pre-rift Gondwanan lithosphere, it is evident that the dynamism of continental break-up imposed heterogeneous magmatic characters within a single plume melting system. This illustrates that plume-derived lava signatures are not inherently defined by their relative spatial positions (i.e., a ’Tristan‘ signature) but by the melt column properties related to their positioning within a region and beneath the lithosphere.

7.4.1.3. Continental and oceanic plumes

By interpreting the transitional plume data set, we observe clear differences that a shift in geodynamic environment has on multi-element, (especially PGE) variability in plume-derived lavas. The third and final data set of this chapter extrapolates the transitional relationship to the extremes of intraplate magmatism, incorporating transitional plumes [H2] with plumes that have always been within an oceanic setting [H1]. This sub-study presents the most complex data structure in the chapter, particularly in regards to clustering and recognising elemental trends in embeddings. The intricacies of global plume geochemistry cannot be succinctly described by a single study, given that we are working with a finite list of elements, a requirement for a full suite of measurements per sample, and a list of localities limited by the elements included in their original study. Our understanding of global plume-derived magma signatures will improve by adding more samples from new work (provided they have measurements for the ten included elements), and this section is envisaged as an evolving model that, as more analyses are added to the global data catalogue, will become more robust with time. Nonetheless, we identify promising trends within the data available in Figures 7.10-7.13, which will serve as a basis for further additions and/or improvements to our model. The major trends from all MLA outcomes for the combined set (summarised in Figure 7.16) are interpreted herein.

Given that the geochemical interpretations of the localities in the amalgamated [H3] data set have been discussed at length in previous models, their role in the combined data set ultimately involves establishing how their multi-element plume signatures compare to samples from outside their own setting (i.e., continental vs. oceanic end-members). Rio Grande Rise and Walvis Ridge lavas are known to exhibit trace element and isotopic similarities with late-stage onshore lavas from their respective continents as remnants of SCLM are incorporated into melting columns (Gibson et al., 2005). Purely oceanic plumes would be expected to contrast strongly with continental and transitional-oceanic plume chemistry. This is exemplified by Canary Islands and Hawaii oceanic samples sharing a reasonably tight cluster (assigned to Group 2) at the bottom right of the embedding for this data set (Figures 7.11a and 7.16). This relationship demonstrates the shared lack of base and precious metal enrichment in the two localities (which constitute seven of the ten variables included in the algorithm)

as illustrated by their absence from prominent PGE eigenvector associations in Figures 7.10b-d. This compares directly with the NAIP and PELIP onshore lavas, which very rarely share an embedding space with Canary Islands or Hawaiian samples in Figure 7.16, inevitably reflecting their different intraplate settings and distinct geochemical reservoirs. With respect to all other localities, Canary Islands and Hawaiian lavas exhibit the lowest degrees of partial melting (1-5% and 4-10%, respectively; Norman and Garcia, 1999; Day et al., 2010). This is reflected in negative MgO-Ni-Cr-Ir-Ru anomalies in our study (i.e., lack of eigenvector association with these elements in Figure 7.10b-d and placement within a low-concentration sector in Figures 7.11a and 7.12).

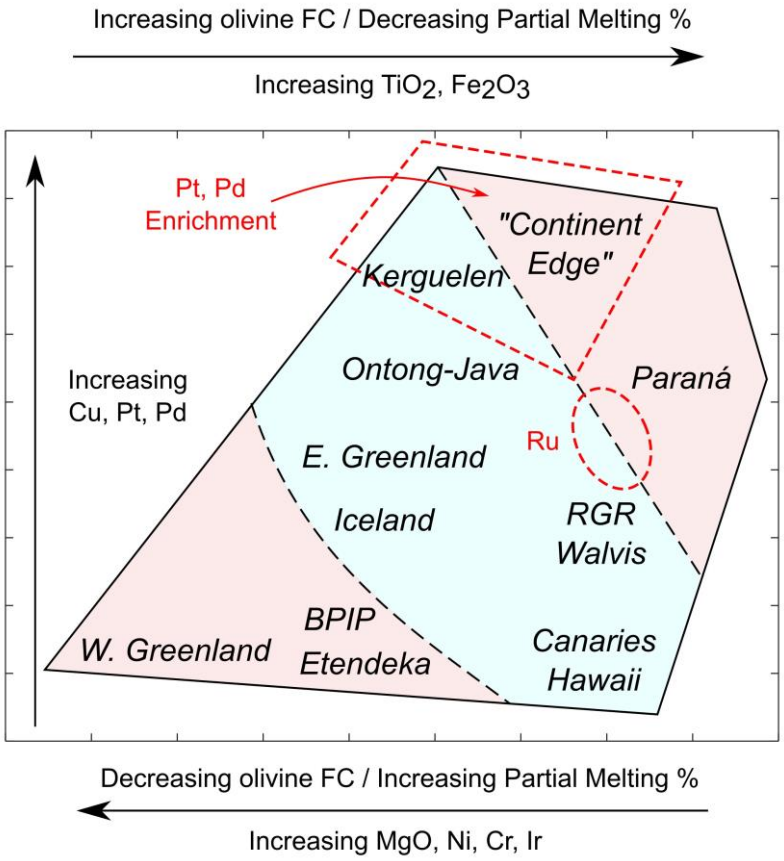

Figure 7.16 – *A summary of information gained from MLA results for the continental vs. oceanic data set, arranged in a simplified embedding shape (Figure 7.11). The dominant trends of multi-element associations are indicated by arrows alongside the geochemical controls implied by each. Individual (i.e., localised) PGE enrichments are highlighted in dashed red outlines. FC – fractional crystallisation, RGR – Rio Grande Rise, SG – Serra Geral, S – Southern. Continent-edge includes East Greenland and Serra Geral Type 1 (Central-Northern). Red and blue shading represents the distribution of continental and oceanic plume lava samples in Figure 7.11, respectively.*

The majority of the remaining oceanic samples (NAIP and PELIP offshore, Ontong-Java, and Kerguelen) are found in the centre of the embedding (Figures 7.11a-b and 7.16), although they are spread across a larger area mainly within the Group 7 sector (Figure 7.13) compared to the more focused Canary-Hawaii association. Nonetheless, the high-MgO/Cr/Ni oceanic NAIP samples tend to plot near to their onshore equivalents rather than the centre of Figure 7.11a, indicating the highest degrees of enrichment in this element association are restricted to a sub-set and isn't inherent throughout all NAIP offshore. In line with Section 4.1.2, East Greenlandic offshore samples tend to plot further from the highest-MgO zones in the embedding for the Atlantic data set (Figures 7.7-7.8). This suggests the younger Icelandic lavas are defined by their anomalous MgO, Cr and Ni concentrations, hence their split in the global model (Figure 7.11a; Appendix E3); this perhaps reflects the more recent addition of significant rift magmatism to Icelandic melts.

For the onshore lavas (belonging to the PELIP and NAIP), we see similar dominant (but not exclusive) areas of the embedding occupied by samples, most easily recognised in Figure 7.11b with two major clusters on the bottom left and top right. By comparing this plot to Figure 7.11a, the left-hand cluster (Groups 1 and 4; Figure 7.13) features NAIP samples, whilst the right-hand cluster (Groups 3, 5 and 6; Figure 7.13) features PELIP samples. The clear split is likely caused by the left-right bimodality shown in the embedding (Figure 7.12), where we will have MgO-enriched and TiO_2-enriched lavas, respectively. We already see significant diversification in these major elements within a single CFB (i.e., PELIP), so it is logical that separate CFB provinces may also be defined in this manner. Multi-element signatures in the NAIP and Etendeka appear to reflect a comparatively high degree of partial melting, incorporating higher abundances of less 'fusible' elements such as Ni, Cr and Ir. In comparison, the Serra Geral CFBs have a diverse range of TiO_2 concentrations in addition to Ru and Pd anomalies, which do not appear to be a function of high melting degree.

High-Ti Serra Geral Type 4 lavas along with Canary Islands and Hawaii plot separately to the rest of the PELIP and within the high-TiO_2 sector on the right of the embedding (Figure 7.11a and 12). Like the Canary Islands and Hawaii, this magma type from Paraná was generated from small degree partial melts (i.e., 10-15 %), but within the SCLM, beneath thick continental lithosphere,

instead of within an oceanic plume column (Chapter 3; Lindsay et al., in review[a]). Despite different physical mechanisms, the small degrees of melting in each of the three locations is likely to be similar, leading to their t-SNE association. Passive melting at depth due to the 'lid' effect of thick lithosphere above a plume source (Serra Geral) (e.g., Arndt et al., 1993) and deep plume melting within the asthenosphere (Canaries/Hawaii; Chapter 4; Lindsay et al., in review[b]) can create similar results and importantly, no positive metal anomalies throughout Figures 7.10-7.13.

The majority of multi-element signatures for each locality through Figures 7.10-7.13 (summarised in Figure 7.16) largely replicate the most distinct trends shown in results for [H1] and [H2] (Figures 7.14 and 7.15), although there are some notable exceptions illustrating quirks in the establishment of a global plume geochemical framework that we are working towards. For example, in Figure 7.16, the three corners of the embedding are occupied by distinct 'flavours' of plume-derived lavas, as described through the previous sections. The first (bottom right) is dominated by small degree partial melts from an oceanic plume sources, with deep melting signatures. The second (bottom left) comprises mostly transitional plumes with the highest degrees of partial melting in the study. The last (top right) hosts continent-edge lavas with moderate TiO_2 and MgO concentrations and PGE anomalies. Between these corners, the continuum represented by Groups 6 and 7 (Figure 7.13) hosts the bulk of the oceanic localities (Ontong-Java, Kerguelen and the offshore trails from the NAIP and PELIP). Given the ability of t-SNE to 'map' multi-element similarities in samples and our previous assessment of Groups 6 and 7 as background geochemical end-members with no prominently anomalous element concentrations, we conclude that this central region of the embedding represent a 'baseline' plume signature within the context of our study. These could perhaps represent tholeiites with negligible crustal contamination and moderate degrees of partial melting. In contrast, the corner end-members in Figure 7.16 exhibit distinct enrichment processes that boost concentrations of one or more of the included elements to anomalous levels (i.e., high z-scores), deviating from the standard intraplate signature. By summarising the trends from the MLA workflow in Figures 7.14, 7.15 and 7.16, we can imply that the distribution of all included samples throughout the embedding space broadly correlates with enrichments/depletions

in the two main multi-element associations along the x-axis, MgO-Ni-Cr-Ir and TiO_2-Fe_2O_3 (i.e., high and low degree partial melts, respectively). In contrast, the contribution to overall data structure from the Ru, Rh, Pt, Pd and Cu are more nuanced in all three plots, and require more explanation (Section 7.4.2).

7.4.2. Reconciling PGE enrichment with geodynamic properties

As discussed in Chapter 2, PGE enrichment in intraplate settings is complex, highly heterogeneous and significantly affected by upper mantle conditions (e.g., Puchtel and Humayun, 2000; Bennett et al., 2000; Brandon and Walker, 2005; Day, 2013; Webber et al., 2013; Barnes et al., 2015). However, our findings in this study provide an insight into some commonalities in the PGE signatures of plume-derived lavas through different settings. Using the Courtillot et al. (2003) study as a basis, we can observe differences in physical and chemical properties between settings that may cause certain plume-derived lavas to become enriched in PGE. This focuses exclusively on mantle, asthenospheric and SCLM-derived controls on magma fertility, to investigate source enrichment prior to later-stage lithospheric upgrading processes. Across all results, as condensed within Figures 7.14-7.16, the lavas with notable enrichments in PGE (and accompanying base metal) concentrations are: Serra Geral Type 1 lavas (Ru-Rh for Southern and Pt-Pd-Cu for Central-Northern); West Greenland (Ni-Ir); East Greenland onshore lavas (Pt-Pd-Cu); Iceland and East Greenland offshore (Ir); Kerguelen (Ir-Pt-Pd); and Ontong-Java (Ir-Pt-Pd). Despite enrichment spanning both onshore and offshore settings, we can draw upon information gleaned from multi-element trends to inform our interpretation of metallogeny in plume systems.

Firstly, there is a distinction between Iridium-group PGE (IPGE – Os, Ir, Ru) and Palladium-group PGE (PPGE – Rh, Pt, Pd) enrichment in all three sub-studies and appears to be related to significant magmatic differentiation processes (Barnes et al., 1985). The two groups are consistently separated throughout most MLA-based data visualisations, establishing their distinct geochemical behaviour in melting systems, the conditions of which vary from plume to plume. The IPGE and Rh are generally more compatible than Pt and Pd of the PPGE during mantle partial melting, because of their mineral-melt partition coefficients within typical mantle phases. The IPGE and Rh tend to form nano-nuggets, alloys and platinum-group minerals (PGM) within the framework of mafic

silicates such as olivine and spinel-group minerals, reflected by Ni and Cr (Mitchell and Keays, 1981; Peach et al., 1990; Barnes and Picard, 1993; Peach et al., 1994; Alard et al., 2000; Maier et al., 2003b; Righter et al., 2004; Helmy and Bragagni, 2017; Hughes et al., 2017; Park et al., 2017). The PPGE are more often found within interstitial base metal sulphides (BMS), arsenides and tellurides (especially Cu-bearing varieties), and have very low compatibility with silicates (Mitchell and Keays, 1981; Barnes et al., 1985; Borisov et al., 1994; Barnes et al., 1997; Holzheid et al., 2000; Lorand and Alard, 2001; Bockrath et al., 2004; Mungall et al., 2005; Righter et al., 2008; Lorand et al., 2013; Mansur and Barnes, 2020). Under partial melting, the more fusible interstitial Pt- and Pd-bearing phases will be consumed before IPGE- bearing PGM (including alloys) or those contained within high-temperature mafic silicate/oxide minerals, fractionating the two sets of PGE at low to moderate degrees of partial melting (Rehkämper et al., 1999; Maier et al., 2003a; Mann et al., 2012). At higher degrees of partial melting, when IPGE phases and olivine and spinel-group minerals begin to melt, we would expect a flatter chondrite-normalised pattern on multi-element PGE plots in resulting magmas, particularly once all mantle BMS are exhausted.

In the global data set in this thesis, the highest Ir concentrations occur in samples with MgO concentrations between 10 and 30 wt.% (Appendix E3). The close relationship between Ir and MgO, Ni and Cr in Figures 7.2, 7.4, 7.6, 7.8, 7.10 and 7.12 establish this link as ubiquitous regardless of plume setting – if degrees of partial melting are high enough, be it in an oceanic or continental setting, IPGE will be introduced to melts from host minerals being consumed in the source. Normally, Ru (of the IPGE) and Rh (that shares silicate partitioning behaviour with the IPGE despite being a PPGE; Capobianco and Drake, 1990) would be included in this multi-element group, given their compatibility in similar mantle phases to Ir and subsequent sensitivity to melting degree. However, when Serra Geral Type 1 (Southern) lavas are included in analyses (i.e., [H2] and [H3]), their significant Ru-Rh enrichment overshadows any correlation with MgO and the relative contribution of other localities to this trend is minimal (i.e., in the PC3-4 spaces in Figures 7.6c and 7.10c). In the oceanic plume data set [H1], we see Ru eigenvectors trend closely with Ir (Figure 7.2b-c), when compared to similar plots from the continent-inclusive data sets.

Base metal sulphides in a mantle source can be exhausted between 12-23 % partial melting for 250 ppm sulphur depending on temperature and pressure (Rehkämper et al., 1999; Luguet et al., 2003), and chalcophiles will only be released in small amounts until this point. The strong link between IPGE enrichment and high degrees of partial melting is evident in our study; West Greenland, East Greenland (offshore) and Iceland exhibit the strongest affinity for MgO-Ni-Cr-Ir eigenvectors (Figures 7.6 and 7.10) indicating high degrees of melting (and Ir incorporation) with minimal olivine fractional crystallisation allowing retention of high MgO signatures. Kerguelen lavas, the most PGE-enriched non-transitional oceanic plume samples (Figure 7.2b-c; Appendix E1) are estimated to be generated from 20-40 % melting of plume material (Chazey and Neal, 2005). Ontong-Java models, also relatively PGE-rich in our study compared to other oceanic plumes (Figure 7.2b-c), suggest ~30 % partial melting of both asthenosphere and plume mantle (Ely and Neal, 2003). Previous work on both Kerguelen and Ontong-Java lavas illustrate their enrichment in Pt and Pd, and modelling implies that the addition of 0.5-1% core material to the CMB-origin plume could satisfy their observed concentrations (Ely and Neal, 2003; Lorand et al., 2004; Chazey and Neal, 2005).

In support of the role of partial melting in PGE collection, we can establish geochemical and physical properties in PGE-poor localities that may have inhibited enrichment. Canary Island, Hawaii, Etendeka and Serra Geral Type 4 lavas regularly exhibit depletions in all included characteristics through MLA outcomes. The bulk of the Canary Islands and Hawaii are formed from notably small degree partial melts (1-6 % and 4-10 %, respectively; Norman and Garcia, 1999; Day et al., 2010) of relatively deep plume components in the upper mantle (Chapter 4; Lindsay et al., in review[b]). This may be an effect of plumes beneath reasonably old and thick oceanic lithosphere, which may impose sub-lithospheric pressures approaching those found under continents. These melting conditions were unlikely to liberate significant amounts of PGE from their sources, given the aforementioned 12-23 % range from the literature. Serra Geral Type 4 and Etendeka parent magmas are some of the deepest-origin melts in the PELIP (< 20 % partial melting in the garnet stability field; Rämö et al., 2016; Licht, 2018; Beccaluva et al., 2020) and are also unlikely to have exhausted mantle sulphides regardless of source enrichment (as modelled in Chapter 3 and Lindsay et al., in

review[a]). The transition from High-Ti (Type 4) to Low-Ti (Type 1) lavas in Paraná synchronises with an increase in partial melting, which may be related to the observed increase in metal basket (Appendix E2). As described in Chapter 3, progressive thinning of the lithosphere above the Tristan plume from ~130 Ma likely allowed shallower, higher degree partial melts to exhaust and incorporate metasomatic SCLM BMS. The contrast between NAIP and PELIP rocks in Figures 7.7 and 7.11a may be connected to more basic mantle properties. The Icelandic plume has notably high $^{3}He/^{4}He$, with strong geophysical connections (slow tomography) to the deep mantle and a high volcanic flux; in contrast, the Tristan plume has low $^{3}He/^{4}He$ with poor tomographic and flux signatures (Courtillot et al., 2003). The thermal anomaly from both plumes is distinct, and this is manifest as different melting properties and subsequently, variable multi-element geochemistry.

The largest and most consistent PGE anomalies in this study are in plume-derived lavas found at the edges of continental margins and/or thinner continental lithosphere from the transitional plume data set, namely Serra Geral Type 1 varieties and East Greenland (onshore) (frequently associated with PGE eigenvectors in Figure 7.10b-c and high-PGE zones within Figure 7.14; also see Appendix E3). The magmatic systems emplaced by plume-rift interactions beneath a thinning continental lithosphere have been highlighted in the literature as particularly prospective locations for ore genesis, being described as “ore factories” by Pirajno and Santosh (2015). The combined effects of dynamic melting conditions shallowing with time, access to metasomatic BMS in the SCLM, and extensional fault systems for magmatic transportation appear to provide an ideal set-up for Ni-Cu-PGE mineralisation on a global scale.

7.4.3. Intraplate PGE Mineral Systems

Melting conditions imposed by geodynamic settings in the mantle dominate the discussion surrounding metal acquisition in intraplate settings, and the multi-element trends featured throughout our results underpin a large proportion of controls on the magmatic system. With a grasp of global plume geochemical signatures (including PGE) and integrated knowledge of the processes that influence lava compositions in plume settings (Sections 7.4.1 and 7.4.2), we can begin to work towards a Mineral Systems model for intraplate metallogenesis, summarised in Figure 7.17. Mineral Systems incorporate the

spectrum of chemical, physical and geological controls on ore body formation, from source to deposition via agents (i.e., magma, fluids) and pathways (i.e., lithospheric migration) (Wyborn et al., 1994; McCuaig et al., 2010; Barnes et al., 2016). The four hypothetical intraplate scenarios from Figure 7.17, attributed to different settings, source, agent, pathway and deposition characteristics, can be applied to all localities in this study to classify metallogenesis. This is also applied to an itemised Mineral System block diagram in Figure 7.18 (adapted from McCuaig et al., 2010), which demonstrates the features of successful intraplate PGE mineralisation at different stages in a magmatic system from district to camp to prospect (i.e., regional to local to deposit).

Beginning with continental plumes, restricted to the NAIP and PELIP here, we illustrate two scenarios; 'failed' and 'successful ore genesis'. In Scenario 1, a plume-derived magma generated within the garnet stability field that may have PGE contributions from the CMB or the plume itself, but negligible amounts from the SCLM. Small degree partial melts (the agent transporting metals away from source) will be insufficient to incorporate mantle BMS and consequently form low MgO, high TiO_2 volcanic and intrusive rocks at surface with low PGE abundances (e.g., Serra Geral Type 4, Etendeka). Higher degree partial melts may liberate PGE from BMS and silicates for moderate concentrations at surface (e.g., West Greenland). Ultimately, source liberation in this scenario is poor and although depositional opportunities may exist in this setting, the parent magma is PGE-poor and unsuitable for upgrading.

Scenario 2 represents a similar setting, but within the shallower spinel stability field beneath thinner continental lithosphere (i.e., continent edges), a product of continued continental break-up. Here, parent magmas are PGE-enriched via mantle and/or SCLM sulphide and PGM exhaustion, and are transported to the surface via extensional and transtensional pathways to form lavas containing elevated but variable metal baskets. The enriched components supplied by the SCLM are themselves geochemically heterogeneous and can boost concentrations of different metals (including PGE) in magmas from locality to locality (as demonstrated in the NAIP; Chapter 5; Hughes et al., 2015; Lindsay et al., 2021). In East Greenland and the BPIP, depositional conditions led to mineralisation in the Skaergaard and Rum Complexes. In Paraná, the Southern and Central-Northern Serra Geral Type 1 lavas indicate promising metal

endowment in parent magmas and multi-element signatures aligned with East Greenland (Chapter 3; Lindsay et al., in review[a]). Recent studies indicate there may be Ni-Cu-PGE mineralised intrusions just west of the region (de Farias and Filho, 2021), validating interpretations in this thesis and indicating fresh mineral exploration potential for Brazil. In the NAIP, the deposition characteristics at a crustal level (i.e., traps, crustal contamination, fractional crystallisation, S-saturation and/or oxidation state) are demonstrably hospitable to the development of significant Ni-Cu-PGE orthomagmatic sulphide mineralisation – these ore bodies align with the optimal model in Figure 7.18.

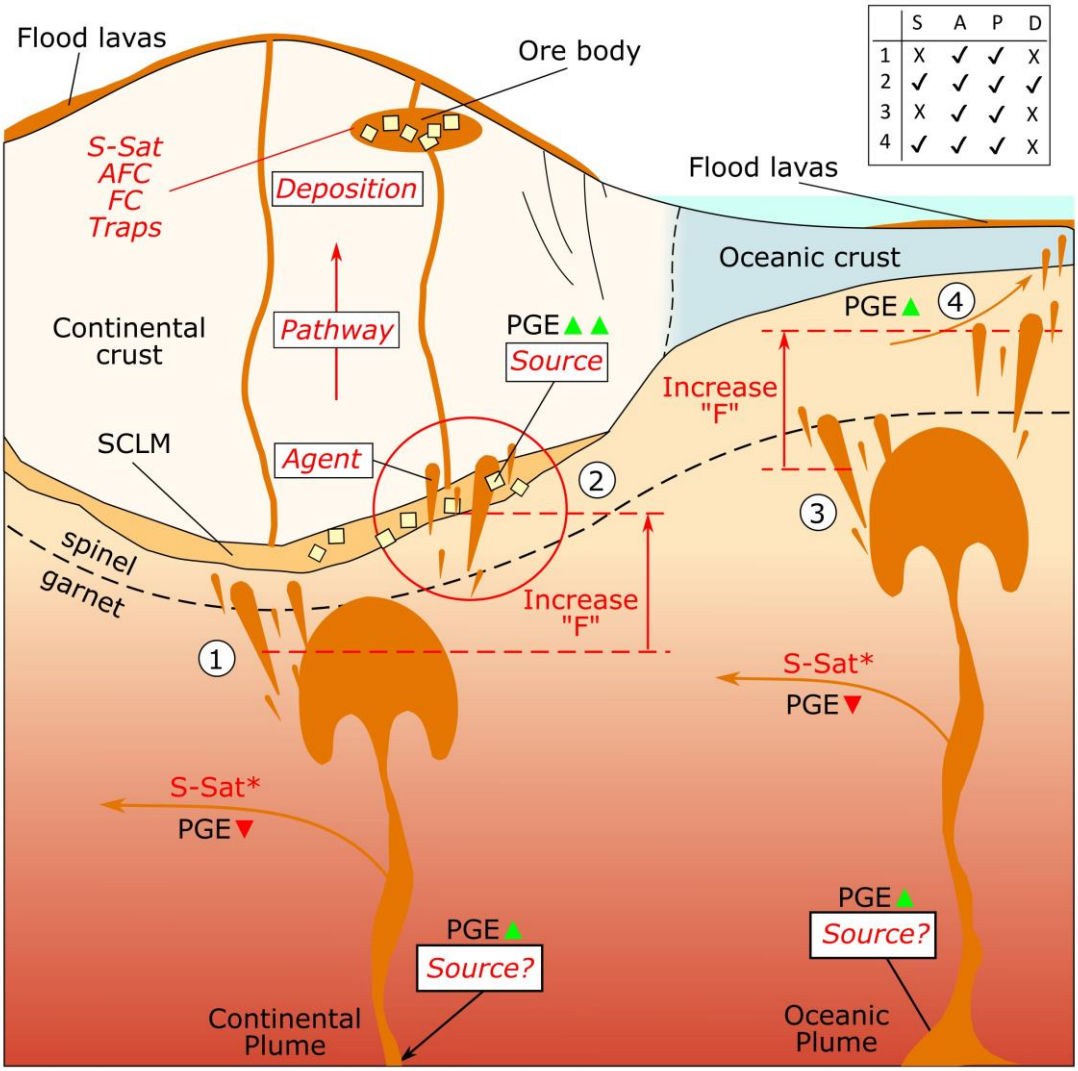

Figure 7.17 – *Schematic cross-section summarising plumes as a Mineral System based on machine learning multi-element information. The four scenarios refer to different plume settings in which Source liberation (S), Agent (A), Pathway (P) and Deposition (D)*

Figure 7.17 (cont'd) - *components vary (inset table); formation of an ore deposit requires all four. Scenarios 1 to 4 are described in-text. Scenario 1 - Serra Geral Type 4 and Etendeka. Scenario 2 - East Greenland, West Greenland, BPIP and Serra Geral Type 1, although only East Greenland and BPIP host significant PGE mineralisation. Scenario 3 - Canary Islands and Hawaii. Scenario 4 - PELIP and NAIP offshore trails, Iceland, Kerguelen and Ontong-Java. Sulphide saturation can occur at any stage in the system and would significantly deplete chalcophiles in the parent magma. Sourcing of PGE from the core is possible, but still requires sufficient partial melting to liberate at the asthenosphere.*

In an oceanic setting, Scenario 3 describes < 10 % partial melts of a plume source, with no significant PGE liberation, even if plume material contains PGE-bearing phases. We observe this in the Canary Islands and Hawaii. The properties of deep mantle components dominate the multi-element signature in these localities in the absence of significant precious and base metal concentrations. In Scenario 4, higher degree partial melting (from ~15 to 30 % or more as observed in Kerguelen and Ontong-Java; Neal et al., 2002; Chazey and Neal, 2005) allows for the incorporation of PGE from sulphides in a plume source. Whilst some oceanic plumes retain small but significant PGE anomalies (namely Rio Grande Rise, Walvis Ridge, Iceland, East Greenland offshore, Kerguelen and Ontong-Java), it is unlikely that oceanic lithosphere will provide the necessary depositional tools to form S-saturated ore bodies. Furthermore, oceanic PGE contents are often orders of magnitudes smaller than those found in continent-edge intraplate lavas (as described by Whitehouse, 2020). As highlighted in Figures 7.17 and 7.18, S-saturation at any stage prior to deposition can negatively influence the chances of PGE mineralisation by depleting a once-fertile magma.

As a final caveat towards PGE Mineral System, the occurrence of S-saturation in a magma at a crustal level is a crucial determining step in plume magma metal content and ore genesis. Sulphide saturation (S-saturation) is the point at which a silicate magma can no longer incorporate S, and a sulphide liquid exsolves from the parent magma as a discrete and immiscible phase (e.g., Shima and Naldrett, 1975; Campbell and Naldrett, 1979; Lesher and Burnham, 2001; Crocket, 2002a; Maier, 2005; Maier and Groves, 2011). This can be activated by addition of excess S to the parent magma from country rocks (usually arkosic sediments, shales or evaporites), changes to fractional crystallisation by addition

of FeO and SiO_2 and changes in pressure/temperature during magma ascent causing chemical instability (Mavrogenes and O'Neill, 1999; Li et al., 2009; Ripley and Li, 2013; Hayes et al., 2015; Lesher, 2017). In a successful PGE Mineral System, S-saturation would ideally occur close to the deposition horizon, to minimise the loss of metals (Naldrett, 1997; Lightfoot, 2007; Hughes et al., 2016). If S-saturation is triggered whilst the fertile magmas are still deep in the lithosphere or even within the asthenosphere or mantle, the majority of the chalcophile load is effectively lost to exsolving sulphide liquids unless physically trapped, as described by chalcophile-depleted associated lava compositions. The time-sensitive nature of S-saturation is thus vital in a prospective intraplate ore system, in addition to the original source of magma enrichment.

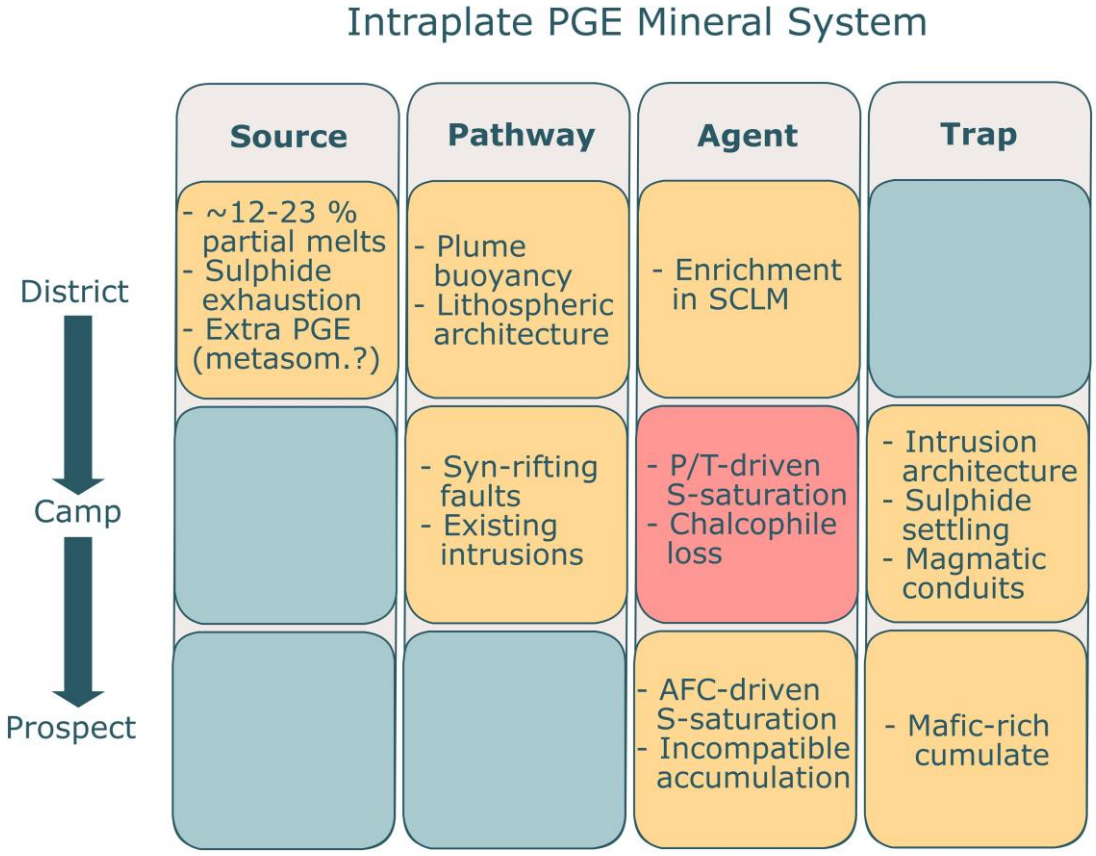

Figure 7.18 – *Mineral System block model based on criteria by McCuaig et al. (2010) for intraplate PGE metallogenesis, using all findings from the MLA-based workflow in this chapter, and information from Chapters 2-6 of this thesis. Agent column refers to chemical processes within the agent (i.e., magma). Orange cells represent key processes at the given scale, blue represent processes are ineffective at the given scale and red cells represent detrimental processes at the given scale; the latter primarily involves early S-saturation. Metasom. – metasomatism.*

The Mineral Systems model presented in this chapter seeks to address the three hypotheses introduced earlier, and unites themes discussed throughout the thesis. Oceanic plumes exhibit different PGE enrichment characteristics [H1], inline with their relative degrees of partial melting. The potential for PGE enrichment at source can only be utilised in high degrees of partial melting (e.g., Kerguelen and Ontong-Java). In transitional plume settings (e.g., Tristan and Iceland), highly changeable mantle melting properties beneath rifting continents, revealed by the MgO-TiO_2 continuum in MLA results, directly impact upon metal acquisition in flood basalts [H2], indicating a "sweet spot" for fertility as lithospheric thinning progresses. In the global data set, we find that it is not the plumes themselves that actively drive metallogenesis but the conditions that the mantle is subject to because of plumes in the upper mantle. The liberation of PGE into magmas in mantle sources(s) is an important starting condition; the subsequent stages in the Mineral System determine the overall potential for mineralisation and this inherently reflects the geodynamic setting [H3]. The PGE enrichment supplied by higher degree partial melts of the SCLM outweighs the highest levels of PGE enrichment in an oceanic setting, conclusively linking intraplate magmas and continental lithosphere to metallogenesis, albeit in a more nuanced manner than initially proposed. As per Fiorentini et al. (2018), this may not necessarily translate to cratonic margins or palaeo-margins hosting canonical layered intrusion type PGE deposits (i.e., Skaergaard) in each case, but rather more likely PGE-rich conduit hosted magmatic systems (i.e., Noril'sk) that work alongside existing crustal architecture to promote mineralisation.

Overall, a machine learning approach has been crucial in interrogating such a large, diverse and wide-reaching data set that incorporates a multitude of "big picture" implications for mantle geochemistry. By reducing dimensionality via PCA and t-SNE, we can effectively summarise complex multi-element variability in intraplate lavas and connect PGE variations to significant major and trace element controls (i.e., Figure 7.14-7.16). The workflow remedies difficulties encountered when comparing bulk geochemistry from different studies with different element suites and missing data, by maximising variability information available for the reduced line-up of elements that *are* common through all studies. Clustering using the *k*-means MLA allows for the simple assessment of similar geochemical trends through all included variables and is particularly useful when

comparing and contrasting variability in lavas from different plume settings. The recognition of geochemical associations transcending different plume settings far removed from each other (i.e., a single *k*-means classification) further exemplifies the necessity of a complete Mineral Systems approach, and a detailed account of what features in an intraplate setting are conducive to ore body genesis beyond a plume conduit and thermal anomaly in a global context.

This study presents an early iteration of a global account of plume metallogenesis with a limited data set, which can only be improved upon with PGE data from other plumes, increased sampling for plumes in this study, and introducing isotopic data such as $^{187}Os/^{188}Os$. Whilst reducing global intraplate metallogeny to a single model is a difficult task, the foundations laid by this detailed MLA-based framework provide many opportunities to assimilate new data and expand our understanding of some of the Earth's rarest and most crucial commodities.

7.5. Conclusions

A machine learning approach to plume-derived lava geochemistry provides an effective and efficient means for analysing global controls on PGE metallogenesis. By resolving complex multi-element variability information for selected major, trace and precious elements through the sample set, and contrasting signatures from oceanic, transitional and continental plumes, we arrive at a Mineral Systems model for intraplate ore genesis.

1. Machine learning analysis of global data sets allows the first Mineral Systems model for plume-related magmatic sulphide metallogenesis.
2. PGE variability in oceanic plumes is intrinsically linked to conditions of partial melting; parental magmas derived from significantly higher degrees of partial melting (e.g., Kerguelen and Ontong-Java) exhibit the most enriched signatures across the data set, due to exhaustion of PGE-bearing mineral phases in the mantle source.
3. In plume settings with continental and oceanic portions (e.g., the Tristan and Icelandic plumes) significant PGE enrichment is linked to the higher-degree partial melts underneath rifting continental lithosphere and subsequent incorporation of BMS *and* PGM from the SCLM, a signature that fades with distance from the continent.
4. On considering continental *and* oceanic plumes as a whole, whilst high-degree partial melts of a purely oceanic source yields notable PGE enrichment, these are orders of magnitude lower than continent-edge transitional lavas in Paraná and East Greenland, which had the opportunity to upgrade fertile magmas into ore bodies in the continental crust.
5. A degree of probability persists through intraplate Mineral Systems, in which source, agent, pathway and deposition factors must align at the right time to produce a final, mineable deposit from plume-derived magmas. By uniting the deterministic properties of a plume melting system, we suggest the current (and recent geologic) optimum metallogenic situation exists in the relatively thin lithosphere of continent-edge localities during rifting intraplate magmatic events (i.e., East Greenland, the British Isles and, potentially, Paraná).

Chapter 8

Concluding Remarks

The new research presented in this thesis spans a variety of locations, methods and scales, and some of the bulk geochemical data sets contained within these research contributions represent the first of their kind for their respective localities. Collectively the five data chapters (chapters 3 to 7; Lindsay et al., 2021; Lindsay et al., accepted; Lindsay et al., in review[a]; Lindsay et al. in review[b]) provide a global account of geochemistry in settings related to mantle plumes, with a focus on PGE concentrations. Throughout the thesis, a combination of new geochemical data collection, modelling and MLA have been used to tackle the aims, objectives and hypotheses set out in Chapter 1.

With reference to the project objectives ***[O1-O5]*** and hypotheses ***[H1-H3]***, the key outcomes of this thesis are as follows:

1. Plume-derived lavas from different localities have a variety of PGE signatures, with the highest levels of enrichment attributed to high degrees of partial melting and incorporation of SCLM material beneath rifting continents in Greenland and Paraná (Chapters 3, 4, 6 and 7) ***[O1, O2, O3] [H1, H2, H3]***.
2. Sulphide, silicate and oxide mineral melting and exhaustion control the majority of the PGE budget in intraplate magmas, quantified using forward-modelled mass balances for high degree partial melts beneath a rifting continent (Chapter 3) and low degree partial melts of an oceanic plume source (Chapter 4) ***[O2, O3, O4] [H2, H3]***.
3. The machine learning algorithm (MLA) workflow developed in the thesis (Chapters 5, 6 and 7) recognised distinct multi-element trends in oceanic and continental plume-derived lava geochemistry, and highlighted the heterogeneous and localised nature of PGE enrichment trends across the data suite, especially the less compatible Pt and Pd ***[O5] [H1, H2, H3]***.
4. Based on geochemical modelling and MLA workflow outcomes, intraplate PGE Mineral Systems rely on metal enrichment inherited from mantle

sources, syn-tectonic transportation of fertile magmas, timely sulphur saturation, and effective physical traps for ore body genesis (Chapter 7) ***[O2, O4] [H2]***.

In Paraná, contemporaneous surface-level tectonics, namely the rifting of Gondwana and formation of the Atlantic Ocean, imposed substantive geochemical controls on magmas generated below the lithosphere by the Tristan plume thermal anomaly (Chapter 3; Lindsay et al., in review[a]). The stark contrast between modelled garnet peridotite melts with no PGE enrichment in Tenerife (Chapter 4 and Lindsay et al., in review[b]) and spinel peridotite melts with notable PGE enrichments in Paraná illustrates the extent to which thinning lithosphere and shallowing melting environments affect resultant lava geochemistry. Modelling results indicate that the presence of an enriched (metasomatic) source in the uppermost mantle was key to producing the observed PGE signatures in Paraná, contributing to the increasingly supported hypothesis that metals may be scavenged from beneath ancient continental crust by ascending magmas.

The type of lithosphere a plume impinges beneath, the thickness of that lithosphere, the proximity to divergent tectonic boundaries (in the case of the Tristan and Icelandic plumes) and even the proximity to separate tectono-magmatic systems have demonstrable impact upon the types of magmas generated in an intraplate setting (Chapter 7). In the asthenosphere, plume-derive melting interacts with tectonics in the upper mantle and lithosphere. For example, the tectonic interplay between Canary Islands volcanism and the Atlas Mountain orogenic belt generated heterogeneous melting regimes in the Canaries ocean island chain, both in terms of temporal distribution and geochemical characteristics (Chapter 4; Lindsay et al., in review[b]). The progressive removal of Gondwanan lithosphere from above the Tristan plume in the PELIP, perhaps exacerbated by the additional thermal erosion from the plume (although this is not tested in this work), resulted in highly variable melting depths across the region, leaving distinctive geochemical ‘fingerprints’ in the huge volume of flood basalts (Chapter 3; Lindsay et al., in review[a]).

The mechanics of plume-derived intraplate melting is generally the same across the settings considered in the thesis – hot and buoyant plume material decompresses in the asthenosphere and fusible mantle phases in the surrounding area partially melt due to the temperature anomaly. The manner in which melts are formed, and the minerals that are incorporated into magmas at the melting source, drive the geochemical diversity in global plume-derived magmas described in Chapter 7. This is inherently linked to geodynamic controls and forms the second major conclusion of the thesis. With regards to the PGE, their predominant hosts in the mantle are PGM (including alloys) and BMS. For PGM and alloys, their highly refractory nature means they will not be liberated from a melting environment until high degrees of partial melting. For BMS, the extreme chalcophile partitioning behaviour of PGE requires the near-total exhaustion of such phases in a melting source before any significant concentration of precious metals can be transferred into magmas. The melting conditions and mineralogy of the mantle involved in each intraplate setting are thus inextricably linked to metallogenesis. The more methodologically traditional Chapters 3 and 4 explored the intricacies that changes in depth, precious metal host phases, peridotite petrology, mantle type and degrees of partial melting can have on magma geochemistry, particularly when considering the mineralisation potential from a Mineral Systems approach for orthomagmatic deposits. The results in Chapters 3 and 4 make a compelling case for a passive plume influence in PGE concentrations in magmas - they supply the essential thermal anomaly for asthenospheric melting, but ultimately the melting degrees and source composition dictate the final metal budget of intraplate magmas.

A core objective to this study [O5] is the creation, testing and validation of an integrated geochemical and machine learning workflow; this is primarily described in Chapter 5 and expanded in Chapters 6 and 7. This process developed an improved data management framework and allowed for identification of clusters and groups based on more criteria than a ‘traditional’ geochemical process. The methodology produced intriguing insights into the variability of bulk element concentrations in plume-derived lavas from local to regional to global scales. For example, the recognition of independence in Pt and Pd variability in continent-edge intraplate magmas when compared to all other elements in the data set supported the theory that such melts can sample

heterogeneous metal-enriched reservoirs in the SCLM, unrelated to major element differentiation (Chapter 5). The workflow was expanded upon in Chapter 6 by applying the techniques to a larger database of more elements from the PELIP, and found that asymmetry in volcanism across this region directly affected precious metal budgets in magmas and focused enriched PGE signatures in Paraná only. In all research chapters, Os isotope analysis could help clarify some specific aspects of source contribution, and would also enhance any MLA-based analysis by adding a further substantial variable into the equation. The addition of any further data to the suite described in this thesis would only serve to bolster interpretations in the high-dimensional space, and the workflow established in Chapter 5 is primed to incorporate any extra measurements, samples or localities from future work.

The potential for application of the workflow to geochemical data sets outside this study is significant, especially considering the increased attention MLA are receiving in the field of geosciences in recent years. However, the conclusions of Chayes (1960) still resonate – geochemical and geophysical data in their default forms (with mixed unit measurements) are unsuitable for immediate multivariate analyses and must be considered with care. A ‘black box’ approach to MLA-based geochemical analyses should always be avoided, and the format of input data must be addressed in all instances. With geochemical data, the scaling issue between percent, ppm and ppb measurements is the key pitfall that can be accommodated using the workflow developed in this thesis (discussed in Chapters 5 and 6). To extract meaningful multi-element information from geochemical data, it must be treated prior to analyses, and the detailed, heuristic development of the final workflow in Chapter 5 is a testament to this. So long as input data is compiled in a high-quality database, with missing values and zeroes accounted for, and standardisation applied to all included variables, the workflow is suitably robust to contribute analytical optimisation as demonstrated by this thesis, and provides an efficient way to manage the high volume of information available to geoscientists.

In the final section of Chapter 7, in which the results of the three sub-studies on specific plume settings, and indeed the thesis as a whole, are synthesised, focus is returned to the potential of intraplate magmatic environments as PGE Mineral Systems. Reducing such a diverse study down to a unifying model may appear reductive, however given the detailed and thorough investigation of intraplate magmas in different settings contained within these five research contributions, the Mineral Systems models of Figure 7.17 and 7.18 have merit beyond a simple summary. The global comparison highlighted the prominence of strongly anomalous PGE compositions of lavas from two main locations - East Greenland and Paraná. As in Andersen et al. (2002), the North Atlantic Igneous Province (from which some of the most prominently PGE-rich Greenlandic lava samples were taken) is one of the most prospective localities for PGE mineralisation, containing the mineralised Skaergaard Intrusion, the Greenlandic mega dykes and the Rum Complex. By studying lavas from Paraná, and recognising overlapping multi-element magmatic signatures in Greenlandic lavas via the MLA workflow (i.e., similar clustering behaviour in Chapters 6 and 7), the continent-edge geodynamic environment is identified as optimal to the PGE Mineral Systems model. Furthermore, the recent discovery of mineralised PGE mafic-ultramafic intrusions west of Paraná, not unlike those found in East Greenland, confirm the long-lived fertility of the ancient Brazilian SCLM (de Farias and Filho, 2021). Whilst these Brazilian intrusions are not contemporaneous with Paraná lavas, they provide promise for PGE exploration in mantle-derived rocks in the region as per the outcomes of Chapter 3, 6 and 7 of this thesis.

The project presented in this thesis is an evolving pursuit in the efforts to understand some of the vital metals to society's next technological age, and introduces a MLA-based foundation for analysing large data suites of plume-derived lava geochemistry that can be extended to other mineral deposit types. The logical progression of the study, beyond adding more localities and/or geochemical variables to the database to improve clustering, is to investigate the effects the age of a plume system may have on PGE budgets in intraplate magmas. Some of the most PGE-enriched lavas in the world reside within greenstone belts (Barnes et al., 2015), which although often associated with intraplate magmatism, are significantly older than any of the rocks discussed in this thesis (often > 1 Ga) and thus subject to significant alteration/metamorphism.

The localities and samples in this thesis were carefully chosen to reflect plume magmas with primary geochemical characteristics, and the inclusion of older, more altered rocks within the MLA would necessitate extra geochemical screening steps to remove the potential effects of mineral phase changes and subsequent element fractionation. However, the combined modelling and MLA approach set out in detail in Chapters 3 to 7 is versatile enough to adapt to such features, provided the data are properly treated before analyses. The exploration of temporal influences on intraplate PGE metallogenesis would complement the conclusions drawn in this thesis regarding the melting, mineralogical and geodynamic controls on metal budgets in plume environments.

Appendix A

(for Chapter 3 - Paraná)

These plots illustrate the alteration conditions within the Paraná (Serra Geral) data set. Overall, the samples are in very good condition, plotting within the expected mafic to intermediate range for unaltered rocks, and far removed from all alteration style vectors. Furthermore, most samples are below 2 wt.% Loss On Ignition (LOI), a further indication of minimal alteration – geochemical signatures in the main body text are thus primary.

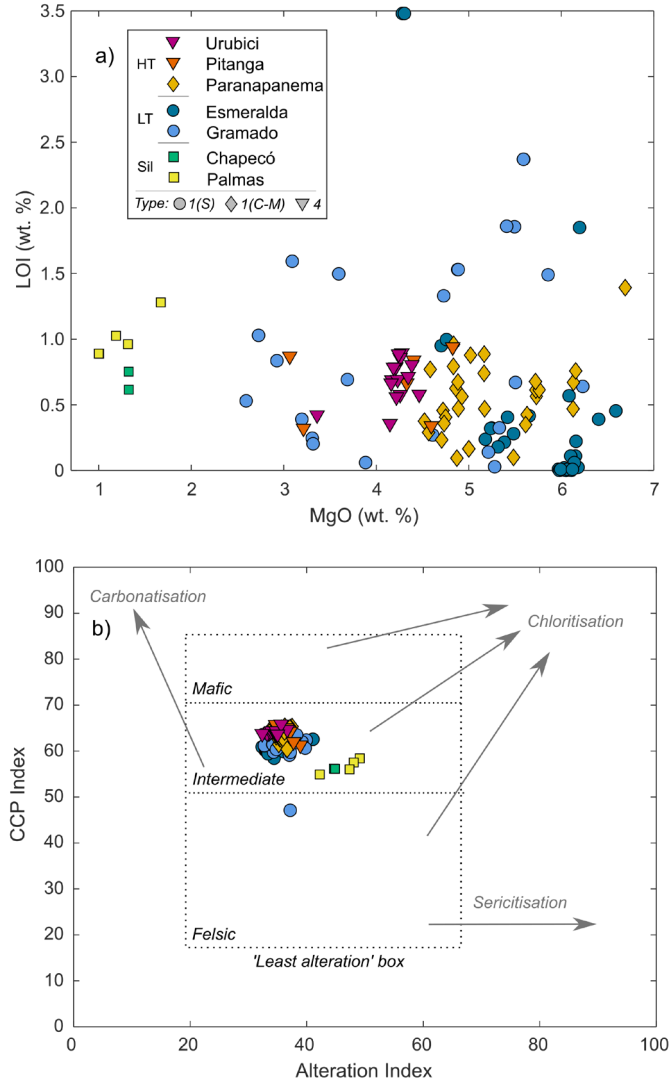

Figure A1 *– Commonly-used alteration plots for (a) LOI with MgO content and (b) Alteration Index and chlorite-carbonate-pyrite index (CCPI) from Mathieu (2018). For Paraná samples.*

Appendix B

(for Chapter 4 - Canary Islands)

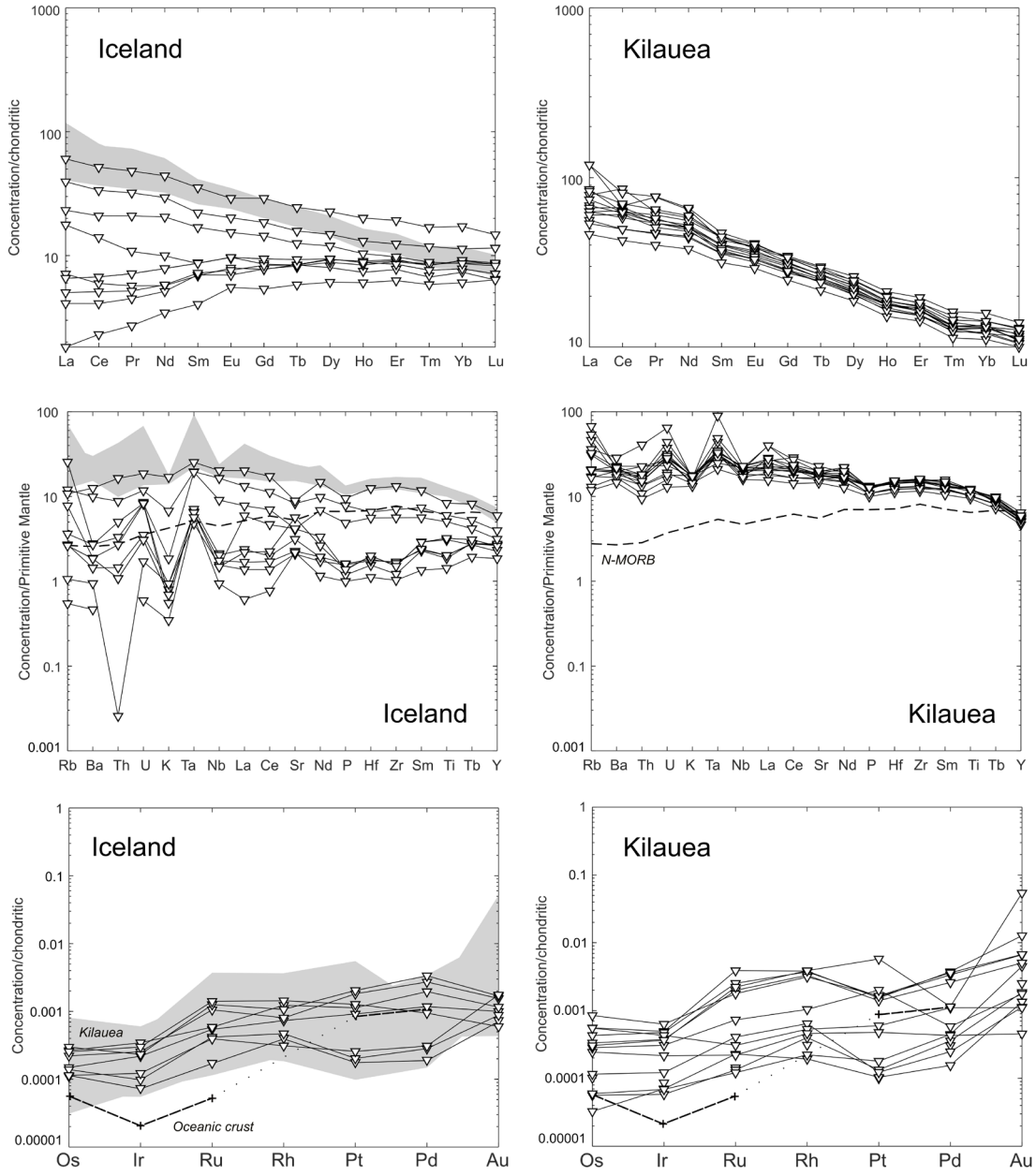

Figure B1 *– Normalised multi-element plots for Iceland and Kilauea samples gathered for this thesis. Top row – rare earth elements normalised by chondritic values (McDonough and Sun, 1995). Middle row – incompatible elements normalised by Primitive Upper Mantle (McDonough et al., 1992). Bottom row – PGE normalised by chondritic values (McDonough and Sun, 1995).*

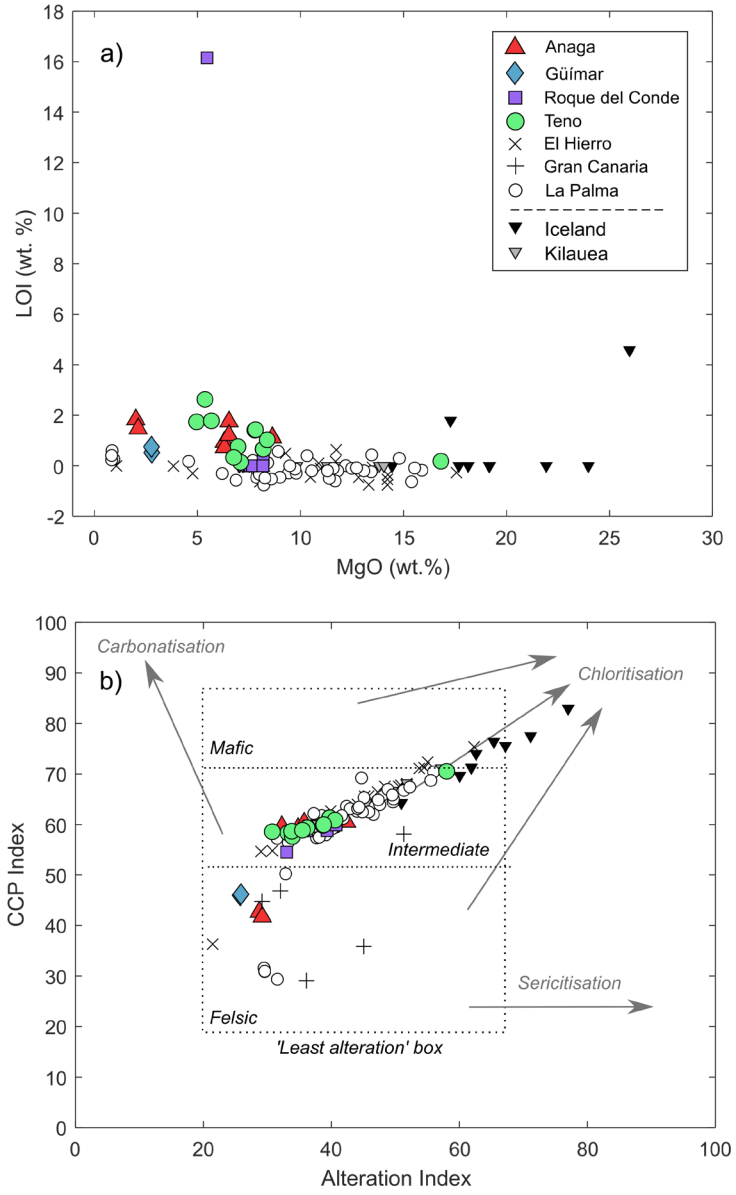

Figure B2 *– Commonly-used alteration plots for (a) LOI with MgO content and (b) Alteration Index and chlorite-carbonate-pyrite index (CCPI) from Mathieu (2018). For Canary Islands samples.*

Appendix C

(for Chapter 5 - NAIP)

These plots demonstrate the variety of input parameters tried and tested through the course of Chapter 5 to ultimately arrive at the optimal set-ups used in analysis and presented in the main text.

Clustering using raw (z-scored) data (C1-C5)

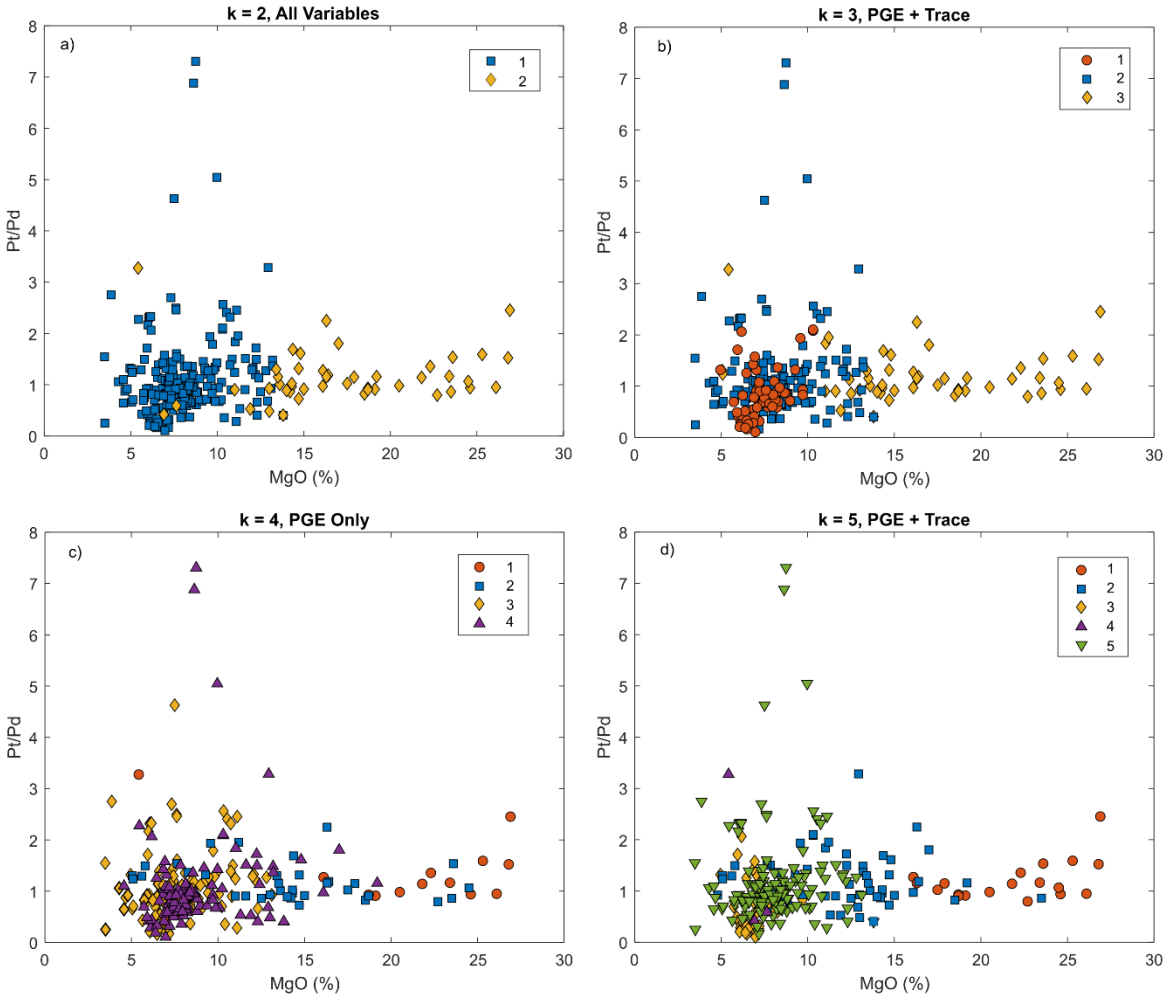

Figure C1 *– A variety of input parameter set-ups for z-scored raw data k-means clustering models. a) k = 2 with all 11 elements as variables; b) k = 3 with five PGE, Cr, Ni and Cu as variables; c) k = 4 with five PGE as variables; d) k = 5 with five PGE, Cr, Ni and Cu as variables.*

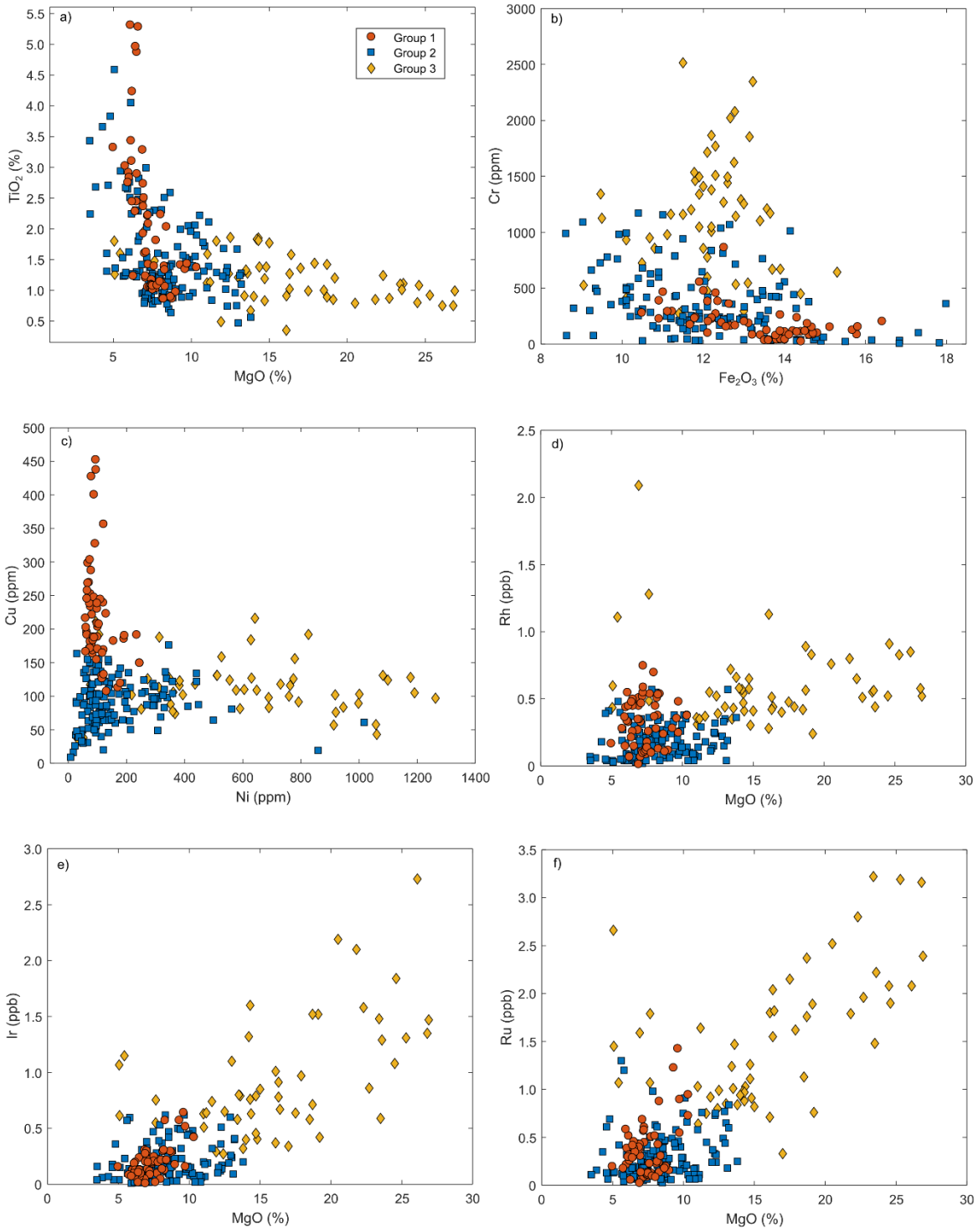

Figure C2 *– Replication of in-text Figure 5.8, displaying the best z-scored model (k = 3 with five PGE, Cr, Ni and Cu as variables) in bivariate space.*

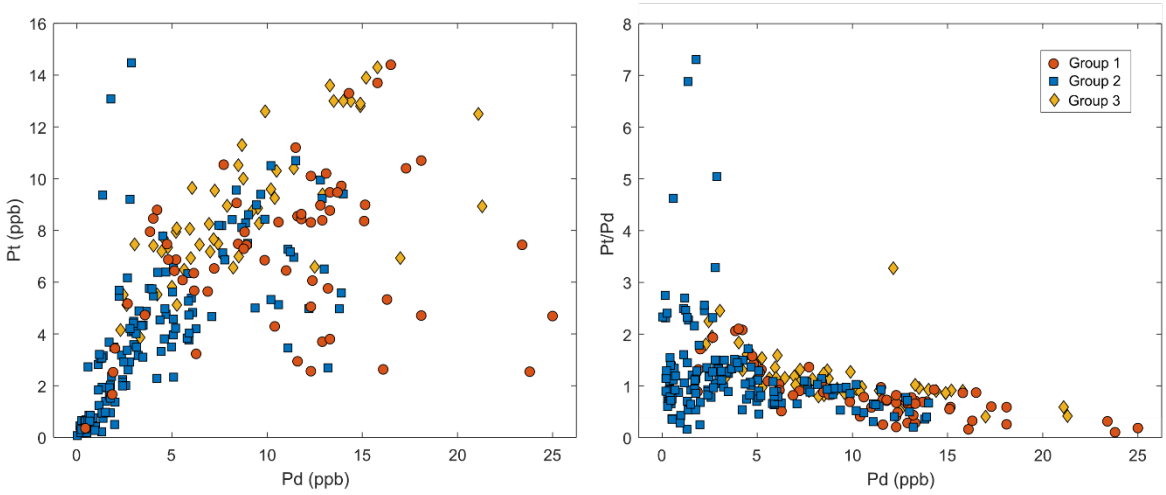

Figure C3 *- Replication of in-text Figure 5.9, displaying the best z-scored model (k = 3 with five PGE, Cr, Ni and Cu as variables) in bivariate space.*

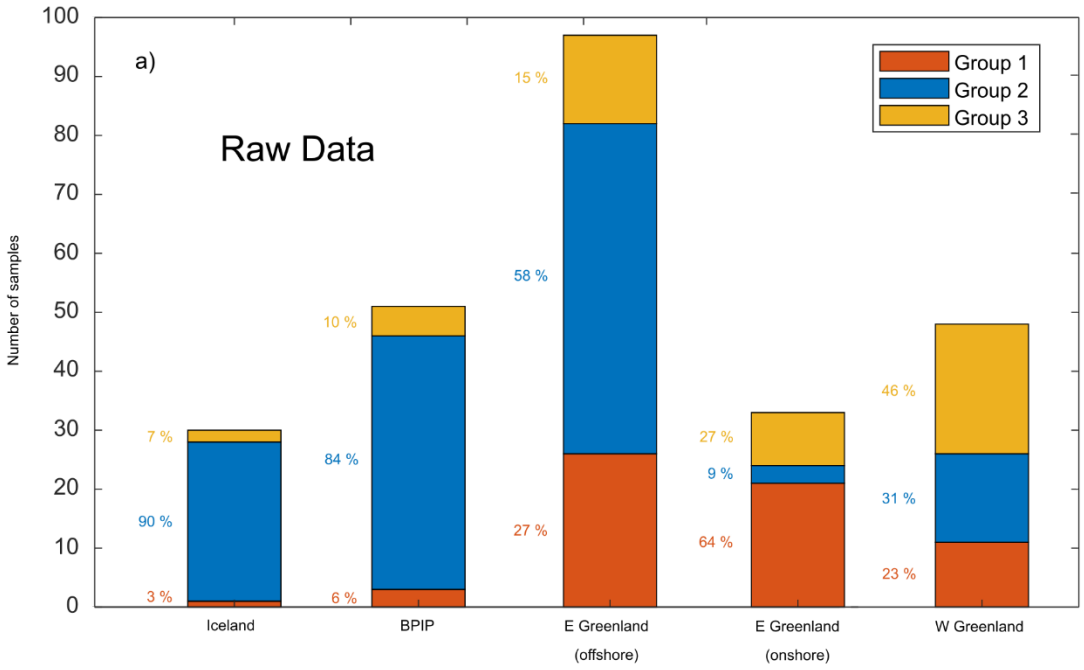

Figure C4 *– Replication of in-text Figure 5.10, with a histogram of the best z-scored model (k = 3 with five PGE, Cr, Ni and Cu as variables)*

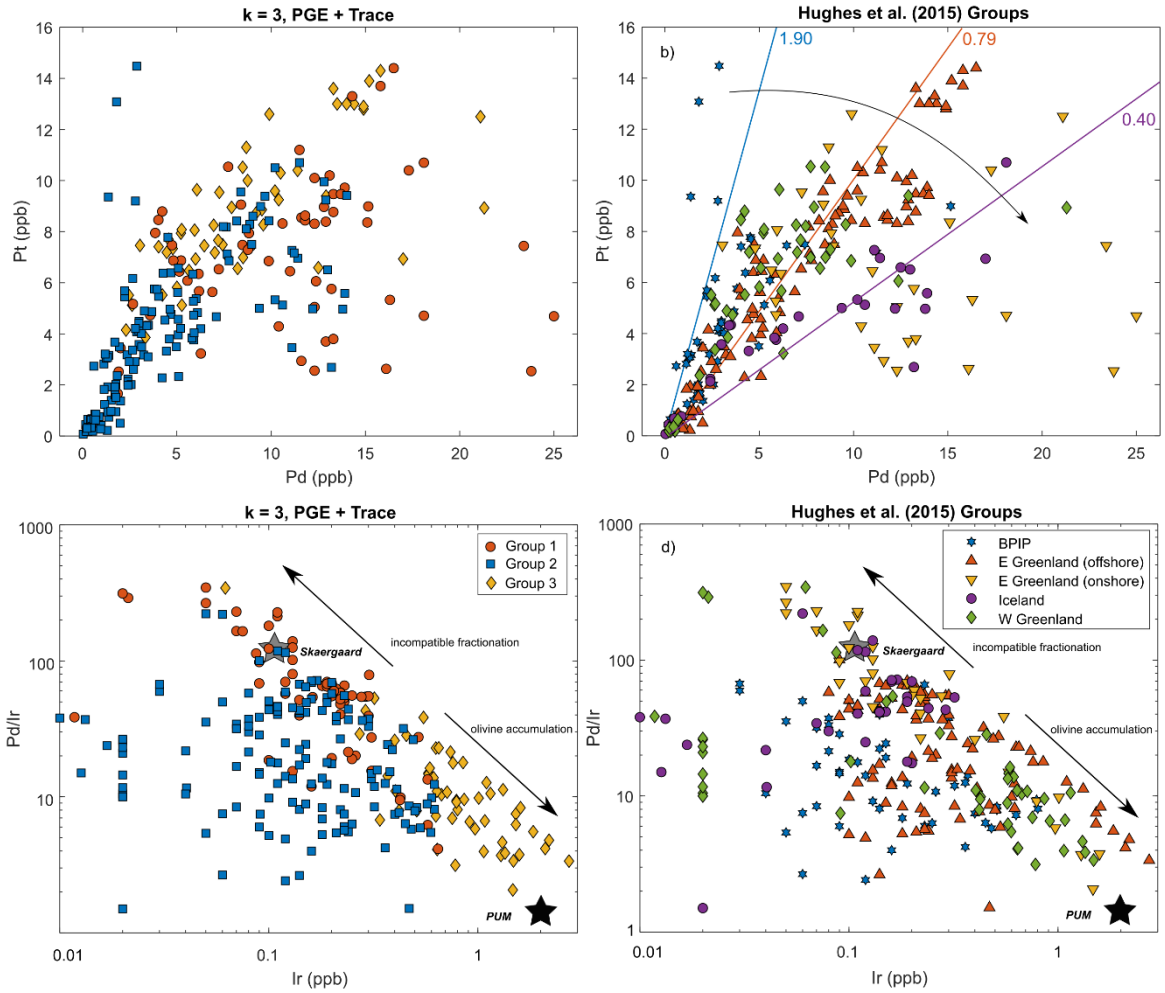

Figure C5 *- Replication of in-manuscript Figure 5.11, displaying the best z-scored model (k = 3 with five PGE, Cr, Ni and Cu as variables) in bivariate space. Plots are recreated from Hughes et al. (2015) and shows geographic categories in comparison to k-means clusters.*

Clustering using PC1-6, extra bivariate displays (C6-C7)

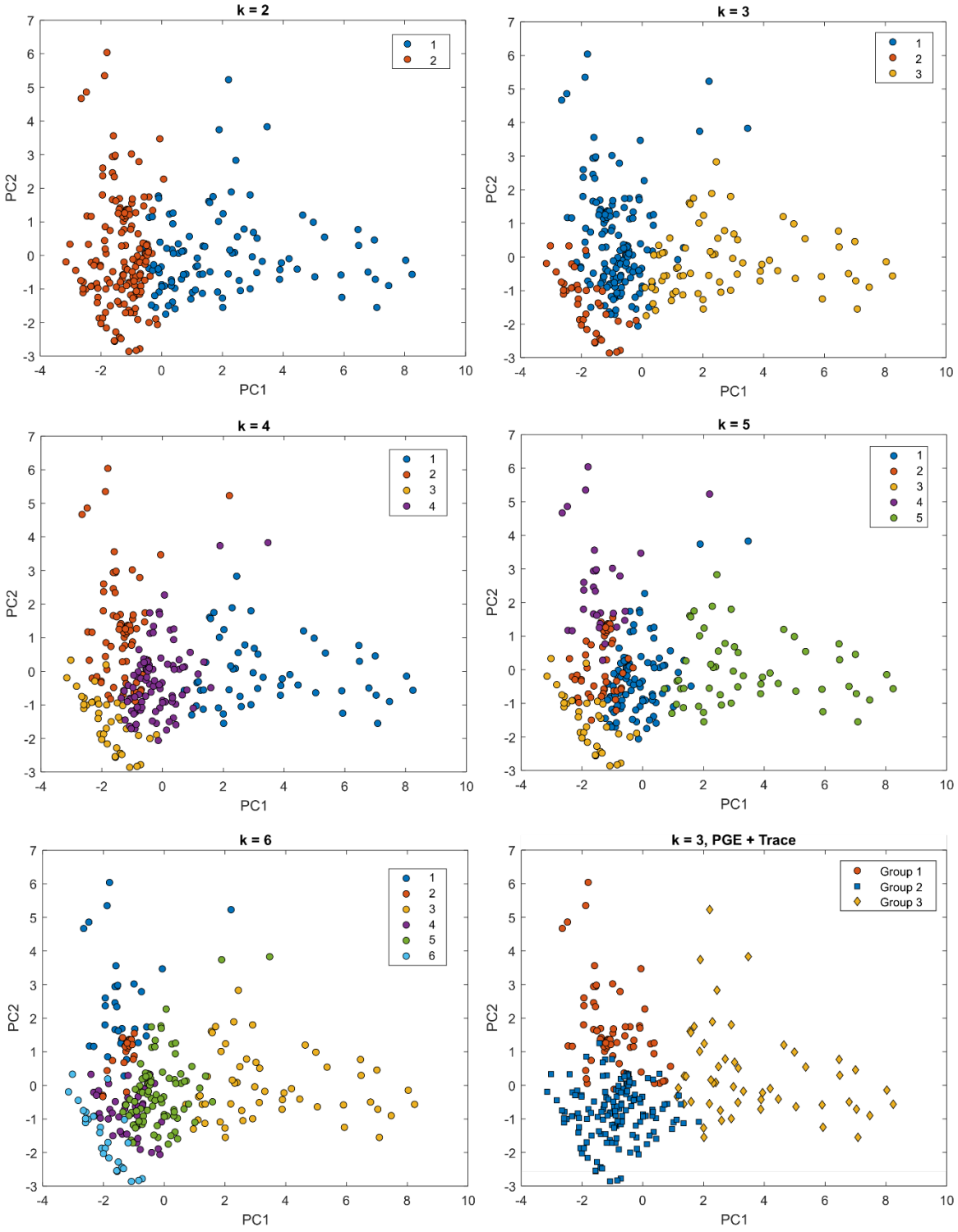

Figure C6 *– Expanded version of in-manuscript Figure 5.7, showing a variety of k-value models for k-means clustering of PC1-6, with a single plot of z-scored raw data clusters for comparison.*

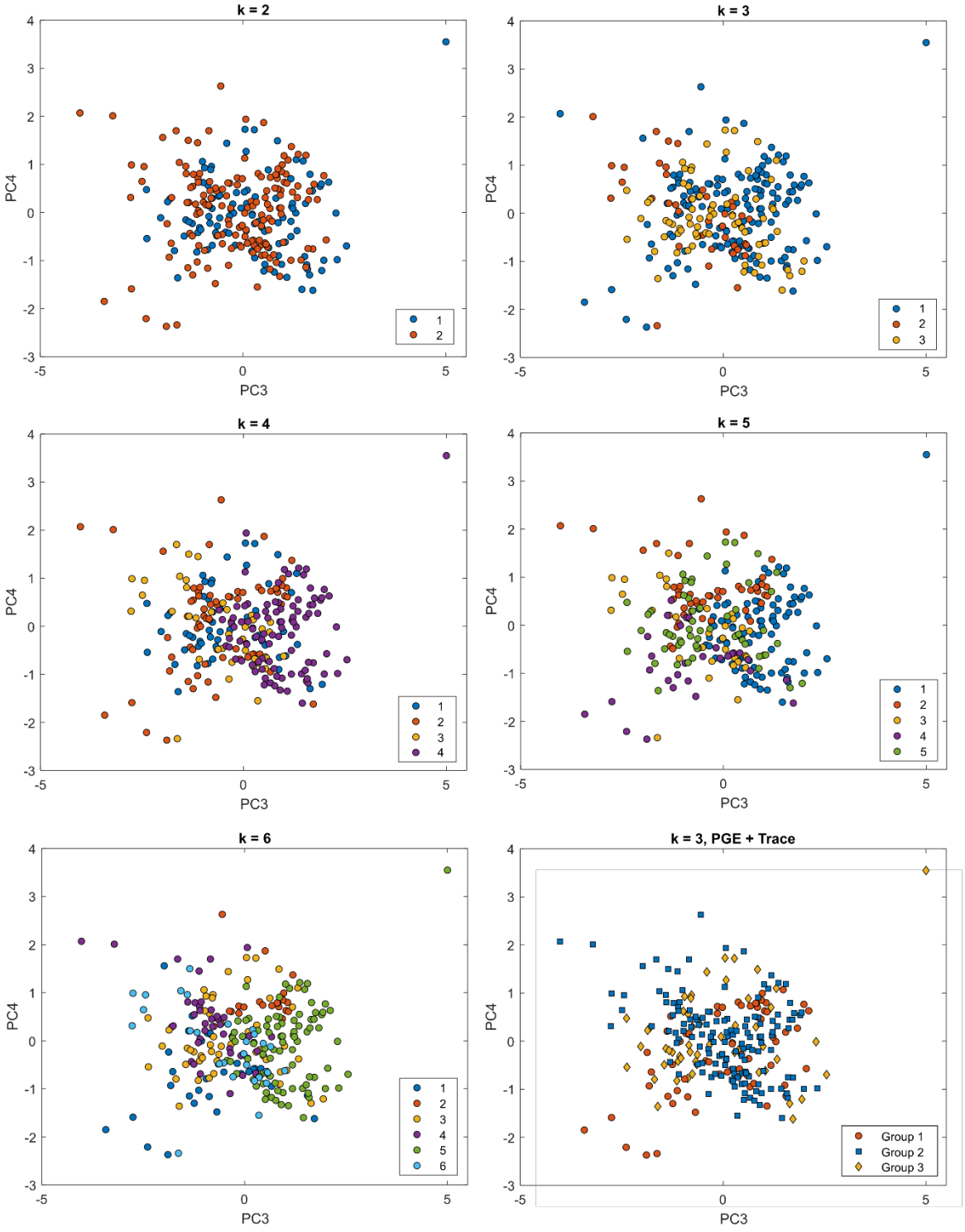

Figure C7 *– Expanded version of in-manuscript Figure 5.7, showing different k-values for k-means clustering models using PC1-6 as variables. This time data points are displayed in bivariate space using PC3 and PC4.*

Appendix D

(for Chapter 6 - PELIP)

Given the large amount of geochemical and MLA-based analyses conducted on the PELIP data set, only the most crucial plots were included in the main body text for Chapter 6. This accompanying Appendix contains traditional geochemical bivariate plots with mineral fractionation vectors, and extra MLA plots exploring different parameter set-ups that support main body outcomes.

Furthermore, a table of summary geochemical data contained within the manuscript version of this chapter has been removed from the main body and placed within the Appendices (below), given its size. It is referred to in-text frequently but is unsuitable to inclusion in the main body.

Table D1 *– Minimum, maximum and mean ($\bar{x}$) values for elemental concentrations measured for each locality in the PELIP, excluding Cr_2O_3, BaO, Te and W. "-" not measured.*

	Etendeka			Rio Grande Rise			SG Silicic			SG Type 1 (C-N)		
wt.%	min	max	$\bar{x}$	min	max	$\bar{x}$	min	max	$\bar{x}$	min	max	$\bar{x}$
LOI	0.1	1.0	0.4	2.4	19.0	6.5	0.6	1.3	0.9	0.1	1.4	0.5
SiO_2	45.5	52.6	49.3	40.9	51.5	48.2	64.3	69.7	67.3	50.1	51.7	50.9
Al_2O_3	9.6	15.7	13.4	8.5	19.5	14.7	12.6	13.5	13.0	12.2	13.8	12.8
Fe_2O_3	10.8	16.2	13.3	9.8	17.0	12.5	6.3	7.5	6.8	13.2	16.1	15.2
CaO	7.6	11.9	9.8	10.4	16.0	11.7	2.7	3.2	3.0	8.5	10.9	9.1
MgO	5.4	14.9	9.3	3.2	18.7	6.9	1.0	1.7	1.3	4.5	6.7	5.2
SO_3	0.06	0.09	0.08	0.07	0.55	0.14	0.01	0.07	0.05	0.01	0.01	0.01
Na_2O	1.46	2.63	2.25	1.95	3.05	2.64	2.77	3.66	3.24	2.18	2.90	2.50
K_2O	0.29	1.03	0.72	0.23	1.32	0.53	3.61	4.27	3.95	0.86	1.89	1.15
TiO_2	0.68	2.50	1.51	0.82	2.54	2.05	0.97	1.45	1.15	1.74	2.53	2.27
P_2O_5	0.08	0.33	0.18	0.08	0.75	0.30	0.27	0.46	0.34	0.19	0.32	0.27
MnO	0.17	0.23	0.18	0.13	0.24	0.18	0.11	0.15	0.12	0.19	0.23	0.22
ppm												
Sc	18	37	26	18	42	37	14	16	15	40	46	42
V	138	396	272	132	386	316	34	102	67	411	549	466
Cr	61	1199	369	72	872	283	6	62	40	33	159	74
Co	35	87	54	42	84	50	10	14	11	46	61	52
Ni	37	776	238	35	408	108	1	133	28	40	86	57
Cu	31	198	97	37	620	262	8	345	138	156	393	257
As	0.5	1.7	1.1	2.5	35.0	9.7	0.4	120.7	21.5	0.5	0.6	0.5
Se	1.5	3.8	2.6	2.2	5.1	4.0	4.3	7.1	5.2	2.1	5.1	3.1

Rb	10	25	18	5	15	9	81	148	122	17	50	29
Sr	111	586	286	105	964	343	104	363	176	226	401	287
Y	17	30	22	15	40	31	34	61	44	23	41	35
Zr	58	156	110	31	185	146	241	702	381	121	208	183
Nb	4	16	7	1	73	15	19	61	32	5	17	13
Ba	74	457	224	7	703	199	531	1087	723	267	398	332
La	7	29	15	1	59	19	36	74	47	17	27	23
Ce	17	60	32	3	112	40	71	146	94	35	57	49
Pr	2.3	7.6	4.2	0.7	12.0	5.2	8.9	20.4	12.3	4.6	7.2	6.4
Nd	9	31	18	4	45	23	34	82	48	19	30	27
Sm	2.4	6.9	4.4	1.8	6.9	5.5	7.2	16.8	10.4	4.4	7.0	6.3
Eu	0.8	2.3	1.5	0.8	2.3	1.9	1.5	4.6	2.5	1.5	2.2	2.0
Gd	3.0	6.8	4.9	2.8	7.9	6.2	7.1	15.8	9.9	4.8	8.0	7.1
Tb	0.5	0.9	0.7	0.5	1.2	0.9	1.1	2.2	1.4	0.7	1.2	1.1
Dy	3.3	5.9	4.6	3.4	8.0	6.2	6.5	12.8	8.6	4.6	7.8	6.8
Ho	0.7	1.2	0.9	0.6	1.6	1.3	1.3	2.4	1.7	0.9	1.6	1.4
Er	1.8	3.5	2.5	1.6	4.7	3.6	3.6	6.6	4.7	2.6	4.6	4.0
Tm	0.21	0.49	0.34	0.20	0.65	0.51	0.53	0.86	0.66	0.36	0.63	0.54
Yb	1.24	3.20	2.14	1.21	4.14	3.21	3.41	5.51	4.23	2.41	4.19	3.62
Lu	0.18	0.49	0.32	0.16	0.60	0.47	0.50	0.78	0.62	0.35	0.61	0.53
Hf	1.73	4.30	3.07	1.21	5.03	3.97	6.63	16.92	9.88	3.19	5.32	4.69
Ta	0.33	1.43	0.76	0.45	4.65	1.43	1.77	4.70	2.63	0.37	1.83	1.21
Pb	0.93	4.14	2.27	1.84	36.61	9.67	8.38	75.75	26.20	3.37	4.57	3.73
Bi	0.01	0.04	0.02	0.01	0.10	0.04	0.02	1.01	0.32	0.01	0.05	0.02
Th	0.91	2.74	1.83	0.08	7.06	1.96	7.60	11.74	10.03	1.60	2.89	2.39
U	0.29	0.73	0.40	0.16	1.63	0.53	1.77	4.36	3.22	0.24	0.74	0.52
ppb												
Os	0.03	0.47	0.12	0.03	0.45	0.18	-	-	-	-	-	-
Ir	0.03	0.4	0.12	0.10	0.54	0.23	0.02	0.03	0.03	0.02	0.29	0.09
Ru	0.12	1.26	0.53	0.50	4.22	1.98	0.10	0.15	0.13	0.12	0.66	0.27
Rh	0.04	0.32	0.14	0.10	2.28	0.87	0.05	0.15	0.10	0.18	0.97	0.53
Pt	2.44	12.9	5.57	2.20	18.9	7.66	1.30	4.51	2.90	3.40	30.53	10.47
Pd	0.42	7.07	1.63	0.60	11	4.04	1.78	3.96	2.87	5.49	30.49	16.17
Au	1.12	4.9	2.71	1.00	3.92	2.25	2.43	3.81	3.12	1.85	19.25	6.46

	SG Type 1 (S)			**SG Type 4**			**Walvis Ridge**		
wt.%	min	max	$\bar{x}$	min	max	$\bar{x}$	min	max	$\bar{x}$
LOI	0.0	3.5	0.8	0.3	0.9	0.7	1.6	2.8	2.2
SiO_2	50.0	60.7	53.1	50.1	54.0	51.0	49.2	49.9	49.5
Al_2O_3	12.5	16.9	13.8	11.6	13.4	12.6	14.8	16.1	15.6
Fe_2O_3	5.5	14.9	13.3	12.1	16.0	14.8	10.0	12.0	11.0
CaO	5.6	11.3	9.2	6.8	8.5	8.1	9.3	10.8	10.1
MgO	2.6	6.6	5.1	3.1	4.8	4.2	6.9	8.8	7.9
SO_3	0.01	0.12	0.07	0.01	0.08	0.03	0.08	0.18	0.12
Na_2O	2.10	4.54	2.57	2.40	2.91	2.65	2.78	3.20	2.98
K_2O	0.39	3.03	1.21	1.17	2.45	1.61	0.12	0.69	0.43

TiO_2	0.74	1.85	1.45	3.20	4.01	3.75	1.67	1.78	1.73
P_2O_5	0.14	0.29	0.20	0.50	1.00	0.61	0.26	0.32	0.28
MnO	0.08	0.35	0.20	0.14	0.24	0.19	0.21	0.30	0.25
ppm									
Sc	12	49	35	19	37	31	36	39	37
V	121	472	357	251	501	396	291	320	308
Cr	10	137	67	5	87	23	108	152	130
Co	20	60	43	32	51	44	32	44	40
Ni	11	124	52	11	81	35	58	75	65
Cu	44	547	204	138	338	217	95	229	139
As	0.2	66.5	10.0	0.4	24.1	2.6	2.4	8.6	4.7
Se	1.5	4.2	3.0	3.6	6.3	4.8	3.0	3.7	3.3
Rb	6	87	39	31	61	40	1	18	10
Sr	149	1096	223	396	713	530	245	307	277
Y	12	42	30	30	56	41	27	33	31
Zr	86	212	138	242	441	300	119	129	125
Nb	4	15	9	9	38	20	16	18	18
Ba	115	721	293	532	755	586	105	155	126
La	9	35	19	39	61	43	13	16	15
Ce	20	73	41	83	141	94	30	35	33
Pr	2.7	8.8	5.2	10.9	17.4	12.1	3.8	4.5	4.2
Nd	12	34	21	45	74	51	18	20	19
Sm	3.5	7.3	5.1	9.8	15.7	10.9	4.3	4.9	4.6
Eu	1.3	1.9	1.5	3.0	4.8	3.4	1.5	1.7	1.6
Gd	4.2	7.7	5.7	9.3	15.3	10.8	4.9	5.8	5.5
Tb	0.5	1.2	0.9	1.2	2.1	1.5	0.8	0.9	0.8
Dy	2.5	7.8	5.8	7.1	11.9	8.6	5.1	6.1	5.7
Ho	0.4	1.6	1.2	1.3	2.2	1.6	1.1	1.3	1.2
Er	1.2	4.6	3.4	3.3	5.9	4.3	3.2	3.9	3.5
Tm	0.15	0.65	0.48	0.42	0.76	0.56	0.45	0.55	0.50
Yb	1.03	4.30	3.11	2.69	4.76	3.57	2.96	3.60	3.23
Lu	0.15	0.63	0.46	0.37	0.67	0.50	0.42	0.55	0.49
Hf	2.52	5.99	3.85	5.90	10.66	7.47	3.16	3.42	3.31
Ta	0.43	4.05	1.10	0.69	3.00	1.56	1.17	1.56	1.43
Pb	2.99	74.35	16.23	4.69	32.34	8.92	3.22	14.72	7.20
Bi	0.01	0.56	0.11	0.01	0.23	0.04	0.02	0.07	0.05
Th	1.50	8.57	4.14	3.46	6.12	4.00	1.37	1.52	1.48
U	0.37	2.24	1.00	0.74	1.51	0.89	0.26	0.51	0.40
ppb									
Os	0.03	1.12	0.29	0.24	0.44	0.37	0.06	0.45	0.25
Ir	0.04	1.17	0.28	0.02	0.50	0.10	0.09	0.47	0.29
Ru	0.16	12.99	2.56	0.08	2.84	0.55	0.28	5.91	2.29
Rh	0.16	5.72	1.11	0.05	1.91	0.38	0.35	2.4	1.19
Pt	0.74	38.06	7.89	0.59	8.37	3.43	1.23	7.51	3.42
Pd	0.51	13.84	4.83	1.24	5.35	2.30	1.02	4.59	2.31
Au	0.18	9.09	2.42	0.37	7.60	2.45	0.08	3.57	1.05

Traditional geochemical accompanying plots (D2-D4)

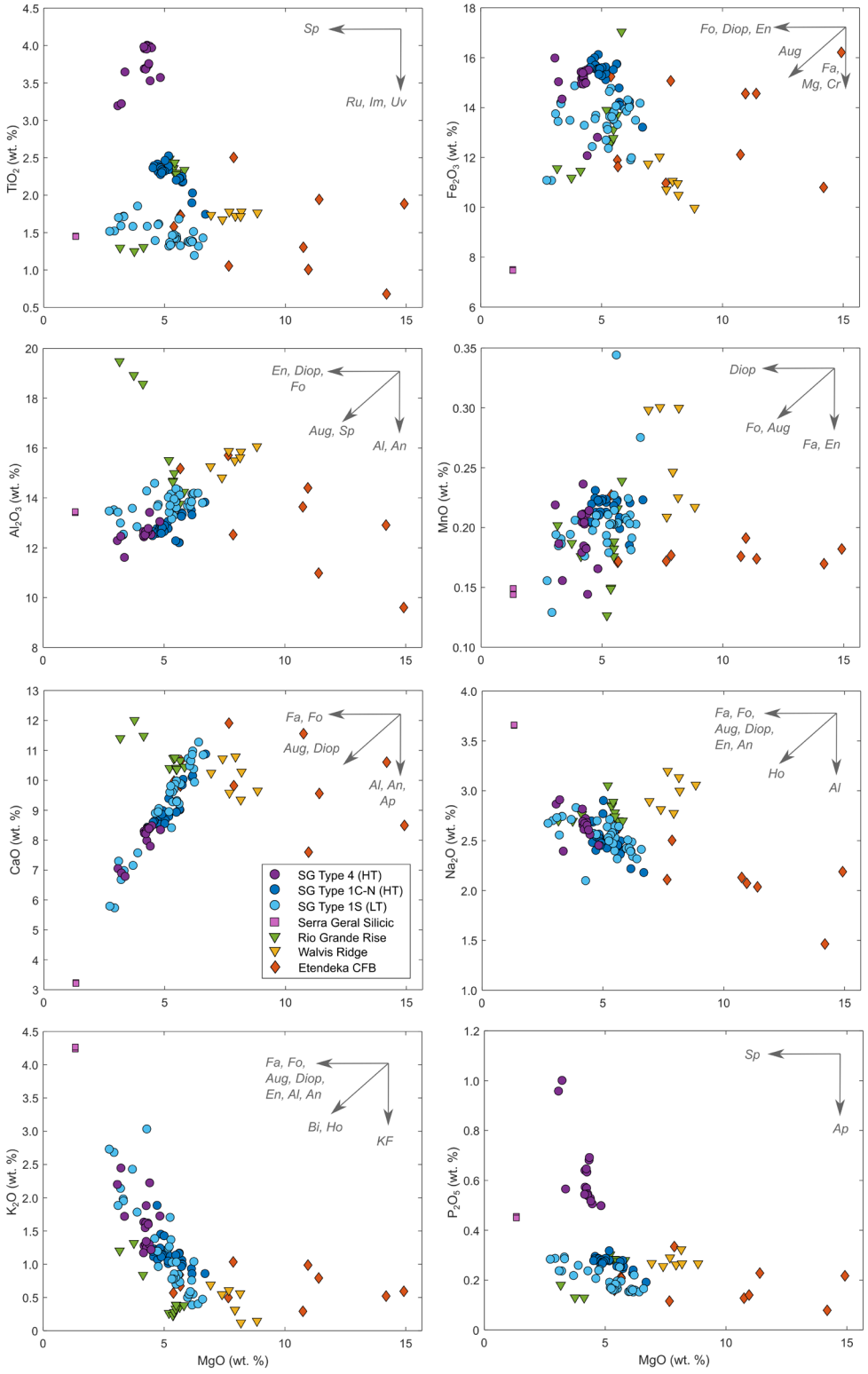

Figure D2 *– Harker plots for major elements with mineral fractionation vectors from Fig. 3b-c. See caption for abbreviations, plus Bi – biotite, Ho – hornblende, KF – F-feldspar, Ap – apatite. Classified by locality.*

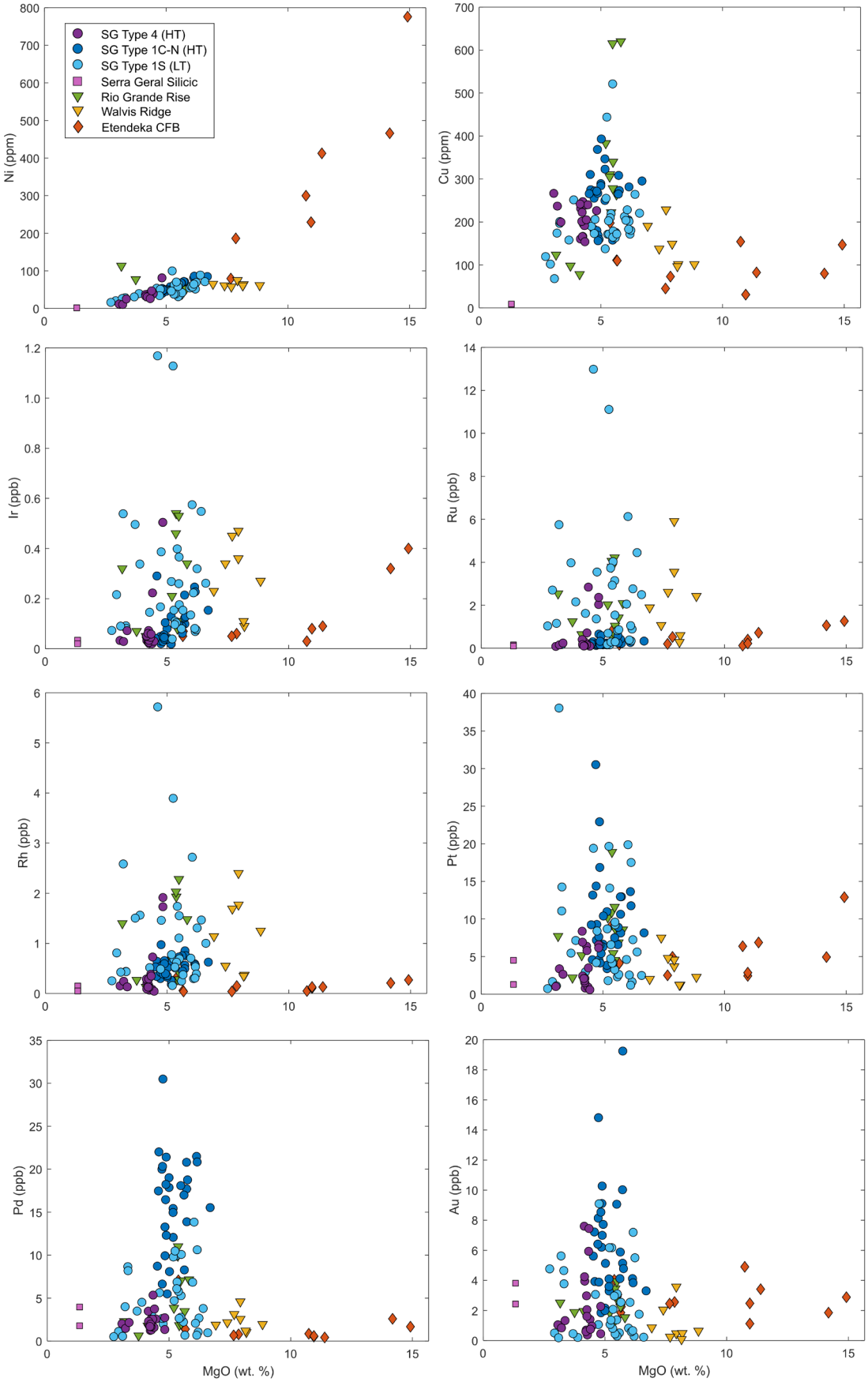

Figure D3 *– Harker plots for Ni, Cu, Ir, Ru, Rh, Pt, Pd and Au. Classified by locality.*

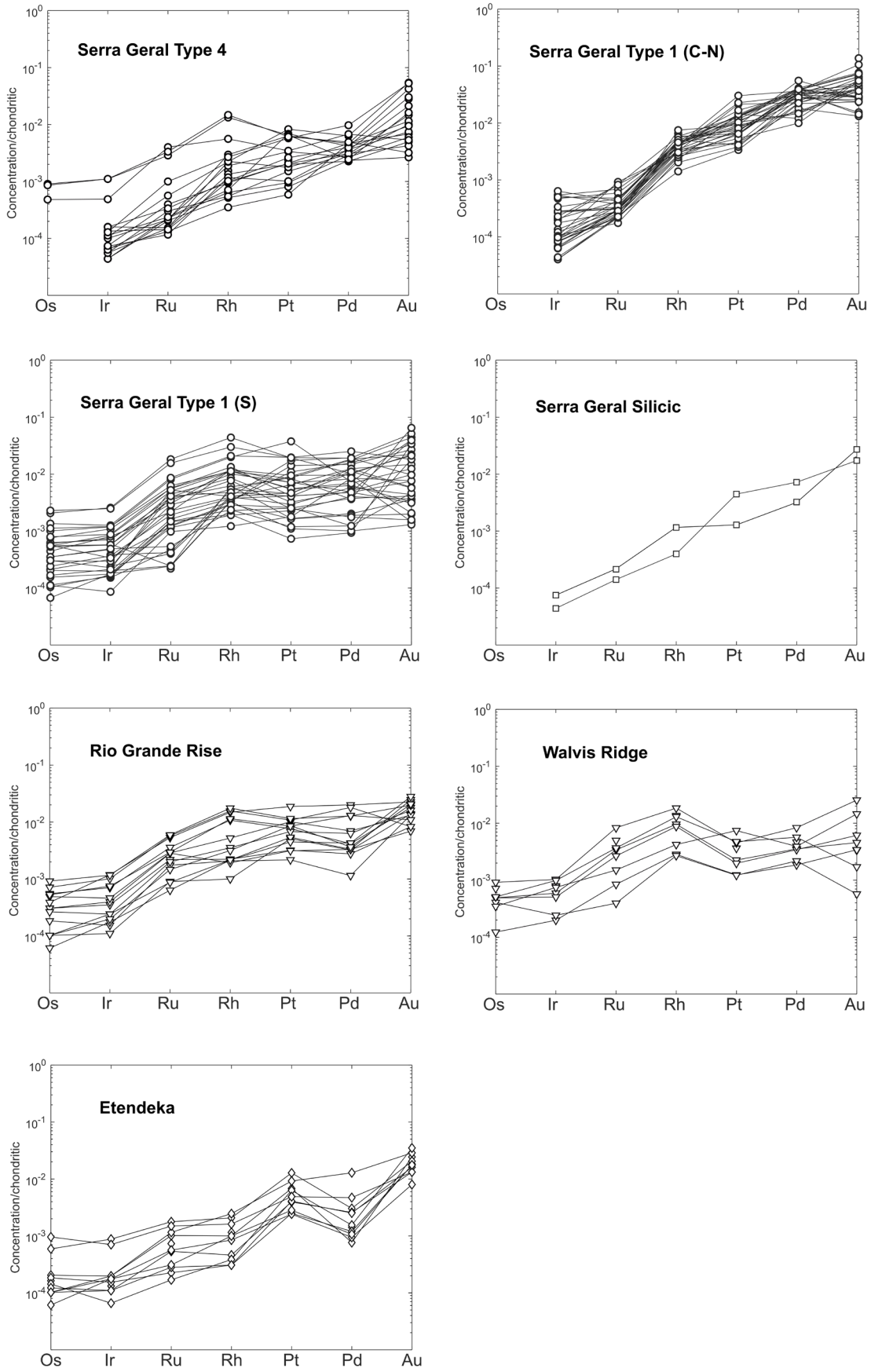

Figure D4 – *Chondrite-normalised* (McDonough and Sun, 1995) *PGE and Au plots for each PELIP sample locality.*

MLA-based plots for the full variable data set (D5-D8)

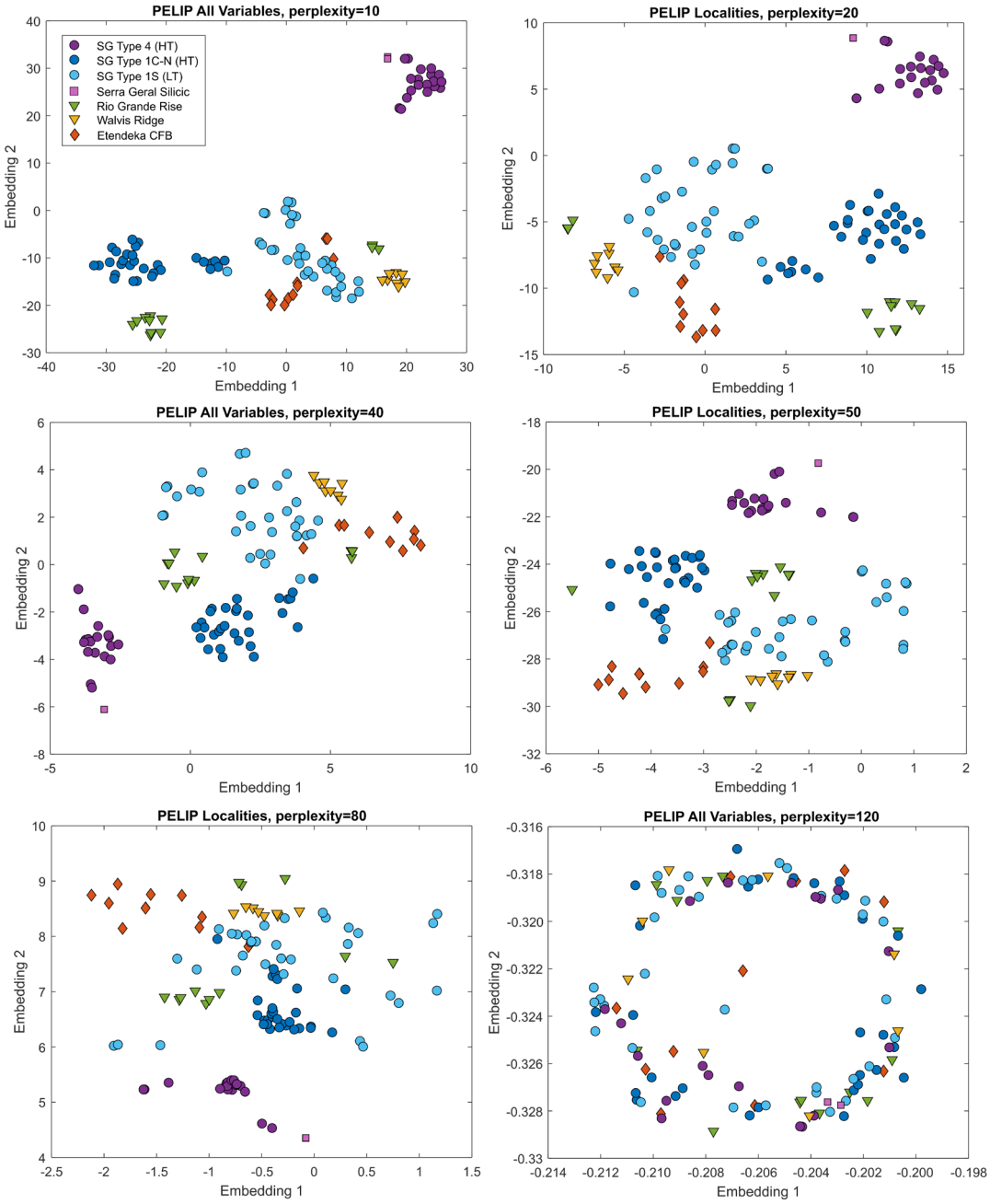

Figure D5 *– t-SNE models using the full data set of 51 variables, with different perplexity values. Perplexity of 50 was selected for full analysis.*

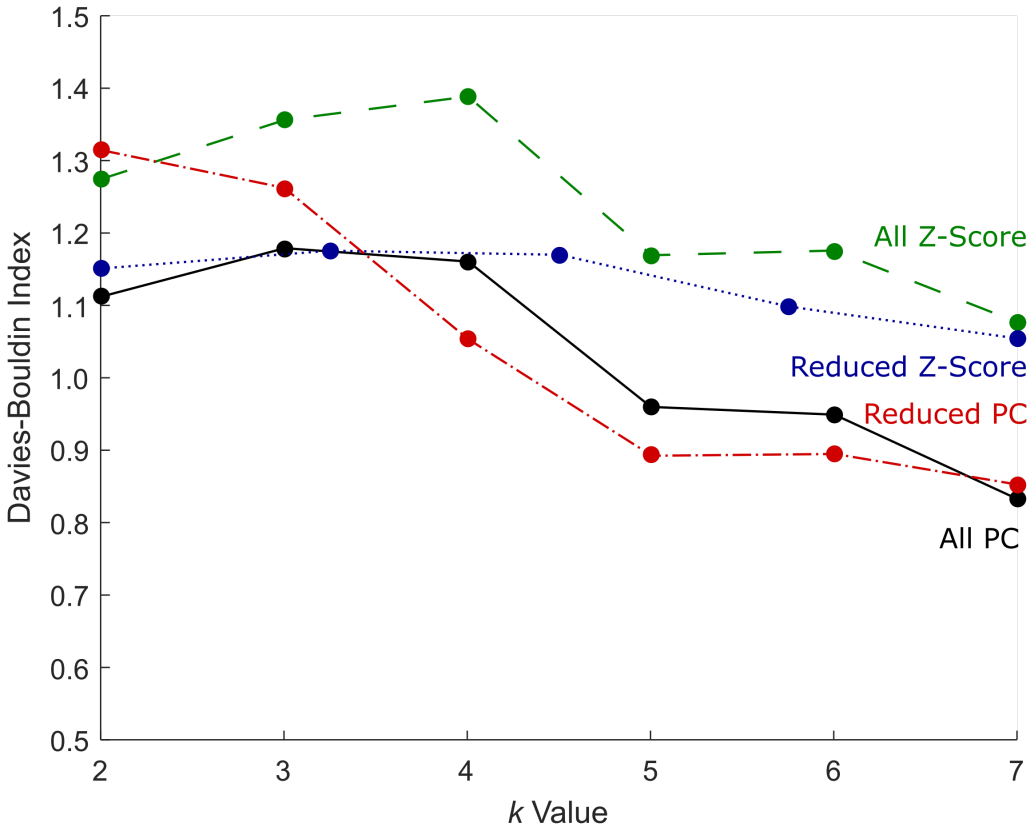

Figure D6 *– Davies-Bouldin Indices (DBI) for all input parameter set-ups used in this study, for both full and reduced data sets. Models are denoted as using z-score or PCs as variables from their respective data sets. Model selected – k=6 for either reduced PC or all PC.*

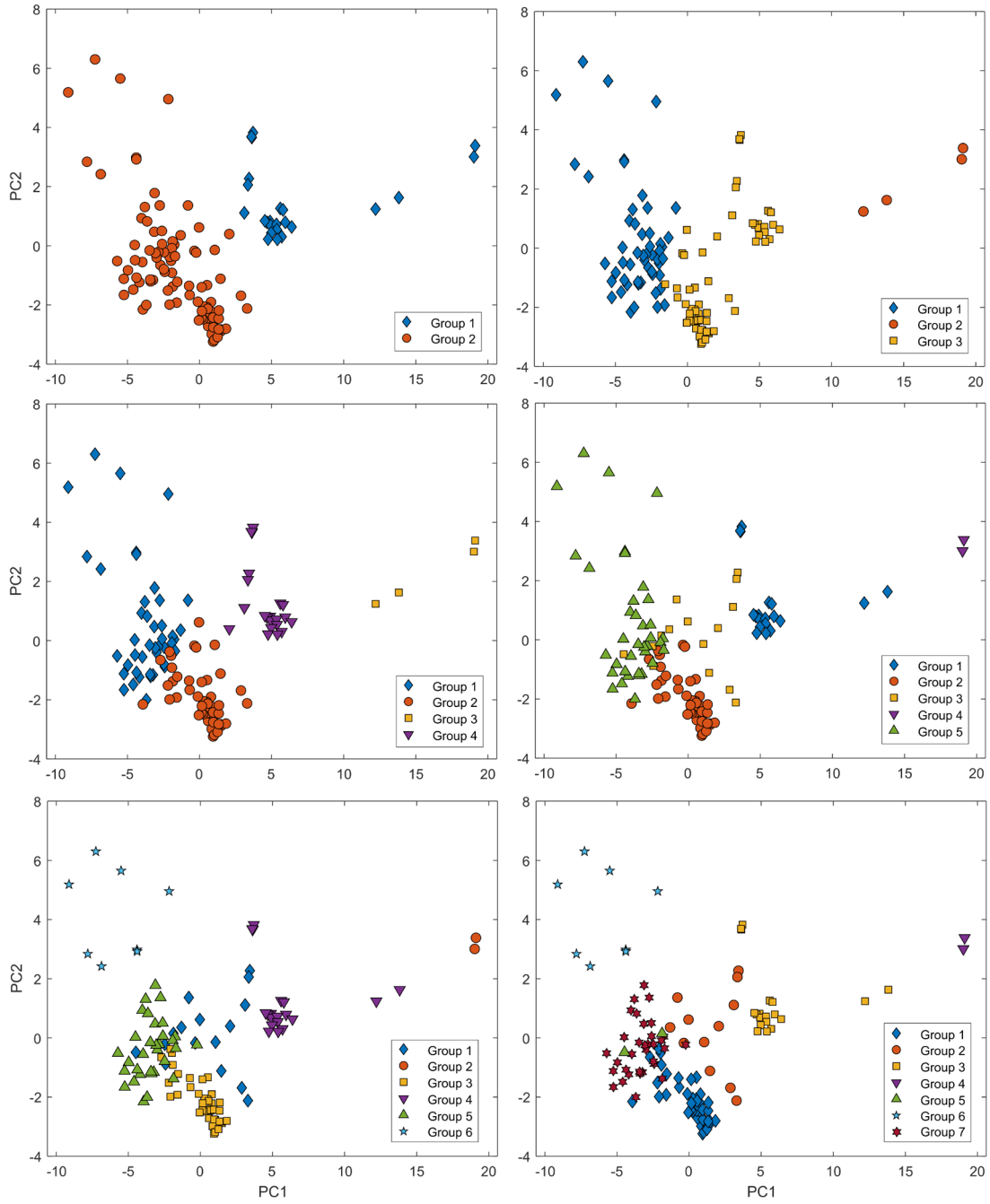

Figure D7 *– k-means clustering models for k-values of 2 to 7, using PC1-8 as variables from Figure 4. Selected model used in the discussion (from Figures 6.8 and 6.9) is shown in the bottom left (k=6).*

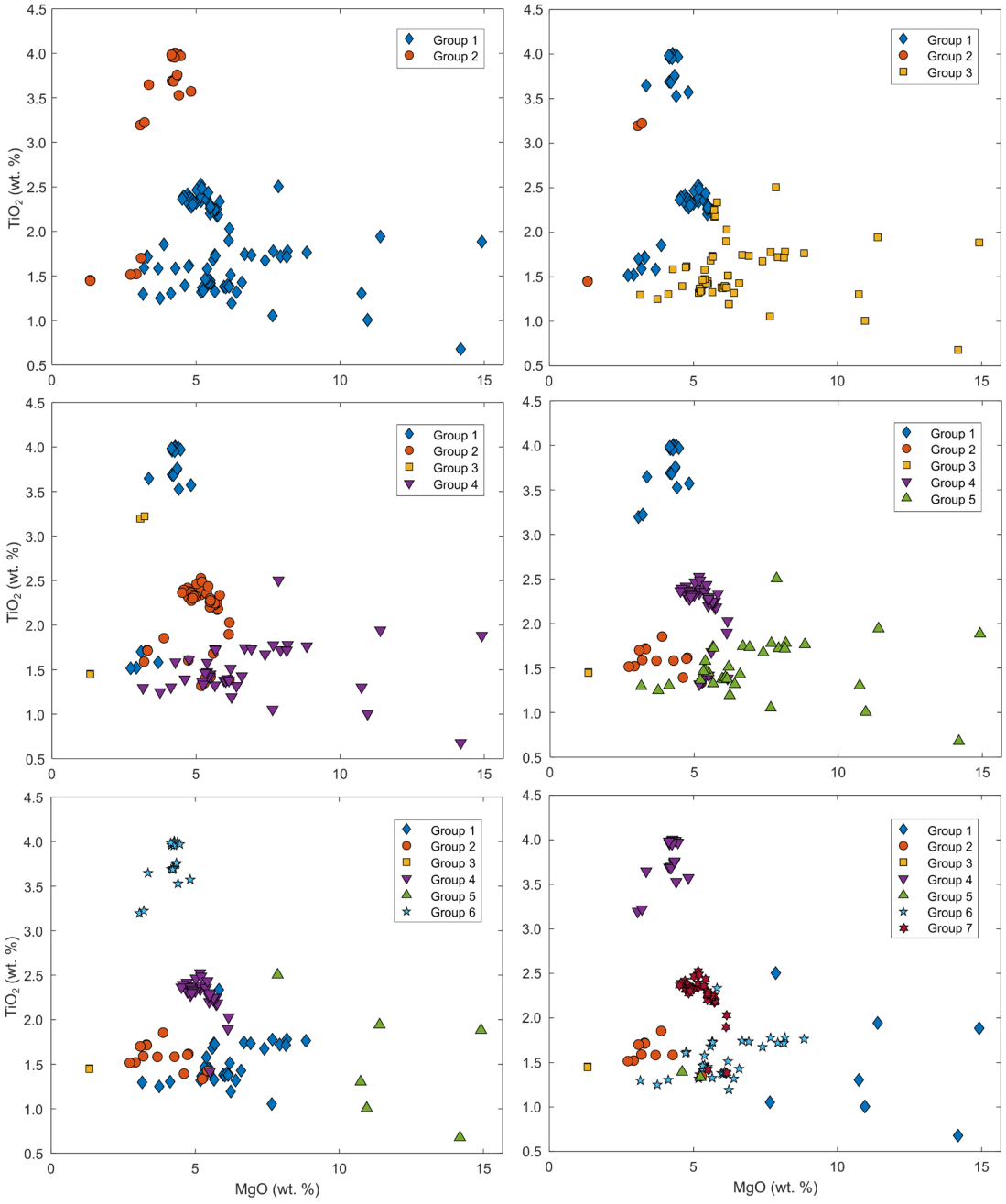

Figure D8 *- k-means clustering models for k-values of 2 to 7, using z-scores of all 51 elements in the full data set as variables (i.e. Table D1). As per DBI assessment (Figure D6), using z-scores gives less robust clustering, hence these models' exclusion from the discussion going forward.*

MLA-based plots for reduced variable data set (D9-D11)

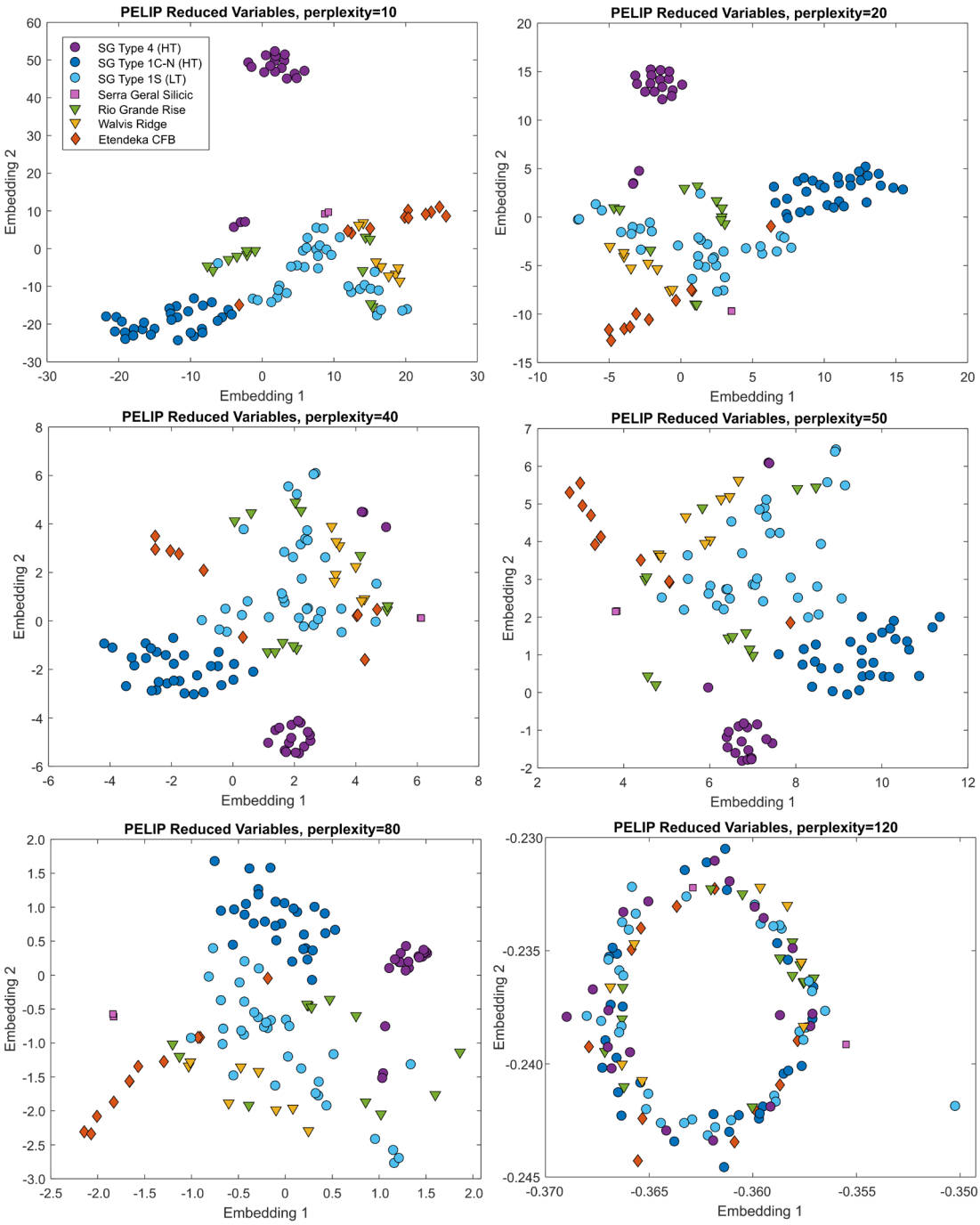

Figure D9 *- t-SNE models using the reduced data set of 11 variables, with different perplexity values. Perplexity of 50 was selected for full analysis.*

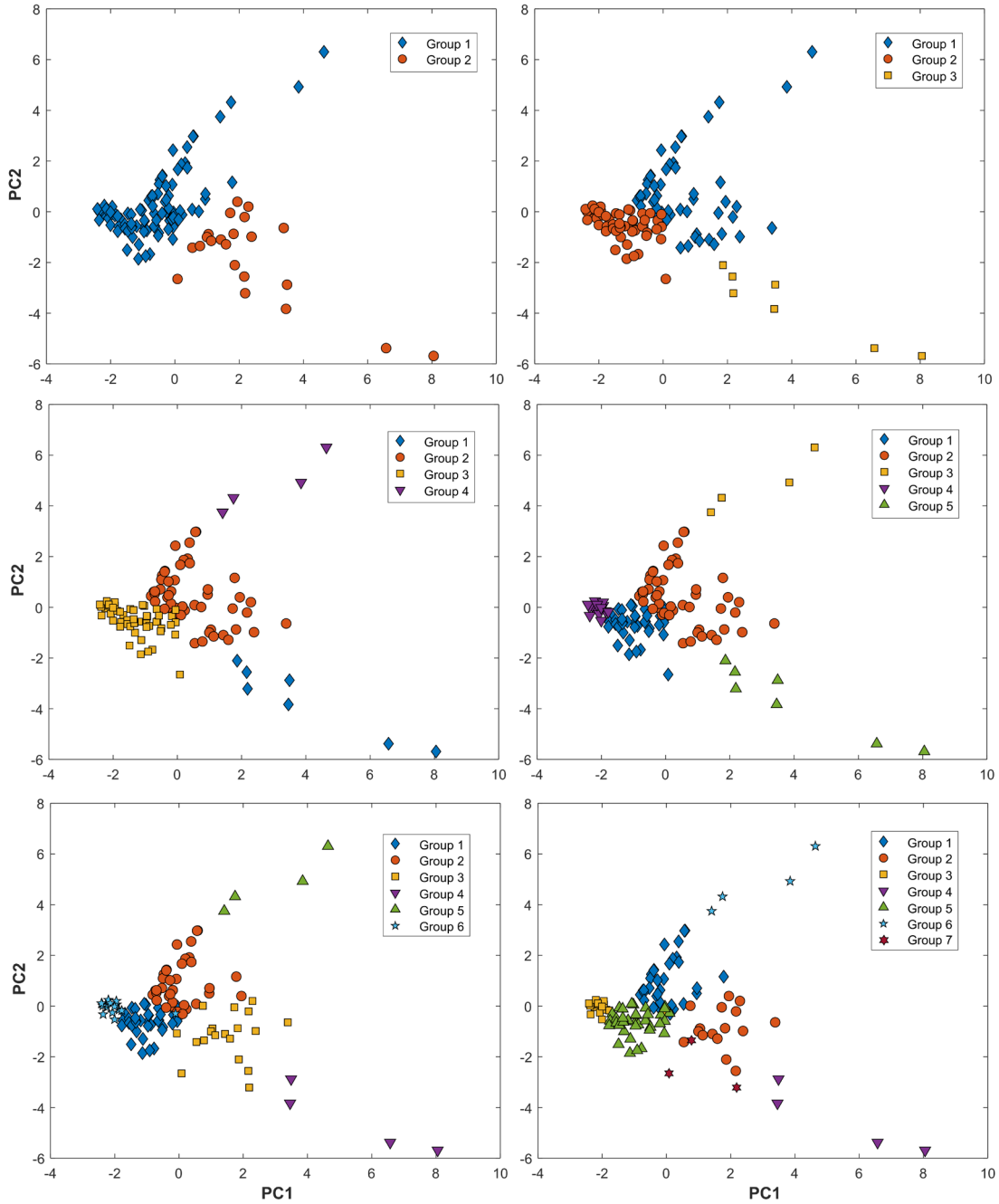

Figure D10 *- k-means clustering models for k-values of 2 to 7, using PC1-6 from the reduced data set (11 elements) as variables. As per DBI assessment (Figure D6), this model set-up gives similar results to the full data set clustered by PCs.*

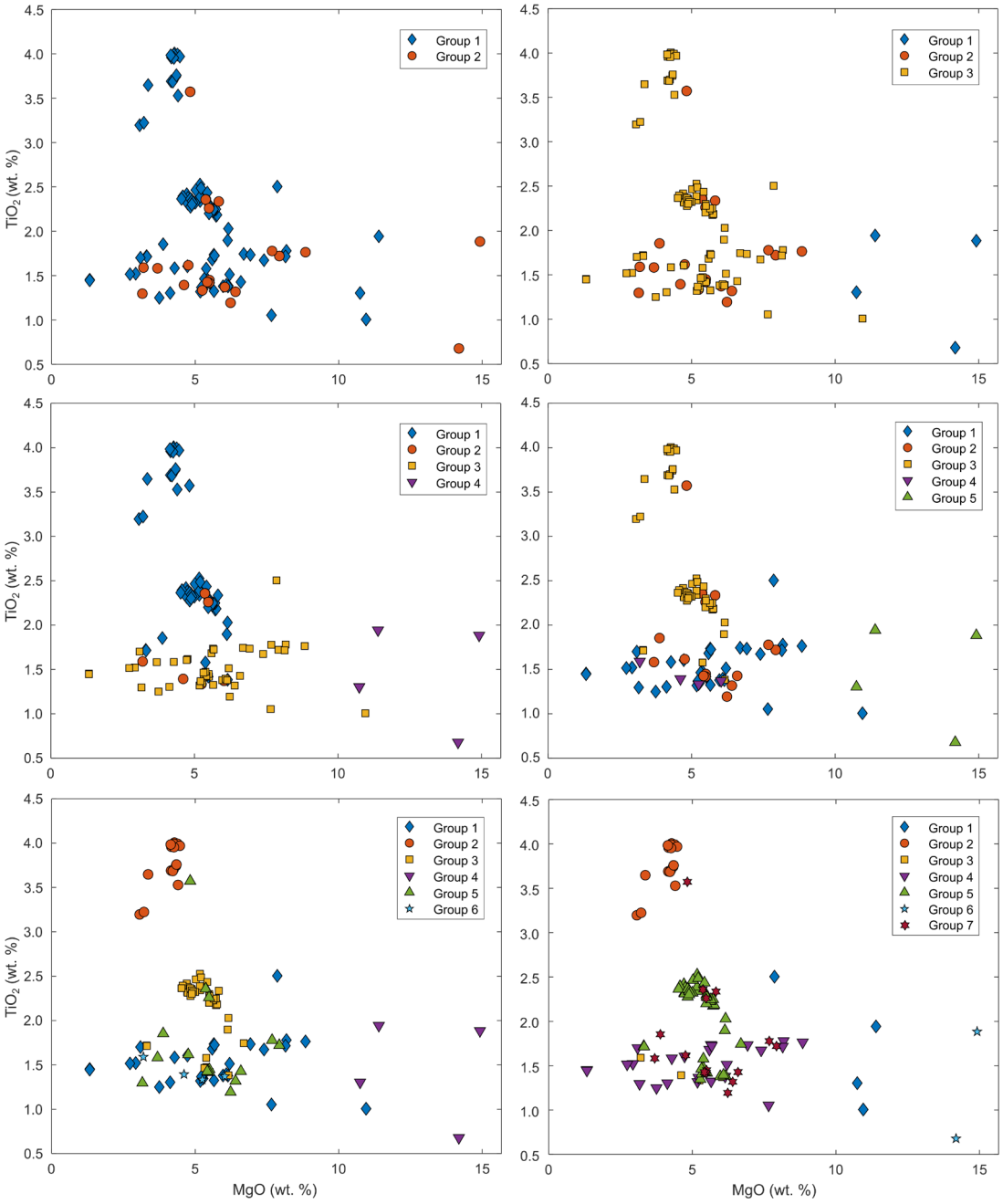

Figure D11 *- k-means clustering models for k-values of 2 to 7, using z-scores of the 11 elements in the reduced data set as variables (i.e. Figure 6.11). As per DBI assessment (Figure D6), using z-scores gives less robust clustering, hence these models' exclusion from the discussion going forward.*

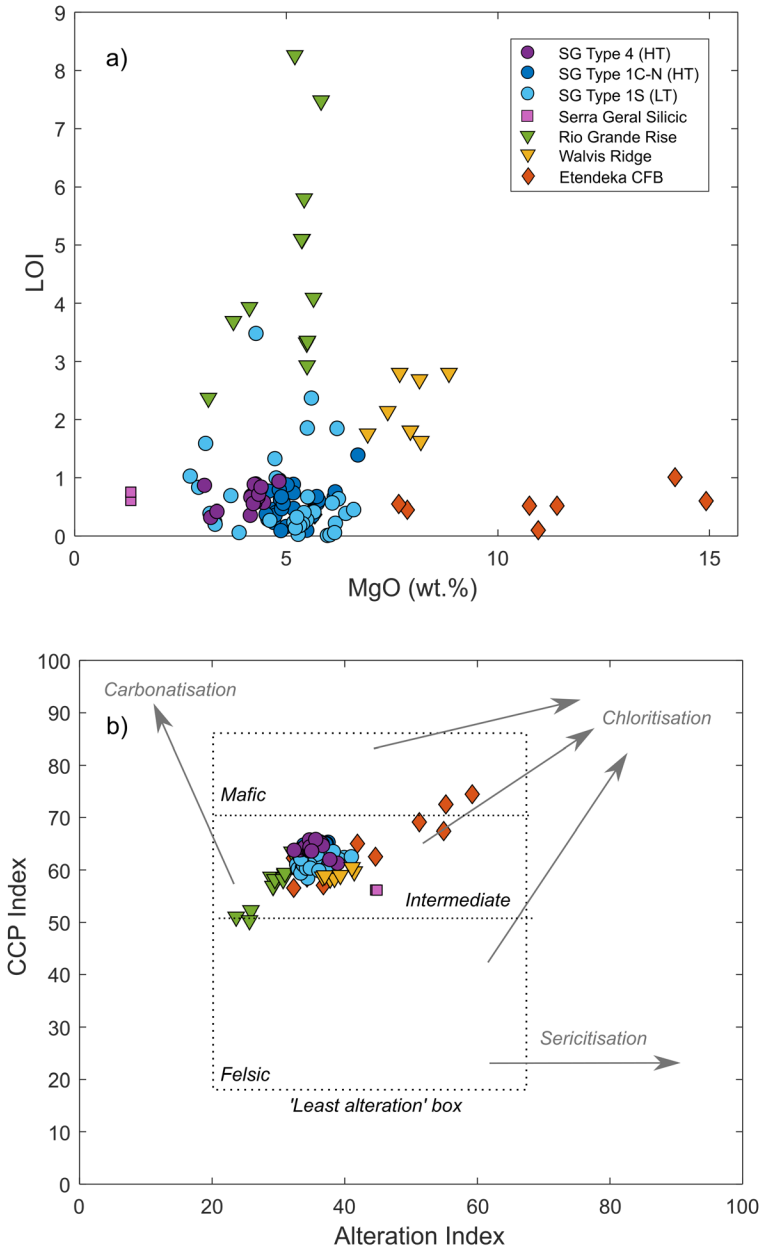

Figure D12 *– Alteration plots for the PELIP data set, ensuring that all geochemical trends in-text are primary signatures. (a) MgO vs. Loss On Ignition (LOI) and (b) alteration index vs. chlorite-carbonate-pyrite index (CCP) from Mathieu (2018).*

Appendix E

(for Chapter 7 - Synthesis)

Given the large amount of geochemical and MLA-based analyses conducted on the global data set, only the most crucial plots were included in the main body text for Chapter 7. This accompanying Appendix contains traditional geochemical bivariate Harker plots, and extra MLA plots exploring different parameter set-ups that support main body outcomes.

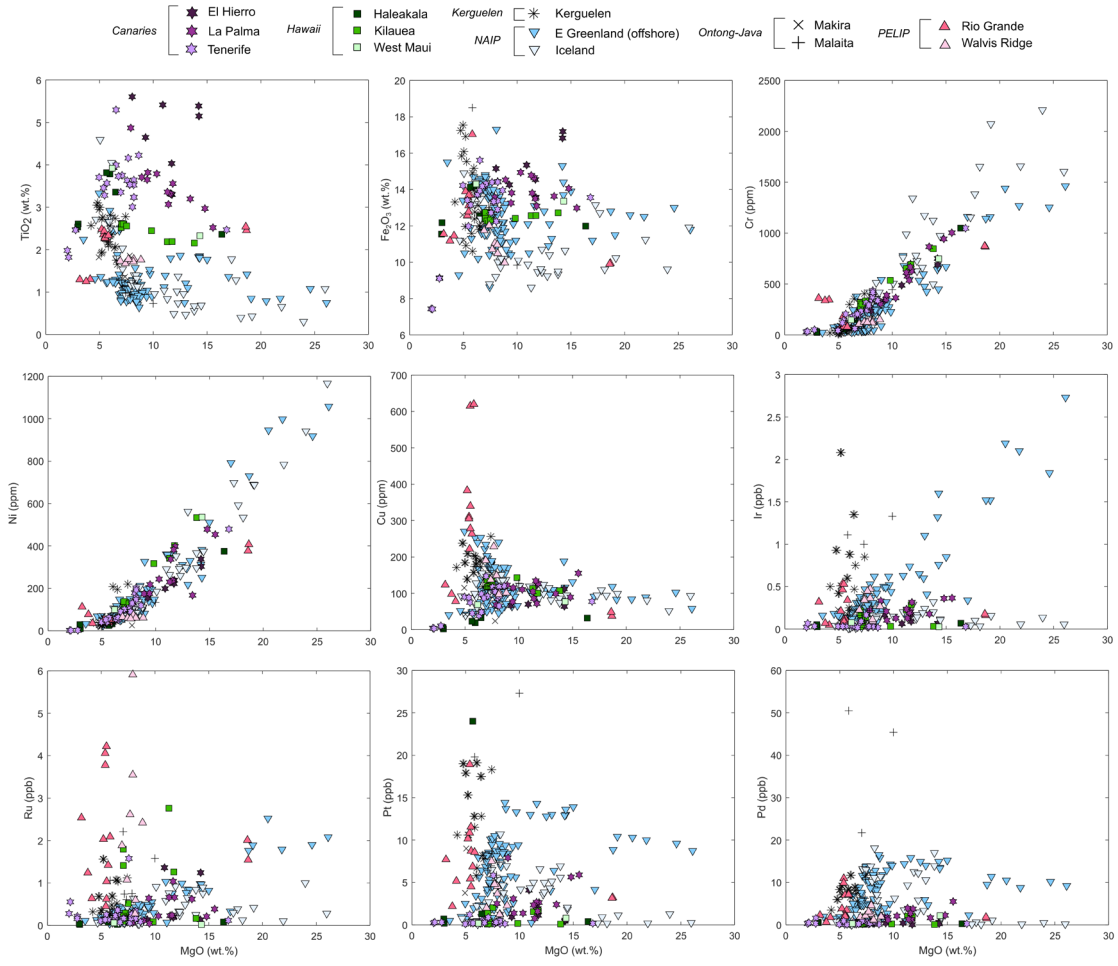

Figure E1 *- Harker plots for all variables in the oceanic plume sub-study, classified by locality.*

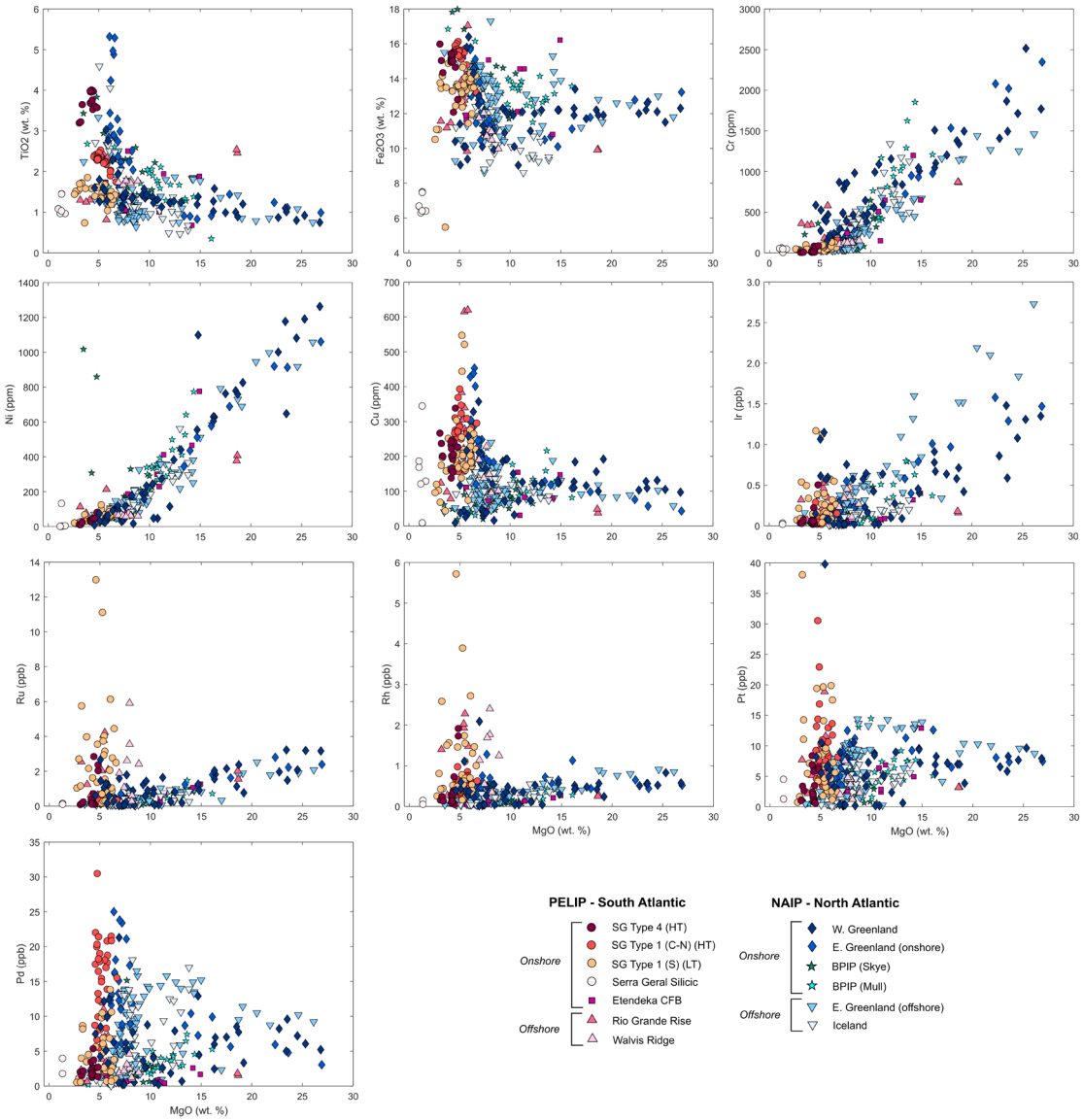

Figure E2 *- Harker plots for all variables in the transitional plume sub-study, classified by locality.*

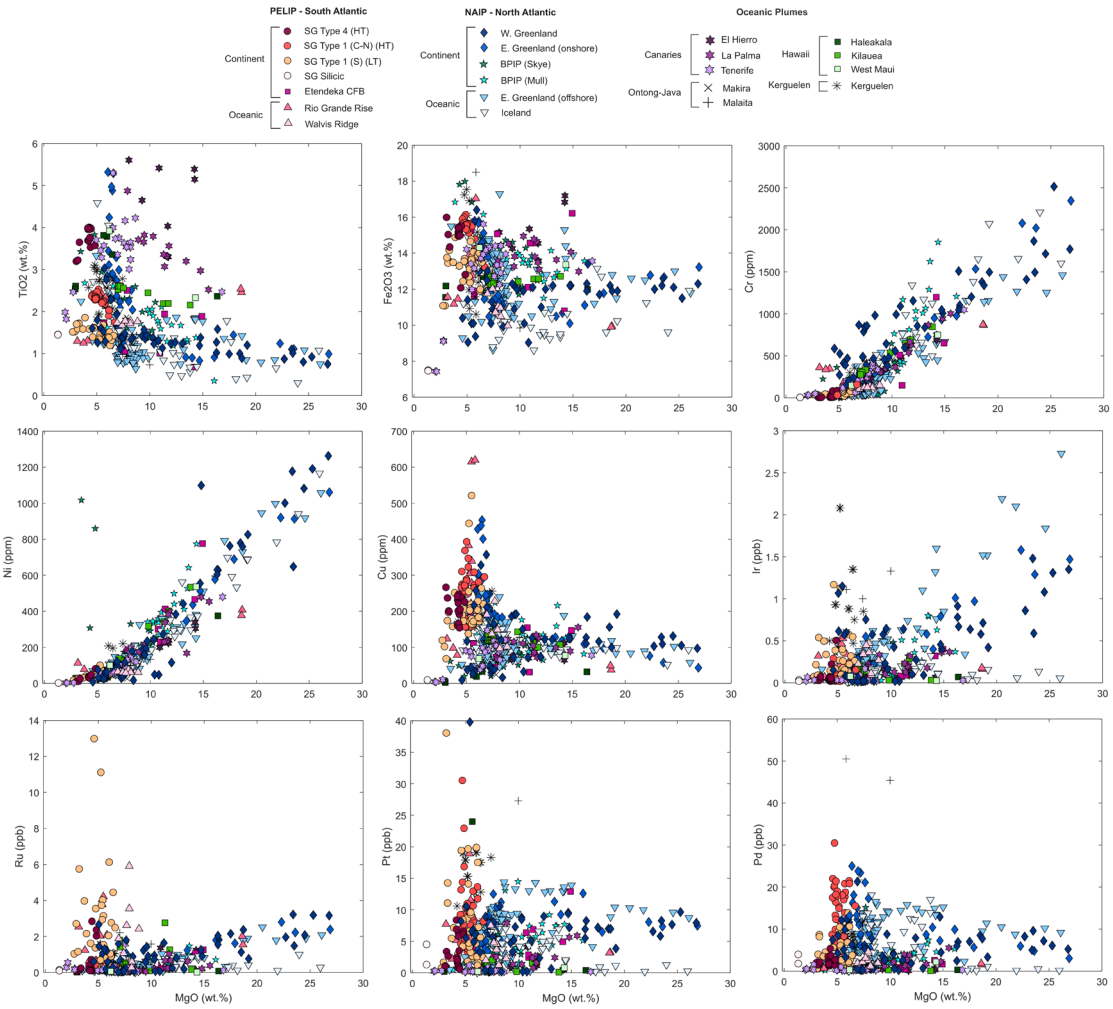

Figure E3 *- Harker plots for all variables in the continental vs. oceanic plume sub-study, classified by locality.*

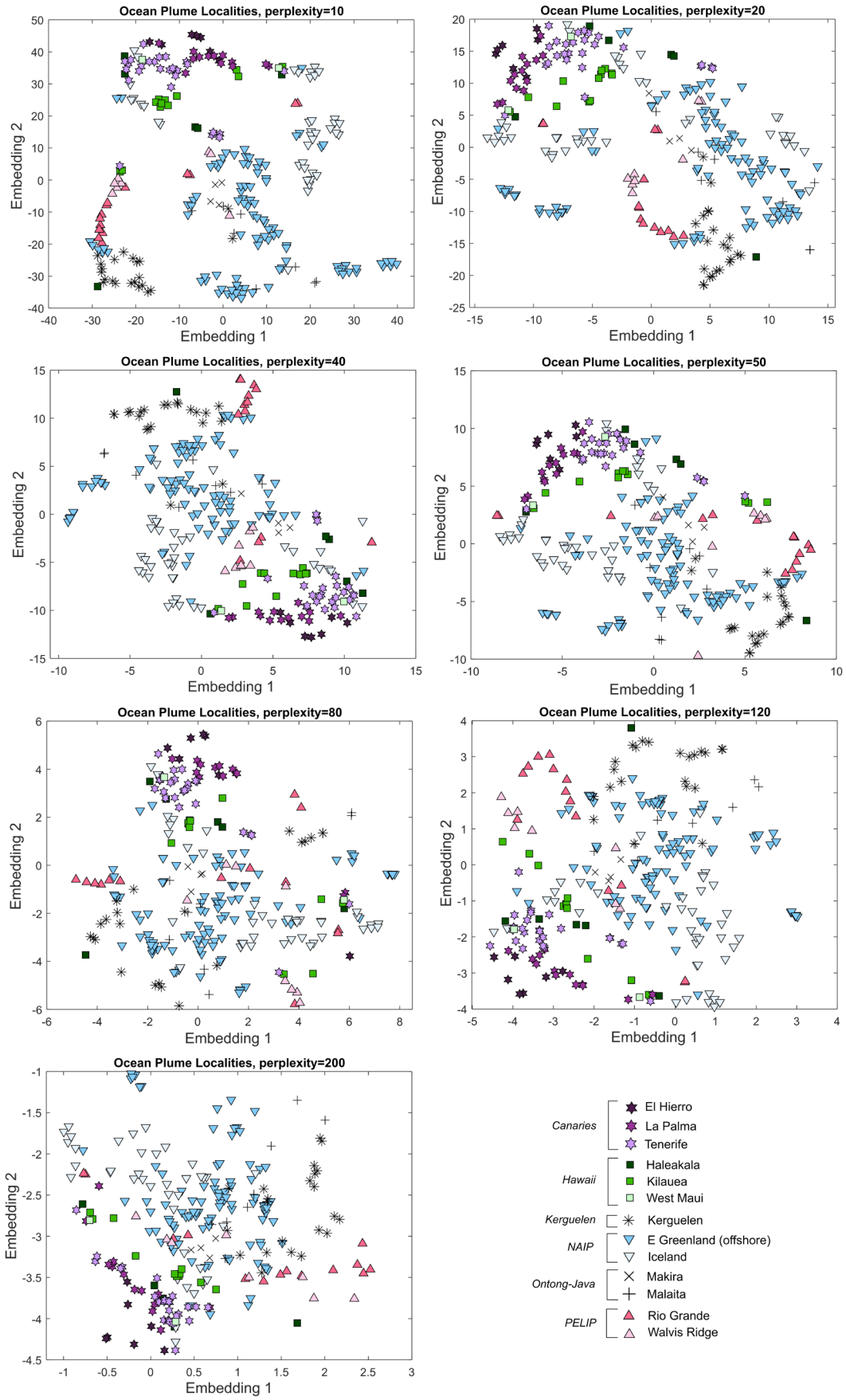

Figure E4 *- Various embeddings generated using t-SNE for oceanic plumes. Perplexity values given for each map. Classified by locality.*

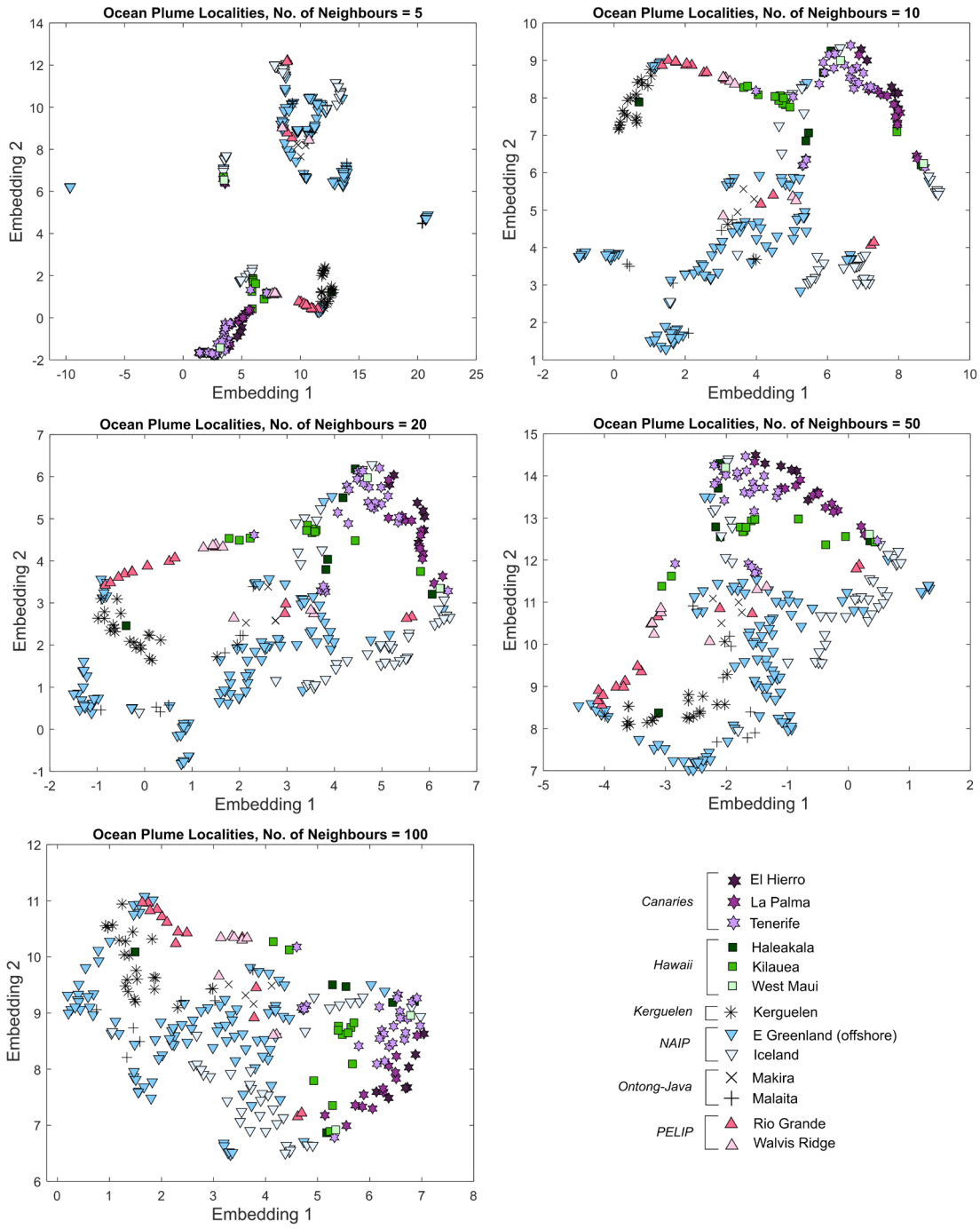

Figure E5 *- Various embeddings generated using UMAP for oceanic plumes. Number of neighbours given for each map. Classified by locality.*

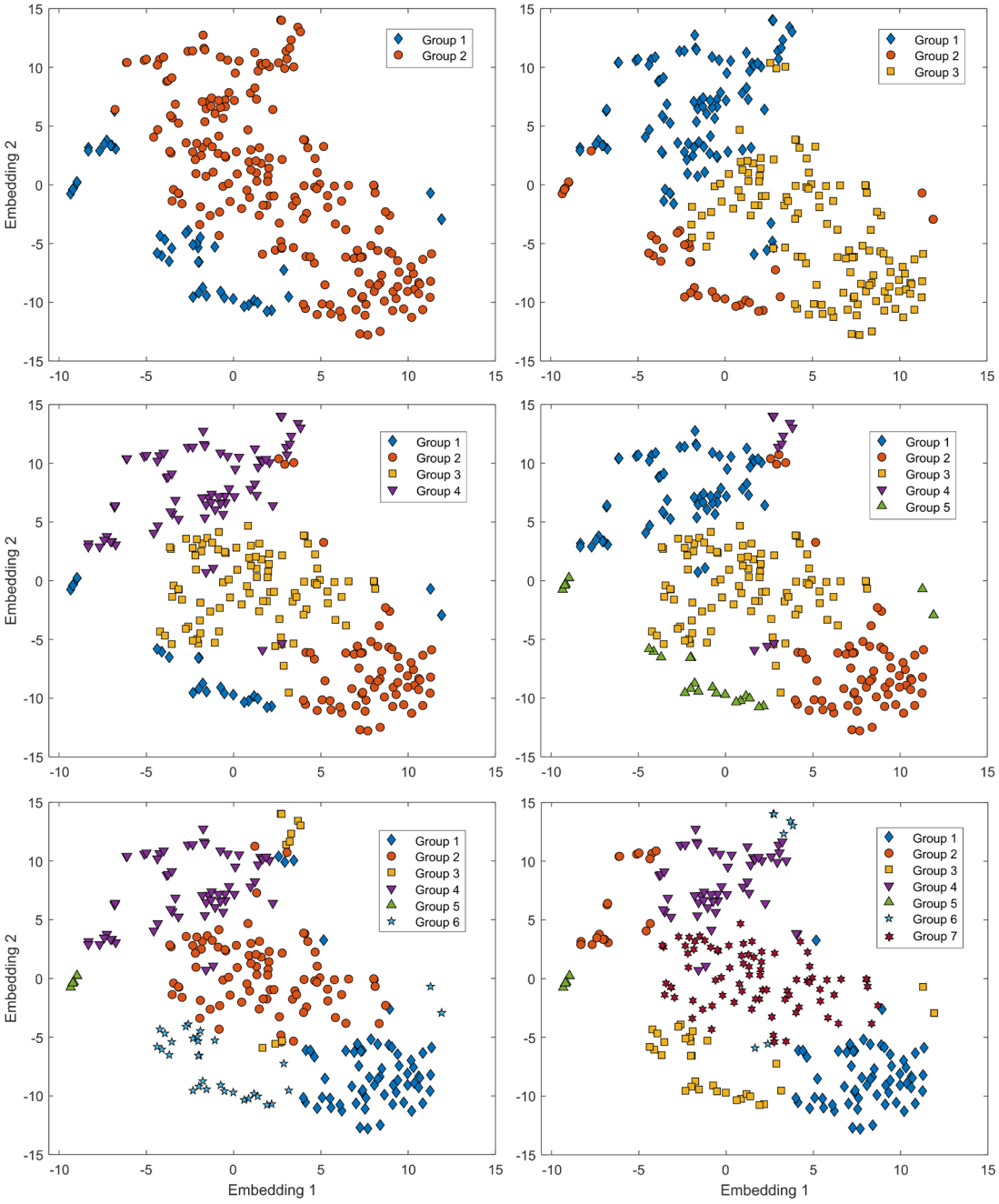

Figure E6 *- Full k-means clustering results for k-values of 2 to 7 for oceanic plumes, using the t-SNE map (Figure 3) as a layout.*

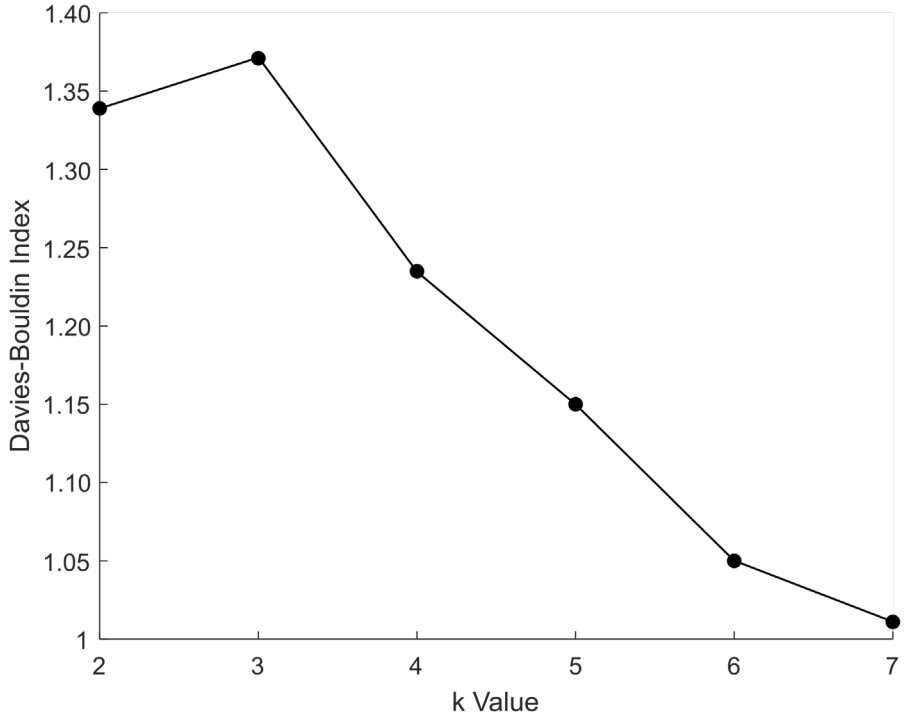

Figure E7 *- DBI assessment of k-means clustering for oceanic plumes; k=7 with PCs as variables was the optimum set-up ultimately chosen for further analyses.*

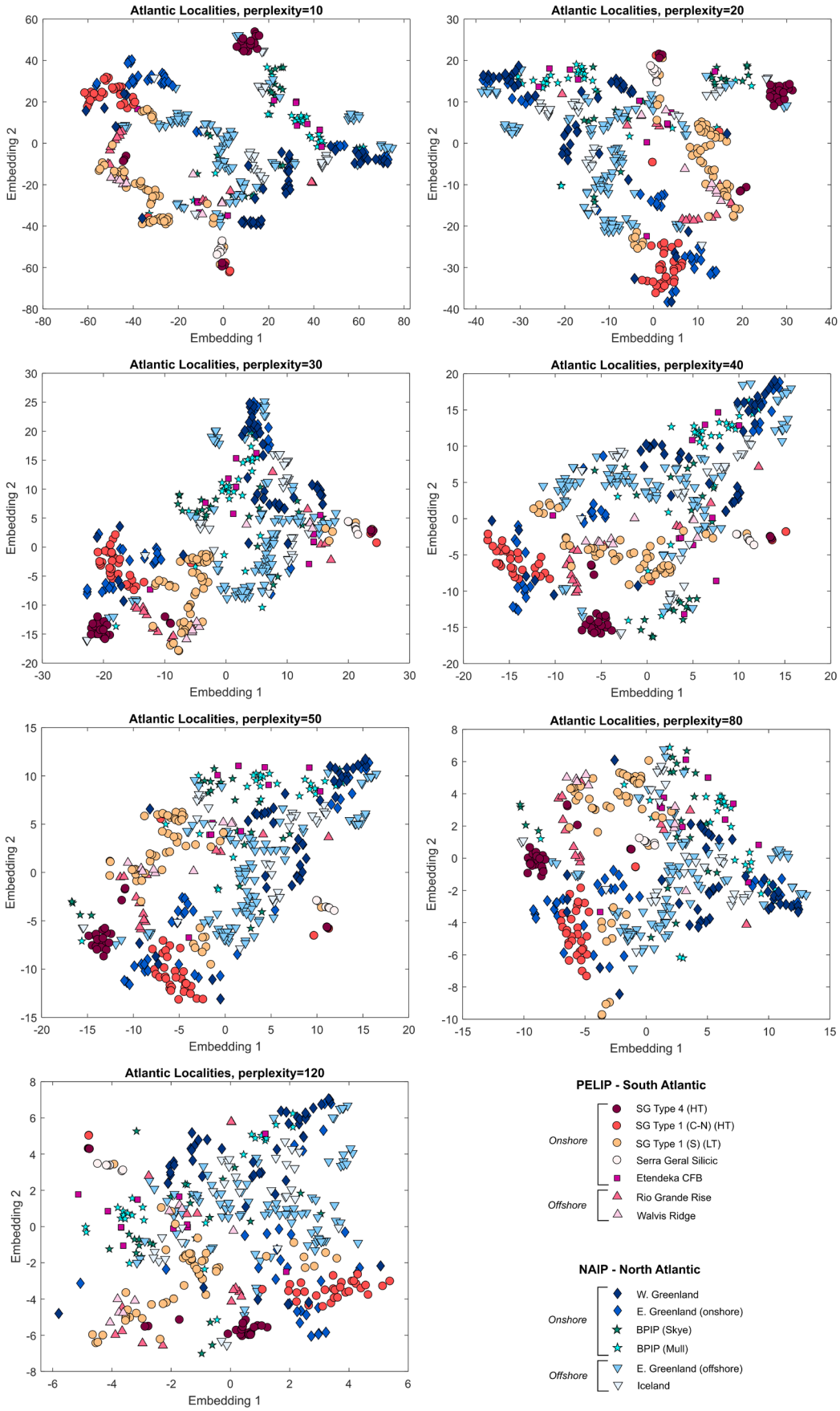

Figure E8 *- Various embeddings generated using t-SNE for transitional (Atlantic) plumes. Perplexity values given for each map. Classified by locality.*

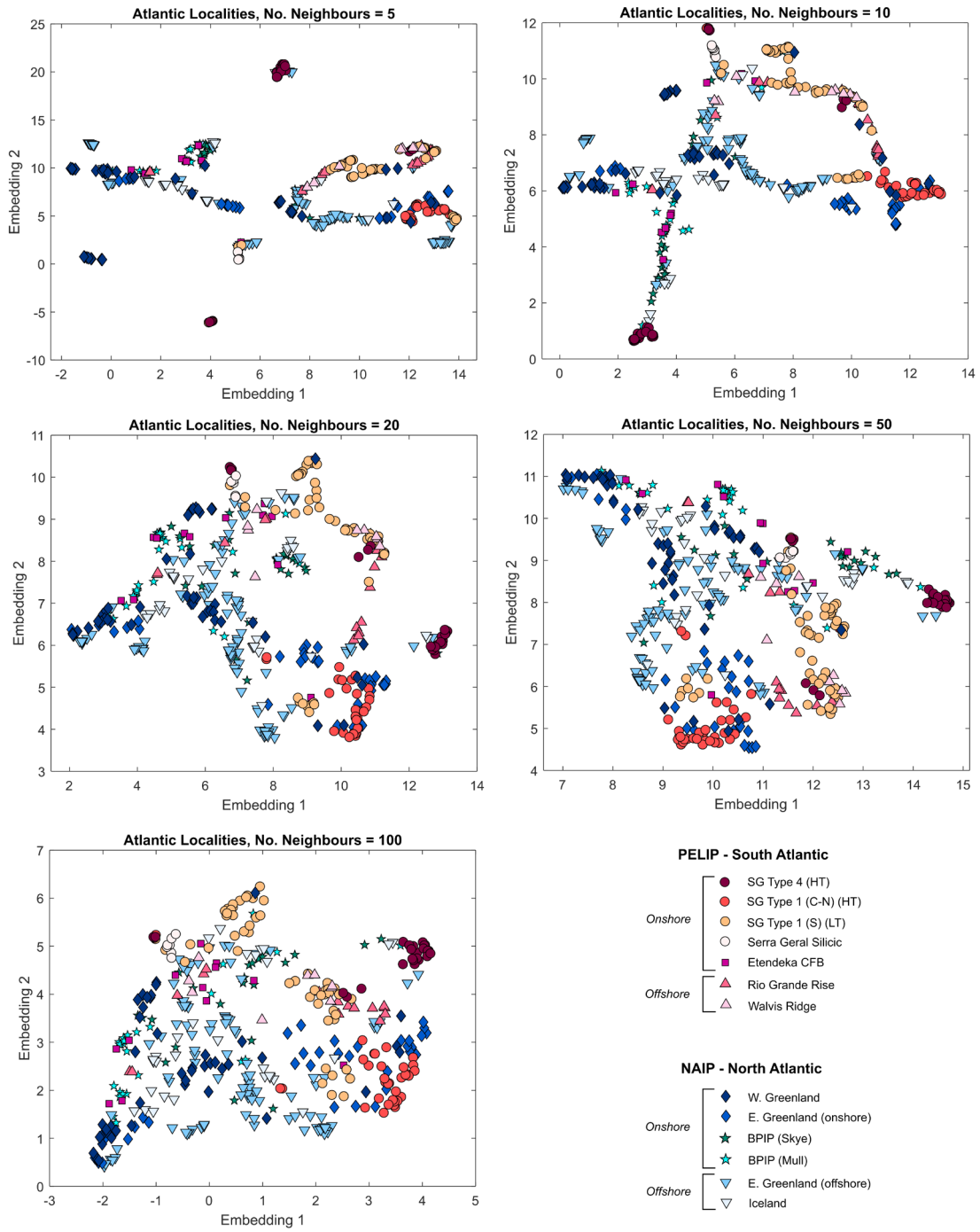

Figure E9 *- Various embeddings generated using UMAP for transitional (Atlantic) plumes. Number of neighbours given for each map. Classified by locality.*

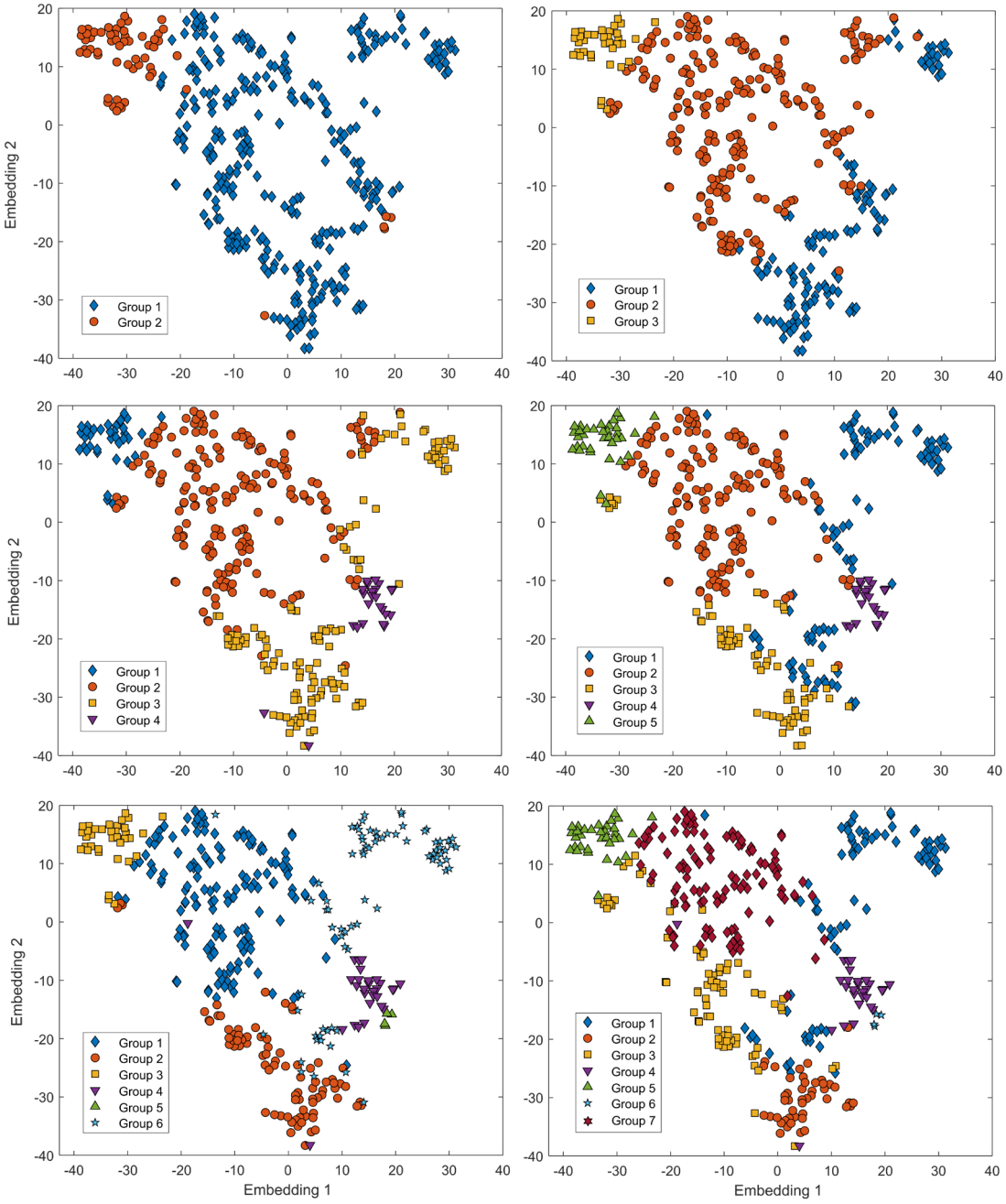

Figure E10 *- Full k-means clustering results for k-values of 2 to 7 for transitional (Atlantic) plumes, using the t-SNE map (Figure 7.7) as a layout.*

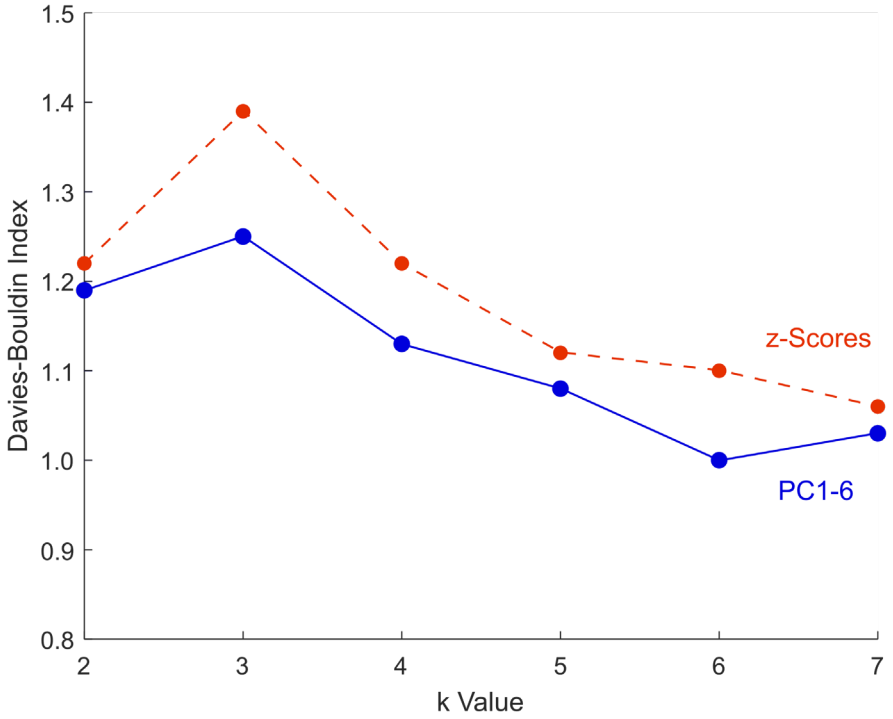

Figure E11 *- DBI assessment of k-means clustering for transitional (Atlantic) plumes; k=6 with PCs as variables was the optimum set-up ultimately chosen for further analyses. Like Chapters 5 and 6, clustering was attempted using z-scores instead of PCs initially, but gave similar results to these chapters – PCs as variable always give the lowest DBIs and thus, the best clusters.*

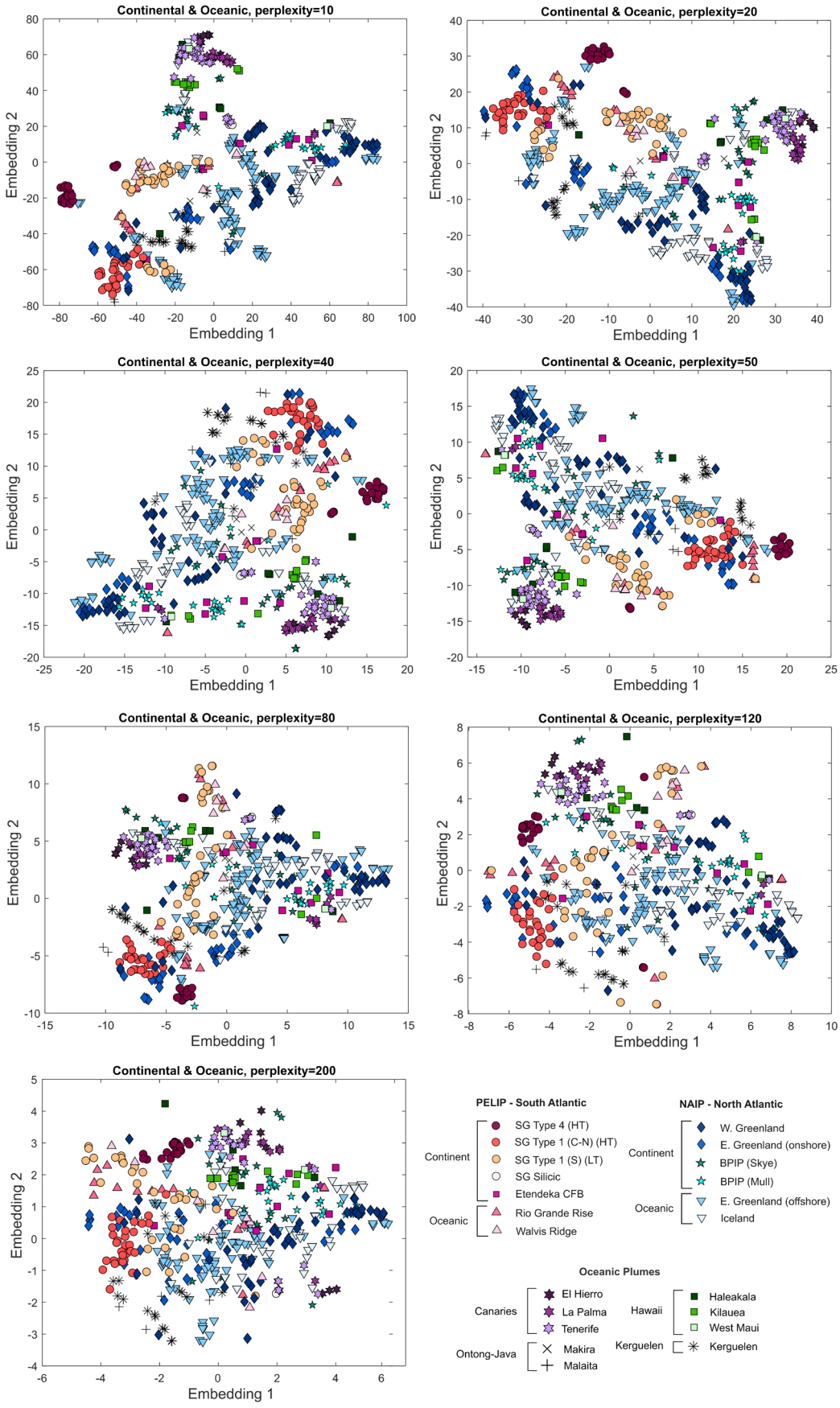

Figure E12 *- Various embeddings generated using t-SNE for continental and oceanic plumes. Perplexity values given for each map. Classified by locality.*

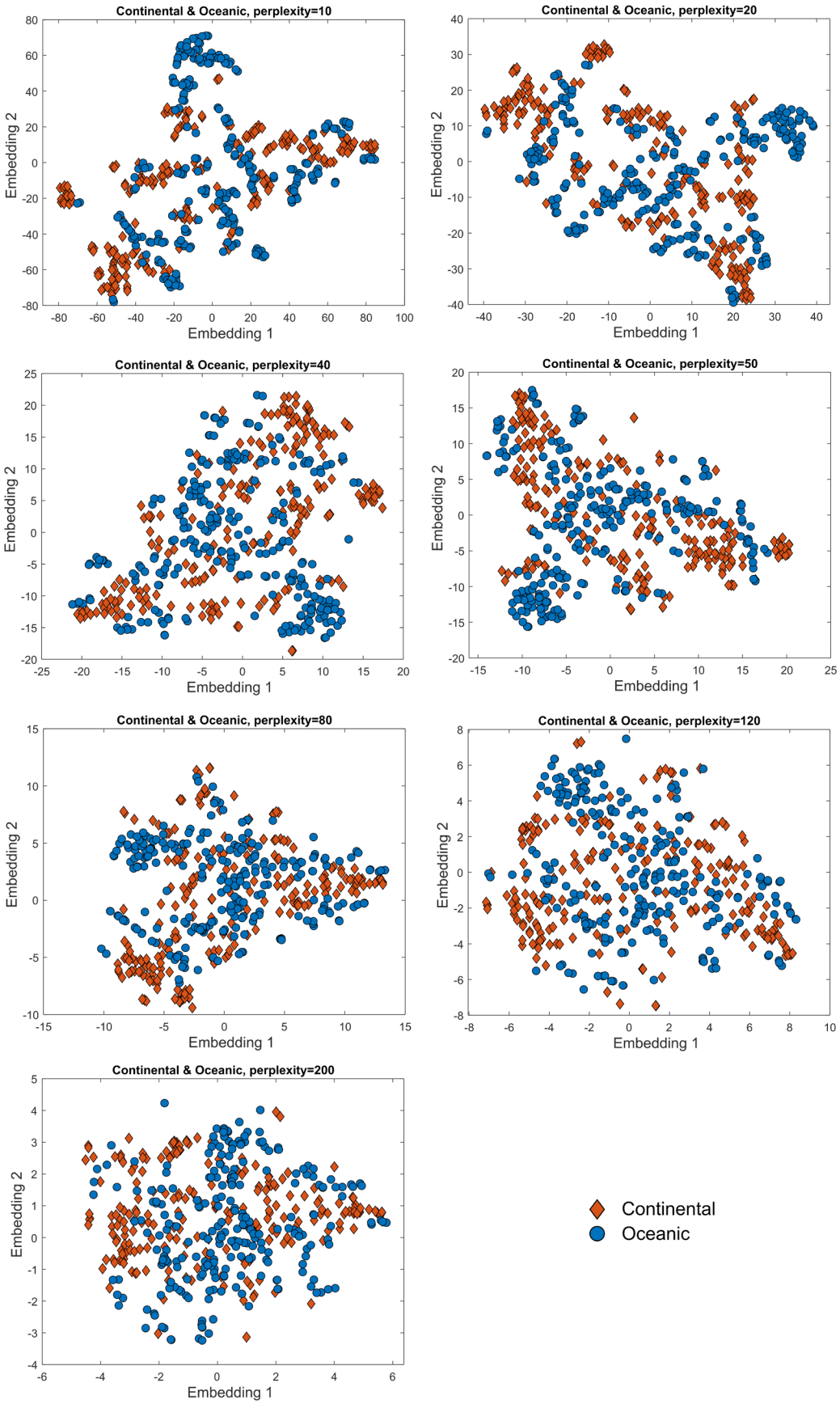

Figure E13 *- Various embeddings generated using t-SNE for continental and oceanic plumes. Perplexity values given for each map. Classified by setting.*

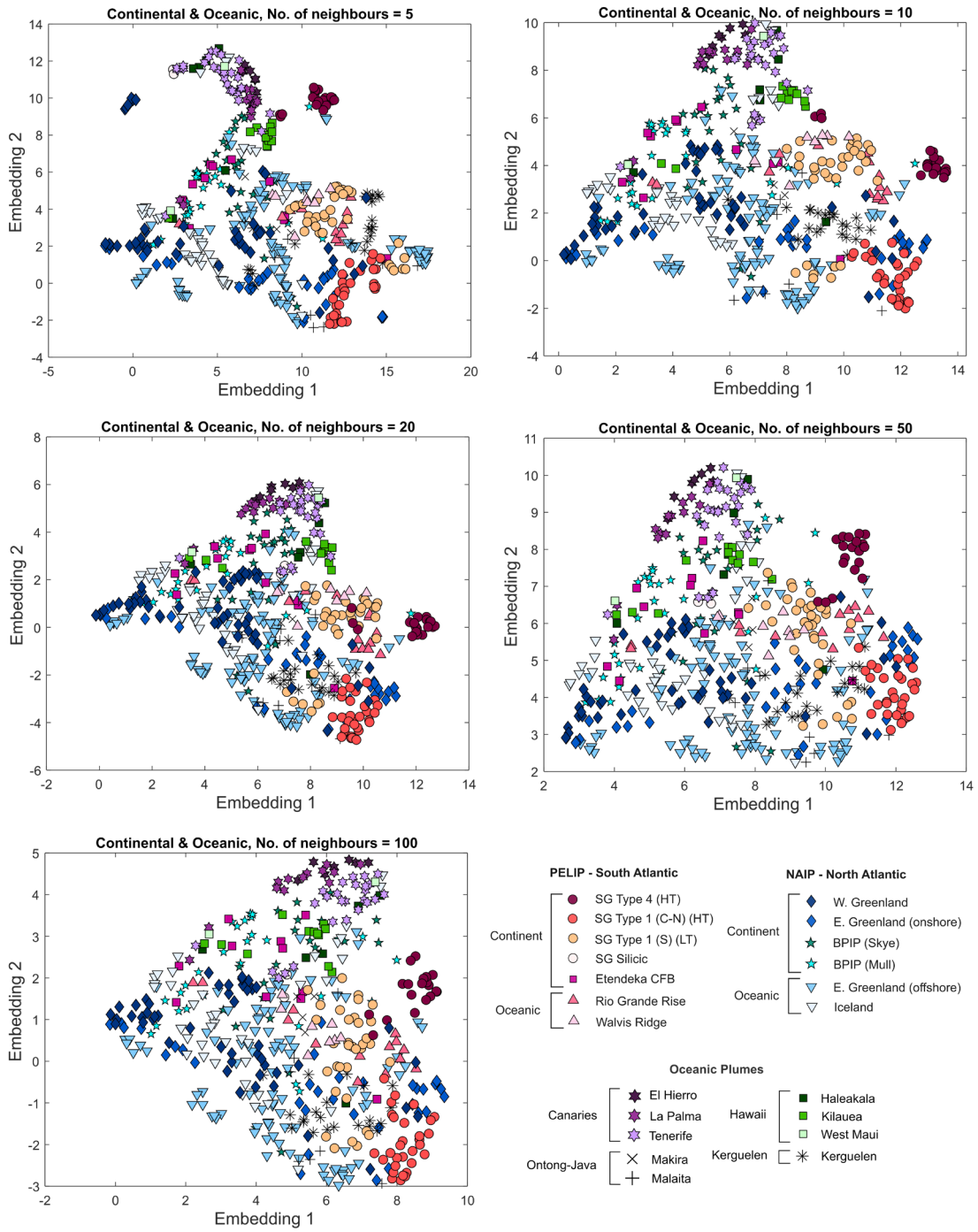

Figure E14 *- Various embeddings generated using UMAP for transitional continental and oceanic plumes. Number of neighbours given for each map. Classified by locality.*

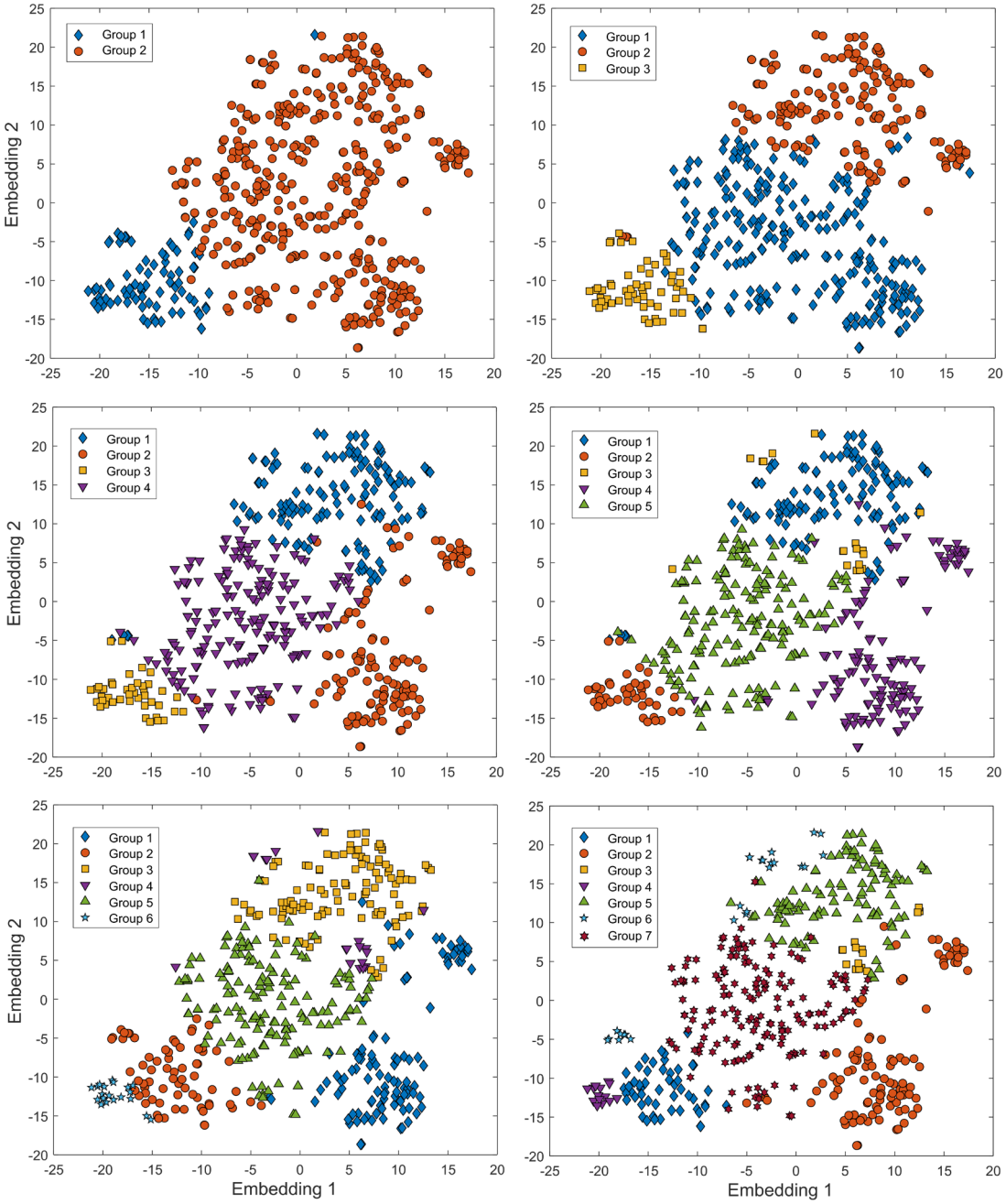

Figure E15 *- Full k-means clustering results for k-values of 2 to 7 for continental and oceanic plumes, using the t-SNE map (Figure 7.11) as a layout.*

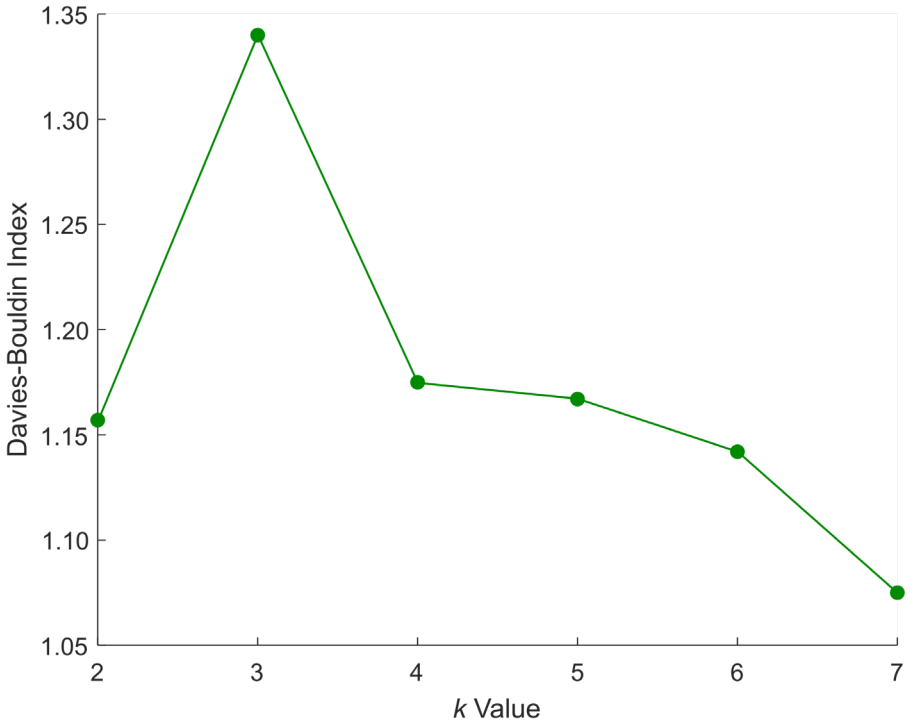

Figure E16 *- DBI assessment of k-means clustering for continental and oceanic plumes; k=7 with PCs as variables was the optimum set-up ultimately chosen for further analyses.*

References

Abdel-Monem A. A., Gast P. W. and Watkins N. D. (1972) Potassium-argon ages, volcanic stratigraphy, and geomagnetic polarity history of the Canary Islands: Tenerife, La Palma, and Hierro. *Am. J. Sci.* **272**, 805–825.

Abeng S. A. E., Ndjigui P-D., Beyanu A. A., Teutsong T. and Bilong P. (2012) Geochemistry of pyroxenites, amphibolites and their weathered products in the Nyong unit, SW Cameroon (NW border of Congo craton): Implications for Au-PGE exploration. *J. of Geochem. Explor.*. **114**, 1-19.

Abdi H. and Williams L. J. (2010) Principal Component Analysis. *Wiley Interdisplinary Rev. Comput. Stat.* **2**, 1–47.

Alard O., Griffin W. L., Lorand J. P., Jackson S. E. and O'Reilly S. Y. (2000) Non-chondritic distribution of the highly siderophile elements in mantle sulphides. *Nature* **407**, 891–894.

Alard O., Lorand J. P., Reisberg L., Bodinier J. L., Dautria J. M. and O'reilly S. Y. (2011) Volatile-rich metasomatism in montferrier xenoliths (Southern France): Implications for the abundances of chalcophile and highly siderophile elements in the subcontinental mantle. *J. Petrol.* **52**, 2009–2045.

Ancochea E., Fuster J., Ibarrola E., Cendrero A., Coello J., Hernan F., Cantagrel J. M. and Jamond C. (1990) Volcanic evolution of the island of Tenerife (Canary Islands) in light of new K-Ar data. *J. Volcanol. Geotherm. Res.* **44**, 231–249.

Andersen J. C. Ø., Power M. R. and Momme P. (2002) Platinum-Group Elements in the Palaeogene North Atlantic Igneous Province. The geology, geochemistry, mineralogy, and mineral beneficiation of platinum-group elements. *L. J. Cabri. Montréal, Québec, Can. Inst. Mining, Metall. Pet.* **CIM Spec.**, 637–667.

Andersen J. C. Ø., Rasmussen H., Nielsen T. F. D. and Rønsbo J. G. (1998) The Triple Group and the Platinova gold and palladium reefs in the Skaergaard Intrusion: stratigraphic and petrographic relations. *Econ. Geol.* **93**, 488–509.

Andersen J. C. Ø., Rollinson G. K., McDonald I., Tegner C. and Lesher C. E. (2017) Platinum-group mineralization at the margin of the Skaergaard intrusion, East Greenland. *Miner. Depos.*, **52**, 929-942. Available at: http://dx.doi.org/10.1007/s00126-016-0707-3.

Anderson D. L. (1998) The helium paradoxes. *Proc. Natl. Acad. Sci. U. S. A.* **95**, 4822–4827.

Anderson D. L. and Natland J. H. (2005) A brief history of the plume hypothesis and its competitors: Concept and controversy. *Spec. Pap. 388 Plates, plumes Paradig.* **388**, 119–145.

Andrew A. M. (1999) Reinforcement Learning: An Introduction (Adaptive

Computation and Machine Learning). *Robotica* **17**, 229–235.

Anguita F. and Hernán F. (2000) The Canary Islands origin: a unifying model. *J. Volcanol. Geotherm. Res.* **103**, 1–26.

Araña V., Martí J., Aparicio A., García-Cacho L. and García-García R. (1994) Magma mixing in alkaline magmas: An example from Tenerife, Canary Islands. *Lithos* **32**, 1–19.

Arndt N. T., Chauvel C., Czamanske G. and Fedorenko V. (1998) Two mantle sources, two plumbing systems: Tholeiitic and alkaline magmatism of the Maymecha River basin, Siberian flood volcanic province. *Contrib. to Mineral. Petrol.* **133**, 297–313.

Arndt N. T., Czamanske G. K., Walker R. J., Chauvel C. and Fedorenko V. a. (2003) Geochemistry and Origin of the Intrusive Hosts of the Noril'sk-TalnakhCu-Ni-PGE Sulfide Deposits. *Econ. Geol.* **98**, 495–515.

Arndt N. T., Czamanske G. K., Wooden J. L. and Fedorenko V. A. (1993) Mantle and crustal contributions to continental flood volcanism. *Tectonophysics* **223**, 39–52.

Arndt N. T. and Goldstein S. L. (1987) Use and abuse of crust-formation ages. *Geology* **15**, 893–895.

Asavin A. M., Kogarko L. N., Kryuchkova O. I., Tyurin D. A. and Kolesov G. M. (1997) The Grand Canary, Saint Helena, and Tristan Da Cunha oceanic islands: Variations of trace element partition coefficients in pyroxene-melt equilibria during alkaline magma evolution. *Geochemistry Int.* **35**, 415–423.

Aulbach S., Giuliani A., Fiorentini M. L., Baumgartner R. J., Savard D., Kamenetsky V. S., Caruso S., Danyushevky L. V., Powell W., Griffin W. L. (2021) Siderophile and chalcophile elements in spinels, sulphides and native Ni in strongly metasomatised xenoliths from the Bultfontein kimberlite (South Africa). *Lithos*. **380–381**, 105880.

Aulinas M., Gimeno D., Fernandez-Turiel J. L., Font L., Perez-Torrado F. J., Rodriguez-Gonzalez A. and Nowell G. M. (2010) Small-scale mantle heterogeneity on the source of the Gran Canaria (Canary Islands) Pliocene-Quaternary magmas. *Lithos* **119**, 377–392.

Balamurali M. and Melkumyan A. (2016) t-SNE Based Visualisation and Clustering of Geological Domain. In *International Conference on Neural Information Processing*

Ballhaus C., Bockrath C., Wohlgemuth-Ueberwasser C., Laurenz V. and Berndt J. (2006) Fractionation of the noble metals by physical processes. *Contrib. to Mineral. Petrol.* **152**, 667–684.

Ballhaus C., Laurenz V., Münker C., Fonseca R. O. C., Albarède F., Rohrbach A., Lagos M., Schmidt M. W., Jochum K. P., Stoll B., Weis U. and Helmy H. M. (2013) The U/Pb ratio of the Earth's mantle-A signature of late volatile addition. *Earth Planet. Sci. Lett.* **362**, 237–245.

Ballhaus C., Tredoux M. and Späth A. (2001) Phase relations in the Fe-Ni-Cu-PGE-S system at magmatic temperature and application to massive

sulphide ores of the the sudbury igneous complex. *J. Petrol.* **42**, 1911–1926.

Barnes S. J., Cruden A. R., Arndt N. and Saumur B. M. (2016) The mineral system approach applied to magmatic Ni–Cu–PGE sulphide deposits. *Ore Geol. Rev.* **76**, 296–316. Available at: http://dx.doi.org/10.1016/j.oregeorev.2015.06.012.

Barnes S. J., Makovicky E., Makovicky J., Rose-Hansen J. and Karup-Moller S. (1997) Partition coefficients for Ni, Cu, Pd, Pt, Rh, and Ir between monosulfide solid solution and sulfide liquid and the formation of compositionally zoned Ni – Cu sulfide bodies by fractional crystallization of sulfide liquid. *Can. J. Earth Sci.* **34**, 366–374.

Barnes S. J., Mungall J. E. and Maier W. D. (2015) Platinum group elements in mantle melts and mantle samples. *Lithos* **232**, 395–417. Available at: http://dx.doi.org/10.1016/j.lithos.2015.07.007.

Barnes S. J., Naldrett A. J. and Gorton M. P. (1985) The origin of the fractionation of platinum-group elements in terrestrial magmas. *Chem. Geol*. **53**, 303–323.

Barnes S. J. and Picard C. P. (1993) The behaviour of platinum-group elements during partial melting, crystal fractionation, and sulphide segregation: An example from the Cape Smith Fold Belt, northern Quebec. *Geochim. Cosmochim. Acta* **57**, 79–87.

Barnes S. J. and Robertson J. C. (2019) Time scales and length scales in magma flow pathways and the origin of magmatic Ni–Cu–PGE ore deposits. *Geosci. Front.* **10**, 77–87.

Beattie P., Drake M., Jones J., Leeman W., Longhi J., McKay G., Nielsen R., Palme H., Shaw D., Takahashi E. and Watson B. (1993) Terminology for trace-element partitioning. *Geochim. Cosmochim. Acta* **57**, 1605–1606.

Beattie P., Ford C. and Russell D. (1991) Partition coefficients for olivine-melt and orthopyroxene-melt systems. *Contrib. to Mineral. Petrol.* **109**, 212–224.

Beccaluva L., Bianchini G., Natali C. and Siena F. (2020) Plume-related Paranà-Etendeka igneous province: An evolution from plateau to continental rifting and breakup. *Lithos* **362**–**363**, 105484. Available at: https://doi.org/10.1016/j.lithos.2020.105484.

Becht E., McInnes L., Healy J., Dutertre C. A., Kwok I. W. H., Ng L. G., Ginhoux F. and Newell E. W. (2019) Dimensionality reduction for visualizing single-cell data using UMAP. *Nat. Biotechnol.* **37**, 38–47.

Becker H., Horan M. F., Walker R. J., Gao S., Lorand J. P. and Rudnick R. L. (2006) Highly siderophile element composition of the Earth's primitive upper mantle: Constraints from new data on peridotite massifs and xenoliths. *Geochim. Cosmochim. Acta* **70**, 4528–4550.

Becker T. W. and Boschi L. (2002) A comparison of tomographic and geodynamic mantle models. *Geochemistry, Geophys. Geosystems* **3**, 1–48.

Begg, G. C., Hronsky, J. A.M., Arndt, N. T., Griffin, W. L. O'Reilly, S. Y. and

Hayward, N. (2010) Lithospheric, Cratonic and Geodynamic Setting of Ni-Cu-PGE Sulfide Deposits. *Economic Geology*. **105** (6), 1057-1070.

Béguelin P., Bizimis M., Beier C. and Turner S. (2017) Rift–plume interaction reveals multiple generations of recycled oceanic crust in Azores lavas. *Geochim. Cosmochim. Acta* **218**, 132–152.

Béguelin P., Bizimis M., McIntosh E. C., Cousens B. and Clague D. A. (2019) Sources vs processes: Unraveling the compositional heterogeneity of rejuvenated-type Hawaiian magmas. *Earth Planet. Sci. Lett.* **514**, 119–129.

Belay I. G., Tanaka R., Kitagawa H., Kobayashi K. and Nakamura E. (2019) Origin of ocean island basalts in the West African passive margin without mantle plume involvement. *Nat. Commun.* **10**, 1–12.

Bellieni G., Comin-Chiaramonti P., Marques L. ., Melfi A. J., Piccirillo E. . and Nardy A. J. (1984) High- and low-TiO2 flood basalts from the Paraná plateau (Brasil): Petrology and geochemical aspects bearing on thier mantle origin. *Neues Jahrb. für Mineral.* **150**, 273–306.

Bennett V. C., Esat T. M. and Norman M. D. (1996) Two mantle-plume components in Hawaiian picrites inferred from correlated Os-Pb isotopes. *Nature* **v. 381**, 221–224.

Bennett V. C., Norman M. D. and Garcia M. O. (2000) Rhenium and platinum group element abundances correlated with mantle source components in Hawaiian picrites: sulphides in the plume. *Earth Planet. Sci. Lett.* **183**, 513–526.

Bercovici D. and Kelly A. (1997) The non-linear initiation of diapirs and plume heads. *Phys. Earth Planet. Inter.* **101**, 119–130.

Berggren W. A., Kent D. V., Swisher C. C. and Aubry M. P. (1995) A revised Cenozoic geochronology and chronostratigraphy. *Geochronol. Time Scales Glob. Stratigr. Correl. SEPM Spec. Publ.* **54**, 129–212.

Besser M. L., Maria E., Vasconcellos G., José A. and Nardy R. (2018) Morphology and stratigraphy of Serra Geral silicic lava flows in the northern segment of the Torres Trough , Paraná Igneous Province. *Brazilian J. Geol.* **48**, 201–219.

Bézos A., Lorand J.-P., Humler E. and Gros M. (2005) Platinum-group element systematics in Mid-Oceanic Ridge basaltic glasses from the Pacific, Atlantic, and Indian Oceans. *Geochim. Cosmochim. Acta* **69**, 2613–2627.

BGS (2015) Risk List 2015. *Br. Geol. Surv.* Available at: https://www2.bgs.ac.uk/mineralsuk/download/statistics/risk_list_2015.pdf [Accessed February 28, 2021]

Bierlein F. P., Groves D. I. and Cawood P. A. (2009) Metallogeny of accretionary orogens - The connection between lithospheric processes and metal endowment. *Ore Geol. Rev.* **36**, 282–292. Available at: http://dx.doi.org/10.1016/j.oregeorev.2009.04.002.

Bird D. K., Brooks C. K., Gannicott R. A. and Turner P. A. (1991) A gold-bearing horizon in the Skaergaard Intrusion, East Greenland. *Econ. Geol.* **86**, 1083–1092.

Birke M., Rauch U., Stummeyer J., Lorenz H. and Keilert B. (2017) A review of platinum group element (PGE) geochemistry and a study of the changes of PGE contents in the topsoil of Berlin, Germany, between 1992 and 2013. *J. Geochemical Explor.* **187**, 72–96.

Blanks D., Holwell D. A., Fiorentini M. L., Moroni M., Giuliani A., Tassara S., González-Jiménez J. M., Boyce A. & Ferrari E. (2020) Fluxing of mantle carbon as a physical agent for metallogenic fertilization of the crust. *Nature Comm.* **11**, 4342, 1-11.

Bockrath C., Ballhaus C. and Holzheid A. (2004) Fractionation of the platinum-group elements during mantle melting. *Science.* **305**, 1951–1953.

Bohrson W. A. and Reid M. R. (1995) Petrogenesis of alkaline basalts from Socorro Island , ocean ocean and abundances Tectonic Setting and Geologic History. *J. Geophys. Res.* **100**, 555–576.

Borisov A., Palme H. and Spettel B. (1994) Solubility of palladium in silicate melts: Implications for core formation in the Earth. *Geochim. Cosmochim. Acta* **58**, 705–716.

Boschi L., Becker T. W. and Steinberger B. (2007) Mantle plumes: Dynamic models and seismic images. *Geochemistry, Geophys. Geosystems* **8**, 1–20.

Bowen N. L. (1979) *The Evolution of Igneous Rocks: Fiftieth Anniversary Perspectives*. ed. H. S. Yoder, Princeton University Press.

Brandon A. D., Norman M. D., Walker R. J. and Morgan J. W. (1999) 186Os-187Os systematics of Hawaiian picrites. *Earth Planet. Sci. Lett.* **174**, 25–42.

Brandon A. D. and Walker R. J. (2005) The debate over core-mantle interaction. *Earth Planet. Sci. Lett.* **232**, 211–225.

Brandon A. D., Walker R. J., Morgan J. W., Norman M. D. and Prichard H. M. (1998) Coupled 186Os and 187Os Evidence for Core-Mantle Interaction. *Science (80-.).* **280**, 1570–1573.

Brenan J. M. and Andrews D. (2001) High-temperature stability of laurite and Ru-Os-Ir alloy and their role in PGE fractionation in mafic magmas: Erratum. *Can. Mineral.* **39**, 341–360.

Brenan J. M., Bennett N. R. and Zajacz Z. (2016) Experimental results on fractionation of the highly siderophile elements (HSE) at variable pressures and temperatures during planetary and magmatic differentiation. *Rev. Mineral. Geochemistry* **81**, 1–87.

Brenan J. M. and McDonough W. F. (2009) Core formation and metal-silicate fractionation of osmium and iridium from gold. *Nat. Geosci.* **2**, 798–801.

Brenan J. M., McDonough W. F. and Dalpé C. (2003) Experimental constraints on the partitioning of rhenium and some platinum-group elements between olivine and silicate melt. *Earth Planet. Sci. Lett.* **212**, 135–150.

ten Brink U. (1991) Volcano spacing and plate rigidity. *Geology* **19**, 397–400.

Brovchenko V. D., Sluzhenikin S. F., Kovalchuk, E. V., Kovrigina S. V., Abramova V. D. and Yudovskaya M. A. (2020) Platinum-Group Element Enrichment of Natural Quenched Sulfide Solid Solutions, the Noril'sk 1 Depsoit, Russia. *Economic Geology* **115** (6), 1343-1361.

Bryan S. E., Martí J. and Leosson M. (2002) Petrology and geochemistry of the Bandas des Sur Formation, Las Cañadas Edifice, Tenerife (Canary Islands). *J. Petrol.* **43**, 1815–1856.

Buccianti A. and Grunsky E. C. (2014) Compositional data analysis in geochemistry: Are we sure to see what really occurs during natural processes? *J. Geochemical Explor.* **141**, 1–5.

Burke K., Steinberger B., Torsvik T. H. and Smethurst M. A. (2008) Plume Generation Zones at the margins of Large Low Shear Velocity Provinces on the core-mantle boundary. *Earth Planet. Sci. Lett.* **265**, 49–60.

Bushkovskyi O. (2020) Unsupervised Machine Learning Blog. *App Solut.* Available at: https://theappsolutions.com/blog/development/unsupervised-machine-learning/ [Accessed March 1, 2021].

Butcher A. R., Pirrie D., Prichard H. M. and Fisher P. C. (1999) Platinum-group mineralization in the Rum layered intrusion, Scottish Hebrides, UK. *J. Geol. Soc. London.* **156**, 213–216. Available at: http://jgs.lyellcollection.org/cgi/doi/10.1144/gsjgs.156.2.0213.

Cagney N., Crameri F., Newsome W. H., Lithgow-Bertelloni C., Cotel A., Hart S. R. and Whitehead J. A. (2016) Constraining the source of mantle plumes. *Earth Planet. Sci. Lett.* **435**, 55–63.

Camboa L. A. P. and Rabinowitz P. D. (1984) The evolution of the Rio Grande Rise in the southwest Atlantic Ocean. *Mar. Geol.* **58**, 35–58.

Campbell I. H. and Griffiths R. W. (1990) Implications of mantle plume structure for the evolution of flood basalts. *Earth Planet. Sci. Lett.* **99**, 79–93.

Campbell I. H. and Naldrett A. J. (1979) The influence of silicate:sulfide ratios on the geochemistry of magmatic sulfides. *Econ. Geol.* **74**, 1503–1506.

Cantagrel J. M., Arnaud N. O., Ancochea E., Fúster J. M. and Huertas M. J. (1999) Repeated debris avalanches on Tenerife and genesis of Las Cañadas caldera wall (Canary Islands). *Geology* **27**, 739.

Cantagrel J. M., Cendrero A., Fuster J. M., Ibarrola E. and Jamond C. (1984) K-Ar chronology of the volcanic eruptions in the Canarian archipelago: Island of La Gomera. *Bull. Volcanol.* **47**, 597–609.

Cantagrel J. M., Fuster J. M., Pin C., Renaud U. and Ibarrola E. (1993) Age miocène inférieur des carbonatites de Fuerteventura (23 Ma : U-Pb zircon) et le magmatisme précoce d'une île océanique (îles Canaries). *Comptes Rendues l'Academie des Sci. Paris* **316**, 1147–1153.

Capobianco C. J. and Drake M. J. (1990) Partitioning of ruthenium, rhodium, and palladium between spinel and silicate melt and implications for platinum group element fractionation trends. *Geochim. Cosmochim. Acta* **54**, 869–874.

Carlson R. W., Araujo A. L. N., Junqueira-Brod T. C., Gaspar J. C., Brod J. A.,

Petrinovic I. A., Hollanda M. H. B. M., Pimentel M. M. and Sichel S. (2007) Chemical and isotopic relationships between peridotite xenoliths and mafic-ultrapotassic rocks from Southern Brazil. *Chem. Geol.* **242**, 415–434.

Carracedo J. C. (1994) The Canary Islands : an example of structural control on the growth of large oceanic-island volcanoes. *J. Vis. Exp.* **60**, 225–241.

Carracedo J. C., Badiola E. R., Guillou H., Paterne M., Scaillet S., Perez-Torrado, F.J. Paris R., Fra-Paleo U. and Hansen A. (2007) Eruptive and structural history of Teide Volcano and rift zones of Tenerife, Canary Islands. *Geol. Soc. Am. Bull.* **119**, 1027–1051.

Carracedo J. C., Day S., Guillou H., Rodríguez Badiola E., Canas J. A. and Pérez Torrado F. J. (1998) Hotspot volcanism close to a passive continental margin: the Canary Islands. *Geol. Mag.* **135**, 591–604.

Carracedo J. C., Pérez F. J., Ancochea E., J. M., Hernán F., Cubas C. R., Casillas R., Rodriguez E. and Ahijado A. (2002) Cenozoic volcanism II: The Canary Islands. In *The Geology of Spain* (eds. W. Gibbons and T. Moreno). Geological Society of London Special Publications. pp. 439–472.

Chang W. C. (1983) On Using Principal Components Before Separating a Mixture of Two Multivariate Normal Distributions. *Appl. Stat.* **32**, 267–275.

Chassé M., Griffin W. L., Alard O., O'Reilly S. Y. and Calas G. (2018) Insights into the mantle geochemistry of scandium from a meta-analysis of garnet data. *Lithos* **310**–**311**, 409–421. Available at: https://doi.org/10.1016/j.lithos.2018.03.026.

Chauvel C., Hofmann A. W. and Vidal P. (1992) HIMU-EM: The French Polynesian connection. *Earth Planet. Sci. Lett.* **110**, 99–119.

Chauvel C., Maury R. C., Blais S., Lewin E., Guillou H., Rossi P. and Gutscher M.-A. (2012) The size of plume heterogeneities constrained by Marquesas isotopic stripes. *Geochemistry Int.* **13**, 1–23.

Chayes F. (1960) On Correlation between Variables of Constant Sum, *Journal of Geophysical Research* **65** (12), 4185–4193.

Chazey W. J. and Neal C. R. (2004) Large igneous province magma petrogenesis from source to surface: platinum-group element evidence from Ontong Java Plateau basalts recovered during ODP Legs 130 and 192. *Geol. Soc. London, Spec. Publ.* **229**, 219–238.

Chazey W. J. and Neal C. R. (2005) Platinum-group element constraints on source composition and magma evolution of the Kerguelen Plateau using basalts from ODP Leg 183. *Geochim. Cosmochim. Acta* **69**, 4685–4701.

Ching T., Himmelstein D. S., Beaulieu-Jones B. K., Kalinin A. A., Do B. T., Way G. P., Ferrero E., Agapow P. M., Zietz M., Hoffman M. M., Xie W., Rosen G. L., Lengerich B. J., Israeli J., Lanchantin J., Woloszynek S., Carpenter A. E., Shrikumar A., Xu J., Cofer E. M., Lavender C. A., Turaga S. C., Alexandari A. M., Lu Z., Harris D. J., DeCaprio D., Qi Y., Kundaje A., Peng Y., Wiley L. K., Segler M. H. S., Boca S. M., Swamidass S. J., Huang A., Gitter A. and Greene C. S. (2018) Opportunities and obstacles for deep learning in biology and medicine. *J. R. Soc. Interface* **15**, 1–47.

Choi E., Fiorentini M. L., Hughes H. S. R. and Giuliani A. (2020) Platinum-group element and Au geochemistry of Late Archean to Proterozoic calc-alkaline and alkaline magmas in the Yilgarn Craton, Western Australia. *Lithos* **374**–**375**, 105716. Available at: https://doi.org/10.1016/j.lithos.2020.105716.

Christensen U. R. and Hofmann A. W. (1994) Segregation of subducted oceanic crust in the convecting mantle. *J. Geophys. Res. Solid Earth* **99**, 19867–19884.

Clare A. P. and Cohen D. R. (2001) A comparison of unsupervised neural networks and k-means clustering in the analysis of multi-element stream sediment data. *Geochemistry Explor. Environ. Anal.* **1**, 119–134.

Coffin M. F. and Eldholm O. (1994) Large igneous provinces: Crustal structure, dimensions, and external consequences. *Rev. Geophys.* **32**, 1–36.

Comin-Chiaramonti P., Marzoli A., de Barros Gomes C., Milan A., Riccomini C., Velázquez V. F., Mantovani M. M. S., Renne P., Tassinari C. C. and Vasconcelos P. M. (2007) The origin of post-Paleozoic magmatism in eastern Paraguay. In *Plates, Plumes and Planetary Processes* (eds. Foulger G. R. and Jurdy D. M.). Geological Society of America Publications 430.

Cone K. A., Palin R. M. and Singha K. (2020) Unsupervised machine learning with petrological database ApolloBasaltDB reveals complexity in lunar basalt major element oxide and mineral distribution patterns. *Icarus*. Available at: https://linkinghub.elsevier.com/retrieve/pii/S0019103520301731.

Cordani U. G. and Vandoros P. (1967) Basaltic Rocks of the Paraná Basin. In *Problems in Brazilian Gondwana Geology* (eds. J. J. Bigarella, R. D. Becker, and J. D. Pinto). pp. 207–231.

Cottrell E. and Walker D. (2006) Constraints on core formation from Pt partitioning in mafic silicate liquids at high temperatures. *Geochim. Cosmochim. Acta* **70**, 1565–1580.

Courtillot V., Davaille A., Besse J. and Stock J. (2003) Three distinct types of hotspots in the Earth's mantle. *Earth Planet. Sci. Lett.* **205**, 295–308.

Cox K. G., Bell J. D. and Pankhurst R. J. (1979) The interpretation of igneous rocks. *George, Allen and Ulwin*, London.

Cracknell M. J. (2014) Machine Learning for Geological Mapping: Algorithms and Applications. *University of Tasmania*, 1–275.

Cracknell M. J. and de Caritat, P. (2017) Catchment-based gold prospectivity analysis combining geochemical, geophysical and geological data across northern Australia. *Geochemistry: Exploration, Environment, Analysis*. **17** (3), 204-216.

Creaser R. A., Papanastassiou D. A. and Wasserburg G. J. (1991) Negative thermal ion mass spectrometry of osmium, rhenium, and iridium. *Geochim. Cosmochim. Acta* **55**, 397–401.

Crocket J. H. (2002a) Platinum-group element geochemistry of mafic and ultramafic rocks. *Geol. geochemistry, Mineral. Miner. Benef. Platinum-gr.*

Elem. Can. Inst. Mining, Metall. Pet. **Special Vo**, 177–210.

Crocket J. H. (2002b) Platinum-group elements in basalts from Maui, Hawai'i: Low abundances in Alkali basalts. *Can. Mineral.* **40**, 595–609.

Danielson L. R., Sharp T. G. and Hervig R. L. (2005) Implications for core formation of the Earth from high pressure-temperature Au partitioning experiments. In *Lunar and Planetary Science Conference XXXVI, 1955* pp. 12–13.

Davidson J., Turner S. and Plank T. (2013) Dy/Dy*: Variations arising from mantle sources and petrogenetic processes. *J. Petrol.* **54**, 525–537.

Davies D. L. and Bouldin D. W. (1979) A Cluster Separation Measure. *IEEE Trans. Pattern Anal. Mach. Intell.* **PAMI**-**1**, 224–227.

Davies D. R. and Davies J. H. (2009) *Mantle Convection at Earth-like Vigor : Thermal Plumes Reconcile Hot–spot Observations*. School of Earth and Ocean Sciences, Cardiff University, pp. 7.

Davies G. (1993) Cooling the core and mantle by plume and plate flows. *Geophys. J. Int.* **115**, 132–146.

Davis J. C. (2002) *Statistics and Data Analysis in Geology*. 3rd ed., John Wiley & Sons Inc.

Day J. M. D. (2013) Hotspot volcanism and highly siderophile elements. *Chem. Geol.* **341**, 50–74.

Day J. M. D. and Hilton D. R. (2011) Origin of 3He/4He ratios in HIMU-type basalts constrained from Canary Island lavas. *Earth Planet. Sci. Lett.* **305**, 226–234.

Day J. M. D. and Hilton D. R. (2020) Heterogeneous mantle-derived helium isotopes in the Canary Islands and other ocean islands. *Geology* **49**, 120–124.

Day J. M. D., Pearson D. G. and Hulbert L. J. (2013) Highly siderophile element behaviour during flood basalt genesis and evidence for melts from intrusive chromitite formation in the Mackenzie large igneous province. *Lithos* **182**–**183**, 242–258.

Day J. M. D., Pearson D. G., Macpherson C. G., Lowry D. and Carracedo J. C. (2010) Evidence for distinct proportions of subducted oceanic crust and lithosphere in HIMU-type mantle beneath El Hierro and La Palma, Canary Islands. *Geochim. Cosmochim. Acta* **74**, 6565–6589.

Dayan P. and Niv Y. (2008) Reinforcement learning: The Good, The Bad and The Ugly. *Curr. Opin. Neurobiol.* **18**, 185–196.

DeFelice C., Mallick S., Saal A. E. and Huang S. (2019) An isotopically depleted lower mantle component is intrinsic to the Hawaiian mantle plume. *Nat. Geosci.* **12**.

Delpech G., Lorand J. P., Grégoire M., Cottin J. Y. and O'Reilly S. Y. (2012) In-situ geochemistry of sulfides in highly metasomatized mantle xenoliths from Kerguelen, southern Indian Ocean. *Lithos* **154**, 296–314. Available at:

http://dx.doi.org/10.1016/j.lithos.2012.07.018.

DePaolo D. J., Linn A. M. and Schubert G. (1991) The continental crustal age distribution: Methods of determining mantle separation ages from Sm–Nd isotopic data and application to the southwestern United States. *J. Geophys. Res.* **96**, 2071–2088.

DePaolo D. J. and Manga M. (2003) Deep origin of hotspots -The mantle plume model. *Science (80-.).* **300**, 920–921.

DePaolo D. J. and Wasserburg G. J. (1976) Nd isotopic variations and petrogenetic models. *Geophys. Res. Lett.* **3**, 249–252.

Deschamps F., Kaminski E. and Tackley P. J. (2011) A deep mantle origin for the primitive signature of ocean island basalt. *Nat. Geosci.* **4**, 879–882. Available at: http://dx.doi.org/10.1038/ngeo1295.

Dominy S. C., Platten I. M. and Raine M. D. (2003) Grade and geological continuity in high-nugget effect gold-quartz reefs: Implications for resource estimation and reporting. *Trans. Inst. Min. Metall. Sect. B Appl. Earth Sci.* **112**, 239–259.

Douglass J., Schilling J. G. and Fontignie D. (1999) Plume-ridge interactions of the Discovery and Shona mantle plumes with the southern Mid-Atlantic Ridge (40°-55° S). *J. Geophys. Res. Solid Earth* **104**, 2941–2962.

Downes H. (2001) Formation and modification of the shallow sub-continental lithospheric mantle: A review of geochemical evidence from ultramatic xenolith suites and tectonically emplaced ultramafic massifs of Western and Central Europe. *J. Petrol.* **42**, 233–250.

Drake M. and Righter K. (2002) Determining the composition of the Earth. *Nature* **416**, 39–44.

Driscoll B. O. (2016) Petrogenesis of the Platinum-Group Minerals. *Rev. Mineral. Geochemistry* **81**, 489–578.

Duggen S., Hoernle K. A., Hauff F., Kluegel A., Bouabdellah M. and Thirlwall M. F. (2009) Flow of Canary mantle plume material through a subcontinental lithospheric corridor beneath Africa to the Mediterranean. *Geology* **37**, 283–286.

Duncombe J. (2019) The Unsolved Mystery of the Earth Blobs. *Eos (Washington. DC).* Available at: https://eos.org/features/the-unsolved-mystery-of-the-earth-blobs?utm_source=eos&utm_medium=email&utm_campaign=EosBuzz030119 [Accessed March 1, 2019].

Duque A., González K., Pérez N., Benitez D., Grijalva F., Lara-Cueva R. and Ruiz M. (2020) Exploring the unsupervised classification of seismic events of Cotopaxi volcano. *J. Volcanol. Geotherm. Res.* **403**, 107009.

Dziewonski A. M., Lekic V. and Romanowicz B. A. (2010) Mantle Anchor Structure: An argument for bottom up tectonics. *Earth Planet. Sci. Lett.* **299**, 69–79.

Eldholm O. and Grue K. (1994) North Atlantic volcanic margins : Dimensions and production rates a volume of flood basalts a mean eruption rate of the basalts were emplaced within volume in a mean crustal accretion rate. *J. Geophys. Res.* **99**, 2955–2968.

Ellam R. M. (1992) Lithospheric thickness as a control on basalt geochemistry. *Geology* **20**, 153–156.

Ellam R. M. and Stuart F. M. (2000) The sub-lithospheric source of North Atlantic basalts: Evidence for, and significance of, a common end-member. *J. Petrol.* **41**, 919–932.

Ely J. C. and Neal C. R. (2003) Using platinum-group elements to investigate the origin of the Ontong Java Plateau, SW Pacific. *Chem. Geol.* **196**, 235–257.

Erlank A. J., Marsh J. S., Duncan A. R., Miller R. M., Hawkesworth C. J., Betton P. J. and Rex D. C. (1984) Geochemistry and petrogenesis of the Etendeka volcanic rocks from South West Africa/Namibia. *Geol. Soc. South African Spec. Publ.* **13**, 195–246.

Ernst R. E. and Peck, D. C. (2010) Using Large Igneous Provinces for Mineral Exploration (e.g., for Ni-Cu-PGE Deposits). *11th International Platinum Symposium June 21-24 2010.*

Esser B. K. and Turekian K. K. (1993) The osmium isotopic composition of the continental-crust. *Geochim. Cosmochim. Acta* **57**, 3093–3104.

European Commission. (2020a) Critical Raw Materials Factsheets. *Eur. Comm.* Available at: https://ec.europa.eu/growth/sectors/raw-materials/specific-interest/critical_en [Accessed February 28, 2021].

European Commission (2020b) Critical Raw Materials Resilience: Charting a Path towards greater Security and Sustainability. *Eur. Comm.* Available at: https://eur-lex.europa.eu/legal-content/EN/TXT/PDF/?uri=CELEX:52020DC0474&from=EN [Accessed February 28, 2021].

Ewart A. (2004) Petrology and Geochemistry of Early Cretaceous Bimodal Continental Flood Volcanism of the NW Etendeka, Namibia. Part 1: Introduction, Mafic Lavas and Re-evaluation of Mantle Source Components. *J. Petrol.* **45**, 59–105. Available at: https://academic.oup.com/petrology/article-lookup/doi/10.1093/petrology/egg083.

Ewart A., Milner S. C., Armstrong R. A. and Duncan A. R. (1998a) Etendeka volcanism of the Goboboseb Mountains and Messum Igneous Complex, Namibia. Part I: Geochemical evidence of early Cretaceous Tristan plume melts and the role of crustal contamination in the Paraná-Etendeka CFB. *J. Petrol.* **39**, 191–225.

Ewart A., Milner S. C., Armstrong R. A. and Duncan A. R. (1998b) Etendeka volcanism of the Goboboseb Mountains and Messum Igneous Complex, Namibia. Part II: Voluminous quartz latite volcanism of the Awahab magma system. *J. Petrol.* **39**, 227–253.

de Farias J. S. and Filho C. F. F. (2021) Ultramafic intrusions hosting Ni–Cu

sulfide mineralization along a suture zone in the southwestern margin of the Amazonian craton, Brazil: Examples from Morro Sem Boné, Morro do Leme and their satellite intrusions. *J. of S. American Earth Sci.* **108**, 103240.

Farnham I. M., Singh A. K., Stetzenbach K. J. and Johannesson K. H. (2002) Treatment of nondetects in multivariate analysis of groundwater geochemistry data. *Chemom. Intell. Lab. Syst.* **60**, 265–281.

FCH (2017) Fuel Cells and Hydrogen Technology: Europe's Journey to a Greener World. 10th Stakeholder Forum. In *Fuel Cell and Hydrogen Joint Undertaking*

FCHEA (2018) Fuel Cell Basics. *Fuel Cell Hydrog. Energy Assoc.* Available at: http://www.fchea.org/ [Accessed February 28, 2021].

Fernandez V. (2017) Some facts on the platinum-group elements. *Int. Rev. Financ. Anal.* **52**, 333–347.

Fiorentini M. L., Barnes S. J., Lesher M., Heggie G. J., Keays R. R., and Burnham O. M. (2010) Platinum Group Element Geochemistry of Mineralized and Nonmineralized Komatiites and Basalts. *Econ. Geo.* **105**, 795–823.

Fiorentini M. L., Barnes S. J., Maier M. D., Burnham O. M. and Heggie G. (2011) Global Variability in the Platinum-group Element Contents of Komatiites. *J. Petrology* **52**, 83–112.

Fiorentini M. L., LaFlamme C., Denyszyna S., Moleb D., Maasc R., Locmelis M., Carusoa S. and Buie T. (2018) Post-collisional alkaline magmatism as gateway for metal and sulfur enrichment of the continental lower crust. *Geochim. Cosmochim. Acta* **223**, 175-197.

Fiorentini M. L., O'Neill C., Giuliani A., Choi E., Maas R., Pirajno F. and Foley S. (2020) Bushveld superplume drove Proterozoic magmatism and metallogenesis in Australia. *Sci. Reports* **10**, 19729.

Fitton J., Saunders A., Norry M., Hardarson B. and Taylor R. (1997) Thermal and chemical structure of the Iceland plume. *Earth Planet. Sci. Lett. Planet. Sci. Lett.* **153**, 197–208.

Fleet M. E., Crocket J. H., Liu M. and Stone W. E. (1999) Laboratory partitioning of platinum-group elements (PGE) and gold with application to magmatic sulfide-PGE deposits. *Lithos* **47**, 127–142.

Fleet M. E., Crocket J. H. and Stone W. E. (1996) Partitioning of platinum-group elements (Os, Ir, Ru, Pt, Pd) and gold between sulfide liquid and basalt melt. *Geochim. Cosmochim. Acta* **60**, 2397–2412.

Fodor R. V. (1987) Low- and high-TiO2 flood basalts of southern Brazil: origin from picritic parentage and a common mantle source. *Earth Planet. Sci. Lett.* **84**, 423–430. Available at: https://linkinghub.elsevier.com/retrieve/pii/0012821X87900070.

Fodor R. V., McKee E. H. and Roisenberg A. (1989) Age distribution of Serra Geral (Paraná) flood basalts, southern Brazil. *J. South Am. Earth Sci.* **2**, 343–349.

Fodor R. V., Sial A. N. and Gandhok G. (2002) Petrology of spinel peridotite xenoliths from northeastern Brazil: Lithosphere with a high geothermal gradient imparted by Fernando de Noronha plume. *J. South Am. Earth Sci.* **15**, 199–214.

Fodor R. V. and Vetter S. K. (1984) Rift-zone magmatism: Petrology of basaltic rocks transitional from CFB to MORB, southeastern Brazil margin. *Contrib. to Mineral. Petrol.* **88**, 307–321.

Foulger G. R., Natland J. H. and Anderson D. L. (2005) A source for Icelandic magmas in remelted Iapetus crust. *J. Volcanol. Geotherm. Res.* **141**, 23–44. Available at: https://linkinghub.elsevier.com/retrieve/pii/S0377027304003312.

Foulger G. R., Pritchard M. J., Julian B. R., Evans J. R., Allen R. M., Nolet G., Morgan W. J., Bergsson B. H., Erlendsson P., Jakobsdottir S., Ragnarsson S., Stefansson R. and Vogfjord K. (2000) The seismic anomaly beneath Iceland extends down to the mantle transition zone and no deeper. *Geophys. J. Int.* **142**, 1–5.

French S. W. and Romanowicz B. (2015) Broad plumes rooted at the base of the Earth's mantle beneath major hotspots. *Nature* **525**, 95–99.

Fretzdorff S., Haase K. M. and Garbe-Schönberg C.-D. (1996) Petrogenesis of lavas from the Umu Volcanic Field in the young Hotspot Region west of Easter Island, southeastern Pacific. *Lithos* **38**, 23–40.

Fromm T., Jokat W. and Behrmann J. H. (2017) Interaction between a hotspot and a fracture zone: The crustal structure of Walvis Ridge at 6° E. *Tectonophysics* **716**, 108–120. Available at: http://dx.doi.org/10.1016/j.tecto.2017.03.001.

Fromm T., Planert L., Jokat W., Ryberg T., Behrmann J. H., Weber M. H. and Haberland C. (2015) South Atlantic opening: A plume-induced breakup? *Geology* **43**, 931–935.

Fullea J., Camacho A. G., Negredo A. M. and Fernández J. (2015) The Canary Islands hot spot: New insights from 3D coupled geophysical-petrological modelling of the lithosphere and uppermost mantle. *Earth Planet. Sci. Lett.* **409**, 71–88.

Gale A., Dalton C. A., Langmuir C. H., Su Y. and Schilling J. G. (2013) The mean composition of ocean ridge basalts. *Geochemistry, Geophys. Geosystems* **14**, 489–518.

Gallagher, K. and Hawkesworth C. J. (1994) Mantle plumes, continental magmatism and asymmetry in the South Atlantic. *Earth and Planetary Science Letters*. **123**, 105-117.

Garland F., Hawkesworth C. J. and Mantovani M. S. M. (1995) Description and Petrogenesis of the Paraná Rhyolites, Southern Brazil. *J. Petrol.* **36**, 1193–1227.

Garnero E. J. and McNamara A. K. (2008) Structure and dynamics of earth's lower mantle. *Science (80-.).* **320**, 626–628.

Geyer A. and Martí J. (2010) The distribution of basaltic volcanism on Tenerife, Canary Islands: Implications on the origin and dynamics of the rift systems. *Tectonophysics* **483**, 310–326.

Ghannadpour S., Hezarkhani A. and Farahbakhsh E. (2013) An Investigation of Pb Geochemical Behavior Respect to Those of Fe and Zn Based on k-Means Clustering Method. *J. Tethys* **1**, 291–302.

Gibson S. A., Thompson R. N. and Day J. A. (2006) Timescales and mechanisms of plume-lithosphere interactions: 40Ar/39Ar geochronology and geochemistry of alkaline igneous rocks from the Paraná-Etendeka large igneous province. *Earth Planet. Sci. Lett.* **251**, 1–17.

Gibson S. A., Thompson R. N., Day J. A., Humphris S. E. and Dickin A. P. (2005) Melt-generation processes associated with the Tristan mantle plume: Constraints on the origin of EM-1. *Earth Planet. Sci. Lett.* **237**, 744–767.

Gibson S. A., Thompson R. N., Dickin A. P. and Leonardos O. H. (1995) High-Ti and low-Ti mafic potassic magmas: Key to plume-lithosphere interactions and continental flood-basalt genesis. *Earth Planet. Sci. Lett.* **136**, 149–165.

Gibson S. A., Thompson R. N., Leonardos O. H., Dickin A. P. and Mitchell J. G. (1999) The limited extent of plume-lithosphere interactions during continental flood-basalt genesis: Geochemical evidence from Cretaceous magmatism in southern Brazil. *Contrib. to Mineral. Petrol.* **137**, 147–169.

Godel B., Barnes S. J. and Maier W. D. (2007) Platinum-group elements in sulphide minerals, platinum-group minerals, and whole-rocks of the Merensky Reef (Bushveld Complex, South Africa): Implications for the formation of the reef. *J. Petrol.* **48**, 1569–1604.

Godel B. and Barnes S. J. (2008) Platinum-group elements in sulfide minerals and the whole rocks of the J-M Reef (Stillwater Complex): Implication for the formation of the reef. *Chem. Geol.* **248**, 272-294.

Goldschmidt V. M. (1937) The principles of distribution of chemical elements in minerals and rocks. *J Chem Soc* **7th Hugo M**, 655–673.

Gomes A. S., Licht O. A. B., Vasconcellos E. M. G. and Soares J. S. (2018) Chemostratigraphy and evolution of the Paraná Igneous Province volcanism in the central portion of the state of Paraná Southern Brazil. *J. Volcanol. Geotherm. Res.* **355**, 253–269. Available at: https://doi.org/10.1016/j.jvolgeores.2017.09.002.

González-Jiménez J. M., Mondal S. K., Ghosh B., Griffin W. L. and O'Reilly S. Y. (2020) Re-Os Isotope Systematics of Sulfides in Chromitites and Host Lherzolites of the Andaman Ophiolite, India. *Minerals* **10**, 1–21.

Gordon J. M. (1947) Classification of the Gondwanic Rocks of Paraná, Santa Catarina and Rio Grande do Sul. Rio de. *Dept. Nac. Prod. Min., Div. Geol. e Min., Notas Prelim.* **no. 38a**, 1–19.

Graça M. C., Kusznir N. and Gomes Stanton N. S. (2019) Crustal thickness mapping of the central South Atlantic and the geodynamic development of the Rio Grande Rise and Walvis Ridge. *Mar. Pet. Geol.* **101**, 230–242.

Available at: https://doi.org/10.1016/j.marpetgeo.2018.12.011.

Griffin W. L., Begg G. C. and O'Reilly S. Y. (2013) Continental-root control on the genesis of magmatic ore deposits. *Nat. Geosci.* **6**, 905–910. Available at: http://dx.doi.org/10.1038/ngeo1954.

Griffiths R. W. and Campbell I. H. (1990) Stirring and structure in mantle starting plumes. *Earth Planet. Sci. Lett.* **99**, 66–78.

Guillou H., Carracedo J. C., Paris R. and Torrado F. J. P. (2004) Implications for the early shield-stage evolution of Tenerife from K/Ar ages and magnetic stratigraphy. *Earth Planet. Sci. Lett.* **222**, 599–614.

Gunn G., Benham A. and Minks A. (2009) Minerals profile: Platinum. *Br. Geol. Surv.*, 1–32. Available at: http://www.MineralsUK.com.

Günther T., Haase K. M., Klemd R. and Teschner C. (2018) Mantle sources and magma evolution of the Rooiberg lavas, Bushveld Large Igneous Province, South Africa. *Contrib. to Mineral. Petrol.* **173**.

Gurenko A. A., Hoernle K. A., Miura Y. N., Schmincke H.-U., Kaneoka I., Hauff F. and Han D. (2006) Major, trace element and Nd–Sr–Pb–O–He–Ar isotope signatures of shield stage lavas from the central and western Canary Islands: Insights into mantle and crustal processes. *Chem. Geol.* **233**, 75–112.

Gurenko A. A., Hoernle K. A., Sobolev A. V., Schmincke H.-U. U., Hauff F., Hoernle K. A., Hauff F. and Schmincke H.-U. U. (2009) Enriched, HIMU-type peridotite and depleted recycled pyroxenite in the Canary plume: A mixed-up mantle. *Earth Planet. Sci. Lett.* **277**, 514–524.

Hamlyn P. R. and Keays R. R. (1986) Sulfur saturation and second-stage melts: application to the Bushveld platinum metal deposits. *Econ. Geol.* **81**, 1431–1445.

Hamlyn P. R., Keays R. R., Cameron W. E., Crawford A. J. and Waldron H. M. (1985) Precious metals in magnesian low-Ti lavas: Implications for metallogenesis and sulfur saturation in primary magmas. *Geochim. Cosmochim. Acta* **49**, 1797–1811.

Hanano D., Weis D., Scoates J. S., Aciego S. and DePaolo D. J. (2010) Horizontal and vertical zoning of heterogeneities in the Hawaiian mantle plume from the geochemistry of consecutive postshield volcano pairs: Kohala-Mahukona and Mauna Kea-Hualalai. *Geochemistry, Geophys. Geosystems* **11**, 1–23.

Handler M. R. and Bennett V. C. (1999) Behaviour of Platinum-group elements in the subcontinental mantle of eastern Australia during variable metasomatism and melt depletion. *Geochim. Cosmochim. Acta* **63**, 3597–3618.

Harpp K. S. and Geist D. J. (2018) The evolution of galápagos volcanoes: An alternative perspective. *Front. Earth Sci.* **6**, 1–16.

Harris C. R., Millman K. J., van der Walt S. J., Gommers R., Virtanen P., Cournapeau D., Wieser E., Taylor J., Berg S., Smith N. J., Kern R., Picus M., Hoyer S., van Kerkwijk M. H., Brett M., Haldane A., del Río J. F., Wiebe

M., Peterson P., Gérard-Marchant P., Sheppard K., Reddy T., Weckesser W., Abbasi H., Gohlke C. and Oliphant T. E. (2020) Array programming with NumPy. *Nature* **585**, 357–362. Available at: http://dx.doi.org/10.1038/s41586-020-2649-2.

Harrison L. N., Weis D. and Garcia M. O. (2017) The link between Hawaiian mantle plume composition, magmatic flux, and deep mantle geodynamics. *Earth Planet. Sci. Lett.* **463**, 298–309.

Harrison L. N., Weis D. and Garcia M. O. (2020) The multiple depleted mantle components in the Hawaiian-Emperor chain. *Chem. Geol.* **532**, 119324.

Hart S. R., E.H H., J.A O. and J.A W. (1992) Mantle Plumes and Entrainment: Isotopic Evidence. *Science (80-.).* **256**, 517–520.

Hartmann, L. A., Baggio, S. B., Brückmann, M. P., Knijnik, D. B., Lana, C., Massonne, H-J., Opitz, J., Pinto, V. M., Sato, K., Tassinari, C. C. G. and Arena, K. R. (2019) U-Pb Geochronology of Paraná Volcanics Combined with Trace Element Geochemistry of the Zircon Crystals and Zircon Hf Isotope Data. *Journal of South American Earth Sciences*, **89**, 219–26. Available at: https://doi.org/10.1016/j.jsames.2018.11.026

Hassan R., Flament N., Gurnis M., Bower D. J. and Muller D. (2015) Provenance of plumes in global convection models. *Geochemistry Geophys. Geosystems* **18**, 1465–1489.

Hastie A. R., Fitton J. G., Bromiley G. D., Butler I. B. and Odling N. W. A. (2016) The origin of Earth's first continents and the onset of plate tectonics. *Geology* **44**, 855–858.

Hastie A. R., Fitton J. G., Kerr A. C., McDonald I., Schwindrofska A. and Hoernle K. (2016) The composition of mantle plumes and the deep Earth. *Earth Planet. Sci. Lett.* **444**, 13–25.

Hastie T., Tibshirani R. and Friedman J. (2009) *The Elements of Statistical Learning: Data Mining, Inference, and Prediction*. 2nd ed., Springer.

Hauri E. H. and Hart S. R. (1997) Rhenium abundances and systematics in oceanic basalts. *Chem. Geol.* **139**, 185–205.

Hawkesworth C., Mantovani M. and Peate D. (1988) Lithosphere remobilization during Paraná CFB magmatism. *J. Petrol.* **Special Issue**, 205–223.

Hawkesworth C. and Scherstén A. (2007) Mantle plumes and geochemistry. *Chem. Geol.* **241**, 319–331.

Hayes B., Bédard J. H., Hryciuk M., Wing B., Nabelek P., Macdonald W. D. and Lissenberg C. J. (2015) Sulfide Immiscibility Induced by Wall-Rock Assimilation in a Fault-Guided Basaltic Feeder System, Franklin Large Igneous Province, Victoria Island (Arctic Canada). *Econ. Geol.* **110**, 1697–1717.

Helmy H. M. and Bragagni A. (2017) Platinum-group elements fractionation by selective complexing, the Os, Ir, Ru, Rh-arsenide-sulfide systems above 1020 °C. *Geochim. Cosmochim. Acta* **216**, 169–183. Available at: http://dx.doi.org/10.1016/j.gca.2017.01.040.

Helmy H. M. and Fonseca R. O. C. (2017) The behavior of Pt, Pd, Cu and Ni in the Se-sulfide system between 1050 and 700 ° C and the role of Se in platinum-group elements fractionation in sulfide melts. *Geochim. Cosmochim. Acta*, 0–12. Available at: http://linkinghub.elsevier.com/retrieve/pii/S0016703717302831.

Hernández-Pacheco A. and Ibarrola E. (1973) Geochemical variation trends between the different Canary Islands in relation to their geological position. *Lithos* **6**, 389–402.

Hieronymus C. F. and Bercovici D. (2001) A theoretical model of hotspot volcanism : Control on volcanic spacing and patterns via magma dynamics and lithospheric stresses model Aside from explaining the equidistant spacing of shield senting the lithosphere as a fluid with unrealistically low a co. *Stress Int. J. Biol. Stress* **106**, 683–702.

Hieronymus C. F. and Bercovici D. (1999) Discrete alternating hotspot islands formed by interaction of magma transport and lithospheric flexure. *Nature* **397**, 604–607.

Hill E., Wood B. J. and Blundy J. D. (2000) The effect of Ca-Tschermaks component on trace element partitioning between clinopyroxene and silicate melt. *Lithos* **53**, 203–215.

Hirt B., Tilton G. R., Herr W. and Hoffmeister W. (1963) The Half-Life of 187-Re. In *Earth science and meteorites* (eds. J. Geiss and E. D. Goldberg). North Holland. pp. 273–280.

Hoernle K. (1998) Geochemistry of Jurassic oceanic crust beneath Gran Canaria (Canary Islands): implications for crustal recycling and assimilation. *J. Petrol.* **39**, 859–880.

Hoernle K. and Carracedo J. C. (2009) Canary Islands, Geology. In *Encyclopedia of Islands* pp. 133–143.

Hoernle K., Rohde J., Hauff F., Garbe-Schönberg D., Homrighausen S., Werner R. and Morgan J. P. (2015) How and when plume zonation appeared during the 132 Myr evolution of the Tristan Hotspot. *Nat. Commun.* **6**, 7799.

Hoernle K. and Schmincke H. U. (1993) The role of partial melting in the 15-MA geochemical evolution of gran canaria: A blob model for the Canary hotspot. *J. Petrol.* **34**, 599–626.

Hofmann A. W. (1997) Mantle geochemistry: The message from oceanic volcanism. *Nature* **385**, 218–229.

Hofmann A. W. (2003) Sampling Mantle Heterogeneity through Oceanic Basalts: Isotopes and Trace Elements. In *The Mantle and Core - Treatise on Geochemistry* (ed. R. W. Carlson). Elsevier-Pergamon, Oxford. pp. 61–102.

Hofmann A. W. and Farnetani C. G. (2013) Two views of Hawaiian plume structure. *Geochemistry, Geophys. Geosystems* **14**, 5308–5322.

Hole M. J. and Natland J. H. (2019) Magmatism in the North Atlantic Igneous Province; mantle temperatures, rifting and geodynamics. *Earth-Science*

Rev., 1–24. Available at: https://doi.org/10.1016/j.earscirev.2019.02.011.

Holm P. M. (1988) Nd, Sr and Pb isotope geochemistry of the Lower Lavas, E Greenland Tertiary Igneous Province. *Geol. Soc. Spec. Publ.* **39**, 181–195.

Holwell D. A., Abraham-James T., Keays R. R. and Boyce A. J. (2012) The nature and genesis of marginal Cu-PGE-Au sulphide mineralisation in Paleogene Macrodykes of the Kangerlussuaq region, East Greenland. *Miner. Depos.* **47**, 3–21.

Holwell D. A., Fiorentini M., McDonald I., Lu Y., Giuliani A., Smith D. J., Keith M. and Locmelis M. (2019) A metasomatized lithospheric mantle control on the metallogenic signature of post-subduction magmatism. *Nat. Commun.* **10**, 1–10. Available at: http://dx.doi.org/10.1038/s41467-019-11065-4.

Holwell D. A. and McDonald I. (2010) A Review of the Behaviour of Platinum Group Elements within Natural Magmatic Sulfide Ore Systems. *Platin. Met. Rev.* **54**, 26–36. Available at: http://openurl.ingenta.com/content/xref?genre=article&issn=0032-1400&volume=54&issue=1&spage=26.

Holwell D. A., McDonald I. and Butler I. B. (2011) Precious metal enrichment in the Platreef, Bushveld Complex, South Africa: Evidence from homogenized magmatic sulfide melt inclusions. *Contrib. to Mineral. Petrol.* **161**, 1011–1026.

Holzheid A., Sylvester P., O'Neill H., Rubie D. C. and Palme H. (2000) Evidence for a late chondritic veneer in the Earth´s mantle from high pressure partitioning of palladium and platinum. *Nature* **406**, 396–399.

Homrighausen S., Hoernle K., Hauff F., Wartho J.-A., van den Bogaard P. and Garbe-Schönberg D. (2019) New age and geochemical data from the Walvis Ridge: The temporal and spatial diversity of South Atlantic intraplate volcanism and its possible origin. *Geochim. Cosmochim. Acta* **245**, 16–34. Available at: https://linkinghub.elsevier.com/retrieve/pii/S0016703718305076.

Hopp J. and Trieloff M. (2005) Refining the noble gas record of the Réunion mantle plume source: Implications on mantle geochemistry. *Earth Planet. Sci. Lett.* **240**, 573–588.

Horni J. Á. ., Hopper J. R., Blischke A., Geisler W. H., Stewart M., McDermott K., Judge M., Erlendsson Ö. and Árting U. (2017) Regional distribution of volcanism within the North Atlantic Igneous Province. *Geol. Soc. London, Spec. Publ.* **447**, 105–125. Available at: http://sp.lyellcollection.org/lookup/doi/10.1144/SP447.18.

Horrocks T., Holden E. J., Wedge D., Wijns C. and Fiorentini M. (2019) Geochemical characterisation of rock hydration processes using t-SNE. *Comput. Geosci.* **124**, 46–57. Available at: https://doi.org/10.1016/j.cageo.2018.12.005.

Hotelling H. (1933) Analysis of a complex of statistical variables into principal components. *J. Educ. Psychol.* **25**, 417–441.

Howarth G. H. and Harris C. (2017) Discriminating between pyroxenite and

peridotite sources for continental flood basalts (CFB) in southern Africa using olivine chemistry. *Earth Planet. Sci. Lett.* **475**, 143–151. Available at: http://dx.doi.org/10.1016/j.epsl.2017.07.043.

Howarth R. J. (1983) Statistics and Data Analysis in Geochemical Prospecting. In *Handbook ofExploration Geochemistry* (ed. G. J. S. Govett). Elsevier, Amsterdam.

Huang S., Hall P. S. and Jackson M. G. (2011) Geochemical zoning of volcanic chains associated with Pacific hotspots. *Nat. Geosci.* **4**, 874–878.

Huber H., Koeberl C., McDonald I. and Reimold W. U. (2001) Geochemistry and petrology of Witwatersrand and dwyka diamictites from south Africa: Search for an extraterrestrial component. *Geochim. Cosmochim. Acta* **65**, 2007–2016.

Hughes H. S. R. (2015) Temporal, lithospheric and magmatic process controls on Ni, Cu and platinum-group element (PGE) mineralisation: a case study from Scotland. Doctoral dissertation, Cardiff University.

Hughes H. S. R., Compton-Jones C., McDonald I., Kiseeva E. S., Kamenetsky V. S., Rollinson G., Coggon J. A., Kinnaird J. A. and Bybee G. M. (2021) Base metal sulphide geochemistry of southern African mantle eclogites (Roberts Victor): Implications for cratonic mafic magmatism and metallogenesis. *Lithos* **382**–**383**, 105918.

Hughes H. S. R., McDonald I., Goodenough K. M., Ciborowski T. J. R., Kerr A. C., Davies J. H. F. L. and Selby D. (2014) Enriched lithospheric mantle keel below the Scottish margin of the North Atlantic Craton: Evidence from the Palaeoproterozoic Scourie Dyke Swarm and mantle xenoliths. *Precambrian Res.* **250**, 97–126. Available at: http://dx.doi.org/10.1016/j.precamres.2014.05.026.

Hughes H. S. R., McDonald I., Boyce A. J., Holwell D. A. and Kerr A. C. (2016) Sulphide sinking in magma conduits: Evidence from mafic-ultramafic plugs on rum and the wider north atlantic igneous province. *J. Petrol.* **57**, 1–33.

Hughes H. S. R., McDonald I. and Kerr A. C. (2015) Platinum-group element signatures in the North Atlantic Igneous Province: Implications for mantle controls on metal budgets during continental breakup. *Lithos* **233**, 89–110. Available at: http://dx.doi.org/10.1016/j.lithos.2015.05.005.

Hughes H. S. R., McDonald I., Loocke M., Butler I. B., Upton B. G. J. and Faithfull J. W. (2017) Paradoxical co-existing base metal sulphides in the mantle: The multi-event record preserved in Loch Roag peridotite xenoliths, North Atlantic Craton. *Lithos* **276**, 103–121. Available at: http://dx.doi.org/10.1016/j.lithos.2016.09.035.

Humayun M. (2011) A model for osmium isotopic evolution of metallic solids at the core-mantle boundary. *Geochemistry, Geophys. Geosystems* **12**, Q03007.

Humayun M., Qiu L. and Norman M. D. (2004) Geochemical evidence for excess iron in the Hawaiian mantle: Implications for mantle dynamics. *Sci.* **306**, 91–94.

Hyvärinen A., Karhunen J. and Oja E. (2001) Introduction. In *Independent Component Analysis* (ed. S. Haykin). John Wiley & Sons, Inc., New York.

Irving A. J. (1978) A review of experimental studies of crystal/liquid trace element partitioning. *Geochim. Cosmochim. Acta* **42**, 743–770.

Iwamori H., Yoshida K., Najamura H., Kuwatani T., Hamada M., Haraguchi S. and Ueki K. (2017) Classification of geochemical data based on multivariate statistical analyses: Complementary roles of cluster, principal component, and independent component analyses. *Geochemistry, Geophys. Geosystems* **18**, 994–1012.

Izokh A. E., Medvedev A. Y., Fedoseev G. S., Polyakov G. V., Nikolaeva I. V. and Palesskii S. V. (2016) Distribution of PGE in Permo-Triassic basalts of the Siberian Large Igneous Province. *Russ. Geol. Geophys.* **57**, 809–821.

Jackson E. D., Silver E. A. and Dalrymple G. B. (1972) Hawaiian-Emperor Chain and Its Relation to Cenozoic Circumpacific Tectonics. *GSA Bull.* **83**, 601–618.

Jackson M. G., Hart S. R., Konter J. G., Kurz M. D., Blusztajn J. and Farley K. A. (2014) Helium and lead isotopes reveal the geochemical geometry of the Samoan plume. *Nature* **514**, 355–358.

Jackson M. G., Weis D. and Huang S. (2012) Major element variations in Hawaiian shield lavas: Source features and perspectives from global ocean island basalt (OIB) systematics. *Geochemistry, Geophys. Geosystems* **13**, 1–24.

Javoy M., Kaminski E., Guyot F., Andrault D., Sanloup C., Moreira M., Labrosse S., Jambon A., Agrinier P., Davaille A. and Jaupart C. (2010) The chemical composition of the Earth: Enstatite chondrite models. *Earth Planet. Sci. Lett.* **293**, 259–268.

Jeffreys H. (1926) The Rigidity of the Earth's Central Core. *Geophys. Suppl. to Mon. Not. R. Astron. Soc.* **1**, 371–383.

Jellinek A. M. and Manga M. (2004) Links Between Long-lived Hot Spots, Mantle Plumes, D", And Plate Tectonics. *Rev. Geophys.* **42**, 1–35. Available at: http://www.seismo.berkeley.edu/~manga/paper72.pdf.

Jennings E. S., Gibson S. A. and Maclennan J. (2019) Hot primary melts and mantle source for the Paraná-Etendeka flood basalt province: New constraints from Al-in-olivine thermometry. *Chem. Geol.* **529**, 119287. Available at: https://doi.org/10.1016/j.chemgeo.2019.119287.

Jennings E. S., Gibson S. A., Maclennan J. and Heinonen J. S. (2017) Deep mixing of mantle melts beneath continental flood basalt provinces: Constraints from olivine-hosted melt inclusions in primitive magmas. *Geochim. Cosmochim. Acta* **196**, 36–57. Available at: http://dx.doi.org/10.1016/j.gca.2016.09.015.

Jerram D. A., Goodenough K. M. and Troll V. R. (2009) Introduction: from the British Tertiary into the future: modern perspectives on the British Palaeogene and North Atlantic Igneous provinces. *Geol. Mag.* **146**, 305–

308.

Jerram D. A. and Widdowson M. (2005) The anatomy of Continental Flood Basalt Provinces: Geological constraints on the processes and products of flood volcanism. *Lithos* **79**, 385–405.

Johnson K. T. M. (1998) Experimental determination of partition coefficients for rare earth and high-field-strength elements between clinopyroxene, garnet, and basaltic melt at high pressures. *Contrib. to Mineral. Petrol.* **133**, 60–68.

Johnson Matthey (2021) Platinum - Prices. *Johnson Matthey.* Available at: http://www.platinum.matthey.com/prices/price-tables#.

Jokat W. and Reents S. (2017) Hotspot volcanism in the southern South Atlantic: Geophysical constraints on the evolution of the southern Walvis Ridge and the Discovery Seamounts. *Tectonophysics* **716**, 77–89. Available at: http://dx.doi.org/10.1016/j.tecto.2016.12.011.

Jolayemi O. O., Robb L., Lenhardt N. and Hughes H. S. R. (2020) Different melt source regions for the volcanics of the Bushveld large igneous province: New observations from MELTS modeling of the Palaeoproterozoic Rooiberg Group (South Africa). *J. African Earth Sci.* **172**, 103999.

Jolliffe I. T. (2002) *Principal Component Analysis*. 2nd ed., Springer, New York.

Jones T. D., Davies D. R., Campbell I. H., Iaffaldano G., Yaxley G., Kramer S. C. and Wilson C. R. (2017) The concurrent emergence and causes of double volcanic hotspot tracks on the Pacific plate. *Nature* **545**, 472–476.

Jones T. D., Davies D. R., Campbell I. H., Wilson C. R. and Kramer S. C. (2016) Do mantle plumes preserve the heterogeneous structure of their deep-mantle source? *Earth Planet. Sci. Lett.* **434**, 10–17.

Jones T. D., Davies D. R. and Sossi P. A. (2019) Tungsten isotopes in mantle plumes: Heads it's positive, tails it's negative. *Earth Planet. Sci. Lett.* **506**, 255–267.

Jourdan F., Bertrand H., Schärer U., Blichert-Toft J., Féraud G. and Kampunzu A. B. (2007) Major and trace element and Sr, Nd, Hf, and Pb isotope compositions of the Karoo large igneous province, Botswana - Zimbabwe: Lithosphere vs Mantle Plume Contribution. *J. Petrol.* **48**, 1043–1077.

Kaminski E. and Javoy M. (2013) A two-stage scenario for the formation of the Earth's mantle and core. *Earth Planet. Sci. Lett.* **365**, 97–107.

Kargel J. S. and Lewis J. S. (1993) The Composition and Early Evolution of Earth. *Icarus* **105**, 1–25.

Keays R. R. (1982) Palladium and iridium in komatiites and associated rocks: application to petrogenetic problems. In *Komatiites* (eds. N. T. Arndt and E. G. Nisbet). George Allen and Unwin, London. pp. 435–455.

Keays R. R. (1995) The role of komatiitic and picritic magmatism and S-saturation in the formation of ore deposits. *Lithos*. **34** (1-3), 1-18.

Keays R. R. and Lightfoot P. C. (2007) Siderophile and chalcophile metal variations in Tertiary picrites and basalts from West Greenland with

implications for the sulphide saturation history of continental flood basalt magmas. *Miner. Depos.* **42**, 319–336.

Keays R. R. and Lightfoot P. C. (2010) Crustal sulfur is required to form magmatic Ni-Cu sulfide deposits: Evidence from chalcophile element signatures of Siberian and Deccan Trap basalts. *Miner. Depos.* **45**, 241–257.

Keays R. R., Nickel E. H., Groves D. I. and McGoldrick P. J. (1982) Iridium and Palladium as Discriminants of Volcanic-Exhalative, Hydrothermal, and Magmatic Nickel Sulfide Mineralization. *Econ. Geol.* **77**, 1535–1547.

Kellogg L. H. and King S. D. (1993) Effect of mantle plumes on the growth of D" by reaction between the core and mantle. *Geophys. Res. Lett.* **20**, 379–382.

Kent R. Y. W. and Fitton J. G. (2000) Mantle Sources and Melting Dynamics in the British Palaeogene Igneous Province. *J. Petrol.* **41**, 1023–1040.

Kepezhinskas P., Defant M. J. and Widom E. (2002) Abundance and distribution of PGE and Au in the island-arc mantle: Implications for sub-arc metasomatism. *Lithos* **60**, 113–128.

Kerr A. C. (1997) The geochemistry and significance of plugs intruding the Tertiary Mull-Morvern lava succession, western Scotland. *Scottish J. Geol.* **33**, 157–167.

Kerr A. C. (1995) The geochemistry of the Mull-Morvern Tertiary lava succession, NW Scotland: an assessment of mantle sources during plume-related volcanism. *Chem. Geol.* **122**, 43–58.

Kerr A. C. and Leitch A. M. (2005) Self-destructive sulfide segregation systems and the formation of high-grade magmatic ore deposits. *Econ. Geol.* **100**, 311–332.

Kimura K., Lewis R. S. and Anders E. (1974) Distribution of gold and rhenium between nickel-iron and silicate melts: implications for the abundance of siderophile elements on the Earth and Moon. *Geochim. Cosmochim. Acta* **38**, 683–701.

Kinzler R. J. (1997) Melting of mantle peridotite at pressures approaching the spinel to garnet transition: Application to mid-ocean ridge basalt petrogenesis. *J. Geophys. Res. B Solid Earth* **102**, 853–874.

Kirkwood C., Cave M., Beamish D., Grebby S. and Ferreira A. (2016) A machine learning approach to geochemical mapping. *J. Geochemical Explor.* **167**, 49–61.

Kleine T. (2011) Earth's patchy late veneer. *Nature* **477**, 168–169.

Kleine T., Mezger K., Palme H. and Münker C. (2004) The W isotope evolution of the bulk silicate Earth: Constraints on the timing and mechanisms of core formation and accretion. *Earth Planet. Sci. Lett.* **228**, 109–123.

Kleine T., Münker C., Mezger K. and Palme H. (2002) Rapid accretion and early core formation on asteroids and the terrestrial planets from Hf-W chronometry. *Nature* **418**, 952–955.

Kleine T., Touboul M., Bourdon B., Nimmo F., Mezger K., Palme H., Jacobsen S. B., Yin Q. Z. and Halliday A. N. (2009) Hf-W chronology of the accretion and early evolution of asteroids and terrestrial planets. *Geochim. Cosmochim. Acta* **73**, 5150–5188.

Klemme S. (2004) The influence of Cr on the garnet-spinel transition in the Earth's mantle: Experiments in the system MgO-Cr2O3-SiO2 and thermodynamic modelling. *Lithos* **77**, 639–646.

Klemme S. and O'Neill H. S. C. (2000) The near-solidus transition from garnet lherzolite to spinel lherzolite. *Contrib. to Mineral. Petrol.* **138**, 237–248.

Klosko E. R., Russo R. M., Okal E. A. and Richardson W. P. (2001) Evidence for a rheologically strong chemical mantle root beneath the Ontong-Java Plateau. *Earth Planet. Sci. Lett.* **186**, 347–361.

Koornneef J. M., Stracke A., Bourdon B., Meier M. A., Jochum K. P., Stoll B. and Grönvold K. (2012) Melting of a two-component source beneath Iceland. *J. Petrol.* **53**, 127–157.

Korenaga J. and Kelemen P. B. (2000) Major element heterogeneity in the mantle source of the North Atlantic igneous province. *Earth Planet. Sci. Lett.* **184**, 251–268.

Kotsiantis S. B. (2007) Supervised Machine Learning: A Review of Classification Techniques. *Informatica* **31**, 249–268.

Kreyszig E. (1979) *Advanced Engineering Mathematics*. 4th ed., Wiley.

Krijthe J. H. (2015) Rtsne: T-Distributed Stochastic Neighbor Embedding using a Barnes-Hut Implementation. Available at: https://github.com/jkrijthe/Rtsne [Accessed April 30, 2020].

Kullback S. and Leibler R. A. (1959) *Information Theory and Statistics*. 3rd ed., John Wiley & Sons Inc. Available at: http://arxiv.org/abs/1706.01538.

Kuno, H. (1968) Differentiation of basalt magmas. In: *Basalts: The Poldervaart treatsie on rocks of basaltic composition*. Vol. 2, Interscience, 623-688.

Kystol J. and Larsen L. M. (1999) Analytical procedures in the Rock Geochemical Laboratory of the Geological Survey of Denmark and Greenland, *Geology Greenland Survey Bulletin,* **184**, 59-62.

Large R. R., Gemmell J. B., Paulick H. and Huston D. L. (2001) The alteration box plot: A simple approach to understanding the relationship between alteration mineralogy and lithogeochemistry associated with volcanic-hosted massive sulfide deposits. *Econ. Geol. Geol.* **96**, 957–971.

Larsen L. M. and Pedersen A. K. (2000) Processes in high-Mg, high-T magmas: Evidence from olivine, chromite and glass in palaeogene picrites from West Greenland. *J. Petrol.* **41**, 1071–1098.

Larsen L. M., Pedersen A. K., Sundvoll B. and Frei R. (2003) Alkali picrites formed by melting of old metasomatized lithospheric mantle: Manîtdlat member, vaigat formation, Palaeocene of West Greenland. *J. Petrol.* **44**, 3–38.

Latyshev A. V., Rad'ko V. A., Veselovskiy R. V., Fetisova, A. M. and Pavlov, V.

E. (2020) Correlation of the Permian-Triassic Ore-Bearing Intrusions of the Norilsk Region with the Volcanic Sequence of the Siberian Traps Based on the Paleomagnetic Data. *Economic Geology* **115** (6), 1173-1193.

Laurenz V., Rubie D. C., Frost D. J. and Vogel A. K. (2016) The importance of sulfur for the behavior of highly-siderophile elements during Earth's differentiation. *Geochim. Cosmochim. Acta* **194**, 123–138.

Lawver L. A. and Muller R. D. (1994) Iceland hotspot track. *Geology* **22**, 311–314.

Lay T., Garnero E. J. and Williams Q. (2004) Partial melting in a thermo-chemical boundary layer at the base of the mantle. *Phys. Earth Planet. Inter.* **146**, 441–467.

Ledevin M., Arndt N. T., Cooper M., Earls G., Lyle P., Auborg C. and Lewin E. (2012) Intrusion history of the Portrush Sill, County Antrim, Northern Ireland: evidence for rapid emplacement and high-temperature contact metamorphism. *Geol. Mag.* **149**, 67–79.

de Leeuw G. A. M., Ellam R. M., Stuart F. M. and Carlson R. W. (2017) 142Nd/144Nd inferences on the nature and origin of the source of high3He/4He magmas. *Earth Planet. Sci. Lett.* **472**, 62–68.

Leinz V. (1949) Contribuição à Geologia dos Derrames Basálticos do Sul do Brasil. *Bol. da Fac. Filos. Ciências e Let. Univ. São Paulo. Geol.*, 1. Available at: http://www.revistas.usp.br/bffcluspgeologia/article/view/121703.

Leinz V., Bartorelli A., Sadowski G. R. and Isotta C. A. L. (1966) Sobre o comportamento do trapp basaltico da Bacia do Paraná. *Bol. da Soc. Bras. Geol.* **15**, 79–91.

Leonhardt R. and Soffel H. C. (2006) The growth, collapse and quiescence of Teno volcano, Tenerife: New constraints from paleomagnetic data. *Int. J. Earth Sci.* **95**, 1053–1064.

Lesher C. M. (2017) Roles of xenomelts, xenoliths, xenocrysts, xenovolatiles, residues, and skarns in the genesis, transport, and localization of magmatic Fe-Ni-Cu-PGE sulfides and chromite. *Ore Geol. Rev.* **90**, 465–484.

Lesher C. M. and Burnham O. M. (2001) Multicomponent elemental and isotopic mixing in Ni-Cu-(PGE) ores at Kambalda, Western Australia. *Can. Mineral.* **39**, 421–446.

Li C., Maier W. D. and de Waal S. A. (2001) The role of magma mixing in the genesis of pge mineralization in the bushveld complex: Thermodynamic calculations and new interpretations-a discussion. *Econ. Geol.* **96**, 653–662.

Li C., Ripley E. M. and Naldrett A. J. (2009) A new genetic model for the giant Ni-Cu-pge sulfide deposits associated with the siberian flood basalts. *Econ. Geol.* **104**, 291–301.

Li Y. and Nguyen T. Van (2018) Core-shell rhodium sulfide catalyst for hydrogen evolution reaction / hydrogen oxidation reaction in hydrogen-bromine reversible fuel cell. *J. Power Sources* **382**, 152–159.

Li M. and Zhong S. (2017) The source location of mantle plumes from 3D spherical models of mantle convection. *Earth Planet. Sci. Lett.* **478**, 47–57. Available at: http://linkinghub.elsevier.com/retrieve/pii/S0012821X17304806.

Licht O. A. B. (2018) A revised chemo-chrono-stratigraphic 4-D model for the extrusive rocks of the Paraná Igneous Province. *J. Volcanol. Geotherm. Res.* **355**, 32–54. Available at: https://doi.org/10.1016/j.jvolgeores.2016.12.003.

Lightfoot P. C. (2007) Advances in Ni-Cu-PGE Sulphide Deposit Models and Implications for Exploration Technologies. *Ore Depos. Explor. Technol. Proc. Explor. 07 Decenn. Int. Conf. Miner. Explor.* **Paper 44**, 629–646.

Lightfoot P. C., Hawkesworth C. J., Hergt J., Naldrett A. J., Gorbachev N. S., Fedorenko V. A. and Doherty W. (1993) Remobilisation of the continental lithosphere by a mantle plume: from picritic and tholeiitic iavas of the Noril'sk District, Siberian Trap, Russia. *Contrib. to Mineral. Petrol.* **114**, 171–188.

Lightfoot P. C., Hawkesworth C. J., Olshefsky K., Green T., Doherty W. and Keays R. R. (1997) Geochemistry of Tertiary tholeiites and picrites from Qeqertarssuaq (Disko Island) and Nuussuaq, West Greenland with implications for the mineral potential of comagmatic intrusions. *Contrib. to Mineral. Petrol.* **128**, 139–163.

Lightfoot P. C. and Keays, R. (2005) Siderophile and chalcophile metal variations in flood basalts from the Siberian trap, Noril'sk region: Implications for the origin of the Ni-Cu-PGE sulfide ores. *Economic Geology*. **100** (3), 439-462.

Lindsay J. J., Hughes H. S. R., Yeomans C. M., Andersen J. C. Ø. and McDonald I. (2021) A Machine Learning approach for regional geochemical data: Platinum-Group Element geochemistry vs geodynamic settings of the North Atlantic Igneous Province. *Geosci. Front.* **12**, 101098. Available at: https://doi.org/10.1016/j.gsf.2020.10.005.

Lindsay J. J., Hughes H. S. R., Yeomans C. M., Andersen J. C. Ø. and McDonald I. (accepted) From Continent to Ocean: Investigate the multi-element and precious metal geochemistry of the Paraná-Etendeka Large Igneous Province using machine learning. *Earth Science, Systems and Society*.

Lindsay J. J., Andersen J. C. Ø., Hughes H. S. R., McDonald I., Hastie A. R., Besser M. L., Licht O. A. B. and Arioli E. E. (in review[a]) Platinum-group element geochemistry of the Paraná flood basalts – modelling metallogenesis in rifting continental plume environments. *Geochim. Et Cosmochim. Acta*.

Lindsay J. J., Hughes H. S. R., Andersen J. C. Ø., McDonald I. and Hastie A. R. (in review[b]) Precious metals in Tenerife: Investigating metallogeny in plume-derived lavas from the western Canary Islands and beyond. *Geosi. Front.*

Liu X., Xiong X., Audétat A., Li Y., Song M., Li L., Sun W. and Ding X. (2014) Partitioning of copper between olivine, orthopyroxene, clinopyroxene,

spinel, garnet and silicate melts at upper mantle conditions. *Geochim. Cosmochim. Acta* **125**, 1–22.

Liu Y., Cheng Q., Zhou K., Xia Q. and Wang X. (2016) Multivariate analysis for geochemical process identification using stream sediment geochemical data: A perspective from compositional data. *Geochem. J.* **50**, 293–314.

Locmelis M., Fiorentini M. L., Barnes S. J. and Pearson N. J. (2013) Ruthenium Variation in Chromite from Komatiites and Komatiitic Basalts—A Potential Mineralogical Indicator for Nickel Sulfide Mineralization. *Econ. Geol.* **108**, 355–364.

Locmelis M., Fiorentini M. L., Rushmer T., Arevalo Jr. R., Adam J. and Denyszyn S. W. (2016) Sulfur and metal fertilization of the lower continental crust. *Lithos* **244**, 74-93.

Loewen M. W., Duncan R. A., Kent A. J. R. and Krawl K. (2013) Prolonged plume volcanism in the Caribbean Large Igneous Province: New insights from Curacao and Haiti. *Geochemistry, Geophys. Geosystems* **14**, 4241–4259.

Long L. E. (1964) Rb-Sr chronology of the Carn Chuinneag Intrusion, Ross-shire, Scotland. *J. Geophys. Res.* **69**, 1589–1597.

Longpré M. A., Troll V. R., Walter T. R. and Hansteen T. H. (2009) Volcanic and geochemical evolution of the Teno Massif, Tenerife, Canary Islands: Some repercussions of giant landslides on ocean island magmatism. *Geochemistry, Geophys. Geosystems* **10**.

Lorand J. P. and Alard O. (2001) Platinum-group element abundances in the upper mantle: New constraints from in situ and whole-rock analyses of massif central xenoliths (France). *Geochim. Cosmochim. Acta* **65**, 2789–2806.

Lorand J. P., Alard O. and Godard M. (2009) Platinum-group element signature of the primitive mantle rejuvenated by melt-rock reactions: Evidence from Sumail peridotites (Oman Ophiolite). *Terra Nov.* **21**, 35–40.

Lorand J. P., Delpech G., Grégoire M., Moine B., O'Reilly S. Y. and Cottin J. Y. (2004) Platinum-group elements and the multistage metasomatic history of Kerguelen lithospheric mantle (South Indian Ocean). *Chem. Geol.* **208**, 195–215.

Lorand J. P. and Luguet A. (2016) Chalcophile and siderophile elements in mantle rocks: Trace elements controlled by trace minerals. *Rev. Mineral. Geochemistry* **81**, 441–488. Available at: http://rimg.geoscienceworld.org/lookup/doi/10.2138/rmg.2016.81.08.

Lorand J. P., Luguet A. and Alard O. (2008) Platinum-group elements: A new set of key tracers for the Earth's interior. *Elements* **4**, 247–252.

Lorand J. P., Luguet A. and Alard O. (2013) Platinum-group element systematics and petrogenetic processing of the continental upper mantle: A review. *Lithos* **164**–**167**, 2–21. Available at: http://dx.doi.org/10.1016/j.lithos.2012.08.017.

Lorand J. P., Pattou L. and Gros M. (1999) Fractionation of Platinum-group

elements and gold in the upper mantle: A detailed study in Pyrenean orogenic lherzolites. *J. Petrol.* **40**, 957–981.

Lorand J. P., Reisberg L. and Bedini R. M. (2003) Platinum-group elements and melt percolation processes in Sidamo spinel peridotite xenoliths, Ethiopia, East African Rift. *Chem. Geol.* **196**, 57–75.

Lugmair G. W. and Marti K. (1978) Lugmair 1978 Lunar Initial 143Nd-144Nd differential evolution of the lunar crust and mantle. **39**, 349–357.

Luguet A., Lorand J. P. and Seyler M. (2003) Sulfide petrology and highly siderophile element geochemistry of abyssal peridotites: A coupled study of samples from the Kane Fracture Zone (45°W 23°20N, MARK area, Atlantic Ocean). *Geochim. Cosmochim. Acta* **67**, 1553–1570.

Luguet A. and Reisberg L. (2016) Highly Siderophile Element and 187Os Signatures in Non-cratonic Basalt-hosted Peridotite Xenoliths: Unravelling the Origin and Evolution of the Post-Archean Lithospheric Mantle. *Rev. Mineral. Geochemistry* **81**, 305–367. Available at: http://rimg.geoscienceworld.org/content/81/1/305.short.

van der Maaten L. (2014) Accelerating t-SNE using tree-based algorithms. *J. Mach. Learn. Res.* **15**, 3221–3245.

van der Maaten L. and Hinton G. (2008) Visualizing Data using t-SNE. *J. Mach. Learn. Res.* **9**, 2579–2605.

MacQueen J. (1967) Some methods for classification and analysis of multivariate observations. *Proc. Fifth Berkeley Symp. Math. Stat. Probab.* **1**, 281–297.

Maier W. D. (2005) Platinum-group element (PGE) deposits and occurrences: Mineralization styles, genetic concepts, and exploration criteria. *J. African Earth Sci.* **41**, 165–191.

Maier W. D., Barnes S. J., Campbell I. H., Fiorentini M. L., Peltonen P., Barnes Sarah Jane and Smithies R. H. (2009) Progressive mixing of meteoritic veneer into the early Earths deep mantle. *Nature* **460**, 620–623.

Maier W. D., Barnes S. J. and Marsh J. S. (2003a) The concentrations of the noble metals in Southern African flood-type basalts and MORB: Implications for petrogenesis and magmatic sulphide exploration. *Contrib. to Mineral. Petrol.* **146**, 44–61.

Maier W. D. and Groves D. I. (2011) Temporal and spatial controls on the formation of magmatic PGE and Ni-Cu deposits. *Miner. Depos.* **46**, 841–857.

Maier W. D., O'Brien H., Peltonen P. and Barnes S. J. (2017) Platinum-group element contents of Karelian kimberlites: Implications for the PGE budget of the sub-continental lithospheric mantle. *Geochim. Cosmochim. Acta* **216**, 358–371.

Maier W. D., Peltonen P., McDonald I., Barnes S. J., Barnes S. J., Hatton C. and Viljoen F. (2012) The concentration of platinum-group elements and gold in southern African and Karelian kimberlite-hosted mantle xenoliths: Implications for the noble metal content of the Earth's mantle. *Chem. Geol.*

302–**303**, 119–135. Available at: http://dx.doi.org/10.1016/j.chemgeo.2011.06.014.

Maier W. D., Roelofse F. and Barnes S.-J. (2003b) The Concentration of the Platinum-Group Elements in South African Komatiites: Implications for Mantle Sources, Melting Regime and PGE Fractionation during Crystallization. *J. Petrol.* **44**, 1787–1804.

Mann U., Frost D. J. and Rubie D. C. (2009) Evidence for high-pressure core-mantle differentiation from the metal-silicate partitioning of lithophile and weakly-siderophile elements. *Geochim. Cosmochim. Acta* **73**, 7360–7386.

Mann U., Frost D. J., Rubie D. C., Becker H. and Audétat A. (2012) Partitioning of Ru, Rh, Pd, Re, Ir and Pt between liquid metal and silicate at high pressures and high temperatures - Implications for the origin of highly siderophile element concentrations in the Earth's mantle. *Geochim. Cosmochim. Acta* **84**, 593–613.

Mansur E. T. and Barnes S. J. (2020) The role of Te, As, Bi, Sn and Sb during the formation of platinum-group-element reef deposits: Examples from the Bushveld and Stillwater Complexes. *Geochim. Cosmochim. Acta* **272**, 235–258. Available at: https://doi.org/10.1016/j.gca.2020.01.008.

Marcantonio F., Zindler A., Elliott T. and Staudigel H. (1995) Os isotope systematics of La Palma, Canary Islands: Evidence for recycled crust in the mantle source of HIMU ocean islands. *Earth Planet. Sci. Lett.* **133**, 397–410.

Marchi S., Canup R. M. and Walker R. J. (2017) Heterogeneous delivery of silicate and metal to the Earth by large planetesimals. *Nat. Geosci.*

Marques, L. S., B. Dupré, and E. M. Piccirillo (1999) Mantle Source Compositions of the Parana Magmatic Province (Southern Brazil): Evidence from Trace Element and Sr-Nd-Pb Isotope Geochemistry. *Journal of Geodynamics*, **28** (4–5), 439–58. Available at: https://doi.org/10.1016/S0264-3707(99)00020-4

Marques L. S., De Min A., Rocha-Júnior E. R. V, Babinski M., Bellieni G. and Figueiredo A. M. G. (2018) Elemental and Sr-Nd-Pb isotope geochemistry of the Florianópolis Dyke Swarm (Paraná Magmatic Province): crustal contamination and mantle source constraints. *J. Volcanol. Geotherm. Res.* **355**, 149–164. Available at: https://doi.org/10.1016/j.jvolgeores.2017.07.005.

Marsh J. S., Ewart A., Milner S. C., Duncan A. R. and Miller R. M. G. (2001) The Etendeka Igneous Province: Magma types and their stratigraphic distribution with implications for the evolution of the Paraná-Etendeka flood basalt province. *Bull. Volcanol.* **62**, 464–486.

Marsland S. (2009) *Machine Learning An Algorithmic Perspective Second Edition*. 2nd ed. eds. R. Herbrich and T. Graepel, CRC Press.

Martín-Fernández J. A., Hron K., Templ M., Filzmoser P. and Palarea-Albaladejo J. (2012) Model-based replacement of rounded zeros in compositional data: Classical and robust approaches. *Comput. Stat. Data Anal.* **56**, 2688–2704. Available at:

https://linkinghub.elsevier.com/retrieve/pii/S0167947312000941.

Martín-Fernández J. A. and Thió-Hernestrosa S. (2006) Rounded zeros: some practical aspects for compositional data. In *Compositional Data Analysis in the Geosciences: From Theory to Practice* Geological Society of London Special Publications. pp. 191–201.

Martins-Ferreira M. A. C., Dias A. N. C., Chemale F. and Campos J. E. G. (2020) Intracontinental uplift of the Brazilian Central Plateau linked to continental breakup, orogenies, and basin filling, supported by apatite and zircon fission-track data. *Arab. J. Geosci.* **13**.

Mathieu, L. (2018) Quantifying hydrothermal alteration: a review of methods. *Geosciences*. **8**, 1-27.

Matzen A. K., Wood B. J., Baker M. B. and Stolper E. M. (2017) The roles of pyroxenite and peridotite in the mantle sources of oceanic basalts. *Nat. Geosci.* **10**, 530–535.

Mavrogenes J. A. and O'Neill H. S. C. (1999) The relative effects of pressure, temperature and oxygen fugacity on the solubility of sulfide in mafic magmas. *Geochim. Cosmochim. Acta* **63**, 1173–1180.

McBirney A. R. and Noyes R. M. (1979) Crystallization and layering of the skaergaard intrusion. *J. Petrol.* **20**, 487–554.

McCuaig T. C., Beresford S. and Hronsky J. (2010) Translating the mineral systems approach into an effective exploration targeting system. *Ore Geol. Rev.* **38**, 128–138. Available at: http://dx.doi.org/10.1016/j.oregeorev.2010.05.008.

McCulloch M. T. and Wasserburg G. J. (1978) Sm-Nd and Rb-Sr Chronology of Continental Crust Formation. *Science (80-.).* **200**, 1003–1011.

McDonald I., Hughes H. S. R., Butler I. B., Harris J. W. and Muir D. (2017) Homogenisation of sulphide inclusions within diamonds: A new approach to diamond inclusion geochemistry. *Geochim. Cosmochim. Acta* **216**, 335–357. Available at: http://dx.doi.org/10.1016/j.gca.2017.04.039.

McDonald I. and Viljoen K. S. (2006) Platinum-group element geochemistry of mantle eclogites: a reconnaissance study of xenoliths from the Orapa kimberlite, Botswana. *Appl. Earth Sci.* **115**, 81–93. Available at: http://www.tandfonline.com/doi/full/10.1179/174327506X138904.

McDonough W. F. and Sun S. S. (1995) The composition of Earth. *Chem. Geol.* **120**, 223–253.

McDonough W. F., Sun S. S., Ringwood A. E., Jagoutz E. and Hofmann A. W. (1992) Potassium, rubidium, and cesium in the Earth and Moon and the evolution of the mantle of the Earth. *Geochim. Cosmochim. Acta* **56**, 1001–1012.

McInnes L., Healy J. and Melville J. (2018) UMAP: Uniform manifold approximation and projection for dimension reduction. *arXiv*.

McIntire W. L. (1963) Trace element partition coefficients-a review of theory and applications to geology. *Geochim. Cosmochim. Acta* **27**, 1209–1264.

McKenzie, D. and Bickle, M. J. (1988) The Volume and Composition of Melt Generated by Extension of the Lithosphere. *Journal of Petrology* **29** (3), 625-679.

McKenzie D. and O'Nions R. K. (1991) Partial melt coefficients from inversion of rare earth element concentrations. *J. Petrol.* **23**, 1021–1091.

McKenzie D. and White R. (1989) Magmatism at rift zones: The generation of volcanic continental margins and flood basalts. *J. Geophys. Res.* **94**, 7685–7729.

McKinney W. (2010) Data Structures for Statistical Computing in Python. *Proc. 9th Python Sci. Conf.* **1**, 56–61.

Médard E., Schmidt M. W., Wälle M., Keller N. S. and Günther D. (2015) Platinum partitioning between metal and silicate melts: Core formation, late veneer and the nanonuggets issue. *Geochim. Cosmochim. Acta* **162**, 183–201.

Meisel T. and Horan M. F. (2016) Analytical Methods for the Highly Siderophile Elements. *Rev. Mineral. Geochemistry* **81**, 89–106.

Michie D., Spiegelhalter D. J. and Taylor C. C. (1994) *Machine Learning, Neural and Statistical Classification*., Ellise Horwood Limited.

Milholland C. S. and Presnall D. C. (1998) Liquidus phase relations in the CaO-MgO-Al2O3-SiO2 system at 3·0 GPa: The aluminous pyroxene thermal divide and high-pressure fractionation of picritic and komatiitic magmas. *J. Petrol.* **39**, 3–27.

Miller R. M. (2008) *The Geology of Namibia*., Ministry of Mines and Energy, Geological Survey of Namibia.

Milner S. C., Duncan A. R., Ewart A. and Marsh J. S. (1995a) Promotion of the Etendeka Formation to Group status : A new integrated stratigraphy. *Commun. Geol. Surv. Namib* **9**, 5–11.

Milner S. C., Duncan A. R., Whittingham A. M. and Ewart A. (1995b) Trans-Atlantic correlation of eruptive sequences and individual silicic volcanic units within the Paraná-Etendeka igneous province. *J. Volcanol. Geotherm. Res.* **69**, 137–157.

Milner S. C., Le Roex A. P. and O'Connor J. M. (1995c) Age of Mesozoic igneous rocks in northwestern Namibia, and their relationship to continental breakup. *J. - Geol. Soc.* **152**, 97–104.

de Min A., Callegaro S., Marzoli A., Nardy A. J., Chiaradia M., Marques L. S. and Gabbarrini I. (2017) Insights into the petrogenesis of low- and high-Ti basalts: Stratigraphy and geochemistry of four lava sequences from the central Paraná basin. *J. Volcanol. Geotherm. Res.* **355**, 232–252. Available at: https://doi.org/10.1016/j.jvolgeores.2017.08.009.

Minster J. F., Birck J. L. and Allègre C. J. (1982) Absolute age of formation of chondrites studied by the 87Rb- 87Sr method. *Nature* **300**, 414–419.

Mitchell R. H. and Keays R. R. (1981) Abundance and distribution of gold, palladium and iridium in some spinel and garnet lherzolites: implications for

the nature and origin of precious metal-rich intergranular components in the upper mantle. *Geochim. Cosmochim. Acta* **45**, 2425–2442.

Mitchell W. I., Cooper M. R., Hards V. L. and Meighan I. G. (1999) An occurrence of silicic volcanic rocks in the early Palaeogene Antrim Lava Group of Northern Ireland. *Scottish J. Geol.* **35**, 179–185.

Momme P., Óskarsson N. and Keays R. R. (2003) Platinum-group elements in the Icelandic rift system: melting processes and mantle sources beneath Iceland. *Chem. Geol.* **196**, 209–234. Available at: https://linkinghub.elsevier.com/retrieve/pii/S000925410200414X.

Momme P., Tegner C., Brooks C. K. and Keays R. R. (2002) The behaviour of platinum-group elements in basalts from the East Greenland rifted margin. *Contrib. to Mineral. Petrol.* **143**, 133–153.

Momme P., Tegner C., Brooks C. K. and Keays R. R. (2006) Two melting regimes during Paleogene flood basalt generation in East Greenland: combined REE and PGE modelling. *Contrib. to Mineral. Petrol.* **151**, 88–100. Available at: http://link.springer.com/10.1007/s00410-005-0047-2.

Moreira M., Doucelance R., Kurz M. D., Dupré B. and Allègre C. J. (1999) Helium and lead isotope geochemistry of the Azores archipelago. *Earth Planet. Sci. Lett.* **169**, 189–205.

Moreira M., Kanzari A. and Madureira P. (2012) Helium and neon isotopes in São Miguel island basalts, Azores Archipelago: New constraints on the “low 3He” hotspot origin. *Chem. Geol.* **322**–**323**, 91–98.

Morgan W. J. (1971) Convection plumes in the lower mantle. *Nature* **230**, 42–43.

Morgan W. J. (1972) Deep Mantle Convection Plumes and Plate Motions. *Am. Assoc. Pet. Geol. Bull.* **56**, 203–213.

Mudd G. M., Jowitt S. M. and Werner T. T. (2018) Global platinum group element resources, reserves and mining – A critical assessment. *Sci. Total Environ.* **622**–**623**, 614–625.

Mukhopadhyay S., Lassiter J. C., Farley K. A. and Bogue S. W. (2003) Geochemistry of Kauai shield-stage lavas: Implications for the chemical evolution of the Hawaiian plume. *Geochemistry, Geophys. Geosystems* **4**.

Mundl-Petermeier A., Walker R. J., Jackson M. G., Blichert-Toft J., Kurz M. D. and Halldórsson S. A. (2019) Temporal evolution of primordial tungsten-182 and 3He/4He signatures in the Iceland mantle plume. *Chem. Geol.* **525**, 245–259.

Mundl A., Touboul M., Jackson M. G., Day J. M. D., Kurz M. D., Lekic V., Helz R. T. and Walker R. J. (2017) Tungsten-182 heterogeneity in modern ocean island basalts. *Science (80-.).* **356**, 66–69.

Mungall J. E., Andrews D. R. A., Cabri L. J., Sylvester P. J. and Tubrett M. (2005) Partitioning of Cu, Ni, Au, and platinum-group elements between monosulfide solid solution and sulfide melt under controlled oxygen and sulfur fugacities. *Geochim. Cosmochim. Acta* **69**, 4349–4360.

Mungall J. E. and Brenan J. (2014) Partitioning of platinum-group elements and Au between sulfide liquid and basalt and the origins of mantle-crust fractionation of the chalcophile elements. *Geochim. Cosmochim. Acta* **125**, 265–289. Available at: http://dx.doi.org/10.1016/j.gca.2013.10.002.

Münker C., Pfänder J. A., Weyer S., Büchl A., Kleine T. and Mezger K. (2003) Evolution of Planetary Cores and the Earth-Moon System from Nb/Ta Systematics. *Science (80-.).* **301**, 84–87.

Naldrett A. J. (1997) Key factors in the genesis of Noril'sk, Sudbury, Jinchuan, Voisey's Bay and other world-class Ni-Cu-PGE deposits: implications for exploration. *Aust. J. Earth Sci.*, 283–315.

Naldrett A. J. (2004) *Magmatic Sulfide Deposits*., Available at: http://www.minersoc.org/pages/Archive-MM/Volume_54/54-377-675.pdf.

Naldrett A. J. (2010) From the mantle to the bank: The life of a Ni-Cu-(PGE) sulfide deposit. *South African J. Geol.* **113**, 1–32.

Naldrett A. J. (2011) Fundamentals of Magmatic Sulfide Deposits. *Rev. Econ. Geol.* **17**, 1–50.

Naldrett A. J., Lightfoot P. C., Fedorenko V., Doherty W. and Gorbachev N. S. (1992) Geology and geochemistry of intrusions and flood basalts of the Noril'sk region, USSR, with implications for the origin of the Ni-Cu ores. *Econ. Geol.* **87**, 975–1004.

Naldrett A. J. and MacDonald A. J. (1980) Tectonic Setting of some Ni-Cu Sulphide Ores: Their Importance in Genesis and Exploration. *Geol. Assoc. Canada, Spec. Pap.* **20**, 93–109.

Natali C., Beccaluva L., Bianchini G. and Siena F. (2017) Comparison among Ethiopia-Yemen, Deccan, and Karoo continental flood basalts of central Gondwana: Insights on lithosphere versus asthenosphere contributions in compositionally zoned magmatic provinces. *Spec. Pap. Geol. Soc. Am.* **526**, 191–215.

Neal C. R., Mahoney J. J. and Chazey W. J. (2002) Mantle sources and the highly variable role of continental lithosphere in basalt petrogenesis of the Kerguelen plateau and broken ridge LIP: Results from ODP Leg 183. *J. Petrol.* **43**, 1177–1205.

Nielsen T. F. D. (2004) The shape and volume of the Skaergaard intrusion, Greenland: Implications for mass balance and bulk composition. *J. Petrol.* **45**, 507–530.

Nielsen T. F. D., Andersen J. C. Ø., Holness M. B., Keiding J. K., Rudashevsky N. S., Rudashevsky V. N., Salmonsen L. P., Tegner C. and Veksler I. V. (2014) The Skaergaard PGE and gold deposit: The result of in situ fractionation, sulphide saturation, and magma chamber-scale precious metal redistribution by immiscible Fe-rich melt. *J. Petrol.* **56**, 1643–1676.

Nguyen L. H. and Holmes S. (2019) Ten quick tips for effective dimensionality reduction. *PLoS Comput. Biol.* **15**, 1–19.

Norman M. D. and Garcia M. O. (1999) Primitive magmas and source

characteristics of the Hawaiian plume: Petrology and geochemistry of shield picrites. *Earth Planet. Sci. Lett.* **168**, 27–44.

O'Brien D. P., Morbidelli A. and Levison H. F. (2006) Terrestrial planet formation with strong dynamical friction. *Icarus* **184**, 39–58.

O'Connor J. M. and Duncan R. A. (1990) Evolution of the Walvis Ridge-Rio Grande Rise Hot Spot System: Implications for African and South American Plate motions over plumes. *J. Geophys. Res.* **95**, 17475. Available at: http://doi.wiley.com/10.1029/JB095iB11p17475.

O'Connor J. M. and Jokat W. (2015) Tracking the Tristan-Gough mantle plume using discrete chains of intraplate volcanic centers buried in the Walvis Ridge. *Geology* **43**, 715–718.

O'Connor J., Jokat W., Wijbrans J. and Colli L. (2018) Hotspot tracks in the South Atlantic located above bands of fast flowing asthenosphere driven by waning pulsations from the African LLSVP. *Gondwana Res.* **53**, 197–208.

O'Driscoll B., Butcher A. R. and Latypov R. (2014) New insights into precious metal enrichment on the Isle of Rum, Scotland. *Geol. Today* **30**, 134–141.

O'Driscoll B., Day J. M. D., Daly J. S., Walker R. J. and McDonough W. F. (2009) Rhenium-osmium isotopes and platinum-group elements in the Rum Layered Suite, Scotland: Implications for Cr-spinel seam formation and the composition of the Iceland mantle anomaly. *Earth Planet. Sci. Lett.* **286**, 41–51.

O'Driscoll B., Emeleus C. H., Donaldson C. H. and Daly J. S. (2010) Cr-spinel seam petrogenesis in the rum layered suite, NWScotland: Cumulate assimilation and in situ crystallization in a deforming crystal mush. *J. Petrol.* **51**, 1171–1201.

Ozima M. and Podosek F. (1983) *Noble Gas Geochemistry*., Cambridge University Press, Cambridge.

Pagé P., Barnes S. J., Bédard J. H. and Zientek M. L. (2012) In situ determination of Os, Ir, and Ru in chromites formed from komatiite, tholeiite and boninite magmas: Implications for chromite control of Os, Ir and Ru during partial melting and crystal fractionation. *Chem. Geol.* **302–303**, 3–15. Available at: http://dx.doi.org/10.1016/j.chemgeo.2011.06.006.

Palme H. and O'Neill H. S. C. (2003) Cosmochemical Estimates of Mantle Composition. In *The Mantle and Core - Treatise on Geochemistry* (ed. R. W. Carlson). Elsevier-Pergamon, Oxford. pp. 1–38.

Palowsky-Glahn, V., and Egozcue, J. J. (2006) Compositional Data and Their Analysis: An Introduction. *Geological Society Special Publications* **264** (1), 1–10

Park J. W., Kamenetsky V., Campbell I., Park G., Hanski E. and Pushkarev E. (2017) Empirical constraints on partitioning of platinum group elements between Cr-spinel and primitive terrestrial magmas. *Geochim. Cosmochim. Acta* **216**, 393–416. Available at: http://dx.doi.org/10.1016/j.gca.2017.05.039.

Peach C. L., Mathez E. A. and Keays R. R. (1990) Sulfide melt-silicate melt distribution coefficients for noble metals and other chalcophile elements as deduced from MORB: Implications for partial melting. *Geochim. Cosmochim. Acta* **54**, 3379–3389.

Peach C. L., Mathez E. A., Keays R. R. and Reeves S. J. (1994) Experimentally determined sulfide melt-silicate melt partition coefficients for iridium and palladium. *Chem. Geol.* **117**, 361–377.

Pearson K. (1901) On lines and planes of closest fit to systems of points in space. *Phil. Mag. J. Sci.* **2**, 559–572.

Pearce J. A. (2008) Geochemical fingerprinting of oceanic basalts with applications to ophiolite classification and the search for Archean oceanic crust. *Lithos* **100**, 14–48.

Pearson K. (1901) On lines and planes of closest fit to systems of points in space. *Phil. Mag. J. Sci.* **2**, 559–572.

Peate D. W. (1997) The Paraná-Etendeka province. *Geophys. Monogr. Ser. Ser* **100**, 217–245.

Peate D. W., Breddam K., Baker J. A., Kurz M. D., Barker A. K., Prestvik T., Grassineau N. and Skovgaard A. C. (2010) Compositional characteristics and spatial distribution of enriched Icelandic mantle components. *J. Petrol.* **51**, 1447–1475.

Peate D. W. and Hawkesworth C. J. (1996) Lithospheric to asthenospheric transition in low-Ti flood basalts from southern Paraná, Brazil. *Chem. Geol.* **127**, 1–24.

Peate D. W., Hawkesworth C. J. and Mantovani M. S. M. (1992) Chemical stratigraphy of the Paraná lavas (South America): classification of magma types and their spatial distribution. *Bull. Volcanol.* **55**, 119–139.

Peate D. W., Hawkesworth C. J., Mantovani M. S. M., Rogers N. W. and Turner S. P. (1999) Petrogenesis and stratigraphy of the high-Ti/Y Urubici magma type in the Parana Flood Basalt Province and implications for the nature of 'Dupal'-type mantle in the South Atlantic Region. *J. Petrol.* **40**, 451–473.

Peate D. W., Hawkesworth C. J., Mantovani M. S. M. and Shukowsky W. (1990) Mantle plumes and flood-basalt stratigraphy in the Parana, South America. *Geology* **18**, 1223–1226.

Peate D. W. and Stecher O. (2003) Pb isotope evidence for contributions from different Iceland mantle components to Palaeogene East Greenland flood basalts. *Lithos* **67**, 39–52.

Pedregosa F., Varoquaux G., Gramfort A., Michel V., Thirion B., Grisel O., Blondel M., Prettenhofer P., Weiss R., Dubourg V., Vanderplas J., Passos A., Cournapeau D., Brucher M., Perrot M. and Duchesnay E. (2011) Scikit-learn: Machine Learning in Python. *J. Ma* **12**, 2825–2830.

Peplow M. (2020) Rhodium photocatalyst does double duty to generate hydrogen: Air-stable complex uses light to catalyze production of solar fuel. *Chem. Eng. News* **98**.

Peucker-Ehrenbrink B., Bach W., Hart S. R., Blusztajn J. S. and Abbruzzese T. (2003) Rhenium-osmium isotope systematics and platinum group element concentrations in oceanic crust from DSDP/ODP Sites 504 and 417/418. *Geochemistry, Geophys. Geosystems* **4**, 1–28.

Philipp H., Eckhardt J.-D. and Puchelt H. (2001) Platinum-Group Elements (PGE) in Basalts of the Seaward-Dipping Reflector Sequence, SE Greenland Coast. *J. Petrol.* **42**, 407–432.

Piccirillo E. M., Melfi A. J., Comin-Chiaramonti P., Bellieni G., Ernesto M., Marques L. S., Nardy A. J. R., Pacca I. G., Roisenberg A. and Stolfa D. (1988) Continental Flood Volcanism From the Paraná Basin (Brazil). In *Continental Flood Basalts* (ed. J. D. McDougall). Kluwer. pp. 195–238.

Pirajno F. and Santosh M. (2015) Mantle plumes, supercontinents, intracontinental rifting and mineral systems. *Precambrian Res.* **259**, 243–261. Available at: http://dx.doi.org/10.1016/j.precamres.2014.12.016.

Pirrie D., Power M. R., Andersen J. C. Ø. and Butcher A. R. (2000) Platinum-group mineralization in the Tertiary Igneous Province: new data from Mull and Skye, Scottish Inner Hebrides, UK. *Geol. Mag.* **137**, 651–658.

Pitcher L., Helz R. T., Walker R. J. and Piccoli P. (2009) Fractionation of the platinum-group elments and Re during crystallization of basalt in Kilauea Iki Lava Lake, Hawaii. *Chem. Geol.* **260**, 196–210. Available at: http://dx.doi.org/10.1016/j.chemgeo.2008.12.022.

Polo L. A., Giordano D., Janasi V. A. and Guimarães L. F. (2018) Effusive silicic volcanism in the Paraná Magmatic Province, South Brazil: Physico-chemical conditions of storage and eruption and considerations on the rheological behavior during emplacement. *J. Volcanol. Geotherm. Res.* **355**, 115–135. Available at: https://doi.org/10.1016/j.jvolgeores.2017.05.027.

Powell W. and O'Reilly S. (2007) Metasomatism and sulfide mobility in lithospheric mantle beneath eastern Australia: Implications for mantle Re-Os chronology. *Lithos* **94**, 132–147.

Power M. R., Pirrie D. and Andersen J. C. Ø. (2003) Diversity of platinum-group element mineralization styles in the North Atlantic Igneous Province: new evidence from Rum, UK. *Geol. Mag.* **140**, 499–512.

Power M. R., Pirrie D., Andersen J. C. Ø. and Wheeler P. D. (2000) Testing the validity of chrome spinel chemistry as a provenance and petrogenetic indicator. *Geology* **28**, 1027–1030.

Prichard H. M., Fisher P. C., McDonald I., Knight R. D., Sharp D. R. and Williams J. P. (2013) The Distribution of PGE and the role of arsenic as a collector of pge in the spotted quoll nickel ore deposit in the forrestania Greenstone Belt, Western Australia. *Econ. Geol.* **108**, 1903–1921.

Prytulak J. and Elliott T. (2007) TiO2-enrichment in ocean island basalts. *Earth Planet. Sci. Lett.* **263**, 388–403.

Puchtel I. and Humayun M. (2000) Platinum group elements in Kostomuksha komatiites and basalts: Implications for oceanic crust recycling and core-

mantle interaction. *Geochim. Cosmochim. Acta* **64**, 4227–4242.

Puchtel I. S., Walker R. J., Brandon A. D. and Nisbet E. G. (2009) Pt-Re-Os and Sm-Nd isotope and HSE and REE systematics of the 2.7 Ga Belingwe and Abitibi komatiites. *Geochim. Cosmochim. Acta* **73**, 6367–6389.

Rämö O. T., Heikkilä P. A. and Pulkkinen A. H. (2016) Geochemistry of Paraná-Etendeka basalts from Misiones, Argentina: Some new insights into the petrogenesis of high-Ti continental flood basalts. *J. South Am. Earth Sci.* **67**, 25–39.

Rehkämper M., Halliday A. N., Barfod D., Fitton J. G. and Dawson J. B. (1997) Platinum-group element abundance patterns in different mantle environments. *Science* **278**, 1595–1598.

Rehkämper M., Halliday A. N., Fitton J. G., Lee D. C., Wieneke M. and Arndt N. T. (1999) Ir, Ru, Pt, and Pd in basalts and komatiites: New constraints for the geochemical behavior of the platinum-group elements in the mantle. *Geochim. Cosmochim. Acta* **63**, 3915–3934.

Ren Z. Y., Ingle S., Takahashi E., Hirano N. and Hirata T. (2005) The chemical structure of the Hawaiian mantle plume. *Nature* **436**, 837–840.

Renne P. R., Glen J. M., Milner S. C. and Duncan A. R. (1996) Age of Etendeka flood volcanism and associated intrusions in southwestern Africa. *Geology* **24**, 659–662.

Richards M. A., Hager B. H. and Sleep N. H. (1988) Dynamically supported geoid highs over hotspots: Observation and theory. *J. Geophys. Res. Atmos.* **93 (B7)**, 7690–7708.

Richardson S. H., Erlank A. J., Duncan A. R. and Reid D. L. (1982) Correlated Nd, Sr and Pb isotope variation in Walvis Ridge basalts and implications for the evolution of their mantle source. *Earth Planet. Sci. Lett.* **59**, 327–342.

Richter, D.H. and Moore, J. G. (1966) Petrology of the Kilauea Iki lava lake, Hawaii. *U.S. Geol. Surv. Prof. Paper*. **537-B**, B1-B26.

Rielli A., Tomkins A. G., Nebel O., Raveggi M., Jeon H., Martin L. and Ávila J. N. (2018) Sulfur isotope and PGE systematics of metasomatised mantle wedge. *Earth Planet. Sci. Lett.* **497**, 181–192. Available at: https://doi.org/10.1016/j.epsl.2018.06.012.

Righter K. (2003) Metal-Silicate Partitioning of Siderophile Elements and Core Formation in the Early Earth. *Annu. Rev. Earth Planet. Sci.* **31**, 135–174.

Righter K. (2011) Prediction of metal-silicate partition coefficients for siderophile elements: An update and assessment of PT conditions for metal-silicate equilibrium during accretion of the Earth. *Earth Planet. Sci. Lett.* **304**, 158–167.

Righter K., Campbell A. J., Humayun M. and Hervig R. L. (2004) Partitioning of Ru, Rh, Pd, Re, Ir, and Au between Cr-bearing spinel, olivine, pyroxene and silicate melts. *Geochim. Cosmochim. Acta* **68**, 867–880.

Righter K. and Drake M. (1997) Metal-silicate equilibrium in a homogeneously accreting earth: new results for Re. *Earth Planet. Sci. Lett.* **146**, 541–553.

Righter K., Humayun M. and Danielson L. (2008) Partitioning of palladium at high pressures and temperatures during core formation. *Nat. Geosci.* **1**, 321–323.

Ripley B. D. (1996) *Pattern Recognition and Neural Networks*., Cambridge University Press.

Ripley E. M. and Li C. (2013) Sulfide saturation in mafic magmas: Is external sulfur required for magmatic Ni-Cu-(PGE) ore genesis? *Econ. Geol.* **108**, 45–58.

Ripley, E. M., Lightfoot P. C., Li, C. and Elswick, E. R. (2003) Sulfur isotopic studies of continental flood basalts in the Noril'sk region: Implications for the association between lavas and ore-bearing intrusions. *Geochim. Cosmochim. Acta* **67** (15), 2805-2817.

Rivalenti G., Mazzucchelli M., Girardi V. A. V., Vannucci R., Barbieri M. A., Zanetti A. and Goldstein S. L. (2000) Composition and processes of the mantle lithosphere in northeastern Brazil and Fernando de Noronha: Evidence from mantle xenoliths. *Contrib. to Mineral. Petrol.* **138**, 308–325.

Rizo H., Andrault D., Bennett N. R., Humayun M., Brandon A., Vlastelic I., Moine B., Poirier A., Bouhifd M. A. and Murphy D. T. (2019) 182W evidence for core-mantle interaction in the source of mantle plumes. *Geochemical Perspect. Lett.* **11**, 6–11.

Rocha-Júnior E. R. V, Marques L. S., Babinski M., Nardy A. J. R., Figueiredo A. M. G. and Machado F. B. (2013) Sr-Nd-Pb isotopic constraints on the nature of the mantle sources involved in the genesis of the high-Ti tholeiites from northern Paraná Continental Flood Basalts (Brazil). *J. South Am. Earth Sci.* **46**, 9–25. Available at: http://dx.doi.org/10.1016/j.jsames.2013.04.004.

Rocha-Júnior, E. R. V., Puchtel, I. S., Marques, L. S., Walker, R. J., Machado, F. B., Nardy, A. J.R., Babinski, M. and Figueiredo, A. N. (2012) Re-Os Isotope and Highly Siderophile Element Systematics of the Paraná Continental Flood Basalts (Brazil). *Earth and Planetary Science Letters*, **337–338**, 164–73. Available at: https://doi.org/10.1016/j.epsl.2012.04.050

Le Roex A. P., Cliff R. A. and Adair B. J. I. (1990) Tristan da Cunha, South Atlantic: Geochemistry and Petrogenesis of a Basanite-Phonolite Lava Series. *J. Petrol.* **31**, 779–812.

Rohde J., van den Bogaard P., Hoernle K., Hauff F. and Werner R. (2013a) Evidence for an age progression along the Tristan-Gough volcanic track from new40Ar/39Ar ages on phenocryst phases. *Tectonophysics* **604**, 60–71. Available at: http://dx.doi.org/10.1016/j.tecto.2012.08.026.

Rohde J., Hoernle K., Hauff F., Werner R., O'Connor J., Class C., Garbe-Schönberg D. and Jokat W. (2013b) 70 Ma chemical zonation of the Tristan-Gough hotspot track. *Geology* **41**, 335–338.

Rollinson, H. R. (1993) Using Geochemical Data, *Pearson*, pp. 352.

Rossetti L., Lima E. F., Waichel B. L., Hole M. J., Simões M. S. and Scherer C. M. S. (2018) Lithostratigraphy and volcanology of the Serra Geral Group, Paraná-Etendeka Igneous Province in Southern Brazil: Towards a formal

stratigraphical framework. *J. Volcanol. Geotherm. Res.* **355**, 98–114. Available at: https://doi.org/10.1016/j.jvolgeores.2017.05.008.

Le Roux P. J., Le Roex A. P., Schilling J. G., Shimizu N., Perkins W. W. and Pearce N. J. G. (2002) Mantle heterogeneity beneath the southern Mid-Atlantic Ridge: Trace element evidence for contamination of ambient asthenospheric mantle. *Earth Planet. Sci. Lett.* **203**, 479–498.

Rubie D. C. (2004) Partitioning of oxygen during core formation on the Earth and Mars. *Nature* **429**, 58–61.

Rubie D. C., Frost D. J., Mann U., Asahara Y., Nimmo F., Tsuno K., Kegler P., Holzheid A. and Palme H. (2011) Heterogeneous accretion, composition and core-mantle differentiation of the Earth. *Earth Planet. Sci. Lett.* **301**, 31–42.

Rummel L., Baumann T. S. and Kaus B. J. P. (2020) An autonomous petrological database for geodynamic simulations of magmatic systems. *Geophys. J. Int.* **223**, 1820–1836.

Ryabchikov I. D. and Kogarko L. N. (2016) Physicochemical parameters of deep-seated mantle plumes. *Russ. Geol. Geophys.* **57**, 687–697.

Salters V. J. M. and Stracke A. (2004) Composition of the depleted mantle. *Geochemistry, Geophys. Geosystems* **5** (5), 1-127.

Saunders A. D., Fitton J. G., Kerr A. C., Norry M. J. and Kent R. W. (1997) The North Atlantic Igneous Province. In *Large Igneous Provinces: Continental, Oceanic and Planetary Flood Volcanism* (eds. J. J. Mahoney and M. . Coffin). American Geophysical Union Monograph. pp. 45–93. Available at: http://doi.wiley.com/10.1029/GM100p0045.

Schmidt G., Witt-Eickschen G., Palme H., Seck H., Spettel B. and Kratz K. L. (2003) Highly siderophile elements (PGE, Re and Au) in mantle xenoliths from the West Eifel volcanic field (Germany). *Chem. Geol.* **196**, 77–105.

Schnitzler N., Ross P.-S. and Gloaguen E. (2019) Using machine learning to estimate a key missing geochemical variable in mining exploration: Application of the Random Forest algorithm to multi-sensor core logging data. *J. Geochemical Explor.* **205**, 106344.

Shannon M. C. and Agee C. B. (1998) Percolation of Core Melts at Lower Mantle Conditions. *Sci. New Ser.* **280**, 1059–1061.

Shaw D. M. (1970) Trace element fractionation during anatexis. *Geochim. Cosmochim. Acta* **34**, 237–243.

Sharkov E., Bogina M. and Chistyakov A. (2017) Magmatic systems of large continental igneous provinces. *Geosci. Front.* **8**, 621–640.

Shorttle O., Maclennan J. and Piotrowski A. M. (2013) Geochemical provincialism in the Iceland plume. *Geochim. Cosmochim. Acta* **122**, 363–397.

Shima H. and Naldrett A. J. (1975) Solubility of sulfur in an ultramafic melt and the relevance of the system Fe-S-O. *Econ. Geol.* **70**, 960–967.

Shirey S. B. and Walker R. J. (1998) The Re-Os Isotope System in

Cosmochemistry and High-Temperature Geochemistry. *Annu. Rev. Earth Planet. Sci.* **26**, 423–500.

Siebert J., Badro J., Antonangeli D. and Ryerson F. J. (2012) Metal-silicate partitioning of Ni and Co in a deep magma ocean. *Earth Planet. Sci. Lett.* **321**–**322**, 189–197.

Siebert J., Corgne A. and Ryerson F. J. (2011) Systematics of metal-silicate partitioning for many siderophile elements applied to Earth's core formation. *Geochim. Cosmochim. Acta* **75**, 1451–1489.

Simões M. S., Lima E. F., Rossetti L. M. M. and Sommer C. A. (2019) The low-Ti high-temperature dacitic volcanism of the southern Paraná-Etendeka LIP: Geochemistry, implications for trans-Atlantic correlations and comparison with other Phanerozoic LIPs. *Lithos* **342**–**343**, 187–205.

Sleep N. H. (1990) Hotspots and Mantle Plumes: Some Phenomenology. *Geology* **95**, 6715–6736.

Sobolev A. V., Krivolutskaya N. A. and Kuzmin D. V. (2009) Petrology of the parental melts and mantle sources of Siberian trap magmatism. *Petrology* **17**, 253–286.

Song X. Y., Qi H. W., Robinson P. T., Zhou M. F., Cao Z. M. and Chen L. M. (2008) Melting of the subcontinental lithospheric mantle by the Emeishan mantle plume; evidence from the basal alkaline basalts in Dongchuan, Yunnan, Southwestern China. *Lithos* **100**, 93–111.

Spandler C. and O'Neill H. S. C. (2010) Diffusion and partition coefficients of minor and trace elements in San Carlos olivine at 1,300°C with some geochemical implications. *Contrib. to Mineral. Petrol.* **159**, 1–28.

Starkey N. A., Stuart F. M., Ellam R. M., Fitton J. G., Basu S. and Larsen L. M. (2009) Helium isotopes in early Iceland plume picrites: Constraints on the composition of high3He/4He mantle. *Earth Planet. Sci. Lett.* **277**, 91–100.

Steiger R. H. and Jäger E. (1977) Subcommission on geochronology: Convention on the use of decay constants in geo- and cosmochronology. *Earth Planet. Sci. Lett.* **36**, 359–362.

Stein C. A. and Stein S. S. (1992) A model for the global variation in oceanic depth and heat flow with lithospheric age. *Nature* **359**, 123–129.

Steiner B. M., Rollinson G. K. and Condron J. M. (2019) An exploration study of the Kagenfels and Natzwiller granites, Northern Vosges Mountains, France: a combined approach of stream sediment geochemistry and automated mineralogy. *Minerals* **9**, 1–28.

Steiner C., Hobson A., Favre P., Stampfli G. M. and Hernandez J. (1998) Mesozoic sequence of Fuerteventura (Canary Islands): Witness of early Jurassic sea-floor spreading in the central Atlantic. *Bull. Geol. Soc. Am.* **110**, 1304–1317.

Stewart K., Turner S. P., Kelley S., Hawkesworth C., Kirstein L. and Mantovani M. (1996) 3-D, 40Ar-39Ar geochronology in the Paraná continental flood basalt province. *Earth Planet. Sci. Lett.* **143**, 95–109. Available at:

http://medcontent.metapress.com/index/A65RM03P4874243N.pdf.

Storey M., Duncan R. A. and Tegner C. (2007) Timing and duration of volcanism in the North Atlantic Igneous Province: Implications for geodynamics and links to the Iceland hotspot. *Chem. Geol.* **241**, 264–281.

Stracke A., Hofmann A. W. and Hart S. R. (2005) FOZO, HIMU, and the rest of the mantle zoo. *Geochemistry, Geophys. Geosystems* **6**.

Stroncik N. A., Trumbull R. B., Krienitz M. S., Niedermann S., Romer R. L., Harris C. and Day J. M. D. (2017) Helium isotope evidence for a deep-seated mantle plume involved in South Atlantic breakup. *Geology* **45**, 827–830.

Sushchevskaya N. M., Belyatsky B. V., Dubinin E. P. and Levchenko O. V. (2017) Evolution of the Kerguelen plume and its impact upon the continental and oceanic magmatism of East Antarctica. *Geochemistry Int.* **55**.

Tassara S., González-Jiménez J. M., Reich M., Schilling M. E., Morata D., Begg G., Saunders E., Griffin W. L., O'Reilly S. Y., Grégoire M., Barra F. and Corgne A. (2017) Plume-subduction interaction forms large auriferous provinces. *Nat. Commun.* **8**, 1–7.

Tatsumoto M., Knight R. J. and Allegre C. J. (1973) Time differences in the formation of meteorites as determined from the ratio of lead-207 to lead-206. *Science (80-.).* **180**, 1279–1283.

Taylor G. J., Martel L. M. V., Karunatillake S., Gasnault O. and Boynton W. V. (2010) Mapping Mars geochemically. *Geology* **38**, 183–186.

Taylor R. N., Davila-Harris P., Branney M. J., Farley E. M. R., Gernon T. M., Palmer M. R., Potosino I., Científica D. I. and Potosí S. L. (2020) Dynamics of a chemically pulsing mantle plume. *Earth Planet. Sci. Lett.* **537**, 116182.

Tegner C., Duncan R. A., Bernstein S., Brooks C. K., Bird D. K. and Storey M. (1998) 40Ar-39Ar geochronology of Tertiary mafic intrusions along the East Greenland rifted margin: Relation to flood basalts and the iceland hotspot track. *Earth Planet. Sci. Lett.* **156**, 75–88.

Tegner C., Thy P., Holness M. B., Jakobsen J. K. and Lesher C. E. (2009) Differentiation and compaction in the Skaergaard intrusion. *J. Petrol.* **50**, 813–840.

Tejada M. L. G., Mahoney J. J., Duncan R. A. and Hawkins M. P. (1996) Age and Geochemistry of Basement and Alkalic Rocks of Malaita and Santa Isabel , Solomon Islands , Southern Margin of Ontong Java Plateau. *J. Petrol.* **37**, 361–394.

Tejada M. L. G., Mahoney J. J., Neal C. R., Duncan R. A. and Petterson M. G. (2002) Basement Geochemistry and Geochronology of Central Malaita, Solomon Islands, with Implications for the Origin and Evolution of the Ontong Java Plateau. *J. Petrol.* **43**, 449–484.

Teklay M., Wirth K., Mezger K. and Thole J. (2020) Picrites of the Jungfrau and Sargdeckel, central Namibia: Relative roles of mantle and crust in the Southern Etendeka large igneous province. *Lithos* **354**–**355**, 105283.

Available at: https://doi.org/10.1016/j.lithos.2019.105283.

Thériault R. D., Barnes S. J. and Severson M. J. (1997) The Influence Of Country-Rock Assimilation and Silicate to Sulfide Ratios (R Factor) On the Genesis Of the Dunka Road Cu-Ni-Platinum-Group Element Deposit, Duluth Complex, Minnesota. *Can. J. Earth Sci.* **34**, 375–389.

Thiede D. S. and Vasconcelos P. M. (2010) Paraná flood basalts: Rapid extrusion hypothesis confirmed by new 40Ar/39Ar results. *Geology* **38**, 747–750.

Thirlwall M. F., Singer B. S. and Marriner G. F. (2000) 39 Ar 40 Ar ages and geochemistry of the basaltic shieldstage of Tenerife, Canary Islands, Spain. *J. Volcanol. Geotherm. Res.* **103**, 247–297.

Thompson R. N. and Gibson S. A. (1991) Subcontinental mantle plumes, hotspots and pre-existing thinspots. *J. Geol. Soc. London.* **148**, 973–977. Available at: http://jgs.lyellcollection.org/cgi/doi/10.1144/gsjgs.148.6.0973.

Thormann L., Buchspies B., Mbohwa C. and Kaltschmitt M. (2017) PGE production in southern Africa, part 1: Production and market trends. *Minerals* **7** (224), 1-22.

Thomson, A., Kohn, S., Prabhu, A. and Walter, M. J. (2021) Evaluating the Formation Pressure of Diamond-Hosted Majoritic Garnets; a Machine Learning Majorite Barometer. *Journal of Geophysical Research: Solid Earth*. **126**. e2020JB020604. Available at: https://doi.org/10.1029/2020JB020604

Torsvik T. H., Burke K., Steinberger B., Webb S. J. and Ashwal L. D. (2010) Diamonds sampled by plumes from the core-mantle boundary. *Nature* **466**, 352–355.

Torsvik T. H., Smethurst M. A., Burke K. and Steinberger B. (2006) Large igneous provinces generated from the margins of the large low-velocity provinces in the deep mantle. *Geophys. J. Int.* **167**, 1447–1460.

Tredoux M., Lindsay N. M., Davies G. and McDonald I. (1995) The fractionation of platinum-group elements in magmatic systems, with the suggestion of a novel casual mechanism. *South African J. Geol.* **98**, 157–167.

Trela J., Vidito C., Gazel E., Herzberg C., Class C., Whalen W., Jicha B., Bizimis M. and Alvarado G. E. (2015) Recycled crust in the Galápagos plume source at 70 ma: Implications for plume evolution. *Earth Planet. Sci. Lett.* **425**, 268–277. Available at: http://dx.doi.org/10.1016/j.epsl.2015.05.036.

Turner S. P., Hawkesworth C., Gallagher K., Stewart K., Peate D. and Mantovani M. (1996) Mantle plumes, flood basalts, and thermal models for melt generation beneath continents: Assessment of a conductive heating model and application to the Paraná. *J. Geophys. Res. Solid Earth* **101**, 11503–11518. Available at: http://doi.wiley.com/10.1029/96JB00430.

Turner S. P., Peate D. W., Hawkesworth C. J. and Mantovani M. S. M. (1999) Chemical stratigraphy of the Parana basalt succession in western Uruguay: Further evidence for the diachronous nature of the Parana magma types. *J. Geodyn.* **28**, 459–469.

Ussami N., Chaves C. A. M., Marques L. S. and Ernesto M. (2013) Origin of the rio grande Rise-Walvis ridge reviewed integrating palaeogeographic reconstruction, isotope geochemistry and flexural modelling. *Geol. Soc. Spec. Publ.* **369**, 129–146.

Der Verfasser A., Behrmann J. H., Shulgin A. and Prokoph A. (2011) High Resolution Bathymetric Survey on the NW Slope of Walvis Ridge, Offshore Namibia. *Berichte der Naturforschenden Gesellschaft zu Freibg. i. Br.* **101**, 97–110.

Vincent E. A. and Smales A. A. (1956) The determination of palladium and gold in igneous rocks by radioactivation analysis. *Geochim. Cosmochim. Acta* **9**, 154–160.

Vinnik L., Breger L. and Romanowicz B. (1998) Anisotropic structures at the base of the Earth's mantle. *Nature* **393**, 564–567.

Wade C. E., Payne J. L., Barovich K. M. and Reid A. J. (2019) Heterogeneity of the sub-continental lithospheric mantle and 'non-juvenile' mantle additions to a Proterozoic silicic large igneous province. *Lithos* **340**–**341**, 87–107. Available at: https://doi.org/10.1016/j.lithos.2019.05.005.

Wager L. R. and Brown G. M. (1968) *Layered Igneous Rocks*., Oliver and Boyd, Edinburgh.

Wagstaff K., Cardie C., Rogers S. and Schrödl S. (2001) Constrained K-means Clustering with Background Knowledge. *Int. Conf. Mach. Learn. ICML*, 577–584.

Wahid A. (2017) Big data and machine learning for Businesses. *Data Anal.* Available at: https://www.slideshare.net/awahid/big-data-and-machine-learning-for-businesses.

Walker R. J. (2009) Highly siderophile elements in the Earth, Moon and Mars: Update and implications for planetary accretion and differentiation. *Chemie der Erde - Geochemistry* **69**, 101–125.

Walker R. J., Bermingham K., Liu J., Puchtel I. S., Touboul M. and Worsham E. A. (2015) In search of late-stage planetary building blocks. *Chem. Geol.* **411**, 125–142.

Walker R. J., Morgan J. W., Naldrett A. J., Li C. and Fassett J. D. (1991) ReOs isotope systematics of NiCu sulfide ores, Sudbury Igneous Complex, Ontario: evidence for a major crustal component. *Earth Planet. Sci. Lett.* **105**, 416–429.

Walter M. J. (1998) Melting of Garnet Peridotite and the Origin of Komatiite and Depleted Lithosphere. *J. Petrol.* **39**, 29–60.

Walter M. J. and Cottrell E. (2013) Assessing uncertainty in geochemical models for core formation in Earth. *Earth Planet. Sci. Lett.* **365**, 165–176.

Walter M. J., Katsura T., Kubo A., Shinmei T., Nishikawa O., Ito E., Lesher C. M. and Funakoshi K. (2002) Spinel–garnet lherzolite transition in the system CaO-MgO-Al2O3-SiO2 revisited: an in situ X-ray study. *Geochim. Cosmochim. Acta* **66**, 2109–2121.

Wang Z., Cheng H., Zong K., Geng X., Liu Y., Yang J., Wu F., Becker H., Foley S. and Wang C. Y. (2020a) Metasomatized lithospheric mantle for Mesozoic giant gold deposits in the North China craton. *Geology* **48**, 169–173.

Wang J., Zuo R. and Caers J. (2017) Discovering geochemical patterns by factor-based cluster analysis. *J. Geochemical Explor.* **181**, 106–115.

Wang, J., Zhou, Y. and Xiao, F. (2020b) Identification of multi-element geochemical anomalies using unsupervised machine learning algorithms: A case study from Ag-Pb-Zn deposits in north-western Zhejiang, China. *Applied Geochemistry* **120**, 104679.

Watson E. B. (1985) Henry's law behavior in simple systems and in magmas: Criteria for discerning concentration-dependent partition coefficients in nature. *Geochim. Cosmochim. Acta* **49**, 917–923.

Weaver B. L. (1991) The origin of ocean island basalt end-member compositions: trace element and isotopic constraints. *Earth Planet. Sci. Lett.* **104**, 381–397.

Webb S. (2018) Deep learning for biology. *Nature* **554**, 555–557.

Webber A. P., Roberts S., Taylor R. N. and Pitcairn I. K. (2013) Golden plumes: Substantial gold enrichment of oceanic crust during ridge-plume interaction. *Geology* **41**, 87–90.

Weis D., Garcia M. O., Rhodes J. M., Jellinek M. and Scoates J. S. (2011) Role of the deep mantle in generating the compositional asymmetry of the Hawaiian mantle plume. *Nat. Geosci.* **4**, 831–838.

Weit A., Trumbull R. B., Keiding J. K., Geissler W. H., Gibson S. A. and Veksler I. V. (2017) The magmatic system beneath the Tristan da Cunha Island: Insights from thermobarometry, melting models and geophysics. *Tectonophysics* **716**, 64–76. Available at: http://dx.doi.org/10.1016/j.tecto.2016.08.010.

White R. S. and McKenzie D. (1995) Mantle plumes and flood basalts. *J. Geophys. Res. Solid Earth* **100**, 17543–17585. Available at: http://doi.wiley.com/10.1029/95JB01585.

White W. M. and Hofmann A. W. (1982) Sr and Nd isotope geochemistry of oceanic basalts and mantle evolution. *Nature* **296**, 821–825.

Whitehouse E. J. (2020) A machine learning approach to understanding multi-element behaviour in the mantle. *University of Exeter*, MSc Thesis.

Whittemore T. J., Xue C., Huang J., Gallucci J. C. and Turro C. (2020) Single-chromophore single-molecule photocatalyst for the production of dihydrogen using low-energy light. *Nat. Chem.* **12**, 180–185.

De Wijs G. A., Kresse G., Vočadlo L., Dobson D., Alfè D., Gillan M. J. and Price G. D. (1998) The viscosity of liquid iron at the physical conditions of the Earth's core. *Nature* **392**, 805–807.

Wildman M., Brown R., Persano C., Beucher R., Stuart F. M., Mackintosh V., Gallagher K., Schwanethal J. and Carter A. (2017) Contrasting Mesozoic

evolution across the boundary between on and off craton regions of the South African plateau inferred from apatite fission track and (U-Th-Sm)/He thermochronology. *J. Geophys. Res. Solid Earth* **122**, 1517–1547.

Willbold M., Elliott T. and Moorbath S. (2011) The tungsten isotopic composition of the Earth's mantle before the terminal bombardment. *Nature* **477**, 195–198.

Willbold M. and Stracke A. (2006) Trace element composition of mantle end-members: Implications for recycling of oceanic and upper and lower continental crust. *Geochemistry, Geophys. Geosystems* **7**, 1–30.

Wilson M. (1992) Magmatism and continental rifting during the opening of the South Atlantic Ocean: a consequence of Lower Cretaceous super-plume activity? *Geol. Soc. London, Spec. Publ.* **68**, 241–255. Available at: http://sp.lyellcollection.org/lookup/doi/10.1144/GSL.SP.1992.068.01.15.

Wilson M. R., Kyser T. K. and Fagan R. (1996) Sulfur isotope systematics and platinum group element behavior in REE-enriched metasomatic fluids: A study of mantle xenoliths from Dish Hill, California, USA. *Geochim. Cosmochim. Acta* **60**, 1933–1942.

de Wit M. J., Stankiewicz J. and Reeves C. (2008) Restoring Pan-African-Brasiliano connections: more Gondwana control, less Trans-Atlantic corruption. *Geol. Soc. London, Spec. Publ.* **294**, 399–412. Available at: http://sp.lyellcollection.org/lookup/doi/10.1144/SP294.20.

de Wit M. J. and Thiart, C. (2005) Metallogenic fingerprints of Archaean cratons. *Geol. Soc. Spec. Pub.* **248**, 59-70.

Witten I. H., Frank E. and Hall M. a (2016) *Data Mining: Practical Machine Learning Tools and Techniques*. 4th ed., Elsevier. Available at: http://books.google.com/books?id=bDtLM8CODsQC&pgis=1.

Wittig N., Pearson D. G., Baker J. A., Duggen S. and Hoernle K. (2010a) A major element, PGE and Re-Os isotope study of Middle Atlas (Morocco) peridotite xenoliths: Evidence for coupled introduction of metasomatic sulphides and clinopyroxene. *Lithos* **115**, 15–26.

Wittig N., Webb M., Pearson D. G., Dale C. W., Ottley C. J., Hutchison M., Jensen S. M. and Luguet A. (2010b) Formation of the North Atlantic Craton: Timing and mechanisms constrained from Re-Os isotope and PGE data of peridotite xenoliths from S.W. Greenland. *Chem. Geol.* **276**, 166–187. Available at: http://dx.doi.org/10.1016/j.chemgeo.2010.06.002.

Wood B. J., Walter M. J. and Wade J. (2006) Accretion of the Earth and segregation of its core. *Nature* **441**, 825–833.

Wooden J. L., Czamanske G. K., Fedorenko V. A., Arndt N. T., Chauvel C., Bouse R. M., King B. S. W., Knight R. J. and Siems D. F. (1993) Isotopic and trace-element constraints on mantle and crustal contributions to Siberian continental flood basalts, Noril'sk area, Siberia. *Geochim. Cosmochim. Acta* **57**, 3677–3704.

Woodland A. B., Uenver-Thiele L. and Seitz H. M. (2018) Influence of metasomatism on vanadium-based redox proxies for mantle peridotite. *Geochemical Perspect. Lett.* **8**, 11–16.

Woodland S. J., Pearson D. G. and Thirlwall M. F. (2002) A Platinum Group Element and Re–Os Isotope Investigation of Siderophile Element Recycling in Subduction Zones: Comparison of Grenada, Lesser Antilles Arc, and the Izu–Bonin Arc. *J. Petrol.* **43**, 171–198. Available at: http://academic.oup.com/petrology/article/43/1/171/1399902.

WPIC (2020) Platinum Perspectives. Platinum's role in hydrogen and decarbonisation is a big driver in platinum investment demand. *World Platin. Invest. Counc.* Available at: https://platinuminvestment.com/files/743383/WPIC_Platinum_Perspectives_October_2020.pdf [Accessed February 27, 2021].

Wyborn L. A. I., Heinrich C. A. and Jaques A. L. (1994) Australian Proterozoic Mineral Systems: Essential Ingredients and Mappable Criteria. *Aust. Inst. od Min. Metall. Annu. Conf.*, 109–115.

Wysession M. E., Wilson J., Bartko L. and Sakata R. (1995) Intraplate seismicity in the Atlantic Ocean Basin; a teleseismic catalog. *Bull. Seismol. Soc. Am.* **85**, 755–774.

Xia L. and Li X. (2019) Basalt geochemistry as a diagnostic indicator of tectonic setting. *Gondwana Res.* **65**, 43–67.

Xiao L., Xu Y. G., Mei H. J., Zheng Y. F., He B. and Pirajno F. (2004) Distinct mantle sources of low-Ti and high-Ti basalts from the western Emeishan large igneous province, SW China: Implications for plume-lithosphere interaction. *Earth Planet. Sci. Lett.* **228**, 525–546.

Yeomans C. M., Shail R. K., Grebby S., Nykänen V., Middleton M. and Lusty P. A. J. (2020) A machine learning approach to tungsten prospectivity modelling using knowledge-driven feature extraction and model confidence. *Geosci. Front.* **11**, 2067–2081.

Zhang M., O'Reilly S. Y., Wang K. L., Hronsky J. and Griffin W. L. (2008) Flood basalts and metallogeny: The lithospheric mantle connection. *Earth Sci. Rev.* **86**, 145–174.

Zhou H., Hoernle K., Geldmacher J., Hauff F., Homrighausen S., Garbe-schönberg D. and Jung S. (2020) Geochemistry of Etendeka magmatism : Spatial heterogeneity in the Tristan-Gough plume head. *Earth Planet. Sci. Lett.* **535**, 116123. Available at: https://doi.org/10.1016/j.epsl.2020.116123.

Ziberna L., Klemme S. and Nimis P. (2013) Garnet and spinel in fertile and depleted mantle: Insights from thermodynamic modelling. *Contrib. to Mineral. Petrol.* **166**, 411–421.

Zientek M. L., Loferski P. J., Parks H. L., Schulte R. F. and Seal R. R. (2017) Platinum-Group Elements. In *Mineral Resources of the United States - Economic and Environmental Geology and Prospects for Future Supply* USGS.

Zindler A. and Hart S. R. (1986) Chemical Geodynamics. *Ann. Rev. Earth Planet. Sci* **14**, 493–571.

Zitnik M., Nguyen F., Wang B., Leskovec J., Goldenberg A. and Hoffman M. M. (2019) Machine learning for integrating data in biology and medicine: Principles, practice, and opportunities. *Inf. Fusion* **50**, 71–91.

Zuo R. (2011) Identifying geochemical anomalies associated with Cu and Pb-Zn skarn mineralization using principal component analysis and spectrum-area fractal modeling in the Gangdese Belt, Tibet (China). *J. Geochemical Explor.* **111**, 13–22.

Zuo R. (2017) Machine Learning of Mineralization-Related Geochemical Anomalies: A Review of Potential Methods. *Nat. Resour. Res.* **26**, 457–464.